Edited by
John Clarke and Alex I. Braginski

WILEY-VCH

The SQUID Handbook

Vol. I Fundamentals and Technology of SQUIDs and SQUID Systems

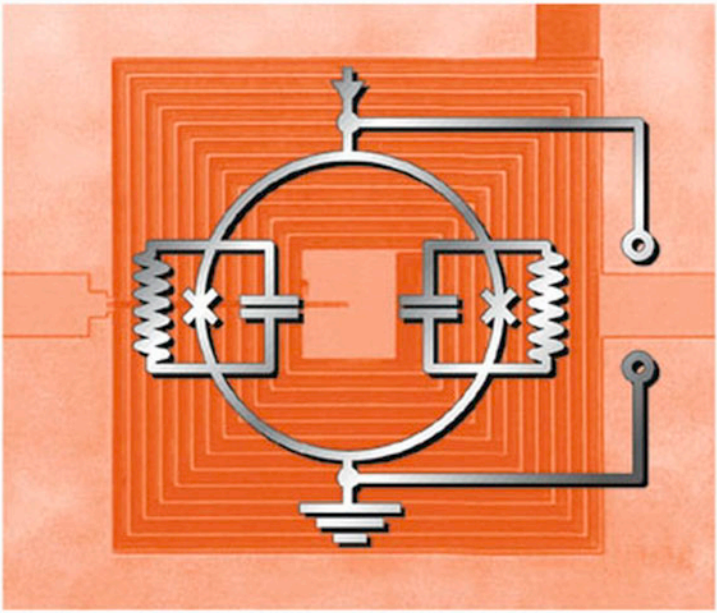

J. Clarke, A. I. Braginski (Eds.)

The SQUID Handbook

Vol. I Fundamentals and Technology of SQUIDs and SQUID Systems

WILEY-VCH Verlag GmbH & Co. KGaA

J. Clarke, A. I. Braginski (Eds.)

The SQUID Handbook

Vol. I

J. Clarke, A. I. Braginski (Eds.)

The SQUID Handbook

Vol. I Fundamentals and Technology of SQUIDs and SQUID Systems

WILEY-VCH Verlag GmbH & Co. KGaA

Editors

Prof. Dr. John Clarke
University of California
Department of Physics
366 LeConte Hal
Berkeley, CA 94720-7300
USA

Prof. Dr. Alex I. Braginski
Research Center Jülich
ISG-2
D-52425 Jülich
Germany

Library of Congress Card No. applied for

British Library Cataloguing-in-Publication Data
A catalogue record for this book is available from the British Library.

Bibliographic information published by

Die Deutsche Bibliothek
Die Deutsche Bibliothek lists this publication in the Deutsche Nationalbibliografie; detailed bibliographic data is available in the Internet at <http://dnb.ddb.de>.

Printed in the Federal Republic of Germany.

Printed on acid-free paper.

Typesetting Kühn & Weyh, Satz und Medien, Freiburg
Printing betz-druck GmbH, Darmstadt
Bookbinding Großbuchbinderei J. Schäffer GmbH & Co. KG, Grünstadt

ISBN 3-527-40229-2

Contents

Preface

We hope that this Handbook will provide an in-depth, systematic treatment of Superconducting QUantum Interference Devices (SQUIDs) and their many applications. Extended reviews of this subject have appeared previously in journals, books and textbooks devoted to broader aspects of superconductivity, and several proceedings of NATO Advanced Study Institutes (ASI) covering various aspects of superconducting electronics. In particular, the NATO proceedings,[1] "SQUID Sensors: Fundamentals, Fabrication and Applications", the most comprehensive review previously available, has become the "bible" for those in the field. However, NATO proceedings are written by individual summer school lecturers, so that some aspects of the subject may be omitted while there may be unavoidable overlaps in others. Furthermore, most of the material in this book was written almost a decade ago.

Our intent is to offer the reader a reasonably complete, balanced and up-to-date presentation of the entire field, with as few omissions and duplications as possible. Initially, our publisher suggested that one or two of us write the book, but we pointed out that this was an impossible workload for anyone actively working in the field. Furthermore, many aspects of SQUIDs, especially applications, have become so specialized that no one person is likely to be able to provide adequate coverage. For these reasons, we invited many colleagues collectively to write a comprehensive treatise. Virtually all of those who were asked graciously agreed. This team comprises many of the leading specialists who have been involved in all aspects of SQUIDs and their applications; many of them are former NATO lecturers who contributed to the "bible".

The Handbook is organized into two volumes, the first being devoted to the fundamentals and technology of SQUIDs and SQUID systems. The second volume is concerned with applications using SQUIDs as sensors and readout devices, with an inevitable emphasis on magnetometers. SQUIDs as building blocks for digital circuits are beyond our scope.

In Chapter 1 of the first volume we offer a broad, phenomenological introduction to SQUIDs and their operation as sensors and readout devices. We include some historical highlights and an overview of existing and future applications. Our intro-

1) SQUID Sensors: Fundamentals, Fabrication and Applications, Ed. Harold Weinstock, Kluwer Academic Publishers (1996).

duction is aimed mainly at readers who are unfamiliar with SQUIDs, and who hopefully will benefit from reading this chapter before delving into the more advanced material in subsequent chapters.

In Chapter 2, Chesca, Kleiner and Koelle present the theoretical foundations of direct-current (dc) and radio-frequency (rf) SQUIDs, starting with a discussion of the Josephson junction. The authors include analytical theories for low and high levels of thermal fluctuations for both kinds of SQUIDs. They address numerical simulations only for the dc SQUID, since no such work yet exists for the rf SQUID.

Subsequently, in Chapter 3, Cantor and Ludwig discuss the fabrication of Josephson junctions and SQUIDs using low-temperature-superconducting (LTS) and HTS thin films, dielectric insulators and normal metals.

In Chapter 4, Drung and Mück give the essentials of analog and digital room-temperature readout electronics for dc and rf SQUIDs with broad bandwidth, high dynamic range and low noise. They present several approaches to the flux-locked loop, as well as issues such as the suppression of low-frequency noise in a dc SQUID and the coupling of an rf SQUID to its readout preamplifier.

In Chapter 5, Cantor and Koelle describe practical LTS and HTS dc SQUIDs, beginning with a brief historical overview. They include the analytical and numerical design of SQUID parameters, and the performance of typical devices. Many of the expressions introduced are also applicable to rf SQUIDs. They discuss magnetometers and gradiometers, including thin-film and wire-wound pickup coils.

In Chapter 6, Braginski and Zhang describe practical thin-film rf SQUIDs with an emphasis on HTS devices, since LTS rf SQUIDs are rarely used today. Their historical overview includes bulk rf SQUIDs, which dominated the first decade of SQUID research and application. In contrast to Chapter 5, they do not address analytical and numerical design issues, since HTS rf SQUIDs were developed empirically, with little recourse to simulations.

In Chapter 7, Foley, Keene, ter Brake and Vrba address SQUID system issues, beginning with such requirements as cryogenics and cabling. They briefly discuss data acquisition and processing as well as methods of testing and calibration. They consider situations in which one needs to measure very low-level signals in an open environment where the ambient noise levels are high. This case requires sophisticated techniques for noise suppression, for example, synthetic gradiometry. They discuss design and noise considerations for both static and mobile SQUID systems.

Finally, in Appendix A.1, Kleiner and Koelle give a brief overview of the relevant properties of superconductors.

The second volume begins with a description of SQUID amplifiers, followed by a chapter on the applications of SQUIDs to standards. The next chapter outlines the inverse problem, which is of central importance in imaging applications. Subsequent chapters deal with practical applications in biomagnetism, nondestructive evaluation of materials and structures, geophysical exploration and gravity and motion sensors.

The handbook would be suitable as a textbook for graduate students in physics and engineering, and hopefully will serve as a general reference for professionals working on SQUIDs and their applications. We hope that researchers who are not

SQUID specialists – for example, physicians working in neuromagnetism and magnetocardiography – will also study relevant chapters.

In concluding, we express our heartfelt thanks to all the contributors to this volume, not least for their patience and persistence during the editing process. We owe an enormous debt of gratitude to Dr. Michael Bär, Mrs. Vera Palmer and Mrs. Ulrike Werner of Wiley-VCH, without whose expert guidance and extraordinary patience this book would never have surfaced.

Alex Braginski and John Clarke

List of Contributors

Alex I. Braginski
(Chapters 1 and 6)
Forschungszentrum Jülich, ISG-2,
D-52425 Jülich, Germany, (retired)
and
Fachbereich C, Fachgruppe Physik,
Bergische Universität Wuppertal,
D-42097 Wuppertal, Germany
A.Braginski@fz-juelich.de

Robin Cantor
(Chapters 3 and 5)
STAR Cryoelectronics,
25-A Bisbee Court,
NM 87508 Santa Fe, USA
rcantor@starcryo.com

Boris Chesca
(Chapter 2)
Physikalisches Institut,
Universität Tübingen,
Auf der Morgenstelle 14,
D-72076 Tübingen, Germany
boris.chesca@uni-tuebingen.de

John Clarke
(Chapter 1)
Department of Physics, University of
California, 366 LeConte Hall,
Berkeley CA 94720-7300, USA,
and
Materials Science Division,
Lawrence Berkeley National
Laboratory, One Cyclotron Road,
Berkeley CA 94720, USA
jclarke@physics.berkeley.edu

Dietmar Drung
(Chapter 4, Appendix 2)
Physikalisch-Technische
Bundesanstalt, Abbestrasse 2–12,
D-10587 Berlin, Germany
Dietmar.Drung@ptb.de

C. P. Foley
(Chapter 7)
CSIRO Telecommunications
and Industrial Physics, P.O. Box 218,
Lindfield, NSW 2070 Australia
Cathy.Foley@tip.csiro.au

M. N. Keene
(Chapter 7)
QinetiQ Ltd., St. Andrews Road,
Malvern, Worcestershire WR14 3PS,
United Kingdom
mnkeene@QinetiQ.com

Reinhold Kleiner
(Chapter 2, Appendix 1)
Physikalisches Institut,
Experimentalphysik II,
Universität Tübingen,
Auf der Morgenstelle 14,
D-72076 Tübingen, Germany
kleiner@uni-tuebingen.de

Dieter Koelle
(Chapter 2, Appendices 1 and 2)
Physikalisches Institut,
Experimentalphysik II,
Universität Tübingen,
Auf der Morgenstelle 14,
D-72076 Tübingen, Germany
koelle@uni-tuebingen.de

Frank Ludwig
(Chapter 3)
Institut für elektrische Meßtechnik
und Grundlagen der Elektrotechnik,
Technische Universität Braunschweig,
D-38092 Braunschweig, Germany
f.ludwig@tu-bs.de

Michael Mück
(Chapter 4)
Institut für Angewandte Physik,
Justus-Liebig-Universität Gießen,
Heinrich-Buff-Ring 16,
D-35392 Gießen, Germany
Michael.Mueck@ap.physik.uni-giessen.de

H. J. M. ter Brake
(Chapter 7)
Twente University of Technology,
Department of Applied Physics,
P.O. Box 217, 7500AE Enschede,
The Netherlands
H.J.M.terBrake@tn.utwente.nl

Jiri Vrba
(Chapter 7) CTF Systems Inc.,
VSM MedTech Ltd, 7 Burbridge Street
Coquitlam, B.C., Canada
jvrba@vsmmedtech.com

Yi Zhang
(Chapter 6)
Forschungszentrum Jülich, ISG-2,
D-52425 Jülich, Germany
y.zhang@fz-juelich.de

1
Introduction

Alex Braginski and John Clarke

1.1 The Beginning

The Superconducting QUantum Interference Device (SQUID) combines the physical phenomena of flux quantization and Josephson tunneling. First predicted by F. London [1], flux quantization was observed experimentally by Deaver and Fairbank [2] and Doll and Näbauer [3] in 1961. They showed that the flux contained in a closed superconducting loop is quantized in units of the flux quantum $\Phi_0 = h/2e \approx 2.07 \times 10^{-15}$ Wb. Here, $h \equiv 2\pi\hbar$ is Planck's constant, and e is the electronic charge. Flux quantization arises from the fact that the macroscopic wave function

$$\Psi(\vec{r},t) = \left| \Psi(\vec{r},t) \right| \exp\left[i\varphi\,(\vec{r},t)\right] \tag{1.1}$$

must be single-valued in going once around a superconducting loop; this result is derived in Appendix A.1, Eq. (A.1.3). In the absence of applied fields or currents, the phase $\varphi\ (\vec{r},t)$ takes the same value throughout the superconductor for all Cooper pairs, which have charge $2e$ [4]. In the case of a loop threaded by a magnetic flux, however, the phase around the loop changes by 2πn, where n is the number of enclosed flux quanta.

In the year preceding the observation of flux quantization, Giaever [5] demonstrated the tunneling of single electrons between a superconductor (S) and a normal metal (N) separated by a thin insulating (I) layer. When he cooled SIN junctions below the critical temperature T_c of the superconductor, he found that the tunneling resistance increased for voltages below Δ/e, where $\Delta(T)$ is the energy gap at temperature T. As the current was increased, the resistance decreased sharply at a voltage Δ/e, and tended asymptotically to the value observed when the superconductor was at a temperature just above T_c. Subsequently, Giaever investigated the tunneling of single electrons through SIS junctions, and observed a steep increase in the current at a voltage corresponding to the sum of the two energy gaps [6].

Against this backdrop of single electron tunneling and flux quantization, in 1962 Josephson predicted the tunneling of Cooper pairs through a barrier separating two superconductors – the phenomenon now known as Josephson tunneling [7]. Josephson showed that the current I flowing through a junction is given by

$$I = I_0 \sin\delta\ , \tag{1.2}$$

where $\delta = \varphi_1 - \varphi_2$ is the difference between the phases φ_1 and φ_2 of the condensates in the two superconducting electrodes and I_0 is the critical current. Furthermore, in the presence of a voltage U between the electrodes, δ evolves with time t according to

$$d\delta/dt = 2eU/\hbar = 2\pi U/\Phi_0 \,. \tag{1.3}$$

Equations (1.2) and (1.3), discussed in Sec. 2 and Appendix A.1, describe the static ("dc") and dynamic ("ac") properties of a Josephson junction. In the absence of fluctuations, as the current through a junction is increased from zero, the flow of Cooper pairs constitutes a supercurrent and the voltage across the junction remains zero until the current exceeds the critical current. At higher currents, the phase difference evolves according to Eq. (1.3), and there is a voltage across the junction. Subsequently, it became clear that this behavior is generally valid for all *weakly-coupled* superconductors, for example, when the two superconductors are connected by a normal metal or a narrow constriction; however, there may be departures from the sinusoidal current-phase relation. The term "Josephson current" is commonly used for the pair current through any "Josephson junction."

Just one year later, Anderson and Rowell [8] made the first observation of the dc Josephson effect, using a thin-film, Sn-SnO_x-Pb junction cooled to 1.5 K in liquid helium. The current-voltage (I–V) characteristic is reproduced in Figure 1.1. Subsequently, Rowell [9] showed that a magnetic field B, applied in the plane of the thin films, caused the critical current to be modulated according to

$$I_0(\Phi) = I_0(0) \; \left| \; \sin(\pi\Phi/\Phi_0) \; / \; (\pi\Phi/\Phi_0) \; \right| \,. \tag{1.4}$$

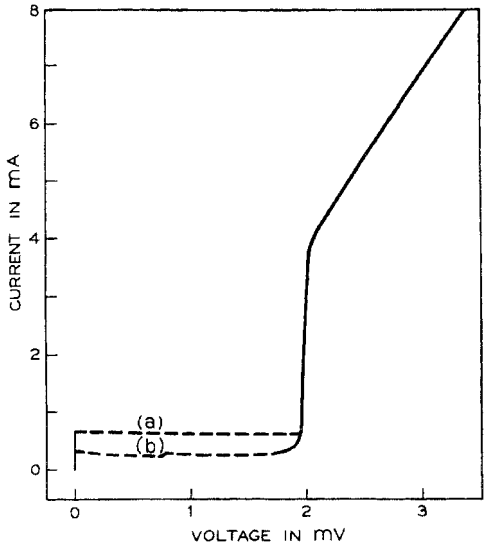

Fig. 1.1 Current-voltage characteristic for a tin-tin oxide-lead tunnel junction at ~1.5 K. Branch (a) – current increasing, branch (b) – current decreasing (reproduced with permission from ref. [8].)

Thus, the critical current becomes zero for $\Phi = \Phi_0 = \pm 1, 2, 3, \ldots n$. Here, $\Phi = Bw(d + \lambda_1 + \lambda_2)$ is the flux threading an area defined by the width w of the barrier and the magnetic thickness of the junction given by the sum of the barrier thickness d and the penetration depths λ_1 and λ_2 of the two superconductors (see Appendix A.1). Equation (1.4) is valid only provided that the self-field produced by the current through the junction is negligible compared with the applied magnetic field. The observation of this Fraunhofer-like result – which is analogous to the diffraction of monochromatic, coherent light passing through a slit – is a dramatic validation of the sinusoidal current phase relation. In the same year, Shapiro [10] showed that microwaves at frequency f induced current steps on the I–V characteristic of a Josephson junction at voltages $\pm nhf/2e$, thereby confirming the ac relation (1.3).

A few months later, Jaklevic *et al.* [11] demonstrated quantum interference between two thin-film Josephson junctions connected in parallel on a superconducting loop. The dependence of the critical current on the applied magnetic field is shown in Figure 1.2. The slowly varying modulation arises from the diffraction-like effects

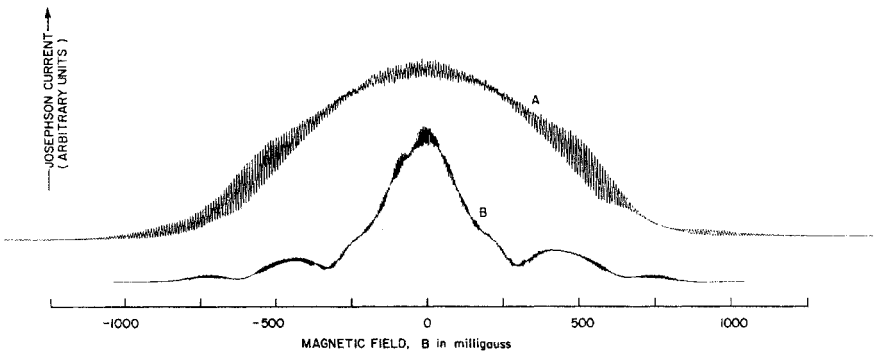

Fig. 1.2 Josephson current vs. magnetic field for two junctions in parallel showing interference effects. Magnetic field applied normal to the area between junctions. Curve (A) shows interference maxima spaced at $\Delta B = 8.7 \times 10^{-3}$ G for one pair of junctions, curve (B) with spacing $\Delta B = 4.8 \times 10^{-3}$ G is for another pair. Maximum Josephson current indicated here is approximately 10^{-3} A. (Reproduced with permission from ref. [11].)

of the two junctions. The rapid oscillations are due to quantum interference between the two junctions, and their period is given by the field required to generate one flux quantum in the loop: thus, critical current maxima occur at $\Phi/\Phi_0 = 0, \pm 1, \pm 2, \ldots \pm n$. The observation of these oscillations – which are analogous to two-slit interference in optics – set the stage for the dc SQUID.

Some three years later, Silver and Zimmerman introduced the rf SQUID – a single Josephson junction interrupting a superconducting loop [12]. In its subsequent implementation, no leads are attached to the device, but rather the loop is inductively coupled to the inductor of a parallel resonant tank circuit in which a capacitor is connected across the inductor. When the tank circuit is excited at or near its resonant frequency by a radio-frequency current, the amplitude of the oscillating voltage

across it is periodic in the magnetic flux threading the SQUID with a period Φ_0. If one rectifies this oscillating voltage to produce a quasistatic voltage, the rf SQUID behaves operationally as a dc SQUID. In fact, the rf SQUID is misnamed as no interference takes place!

In both kinds of SQUID it is possible to detect a change in applied magnetic flux corresponding to a tiny fraction of one flux quantum – typically $10^{-6}\ \Phi_0\ \mathrm{Hz}^{-1/2}$ in today's devices. SQUIDs – which are intrinsically flux-to-voltage transducers – are the most sensitive detectors of magnetic flux known. Their operational bandwidth is enormous, extending from quasistatic measurements to well over 1 GHz. They are amazingly versatile, being able to measure any physical quantity that can be converted to magnetic flux, for example, magnetic field, magnetic field gradient, magnetic susceptibility, current, voltage, and mechanical displacement. As a consequence, the applications of SQUIDs are extraordinarily wide-ranging, and are very briefly summarized in Sec. 1.7. Detailed reviews of the many applications of SQUIDs appear in Volume II.

1.2 Subsequent Developments

We now give a brief overview of the evolution of SQUIDs after their initial invention; more detailed histories are to be found in Chapters 5 and 6.

In the early days of the dc SQUID it was recognized that the thin-film devices used for the initial discoveries were not sufficiently robust for use in measurement instruments, and alternative means of making a suitable junction were sought. It was quickly found that one could make a junction by pressing together two pieces of oxidized Nb wire at right angles to each other, or by pushing a sharpened – and presumably oxidized – Nb point against a piece of Nb [13]. The famous "point contact" provided a simple means of making a junction that could easily be emulated in any low-temperature laboratory, and is used even today in undergraduate classes. Another simple device was the SLUG – Superconducting Low-inductance Undulatory Galvanometer [14]. This device consisted of a bead of PbSn solder frozen around a length of oxidized Nb wire. The I–V characteristic measured between the solder and the wire exhibited Josephson-like behavior, with a critical current that was periodic in an additional current passed along the Nb wire. With a small resistor connected in series with the wire, the SLUG was a voltmeter with a voltage noise of $10\ \mathrm{fV\ Hz}^{-1/2}$, an improvement of five orders of magnitude over the noise of semiconductor voltmeters. This device also enabled a demonstration of the flux transformer – a means of enhancing the magnetic field sensitivity of a magnetometer – and of the use of a second SQUID to read out a first-stage SQUID [15].

The invention of the rf SQUID had a major impact, largely because it required only a single junction which, at the time, was easier to manufacture than a pair of junctions. The first commercially available devices involved either a single point contact in a loop made of bulk Nb or a constriction in a thin-film superconducting

cylinder deposited on a quartz tube. By the early 1970's, the rf SQUID, operated at typically 30 MHz, was the device of choice.

The situation was reversed, however, by the development of the cylindrical dc SQUID [16]. This device showed first, that thin-film Nb-NbO_x-PbIn junctions – suitably coated for protection – could have a useful life in an instrument, and second, that with the use of a cold tank circuit to couple the SQUID to the room-temperature amplifier, the flux noise could readily be made much lower than that of rf SQUIDs. Subsequently, a theory for the noise in the dc SQUID involving the solution of the equations of motion including a noise term [17] showed that the intrinsic flux noise of the dc SQUID is indeed much lower than that predicted for the rf SQUID, unless the latter is operated at microwave frequencies [18].

Two subsequent events secured the dominance of the dc SQUID. First, the development of the planar dc SQUID with an integrated, multiturn input coil [19] quickly paved the way for wafer-scale production. Second, the invention of the highly reproducible and nearly indestructible Nb-AlO_x-Nb tunnel junction [20] ensured that most of the devices on a wafer would function, and that they would continue to function almost indefinitely. The majority of low-T_c SQUIDs produced in the last two decades embrace these two technologies; in fact, the essentials of the basic device have changed little over that time period. These devices are grown with a series of depositions and patterning processes – taken over from the semiconductor industry – on 2-, 3-, or 4-inch silicon wafers.

The advent of high-T_c superconductivity in 1986 [21] resulted in a worldwide upsurge in the development of new types of SQUID; indeed many groups chose the SQUID as a vehicle to develop their high-T_c thin-film technology [22, 23]. The first rf SQUIDs involved a pellet of granular $YBa_2Cu_3O_{7-x}$ (YBCO) with the inductor of the tank circuit wound around it [24]: weak links between grains in the pellet produced SQUID-like behavior at 77K. Subsequently, an rf SQUID made from bulk YBCO with a "break junction" showed a quite low noise [25]. The first thin-film dc SQUID was made from YBCO with "grain boundary" junctions formed between randomly-oriented grains in the film [26]. The majority of high-T_c SQUIDs made since then have relied on rather more controlled grain boundary junctions made in one of two ways. The first technique involves depositing the YBCO film on a bicrystal substrate of $SrTiO_3$, $LaAlO_3$ or MgO in which there is an in-plane misorientation of (say) 24° or 30° [27]. The film grows epitaxially on the substrate, forming a grain boundary that is subsequently patterned into one or two bridges, typically a few micrometers wide. The second technique involves depositing the YBCO film over a step edge formed in the substrate [28]. A grain boundary is formed in the film at top and bottom of the step.

The next challenge to be met – required if high-T_c magnetometers are to emulate the multilayer structures of their low-T_c counterparts – was the development of a multilayer technology involving a YBCO-$SrTiO_3$-YBCO insulating crossover, together with a via technology to enable the YBCO films to be connected together with a superconducting pathway [29]. In contrast to the Nb-based technology, the high-T_c multilayers require epitaxial growth throughout the stack, together with correct oxy-

genation. Such structures have now been demonstrated by several groups, but are still difficult to fabricate.

The 1990's saw a steady progression in the performance of both dc and rf high-T_c SQUIDs. A major noise issue that was recognized early on was the prevalence of $1/f$ noise at low frequencies, that is, noise with a power spectral density scaling inversely with frequency f. There are in fact two independent sources of such noise: $1/f$ noise in the critical current of the junctions and $1/f$ "flux noise" produced by the uncorrelated hopping of flux vortices among pinning sites in the films [30]. In both cases, the fundamental process is a random telegraph signal (RTS) – random transitions between two states; a superposition of uncorrelated RTSs yields a $1/f$ power spectrum. In the case of junctions, the RTSs arise from the trapping and release of electrons in the barrier [31]. In both dc and rf SQUIDs, the use of two modulations eliminates this source of $1/f$ noise. The level of flux noise was greatly reduced by the progressive improvement in the quality of the films, which lowered the density of weak pinning sites amongst which vortices could hop under thermal activation. The use of slots or holes in the films effectively eliminated the generation of $1/f$ noise in devices cooled in weak fields, such as that of the Earth [32]. The applied field penetrates the voids, rather than the film, so that no additional vortices are created at pinning sites.

The high-T_c dc SQUID magnetometers currently in use fall into two groups. The lowest white magnetic field noise is achieved with mulitlayer devices, either integrated on a single chip or made in a "flip-chip" arrangement in which a multilayer structure on one chip is pressed against a SQUID on a second chip. The second – and more popular devices – consist of a single layer of YBCO. These are much simpler to fabricate than the multilayer devices, but have a higher level of magnetic field noise. The rf SQUIDs, on the other hand, are almost always single-layer devices, often with a single-layer "flux focuser" added in a flip-chip configuration. The magnetic field noise of the best of these devices lies midway between that of the two groups of dc SQUIDs.

We now turn to a brief overview of the principles, fabrication, operation and performance of the dc and rf SQUIDs.

1.3 The dc SQUID: A First Look

The dc SQUID [Figure 1.3(a)] consists of two Josephson junctions connected in parallel on a superconducting loop. In most – but not all – operating schemes each junction has a resistive shunt to eliminate hysteresis on its I–V characteristic, and we begin with a brief review of the resistively- and capacitively-shunted junction (RCSJ).

In the absence of any added damping resistance, generally speaking, the I–V characteristic of a Josephson junction is hysteretic. As the current is raised from zero, eventually the voltage switches to $2\Delta/e$; the voltage remains there as the current is reduced until it attains a relatively low value, at which the voltage switches back to

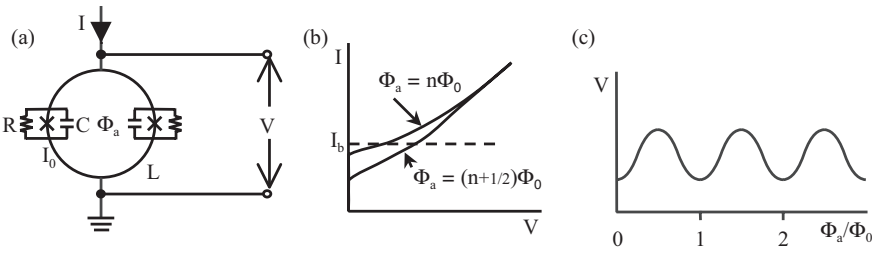

Fig. 1.3 The dc SQUID: (a) Schematic; (b) current-voltage characteristics at integer and half-integer values of applied flux; the operation point is set by the bias current I_b; (c) voltage vs. flux Φ_a/Φ_0 for constant bias current.

zero. For a junction with critical current I_0 and self-capacitance C, this hysteresis is removed by the addition of a shunt of resistance R provided that [33, 34]

$$\beta_c \equiv 2\pi I_0 R^2 C/\Phi_0 = \omega_J RC \leq 1 . \tag{1.5}$$

Here, $\omega_J/2\pi \equiv I_0R/\Phi_0$ is the Josephson frequency at voltage I_0R. For $\beta_c << 1$, the I–V characteristic is given by

$$V = R(I^2 - I_0^2)^{1/2} , \tag{1.6}$$

which tends asymptotically to IR for $I >> I_0$. The resistive shunt has an associated Nyquist noise current with a spectral density $S_I(f) = 4k_BT/R$, where k_B is Boltzmann's constant. This noise has two effects. First, it rounds the I–V characteristic at low voltages and reduces the apparent critical current. To maintain a reasonable degree of Josephson coupling one requires $I_0\Phi_0/2\pi >> k_BT$; $I_0\Phi_0/2\pi$ is the Josephson coupling energy. This inequality is conveniently written as $\Gamma \equiv 2\pi k_BT/I_0\Phi_0 << 1$. Second, the noise current induces a voltage noise across the junction at nonzero voltages. Computer simulations of the dc SQUID are invariably based on the RCSJ.

When the dc SQUID is biased at an appropriate constant current I_b [Figure 1.3(b)], changes in applied magnetic flux cause the voltage to swing between two extrema, producing the oscillations with period Φ_0 shown in Figure 1.3(c). The maximum response to a small flux change $\delta\Phi_a << \Phi_0$ is obtained when $\Phi_a \approx (2n + 1)\Phi_0/4$, where the flux-to-voltage transfer coefficient $V_\Phi \equiv |(\partial V/\partial\Phi_a)_I|$ is a maximum. The resulting voltage change $\delta V = V_\Phi\, \delta\Phi_a$ is approximately linear in $\delta\Phi_a$ in this regime. Detailed computer simulations [17] show that the response is optimized when β_c is at a value just below the onset of hysteresis and when

$$\beta_L \equiv 2LI_0/\Phi_0 = 1, \tag{1.7}$$

where L is the loop inductance and I_0 is the critical current per junction. For this value of β_L the critical current at $(2n + 1)\Phi_0/2$ is approximately one-half that at $n\Phi_0$. The transfer function is predicted to be

$$V_\Phi \approx R/L \approx 1/(\pi LC)^{1/2}\,, \tag{1.8}$$

where we have set $\beta_c = \beta_L = 1$.

Nyquist noise in the shunt resistors imposes an upper limit on the SQUID inductance, namely $\Phi_0^2/2L >> 2\pi k_B T$. Quantum interference is unobservable unless this criterion is satisfied. In addition, the Nyquist noise introduces a white voltage noise across the SQUID with a flux- and bias-current-dependent spectral density $S_v(f)$, which is equivalent to a flux noise with spectral density $S_\Phi(f) = S_v(f)/V_\Phi^2$. Under optimum conditions, one finds [17]

$$S_\Phi(f) \approx 16 k_B T L^2/R\,. \tag{1.9}$$

It is often useful to characterize SQUIDs in terms of their *noise energy*

$\varepsilon(f) = S_\Phi(f)/2L$, whence

$$\varepsilon(f) \approx 9 k_B T L/R \approx 16\, k_B T (LC)^{1/2}. \tag{1.10}$$

We have set $\beta_c = \beta_L = 1$ to obtain the last expression. The white noise of a large number of low-T_c SQUIDs has been found to be generally in good agreement with these predictions. It is common practice to quote noise energy in units of $\hbar$. A comprehensive overview of the theory appears in Chapter 2.

We note that $\varepsilon(f)$ is not a *complete* characterization of the white noise in the dc SQUID since it does not take into account the accompanying noise current in the SQUID loop, which induces a noise voltage into any input circuit coupled to the SQUID. This topic is deferred to Vol. II. Furthermore, this brief discussion has not addressed issues of $1/f$ noise, which are dealt with in Chapters 2, 5 and 6.

As mentioned earlier, low-T_c dc SQUIDs are almost invariably fabricated from thin, polycrystalline films of Nb, most often with Nb-AlO_x-Nb junctions fabricated *in situ*, that is, by sequential deposition and Al oxidation without breaking vacuum. This process can yield spreads in critical current of only a few percent across the wafer. The trilayers are patterned with reactive ion etching, and their sides protected by anodization. Subsequently, thin-film shunt resistors of Pd, Mo, W or AuCu are deposited. Chapter 3 gives a detailed account of these processes. The multiturn, spiral input coil – to be connected to an appropriate input circuit – is integrated on top of the SQUID washer, insulated from it by silicon oxide. An example is shown in Figure 1.4. The washer acts as a ground plane for the coil, providing efficient flux coupling into the SQUID. A second coil to provide flux modulation and feedback may also be fabricated on the chip.

For high-T_c dc SQUIDs in the low-fluctuation regime $\Gamma << 1$, the expressions $V_\Phi \approx R/L$ [Eq. (1.8)] and $\varepsilon(f) \approx 9 k_B T L/R$ [Eq. (1.10)] remain valid. However, since high-T_c Josephson junctions are self-shunted and require no external shunt, the extensions of these two expressions differ from those for the low-T_c case. We assume that $I_0 R = V_c$ for a given technology, and that this expression remains valid as the width of the junction (parallel to the barrier or weak-link interlayer) is varied. Thus, one

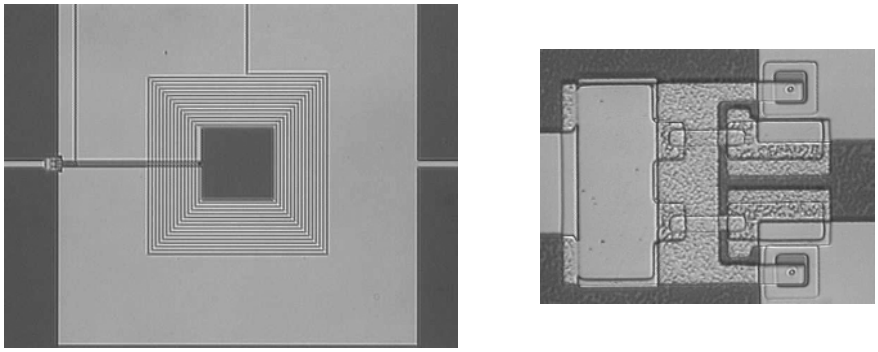

Fig. 1.4 (a) Square-washer dc SQUID with overlaid 15-turn input coil. (b) Expanded view of the left-hand end of the slit showing the junction on each side of the slit, and the resistive shunts.

can vary I_0 simply by changing the width. Under these circumstances, with $\beta_L = 2LI_0/\Phi_0 = 1$, we find

$$V_\Phi \approx R/L \approx 2V_c/\Phi_0 \tag{1.11}$$

and

$$\varepsilon(f) \approx 4k_B T\Phi_0/V_c\,. \tag{1.12}$$

Remarkably, for fixed V_0 and in the limit $\Gamma << 1$, V_Φ and hence $\varepsilon(f)$ are independent of the dc SQUID parameters. Thus, V_0 becomes an alternative figure of merit for the high-T_c dc SQUID.

High-T_c dc SQUIDs are fabricated from thin films of YBCO, mostly on bicrystals to form grain boundary junctions. Devices with integrated input coils following the design for low-T_c SQUIDs have been successfully made and tested, but their production is nowhere near as routine as that of Nb-based devices. Thus, single-layer devices are more commonly used. Chapter 3 presents a detailed account of the fabrication of high-T_c devices.

Except for high-frequency applications – above, say, a few megahertz – the dc SQUID is almost invariably operated in a flux-locked feedback loop. A detailed account appears in Chapter 4. Feedback serves several purposes: it linearizes the response of the SQUID to applied flux, it enables one to track changes in flux corresponding to many flux quanta, and it enables one to detect changes in flux corresponding to a tiny fraction of a flux quantum. An example – in which a modulating flux is applied to the SQUID at frequencies f_m ranging from perhaps 100 kHz to 10 MHz – is shown in Figure 1.5. The flux has a peak-to-peak value of $\Phi_0/2$. When the flux in the SQUID is $n\Phi_0$, the resulting voltage is a "rectified" sine wave, as

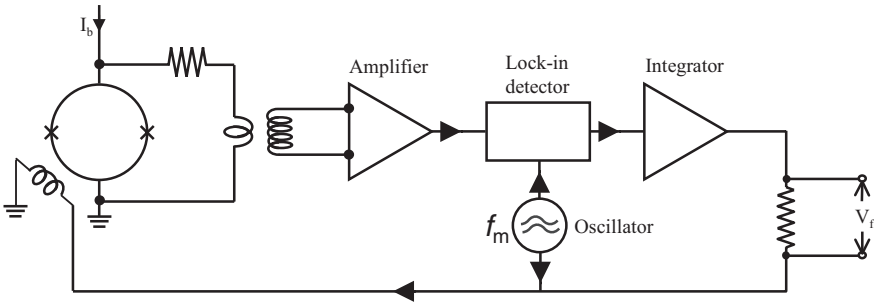

Fig. 1.5 Flux modulation and feedback circuit for the dc SQUID. The modulation oscillator shown operates at the frequency f_m.

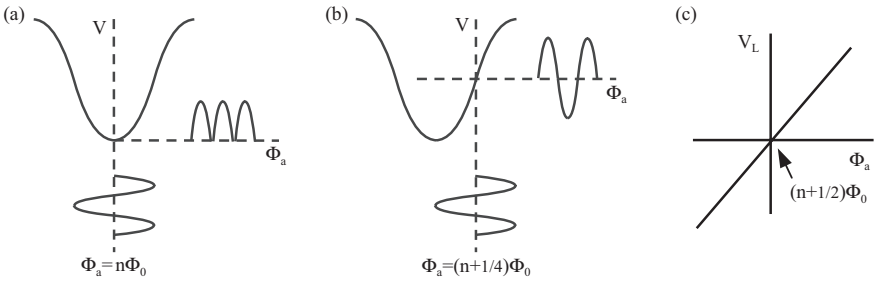

Fig. 1.6 Flux modulation scheme showing voltage across the dc SQUID for (a) $\Phi_a = n\Phi_0$ and (b) $\Phi_a = (n+1/4)\Phi_0$. The output V_L from the lock-in detector versus Φ_a is shown in (c).

shown in Figure 1.6(a). When this voltage is connected to a lock-in detector referenced to f_m, the output is zero. On the other hand, when the flux is $(n + 1/4)\Phi_0$ [Figure 1.6(b)], the output from the lock-in is a maximum. Thus, as one increases the flux from $n\Phi_0$ to $(n + 1/4)\Phi_0$, the output from the lock-in steadily increases; if instead we decrease the flux from $n\Phi_0$ to $(n - 1/4)\Phi_0$, the output from the lock-in is negative [Figure 1.6(c)]. After integration, the signal from the lock-in is coupled, via a resistor, to the same coil as that producing the flux modulation. A flux $\delta\Phi_a$ applied to the SQUID results in an opposing flux $-\delta\Phi_a$ from the feedback loop to maintain (ideally) a constant flux in the SQUID, while producing an output voltage across the resistor proportional to $\delta\Phi_a$.

With judicious design, the electronics adds very little noise to the intrinsic noise of a dc SQUID at 4.2K. The oscillating voltage across the SQUID is amplified by either a tank circuit or more commonly a transformer that boosts the dynamic resistance of the SQUID – typically of the order of 10Ω – to the value required to optimize the noise temperature of the preamplifier which is typically a few kilohms. Since the noise temperature of the optimally-coupled preamplifier is typically about 1K at frequencies of a few hundred kilohertz, it does not contribute significantly to the system noise. Typically, the white flux noise for a low-T_c SQUID at 4.2K is

10^{-6} Φ_0 $Hz^{-1/2}$ with an onset of $1/f$ noise below 1 Hz, the dynamic range is in excess of 120 dB and the slew rate – the maximum rate at which the flux-locked loop can track changes in flux without losing lock – is $10^6 - 10^7$ Φ_0/s. For high-T_c SQUIDs, a typical white flux noise is a few $\mu\Phi_0$ $Hz^{-1/2}$, with an onset of $1/f$ noise below 10 Hz (with bias reversal – see below). Chapter 5 presents typical noise data.

The flux modulation scheme eliminates low-frequency $1/f$ noise due to noise in the current bias and to the components of noise in the critical current of the junctions that fluctuate "in-phase". However, this scheme does not eliminate "out-of-phase" critical current $1/f$ noise in the junctions that induces current noise around the SQUID loop, and hence a flux noise in the SQUID. Fortunately, this noise component can be eliminated by one of several methods in which the bias current is periodically reversed. This latter scheme is rarely implemented for low-T_c SQUIDs where the critical current $1/f$ noise is low, but is essential for high-T_c SQUIDs where it is relatively high.

Several other read-out schemes are in use, and are described in Chapter 4. Of these, the most widely used is the direct read-out scheme [35] in which the voltage across the SQUID is coupled directly to the room-temperature amplifier. A positive feedback scheme – in which part of the flux-induced change in voltage across the SQUID is fed back inductively into the SQUID – increases V_Φ for flux between (say) $n\Phi_0$ and $(n + 1/2)$ Φ_0, so that the preamplifier noise is relatively unimportant. This electronics package involves fewer components than is required for the flux-modulated case; bias reversal can be incorporated to reduce the $1/f$ noise in high-T_c SQUIDs.

Modern SQUID controllers – especially those for large numbers of SQUIDs – are often equipped with microprocessors that automatically optimize the working point of each SQUID, or reset it if the flux-lock is lost due to momentary overload. Increasingly, the feedback electronics is becoming digital. The signal output and control inputs are usually digitized, enabling the user to operate the system from a computer.

1.4 The rf SQUID: A First Look

The rf SQUID, shown in Figure 1.7, employs only a single junction in a superconducting loop. The loop inductance L is coupled to the inductor L_T of a tank circuit via a mutual inductance $M = k(LL_T)^{1/2}$. The tank circuit is driven by a current oscillating at or near the resonant frequency, $f_0 = \omega_0/2\pi$, which may vary from 20 MHz to 10 GHz. The resistance R_T represents the loss in the tank circuit, so that the unloaded quality factor is $Q_0 = \omega_0 L_T/R_T$ in the absence of the SQUID. On resonance, and with the SQUID in place, the oscillating bias current $I_{rf} \sin \omega_{rf} t$ thus induces a current $I_T \sin \omega_{rf} t = QI_{rf} \sin \omega_{rf} t$ in the inductor; here Q is the loaded quality factor. The peak rf flux in the SQUID loop is $\Phi_{rf} = MI_T$. The tank circuit, which is connected to a preamplifier, also serves to read out the applied flux Φ_a in the SQUID: the amplitude of the rf voltage $V_T \sin \omega_{rf} t$ is periodic in Φ_a with period Φ_0.

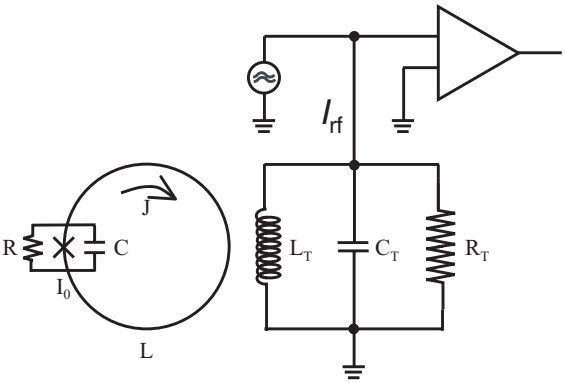

Fig. 1.7 Schematic representation of the rf SQUID, with tank circuit and preamplifier; the operation point is set by the amplitude of the rf bias current, I_{rf}.

We briefly describe the behavior of the rf SQUID [36–39]; a detailed account of the theory is given in Chapter 2. We assume that the junction is damped sufficiently to eliminate hysteresis. Flux quantization imposes the constraint

$$\delta + 2\pi\Phi_T/\Phi_0 = 2\pi n \tag{1.13}$$

on the *total* flux Φ_T in the loop, where n is an integer. In turn, the phase difference δ across the junction determines the supercurrent

$$J = -I_0 \sin(2\pi\Phi_T/\Phi_0) \tag{1.14}$$

flowing around the loop. The total flux can thus be written

$$\Phi_T = \Phi_a - LI_0 \sin(2\pi\Phi_T/\Phi_0)\ . \tag{1.15}$$

Inspection of (1.15) shows that there are two distinct kinds of behavior, plotted in Figure 1.8. For $\beta_{rf} \equiv 2\pi LI_0/\Phi_0 < 1$, the slope $d\Phi_T/d\Phi_a = 1/[1 + \beta_{rf}\cos(2\pi\Phi_T/\Phi_0)]$ is everywhere positive and the Φ_T vs. Φ_a curve is nonhysteretic. On the other hand, for $\beta_{rf} > 1$ there are regions in which $d\Phi_T/d\Phi_a$ are positive, negative or divergent, so that the device makes transitions between flux states [Figure 1.9(a)]. As a result, the Φ_T vs. Φ_a plot is hysteretic. The rf SQUID may be operated in either regime. For high thermal fluctuations ($\Gamma > 1$), the nonhysteretic regime extends to higher values of β_{rf} predicted and experimentally verified to be about 3 [40, 41]. The hysteretic regime for $\Gamma > 1$ has not yet been analyzed.

In the hysteretic mode, the rf drive causes the SQUID to make transitions between quantum states and to dissipate energy at a rate that is periodic in Φ_a: hence, this is termed the "dissipative mode". This periodic dissipation in turn modulates the Q of the tank circuit, so that when it is driven on resonance with a current of constant amplitude, the rf voltage is periodic in Φ_a. Figure 1.9(b) shows the ampli-

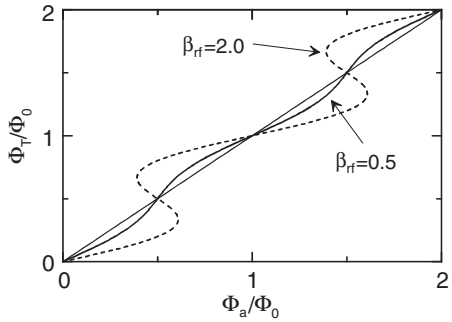

Fig. 1.8 Dependence of total flux Φ_T in the rf SQUID loop on applied flux Φ_a in the absence of noise for the dispersive ($\beta_{rf} = 0.5$) and hysteretic ($\beta_{rf} = 2$) modes of operation.

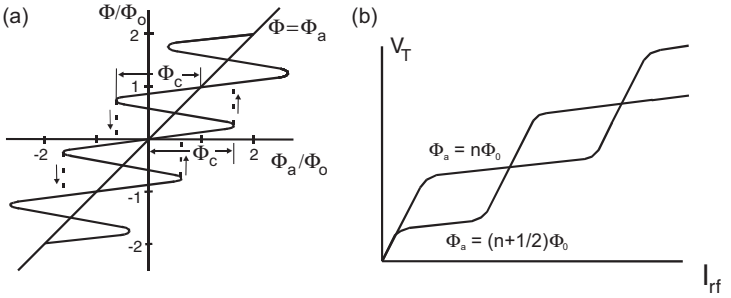

Fig. 1.9 (a) Total flux Φ_T vs. applied flux Φ_a for rf SQUID in the hysteretic mode ($\beta_{rf} = 5\pi/2$) showing transitions between quantum states. (b) Corresponding amplitude of rf voltage across the tank circuit vs. rf drive current at applied fluxes of $n\Phi_0$ and $(n + 1/2)\ \Phi_0$.

tude of the rf voltage across the tank circuit vs. the amplitude of the applied rf current for two values of applied flux. The characteristic "steps and risers" are evident, as is the change in amplitude of V_T with Φ_a at appropriate values of I_{rf}. The nonzero slope of the steps is due to thermal noise. A detailed analysis shows that the device is optimized when [36–39]

$$k^2 Q \approx 1, \tag{1.16}$$

at which value the flux-to-voltage transfer coefficient becomes

$$\partial V_T/\partial \Phi_a \approx \omega_{rf}(QL_T/L)^{1/2} \approx \omega_{rf}(L_T/L)^{1/2}/k\,. \tag{1.17}$$

We note that V_Φ scales as ω_{rf} and as $1/L^{1/2}$. The *intrinsic* noise energy is given by [18]

$$\varepsilon\,(f) \approx LI_0^2\Gamma^{4/3}/2\omega_{rf}\,. \tag{1.18}$$

However, for rf SQUIDs at 4.2K and a room-temperature preamplifier, it should be stressed that there are *extrinsic* contributions to the noise energy that may far exceed the intrinsic value. These contributions arise in part because the noise temperature of the rf preamplifier tends to be significantly higher than the bath temperature and in part because portions of the coaxial line connecting the tank circuit to the preamplifier are at room temperature. The latter contribution can be eliminated by cooling the preamplifier; however, this is an additional complication. Furthermore, one needs to operate the SQUID at high values of ω_{rf} – perhaps as high as $R/10L$ [18] – to achieve an intrinsic noise energy comparable to that of the dc SQUID at 4.2K. It is for these reasons that rf SQUIDs are rarely used today at liquid helium temperature.

A corollary to this behavior, however, is that when one increases the operating temperature of an rf SQUID coupled to a room-temperature amplifier from 4.2K to 77K, the system noise energy is virtually unchanged. For the dc SQUID, however, the noise energy scales with the temperature for fixed SQUID parameters, and the noise advantage of the dc SQUID over the rf SQUID is diminished.

In the nonhysteretic regime ("dispersive mode") the rf SQUID behaves as a flux-sensitive inductor [36, 38–40, 42, 43]. When the tank circuit is operated off-resonance, a flux change in the SQUID thus changes the resonant frequency, causing the rf voltage across the tank circuit to be periodic in Φ_a at constant drive amplitude and frequency. The "steps and risers" in the plot of rf voltage vs. current are qualitatively similar to those for the dissipative mode. However, when $kQ^2\beta_{rf} > 1$, that is, when the tank circuit is rather strongly coupled to the SQUID and Q is high, the resonance curve $V_T(f)$ is nonlinearly dependent on Φ_a, becoming asymmetrical and even multivalued. Consequently, when the bias frequency is set near a point of infinite slope, the transfer coefficient can be arbitrarily high, but at the cost of reduced bandwidth and strong dependence on SQUID parameters. In practice, when the detuning from resonance is appropriately chosen, a very high value of $\partial V_T/\partial \Phi_a$ can be obtained with wide bandwidth and acceptable stability. Under these circumstances, the transfer coefficient cannot be expressed by a simple functional form; the full expression is discussed in Chapter 2.

In the low fluctuation limit, $\Gamma << 1$, the intrinsic noise energy can be approximated by [40]

$$\varepsilon(f) \approx 3k_B TL/\beta_{rf}^2 R\,. \tag{1.19}$$

The intrinsic noise energy may be lower than in the dissipative mode. Furthermore, in contrast to the dissipative mode, the noise of a room-temperature preamplifier and coaxial line may not dominate, even for a 4.2 K SQUID. This becomes possible when the SQUID is interacting strongly with the tank circuit, i.e., $k^2Q\beta_L \geq 1$. Discussion of this case is deferred to Chapter 6, but we note that the lowest flux noise and energy resolution of any rf SQUID were reported for a microwave SQUID operating in this regime [44]. As shown in Chapter 2, the intrinsic noise energy of dispersive SQUIDs remains low even in the high fluctuation limit, making it possible for them to operate with relatively large loop inductances, somewhat higher than those

of dc SQUIDs. Large inductances, and correspondingly large loop areas, help one to attain high field sensitivities in single-layer high-T_c SQUIDs.

Almost all practical high-T_c rf SQUIDs are made from a single layer of YBCO – see Chapter 6. The grain boundary junctions are formed either on a bicrystal or more often on a step edge. Most of the structures used to improve the magnetic field sensitivity – for example, by flux focusing – are also fabricated from single-layer YBCO films. Early devices were operated with lumped tank circuits consisting of a wire-wound coil and a capacitor; however, this technology is limited to perhaps 200 MHz. Recent, more sensitive designs involve microwave resonators at frequencies of 0.5–1 GHz. For practical reasons, higher frequencies are rarely used. A multiturn flux transformer has been demonstrated [45] but not implemented in practical applications.

Although cooled preamplifiers have been explored, current practice uses room-temperature amplifiers, since the advantages of cooling them to 77K are relatively modest. After amplification, the rf signal is usually rectified and smoothed to give a quasistatic voltage that is periodic in the flux applied to the SQUID. The rf SQUID is almost invariably operated in a flux-locked loop, with flux modulation as for the dc SQUID. It is noteworthy that the combination of rf bias and flux modulation eliminates l/f noise due to fluctuations in the critical current of the junction, analogously to the combination of flux modulation and bias reversal for the dc SQUID. Typical values of white flux noise in high-T_c rf SQUIDs are somewhat below $10^{-5}\ \Phi_0\ \mathrm{Hz}^{1/2}$; furthermore, the l/*f* flux noise is higher than that of single-layer dc SQUIDs operating with bias reversal.

1.5 Cryogenics and Systems

Low-T_c and high-T_c SQUIDs are traditionally operated at liquid ^{4}He temperatures ($\leq$ 4.2K) and liquid nitrogen temperatures ($\leq$ 77K), respectively. For some applications the SQUID and its associated circuitry are immersed in the cryogen, which is contained in a suitable dewar made of glass, metal, or (most commonly) fiberglass. In other applications, it is more convenient to operate the device in a vacuum, with conductive cooling. In recent years, some commercial systems make use of a cryocooler, thus obviating the need to replenish the liquid cryogen: this is an important step in improving the user-friendliness of SQUIDs.

SQUIDs are often encapsulated to protect them against environmental damage, and provided with a heater to expel trapped flux. Broadly speaking, there are two kinds of SQUID applications: those in which the signal is generated at low temperature and those in which the signal source is at room temperature. In the former case, the entire experiment – SQUID, input circuit and sample – is usually surrounded by a superconducting shield to exclude ambient magnetic field fluctuations. If a low static field is desirable, the Earth's field may be attenuated by surrounding the dewar with one or more shields made from a high permeability material such as mu-metal. In the latter case, the SQUID or the pickup loop of an appro-

priate flux transformer must obviously be exposed to the signal source outside of the dewar. When a flux transformer is used, the SQUID itself may be enclosed in a superconducting shield with leads connecting its input coil to the flux transformer. For such measurements, it is vital that the dewar and its components generate very low levels of magnetic noise. Furthermore, to maximize the signal, the room-temperature source must be brought as close as possible to the cooled dewar. This requirement calls for a dewar with thin walls and minimal separation between the inner (cold) and outer (warm) wall. The necessary reduction in the number of layers of superinsulation results in a higher boil-off rate of the cryogen or an increased load on the cryocooler. In some cases, notably high-T_c "SQUID microscopes", the SQUID and sample may be separated by a single window only a few micrometers thick.

Given the extraordinarily high sensitivity of SQUIDs, it goes without saying that suppressing environment noise is a major undertaking. There are two broad issues. The first is magnetic noise in the signal bandwidth, most notably from power lines at frequencies of 50 or 60 Hz and their harmonics. These disturbances can be suppressed substantially by the use of spatial gradiometers, but a high-permeability enclosure for the cryostat and, for example, a human subject may be required when the signals are weak. Such magnetically shielded rooms usually incorporate both high-permeability shields and eddy-current shields made of high-conductivity aluminum. The second – and often even more insidious issue – is radio frequency noise from radio and televisions stations, and particularly from nearby computers and other digital equipment which produce copious levels of electromagnetic interference. Elimination of such noise is a skilled art: the essential principle is to surround the cryogenic components, the leads connecting them to the room-temperature electronics and the electronics themselves with a Faraday cage. In the case of dc SQUIDs, the leads are preferably twisted pairs inside metal tubes, whereas the higher frequencies associated with rf SQUIDs demand coaxial cable – which has a higher thermal loss than a twisted pair.

Chapter 7 is devoted to these various, practical issues. Since many magnetometer and gradiometer systems consist of multiple SQUID and electronics channels – up to 300 or more – some system issues stem from the need for simultaneous and synchronous measurements in these multiple channels.

1.6 Instruments: Amplifiers, Magnetometers and Gradiometers

There is a wide range of input circuits that can be coupled to a dc or an rf SQUID. For example, by connecting a signal source in series with a resistor and the superconducting input coil of a SQUID one can make a voltmeter – for quasistatic signals – or an amplifier with a bandwidth that may extend up to 100 MHz. The amplifier may be tuned with the addition of a series capacitor. The operating frequency may be extended to several gigahertz by using the input coil as a microstrip resonator.

The noise temperature of SQUID amplifiers may be many orders of magnitude lower than that of state-of-the-art semiconductor amplifiers.

The majority of applications, however, involve a superconducting input circuit, configured, for example, as a magnetometer or gradiometer. In contrast to various types of absolute field measuring instruments, SQUID magnetometers (and naturally gradiometers) are vector devices, and measure only changes in the magnetic field component perpendicular to the plane of the flux pickup loop. Given the widespread use of these devices, an overview of their configuration and optimization is in order. Chapters 5 and 6 present comprehensive surveys.

Because of the need to satisfy the constraint $L << \Phi_0^2/2\pi k_B T$, the inductances of SQUIDs are necessarily small, and the corresponding areas A_s of planar devices are also small (typically 10^{-4} to 10^{-2} mm^2). (An exception is the cylindrical SQUID, which is not used today.) Consequently, although the magnetic flux noise $\Phi_N(f)$ may be very low, the magnetic *field* noise $B_N(f) = \Phi_N(f)/A_s$ is often too high for many applications – most notably biomagnetism. The essential feature of a magnetometer is to enhance the effective area to a value

$$A_{eff} = \Phi_s/B_a \tag{1.20}$$

that may be 2 or 3 orders of magnitude higher than that of the bare SQUID, with a concomitant reduction in the magnetic field noise. Here, Φ_s is the flux coupled into the SQUID by a flux transformer in response to an applied field B_a.

One way of increasing the effective area of a square washer SQUID is simply to make its outer dimension D much larger than that of the hole in the washer, d. Since the effective area is dD [19], the sensitivity increases linearly with the outer dimension. This approach has been very successful for high-T_c rf SQUIDs, and has the advantage of using a single-layer technology. However, for a given size, it has a much lower effective area than multiturn flux transformers and multiloop (fractional turn) SQUIDs.

Indeed, the majority of magnetometers and gradiometers – particularly for low-T_c dc SQUIDs – involve a superconducting pickup circuit connected to the superconducting input coil, that is, a flux transformer. In low-T_c technology, gradiometers may be planar, in which case they are generally patterned in a film of Nb, or axial, in which case they are invariably wound from Nb wire. In the case of high-T_c devices, given the absence of a flexible, bondable high-T_c wire, to date only planar structures have been used. Figure 1.10(a) shows the configuration of a magnetometer, with a pickup loop of inductance L_p connected to an input coil of inductance L_i that is coupled, in turn, to the SQUID via a mutual inductance $M_i = k_i(LL_i)^{1/2}$. We assume that the SQUID is isolated from the applied field by a superconducting shield. In the simplified analysis that follows, we neglect the fact that the SQUID inductance is reduced by the presence of the flux transformer, and the fact that there is a voltage noise source induced in the flux transformer by the current noise in the SQUID. Both effects modify the optimization.

A flux change $\delta\Phi_a^{(p)}$ in the pickup loop induces a current J_s in the flux transformer determined by flux quantization:

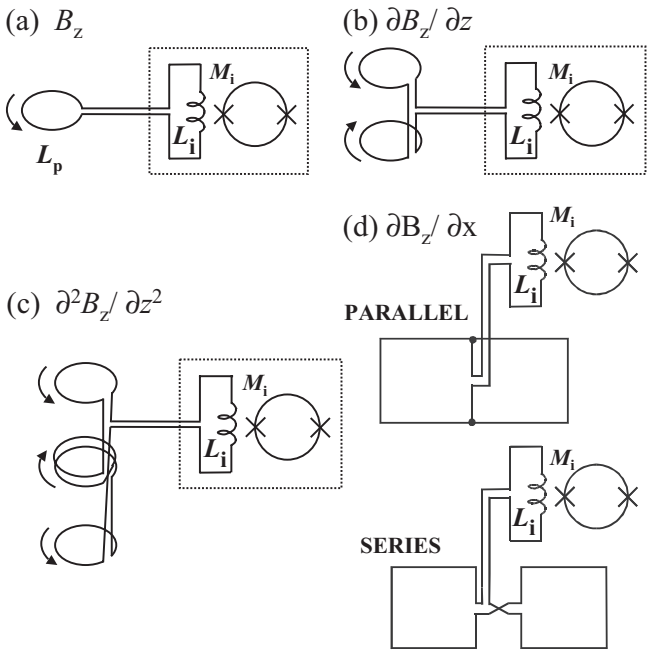

Fig. 1.10 Superconducting flux transformers: wire-wound devices (a) magnetometer, (b) first-derivative axial gradiometer, (c) second-derivative axial gradiometer. The dashed box indicates a superconducting shield enclosing the SQUID, which is in a flux-locked loop. (d) Thin-film, planar first-order gradiometers measuring $\partial B_z/\partial x$ with parallel and series pickup loops.

$$\delta\Phi_a^{(p)} + (L_p + L_i)J_s = 0\,. \tag{1.21}$$

We have neglected parasitic inductance in the leads connecting the pickup and input loops. The flux coupled into the SQUID is thus $\delta\Phi_s = M_i\left|J_s\right| = M_i\delta\Phi_a^{(p)}/(L_p + L_i)$. The spectral density of the equivalent flux noise referred to the pickup loop is then

$$S_\Phi^{(p)}(f) = (L_p + L_i)^2\, S_\Phi(f)/M_i^2. \tag{1.22}$$

Correspondingly, the equivalent noise energy referred to the pickup loop is

$$\varepsilon^{(p)}(f) = S_\Phi^{(p)}(f)/2L_p = [(L_p + L_i)^2/L_pL_i]S_\Phi(f)/2k_i^2L\,. \tag{1.23}$$

It is easy to see that the minimum value of $\varepsilon^{(p)}(f)$, $4\varepsilon(f)/k_i^2$, occurs when $L_p = L_i$; here $\varepsilon(f)$ is the noise energy of the SQUID. Thus, a fraction $k_i^2/4$ of the energy in the pickup loop is transferred to the SQUID.

When $L_p = L_i$, the magnetic field noise in a single-turn pickup loop of radius r_p is

$$B_N^{(p)}(f) = (S_\Phi^{(p)})^{1/2}/\pi r_p^2 = 2(2L_p\varepsilon)^{1/2}/k_i\pi r_p^2. \tag{1.24}$$

One can, in principle, improve the magnetic field resolution indefinitely by increasing the size of the pickup coil. Since L_p scales approximately as r_p (neglecting logarithmic corrections), $B_N^{(p)}(f)$ is predicted to scale as $1/r_p^{3/2}$. For a typical low-T_c dc SQUID and r_p ~10 mm, one expects a white magnetic field noise of the order of 1 fT $Hz^{1/2}$. Such noise levels are indeed achieved in practice.

An alternative to the superconducting flux transformer is the multiloop dc SQUID (See Chapter 5). This consists of several relatively large pickup loops all connected in parallel across the same junctions to reduce the SQUID inductance. Practical devices involve a multilayer, thin-film structure with identical loops tightly arranged around the junctions, and resemble a wheel with spokes. The effective area is that of a single loop.

Particularly in biomagnetic measurements, the use of gradiometers – spatial filters – is almost universal. The magnetic field from a dipole falls off with distance r as $1/r^3$, the first-derivative as $1/r^4$, the second-derivative as $1/r^5$, and so on. Thus, a gradiometer with baseline b gives substantial rejection of a noise source at a distance $r >> b$ in favor of a signal from a source at a distance r << b, which is essentially unattenuated. Figure 1.10(b) shows the principle of a first-derivative, axial gradiometer consisting of two pick-up loops of equal areas connected in series; the loops are wound in opposition and are separated by the baseline, b. A uniform magnetic field B_z ideally induces no net flux into the two loops, and hence produces no flux in the SQUID. A gradient $\partial B_z/\partial z$, on the other hand, induces a net flux into the gradiometer, and is thus measured by the SQUID. In practice, balances of 1 part in 100 to 1 part in 1000 are typical. Figure 1.10(c) shows the configuration of a second-derivative, axial gradiometer. The principle of planar gradiometers is identical. Figure 1.10(d) shows parallel and series first-derivative configurations. Such planar gradiometers are always fabricated from thin films, and measure off-diagonal gradients such as $\partial B_z/\partial x$. We note that magnetic susceptibility χ is generally measured with an axial or planar gradiometer. Either the sample is placed in one loop of the gradiometer, and a uniform field is applied, or a uniform field is established and the sample is then introduced. A nonzero value of χ unbalances the gradiometer, enabling one to determine its value.

In the case of high-T_c SQUIDs, only planar hardware gradiometers have been fabricated. However, one can form an axial gradiometer by stacking magnetometers one above the other and subtracting the outputs: two magnetometers form a first-derivative gradiometer and three a second-derivative.

Subtraction is also used with low-T_c first-derivative gradiometers to form higher derivatives, for example, third-order. For *electronic gradiometers* the signals are subtracted electronically, whereas for *synthetic gradiometers* the subtraction is performed in software. Because hardware gradiometers have limited balance in all three directions, one generally subtracts signals from a three-axis (vector) magnetometer to compensate. This approach can improve the balance by several orders of magnitude.

These issues are discussed in detail in Chapter 7, along with the (special) requirements of mobile SQUID systems, where additional reference channels can be used to compensate for flux changes produced by rotational motion in the Earth's magnetic field.

1.7 Applications

Most of the SQUIDs ever made are incorporated into biomagnetic systems, specifically those for magnetoencephalography (MEG). In modern instruments about 300 low-T_c dc SQUIDs – usually configured as first-derivative gradiometers – are installed in a helmet into which the subject inserts his or her head. The system is most often installed in a magnetically-shielded room since brain signals are extremely weak, as low as a few femtotesla. The SQUIDs detect tiny signals produced by neuronal electrical currents in the brain. This completely noninvasive technique has been quite widely used in neurological and psychological research, and is increasingly used as a clinical tool, particularly for neurological screening of brain tissue surrounding tumors prior to surgery and localization of epileptic foci. Another biomagnetic method is magnetocardiography (MCG), the noninvasive characterization of local magnetic activity of the heart muscle, generated by currents. Currently, clinical studies on hundreds of normal subjects and patients with heart disorder are in progress. The goal is the noninvasive diagnosis of various kinds of heart disease – for example, ischemia. The heart signals are substantially larger than those of the brain and have a narrower bandwidth. Therefore, some systems can be operated in an unshielded environment, and if the technique proves clinically viable, one could even envision high-T_c SQUID gradiometers being used. Other biomagnetic techniques include liver susceptometry to monitor the accumulation of excess iron in the human liver (thalassemia) and gastro-magnetometry, where ingested magnetic markers are followed through the gastro-intestinal tract. A recently-developed experimental method is aimed at immunoassay – the qualitative and quantitative detection of very small numbers of antibodies or antigens in biological fluids. Immunoassays are widely used in biology and medical diagnosis. The magnetic method involves the specificity of the binding reaction between two components, one of which is magnetically labeled so that its presence or absence can be detected by a SQUID microscope.

Although most SQUIDs are installed in biomagnetic systems, by far the most widely sold commercial systems involve only one or two SQUIDs and are used to measure magnetic properties such as magnetization and susceptibility. One system makes it possible to study relatively small samples at temperatures ranging from a few kelvin to above room temperature in fields of several tesla. The other, a "rock magnetometer," has a horizontal open access and allows one to study the magnetic properties of core samples, taken from the earth, at room temperature. Both systems employ low-T_c dc SQUIDs and – importantly – are available with cryocoolers that make the cryogenics invisible or at least less cumbersome to the operator.

The advent of high-T_c SQUIDs has heightened interest in nondestructive evaluation (NDE) of materials – for example, aircraft structures and engines, nuclear plants, reinforcing steel in concrete structures, and wires and cables. The goal is to locate flaws – for example, minute cracks, inclusions of unwanted contaminants, and damage due to corrosion or fatigue – before the integrity of the structure is threatened. Broadly speaking, there are two approaches: passive, in which one detects the magnetic field due to ferromagnetism, and active, in which one applies an oscillating magnetic field and measures the "secondary" response magnetic fields of oscillating currents induced in the sample. In each case, the presence of flaws is inferred from maps – obtained by scanning – that show localized anomalies. Active methods are useful in testing electrically conductive, nonferromagnetic materials. The first commercial application of a passive method was the screening of aircraft gas turbine rotors fabricated from a nonmagnetic alloy for magnetic microparticles, the presence of which can cause catastrophic fatigue failures. The first commercial application of an active method was the use of a high-T_c scanning SQUID microscope to detect faults, such as spurious short circuits, in computer multichip modules and packages. In most NDE methods, the very wide dynamic range of the SQUID is of particular importance, whereas the vast reserve in sensitivity is rarely exploited fully, so that high-T_c devices are more than adequate.

Interest in geophysical exploration measurements has also been rekindled by the simplicity of fielding liquid-nitrogen-cooled SQUIDs compared with their liquid-helium-cooled counterparts. Magnetic and electrical measurements made at the Earth's surface can provide information on the conductivity at depths ranging from a few meters to tens of kilometers. For example, the presence and depth of oil and mineral ores can be deduced from local conductivity anomalies.

In magnetotellurics (MT), the low-frequency excitation signals (10^{-4} to 100 Hz) originate in the ionosphere or magnetosphere. Alternatively, in other techniques the signals are provided by a generator, the frequency of which is under the control of the operator. In time-domain methods, pulses of current are applied to the ground via large antennae or buried electrodes, and the subsequent decaying magnetic fields are detected, averaged and mapped. Three-axis SQUID magnetometers are particularly competitive at low frequencies (< 1 Hz), where conventional induction coils become very large in order to maintain sufficient sensitivity. Ground-based time-domain SQUID exploration systems have been successfully demonstrated on four continents, and one has been towed behind an aircraft with considerable success. Related techniques have been demonstrated for the detection of buried ordnance and submarines.

In the classes of applications mentioned thus far, it is often of prime interest to determine the electric currents which are the *sources* of the measured magnetic fields. These sources are mapped by solving the *inverse* and *forward* problems. In the inverse problem, one estimates the unknown spatial distribution and amplitude of electrical current from the measured spatial distribution of the magnetic field. In three dimensions, the inverse problem is ill-defined, that is, the solution is not unique, and the magnetic field data must be supplemented by additional information to obtain unique current estimates. Forward solutions consist of calculating

magnetic field distributions from assumed current distributions and of iteratively matching the results of calculations and measurements until a sufficiently good match is obtained. While the field calculations from given current sources have unique solutions even in three dimensions, to obtain rapid, nearly real-time matching it is desirable to have as much *a priori* information about the sources as possible.

All the applications above involve the detection of magnetic fields, and can be categorized as magnetometric. Although a SQUID always detects magnetic flux, there is another class of applications in which the device is used as an amplifier. One can measure a quasistatic voltage by connecting it to a SQUID input coil in series with a resistor. Such measurements have been made on a great variety of cryogenic sources, and can be extended to frequencies up to several megahertz in a flux-locked loop. A major application – with a superconducting input transformer – is the detection of nuclear magnetic resonance (NMR) or nuclear quadrupole resonance (NQR) at frequencies that may be below 100 Hz. One possible use is the detection of explosives in security screening. At higher frequencies – say up to 100–200 MHz – SQUIDs operated open-loop are used as high-gain, low-noise amplifiers with either an untuned or tuned input circuit. At still higher frequencies – up to several gighertz – the input coil can be configured as a microstrip resonator, again enabling high gain and low noise. A primary goal of this device is as the readout amplifier of a cryogenic axion detector.

Another amplifier application currently undergoing rapid development is the readout of superconducting transition-edge bolometers. Electromagnetic radiation absorbed by the bolometer causes its temperature to rise and the ensuing change in the resistance of the superconductor deposited on it is detected by a low-T_c dc SQUID. These are the most sensitive detectors available in the far-infrared and submillimeter regions of the electromagnetic spectrum, and telescopes are now funded that in a few years will involve arrays of hundreds and subsequently thousands of such sensors. This application is driving the development of SQUID multiplexers. Similar and highly competitive detectors have been developed for X-rays, and are finding an important application in the detection of impurities in semiconductors.

SQUID-based, superconducting accelerometers are used as transducers for gravity wave detectors, and have potential for gravity gradiometers, precision tests of the law of gravity, and inertial navigation. The acceleration of a mass causes it to be displaced, and this movement is converted into a change in magnetic flux that is detected by a low-T_c dc SQUID.

Finally, there are a myriad "one-of" experiments in basic science that are possible only because of the unrivaled sensitivity of the SQUID. These range from the discovery of the phenomenon of charge imbalance in superconductors three decades ago to today's use of a SQUID to study macroscopic quantum coherence in a flux qubit – a superconducting loop interrupted by a Josephson junction (or sometimes several junctions). In many ways, such applications are the most exciting of all because they may lead to new scientific discoveries.

Volume II of the Handbook is devoted to applications.

1.8 Challenges and Perspectives

The concept of the SQUID and its ability to perform ultrasensitive measurements have been around for four decades. What are the remaining challenges and possible future trends?

The theory of the dc SQUID in the small-fluctuation limit ($\Gamma << 1$) has been long established, and experiments on low-T_c devices with a broad range of parameters provide results in good agreement with predictions. The agreement is less satisfactory for high-T_c devices, however, where the measured white noise power is typically an order of magnitude higher than predicted. Resolving this discrepancy would be a significant advance. The theory of rf SQUIDs in both the hysteretic and nonhysteretic regimes is well established for the small fluctuation limit, but only the nonhysteretic regime has been investigated for large fluctuations. Detailed comparisons between experiment and theory tend to be hampered by the practical difficulty of measuring the critical current accurately. Predictions of particularly low noise energy for high-T_c devices in the nonhysteretic rf SQUID at angular frequencies exceeding R/L have yet to receive confirmation.

The wafer-scale fabrication process for low-T_c dc SQUIDs – involving Nb-AlO_x-Nb trilayer junctions – is well established, highly successful, and commercially available. The same is not true, unfortunately, for high-T_c dc and rf SQUIDs. The single greatest challenge in this regard is to develop a junction technology that is not only more reproducible than current methodologies but also capable of providing an I_0R product at 77 K that is substantially higher than the 200 μV or so available today. Multilayer circuit technology is still far from being perfected, and seems inevitably to produce higher levels of $1/f$ noise at low frequencies than single-layer processes. A fabrication technology for high-T_c junctions and multilayers that produces the same narrow spread of parameters, high yields and long-term stability as low-T_c devices would be a marvelous advance, but the challenges are formidable. Despite these difficulties, existing high-T_c SQUIDs are adequate for a number of applications, albeit at a higher cost than one would like.

Today, SQUIDs – especially low-T_c SQUIDs – have the lowest noise energy of any device, and are used for a broad range of applications at frequencies ranging from zero to several gigahertz. At frequencies above about 10 MHz, SQUIDs are operated open-loop. At lower frequencies they are generally operated in a flux-locked loop with room-temperature electronics. Even in SQUID systems with hundreds of channels, each channel is currently operated with its own flux-locked loop. A means of multiplexing groups of channels – say 32 or 64 – could offer a considerable saving, and substantially reduce the number of wires running down the cryostat. Both frequency-domain and time-domain multiplexers have been successfully demonstrated for arrays of superconducting transition-edge bolometers, but their application to biomagnetic measurements is not straightforward. The upper frequency limit of the flux-locked loop is generally set by propagation delays in the cables connecting the SQUID to the room-temperature electronics. The development of cryogenic, low-power semiconductor chips would enable one to place the electronics package much

closer to the SQUID and thus achieve a substantially higher frequency response and slew rate. However, there seems to be insufficient demand to drive this technology. Alternatively, one could imagine very fast on-chip electronics based on superconducting rapid single flux quantum (RSFQ) devices. Although these circuits are feasible in principle, it appears that substantial development and investment will be necessary to make them available in practice at a low enough cost to be attractive.

Obviously, a major factor in the broad application of SQUIDs is the need to cool them – the "cryogenic barrier." Liquid helium is expensive, its availability is geographically restricted, and its handling is relatively difficult and requires training in the necessary safety precautions. Liquid nitrogen is much more appealing with regard to all three issues. The development of inexpensive, long-lifetime, compact, magnetically and mechanically quiet cryocoolers would have a major impact on the exploitation of SQUIDs. It is noteworthy that the two "best-selling" SQUID systems – a magnetic susceptometer and a rock magnetometer – are available with cryocoolers. In both systems, however, the measurement chamber is magnetically shielded from the environment, so that the magnetic and vibrational noise from the cryocooler can be attenuated sufficiently. The task of producing a cryocooler quiet enough for a 300-channel biomagnetic system – which inevitably must be open to the environment – is considerably more challenging.

The two major challenges in the field – an improved high-T_c, thin-film technology and better cryocoolers – are not likely to be resolved inexpensively. One might well question whether current revenue from SQUID products will justify the investment. It is the age-old chicken-and-egg dilemma: "cryocoolers would be cheaper if only the demand were greater, and the demand would be greater if only they were cheaper." One might hope that other cryogenic applications would provide the incentives. For example, a significant growth of high-T_c devices in telecommunications is already beginning to reduce the prices of cryocoolers operating at 70 to 80 K. Similarly, if there were ever to be a significant market for high-T_c electronics – and the growth of such a market is not obvious today – there would be a stronger driver for an improved multilayer thin-film technology.

The future of the field of SQUIDs is more likely to be driven by new or more widespread applications than by advances in the SQUID technology. If there is going to be a large potential market, our crystal ball suggests that it is most likely to be in biomagnetism: for example, magnetoencephalography, magnetocardiography or magnetic resonance imaging. The rapid growth in the use of the SQUID readout of bolometers for far infrared and submillimeter astronomy on telescopes with 1000 or even 10,000 detectors may have a major impact on the field. The creative use of SQUIDs for "one-of" experiments in fundamental science – measurements that would otherwise be impossible – will continue to capture one's imagination. A good example is the use of dc SQUIDs to measure the quantum state of mesoscopic flux "qubits". No other detector is remotely close to having sufficient sensitivity or sufficiently low back-action for such measurements. Nonetheless, one should never underestimate the competition. Advances are being made in flux gate magnetometers, Hall effect sensors, giant and colossal magnetoresistive sensors, proton magnetometers and optical magnetometers that may enable these room-tempera-

ture devices to supplant the SQUID in certain applications. In particular, the feasibility of multichannel optically pumped atomic magnetometers and gradiometers was very recently demonstrated with a white magnetic field noise below 1 $fTHz^{-1/2}$ at frequencies between about 10 and 150 Hz [46]. To paraphrase Harold Weinstock's [47] maxim, "Never use a SQUID when a simpler, cheaper device will do."

1.9 Acknowledgment

This work was supported in part (JC) by the Director, Office of Science, Office of Basic Energy Sciences, Division of Material Sciences and Engineering of the U.S. Department of Energy under Contract No. DE-AC03-76SF00098.

References

1 London, F. (1950) *Superfluids*, Wiley, New York.
2 Deaver, B.S. and Fairbank, W.M. (1961) Experimental evidence for quantized flux in superconducting cylinders, *Phys. Rev. Lett.* **7**, 43–46.
3 Doll, R. and Näbauer, M. (1961) Experimental proof of magnetic flux quantization in a superconducting ring, *Phys. Rev. Lett.* **7**, 51–52.
4 Bardeen, J., Cooper, L.N. and Schrieffer, J.R. (1957) Theory of superconductivity, *Phys. Rev.* **108**, 1175–1204.
5 Giaever, I. (1960) Energy gap in superconductors measured by electron tunneling, *Phys. Rev. Lett.* **5**, 147–148.
6 Giaever, I. (1960) Electron tunneling between two superconductors, *Phys. Rev. Lett.* **5**, 464–466.
7 Josephson, B.D. (1962) Possible new effects in superconductive tunneling, *Phys. Lett.* **1**, 251–253.
8 Anderson, P.W. and Rowell, J.M. (1963) Probable observation of the Josephson superconducting tunneling effect, *Phys. Rev. Lett.* **10**, 230–232.
9 Rowell, J.M. (1963) Magnetic field dependence of the Josephson tunnel current, *Phys. Rev. Lett.* **11**, 200–202.
10 Shapiro, S., (1963) Josephson currents in superconducting tunneling: the effect of microwaves and other observations, *Phys. Rev. Lett.* **11**, 80–82.
11 Jaklevic, R.C., Lambe, J., Silver, A.H. and Mercereau, J.E. (1964) Quantum interference effects in Josephson tunneling, *Phys. Rev. Lett.* **12**, 159–160.
12 Silver, A.H. and Zimmerman, J.E. (1967) Quantum states and transitions in weakly connected superconducting rings, *Phys. Rev.* **157**, 317–341.
13 Zimmerman, J.E and Silver, A.H. (1966) Macroscopic quantum interference effects through superconducting point contacts, *Phys. Rev.* **141**, 367–375.
14 Clarke, J. (1966) A superconducting galvanometer employing Josephson tunneling, *Phil. Mag.* **13**, 115–127.
15 Clarke, J. (1967) Measurement of small voltages using a quantum interference device in *Proc. Symposium on the Physics of Superconducting Devices* B.S. Deaver, Jr. and W.S. Goree (Eds.), University of Virginia, Charlottesville.
16 Clarke, J., Goubau, W.M. and Ketchen, M.B. (1976) Tunnel junction dc SQUID: fabrication, operation and performance, *J. Low Temp. Phys.* **25**, 99–144.
17 Tesche, C.D. and Clarke, J. (1977) dc SQUID: noise and optimization, *J. Low Temp. Phys.* **27**, 301–331.
18 Kurkijärvi, J. (1973) Noise in the superconducting flux detector, *J. Appl. Phys.* **44**, 3729–3733.
19 Ketchen, M.B. and Jaycox, J.M. (1981) Planar coupling scheme for ultra low noise dc

SQUIDs, *IEEE Trans. Magn.* **MAG-17**, 400–403.

20 Gurvitch, M., Washington, M.A. and Huggins, H.A. (1983) High quality refractory Josephson tunnel junctions utilizing thin aluminum layers, *Appl. Phys. Lett.* **42**, 472–474.

21 Bednorz, J.G. and Müller, K.A. (1986) Possible high-T_c superconductivity in the Ba-La-Cu-O system, *Z. Phys.* **B64**, 189–193.

22 Clarke, J. (1988) Small-scale analog applications of high transition temperature superconductors, *Nature* **333**, 29–35.

23 Clarke, J. and Koch, R.H. (1988) The impact of high-temperature superconductivity on SQUID magnetometers, *Science* **242**, 217–223.

24 Colclough, M.S., Gough, C.E., Keene, M., Muirhead, C.M., Thomas, N., Abell, J.S. and Sutton, S. (1987) Radio-frequency SQUID operation using a ceramic high-temperature superconductor, *Nature* **328**, 47–48.

25 Zimmerman, J.E., Beall, J.A., Cromar M.W. and Ono R.H. (1987) Operation of Y-Ba-Cu-O rf SQUID at 81K, *Appl. Phys. Lett.* **51**, 617–618.

26 Koch, R.H., Umbach, C.P., Clark, G.J., Chaudhari, P. and Laibowitz, R.B. (1987) Quantum interference devices made from superconducting oxide thin films, *Appl. Phys. Lett.* **51**, 200–202.

27 Dimos, D., Chaudhari, P., Mannhart, J. and LeGoues, F.K. (1988) Orientation dependence of grain-boundary critical currents in $Yba_2Cu_3O_{7-\delta}$, *Phys. Rev. Lett.* **61**, 219–222.

28 Simon, R.W., Bulman, J.B., Burch, J.F., Coons, S.B., Daly, K.P., Dozier, W.D., Hu, R., Lee, A.E., Luiere, J.A., Platt, C.E., Schwarzbek, S.M., Wire, M.S. and Zani, M.J. (1991) Engineered HTS microbridges, *IEEE Trans. Magn.* **MAG-27**, 3209–3214.

29 Kingston, J.J., Wellstood, F.C., Lerch, Ph., Micklich, A.H. and Clarke, J. (1990) Multilayer $YBa_2Cu_3O_x$-$SrTiO_3$-$YBa_2Cu_3O_x$ films for insulating crossovers, *Appl. Phys. Lett.* **56**, 189–191.

30 Koch, R.H., Clarke, J., Goubau, W.M., Martinis, J.M., Pegrum, C.M. and Van Harlingen, D.J. (1983) *J. Low Temp. Phys.* **51**, 207–224.

31 Rogers, C.T. and Buhrman, R.A. (1984) Composition of l/f noise in metal-insulator-metal tunnel junctions, *Phys. Rev. Lett.* **53**, 1272–1275.

32 Dantsker, E., Tanaka, S. and Clarke, J. (1997) High-T_c SQUIDs with slots or holes: low l/f noise in ambient magnetic field, *Appl. Phys. Lett.* **70**, 2037–2039.

33 Stewart, W.C. (1968) Current-voltage characteristics of Josephson junctions, *Appl. Phys. Lett.* **12**, 277–280.

34 McCumber, D.E. (1968) Effect of ac impedance on dc voltage-current characteristics of superconductor weak-link junctions, *J. Appl. Phys.* **39**, 3113–3118.

35 Drung, D., Cantor, R., Peters, M., Scheer, H.J. and Koch, H. (1990) Low-noise high-speed dc superconducting quantum interference device magnetometer with simplified feedback electronics, *Appl. Phys. Lett.* **57**, 406–408.

36 Jackel, L.D. and Buhrman, R.A. (1975) Noise in the rf SQUID, *J. Low Temp. Phys.* **19**, 201–246.

37 Ehnholm, G.J. (1977) Theory of the signal transfer and noise properties of the rf SQUID, *J. Low Temp. Phys.* **29**, 1–27.

38 Likharev, K.K. (1986) *Dynamics of Josephson Junctions and Circuits*, Gordon Breach, New York.

39 Ryhänen, T., Seppa, H. Ilmoniemi, R. and Knuutila, J. (1989) SQUID magnetometers for low-frequency applications, *J. Low Temp. Phys.* **76**, 287–386.

40 Chesca, B. (1998) Theory of rf SQUIDs operating in the presence of large thermal fluctuations, *J. Low Temp. Phys.* **110**, 963–1001.

41 Zeng, X.H., Zhang, Y., Chesca, B., *et al.* (2000) Experimental study of amplitude-frequency characteristics of high-transition-temperature radio frequency superconducting quantum interference device, *J. Appl. Phys.* **88**, 6781–6787.

42 Hansma, P.K. (1973) Superconducting single-junction interferometers with small critical currents, *J. Appl. Phys.* **44**, 4191–4194.

43 Rifkin, R., Vincent, D.A., Deaver, B.S. and Hansma, P.K. (1976) Rf SQUIDs in the nonhysteretic mode: detailed comparison of theory and experiment, *J. Appl. Phys.* **47**, 2645–2650.

44 Kuzmin, L.S., Likharev, K.K., Migulin, V.V., Polunin, E.A,. Simonov, N.A. (1985) X-band parametric amplifier and microwave SQUID using single-tunnel-junction superconducting interferometer. In *SQUID'85, Superconducting Quantum Interference Devices and*

Their Applications, H.D. Hahlbohm and H. Lübbig, (eds.). Berlin: Walter de Gruyter, p. 1029–1034.

45 Zhang, Y. (2001) Evolution of HTS rf SQUIDs, *IEEE Trans. Appl. Supercond.* **11**, 1038–1042.

46 Kominis, I.K., Kornack, T.W., Allred, J.C. and Romalis, M.V. (2003) A subfemtotesla atomic magnetometer, *Nature* **422**, 596–599.

47 Weinstock, H. (1996) Introduction in *SQUID Sensors: Fundamentals, Fabrication and Applications*, H. Weinstock (Ed.) Kluwer, Dordrecht.

2
SQUID Theory

Boris Chesca, Reinhold Kleiner, Dieter Koelle

2.1 Josephson Junctions

The Josephson junction [1–4] consists of two weakly coupled superconducting electrodes. Different types of Josephson junctions have been investigated and used in practice [4]. Examples are point contact junctions, constriction type weak links, SNS or SIS junctions. In the latter two cases the superconducting electrodes are separated by a thin normal conducting (N) or insulating (I) layer, respectively. For details on the geometry and fabrication of various junction types we refer to Chapter 3. In the widely used SIS junction the current transport occurs via tunneling of Cooper pairs and quasiparticles. In general, if the coupling is weak enough, the supercurrent I_s across the junction is related to the gauge invariant phase difference δ of the phases of the macroscopic wave functions of the two superconducting electrodes via a function f(δ) which is 2π-periodic and which can be expanded in a Fourier series in δ (see Appendix A.1.3). As shown by Josephson [1,2] for the SIS tunnel junction one finds

$$I_s = I_0 \sin\delta \,, \tag{2.1}$$

where I_0 is the maximum supercurrent (critical current). Equation (2.1) is known as the first Josephson equation and holds for many junction types used in practice. Here, we restrict our discussion to the case of small junctions with homogeneous critical current density $j_0 = I_0 / A_J$ within the junction cross-section of area A_J, as only this case is relevant for SQUIDs. In the general case, the critical current density j_0 and the gauge invariant phase difference may vary within the cross-section of the junction (in the x-y-plane in Fig.A.1.3).

If the phase difference δ changes with time, a voltage U is developed across the junction, as given by the second Josephson relation

$$\dot{\delta} \equiv \frac{d\delta}{dt} = \frac{2e}{\hbar} U = \frac{2\pi}{\Phi_0} U. \tag{2.2}$$

Here, $\Phi_0 \equiv h/2e \approx 2.07\times10^{-15}$ Vs is the magnetic flux quantum. For zero applied current, the two electrodes are coupled by the Josephson coupling energy $E_J = I_0\Phi_0/2\pi$, which can be found by direct integration of the product $U \cdot I$, using equations (2.1) and (2.2). In the zero-voltage state, the phase difference is constant

in time (static case) if we neglect plasma oscillations, which are discussed below. In this static regime, according to (2.1) a dc supercurrent with maximum value I_0 can flow across the junction. In the dynamic regime, that is for voltages $U \neq 0$, the Josephson current oscillates with the Josephson frequency $\omega_J \equiv 2\pi V/\Phi_0$ (or $f_J = \omega_J/2\pi = V/\Phi_0 \approx V \times 483.6$ MHz/μV). Note that we here denote V as the time averaged dc voltage across the Josephson junction. In addition one has to consider a displacement current I_d and a quasiparticle current I_{qp}. While the expressions for I_s, I_{qp} and I_d can be quite complex in general [3,4], for many practical situations, e.g. for a resistively shunted tunnel junction, one may simply approximate I_{qp} and I_d by an ohmic shunt resistor and a capacitor, respectively, both connected in parallel to the Josephson element. This leads to the widely used "resistively- and capacitively-shunted junction model" (RCSJ-model) [5,6] which is described in the next section.

2.1.1 RCSJ Model

A high-quality tunnel junction has a hysteretic current–voltage (I–V) characteristic. As the bias current is increased from zero, the voltage switches abruptly to a non-zero value when I exceeds I_0, but returns to zero only when I is reduced to a value much less than I_0. This hysteresis must be eliminated for SQUIDs operated in the conventional manner. For tunnel junctions fabricated from low transition temperature (low-T_c) superconductors this is usually done by shunting the junction with an external shunt resistance. The current–voltage characteristics of such junctions are well-explained by the resistively- and capacitively-shunted junction (RCSJ) model [5,6]. In this model, the Josephson element has a critical current I_0 and is in parallel with its self-capacitance C and a resistance R, which has a current noise source I_N (t) associated with it. We note that the RCSJ model neglects any spatial dependence of junction parameters within the junction cross-section, in other words, this model assumes point-like junctions. The most important simplification is the assumption of a linear resistance R, both below and above the gap voltage. For junction models, which avoid these simplifications, such as the nonlinear resistive (RSJN) model or the tunnel junction microscopic (TJM) model, see [4].

The equivalent circuit of a Josephson junction in the RCSJ-model is shown in Fig. 2.1(a). Using Kirchhoff's law we find

$$C\dot{U} + \frac{U}{R} + I_0 \sin\delta = I + I_N(t)\,. \tag{2.3}$$

Using the second Josephson relation (2.2), and neglecting the noise term for the moment, we find the equation of motion for the phase difference δ across the Josephson junction as

$$\frac{\Phi_0}{2\pi} C\ddot{\delta} + \frac{\Phi_0}{2\pi}\frac{1}{R}\dot{\delta} = I - I_0 \sin\delta = -\frac{2\pi}{\Phi_0}\frac{\partial U_J}{\partial \delta}\,, \tag{2.4}$$

where we define the so-called *tilted washboard potential* U_J of the Josephson junction as

$$U_J \equiv \frac{\Phi_0}{2\pi}\left\{I_0(1-\cos\delta) - I\delta\right\} = E_J\{1-\cos\delta - i\delta\}\,, \tag{2.5}$$

with the normalized bias current $i \equiv I/I_0$. The amplitude of the potential is given by the Josephson coupling energy E_J. As the normalized potential we define $u_J \equiv U_J/E_J = 1\text{–}\cos\,\delta - i\delta$.

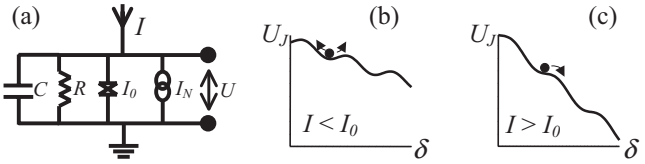

Fig. 2.1 (a) Equivalent circuit of the resistively- and capacitively-shunted Josephson junction; (b) and (c) show the tilted washboard potential for $I < I_0$ and $I > I_0$.

Equation (2.4) describes the dynamics of the phase difference δ in analogy to the motion of a point-like particle of mass m and friction coefficient ξ moving on the tilted washboard potential in a mechanical model (along the coordinate x), which is in a general form governed by the equation of motion

$$m\ddot{x} + \xi\dot{x} = -\frac{\partial w(x)}{\partial x} + F_d = -\frac{\partial[w(x) - F_d x]}{\partial x}. \tag{2.6}$$

Here F_d is an external driving force, which tilts the potential w. Turning from the mechanical model to the Josephson junction, the coordinate x is replaced by δ, and the velocity $\dot{x}$ by $\dot{\delta} \sim U$. The mass corresponds to the capacitance and the friction coefficient to the conductance $1/R$. The bias current I corresponds to the external force, which tilts the cosine-shaped potential. In the static case, for $I<I_0$, the particle is confined to one of the potential minima (cf. Fig. 2.1(b)), where it oscillates back and forth at the plasma frequency

$$\omega_{p,i} = \omega_p\left[1 - i^2\right]^{1/4} \quad \text{with} \quad \omega_p = \left(\frac{2\pi}{\Phi_0}\frac{I_0}{C}\right)^{1/2}. \tag{2.7}$$

The time average of $\dot{\delta}$, and hence the time averaged dc voltage V, is zero in this state. As the current I exceeds I_0, the local minima in the washboard potential disappear (cf. Fig. 2.1(c)), and the phase difference evolves in time. This dynamic case is hence associated with a finite dc voltage V across the junction which increases with increasing bias current.

As the bias current is reduced from above I_0, the particle becomes trapped in one of the wells of the washboard at a current which depends on the inertial term, given by the capacitance of the junction. Rewriting (2.4) with the normalized bias current and with the characteristic frequency $\omega_c \equiv 2\pi I_0 R/\Phi_0$, which is the Josephson frequency at the characteristic voltage $V_c \equiv I_0 R$, we get

$$\frac{\ddot{\delta}}{\omega_p^2} + \frac{\dot{\delta}}{\omega_c} = i - \sin\delta = -\frac{\partial u_J}{\partial \delta}\,, \tag{2.8a}$$

or

$$\beta_c \frac{\ddot{\delta}}{\omega_c^2} + \frac{\dot{\delta}}{\omega_c} = i - \sin\delta = -\frac{\partial u_J}{\partial \delta}. \tag{2.8b}$$

Here we introduce the Stewart–McCumber parameter

$$\beta_c \equiv \left(\frac{\omega_c}{\omega_p}\right)^2 = \frac{2\pi}{\Phi_0} I_0 R^2 C = \frac{2\pi}{\Phi_0} j_0 \rho_J^2 c_J\,, \tag{2.9}$$

with the product of normal resistance times the junction cross-section $\rho_J \equiv R \cdot A_J$ and the capacitance per junction cross-section $c_J \equiv C/A_J$. Note that the characteristic frequencies ω_c, ω_p and $\omega_{RC} = 1/RC$ are related by $\omega_p^2 = \omega_c \omega_{RC}$. Therefore the Stewart–McCumber parameter can be expressed in various ways as the ratios $\beta_c = (\omega_c/\omega_p)^2 = (\omega_p/\omega_{RC})^2 = \omega_c/\omega_{RC}$ of those frequencies. Furthermore, it may be convenient to introduce the normalized time $\tau \equiv t \cdot \omega_c$. In this case, the characteristic frequency disappears in (2.8b).

Equation (2.8), which is valid in the absence of noise, shall be considered for the two limiting cases, (i) if $\beta_c << 1$ (strongly *overdamped limit*) and (ii) if $\beta_c >> 1$ (strongly *underdamped limit*).

In the strongly overdamped limit ($\beta_c << 1$) the inertial term in (2.4) or (2.8) is negligible, which corresponds to a negligible junction capacitance. In this limit the RCSJ model reduces to the so-called RSJ model which is most often used for practical SQUIDs. A negligible inertial term means that by reducing the bias current from above I_0, the particle gets trapped instantly in one of the minima of the washboard potential at $I = I_0$, which results in non-hysteretic I–V characteristics. Solving (2.8) with $\beta_c = 0$ one finds for the normalized time dependent voltage $u = U/I_0 R$

$$u = 0 \quad \text{for} \quad I < I_0 \tag{2.10a}$$

$$u(t) = \frac{i^2 - 1}{i + \cos\omega t} \quad \text{for} \quad I > I_0 \quad \text{with} \quad \omega = \omega_c \sqrt{i^2 - 1}\,. \tag{2.10b}$$

As shown in Fig. 2.2(a) for $i > 1$ the voltage u oscillates with frequency ω, which increases with increasing bias current. The normalized time averaged voltage $v = V/I_0 R$ is zero for $i < 1$ and increases also with increasing i according to

$$v = \sqrt{i^2 - 1} \quad \text{for} \quad i > 1\,, \tag{2.11}$$

as shown in Fig. 2.2(b).

In the strongly underdamped limit ($\beta_c >> 1$) the characteristic Josephson frequency is much higher than the relaxation frequency ω_{RC}. Hence, the dynamics of the junctions is solely determined by the *R-C*-circuit, leading to a simple ohmic response of the average voltage to a dc current drive. Hence, in the dynamic regime

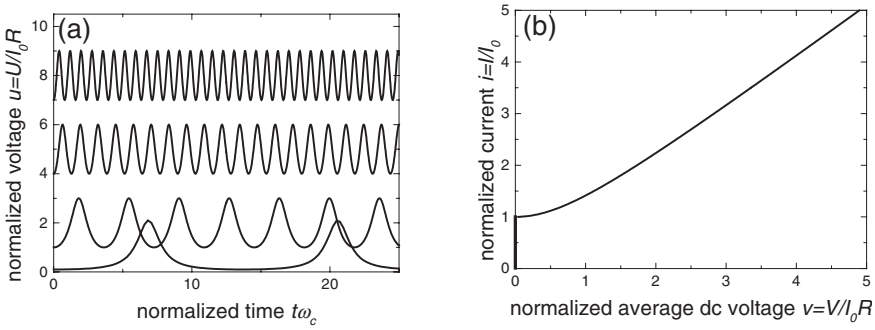

Fig. 2.2 Characteristics for a strongly overdamped junction calculated within the RSJ model: (a) Normalized voltage vs. time [from (2.10b)] for normalized bias currents $i = 1.1$, 2, 5 and 8 (from bottom to top); (b) normalized current vs dc voltage [from (2.11)] .

the dc voltage stays finite even for $i<1$ until the current is reduced to zero. In contrast, when the current is increased from zero the junction stays in the zero voltage state until $i = 1$, resulting in highly hysteretic I–V characteristics.

In the general case of finite β_c the dynamics of the junction can be obtained by numerical solution of (2.8). Figure 2.3(a) shows the result of calculated I–V characteristics for various values of β_c. Decreasing the bias current from above I_0, the zero voltage state is reached at the return critical current $I_r(\beta_c)$. The ratio $i_r = I_r/I_0$ as a function of β_c decreases monotonically from 1 to 0 for increasing β_c, as shown in Fig. 2.3(b) [6]. For comparison we also show the approximated analytical solutions $\beta_c = \{2 - (\pi - 2)i_r\}/i_r^2$ in the limit $0.05< i_r <0.95$ [7] and $i_r = 4/(\pi\sqrt{\beta_c})$, which has been derived in the limit $\beta_c >> 1$ [4].

In order to obtain non-hysteretic I–V characteristics with low-T_c tunnel junctions, one usually places a shunt resistor across the junction to reduce β_c below 1. In the noise-free case discussed above, a significant hysteresis is present for $\beta_c \gtrsim 1$. However, as will be shown below, at nonzero temperature, the thermal noise of the shunt resistor may suppress the hysteresis if β_c is not too large. Furthermore, we note that

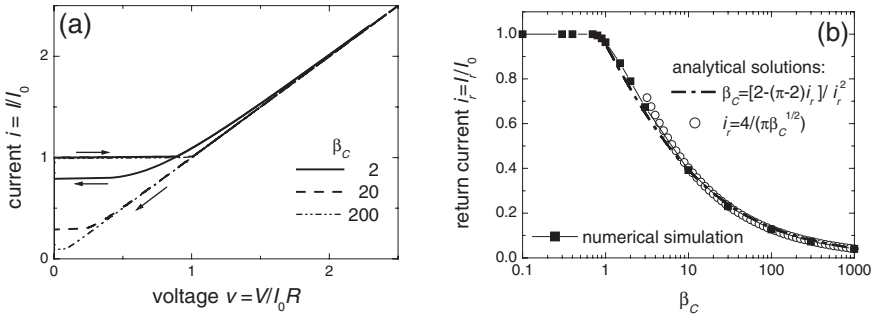

Fig. 2.3 (a) Hysteretic current voltage characteristics, calculated within the RCSJ model for various values of β_c (arrows indicate direction of bias current sweep); (b) return current vs. β_c .

for many high-T_c Josephson junctions the RCSJ-model seems also to be a reasonably good approximation. In fact, most of these junctions seem to be intrinsically shunted [8,9], yielding values of $\beta_c < 1$ for a typical operation temperature of $T = 77$ K.

So far, we have considered only the Josephson junction in the RSJ-model for a dc current drive. An additional feature emerges if we bias the junction with an additional sinusoidal ac current drive $I_{ac}\sin\omega_{ac}t$. Using the RSJ model for strongly overdamped junctions with current bias, one has to solve the modified equation of motion for the phase difference

$$\frac{\dot{\delta}}{\omega_c} = i + i_{ac}\sin\omega_{ac}t - \sin\delta, \tag{2.12}$$

with the normalized ac current amplitude $i_{ac} = I_{ac}/I_0$. The most noticeable consequence of the ac signal is the occurrence of constant voltage steps (Shapiro steps) in the IV-curves [10] at dc voltages

$$V_n = nV_1 = n\frac{\Phi_0}{2\pi}\omega_{ac} \quad (n = 0,1,2...), \tag{2.13}$$

as shown in Fig. 2.4. Using the mechanical analog of a particle in the washboard potential which is now tilted periodically, with an amplitude determined by I_{ac}, around an average tilt determined by the dc bias current I, the appearance of Shapiro steps corresponds to the synchronization of the motion of the particle with the external drive at frequency ω_{ac}. At the n-th Shapiro step the particle moves along n minima of the washboard potential within one period of the external excitation. Hence the velocity of the particle does not depend on the average tilt (dc bias current) within a certain interval which corresponds to the height ΔI_n of the n-th step. In this regime the average velocity, and hence the dc voltage is solely determined by the excitation frequency ω_{ac} as given in (2.13). The normalized height $\Delta i_n = \Delta I_n/I_0$ of the n-th Shapiro step depends strongly on the amplitude and frequency of the ac drive and shows an oscillatory behavior with increasing I_{ac}. In the limit of large ac frequency $\Omega \equiv \omega_{ac}/\omega_c \geq 1$ these oscillations are described by first-kind Bessel functions of order n [11]

$$\Delta i_n = \left| J_n(x) \right| \quad \text{with} \quad x \equiv \frac{i_{ac}}{\Omega}\frac{1}{\sqrt{1+\Omega^2\beta_c}} \tag{2.14}$$

For more details we refer to [4].

To conclude our discussion of the RCSJ model in the noise-free case, we mention that deviations from this simple model are frequently observed which may have various origins. Fist of all, the sinusoidal current-phase-relation (CPR) , equation (2.1), as predicted by Josephson [1,2] for ideal SIS tunnel junctions from conventional superconductors, has been confirmed by various experiments [12]. In contrast, for SNS junctions the supercurrent is still a 2π-periodic function of δ but deviations from the sinusoidal dependence, with a sawtooth-like function that contains higher harmonic components such as $\sin(n\delta)$, can be quite substantial unless the effective spacing between the superconducting electrodes is less than approximately three

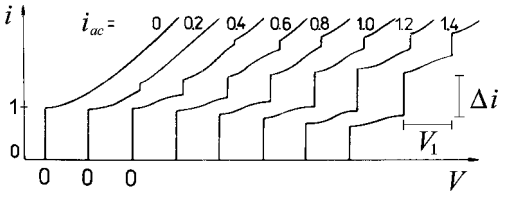

Fig. 2.4 I–V curves of a Josephson junction driven by a dc current and an additional ac current of different normalized amplitudes $i_{ac} = I_{ac}/I_0$ at frequency $\omega_{ac} = \omega_c$, calculated within the RSJ model (adapted from [4]).

times the normal layer coherence length [4]. Analysis of the RCSJ model with a modified CPR shows a significant effect on the *IV*-curves, e.g. the appearance of an "excess current" or a modification of the hysteretic behavior in the *IV*-curves [13]. Other sources of such an excess current are due to superconducting shorts through the barrier, or Andreev reflection at the barrier interfaces. Obviously, the RCSJ model fails in the description of junctions which do not have a linear resistance. In this case the RSJN model or the TJM model provides much better agreement with experimental data. For a more detailed discussion on deviations from the RSJ-model in weak links formed from low-T_c superconductors we refer to references [4,12].

For most high-T_c superconductors there is convincing evidence for a *d*-wave pairing state with an internal phase of the pair potential [14] (see also the Appendix, A.1.2). Important effects of the internal phase on the Josephson current were predicted theoretically. Such predictions are supported by several experiments using high-T_c Josephson junctions and SQUIDs, which detect a π-phase shift between the *a*- and *b*-axis directions and fractional flux quanta. In addition, the existence of new interference effects in the quasiparticle states near surfaces and boundaries has been suggested theoretically and has been supported by tunneling spectroscopy data, which showed zero-bias conductance peaks (ZBCPs). These ZBCPs reflect the formation of zero-energy states (ZES) on the surface due to the π-phase shift of the internal phase in the *d*-wave pairing symmetry. The formation of ZES greatly influences the transport properties of quasiparticles in tunnel junctions. Similar effects are also expected in the dc Josephson current for junctions made from *d*-wave superconductors. For details on tunneling effects in unconventional superconductors we refer to reference [15]. In this context, it should not be surprising to observe deviations from the RCSJ-behavior in high-T_c junctions. Most experimental work regarding this issue has been performed on grain boundary Josephson junctions (GBJs), where the orientation of the crystal axis changes across the barrier [16]. Fortunately, deviations from the RCSJ-model in such junctions seem to be pronounced only for large misorientation angles up to 45°, which are not of importance for practical SQUIDs.

Experiments based on the method developed by Rifkin and Deaver [17] revealed a clear deviation from a sinusoidal CPR only for symmetric 45° [001] tilt grain boundaries in YBCO bicrystal junctions [18]. In contrast, no such deviation was found for other junction types,(e.g. step-edge-, ramp-type or ion irradiated junctions) or for

bicrystal junctions with smaller misorientation angles such as 30° or 24°, which are widely used for high-T_c SQUIDs. The sign of the deviation $\Delta I_s = I_s - I_0 \sin\delta$ which is positive for point contact or SNS junctions from low-T_c superconductors [12], has been shown to be negative (with a shift of the maximum supercurrent towards larger δ) for 45° YBCO GBJs. It has been shown recently [19] that this observation can be attributed to the strongly inhomogeneous nature of large-angle GBJs with a randomly distributed alternating current density [20]. The strong faceting, together with the *d*-wave pairing symmetry favors the formation of π-junctions and leads also to a very irregular $I_c(B)$ pattern in large-angle GBJs [21]. Again, these deviations seem to be most pronounced for large misorientation angles in the case of GBJs, which, however, are not frequently used for practical devices. On the other hand, inhomogeneity is certainly a problem of all high-T_c junctions and probably the most significant source of deviations from the RSJ-model. This tendency to strong nonuniformity is consistent with the large spread in junction parameters.

The physical reason behind this lies in the short and highly anisotropic coherence length. As a result, the properties of high-T_c materials are highly susceptible to structural and chemical changes on atomic length scales. This can lead to a strong suppression of the superconducting order parameter at a superconductor-insulator interface, in turn reducing the I_0R product substantially [22]. Furthermore, the barrier materials are generally oxides close to a metal-insulator transition with a complex crystal structure and a strong sensitivity to defects on an atomic scale. As a result, transport across the barrier is highly dependent on microstructural imperfections in the barrier and at its interface with the electrodes.

2.1.2 Thermal Noise

So far, we have discussed the characteristics of Josephson junctions without the consideration of noise. We will now consider the effect of thermal fluctuations, which can have an appreciable effect, in particular for high-T_c devices operated at 77K. We mainly restrict ourselves to the discussion of thermal noise in the frame of the RCSJ model which, for example, can lead to a significant rounding of the dc current–voltage characteristics.

In the presence of noise, the current $I(t)$ may fluctuate about its mean value, which for simplicity we assume to be zero. An important quantity which describes the correlation of values of $I(t)$ at different times is the correlation function $\langle I(t)I(t+t_i)\rangle$. The brackets specify a statistical average over probabilities of values for I at different times. Note, that in the case of a stationary process, the correlation function does not depend on time t , but only on the time interval t_i. For a description of fluctuation phenomena it is often advantageous to shift from the time domain to the frequency domain. In the latter, an important quantity is the spectral density of current noise S_I, which is the mean-square current noise per unit interval of frequency. Using the RCSJ model, we assume that the conductance of the Josephson junction does not depend on frequency. This results in the classical Nyquist–Johnson formula for thermal noise

$$S_I(\omega) = \frac{2k_B T}{\pi R} \tag{2.15}$$

in the resistor R at temperature T, where k_B is the Boltzmann constant. Using the well-known Wiener–Khintchine theorem

$$\langle I(t)I(t+t_i)\rangle = \int_0^\infty S_I(\omega)\cos(\omega t_i)\, d\omega \tag{2.16}$$

one can calculate the corresponding correlation function

$$\langle I(t)I(t+t_i)\rangle = \frac{2k_B T}{\pi R}\int_0^\infty \cos(\omega t_i)\, d\omega = \frac{2k_B T}{R}\delta(t_i), \tag{2.17}$$

with the definition of the delta function $\delta(t) = \frac{1}{\pi}\int_0^\infty \cos(\omega t)\, d\omega$. Hence, the thermal noise current has no correlation in time, and results in a white (frequency independent) power spectrum, with Gaussian distributed amplitudes and zero average $\langle I(t)\rangle = 0$ (Gaussian white noise). Strictly speaking, (2.15) is only valid in the limit $k_B T >> eV, \hbar\omega$ [4]. At high frequencies, quantum fluctuations may become important.

Using the Langevin approach means that we simply add a random force $F_N(t)$ to the driving force $F_d(t)$ in the equation of motion (2.6). For the description of the Josephson junction, including the effect of noise, this corresponds to the addition of a fluctuating noise current $I_N(t)$ in the RCSJ model, as already included in (2.3). Note that, due to the symmetric distribution of the noise current amplitudes around zero, one can add the term $I_N(t)$ also on the left-hand side in (2.3). Using the tilted washboard potential picture one can modify (2.5) to include the noise current as

$$U_{J,N} = E_J\left\{1 - \cos\delta - \left[i + i_N(t)\right]\delta\right\}, \tag{2.18}$$

which means that the average tilt i of the washboard potential fluctuates with normalized amplitude $i_N \equiv I_N/I_0$. In the thermal limit i_N is treated as white noise with normalized spectral density

$$S_i(\omega) = \frac{2\Gamma}{\pi\omega_c} \quad \text{or} \quad S_i(f) = \frac{4\Gamma}{\omega_c}, \tag{2.19}$$

where we have defined the noise parameter Γ as the ratio of the thermal energy over the Josephson coupling energy

$$\Gamma \equiv \frac{k_B T}{E_J} = \frac{2\pi k_B T}{I_0 \Phi_0}. \tag{2.20}$$

In the time domain, the noise current is described by the statistical properties

$$\langle i_N(t)\rangle = 0 \quad \text{and} \quad \langle i_N(t) i_N(t+t_i)\rangle = \frac{2\Gamma}{\omega_c}\delta(t_i). \tag{2.21}$$

The effect of the fluctuating current on the dc IV-characteristics can easily be understood in the picture of the tilted washboard potential. For $I<I_0$ the fluctuating tilt can cause the total current $I+I_N(t)$ to exceed I_0, which enables the particle to roll out of the potential minimum to the next. For the overdamped junction this produces a series of voltage pulses randomly spaced in time. Hence, the time averaged dc voltage V becomes finite, even for $I<I_0$. As an obvious consequence, the I–V-characteristics are "noise rounded" at low voltages, as shown in Fig. 2.5(a) for negligible junction capacitance ($\beta_c = 0$).

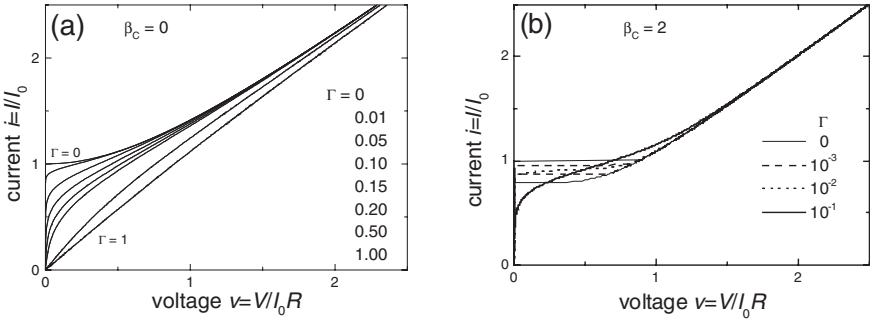

Fig. 2.5 I–V curves of a Josephson junction calculated for various values of the thermal noise parameter Γ within the RCSJ model, for negligible capacitance (a) and finite capacitance (b).

To obtain the dc IV-curves one can numerically solve the Langevin equation

$$\beta_c \frac{\ddot{\delta}}{\omega_c^2} + \frac{\dot{\delta}}{\omega_c} = i + i_N(t) - \sin\delta \equiv f_\delta(\delta) + i_N(t), \tag{2.22}$$

with the effective "force"

$$f_\delta(\delta) \equiv -\frac{\partial u_J}{\partial \delta} = i - \sin\delta \tag{2.23}$$

as obtained from the gradient of the tilted washboard potential. The noise currents are implemented as Gaussian distributed random numbers with the normalization of (2.19) [23]. For details on the numerical simulations we refer to Section 2.2.3.2. Due to the thermal noise, the observed value of the critical current (zero voltage state) is reduced with increasing value of Γ and vanishes at $\Gamma \approx 0.2$, as shown in Fig. 2.5(a). Including a finite junction capacitance, one finds that the hysteresis in the IV-curve is suppressed, as shown in Fig. 2.5(b), which was obtained by numerical solution of (2.22) for $\beta_c = 2$ and various values of Γ.

Obviously, the thermal fluctuations "destroy" the Josephson coupling if T is large enough or I_0 is small enough. Rewriting the expression for the noise parameter as $\Gamma = I_{th}/I_0$, one can define a thermal noise current I_{th} as

$$I_{th} \equiv \Gamma I_0 = \frac{2\pi}{\Phi_0} k_B T\,. \tag{2.24}$$

To maintain a reasonable degree of Josephson coupling, which means keeping $\Gamma \lesssim 1$, results in the requirement $I_{\mathrm{th}} \lesssim I_0$ for the maximum Josephson current, with $I_{th} = 176$ nA at $T = 4.2$ K and $I_{th} = 3.23$ μA at $T = 77$ K. Typical values for Γ used in SQUIDs are below 0.1. However, as discussed in Sections 2.2 and 2.3, for high-T_c SQUIDs it may be advantageous to use rather large values of Γ approaching unity, in order to obtain optimum performance at T=77. In this case the effect of thermal fluctuations becomes very important.

Finally, we mention an alternative approach to the description of the effect of thermal noise on Josephson junctions, which was originally used by Ivanchenko and Zilberman [24] and by Ambegaokar and Halperin [25]. In the limit of thermal fluctuations, $I_N(t)$ is a Markoffian process, which can be described by using the Fokker–Planck equation. As the general theory of Brownian motion shows [26,27], the Langevin equation (2.22), which was obtained within the RCSJ model, is equivalent to the Fokker–Planck equation

$$\frac{1}{\omega_c}\frac{\partial \sigma}{\partial t} + \frac{\partial(\sigma u)}{\partial \delta} + \frac{1}{\beta_c}\frac{\partial}{\partial u}\left\{\sigma\left[f_\delta(\delta) - u\right]\right\} = \frac{\Gamma}{\beta_c^2}\frac{\partial^2 \sigma}{\partial u^2}, \tag{2.25}$$

with the effective "momentum" (normalized voltage) $u = \omega_c^{-1}\dot{\delta}$. The Fokker–Planck equation describes the probability density $\sigma(t, \delta, u)$ of finding the system at the point [δ,u] in phase space at the moment t. From the solution of (2.25) one can then calculate the statistical average of any variable $X(t, \delta, u)$as

$$\langle X\rangle(t) = \int_{-\infty}^{+\infty} d\delta \int_{-\infty}^{+\infty} du\, \sigma(t, \delta, u) X(t, \delta, u). \tag{2.26}$$

In the strongly overdamped limit ($\beta_c \to 0$) for the RSJ model, the Fokker–Planck equation (2.25) can be reduced to the Smoluchowski equation for the distribution function $\sigma(t, \delta) \equiv \int_{-\infty}^{+\infty} du\, \sigma(t, \delta, u)$ in the coordinate space alone

$$\frac{\partial \sigma}{\partial t} = \omega_c \Gamma \frac{\partial^2 \sigma}{\partial \delta^2} - \omega_c \frac{\partial}{\partial \delta}\left[f_\delta \sigma\right] \equiv -\frac{\partial i_\sigma}{\partial \delta}. \tag{2.27}$$

From the probability conservation law we can interpret i_σ as the probability flow

$$i_\sigma \equiv -\omega_c\left[-f_\delta \sigma + \Gamma \frac{\partial \sigma}{\partial \delta}\right] = -\omega_c \Gamma e^{-\frac{u_J}{\Gamma}} \frac{\partial}{\partial \delta}\left[\sigma e^{\frac{u_J}{\Gamma}}\right], \tag{2.28}$$

with the normalized potential $u_J \equiv U_J/E_J$. With the definition of Γ we can also write the exponents in (2.28) as $u_J/\Gamma = U_J/k_BT$. Finding a stationary solution of (2.27) requires i_σ = const. With the normalization of σ to unity, one finds that $1/i_\sigma$ is the average time for the particle to diffuse one period in the washboard potential, that is for the phase difference δ to change by 2π. Hence we get for the average normalized voltage

$$\langle u\rangle \equiv \frac{\langle U\rangle}{V_c} = \frac{1}{\omega_c}\langle \dot{\delta}\rangle = \frac{2\pi i_\sigma}{\omega_c}. \tag{2.29}$$

Finally, with the periodic boundary condition $\sigma(\delta) = \sigma(\delta + 2\pi)$, one finds the solution for the average voltage as

$$\langle u \rangle = 2\pi\Gamma \left(e^{\frac{2\pi i}{\Gamma}} - 1 \right) \left\{ \int_0^{2\pi} d\delta \int_0^{\delta} d\delta' \, e^{\frac{\left[u_J(\delta) - u_J(\delta')\right]}{\Gamma}} + e^{\frac{2\pi i}{\Gamma}} \int_0^{2\pi} d\delta \int_{\delta}^{2\pi} d\delta' \, e^{\frac{\left[u_J(\delta) - u_J(\delta')\right]}{\Gamma}} \right\}^{-1} . \tag{2.30}$$

By numerical integration of (2.30) one can obtain the dc IV-characteristics for various values of Γ [25]. For further details and the treatment for finite β_c we refer to [3,4].

2.1.3 The $1/f$ Noise (I_0, R fluctuations)

The white noise of Josephson junctions due to thermal fluctuations limits the sensitivity of SQUIDs over a wide frequency range in many practical applications. However, some applications, for example in biomagnetism, require operation at low frequencies down to 0.1 Hz or less, where $1/f$ noise ("flicker" noise) becomes important. There are two major sources of $1/f$ noise in SQUIDs. One is due to the motion of flux lines (vortices) trapped in the body of the SQUID, which will be discussed in Sections 5.5 and 6.4. The other source of $1/f$ noise, which will be discussed now, is due to fluctuations in the Josephson junctions.

In contrast to thermal noise, $1/f$ noise is much less understood, even for systems in thermal equilibrium (for a review on $1/f$ noise in condensed matter systems we refer to Refs. [28,29]). Moreover, these fluctuations seem to be more accurately described by system parameter fluctuations rather than by a Langevin force F_N(t). For Josephson tunnel junctions an appropriate description has been developed [30], which is based on fluctuations of the critical current I_0 of the Josephson junction. Such fluctuations may occur in the process of tunneling through the barrier due to trapping and subsequent release of an electron in a defect in the tunneling barrier. Occupation of the trap induces a local change in the height of the tunnel barrier and hence in the critical current density of that region. Hence, a single trap leads to a randomly switching critical current I_0 of the junction between two values. Such a process produces a random telegraph signal (RTS) with a Lorentzian spectral density

$$S(f) \propto \frac{\tau}{1 + (2\pi f \tau)^2} , \tag{2.31}$$

which is white at low frequencies and which falls off as $1/f^2$ above $1/2\pi\tau$. Here, τ is the mean time between pulses and, for a thermally activated trapping process, given by

$$\tau = \tau_0 \, e^{\frac{E}{k_B T}} , \tag{2.32}$$

where τ_0 is a constant and E is the barrier height. Experiments on Nb-Al_2O_3-Nb junctions with a single trap [31] showed approximately Lorentzian switching processes. The temperature dependence of the RTS could be described by (2.32) with $\tau_0 \approx 0.1$ s and $E = 1.8$ meV.

For junctions with several traps one can assume that each trap has its own characteristic time τ_i, producing statistically independent switching. In that case one can superimpose the trapping processes to obtain a spectral density [28]

$$S(f) \propto \int dE\, D(E) \left[\frac{\tau_0\, e^{\frac{E}{k_B T}}}{1+(2\pi f \tau_0)^2\, e^{\frac{2E}{k_B T}}} \right], \tag{2.33}$$

where $D(E)$ is the distribution of activation energies. The term in square brackets is a strongly peaked function of E, centered at $\tilde{E} \equiv k_B T \ln(1/2\pi f \tau_0)$, with a width $\sim k_B T$. Thus, at a given temperature, only traps with energies within a range $\tilde{E} - k_B T < E < \tilde{E} + k_B T$ contribute significantly to the noise. Assuming a broad distribution $D(E)$ with respect to $k_B T$, one can take $D(\tilde{E})$ outside the integral, and obtain a $1/f$-like spectrum

$$S(f, T) \propto \frac{k_B T}{f} D(\tilde{E}), \tag{2.34}$$

even from just a few traps. Traps in the barrier enable electrons to tunnel at voltages below the gap voltage, a process producing both leakage current and $1/f$ noise. Therefore, the magnitudes of the $1/f$ noise from I_0 fluctuations and of the leakage current are related and depend strongly on the quality of the tunnel junction.

Most Josephson junctions made from high-T_c superconductors exhibit large levels of low-frequency $1/f$ noise arising from fluctuations of the critical current and the junction resistance [32–34]. The normalized spectral densities $s_I \equiv S_I / I_0^2$ and $s_R \equiv S_R / I_0^2$ for critical current and resistance fluctuations, respectively, are temperature independent and proportional to the junction resistance [35]. One typically finds $s_I \cdot f \approx 10^{-8} R/\Omega$, which is about three orders of magnitude larger than for Nb tunnel junctions with shunt resistances of a few ohms [31,36]. Furthermore, the relation $(s_I/s_R)^{1/2} \approx 1/(1-p)$ observed for grain boundary junctions (GBJs) [9,34] strongly suggests that the low-frequency noise and the approximate scaling $j_0 \rho_J \propto j_0^p$ with $p \approx 0.5$ [37] have the same microscopic origin. The details of this mechanism are still controversial. One model, which predicts an origin of low-frequency noise similar to the tunnel junctions described above, assumes that resonant tunneling of quasiparticles via localized states in an insulating barrier, acts as an intrinsic normal shunt [8]. This model, known as the intrinsically-shunted junction (ISJ) model, naturally explains the low I_0R product of high-T_c junctions in terms of an intrinsic shunt due to a high density of localized states in the barrier. The trapping and release of charge carriers in localized states lead to fluctuations in the local barrier height which cause I_0 and R to fluctuate with antiphase correlation, as observed experimentally [38], thus explaining the high level of $1/f$ noise in junctions with a high density of localized states.

2.2
Theory of the dc SQUID

2.2.1
Introduction

In the following section we introduce some basic theoretical aspects of dc SQUIDs. We will start with a discussion of dc SQUID operation at zero temperature, i.e., in the absence of thermal fluctuations. The second part of this chapter will address the dc SQUID performance in the presence of thermal fluctuations. The third part addresses effects of SQUID asymmetry, like junction asymmetry or the SQUID's geometrical asymmetry. Throughout this section we will focus on the dc SQUID performance when used as a detector for low-frequency flux signals. We note, however, that there are other modes of operation like its use as an amplifier for rf signals [39–47]. For a broad treatment of dc SQUID operation we also refer to the review articles by Ketchen [48], Clarke [49–51] Ryhänen *et al.* [52] and the text books by Barone and Paterno [3] and by Likharev [4].

The configuration of the dc SQUID is schematically shown in Fig. 2.6. It consists of a superconducting ring biased with a current I. An external magnetic field $H = B/\mu_0$ is applied to the loop. A Josephson junction is incorporated into each of the two arms of the dc SQUID. The Josephson junctions limit the maximum supercurrent I_c that can flow across the ring to a maximum value given by the sum of the critical currents of the two junctions. The magnetic flux enclosed inside the SQUID ring modulates I_c periodically, with a period of one flux quantum $\Phi_0 = h/2e$[1)]. This modulation, caused by an interference of the superconducting wave functions in the two SQUID arms, forms the basis of the working principle of the dc SQUID. The direct way to detect this modulation is to read out I_c directly, e.g., by increasing the bias current at fixed magnetic field until a nonzero dc voltage develops across the junctions. A much simpler method, however, can be used at least for dc SQUIDs with overdamped junctions having a nonhysteretic current–voltage characteristic. Here, the SQUID is biased with a current slightly above the maximum value of I_c and the dc voltage V across the junctions is read out directly as a function of external magnetic field or applied magnetic flux Φ_a. When I_c is maximum, V is minimum and vice versa. Read out this way, the dc SQUID thus directly acts as a flux-to-voltage transducer. To measure small changes $\delta\Phi_a$ in applied flux one generally chooses the bias current to maximize the amplitude of the voltage modulation, and the applied flux to be $(2n+1)\ \Phi_0/4$ $(n = 0, 1, 2,...)$ so that the flux-to-voltage transfer coefficient, $\left|(\partial V/\partial \Phi_a)\right|_I$, is a maximum, which we denote as V_Φ. Thus, the SQUID produces a maximum output voltage signal $\delta V = V_\Phi \delta\Phi_a$ in response to a small applied flux signal $\delta\Phi_a$.

1) The external field also causes the critical currents of the two Josephson junctions to modulate. Since, however, the area of the SQUID loop is usually much larger than the area of the junctions this modulation occurs on a field scale much larger than the modulation period of I_c. It thus can be ignored in most practical cases.

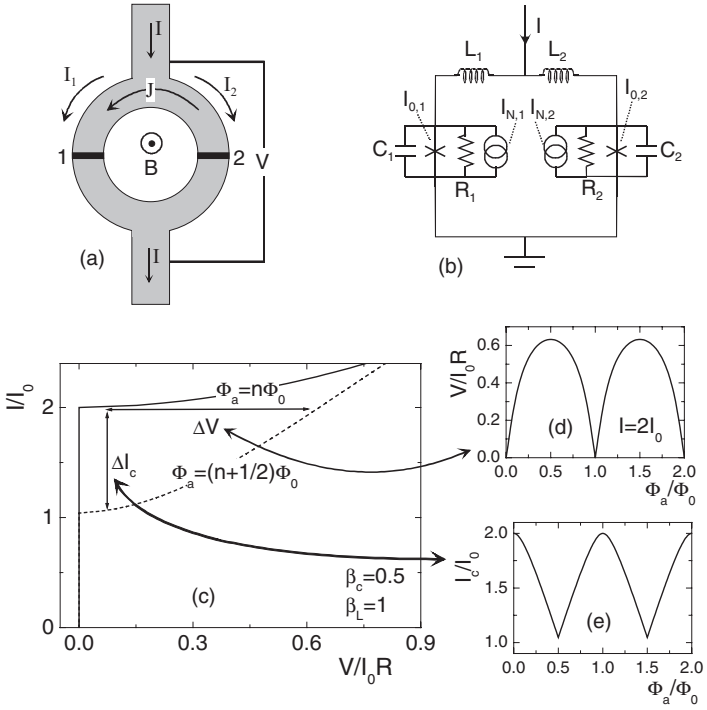

Fig. 2.6 Configuration of the dc SQUID. (a) schematic drawing; (b) equivalent circuit; (c) typical current voltage characteristics; (d) voltage modulation $V(\Phi_a)$; (e) modulation of critical current $I_c(\Phi_a)$. Curves (c) to (e) have been calculated numerically from Eqs. (2.37) to (2.39) for identical junction parameters and $\beta_L = 1$, $\beta_c = 0.5$, as discussed in Section 2.2.2.

2.2.2
Basic Equations, dc SQUID Potential

A quantitative description of the operation of a dc SQUID containing two junctions symmetrically incorporated into the SQUID loop can easily be obtained by using the RCSJ model for the currents flowing through the two Josephson junctions (cf. Section 2.1); in addition, one needs Kirchhoff's laws and an equation relating the phase differences δ_1 and δ_2 of the two junctions, the flux penetrating the SQUID loop and the currents circulating around the loop. We refer to the notation of Fig. 2.6(b). The current through junction 1 can be written as half the bias current I plus the circulating current J, $I_1 = I/2 + J$. Similarly, we can write the current through junction 2 as $I/2–J$. Equating these currents to the sum of supercurrent, quasiparticle current and displacement current through each junction, as in the RCSJ model, we obtain

$$\frac{I}{2} \pm J = I_{0,k} \sin\delta_k + \frac{\Phi_0}{2\pi R_k}\dot{\delta}_k + \frac{\Phi_0}{2\pi} C_k \ddot{\delta}_k + I_{N,k} \tag{2.35}$$

for the two junctions $k = 1,2$ with two independent Nyquist noise currents $I_{N,k}$. The phase differences δ_1 and δ_2 are related by

$$\delta_2 - \delta_1 = \frac{2\pi}{\Phi_0}(\Phi_a + LJ) = \frac{2\pi}{\Phi_0}\Phi_T \,. \tag{2.36}$$

This equation is derived in the Appendix (equations (A.14) and (A.15)). The flux Φ_T is the total flux through the SQUID loop having contributions from the applied magnetic field and from the circulating current J. The first contribution we write as $\Phi_a = B \cdot A_{eff}$, with the effective area A_{eff}. Due to flux compression caused by the superconducting structures A_{eff} is usually quite different from the geometric dimensions of the SQUID hole. For example, for a square hole with diameter d incorporated into a superconducting square washer of diameter D it is given by $A_{eff} = d \cdot D$ [53,54]. The contribution from the circulating current J can be written as LJ where the SQUID inductance L has a geometric contribution as well as a kinetic contribution [55–61]. The latter, although usually small, can play a role, if the film thickness is comparable to or smaller than the London penetration depth λ_L and the linewidth of the superconducting structures is small. For completeness we note that, if the inductances of the two arms of the SQUID are not equal, the bias current I causes a net magnetic flux which should be added to the right-hand side of (2.36) (see Section 2.2.4).

Equations (2.35) and (2.36) form the basis of a description of the dynamics of the dc SQUID. The voltages U_k ($k = 1,2$) across the Josephson junctions are obtained from the phase differences δ_k via the second Josephson relation, $U_k = \frac{\Phi_0}{2\pi}\dot{\delta}_k$. In general, the U_k are time dependent functions with high-frequency contributions, e.g., resulting from the ac Josephson effect. The voltage V read out experimentally from the dc SQUID, is usually a dc or low-frequency voltage. It can be obtained from the U_k by a sufficiently long time average. The time averages of U_1 and U_2 are actually identical, although U_1 and U_2 are usually not. The reason is that the SQUID loop contains no dissipative elements other than the junction resistances able to carry a non vanishing dc voltage.

To further analyze (2.35) and (2.36) it is useful to turn to dimensionless units. We introduce the average critical current $I_0 = (I_{0,1} + I_{0,2})/2$ of the two junctions, (twice) the parallel resistance of the dc SQUID, $R = 2R_1R_2/(R_1 + R_2)$ and capacitance $C = (C_1 + C_2)/2$ and normalize currents to I_0, resistances to R, time to $\tau \equiv \Phi_0/(2\pi I_0 R) = \omega_c^{-1}$, voltage to I_0R and magnetic flux to Φ_0. With these normalizations the dc SQUID equations of the Langevin type transform to

$$\frac{i}{2} + j = (1 - \alpha_I)\sin\delta_1 + (1 - \alpha_R)\cdot\dot{\delta}_1 + \beta_c(1 - \alpha_C)\cdot\ddot{\delta}_1 + i_{N,1}, \tag{2.37}$$

$$\frac{i}{2} - j = (1 + \alpha_I)\sin\delta_2 + (1 + \alpha_R)\cdot\dot{\delta}_2 + \beta_c(1 + \alpha_C)\cdot\ddot{\delta}_2 + i_{N,2} \tag{2.38}$$

and

$$\delta_2 - \delta_1 = 2\pi(\phi_a + \frac{1}{2}\beta_L j). \tag{2.39}$$

Here, α_I, α_R and α_C, respectively, parametrize asymmetries in the junction critical currents, resistances and capacitances and $i_{N,k} \equiv I_{N,k}/I_0$ $(k = 1,2)$. Dots above variables denote derivatives with respect to normalized time τ. $\beta_c = \frac{2\pi}{\Phi_0} I_0 R^2 C$ is the Stewart–McCumber parameter [5,6], and $\beta_L = \frac{2LI_0}{\Phi_0}$ the screening parameter; i and j denote the dimensionless bias and circulating currents, respectively, and ϕ_a is the normalized applied magnetic flux. The dimensionless voltages u_k are obtained via $u_k = \dot{\delta}_k (k = 1,2)$.

In the following we will analyze equations (2.37) to (2.39) in the absence of thermal noise in some limiting cases. For extended treatments of the zero-noise case, see [3,4,62–69]. We will first study static solutions of a dc SQUID with identical junctions. In this case (2.37) and (2.38) greatly simplify to $\frac{i}{2} + j = \sin\delta_1$ and $\frac{i}{2} - j = \sin\delta_2$. We further assume that the SQUID inductance is negligible ($\beta_L << 1$) in which case (2.39) reduces to $\delta_2 - \delta_1 = 2\pi\phi_a$. From these simplified equations we find $i = \sin\delta_1 + \sin\delta_2 = \sin\delta_1 + \sin(\delta_1 + 2\pi\phi_a)$. Defining $\gamma \equiv \delta_1 + \pi\phi_a$ we finally get $i = 2\sin\gamma \cdot \cos(\pi\phi_a)$. For a bias current below the critical current the phase γ will adjust so that the latter equation is fulfilled. The maximum current is obtained for $\sin\gamma = \pm 1$ (depending on the sign of i and the cosine term), yielding $i_c = 2\left|\cos(\pi\phi_a)\right|$ or, in absolute units,

$$I_c = 2I_0 \cdot \left|\cos\left(\pi \frac{\phi_a}{\phi_0}\right)\right| . \tag{2.40}$$

In the case of identical currents and very low inductance, the critical current of the dc SQUID thus modulates between $2I_0$ and 0. A reduction of the modulation depth occurs for nonzero values of β_L (cf. Fig. 2.7). For $\beta_L = 1$ the critical current modulates by 50%, and for $\beta_L >> 1$, $\Delta I_c/I_{c,max}$ decreases as $1/\beta_L$ (cf. Fig. 2.7(b)). The reason for the $1/\beta_L$ decrease can easily be understood from the fact that the SQUID response is periodic in Φ_0. When the applied flux is $\Phi_0/2$ the largest circulating cur-

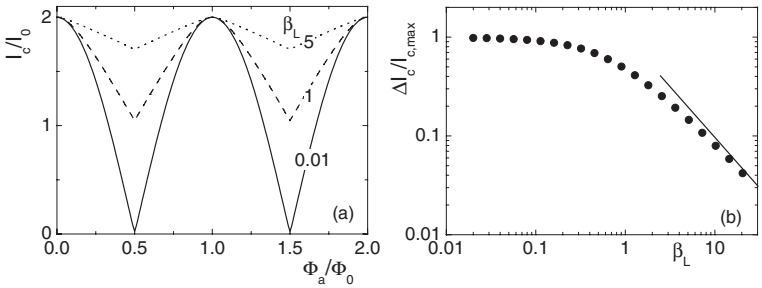

Fig. 2.7 (a) Critical current of the dc SQUID vs. applied flux for 3 values of the screening parameter β_L. Junction parameters are assumed to be identical. (b) Modulation depth $\Delta I_c/I_{c,max}$ vs. β_L. Solid line in (b) is function β_L^{-1}.

rent required to lift the total flux to an integer number is of the order of $J = \Phi_0/2L$, or $j = 1/\beta_L$. The minimum critical current is of the order of $2(I_0–J)$, and thus $\Delta I_c/I_{c,max} \approx j \approx 1/\beta_L$ for $\beta_L >> 1$.

The above considerations illustrate the response of the dc SQUID in the superconducting state. We now turn to the case of a nonzero dc voltage V across the junctions. Figures 2.8(a) to 2.8(d) show current–voltage characteristics for several values of the external flux. The figures are for 4 sets of β_L and β_c. Figure 2.9 shows the modulation $V(\Phi_a)$ for several values of the bias current for two sets of β_L and β_c. All curves have been obtained by numerically solving equations (2.37) to (2.39). We see that the modulation in I_c directly transfers into a modulation of V. Other phenomena arise from the ac Josephson currents interacting, e.g., with geometric resonances of the SQUID, as we will show below.

We start with the case of $\beta_L << 1$ (cf. Fig. 2.8(a)). We assume junction parameters to be identical. Equations (2.37) and (2.38) then reduce to $\frac{i}{2} + j = \sin\delta_1 + \dot{\delta}_1 + \beta_c \cdot \ddot{\delta}_1$ and $\frac{i}{2} - j = \sin\delta_2 + \dot{\delta}_2 + \beta_c \cdot \ddot{\delta}_2$. From (2.39), with $\beta_L << 1$, we find $\dot{\delta}_1 = \dot{\delta}_2$ and $i = \sin\delta_1 + \sin(\delta_1 + 2\pi\phi_a) + 2\dot{\delta}_1 + 2\beta_c\ddot{\delta}_1$. With $\gamma = \delta_1 + \pi\phi_a$ we get $i = 2[\cos\pi\phi_a \cdot \sin\gamma + \dot{\gamma} + \beta_c\ddot{\gamma}]$ or, in absolute units

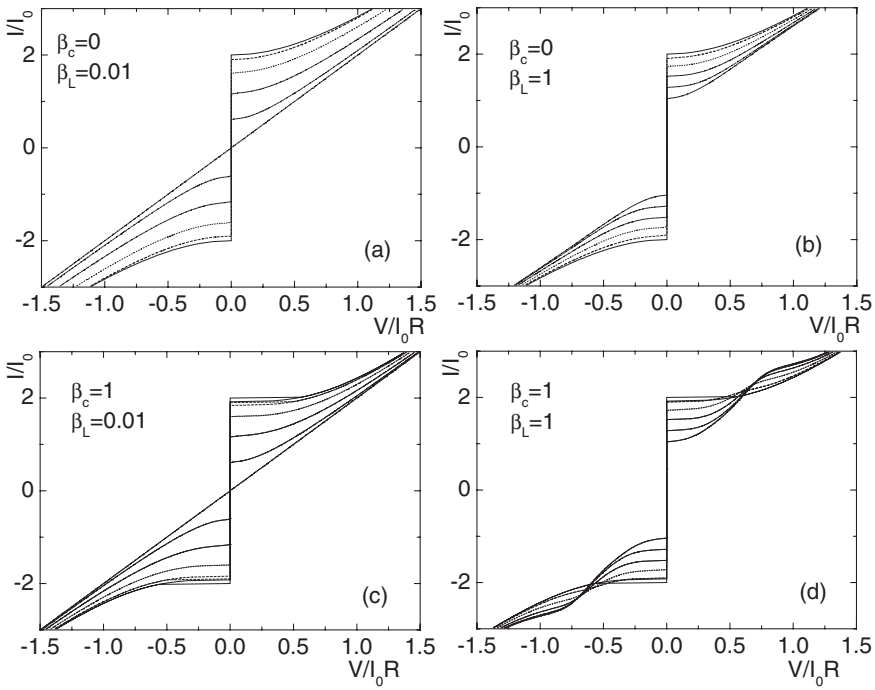

Fig. 2.8 Current voltage characteristics of dc SQUIDs for $\beta_L = 0.01$, 1 and $\beta_c = 0$, 1. Applied flux is increased from 0 (solid line) to $\Phi_0/2$ (short dashed line) in steps of $0.1\Phi_0$.

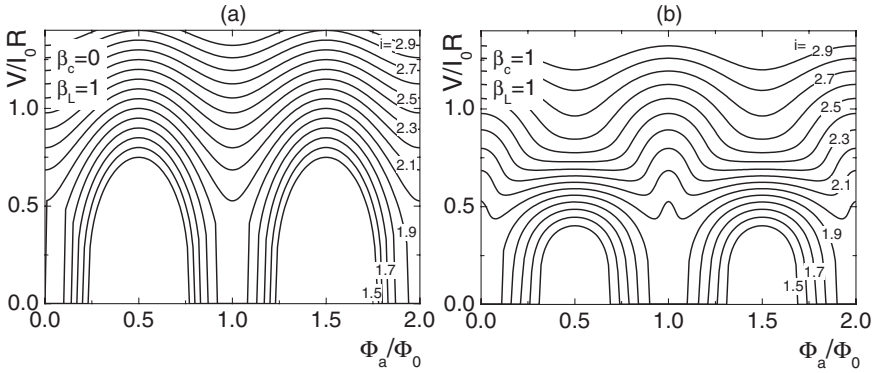

Fig. 2.9 dc SQUID modulation $V(\Phi_a)$ for several values of normalized bias current i from 1.5 to 1.9 calculated for strongly overdamped (a) and intermediately damped (b) junctions.

$I = 2I_0\cos(\pi\Phi_a/\Phi_0)\cdot\sin\gamma + \frac{2\Phi_0}{2\pi R}\dot{\gamma} + \frac{2\Phi_0}{2\pi}C\ddot{\gamma}$. This equation is identical to the RCSJ equation of a single junction if a parallel resistance $R/2$ of the two junctions, a capacitance $2C$ and a critical current $2I_0\cos\pi\varphi_a$ are taken. We thus see that, in the limit $\beta_c<<1$ the current–voltage characteristic for $I>I_c$ is given by

$$V = \frac{R}{2}\sqrt{I^2 - I_c^2}, \tag{2.41}$$

with I_c as in (2.40). Thus the dc voltage oscillates with flux with a period of one flux quantum, with minima at integer multiples of Φ_0. For the slope $\partial V/\partial\Phi_a$ we get $\frac{\partial V}{\partial\Phi_a} = -2\pi\cdot\frac{I_0R}{\Phi_0}\cdot\frac{I_0\cdot\sin\pi\Phi_a/\Phi_0\cdot\cos\pi\Phi_a/\Phi_0}{(I^2-I_c^2)^{1/2}}$. The expression actually diverges for $I = I_c$. However, we will see that in the presence of thermal fluctuations, $\partial V/\partial\Phi_a$ becomes finite for all currents, with a maximum value near its divergence in the noise-free case. We can thus define the SQUID transfer function $V_\Phi = \max(|\partial V/\partial\Phi_a|)$, where maximization is with respect to bias current and flux. From (2.41) we can also see that the peak-to-peak-modulation in $V(\Phi_a)$ is given by $V_{pp} = V(\Phi_a = \Phi_0/2) - V(\Phi_a = 0) = I_0R\cdot\left[\frac{I}{2I_0} - \sqrt{\left(\frac{I}{2I_0}\right)^2 - 1}\right]$, which for $I = 2I_0$ reaches its maximum value I_0R. When the SQUID inductance is taken into account the modulation of both I_c and V decreases (cf. Fig. 2.8(b)). The same actually also holds when the junction parameters R, I_0, C become asymmetric. However, note that this does not mean that a SQUID with identical junctions and $\beta_L = 0$ is the "best" SQUID. A detailed analysis taking fluctuations into account shows that β_L values near 1 are often optimal. Although symmetric junctions are desirable in many cases, asymmetries in the junction parameters can sometimes improve the SQUID performance (cf. Section 2.2.4).

We next discuss the effect of nonzero capacitances on the current–voltage characteristics of the SQUID. We will discuss junctions with $\beta_c \leq 1$. Examples for the current–voltage characteristics, as numerically calculated from equations (2.37) to (2.39) for several values of applied flux, are shown in Fig. 2.8(c) for $\beta_c = 1$ and $\beta_L = 0.01$ and in Fig. 2.8(d) for $\beta_c = 1$ and $\beta_L = 1$. For $\beta_L = 0.01$ and $\Phi_a = 0$ the current voltage characteristic exhibits a small hysteresis which actually appears for McCumber parameters larger than about 0.8 [70]. This small hysteresis, however, disappears when the external flux is increased[2)]. The current–voltage characteristics do not differ greatly from the ones shown in Fig. 2.8(a), although the differential resistance, slightly above the critical current, is larger than for $\beta_c = 0.01$. The curves shown in Fig. 2.8(d) exhibit new features. Here, the curve for $\Phi_a = \Phi_0/2$ intersects the $\Phi_a = 0$ curve defining two regimes where $U(\Phi_a)$ modulates strongly. Note that the crossing of the $\Phi_a = 0$ and the $\Phi_a = \Phi_0/2$ curves means that $U(\Phi_a)$ is phase shifted by a half-flux quantum when passing from one regime to the other. The situation is illustrated in Fig. 2.9(b) where $V(\Phi_a)$ is shown for $\beta_c = 1$ and $\beta_L = 1$ for a number of bias currents. What is the reason for this behavior? As discussed in [71–77] the effect is actually caused by the LC resonance of the SQUID loop getting excited by the ac Josephson currents. Suppose that the frequency $f_J = V/\Phi_0$ of the Josephson currents matches the resonance frequency $1/2\pi\sqrt{L \cdot (C/2)}$ of the SQUID loop. For $\Phi_a = 0$ the two Josephson junctions oscillate in-phase and are unlikely to excite the *LC* resonance. However, strong coupling will occur when the junctions oscillate out-of-phase, as for $\Phi_a = \Phi_0/2$. While the dc component of the Josephson current is small outside the resonance it becomes substantial at the resonance and the voltage across the dc SQUID decreases. Thus, in the resonant regime V is maximum for $\Phi_a = 0$ and minimum for $\Phi_a = \Phi_0/2$, exactly opposite to the non-resonant modulation of V.

Equations (2.37) and (2.38) describing the dc SQUID dynamics may be seen [52,78,79] as the equation of motion of a point mass in a field of force with a two-dimensional (2D) potential $U_{SQUID}(\delta_1, \delta_2)$. For a symmetrical configuration, when the two junctions are identical and symmetrically incorporated into the SQUID ring U_{SQUID} may be written as:

$$\frac{U_{SQUID}}{2E_J} = \frac{1}{\pi\beta_L}\left(\frac{\delta_2 - \delta_1}{2} - \pi\frac{\Phi_a}{\Phi_0}\right)^2 - \cos\frac{\delta_2 - \delta_1}{2}\cos\frac{\delta_1 + \delta_2}{2} - \frac{I}{2I_0}\frac{\delta_1 + \delta_2}{2}, \qquad (2.42)$$

where $E_J = I_0\Phi_0/2\pi$ is the Josephson coupling energy. U_{SQUID} (for 2D and 3D representations see Fig. 2.10 and Fig. 2.11, respectively) has a parabolic shape shifted by an applied flux Φ_a with cosine-shaped bumps that generate multiple metastable states separated by saddle points. With increasing bias current i the potential is tilted in the direction of increasing $\delta_1 + \delta_2$ and the saddle points between the minima are lowered. The critical value of the bias current at which the particle starts to move depends on both β_L and Φ_a. A voltage is created as soon as the SQUID total phase

2) The current–voltage characteristics become again hysteretic for larger values of β_c, with the precise value depending on flux and β_L.

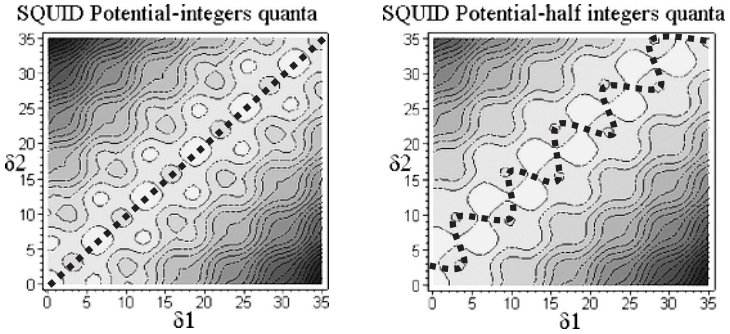

Fig. 2.10 2D representations of the dc SQUID potential $U_{SQUID}(\delta_1, \delta_2)$ for $i = 0$, $\beta_L = 5$ and integers (left side) or half integers (right side) quanta of the externally applied dc flux. Dotted lines are the 2D projection of the SQUID trajectory in the voltage state, when the applied bias current is so high that it tilts the potential until the point when the system starts to move.

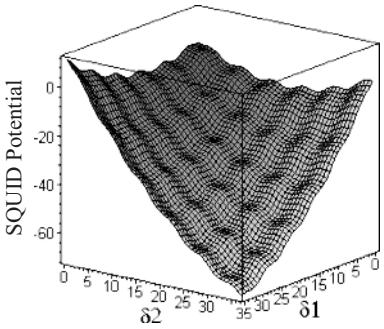

Fig. 2.11 3D representation of the dc SQUID potential $U_{SQUID}(\delta_1, \delta_2)$ for $i = 2$, $\beta_L = 5$ and $\Phi_a = 0$.

$\delta_1 + \delta_2$ changes in time. For $\Phi_a = \Phi_0(2n+1)/2$ (here n is an integer) the path connecting the neighboring relative minima has a serpentine-like shape (dotted line in Fig. 2.10) when viewed from the top. As a result, in this case the movement of the particle in the $\delta_1 + \delta_2$ direction generates oscillations in $\delta_1 - \delta_2$ and therefore, also oscillations of the circulating current in the SQUID loop. On the contrary, when $\Phi_a = \Phi_0 n$, the neighboring relative minima are connected via a straight path when viewed from the top (dotted line on Fig. 2.10) and no such oscillations occur.

2.2.3 Thermal Fluctuations

2.2.3.1 General Considerations

We now turn to the case of nonzero temperature, and discuss the effect of thermal fluctuations on the performance of dc SQUIDs. According to the Nyquist theorem, the junction resistances of the dc SQUID produce a noise voltage with a spectral noise power in a bandwidth of 1 Hz

$$S_V(f) = 4k_B TR. \tag{2.43}$$

These noisy elements produce a voltage noise across the dc SQUID [23,80] and also a current noise around the SQUID loop; in fact, these two noise terms are partially correlated [81].

We can distinguish different regimes of noise, depending on the junction parameters as well as on the SQUID inductance L. To have a qualitative understanding of the effect of L on the noise properties of the SQUID, one should consider the fluctuation amplitude of the total flux Φ_T in the presence of thermal fluctuations. In (2.42) Φ_T enters the SQUID potential quadratically and, from basic principles of thermodynamics, we should relate this term to the total average energy of a classical harmonic oscillator. Following such an approach (Chapter 6 in [4]), one may neglect the periodic term in the SQUID potential (2.42) and integrate this equation over the whole frequency spectrum to get

$$\left\langle \frac{(\delta_2 - \delta_1 - 2\pi\Phi_a/\Phi_0)^2}{4\pi\beta_L} \right\rangle \cong \left\langle \frac{U_{SQUID}}{2E_J} \right\rangle = \frac{k_B T/2}{2E_J}. \tag{2.44}$$

From (2.44), for the mean square of the fluctuations one finds $\left\langle (\delta_2 - \delta_1 - 2\pi\Phi_a/\Phi_0)^2 \right\rangle = L/L_F$, where $L_F \equiv (\Phi_0/2\pi)^2/k_B T$ is the so called fluctuation-threshold inductance. With the introduction of L_F and with the noise parameter $\Gamma = k_B T/E_J = 2\pi k_B T/(I_0\Phi_0)$ one can distinguish the two regimes of small and large thermal fluctuations in SQUIDs. In the regime of small thermal fluctuations, both the noise parameter Γ and the normalized inductance L/L_F are much less than 1. In contrast, the regime of large thermal fluctuations is reached when either Γ or L/L_F is comparable to unity or even larger.

To achieve reasonable input coupling, typical SQUID inductances are of the order of 100 pH, and, as will be shown below, optimized SQUIDs have values of β_L close to unity. Furthermore, the value of L_F is 1.87 nH at 4.2 K and 102 pH at 77 K. Hence, at 4.2 K SQUIDs are usually operated in the regime of small thermal fluctuations, since $L/L_F << 1$ and from $\pi\beta_L\Gamma = L/L_F$, with $\beta_L \approx 1$ also $\Gamma << 1$. In contrast, at 77 K L_F is about 20 times smaller than at 4.2 K, and therefore the regime of large thermal fluctuations is quite often reached, since L/L_F is close to unity. These considerations hold for both dc and rf SQUIDs.

From qualitative basic considerations it was generally believed that SQUIDs should be operated in the small thermal fluctuation limit for the following reasons:

(1) To avoid the suppression of macroscopic quantum interference, the SQUID inductance should satisfy $L < L_F = (\Phi_0/2\pi)^2/k_B T$.
(2) The Josephson coupling energy of the weak link should be substantially greater than the thermal energy $k_B T$, i.e., $\Gamma = 2\pi k_B T/(\Phi_0 I_0) << 1$;

Operation at 4.2 K did not impose the necessity of analyzing this problem quantitatively. The situation, however, changed for operation at 77 K, which raised the

question of how the SQUID performance is affected by an increase of L and Γ up to and beyond these threshold values. To answer this question, analytical approaches have been developed for overdamped systems (characterized by $\beta_c << 1$) of both types: dc and rf SQUIDs [82–85] (we recall here that high-T_c SQUIDs operating at 77 K are made of overdamped junctions). Moreover, for the case of dc SQUIDs, extensive numerical simulations have also been performed [86–94] to clarify this issue.

The spectral density of the voltage fluctuations, (2.43), can be written in dimensionless form by referring bandwidth to $\omega_c = \tau^{-1} = 2\pi I_0 R/\Phi_0$ and voltage to $V_c = I_0 R$, i.e. we normalize S_v to $V_c^2/\omega_c = I_0 R\Phi_0/2\pi$. The Nyquist theorem for the spectral density of the dimensionless voltage noise power thus reads

$$s_v = 4\Gamma, \tag{2.45}$$

with the noise parameter Γ introduced above. A symmetric dc SQUID is now described by three parameters, β_c, β_L and Γ, or alternatively β_c, $\Gamma\beta_L$ and Γ. The noise parameter Γ can in fact be interpreted as the ratio of the thermal noise current $I_{th} = 2\pi k_B T/\Phi_0$ to the critical current of one junction I_0. At 4.2 K we have $I_{th} = 0.18\,\mu A$, and at 77 K, $I_{th} = 3.2\,\mu A$. Γ may also be interpreted as the ratio of the thermal energy $k_B T$ to the coupling energy $E_J = \Phi_0 I_0/(2\pi)$ associated with one Josephson junction. The product $\beta_L\Gamma$ is related to the fluctuation-threshold-inductance as $\Gamma\beta_L = L/\pi L_F$. At 4.2 K, $L_F \approx 1.9$ nH, and at 77 K $L_F \approx 100$ pH. We may also read $\Gamma\beta_L/(2\pi)$ as the ratio of the thermal energy $k_B T$ to the magnetic energy E_M associated with one flux quantum stored in the SQUID loop, and in the same sense $\beta_L/2\pi$ can be interpreted as the ratio of E_J to E_M. From these interpretations we can intuitively expect the SQUID performance to degrade strongly if at least one of the following two conditions is fulfilled: $L > L_F$ (or $\Gamma\beta_L > 1$), or if $\Gamma > 1$.

The important figures of merit to be calculated are the SQUID transfer function V_Φ, the spectral density S_V of the voltage noise power, the flux noise power, defined as $S_\Phi = S_V/V_\Phi^2$, the energy resolution $\varepsilon = S_\Phi/(2L)$ and the magnetic field noise power $S_B = S_\Phi/A_{eff}^2$. While the latter quantity depends on the details of the layout via A_{eff}, the other quantities can be calculated quite generally using the Langevin or Fokker–Planck equations in terms of the white noise produced by the junction resistances. Other sources of noise, e.g., $1/f$ contribution caused by fluctuations of the critical currents of the Josephson junctions, or by the thermally activated motion of flux vortices, need to be addressed separately (cf. Section 2.1.3). In order to optimize the dc SQUID with respect to white noise, optimal values of β_c, β_L and Γ need to be found. Although this optimization depends strongly on many details like temperature or the quantity to be optimized (flux noise, field or energy resolution etc.) it often turns out that there is only a weak dependence on β_c (provided $\beta_c < 1$). Also, often $\beta_L \approx 1$, or somewhat smaller, is close to optimum.

As mentioned above, there are two equivalent ways to treat the frequency independent white noise. The first is to consider the two independent noise currents $I_{N,k}$ $(k = 1,2)$ as included on the right-hand side of (2.35) (see also the equivalent circuit of Fig. 2.6(b)) with a spectral power density of $S_I(f) = 4k_B T/R$ and solve these Langevin equations numerically. This method has been used by many authors both in the context of low T_c [23,52,70,77,80,81,95–98] and high T_c dc SQUIDs [86–94,99]

and is described in detail in Section 2.2.3.2. The other method, which is described in detail in Section 2.2.3.3, is based on a statistical method, namely on the two-dimensional Fokker–Planck equation. An analytical solution of this problem for small values of β_L was found in [82–84].

2.2.3.2 Numerical Simulations (Langevin Equation)

In order to quantitatively discuss the dc SQUID performance in this section we study numerical solutions of the coupled Langevin equations (equations (2.37) to (2.39) together with a stochastic current term in (2.37) and (2.38)). In this section we will calculate important figures of merit in normalized units, such as $v_\phi \equiv V_\Phi \Phi_0 / I_0 R$, $s_v \equiv S_V 2\pi / I_0 R \Phi_0$, $s_\phi \equiv s_v / v_\phi^2 = S_\Phi 2\pi I_0 R / \Phi_0^3$, and $e \equiv s_\phi / 2\Gamma\beta_L = \varepsilon I_0 R / 2\Phi_0 k_B T$, where ε is the energy resolution and e the normalized energy resolution. The noise currents are implemented as Gaussian distributed random numbers with a normalization of (2.45), changing on timescales much faster than τ (typically at most 0.2τ). To generate the data in figures 2.16(a–d) shown below, the Langevin equations were solved using the 5th order Runge–Kutta–Fehlberg method [100].

To illustrate the effect of noise, Fig. 2.12 compares the time dependent voltages U_1 and U_2 across the two Josephson junctions for parameters $\beta_c = 0.5$ and $\beta_L = 0.5$

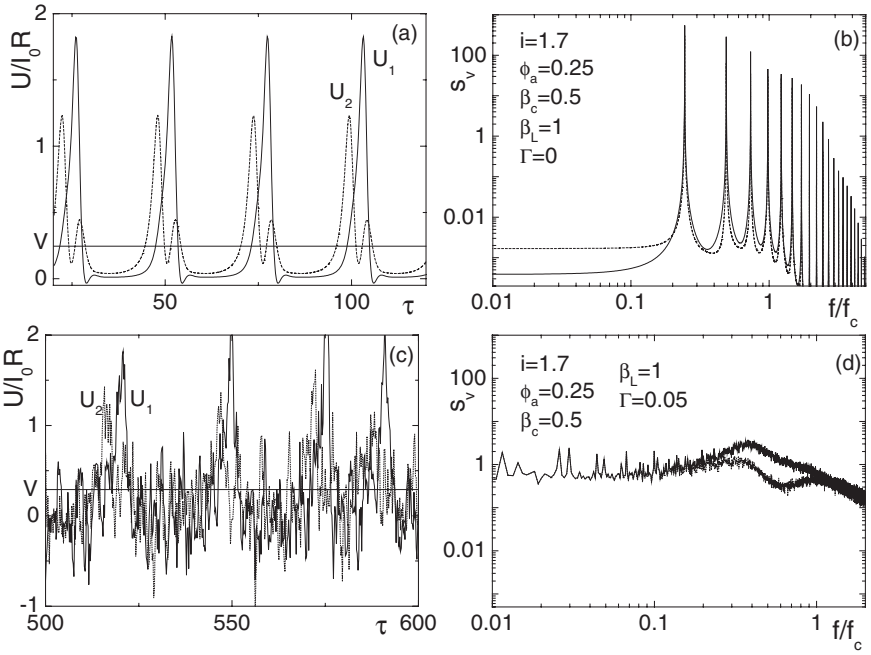

Fig. 2.12 Time dependent voltages across the two junctions of the dc SQUID (a,c) and corresponding Fourier power spectra in units of $I_0 R \Phi_0 / 2\pi$ (b,d) for (a,b) zero temperature and (c,d) $\Gamma = 0.05$. SQUID parameters are $\beta_L = 1$, $\beta_C = 0.5$, $I = 1.7 I_0$, $\Phi_a = \Phi_0/4$. Solid lines are for junction 1 and dashed lines for junction 2. Horizontal lines in (a,c) denote time averaged voltage v.

without fluctuations (Fig. 2.12(a)) and for $\Gamma = 0.05$ (Fig. 2.12(c)). The external flux is set to $0.25\Phi_0$, and the bias current to 1.7 I_0. For $\Gamma = 0$ there is a periodic sequence of voltage pulses. Although voltages U_1 and U_2 differ from each other, the time average voltage V is the same for both junctions. The Fourier power spectra of the two voltages, normalized to $I_0 R\Phi_0/2\pi$ are shown in Fig. 2.12(b,d). In the noise-free case there is a series of peaks, the lowest located at the fundamental frequency $f = V/\Phi_0$ followed by a large number of harmonics. For $\Gamma = 0.05$ the voltage pulses are still visible, however the sequence is no longer periodic. As a result the Fourier spectrum is strongly broadened and only a shallow peak at the fundamental Josephson frequency is left, followed by a smooth roll-off. Note that the voltage noise becomes white for frequencies well below the frequency of the Josephson oscillations.

In order to obtain a well-defined time-averaged voltage from these data one typically has to integrate U_1 and U_2 over 10^4 to 10^7 time units, depending on the accuracy required. For example, the current voltage characteristics shown below in Fig. 2.13 have been integrated for 10^4 time units, while the data for the transfer function shown in Fig. 2.15 (a) required an integration time of 10^5 time units. In order to obtain the Fourier spectrum of Fig. 2.12(d), 100 Fourier transforms of time traces of U were averaged (each calculated for 3200 time units with random numbers for noise changing every 0.2 time units). For larger values of Γ even longer integration times would have been needed, showing that the optimization of a quantity like the SQUID energy resolution apparently requires an enormous computation time, limiting both the number and the accuracy of quantities to be calculated.

Figure 2.13 shows the effect of noise on the current–voltage characteristics for the parameters $\beta_c = 0$, $\beta_L = 1$ (a) and $\beta_c = 1$, $\beta_L = 1$ (b). The calculations are for $\Gamma = 0.05$. In comparison to the noise-free case (cf. Figs. 2.8 (b) and (d)) one can see that the current–voltage characteristics are rounded near the critical current leading to the disappearance of infinite values of the differential resistance. The same effect can be observed in the V(Φ_a) patterns which are shown for the same SQUID parameters in Fig. 2.14 (to be compared with Fig. 2.9 for the noise-free case). Apparently all divergences in $\partial V/\partial \Phi_a$ disappear and the oscillations in V(Φ_a) are almost sinusoidal.

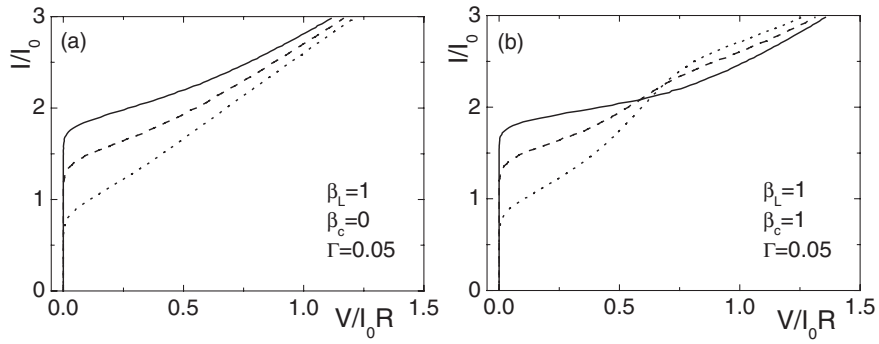

Fig. 2.13 Current–voltage characteristics of dc SQUID with strongly overdamped (a) and intermediately damped (b) junctions in the presence of thermal noise (Γ=0.05).

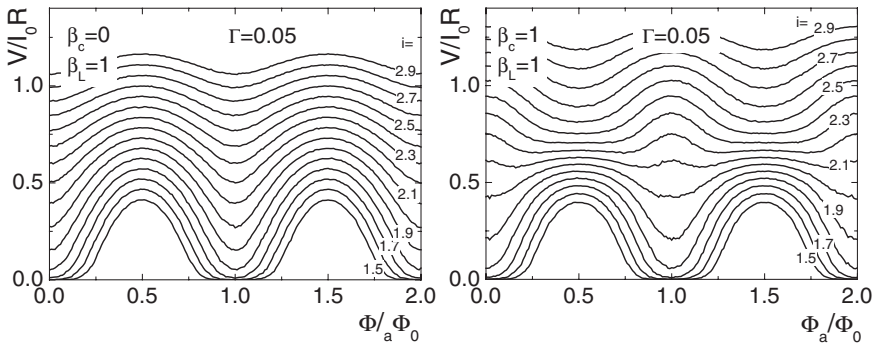

Fig. 2.14 Voltage modulation $V(\Phi_a)$ of dc SQUID for strongly damped (left) and intermediately damped (right) junctions, in the presence of thermal noise for several values of bias current from 1.5 to 2.9.

Consequently, $\partial V/\partial \Phi_a$ can reasonably be calculated for all currents. Fig. 2.15(a) shows $|\partial V/\partial \Phi_a|$ as a function of bias current for the parameters $\beta_L = 1$ and $\Gamma = 0.5$ and 3 values of β_c (0: solid curve; 0.5: dashed curve; 1: dotted curve). The external flux is set to 0.25 Φ_0. For all values of β_c the maximum in $|\partial V/\partial \Phi_a|$ occurs at about the same bias current ($\approx 1.6\, I_0$). Note that the optimum bias current depends on the value of β_L. In the case of $\beta_c = 0$, $|\partial V/\partial \Phi_a|$ decreases smoothly while for nonzero

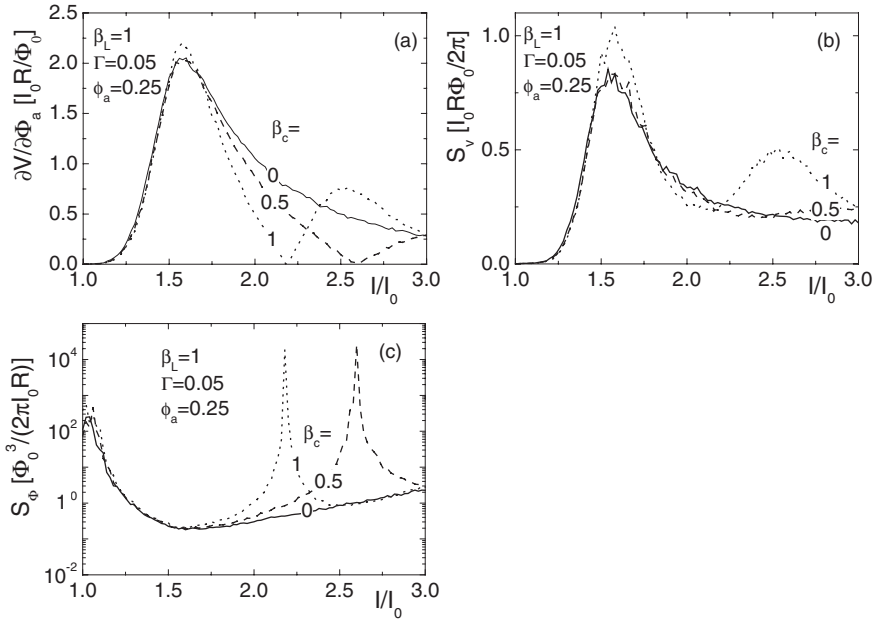

Fig. 2.15 dc SQUID transfer function (a), low-frequency voltage noise (b) and low-frequency flux noise (c) vs. bias current for three values of β_c .

values of the McCumber parameter, the LC resonance leads to a second maximum in the transfer function. In Fig. 2.15(a) the effect can best be seen for $\beta_c = 1$. Note that near its maximum the transfer function is almost independent of β_c.

Fig. 2.15(b) shows the low frequency value S_V of the normalized voltage noise power (i.e. the low-frequency end of spectra as in Fig. 2.12(d)) as a function of bias current for the same SQUID parameters as in Fig. 2.15(a). S_V depends on the bias current in a similar way to the transfer function. From $|\partial V/\partial \Phi_a|$ and S_v we can calculate the flux noise power S_Φ of the dc SQUID as the ratio $S_V/(\partial V/\partial \Phi_a)^2$. The result is shown in Fig. 2.15(c). The S_Φ has a minimum roughly where the maxima in S_v and $\partial V/\partial \Phi_a$ occur. For $\beta_c = 0$, S_Φ increases smoothly with increasing current above the optimum bias current, while for the case of nonzero β_c there is a steep increase in S_Φ when the transfer function reaches its node. Well above the resonance S_Φ approaches the value obtained for $\beta_c = 0$.

The quantities which are most important for the dc SQUID are the optimized transfer function and spectral densities of noise power S_V, S_Φ and ε, to be obtained from curves as in Fig. 2.15 by optimizing with respect to bias current. Usually the optimization is done for a fixed flux $\Phi_a = 0.25\Phi_0$. In principle, the above quantities should be optimized by independently optimizing with respect to both I and Φ_a. This requires an enormous computer effort, and it turns out that optimum values can indeed be obtained for $\Phi_a \approx 0.25\,\Phi_0$. Also, the fact that the maximum in the transfer function and the minimum in S_Φ (and consequently also in $\varepsilon = S_\Phi/2L$) occur at the same bias point, allows us first to find the maximum in the transfer function and then to calculate all other quantities for the optimal bias current.

Until now, no general solutions have been found for V_Φ, S_V, S_Φ and ε, that are valid over a wide range of all relevant parameters. However, many limits can be addressed [23,52,77,80–84, 86–98,101]. In the case of low-temperature superconductors one often has β_L near unity. Both Γ and $\Gamma\beta_L$ are usually much less than 1. In this limit one finds $V_\Phi \propto 1/(1+\beta_L)$ [23,52]. For $\beta_L \approx 1$ and $\Gamma = 0.05$ the expressions $V_\Phi \approx R/L$, $S_v \approx 16k_BTR$, $S_\Phi \approx 16k_BTL^2/R$ and $\varepsilon \approx 9k_BTL/R$ work very well [49–52]. For the noise power of the circulating current one finds $S_j \approx 11k_BT/R$ [81]. There is also a correlation between current and voltage noise yielding $S_{VJ} \approx 12k_BT$ [81]. In the context of high-T_c superconductors operating at 77 K, situations need to be addressed where both Γ and $\Gamma\beta_L$ are comparable to unity. An analytic approach valid for $\beta_L \lesssim 1/\pi$ and a wide range of Γ is discussed in the next section. A widely used expression for the normalized transfer function has been given by Enpuku *et al.* [91,92],

$$v_\phi = \frac{4}{1+\beta_L}\exp\left(-\frac{3.5\pi^2(\delta\Phi_n)^2}{\Phi_0^2}\right) = \frac{4}{1+\beta_L}\exp(-2.75\Gamma\beta_L) \tag{2.46}$$

where $(\delta\Phi_n)^2 = k_BTL$ is the mean-square flux noise. For the flux noise, Enpuku *et al.* give the formula $S_\Phi = \alpha L^2(2k_BT/R)\,[1+(R/LV_\Phi)^2]$, with $\alpha = 1+\exp(1.23–4.82\Gamma)$ [91,92]. In order to keep this chapter simple, only the approach of [94] is described in more detail below. Results of calculations of the maximized transfer function V_Φ and the corresponding values of S_V, S_Φ and ε are shown in Fig. 2.16. To explore the depen-

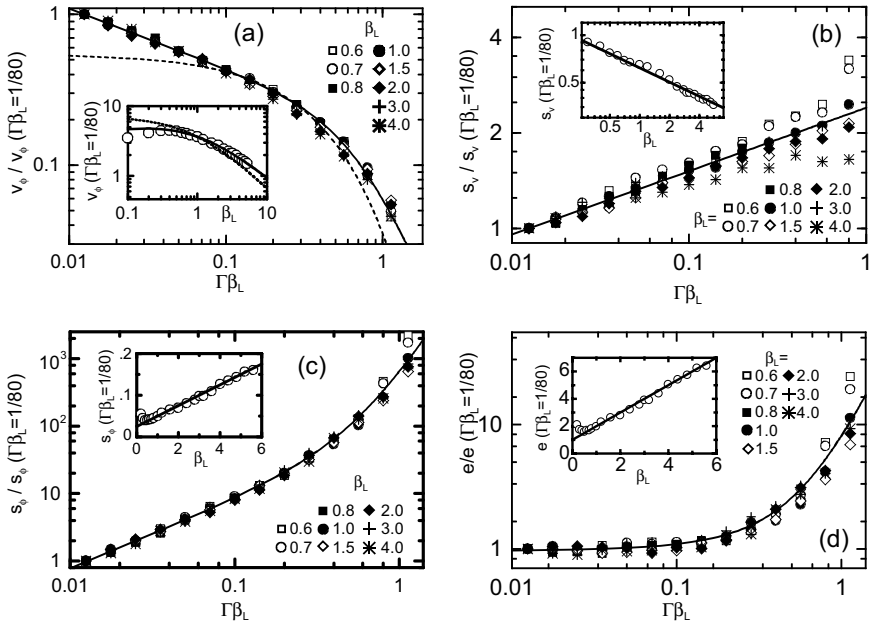

Fig. 2.16 Computed normalized transfer function v_ϕ/v_ϕ (β_L; $\Gamma\beta_L = 1/80$) (a), voltage noise power $s_v/s_v(\Gamma\beta_L = 1/80)$ (b), flux noise power s_ϕ/s_ϕ ($\Gamma\beta_L = 1/80$) (c) and energy resolution $e/e(\Gamma\beta_L = 1/80)$ (d) vs. $\Gamma\beta_L$ for $\beta_c = 0.5$. Solid lines correspond to (a) Eq. (2.47), (b) $s_v \propto (\Gamma\beta_L)^{0.2}$, (c) Eq. (2.49), (d) Eq. (2.51). Dashed line in (a) corresponds to (4/7.3) exp (–2.75$\Gamma\beta_L$). Insets show (a) v_ϕ (β_L; $\Gamma\beta_L = 1/80$) vs. β_L, (b) $s_v(\Gamma\beta_L = 1/80)$ vs. β_L, (c) s_ϕ ($\Gamma\beta_L = 1/80$) vs. β_L and (d) $e(\Gamma\beta_L = 1/80)$ vs. β_L. Solid lines in the insets correspond to (a) Eq. (2.48), (b) $s_v(\Gamma\beta_L = 1/80) = 0.62\beta_L^{-0.3}$, (c) s_ϕ ($\Gamma\beta_L = 1/80$) $= (1 + \beta_L)/40$ and (d) $(1 + \beta_L)$. Dashed line in (a) is $7.3/(1 + \beta_L)$.

dence on the inductance L, it is convenient to plot the above quantities vs. $\Gamma\beta_L = L/\pi L_F$. In Fig. 2.16, $\Gamma\beta_L$ ranges from 0.0125 to 1.25 widely covering the experimental range of interest, At 77 K the above range corresponds to inductances between 4 pH and 400 pH at 77 K. For low-T_c SQUIDs at 4.2 K, the corresponding range is 74 pH to 7.4 nH. For typical low-T_c devices, $\Gamma\beta_L \approx 0.05$ (corresponding to L ≈ 300 pH at 4.2 K), whereas for most high-T_c devices $\Gamma\beta_L \geq 0.1$. Without losing generality, the data are normalized to their respective values at $\Gamma\beta_L = 1/80$ and the normalization factor is shown in the insets of the corresponding figures as a function of β_L.

Fig. 2.16(a) shows $v_\phi(\beta_L; \Gamma\beta_L)/v_\phi(\beta_L; \Gamma\beta_L = 1/80)$ vs. $\Gamma\beta_L$ for 8 values of β_L ranging from 0.6 to 4.0. The results collapse onto a single curve that can be characterized as $v_\phi = f(\beta_L)\ g(\Gamma\beta_L)$. The solid line in Fig. 2.16(a) is an empirical fit to the computed values,

$$g(\Gamma\beta_L) \equiv v_\phi(\beta_L; \Gamma\beta_L)/v_\phi(\beta_L; \Gamma\beta_L = 1/80) = [(80\Gamma\beta_L)^{0.4} + 0.35(4\Gamma\beta_L)^{2.5}]^{-1} \qquad (2.47)$$

For $\Gamma\beta_L < 0.2$, (2.47) can be approximated as $g(\Gamma\beta_L) \approx (80\Gamma\beta_L)^{-0.4}$. The inset of Fig. 2.16(a) shows v_ϕ vs. β_L for the fixed value $\Gamma\beta_L = 1/80$ for $0.1 < \beta_L < 5.2$. Within the range $0.4 < \beta_L < 5.2$, which embraces the values that are of interest experimentally, one can fit the transfer function by the expression

$$f(\beta_L) \equiv v_\phi(\beta_L; \Gamma\beta_L = 1/80) = 7.3\beta_L^{0.15}/(1+\beta_L) \tag{2.48}$$

shown as a solid line in the inset. Note that the expression describes the numerical data well for $\beta_L > 0.4$. It does, however, not follow the decrease in v_ϕ ($\Gamma\beta_L = 1/80$) for small values of β_L. With the aid of the factorisation $v_\phi = f(\beta_L)g(\Gamma\beta_L)$, these two curves or equations (2.47) and (2.48) enable one to calculate v_ϕ immediately for any value of β_L and $\Gamma\beta_L$ within the specified ranges. Note that the factorization cannot hold for values of β_L that are too small, since Γ would become much greater than unity and the SQUID would no longer function. One should restrict the range of validity to $\Gamma < 1$, that is $\Gamma\beta_L < \beta_L$. In the region $\Gamma\beta_L < 0.2$, where one finds $g(\Gamma\beta_L) = (80\Gamma\beta_L)^{-0.4}$, v_ϕ can also be factorized as $\hat{f}(\beta_L)\hat{g}(\Gamma)$, where $\hat{f}(\beta_L) = f(\beta_L)(80\beta_L)^{-0.4}$ and $\hat{g}(\Gamma) = \Gamma^{-0.4}$. For comparison, expression (2.46) is plotted as a dashed line in Fig. 2.16(a). It agrees with the numeric results for $0.1 < \Gamma\beta_L < 0.4$, but underestimates v_ϕ outside this region.

Fig. 2.16(b) shows the normalized low-frequency voltage noise at the optimal bias point for 8 values of β_L. For a given value of β_L, the noise power increases with $\Gamma\beta_L$. However, the overall variation in $S_v(\Gamma\beta_L)$ is weak: within a factor of 2, $s_v \approx 1$ or $S_V \approx I_0 R\,\Phi_0/2\pi$. In contrast to the transfer function (Fig. 2.16(a)), there is no universal behavior for the noise power although roughly speaking s_v scales as $(80\Gamma\beta_L)^{0.2}$ (line in Fig. 2.16(b)). The inset to Fig. 2.16(b) shows $s_v(\beta_L; \Gamma\beta_L = 1/80)$ vs. β_L. At fixed $\Gamma\beta_L$, the normalized noise power decreases as β_L is increased, reflecting the decrease in temperature. The line is a fit to $s_v(\beta_L; \Gamma\beta_L = 1/80) = 0.62\beta_L^{-0.3}$; within the range $0.4 < \beta_L < 5.2$, one can approximate $s_v \approx 1.5\beta_L^{-0.3}(\Gamma\beta_L)^{0.2}$. For $\Gamma = 0.05$ and $\beta_L = 1$, one finds $s_v = 0.82$ or $S_V \approx 16\,k_B TR$, in agreement with the result of Tesche and Clarke [23].

The normalized low-frequency flux noise at optimal bias point, as obtained from the data shown in Figs. 2.16(a) and 2.16 (b), is shown in Fig. 2.16 (c). The data can be fitted well by the expression

$$s_\phi(\beta_L; \Gamma\beta_L)/\, s_\phi(\beta_L; \Gamma\beta_L = 1/80) = 0.8[80\Gamma\beta_L + (1 + 4\Gamma\beta_L)^{4.1} - 1]\,. \tag{2.49}$$

shown as a solid line in Fig. 2.16(c). For $\Gamma\beta_L < 0.1$, $s_\phi(\beta_L; \Gamma\beta_L)/\, s_\phi(\beta_L; \Gamma\beta_L = 1/80)$ reduces to approximately $80\Gamma\beta_L$, while for larger values of $\Gamma\beta_L$ it increases rapidly because of the rapid drop in v_ϕ. In the inset to Fig. 2.16(c) we plot $s_\phi(\beta_L; \Gamma\beta_L = 1/80)$ vs. β_L, together with the fitted curve

$$s_\phi(\beta_L; \Gamma\beta_L = 1/80) = (1 + \beta_L)/40\,, \tag{2.50}$$

describing the numerical data well for $\beta_L > 0.5$. Thus, for the range $\Gamma\beta_L < 0.1$, one finds $s_\phi \approx 2(1+\beta_L)\,\Gamma\beta_L$ or $S_\Phi \approx 4(1+\beta_L)\,\Phi_0 k_B TL/I_0 R$. For $\beta_L = 1$, this result becomes

$16\,k_B T L^2/R$, in excellent agreement with the value of Tesche and Clarke [23]. As an example, from Fig. 2.16(c) for $\Gamma\beta_L = 0.1$ and $\beta_L = 1$ we find $s_\phi \approx 0.4$; with $I_0 R = 200\,\mu V$, this value corresponds to $S_\Phi \approx 0.6 \times 10^{-12} \Phi_0^2\,Hz^{-1}$.

We finally discuss the optimized energy resolution $\varepsilon = S_\Phi/2L$; in dimensionless units, $e = \varepsilon I_0 R/2\Phi_0 k_B T = s_\phi/2\Gamma\beta_L$. Figure 2.16(d) shows $e(\beta_L; \Gamma\beta_L)/e(\beta_L; \Gamma\beta_L = 1/80)$ vs. $\Gamma\beta_L$, obtained from the results in Figs. 2.16(a) and 2.16(b). To a good approximation we find

$$e(\beta_L; \Gamma\beta_L)/\, e(\beta_L; \Gamma\beta_L = 1/80) = [80\Gamma\beta_L + (1 + 4\Gamma\beta_L)^{4.1} - 1]/(100\Gamma\beta_L). \tag{2.51}$$

For $\Gamma\beta_L < 0.2$, the normalized noise energy e is almost constant (≈ 1), while for higher values of $\Gamma\beta_L$ it increases rapidly. The rapid increase in noise energy arises from the rapid degradation of the transfer function over the same values of $\Gamma\beta_L$ (Fig. 2.16(a)). In the inset of Fig. 2.16(d) we plot $e(\beta_L; \Gamma\beta_L = 1/80)$ as a function of β_L. The dependence is linear for $\beta_L > 0.5$ and to a good approximation

$$e(\beta_L; \Gamma\beta_L = 1/80) \approx (1 + \beta_L). \tag{2.52}$$

From (2.51) and (2.52) we find for the un-normalized energy resolution

$$\varepsilon = \frac{\Phi_0^2}{R}\,\frac{1+\beta_L}{\beta_L}\,\frac{80\Gamma\beta_L + \left(1+4\Gamma\beta_L\right)^{4.1} - 1}{100\pi}. \tag{2.53}$$

For $\Gamma\beta_L < 0.2$ and for an arbitrary value of β_L one finds $\varepsilon \approx 2(1 + \beta_L)\Phi_0 k_B T/I_0 R$ or $e \approx (1 + \beta_L)$.

For a SQUID with $\Gamma = 0.05$ and $\beta_L = 1$, one finds $\varepsilon \approx 9\,k_B T L/R$ [23], corresponding to $e \approx 2.25$. From Fig. 2.16(d), one obtains $e \approx 2$, in good agreement, and observes that this value remains valid for $\Gamma\beta_L < 0.2$.

We conclude this section on numerical simulations by noting that, for low-T_c devices, the measured transfer function and white noise properties follow the numerical predictions closely. In contrast, for high-T_c devices the white noise measured is often one order of magnitude larger than the predicted values [94]. We also note that further improvements of the noise performance may be achieved via asymmetric SQUID parameters [see Section 2.3] or additional elements like a damping resistor across the SQUID loop [77,87,88] and/or a third Josephson junction [90,91]. A detailed analysis is beyond the scope of this section, and we will only refer to the literature cited above.

2.2.3.3 Analytical Theory of the dc SQUID

To complete the understanding of dc SQUIDs operating at large thermal fluctuations (in particular, of high-T_c SQUIDs operating at 77 K) an analytical approach has been developed for overdamped systems having $\beta_c << 1$ (we recall here that high-T_c SQUIDs operating at 77 K are made of overdamped junctions). Analytical expressions can be very useful in that they not only permit more rapid calculations, but also give added insights and allow manipulations such as the taking of derivatives.

The dynamic resistance (the derivative of voltage with respect to bias current), the transfer function (the derivative of voltage with respect to the applied flux), and energy sensitivity (inversely proportional to the square of the derivative of voltage with respect to bias current) are examples of quantities needed in the analysis of dc SQUIDs. Next, a short summary of this analytical treatment is given (for details see [82–84]).

For dc SQUIDs made of overdamped junctions, the dynamics in the presence of thermal fluctuations is described by a simplified version of Langevin-type equations (2.35) of the form:

$$\frac{d\delta_-}{dt} = -\frac{2R}{L}\left(\delta_- - \pi\phi_a\right) - \omega_c \sin\delta_- \cos\delta_+ + \frac{i_{N1}+i_{N2}}{2}\omega_c, \tag{2.54a}$$

$$\frac{d\delta_+}{dt} = \frac{i}{2}\omega_c - \omega_c \sin\delta_+ \cos\delta_- + \frac{i_{N1}-i_{N2}}{2}\omega_c\,, \tag{2.54b}$$

where $\delta_- = (\delta_2 - \delta_1)/2$, $\delta_+ = (\delta_1+\delta_2)/2$, $\delta_k(t)$ is the phase difference across the Josephson junction (JJ) k (k= 1,2; the two JJ are identical, overdamped and symmetrically incorporated into the SQUID inductance L), t is time, $\delta_- = \pi\Phi_T/\Phi_0$, Φ_T is the total flux inside the SQUID loop, and $i_{Nk}(t) = I_{Nk}(t)/I_0$ are the two independent Nyquist normalized noise currents.

As the general theory of the Brownian motion shows [102], the two coupled Langevin equations (2.54a) and (2.54b) (written for the phases δ_- and δ_+) are equivalent to a single two dimensional Fokker–Planck equation written for $\lambda(t,\delta_-,\delta_+)$ – the probability density distribution of finding the dc SQUID in a state (δ_-,δ_+) at time t:

$$\begin{aligned}&\frac{L}{2R}\frac{\partial}{\partial t}\lambda + \frac{\pi\beta_L i}{4}\frac{\partial}{\partial\delta_+}\lambda - \frac{\partial}{\partial\delta_-}\left[\left(\delta_- - \pi\phi_a\right)\lambda\right] - \alpha\left(\frac{\partial^2}{\partial\delta_-^2} + \frac{\partial^2}{\partial\delta_+^2}\right)\lambda \\ &= \frac{\pi\beta}{2}\left[\cos\delta_+ \frac{\partial}{\partial\delta_-}\left(\lambda\sin\delta_-\right) + \cos\delta_- \frac{\partial}{\partial\delta_+}\left(\lambda\sin\delta_+\right)\right]\end{aligned} \tag{2.55}$$

where $\alpha = L/4L_F$. With (2.55) we introduce the concept of the probability density distribution to characterize the operation of dc SQUIDs in the presence of large thermal fluctuations. The probability density distribution concept shows us that, in the presence of thermal fluctuations, although the external applied flux Φ_a is fixed, the total flux Φ_T inside the SQUID ring does not have a unique solution and should be considered a probabilistic variable instead. By solving the Fokker–Planck equation (2.55) it has been found that the probability density distribution is a Gaussian type function whose dispersion increases with increasing normalized SQUID inductance L/L_F (see Fig. 2.17a). The probability density distribution concept is relevant when the dispersion becomes comparable to the flux quantum Φ_0 – which gives the fundamental periodicity for the Josephson effect. At 77 K, SQUIDs may have inductances around L_F or even higher, in which case fluctuations play an important role. When $L >> L_F$, the dispersion becomes larger than Φ_0, and there is no longer any flux quantization: the SQUID simply does not work. On the contrary, SQUIDs operated at 4 K typically have inductances of $L << L_F$ and the probability density distribu-

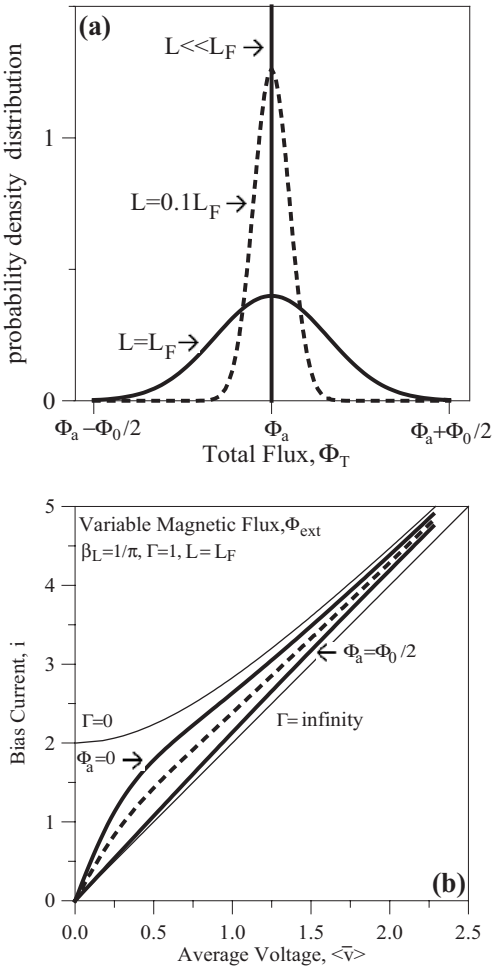

Fig. 2.17 (a): Probability density distribution vs. total flux inside the SQUID ring for different values of normalized inductance L/L_F. For $L << L_F$ the probability density distribution is a Dirac-type function, and with increasing L/L_F the dispersion of the probability density distribution increases. (b) Current–voltage characteristics of the dc SQUID as given by (2.58) for three values of the applied flux (the dashed line is for a quarter of a flux quanta). Thin solid lines show the extreme cases $\Gamma = 0$ and $\Gamma =$ infinity.

tion is close to a Dirac-type function. In this case thermal fluctuations can be considered as a small perturbation in the Langevin equations (2.54).

Adopting the probability density distribution concept, one can calculate the average normalized circulating current $\langle \bar{j} \rangle = \langle \bar{J} \rangle / I_0$ in the ring and the average normalized voltage $\langle v \rangle = \langle \bar{u} \rangle = \langle \bar{U} \rangle / I_0 R$ across the SQUID in the usual way, as is done in statistical physics, i.e., as statistical momenta (the statistical average of x is denoted by $\langle x \rangle$, and the temporal average by $\bar{x}$):

$$\langle \bar{j} \rangle = \int_{-\infty}^{\infty} \int_{0}^{2\pi} \overline{j\lambda\left(t, \delta_-, \delta_+\right)} d\delta_- d\delta_+ = \frac{\pi \beta_L}{8} S_1 \sin 2\pi\phi_a, \tag{2.56}$$

with

$$S_1(\alpha,\Gamma,i)=\frac{e^{-\alpha}}{\alpha^2+(\alpha i/\Gamma)^2}\left[\alpha e^{-\alpha}-\sum_{m=0}^{\infty}\frac{(-\alpha)^m}{m!}\frac{(2\alpha+m+1)(\alpha i/\Gamma)^2}{(\alpha+m+1)^2+(\alpha i/\Gamma)^2}\right],$$

and

$$<\overline{v}>=<\overline{u}>=\int_{-\infty}^{\infty}\int_{0}^{2\pi}\overline{u\lambda(t,\delta_-,\delta_+)}d\delta_-\,d\delta_+=\frac{i}{2}\left\{1-\frac{e^{-\alpha}(\alpha/\Gamma)^2}{\alpha^2+(\alpha i/\Gamma)^2}\right.$$
$$\left.\times\left[(e^{-\alpha}+S_{i-})\cos 2\pi\phi_a+(e^{\alpha}-S_{i+})\right]\right\}, \tag{2.57a}$$

$$S_{i\pm}(\alpha,\Gamma,i)=\sum_{m=0}^{\infty}\frac{(\pm\alpha)^m}{m!}\frac{\alpha(\alpha+m+1)-(\alpha i/\Gamma)^2}{(\alpha+m+1)^2+(\alpha i/\Gamma)^2}. \tag{2.57b}$$

Equation (2.56) contains an important physical insight of SQUID operation under the influence of large thermal fluctuations: the screening current in the SQUID ring is suppressed with increasing L/L_F and Γ. As we shall see later on in this section, it is exactly this fact that limits the SQUID sensitivity at large values of the SQUID inductance and noise parameter. Equations (2.56) and (2.57) are accurate when $\pi\Gamma < \exp(-\alpha)$. When $\pi\Gamma > \exp(-\alpha)$, a better solution has been found [83] for the *IV*-curves in the reverse form $i=i(v)$,

$$<i>=2v\left\{1+\frac{e^{-\alpha}(\alpha/\Gamma)^2}{\alpha^2+(2\alpha v/\Gamma)^2}\left[(e^{-\alpha}+S_{v-})\cos 2\pi\phi_a+(e^{\alpha}-S_{v+})\right]\right\}, \tag{2.58a}$$

$$S_{v\pm}(\alpha,\Gamma,v)=\sum_{m=0}^{\infty}\frac{(\pm\alpha)^m}{m!}\frac{\alpha(\alpha+m+1)-(2\alpha v/\Gamma)^2}{(\alpha+m+1)^2+(2\alpha v/\Gamma)^2}. \tag{2.58b}$$

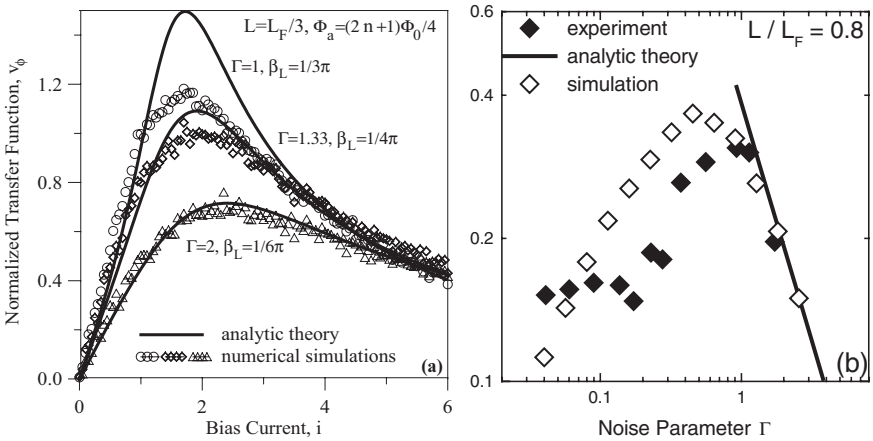

Fig. 2.18 Normalized dc SQUID transfer function (a) vs. bias current and (b) vs. noise parameter Γ. Analytical calculations (the inverse of the voltage derivative of current in (2.58), namely $1/(\partial<i>/\partial v)$ in (a) and (2.59) in (b)) and numerical simulations are shown together with experimental data (in (b)) from a typical high-T_c dc SQUID.

Expressions (2.57) and (2.58) form a complementary set of equations for the dc SQUID operating in the presence of thermal fluctuations obtained in the limit $\Gamma > 4\alpha$, or equivalently, $\beta_L < 1/\pi$. These equations can be used to calculate all important SQUID characteristics: the *IV*-curves (Fig. 2.17b), the dynamic resistance $\partial\langle v\rangle/\partial i$, the transfer function $\partial\langle v\rangle/\partial\phi_a$ (Fig. 2.18), and the energy sensitivity ε (Fig. 2.19). The sums S_1, $S_{i\pm}$ and $S_{v\pm}$ converge rapidly so that for practical purposes it is sufficient to consider only the first terms, namely, $m = 0, 1, 2$ which simplifies the use of equations (2.56), (2.57), and (2.58).

As an example (2.58) has been used in Fig. 2.18(a) to represent the normalized transfer function $\partial\langle v\rangle/\partial\phi_a$ versus bias current. It follows that this characteristic has a maximum at optimum bias current $i = i_{opt}$. It was found that $i_{opt} \approx 1.6$, practically independent of Γ if $\Gamma < 1.6$, while $i_{opt} = \Gamma$ for $\Gamma > 1.6$. These results have been confirmed by experiments [103]. One can insert the calculated optimal values $i = i_{opt}$ into (2.57) and (2.58) and get a unique analytical expression (valid for all cases, no matter whether $\pi\Gamma$ is larger or smaller than $\exp(-\alpha)$) for the optimal transfer function:

$$\left(\frac{\partial\langle v\rangle}{\partial\phi_a}\right)_{opt} = \left(\frac{i_{opt}}{\Gamma} + \frac{\Gamma}{i_{opt}}\right)^{-1} \frac{\pi e^{-\alpha}}{\Gamma}\left(e^{-\alpha} + S_{i-,opt}\right)\sin 2\pi\phi_a \tag{2.59}$$

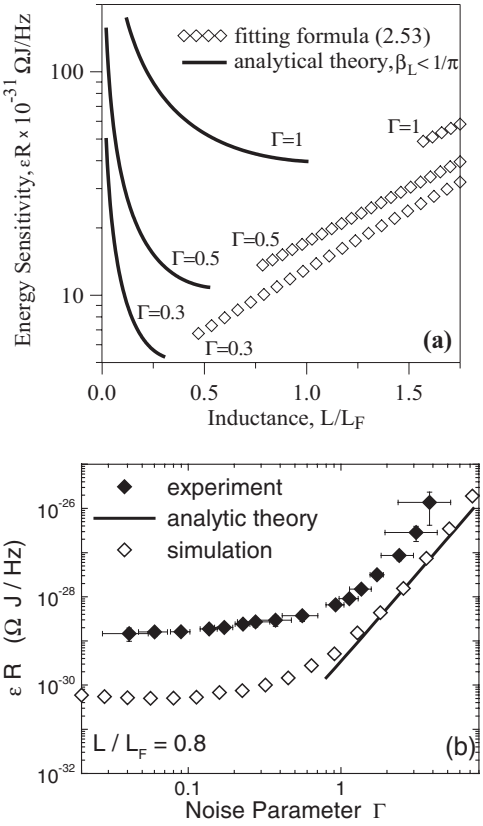

Fig. 2.19 Energy sensitivity ε of the dc SQUID (a) vs. normalized inductance L/L_F for three different values of the noise parameter Γ and (b) vs. Γ for three different values of L/L_F. Analytical calculations (from (2.61); the curves stop at the theory applicability limit $\beta_L < 1/\pi$) and numerical simulations of the fitting formula (2.53)) are shown together with experimental data (in (b)) from a typical high-T_c dc SQUID.

where $S_{i-,opt}$ is given by (2.57b) with $i = i_{opt}$. Neglecting the preamplifier noise, the dc SQUID energy sensitivity ε calculated in [52] can be written as:

$$\varepsilon = \frac{k_B TL}{R} + \frac{2k_B TR_{dyn}/L}{\left(\partial <\overline{V}> /\partial \Phi_a\right)^2_{opt}}, \tag{2.60}$$

where R_{dyn} is the SQUID dynamic resistance. Taking the derivative of the average voltage with respect to bias current in (2.57) and (2.58) one finds that the normalized dynamic resistance $\partial <v>/\partial i$ takes values around 1/2 at optimum bias and large thermal fluctuations, and for that reason a good approximation is to set $R_{dyn}/R = 1/2$ in (2.60). Considering this and by introducing (2.59) into (2.60) one gets for the energy sensitivity in units of 10^{-31} ΩJ/Hz (see also (33a) in [82]):

$$\varepsilon R = 4\alpha + \Gamma^4 \frac{e^{2\alpha}}{\alpha}\left(\frac{i_{opt}}{\Gamma} + \frac{\Gamma}{i_{opt}}\right)^2 \frac{1}{\left[\left(e^{-\alpha} + S_{i-,opt}\right)\sin 2\pi\phi_a\right]^2}. \tag{2.61}$$

The energy sensitivity vs. normalized inductance $L/L_F = 4\alpha$ and the noise parameter Γ as given by (2.61) is shown in Fig. 2.19. Also shown are experimental data of a high-T_c dc SQUID which typically are about one order of magnitude higher than calculations predict, an issue that remains still unclear at present [104].

As seen in Fig. 2.19(a) the energy sensitivity of dc SQUIDs has a minimum with increasing L/L_F. The physics behind this result can be summarized as follows [85]. First, it is natural to expect better output characteristics with improvement of the SQUID screening properties with respect to the applied flux (one of the basic requirements for SQUID operation). Consequently, the higher the L/L_F parameter, which is proportional to the screening parameter β_L, the bigger the difference of the total flux in the SQUID ring and the value of the applied flux; as a result, the better the screening properties. On the other hand it has been shown (see (2.56)) that the screening current in the SQUID ring is suppressed with increasing L/L_F (the suppression becomes noticeable at large thermal fluctuations and increases with Γ). Therefore, from this point of view, the SQUID screening properties degrade with increasing L/L_F. These two physically opposing aspects are responsible for the minimum of SQUID energy sensitivity. In addition, from Fig. 2.19(a) it follows that at large thermal fluctuations (for $\Gamma \geq 0.3$) the minimum in energy sensitivity occurs at $\Gamma \approx L/L_F$, corresponding to $\beta_L \approx 1/\pi$. This is different from the case of small thermal fluctuations when the optimum value of the screening parameter $\beta_L \approx 1$ (see Table 2.1).

To reach the small thermal fluctuations case one has to take the limit $L << L_F$, i.e., $\alpha \to 0$ in Eqs. (2.57), (2.59) and (2.61). We note that by taking this limit $\alpha/\Gamma = \pi\beta_L/4$ remains finite. An excellent agreement (see Table 2.1) is found with the numerical simulations performed for the case of small thermal fluctuations with $\Gamma \cong 0.05$ [23,80,81,52]. This fact shows the generality and applicability of the analytical treatment.

Table 2.1 Analytical vs. numerical simulations of dc SQUIDs at small thermal fluctuations.

Method	β_L optimal	Dynamic Resistance	Transfer Function		Energy Sensitivity	
Analytical	0.9	$3R/4$	$R/2L$		$8\,k_BTL/R$	
Numerical Simulation	≈1	$R/\sqrt{2}$	R/L from [23], [70]	$\approx R/2L$ from [52]	$(9\pm1)\,k_BTL/R$ from [23], [80], [81]	$6.7\,k_BTL/R$ from [52]

2.2.4 Effect of Asymmetry

So far, we have largely neglected the asymmetries in dc SQUID parameters. For high-T_c dc SQUIDs such an asymmetry may occur due to the large spread in the critical current I_0 and resistance R of high-T_c Josephson junctions. It may lead to asymmetric $I_c(\Phi_a)$- or $V(\Phi_a)$-characteristics and can affect the SQUID performance, namely transfer function and flux noise. In this subsection we will therefore discuss the effect of asymmetry in parameters of the two Josephson junctions and in the inductance of the SQUID loop.

In equations (2.37) and (2.38) for the normalized currents flowing across the two junctions (1 and 2) we have already introduced possible asymmetries in the junction critical currents, resistances and capacitances with asymmetry parameters α defined as follows

$$\begin{aligned} I_{0,1} &= I_0\,(1-\alpha_I)\,, \quad R_1 = R\,/(1-\alpha_R)\,, C_1 = C\,(1-\alpha_C) \\ I_{0,2} &= I_0\,(1+\alpha_I)\,, \quad R_2 = R\,/(1+\alpha_R)\,, C_2 = C\,(1+\alpha_C)\,. \end{aligned} \tag{2.62}$$

Considering also an asymmetry in the SQUID inductance, we write the total magnetic flux in the SQUID loop as

$$\Phi_T = \Phi_a + L_1 I_1 - L_2 I_2 = \Phi_a + LJ - \alpha_L LI/2\,, \tag{2.63}$$

where we introduced the parameter $\alpha_L = (L_2 - L_1)/L$ for the asymmetry in the inductance of the two arms forming the SQUID loop as $L_1 = L\,(1-\alpha_L)/2$ and $L_2 = L\,(1+\alpha_L)/2$. We note that our definition of the two inductances L_1, L_2 includes the self-inductance of the two arms of the SQUID loop and their mutual inductance [23], with $L_1 + L_2 = L$. Comparing (2.63) with (2.36) we have now added the "self-flux" $-\alpha_L LI/2$ which increases linearly with bias current I. Including the inductance asymmetry, (2.39) transforms into

$$\delta_2 - \delta_1 = 2\pi\left(\phi_a + \frac{1}{2}\beta_L j - \frac{1}{4}\alpha_L\beta_L i\right) = 2\pi\phi_a + \pi\beta_L\left(j - \frac{\alpha_L}{2} i\right)\,, \tag{2.64}$$

which has to be solved together with (2.37) and (2.38). We note that (2.64) can be used to express the circulating current as

$$j = \frac{\delta_2 - \delta_1 - 2\pi\phi_a}{\pi\beta_L} + \frac{\alpha_L}{2} i \,. \tag{2.65}$$

The (time dependent) voltage across the SQUID can be written as

$$U = U_1 + L_1 \frac{\mathrm{d}I_1}{\mathrm{d}t} = U_2 + L_2 \frac{\mathrm{d}I_2}{\mathrm{d}t} \tag{2.66}$$

which includes the voltages induced by time-varying currents flowing through the inductances L_1, L_2 through the SQUID arms. With the definition of L_1 and L_2 and with $\mathrm{d}I_1/\mathrm{d}t = -\mathrm{d}I_2/\mathrm{d}t = \mathrm{d}J/\mathrm{d}t$ (for $\mathrm{d}I/\mathrm{d}t = 0$) we get $L_1(\mathrm{d}I_1/\mathrm{d}t) = L(\mathrm{d}J/\mathrm{d}t)(1-\alpha_L)/2$ and $L_2(\mathrm{d}I_2/\mathrm{d}t) = -L(\mathrm{d}J/\mathrm{d}t)(1+\alpha_L)/2$ and hence

$$U = \frac{1}{2}\left[U_1 + \frac{1-\alpha_L}{2} L \frac{\mathrm{d}J}{\mathrm{d}t} + U_2 - \frac{1+\alpha_L}{2} L \frac{\mathrm{d}J}{\mathrm{d}t}\right] = \frac{1}{2}\left[U_1 + U_2 - \alpha_L L \frac{\mathrm{d}J}{\mathrm{d}t}\right]. \tag{2.67}$$

With the normalization of voltage by $I_0 R$ and time by ω_c^{-1} we get then $u = \frac{1}{2}\left[\dot{\delta}_1 + \dot{\delta}_2 - \pi\beta_L \alpha_L \dot{j}\right]$, and using the expression for j in (2.65),

$$u = \frac{1}{2}\left[(1+\alpha_L)\dot{\delta}_1 + (1-\alpha_L)\dot{\delta}_2\right], \tag{2.68}$$

where we assumed the external flux and the bias current to be constant in time. We note that for the time-averaged voltages we still have $V_1 = V_2$.

One can derive the normalized potential $u_{SQUID} = U_{SQUID}/E_J$ for the asymmetric dc SQUID by rewriting (2.37) and (2.38), with the expression (2.65) for the circulating current as

$$\beta_c \ddot{\delta}_k (1 \mp \alpha_C) + \dot{\delta}_k (1 \mp \alpha_R) = -\frac{\partial u_{SQUID}}{\partial \delta_k}, \; (k=1,2) \tag{2.69}$$

with

$$\begin{aligned} u_{SQUID} = {} & \frac{1}{2\pi\beta_L}(\delta_2 - \delta_1 - 2\pi\phi_a)^2 - (1-\alpha_I)\cos\delta_1 - (1+\alpha_I)\cos\delta_2 \\ & - \frac{i}{2}\left\{(1+\alpha_L)\delta_1 + (1-\alpha_L)\delta_2\right\}. \end{aligned} \tag{2.70}$$

Turning to new coordinates $\delta_+ \equiv (\delta_1 + \delta_2)/2$ and $\delta_- \equiv (\delta_2 - \delta_1)/2$ one finds

$$\begin{aligned} \frac{U_{SQUID}}{2E_J} = \frac{u_{SQUID}}{2} = {} & \frac{1}{\pi\beta_L}(\delta_- - \pi\phi_a)^2 - \cos\delta_+ \cos\delta_- + \alpha_I \sin\delta_+ \sin\delta_- \\ & - \frac{i}{2}(\delta_+ - \alpha_L \delta_-), \end{aligned} \tag{2.71}$$

which reduces to the expression (2.42) for the symmetric dc SQUID if $\alpha_I = 0$ and $\alpha_L = 0$. Two consequences of nonzero asymmetry parameters are obvious from (2.71). First, an asymmetry in the critical currents ($\alpha_I \neq 0$) leads to the appearance of

the ($\sin\delta_+ \sin\delta_-$)-term, which breaks the reflection symmetry in the SQUID potential. As a consequence, one obtains voltage rectification if an ac driving current is applied and if the applied flux is $\phi_a \neq \pm n/2$ ($n = 0, 1, 2, \ldots$) [62]. This fact can be used to study ratchet effects [105] with asymmetric dc SQUIDs [106,107]. Secondly, an asymmetry in the SQUID inductance ($\alpha_L \neq 0$) changes the direction of the tilt of the potential (along δ_+ if $\alpha_L = 0$) if a bias current is applied.

To understand the effect of various asymmetries on the dc SQUID operation we neglect the thermal noise for the moment and consider first the static case, which is also treated in [23,62,64–66]. Setting all time derivatives equal to zero we get from (2.37), $\frac{i}{2} + j = (1 - \alpha_I)\sin\delta_1$, and from (2.38), $\frac{i}{2} - j = (1 + \alpha_I)\sin\delta_2$. Summation of the above equations yields

$$i = (1 - \alpha_I)\sin\delta_1 + (1 + \alpha_I)\sin\delta_2 \,, \tag{2.72}$$

and after subtraction we get

$$2j = (1 - \alpha_I)\sin\delta_1 - (1 + \alpha_I)\sin\delta_2 \,, \tag{2.73}$$

which have to be solved together with (2.64).

As expected, the asymmetries in R and C do not contribute in the static case. This means that the $I_c(\Phi_a)$-curves do not depend on α_R and α_C. Furthermore, the above equations imply that the normalized critical current i_c always reaches its maximum possible (positive) value $i^+_{c,\max} = 2$ (corresponding to $\delta_1 = \delta_2 = \pi/2$), for some value of the external flux $\phi^+_{a,\max}$. In this case the circulating current is $j(i^+_{c,\max}) = -\alpha_I$ and the external flux $\phi^+_{a,\max} = \frac{\beta_L}{2}(\alpha_I + \alpha_L)$. Hence, the maxima in the $I_c(\Phi_a)$-characteristics are shifted along the flux axis, as shown in Fig. 2.20. Reversing the polarity of the bias current reverses the sign of the shift but does not change its amplitude ($\phi^-_{a,\max} = -\phi^+_{a,\max}$). This allows experimental determination of $\alpha_I + \alpha_L$ (for known β_L) by measuring the difference $\Delta\Phi = \beta_L(\alpha_I + \alpha_L)/\Phi_0$ of the values of the external flux at which $|I_c|$ is maximum for both polarities of bias current. The same shift

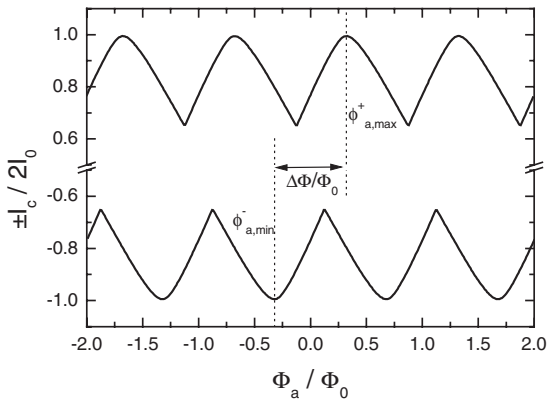

Fig. 2.20 $I_c(\Phi_a)$-curves for dc SQUID with critical current asymmetry $\alpha_I = 0.4$ ($\Gamma = 6 \times 10^{-4}$, $\beta_L = 1.5$, $\alpha_L = 0$) showing the shift of the I_c-maxima for opposite polarity of bias currents

occurs for the minima in the $V(\Phi_a)$ characteristics if $|I_c| \approx 2I_0$. For variable bias current, the minima in the $V(\Phi_a)$ characteristics are shifted along the flux axis proportional to $\alpha_L LI/2$, independent of the value of α_I. This allows the experimental discrimination of asymmetries in critical currents and SQUID inductance. Furthermore, from numerical simulations for nonzero values of $\Gamma \lesssim 0.5$ (for $\alpha_L = 0$) one finds the same relation $\Delta\Phi \approx \beta_L \alpha_I / \Phi_0$ for the flux shift in the maxima of $I_c(\Phi_a)$ and minima of $V(\Phi_a)$ as for the case of $\Gamma = 0$.

Calculations of the $I_c(\Phi_a)$-characteristics for $\Gamma = 0$ for various values of α_I and α_L [23] show that with increasing α_I, the minimum value of the critical current $I_{c,min}$ increases, leading to a reduction of the modulation depth $(I_{c,max} - I_{c,min})/I_0$. In contrast, the modulation depth does not depend on the value of α_L. In the case of an inductance asymmetry ($\alpha_L \neq 0$) the $I_c(\Phi_a)$-curves appear skewed. The value of ϕ_a at $I_{c,min}$ is shifted from $\phi_a = 0.5$ for $\alpha_L = 0$ to $\phi_a = 0.5 - \beta_L \alpha_L i_{c,min}/4$. Moreover, the entire $I_c(\Phi_a)$-curves for $\alpha_L \neq 0$ can be readily generated from the corresponding curve for $\alpha_L = 0$ [23].

Numerical simulations for even moderate values of $\Gamma = 0.05$ show that thermal noise smears out the asymmetry in both the $I_c(\Phi_a)$- and $V(\Phi_a)$-characteristics [99]. We note, that an asymmetry in resistance and capacitance leads to an asymmetric distortion of the $V(\Phi_a)$-characteristics, while an asymmetry in the critical currents only shifts the $V(\Phi_a)$-characteristics. The latter follows directly from (2.64) for constant i. For SQUID operation it is important to understand the effect of asymmetry on the transfer function and noise under the presence of thermal fluctuations. A detailed analysis of the $V(\Phi_a)$-characteristics for various kinds of asymmetries in I_0, R and C is given in [108], where the coupled Langevin equations have been solved numerically, and results are compared with experiments on YBCO dc SQUIDs. In the following we show only results of calculations for the case of 'geometric asymmetry' ($\alpha_I = \alpha_R = \alpha_C$). Due to the asymmetry one finds different values of the maximum transfer function V_Φ^+ and V_Φ^- on the positive and negative slope of the $V(\Phi_a)$-characteristics, respectively. Figure 2.21 shows the calculated normalized transfer function V_Φ^+ and V_Φ^- plotted versus β_L, for fixed $\Gamma\beta_L = 0.2$ and various values of α_I. In most cases one finds for $\beta_L \lesssim 5$ for the asymmetric SQUID a reduction of V_Φ as

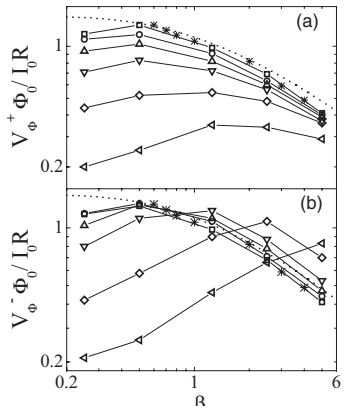

Fig. 2.21 Calculated normalized transfer function V_Φ^+ (a) and $V_{\bar{\Phi}}$ (b) vs. β_L for $\Gamma\beta_L$=0.2 with geometric asymmetry ; $\alpha_I = 0$ (□), 0.2 (○), 0.4 (△), 0.6 (▽), 0.8 (◇), 0.9 (+); solid lines are guide to the eye. For comparison, simulation data (*) from the inset of Fig.2.16(a) together with the according fit-function (dotted line) from eq. (2.48) for symmetric dc SQUIDs, are also shown.

compared to the symmetric SQUID. This reduction increases with decreasing β_L and increasing α_I. However, in the case of geometric asymmetry, for intermediate values of $1 \lesssim \beta_L \lesssim 5$ an increase in V_Φ^- for $\alpha_I \gtrsim 0.5$ is observed, which is due to a strong distortion of the $V(\Phi_a)$-characteristics.

As a main result, the numerical simulations again show factorization of the maximum normalized transfer function $v_\phi \approx g(\Gamma\beta_L) \cdot f(\alpha_I\beta_L)$, similar to the case of the symmetric dc SQUID (see Section 2.2.3.2). Figure 2.22 shows the simulation results for V_Φ^+ in the case of geometric asymmetry. In fact, the function $g(\Gamma\beta_L)$ does not depend on the asymmetry and is identical with (2.47), However, the function $f(\alpha_I\beta_L)$, as shown in the inset, is now strongly dependent on α_I, as already discussed above. The simulation data can now be approximately fitted by

$$f_{geo}^{+} \approx (7.18 \cdot 0.31^{\alpha_I^{8.42}} + 0.45^{\alpha_I^{1.22}}) \frac{\beta_L^{0.18+0.49\cdot\alpha_I^{2.68}}}{1+\beta_L}. \tag{2.74}$$

The effect of asymmetries in critical current and resistance on transfer function, voltage noise, flux noise and energy resolution has been treated by numerically solving the coupled Langevin equations by Testa *et al.* for the case of small thermal fluctuations ($\Gamma = 0.01$) [109] and large thermal fluctuations ($\Gamma = 0.16$) [110]. In both cases strongly overdamped junctions ($\beta_c = 0$) have been assumed and the effect of a damping resistor R_d which shunts the SQUID inductance has been included. With the particular value of $\Gamma = 0.01$ [109] and with $\alpha_I = \alpha_R$ ranging from 0 to 0.6 it is found that the distortion of the $V(\Phi_a)$-curve in the presence of asymmetry can increase V_Φ (if measured on the steeper slope of the $V(\Phi_a)$-curve) within a certain range of values for β_L between 1 and 5. This behavior is also visible in Fig. 2.21(b). However, the absolute maximum of the transfer function is still obtained for the symmetric dc SQUID, if an optimum value of β_L (close to 0.5) is chosen. This is because the improvement in V_Φ with increasing asymmetry is more pronounced for values of β_L which are larger than the optimum value. As the reduction of V_Φ with increasing β_L can be suppressed by the use of a damping resistor, it finally turns out that a combination of asymmetry and damping $\gamma \equiv R/R_d$ may increase the transfer function, even over the optimum value for the symmetric SQUID. For example with

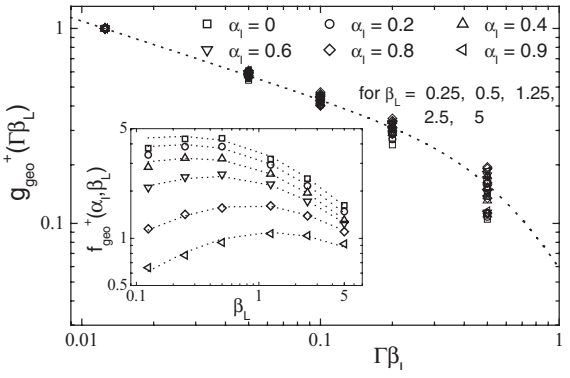

Fig. 2.22 Calculated normalized transfer function V_Φ^+ for geometric asymmetry. The plot shows the function $g(\Gamma\beta_L)$ which does not depend on α_I; the dashed line is calculated from eq.(2.47). The inset shows the normalization function $f(\alpha_I, \beta_L)$; the dashed lines are calculated from eq.(2.74).

$\gamma = 0.5$, $\alpha_I = \alpha_R = 0.6$ and $\beta_L = 5$ one finds a 3% increase in V_Φ over the value obtained for $\gamma = 0$, $\alpha_I = \alpha_R = 0$ and $\beta_L = 0.5$ [109]. It is not the slight increase in V_Φ, which makes this result interesting, but the fact that a high transfer function can be obtained with larger inductance, which allows improvement of the coupling of input signals. The introduction of a damping resistor, however, increases the voltage noise S_V which becomes now also dependent on the asymmetry, leading to an increase of S_V with increasing $\alpha_I = \alpha_R$ [109]. Numerical simulations of the flux noise and the energy resolution indicate that, even with damping, the SQUID performance degrades if one increases β_L from 1 to 5. For $\beta_L = 1$ the flux noise S_Φ is almost independent of the damping γ and the noise improves with increasing asymmetry, for example by roughly a factor of 2 in S_Φ if $\alpha_I = \alpha_R$ is increased from 0 to 0.6 [109]. A similar result has been obtained for larger $\Gamma = 0.16$ [110]. However, it is not clear yet, whether $\beta_L = 1$ is the optimum value in any case. In order to draw a final conclusion on the possible improvement of SQUID performance via introduction of asymmetry, a more detailed analysis is required, in particular regarding the optimization of the flux noise and energy resolution with respect to β_L and Γ. We note that the improvement of the asymmetric SQUID performance relies on the operation on the steeper slope of the $V(\Phi_a)$-curve. Hence, direct readout, instead of flux modulation [c.f. Section 4] should be used in that case.

2.3 Theory of the rf SQUID

2.3.1 Introduction

In this section we analyze the rf SQUID, which consists of a single Josephson junction closed with a superconducting loop that is inductively coupled via a mutual inductance M to an rf current driven tank circuit $L_T C_T$. The principle of rf SQUID operation is clear from Fig. 2.23: the measured flux Φ_a, superimposed over some dc bias flux, changes the average value of the phase δ across the Josephson junction. The non-linearity of the junction expressed by the $\delta(\Phi_a)$ characteristic results in some related change of its impedance for the rf drive oscillations and hence in some change of the amplitude of the rf voltage V_T across the tank circuit. This change,

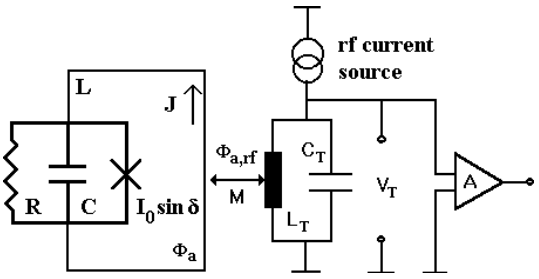

Fig. 2.23 Schematic view of an rf SQUID.

after preliminary amplification, is detected, low-pass filtered and serves as the output signal which is proportional to Φ_a. The dynamics of rf SQUIDs depends fundamentally on whether the rf frequency is smaller than both the junction characteristic frequency ω_c and the cut-off frequency of the SQUID loop, the so-called adiabatic regime. In the adiabatic regime the dynamics is also strongly dependent on whether the junction phase δ as a function of the applied flux Φ_a (see Fig. 2.24b) is single valued (the so-called non-hysteretic operation) or multi-valued (hysteretic operation). In the hysteretic operation dissipative phase jumps occur (schematically shown as AB or CD transitions in Fig. 2.24b) known as the main source for the intrinsic noise of the SQUID. Consequently, the SQUID dissipates energy at a rate that is periodic in Φ_a. This periodic dissipation in turn modulates the quality factor Q of the tank circuit, so that when it is driven on resonance with a constant amplitude, the rf voltage is periodic in Φ_a. To avoid such intrinsic noisy phase transitions in the adiabatic regime, the non-hysteretic operation known as a low-noise regime should be used instead. In this case the SQUID behaves as a parametric inductance, modulating the effective inductance, and hence the resonant frequency of the tank circuit, as the flux is varied. Thus when the tank circuit is driven at constant frequency, the variations in its resonant frequency cause the rf voltage to be periodic in Φ_a. If, on the other hand, the rf frequency is larger than either the junction characteristic frequency ω_c or the cut-off frequency of the SQUID loop the regime of operation is called non-adiabatic. In this regime, although the $\delta(\Phi_a)$ characteristic is hysteretic (see Fig. 2.25a) no discontinuous phase jumps occur which make it a low-intrinsic noise operation as well. Qualitatively, the SQUID operation is somehow similar to the adiabatic non-hysteretic regime, that is, the SQUID behaves as a parametric inductance whose output voltage response results from the Φ_a modulation of the tank circuit resonant frequency. All these regimes will be investigated separately.

Since their first demonstration, rf SQUIDs were used as magnetic field sensors for applications requiring very high sensitivity [111]. Tank frequencies of these early, point-contact rf SQUIDs were in the range of 20 to 40 MHz. Later on in the 1980s, they were gradually replaced by dc SQUIDs, which then offered higher sensitivity. The operation at microwave bias frequencies (a few to tens of GHz) and the use of liquid helium cooled preamplifiers, however, has greatly improved the sensitivity of rf SQUIDs to a value comparable with that of the best dc SQUIDs, in terms of energy resolution. Moreover, the discovery of high transition temperature (high-T_c) superconductors has further increased the interest in rf SQUIDs. As discussed in Chapter 6, due to the different geometry and readout, rf SQUIDs offer interesting advantages when compared to dc SQUIDs. Also, generally, because of the absence of steady Josephson oscillations, in a well coupled input coil no problems usually occur due to resonance, which, in dc SQUIDs, can lead to a reduction in signal voltage and in sensitivity.

Soon after the first demonstration of rf SQUIDs, a consistent theory of their operation was developed, which could explain the experimental results obtained at that time. A complete summary of this theory can be found in the excellent review articles by e.g. Silver and Zimmerman [111], Giffard, Webb and Wheatley [112], Jackel and Buhrman [113], Ryhänen *et al.* [52] and in books by Likharev and Ulrich

[114], Likharev [4] and Gallop [115]. Recent work on high-T_c rf SQUIDs has shown that in some cases this standard theoretical model needs considerable further development. Issues not considered in early theories of the rf SQUIDs were operation at large thermal fluctuations – the case of high-T_c rf SQUIDs –, and low-frequency excess noise in rf SQUIDs. The effect of SQUID inductance on the thermal noise of the SQUID in particular, as well as operation at large thermal fluctuations in general, have been under theoretical investigation only recently [85], after observations that high-T_c rf SQUIDs still function at much higher inductances and thermal fluctuation levels than previously predicted. We briefly present the most important results of all these analytical theories, but refer the reader to the above mentioned papers for a more detailed review. It should be mentioned that in contrast to the case of dc SQUIDs, for rf SQUIDs no extensive numerical simulations performed for a wide range of noise parameter Γ and inductance L have been reported so far.

2.3.2
SQUID Potential and the Equation of Motion for the Phase Difference

The rf SQUID consists of a superconducting ring of inductance L containing a single Josephson junction or weak link having a critical current I_0, a resistance R and capacitance C (Fig. 2.23). The inductance L is inductively coupled to the tank circuit $L_T C_T$ via a mutual inductance M. A rf current generator supplies the tank circuit with a current $I_{rf}\cos(\omega_{rf}t)$, so that the resulting rf magnetic flux applied to the SQUID loop is $\Phi_{a,rf} = [(\Phi_0/2\pi)\nu_T]\cos(\omega_{rf}t + \rho)$, where $(\Phi_0/2\pi)\nu_T$ is the amplitude of the external rf flux, ρ is the phase, t is the time, and Φ_0 is the flux quantum. The voltage that provides the output signal of the rf SQUID is picked up from the amplifier A whose input is connected to the tank circuit. The input signal magnetic flux to be measured Φ_a is applied to the SQUID loop. Because the highest frequency of the Φ_a flux spectrum is usually much less than the pumping frequency ω_{rf}, this flux can be considered quasi-static.

In analogy to (2.36), written for a ring that incorporates two junctions, one has for a single junction loop a similar equation that connects the junction's phase difference δ, the circulating current J in the SQUID loop, and the total applied flux $\Phi_{a,T} = \Phi_{a,rf} + \Phi_a$

$$\delta = \frac{2\pi}{\Phi_0}\left(\Phi_{a,rf} + \Phi_a + LJ\right) = \frac{2\pi}{\Phi_0}\Phi_T \tag{2.75}$$

where Φ_T is the total flux in the SQUID loop. In addition, one assumes that the supercurrent across the junction has again a sinusoidal dependence on δ (see (2.1)). On the basis of (2.1) and (2.75) one can build up the SQUID potential, or, equivalently the Gibbs free energy of the system. It has two components: the Josephson coupling energy and the inductive energy that is due to the screening current flowing into the SQUID loop. Thus, the dynamics of the rf SQUID can be visualized as a motion in a one-dimensional potential – see Fig. 2.24(a)

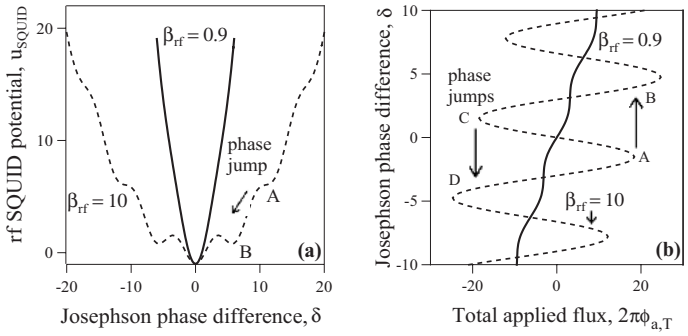

Fig. 2.24 (a) rf SQUID normalized potential $u_{SQUID} = U_{SQUID}/E_J$ as a function of the Josephson phase difference δ (from (2.76)). (b) SQUID phase (flux) diagram in the adiabatic regime at low thermal fluctuations (from (2.80)).

$$\frac{U_{SQUID}(\delta)}{E_J} = \frac{\left(\delta - 2\pi\phi_{a,T}\right)^2}{2\beta_{rf}} - \cos\,\delta \tag{2.76}$$

where $\phi_{a,T} = \Phi_{a,T}/\Phi_0$, and $\beta_{rf} = 2\pi LI_0/\Phi_0$ is the so called SQUID hysteresis parameter (or screening parameter), At $\beta_{\mathrm{rf}} < 1$ the potential has one minimum, corresponding to the only superconducting state of the interferometer. At $\beta_{\mathrm{rf}} > 1$, in addition, there can be several metastable states. Here, the resistive-capacitive shunted junction (RSCJ) model of the Josephson junction is assumed (the Josephson junction is shunted by a resistor R and a capacitor C) so that the equation describing the system dynamics is (see, e.g., Chapter 8 in [114], and Chapter 6 in [4]) of Langevin type

$$C\frac{d^2\delta}{dt^2} + \frac{1}{R}\frac{d\delta}{dt} + \left(\frac{2\pi}{\Phi_0}\right)^2 \frac{dU_{SQUID}}{d\delta} = I_N\frac{2\pi}{\Phi_0}. \tag{2.77}$$

It is also assumed that the input noise in the rf SQUID can be approximated by the Johnson noise in the shunt resistance, so that the term I_N, having a Dirac correlation function and a spectral density $S_{IN}(\omega) = 2\,k_BT/\pi R$, corresponds to the current contribution of the thermal noise generated by the resistance R. Two more parameters have to be defined at this point: the SQUID cutoff frequency $\omega_{cut} = R/L$ and the characteristic frequency of the Josephson junction $\omega_c = 2\pi RI_0/\Phi_0 = \beta_{rf}\omega_{cut}$. The resistance R is usually chosen to have a Stewart–McCumber damping parameter $\beta_c = 2\pi I_0R^2C/\Phi_0 << 1$, so that the current-voltage (I–V) characteristic of the weak link is non-hysteretic. In this overdamped case, effects of C on the SQUID response can be neglected. Consequently, the second derivative of the phase in the equation of motion (2.77) vanishes so that the system dynamics is described by a nonlinear first-order differential Langevin equation:

$$\frac{1}{\omega_{cut}}\frac{d\delta}{dt} + \beta_{rf}\sin\delta + \delta - 2\pi\phi_{a,T} = I_N\frac{2\pi}{\Phi_0} \tag{2.78}$$

From the point of view of bias frequency ω_{rf}, there are two different modes of operation. First, the so called adiabatic mode defined by

$$\omega_{rf} << \min\left(\omega_{cut}, \omega_c\right) \tag{2.79}$$

in which case the first term on the left-hand side of (2.78) can be neglected so that, in the absence of thermal fluctuations, ($I_N = 0$):

$$\beta_{rf}\sin\delta + \delta = 2\pi\phi_{a,T}. \tag{2.80}$$

Equation (2.80) is represented in Fig. 2.24(b). When $\beta_{\mathrm{rf}} < 1$ the phase diagram is single-valued [4], [115–122]. In contrast, when $\beta_{\mathrm{rf}} > 1$, the phase diagram is multi-valued (see for instance [4], [52], [111–115]), and noisy flux transitions occur [123–124]. With increasing flux, the SQUID will follow a segment with positive slope (only the parts having positive slopes are due to stable states of the system) up to a value where the supercurrent in the SQUID reaches the critical current of the weak link. Then the weak link momentarily switches to the resistive state and the SQUID undergoes a quantum transition $n \to n+1$ (the flux through the SQUID changes by one flux quantum). For a system, where $\beta_{\mathrm{c}} > 1$, it may jump through several flux states before stabilizing. The time of the transition is given by $1/\omega_{\mathrm{cut}}$, the response time of the SQUID ring or by the quasiparticle relaxation time of the weak link $1/\omega_{\mathrm{c}}$, depending on which will be larger. In the same way, as the flux is decreased, quantum transitions $n+1 \to n$ take place. As the system undergoes quantum transitions from one state to another and back, a hysteresis loop (like ABCDA in Fig. 2.24(b)) is described on the phase diagram. For that reason this mode of operation is sometimes also called the hysteretic mode. If condition (2.79) is not satisfied then one deals with the so called non-adiabatic mode. In the non-adiabatic case the first term on the left-hand side of (2.78) should be considered in the calculations. This latter mode of operation has been less investigated theoretically [125–129] although it is believed that in this mode rf SQUIDs are at their best in terms of energy sensitivity.

What is the physical difference between the two modes of operation? Before answering this question a simple physical picture has to be introduced (see for instance [4] where the system dynamics can be found by considering the motion in the one-dimension $\mathrm{U_{SQUID}}(\delta)$ potential). When $\beta_{\mathrm{rf}} > 1$, phase transitions are possible between different metastable states when an externally applied magnetic field is changed, so that the parabolic part of U_{SQUID} is shifted along its oscillating part. As a consequence, a gradual change of the applied field $\Phi_{a,rf}$ leads to the general rise in energy of the system (since U_{SQUID} depends on $\Phi_{\mathrm{a,T}} = \Phi_{a,rf} + \Phi_a$), while the phase is "captured" at the bottom of one potential well. As it increases further the external flux $\Phi_{a,rf}$, an energy barrier which separates this well from a lower energy state, decreases, and the system eventually makes a phase transition to one of these

lower states. In the limit of large damping the motion along the SQUID potential U profile is non-inertial. The first stage of the phase transient (with the phase in the vicinity of the energy barrier top) has a duration higher than $1/\omega_c$, while the second stage of the jump (the phase motion along the external side of the energy barrier) will be passed in the time $3/\omega_c$. As a result, in this case, the total transition time between two adjacent metastable states takes a time interval of about $5/\omega_c$. Having the estimates of flux transition time, it is easy to obtain a physical picture of the operating regime for frequencies that satisfy condition (2.79). Simply, the sweep ω_{rf} is much slower than the characteristic time for a flux transition which explains the significance of the term "adiabatic", used to describe this regime. The difference between the two SQUID modes is ultimately due to changes in the system response. For the adiabatic mode, the external flux $\Phi_{a,rf}$ changes sufficiently slowly so that in the one-dinensional space of the basic variable δ, the system always manages to settle in a local minimum of the potential $U_{SQUID}(\delta)$. Thus, δ remains nearly in phase with $\phi_{a,rf} = \Phi_{a,rf}/\Phi_0$. Whenever the barrier separating a local minimum from the next lower minimum disappears, the system makes a flux transition. In contrast, for the non-adiabatic mode, the system's position in the one-dimension space is driven through the same potential so quickly that it cannot settle to the bottom of the local minima, so that δ becomes significantly out of phase with $\phi_{a,rf} = \Phi_{a,rf}/\Phi_0$. Therefore, in 1D space, the system traverses far beyond the point where the barrier to the next lower minimum disappears, without making a transition. Before the system has a chance to transit to the adjacent stable steady state, the external flux $\Phi_{a,rf}$ changes and the barrier reappears.

When phase transitions occur (adiabatic regime at low thermal fluctuations with $\beta_{\mathrm{rf}} > 1$) a considerable intrinsic noise [123–124] is generated that is due to amplification of the junction's thermal noise by multiple flux transitions which deteriorates the SQUID measuring performances. For that reason this mode of operation has been lately avoided in practice. To give an example, for rf SQUIDs with a non-hysteretic phase diagram operating at about 10 GHz, an energy sensitivity as small as $(2.5\pm0.7)10^{-33}$ J/Hz $\approx (23 \pm 7)\,\hbar$ (here $\hbar = h/2\pi$, h is the Planck constant) with a calculated thermal fluctuations level of about $6\hbar$ has been reported in the literature [130]. This is about two orders of magnitude better than for any hysteretic rf SQUID. Consequently, in spite of being historically the first mode used, the hysteretic mode will be only briefly considered here. A more detailed description will be given of the other two, low-noise regimes: adiabatic operation with non-hysteretic phase diagram (this mode of operation is also known as the "dispersive" or "inductive" mode), and non-adiabatic operation. In both of these regimes, rf SQUIDs can be tuned to produce an infinite value of the transfer function. This fact is responsible for the high sensitivity reached in these cases. Around such operating points the energy sensitivity is limited by the intrinsic noise of the SQUID and not by the preamplifier, provided it is appropriately cooled.

It is important to note that the threshold value $\beta_{rf} = 1$, which separates the operation regimes into two categories (see Fig. 2.24(b)), namely, SQUIDs having a hysteretic phase diagram ($\beta_{rf} > 1$) or a non-hysteretic one ($\beta_{rf} < 1$) is valid only under the assumption that the SQUID is operated at low thermal fluctuations. In the presence

of large thermal fluctuations, as we shall see, the non-hysteretic phase diagram characterizes SQUID operation also for $\beta_{rf} > 1$ so that the inductive mode of operation is extended to higher values of β_{rf}.

2.3.3 Unitary Theory for Output Signal and Noise

When thermal fluctuations are important (as is the case of great interest for high-T_c rf SQUIDs) the noise contribution in (2.78) cannot be treated as a small perturbation. For that reason (2.80) as well as the phase diagrams plotted in Fig. 2.24(b) are no longer valid. Instead, signal and noise should be treated simultaneously in a unitary approach. An analytical solution of this problem has recently being given [85]. Its validity, with some restrictions, extends over all existing operating regimes discussed so far: adiabatic with hysteretic phase diagram which at large thermal fluctuations become non-hysteretic, adiabatic with non-hysteretic (single-valued) phase diagram, the non-adiabatic regime, and small and large thermal fluctuation regimes. In comparison with numerical simulations, analytical expressions can be very useful in that they not only permit more rapid calculations, but also give added insight and allow manipulations such as the taking of derivatives. For all these reasons a detailed description of the analytical approach will be given in this section.

As already mentioned at the beginning of Section 2.2.3 it was believed that thermal noise imposed two requirements for a proper operation of SQUIDs: the noise parameter $\Gamma << 1$ and $L < L_F$. First reported evidence to the contrary was published over 20 years ago; Falco and Parker [131]. operated at 2 K some rf SQUIDs with noise parameter Γ as high as 1.7 and $L < L_F$. More recently, high-T_c rf SQUIDs having Γ up to 10 and inductances up to 1 nH ($L_F = 100$ pH at 77 K) have been successfully operated in practice (Zhang *et al.* [132–134], Zakosarenko *et al.* [135], Il'ichev *et al.* [136]). To improve understanding of rf SQUIDs operating at large thermal fluctuations (in particular, of high-T_c SQUIDs operating at 77 K) an analytical approach was developed for overdamped systems ($\beta_c << 1$). When thermal fluctuations are important (which is the case at $T = 77$ K), the processes that take place in the interferometer should be considered to be of a Markoffian type, and for calculations of important SQUID parameters the Fokker–Planck equation should be applied. As the general theory of the Brownian motion shows [102], this equation is equivalent to the Langevin equation (2.78) which describes the SQUID dynamics in the frame of the RSJ model. The first attempt to include the interaction within the rf SQUID between the interferometer and the tank circuit, into the Markoffian-type formalism was made some time ago [137]. In that work, however, the Fokker–Planck equation had not been solved because of its complexity. Nevertheless, the equation was exactly written for the case of a real rf SQUID (i.e., an rf SQUID inductively coupled to a tank circuit) with $\beta_{rf} \geq 1$. It was assumed that the product of the junction capacitance times the resistance is a small but a non-zero parameter. Recently [85], although in a different manner, this problem has been reconsidered for $\beta_{rf} < 3$ and successfully solved in the case when the product CR is negligibly small. In practice this is the case, because for proper high-T_c SQUID operation it is necessary that the Josephson

junction be overdamped ($\beta_c << 1$). Hence, the Fokker–Planck equation is reduced to the Smoluchowski equation:

$$\frac{1}{\beta_{rf}\omega_{cut}}\frac{\partial\sigma}{\partial t} = \frac{d}{d\delta}\left[\frac{1}{E_J}\frac{dU_{SQUID}}{d\delta}\sigma\right] + \Gamma\frac{\partial^2\sigma}{\partial\delta^2} \tag{2.81}$$

where U_{SQUID}/E_J is the normalized rf SQUID potential (2.76), $\sigma(\delta,t)$ is the probability density of finding the interferometer loop in a state δ at time t, and $\omega_{cut} = R/L$ is the cut-off frequency.

For $\beta_{rf} << 1$, an exact solution for the non-stationary Smoluchowski equation (2.81) has been found:

$$\sigma(\delta,t) = \sqrt{\frac{L_F}{2\pi L}}\exp\left\{-\frac{L_F}{2L}\left[\delta - 2\pi\phi_a - v_T^*\sin\left(\omega_{rf}t - \theta\right)\right]^2\right\},\ (\beta_{rf} << 1). \tag{2.82a}$$

Here $v_T^* = v_T/\sqrt{1+\omega_R^2}$, $tg\theta = \omega_R$ and $\omega_R = \omega_{rf}/\omega_{cut}$.

For larger values of the reduced inductance ($0.2 < \beta_{rf} < 3$) an approximate solution valid for operating frequencies much less than the SQUID cut-off frequency (the adiabatic mode of operation) $\omega_{rf} << \omega_{cut}$ is given by

$$\sigma(\delta,t) = \sqrt{\frac{L_F}{2\pi L}}\exp\left\{-\frac{L_F}{2L}\left[\delta - 2\pi\phi_{a,T}(t)\right]^2\right\} \tag{2.82b}$$

with $\phi_{a,T} = 2\pi\phi_a + v_T\sin\omega_{rf}t$. In addition, the statistical average $\langle\delta\rangle$ of the Josephson phase difference and its dispersion has been calculated as

$$\begin{aligned}&\langle\delta\rangle \underset{t>>2\pi\omega_{rf}}{\longrightarrow} 2\pi\phi_a + v_T^*\sin\left(\omega_{rf}t - \theta\right)\\ &\left\langle\left(\delta - \langle\delta\rangle\right)^2\right\rangle \underset{t>>2\pi\omega_{rf}}{\longrightarrow} L/L_F\end{aligned} \tag{2.83}$$

Two important results are incorporated in (2.83). The first equation gives the SQUID phase diagram (or, equivalently the flux diagram), i.e., the total flux in the interferometer loop as a function of the applied flux, represented in Fig. 2.25(a) for different values of the reduced operating frequency $\omega_R = \omega_{rf}/\omega_{cut}$. As can be observed, the flux inside the interferometer is retarded by some phase lag θ with reference to the applied flux, while the oscillation amplitude is reduced by a factor of $1/\sqrt{1+\omega_R^2}$. Both effects are increasing as ω_R increases in which case the rf SQUID will operate in the non-adiabatic mode. In this mode, although $\beta_{rf} << 1$, there is a hysteresis depicted in the flux diagram. The second equation (2.83) implies that the dispersion of the flux inside the interferometer loop (which describes the effect of thermal noise) is proportional to the SQUID inductance L and temperature T.

After the probability density distribution σ has been found, the statistical average of any variable can easily be calculated. Of particular importance is the expression of the average of the screening circulating current <J> flowing in the SQUID induc-

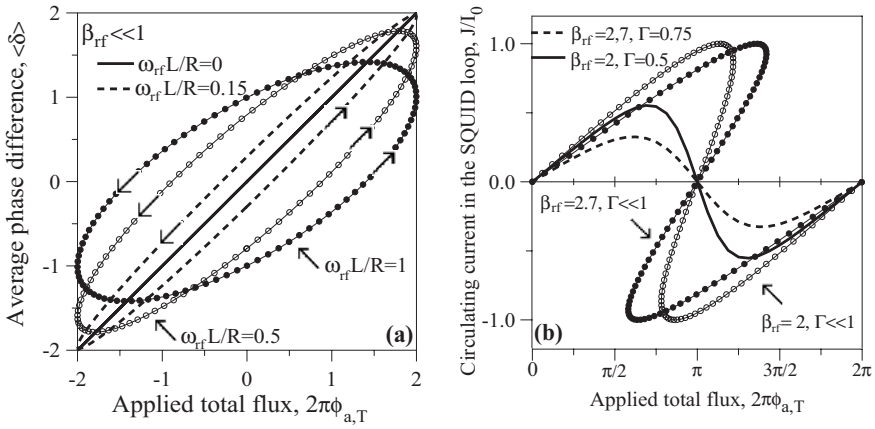

Fig. 2.25 (a) SQUID phase (flux) diagram in the non-adiabatic regime in the presence of thermal fluctuations. The arrows on the curves indicate the direction of time flow. (b) Circulating current in the SQUID loop versus normalized applied flux.

tance L; for $\beta_{rf} << 1$, with the help of (2.82a), it can be written in an explicit form:

$$\begin{aligned}\langle J\rangle &= \left\langle I_0 \sin\delta + \frac{\Phi_0}{2\pi R}\frac{d\delta}{dt}\right\rangle = I_0 \int\limits_{-\infty}^{\infty} \sigma \sin\delta \, d\delta + \frac{\Phi_0}{2\pi R}\frac{d}{dt}\left(\int\limits_{-\infty}^{\infty} \sigma\delta \, d\delta\right) \\ &= I_0 \times \left\{ \exp\left[-L/(2L_F)\right] \sin\left[2\pi\phi_a + \nu_T^* \sin\left(\omega_{rf} t - \theta\right)\right] \right. \\ &\quad \left. + \frac{\omega_R \nu_T^*}{\beta_{rf}} \cos\left(\omega_{rf} t - \theta\right) \right\} \end{aligned} \tag{2.84a}$$

while for $0.2 < \beta_{rf} < 3$ and $\omega_{rf} << \omega_{cut}$ the parametric form (the parameter being x) can be used:

$$\begin{cases} 2\pi\phi_{a,T} = x + \beta_{rf} \exp\left(-\dfrac{L}{L_F} 1.1\right) \sin x \\ \langle J\rangle = I_0 \exp\left(-\dfrac{L}{2L_F} 1.1\right) \sin x \ . \end{cases} \tag{2.84b}$$

Equations (2.84b) are valid for most values of interest for the SQUID parameters: $0.1 < L/L_F < 3$ and $0.3 < \Gamma < 3$. Expressions (2.84a) and (2.84b) differ from the ones that correspond to 4 K, see (2.80). In particular the screening supercurrent is suppressed by a factor of $\exp[-L/(2L_F)]$. It follows from (2.84b) that, in the presence of large thermal fluctuations the circulating current vs. the applied flux diagram (or equivalently, the phase diagram) of SQUIDs with $\beta_{rf} > 1$, which at low thermal fluctuations ($\Gamma << 1$) is hysteretic (see Fig. 2.24(b)), is strongly distorted and becomes non-hysteretic (see Fig. 2.25(b)). In the analysis of the interaction between the

SQUID ring and the tank circuit, the average screening circulating current through L, $\langle J \rangle$ is of prime importance, because the coupling is inductive, via induced currents. As a consequence, the inductive interaction is directly affected and new equations for the output current–voltage (I–V) characteristic, transfer function, flux noise spectral density, and energy sensitivity should be derived at large thermal fluctuations.

To obtain the output IV characteristics, one can use the analysis from [114] (Chapter 13), [4] (Chapter 14), and [116,117] describing the interaction between the interferometer loop and the tank circuit coupled to it. Taking into account the calculated average $\langle J \rangle$ (see (2.84a) and (2.84b)), the output rf SQUID I–V's, or equivalently $i_{rf} = i_{rf}(v_T)$, can be obtained. Here only the result for $0.2 < \beta_{\mathrm{rf}} < 3$ and $\omega_{rf} << \omega_{cut}$ is shown:

$$i_{rf} = \frac{v_T}{Z(v_T)} \tag{2.85a}$$

$$\left[\frac{v_T}{Z(v_T)}\right]^2 = \left(\frac{v_T}{Q}\right)^2 + 4\left(v_T \xi - k^2 F^*\right)^2, \tag{2.85b}$$

$$F^* = \beta_{rf} \exp\left(-\frac{L}{2L_F}\right) g\left[J_1(v_T)\cos\left(2\pi\phi_a\right) - \frac{f}{2} J_1(2v_T)\cos\left(4\pi\phi_a\right)\right], \tag{2.85c}$$

$$g = \exp\left\{-\frac{\beta_{rf}/2}{\exp[3.5(\Gamma - 0.5)] + \beta_{rf}}\right\} \text{ for } 0.2 < \beta_{\mathrm{rf}} < 3 \text{ and } \omega_{rf} << \omega_{cut}. \tag{2.85d}$$

The coefficient f takes values in the range (0.1, 1). For $\beta_{\mathrm{rf}} << 1$, $g \to 1$, $f \to 0$. Here the output impedance Z is an output-voltage-dependent function $Z = Z(v_T)$, where the amplitude $v_T \Phi_0 / 2\pi$ of the external applied rf flux is proportional to the SQUID output voltage amplitude V_T: $v_T \Phi_0/(2\pi) = V_T (k/\omega_{rf})(L/L_T)^{1/2}$. Then, i_{rf} is the normalized drive current in the tank circuit, $i_{rf} \Phi_0/(2\pi) = I_{rf} k \sqrt{L L_T}$, I_{rf} is the rf pump current amplitude, J_1 is the Bessel function of the first kind, of order 1; $Q = \omega_{rf} L_T / R_T$ is the quality factor of the tank circuit (L_T, R_T are, respectively, the tank circuit inductance and the resistance), $k = M/(L L_T)^{1/2}$ is the coupling coefficient between the interferometer loop and the tank circuit, and $\xi = (\omega_{rf} - \omega_0)/\omega_0$ is the detuning of the drive frequency from the tank circuit resonant frequency $\omega_0 = 1/(L_T C_T)^{1/2}$.

The flux modulation of the I–V characteristics is qualitatively similar to the case of small thermal fluctuations (see [118–121]), namely it consists of a few maxima of magnitude decreasing with increasing rf pump current amplitude (see Fig. 2.26(a)). The dependence of the output voltage modulation on the detuning parameter ξ shown in Fig. 2.26(b) is again, qualitatively only, similar to the case of small thermal fluctuations (see [119], [121]). The same is true for the resonance curve $v_T(\xi)$ (compare the figure from [4] p.492 for the case of small thermal fluctuations and Fig. 2.27(a)). From (2.85) the SQUID transfer function proportional to $\partial v_T / \partial \phi_a$ can easily be calculated. $\partial v_T / \partial \phi_a$ is a rather complicated functional that depends on inter-

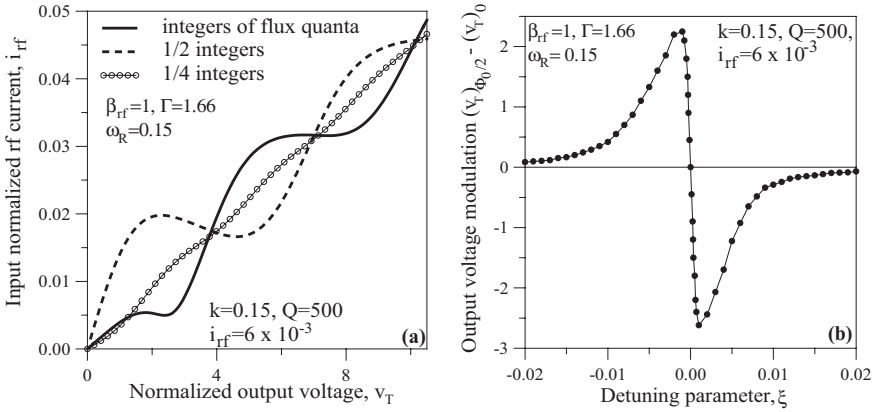

Fig. 2.26 (a) Calculated output current–voltage voltage characteristic (in normalized units i_{rf} vs v_T) for 3 different values of the measured flux (from (2.85)). (b) Maximum flux modulation of the output voltage amplitude vs. detuning parameter (from (2.85)).

ferometer parameters (I_c, L, R) and all tank circuit parameters. In Fig. 2.27 (a) it is shown that when $k^2Q\beta_{rf}>1$ the output voltage versus detuning ξ is multivalued and that a change in the applied flux has a drastic impact on the sign of the slope of the $v_T(\xi)$ characteristics. From this, it immediately follows that when $k^2Q\beta_{rf}>1$ the transfer function may diverge. This property determines both advantages and drawbacks of such a regime of operation [4]. On one hand, the large possible values of the transfer results in a negligible amplifier noise contribution to the overall device noise and thus improves its sensitivity. On the other hand, at bias points with large transfer function the SQUID is extremely sensitive to small variations of ac drive amplitude i_{rf} and the detuning ξ. In addition, the SQUID signal bandwidth narrows when the transfer function increases, and *vice versa*. For these reasons the optimum SQUID performance is not reached at maximum transfer function. Optimization has to be done with respect to the energy sensitivity. Calculated energy sensitivity has a rather complicated expression [85] which considerably simplifies by imposing several optimizing conditions. First the flux modulation of the output voltage has to be maximum, a condition fulfilled for $v_T/(1+\omega_r^2)^{1/2}=1.84$ and when the signal to be measured is superimposed on an additional dc flux of $(2n+1)\Phi_0/4$ (here n is an integer). Secondly, an additional optimization condition is to have the inverse of the effective tank circuit quality factor much smaller than twice the effective detuning from the resonant frequency of the tank circuit. Finally one finds that the energy sensitivity in units of 10^{-31} ΩJ/Hz is given by:

$$\varepsilon R = 3\Gamma^2\left(1+\frac{T_k}{T}\frac{1}{k^2Q}\frac{1}{\omega_R}\right)\frac{\exp(L/L_F)}{L/L_F}\frac{1}{g^2} \tag{2.86}$$

where $g=\left(1+\omega_R^2\right)^{-1/2}$ for $\beta_{rf}<<1$

while for $0.2 < \beta_{rf} < 3$ and $\omega_{rf} << \omega_{cut}$ g is given by (2.85d). Here T_k is the tank circuit temperature. Thus, in contrast to the case of small thermal fluctuations (4 K) the energy resolution exhibits a minimum with respect to two parameters: the bias frequency and the SQUID inductance L. From Fig. 2.27(b), where (2.86) is represented,

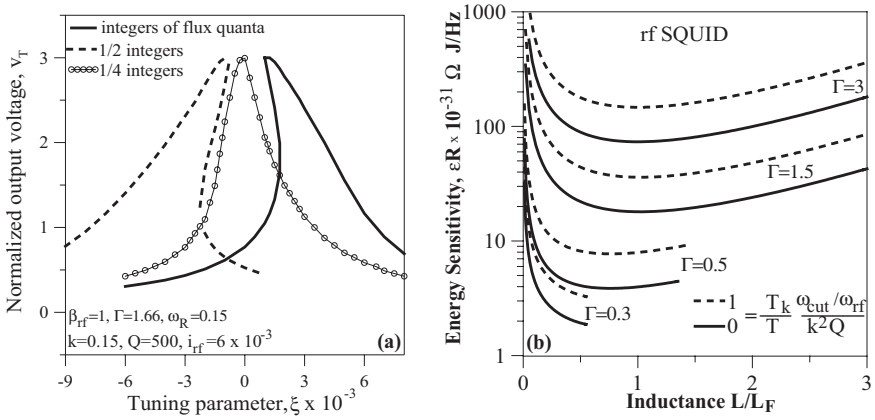

Fig. 2.27 (a) The output resonant curve for 3 different values of the applied dc flux (from (2.85)). (b) The rf SQUID energy sensitivity for several values of the noise parameter Γ as a function of the normalized inductance (from (2.86)). Solid lines are for $(T_k/T) / (k^2 Q \omega_R) << 1$.

one finds the optimal value for the SQUID inductance: $L = L^*$ if $\Gamma \leq 0.335$, and $L = L_F = 100$ pH if $\Gamma > 0.335$. Here L^* is a monotonically increasing function of the noise parameter and takes values from $L^*/L_F = 0.55$ for $\Gamma = 0.3$ to $L^*/L_F = 0.9$ for $\Gamma = 0.335$. The minimum of energy sensitivity ε with respect to the SQUID inductance (or equivalently the screening parameter β_{rf}) – see (2.86) – can be understood as follows [85]. The SQUID is a superconducting device, so that it is natural to expect better output characteristics with improvement in its screening properties with respect to the applied flux (the basic feature of superconductors). The dependence of ε upon β_{rf} contains two important terms: $1/\beta_{rf}$ and exp $(\beta_{rf}\Gamma)$. The significance of the first one is obvious: the higher the β_{rf} parameter (in the range considered in this paper, i.e., up to about 3 – this is also the range of practical interest) the bigger the difference of the flux inside the SQUID ring from the value of the applied flux, and as a result, the better the screening properties. The second term is a result of the influence of thermal fluctuations. It has been shown that the screening current in the SQUID ring is suppressed with increasing β_{rf} (the suppression becomes noticeable at large thermal fluctuations and increases with Γ). Therefore, from this point of view, the SQUID screening properties degrade with increasing β_{rf}. These two physically opposing aspects are responsible for the minimum of energy sensitivity versus β_{rf} in the high-T_c rf SQUID.

The analytical analysis presented here also includes the case of small thermal fluctuations. Indeed, by taking the limit $L << L_F$, or equivalently $\beta_{rf}\Gamma << 1$ the expo-

nent $\exp(-L/2L_F) \rightarrow 1$. By taking this limit in (2.84b), (2.85) and (2.86) one gets the well known results of low thermal fluctuations for the phase diagram (2.80) (and the current in the SQUID loop), output current–voltage characteristic, and energy sensitivity, respectively (see [114] p.270, [4] p.490, and [116,117]).

Extensive measurements recently performed [138,139] on high-T_c rf SQUIDs have confirmed the validity of the analytical analysis presented. In Table 2.2 a brief example is given of the calculated and experimentally measured values of the energy sensitivity of some rf SQUIDs. All quantities marked with the superscript * were not directly measured, but indirectly estimated since in practice it is difficult to measure the SQUID critical current in the presence of large thermal fluctuations. The first column for the theoretical estimates of ε is for the ideal case when in (2.86) the term $(T/T_k)/k^2 Q\omega_R << 1$. In this case, for a given inductance, the optimum sensitivity is reached experimentally. The theoretical estimates are in good agreement with the measurements. We note that the numbers given in the second column of Table 2.2 are for practical, non-zero, values of the term $(T/T_k)/k^2 Q\omega_R$. Finally, we note that the analytical theory from [85] was extended to a second-order approximation in [140].

Table 2.2 Calculated (using Eq.(2.86)) and experimental values of the energy sensitivity for five different high-T_c rf SQUIDs.

	Josephson junction parameters			**Tank circuit parameters**			**Derived SQUID parameters**			**Energy sensitivity (thermal noise only) $\varepsilon \times 10^{-31}$ (J/Hz)**		
	$I_0{}^*$	L	R^*	k^*	Q^*	$\omega/(2\pi)$	$\beta_{rf}{}^*$	Γ^*	$\omega_R{}^*$	Theory		Experiment
#	(μA)	(pH)	(Ω)		loaded	(MHz)						
1	1.1	150	8	0.15	500	850	0.5	3	0.15	10	16	14
2	1.7	230	8	0.15	500	850	1.3	1.8	0.1	5.5	10	6.4
3	1.8	260	8	0.15	500	850	1.5	1.7	0.17	5.8	8.8	5.6
4	1.1	450	6	–	–	300	1.5	5	0.15	110	–	230
5	0.8	900	6	–	–	300	2.3	4	0.28	7200	–	7600

Concluding, at low thermal fluctuations and for operating frequencies smaller than both the SQUID cut-off frequency ω_{cut} and the characteristic frequency of the Josephson junction ω_c, the presented analytical analysis reduces to the well known theories of rf SQUIDs operating in the inductive mode $\beta_{rf} < 1$ [4], [115], [116–122]. For operating frequencies exceeding ω_{cut} and for $\beta_{rf} << 1$ it contains also the non-adiabatic case studied in [125–129]. The approach also extends to the case of large thermal fluctuations where it gives a fundamentally based explanation for the well known experimental fact that rf SQUIDs preserve a remarkable energy resolution even at higher values of the inductance L/L_F (up to about 3) and the noise parameter Γ (up to about 2). Table 2.3 contains a summary of some results in different regimes.

Tab. 2.3 Summary of the different rf SQUID operating regimes.

Operating regime	β_{rf}	Phase-flux diagram	Intrinsic energy sensitivity* ε (or noise spectral density S_Φ)
adiabatic; $\omega_{rf} << \min(\omega_{cut}, \omega_c)$	$\beta_{rf} < 1$ (**low TF**; $\Gamma << 1$ and $L/L_F << 1$)	**non-hysteretic** (Fig.2.24 b)	$\varepsilon R = 3\Gamma^2\left(1 + \frac{T_k}{T}\frac{1}{k^2 Q}\frac{1}{\omega_R}\right)$
	$\beta_{rf} < 3$ (**large TF**; either $\Gamma << 1$ or $L/L_F << 1$ is not fulfilled)		$\varepsilon R = 3\Gamma^2\left(1 + \frac{T_k}{T}\frac{1}{k^2 Q}\frac{1}{\omega_R}\right)\frac{\exp(L/L_F)}{L/L_F}\frac{1}{g^2}$ with g given by (2.85d)
adiabatic; $\omega_{rf} << \min(\omega_{cut}, \omega_c)$	$\beta_{rf} > 1$ (**low TF**, $\Gamma << 1$ and $L/L_F << 1$);	**hysteretic** (Fig.2.24 b) flux transitions occur	$S_\Phi{}^{1/2} \approx 1.16\,(1/\omega_{rf})^{1/2}\,LI_0{}^{1/3}\,(k_B T/\Phi_0)^{2/3}$
non-adiabatic; $\omega_{rf} << \min(\omega_{cut}, \omega_c)$ is not fulfilled	β_{rf} arbitrary (**low TF**)	**hysteretic** (Fig.2.25 a) **no** flux transitions occur	$\varepsilon = k_B T L/R$
	$\beta_{rf} << 1$ (**large TF**)		$\varepsilon R = 3\Gamma^2\left(1 + \frac{T_k}{T}\frac{1}{k^2 Q}\frac{1}{\omega_R}\right)\frac{\exp(L/L_F)}{L/L_F}\frac{1}{g^2}$ with $g = \left(1 + \omega_R^2\right)^{-1/2}$

* expressions for εR are in units of 10^{-31} ΩJ/Hz

2.3.4 Noise as a Small Perturbation

2.3.4.1 Introduction

So far, noise and signal were treated simultaneously in a unitary approach (its analytical version has been summarized) which is the proper way of solving the problem at large thermal fluctuations (in particular, the case of high-T_c rf SQUIDs operating at 77 K). However, when thermal fluctuations are small (the case of low-temperature superconductors rf SQUIDs at 4 K), alternatively, a more simple two-step approximate approach may be used instead. First, by solving (2.78) SQUID signal characteristics are calculated in the absence of noise, and then noise is included as a small perturbation. As already pointed out, at low thermal fluctuations in the adiabatic regime, rf SQUIDs operate either in the hysteretic mode ($\beta_{\rm rf} > 1$) or non-hysteretic mode ($\beta_{\rm rf} < 1$). Since the latter case can easily by obtained by taking the limit $\exp(-L/2L_F) \to 1$, in the analysis presented in the previous section for the case of large thermal fluctuations, it will not be considered further. Instead, a few details

will be given about rf SQUID output characteristics calculated in the frame of small perturbation theories of hysteretic rf SQUIDs operating in the adiabatic mode and systems operating in the non-adiabatic mode.

2.3.4.2 Adiabatic Operation; Hysteretic Phase Diagram

In the adiabatic hysteretic mode and at low thermal fluctuations, (2.80) is applicable and the phase diagram of the SQUID (see Fig. 2.24(b)) is characterized by phase jumps. As long as the supercurrent induced in the interferometer by the applied rf flux $\Phi_{a,rf}$ does not exceed the critical current I_0, no phase transitions occur, and V_T is a linear function of rf current bias i_{rf}. As soon as the current in the SQUID ring exceeds I_0, the Josephson junction switches to the resistive state. The current in the ring then decays exponentially with a time constant L/R, until the Josephson junction switches back to the superconducting state. At higher i_{rf}, dissipation in the SQUID limits the tank circuit voltage V_T to a constant value, until at the positive and negative peak of every rf cycle, the current in the SQUID exceeds I_0. A further increase in i_{rf} increases V_T linearly again up to a point where, during a rf cycle, a third quantum transition takes place (I_0 is exceeded twice during the positive half of the rf cycle), which again limits V_T. The rf SQUID output characteristics $V_T \propto v_T = v_T(i_{rf})$ thus looks like a staircase (see Fig. 2.28(a)). An applied external flux leads to an additional supercurrent in the SQUID, which adds to i_k and leads to a shifting of the step in the $v_T(i_{rf})$ characteristics towards lower values of the normalized voltage (see Fig. 2.28(a)). If the SQUID is biased at a constant i_{rf}, $V_T \propto v_T$ is periodically changed by varying flux, with maximum values at $\Phi = n\Phi_0$ and minima at $\Phi = (2n-1)\Phi_o$. The flux induced maximum voltage change and thus the modulation amplitude is $\Delta V_T = V_T(n\Phi_0) - V_T((2n-1)\Phi_0/2) = \omega_{rf} L_T \Phi_0/2M$. This result suggests that the transfer coefficient can be made arbitrarily large by reducing M, i.e, the coupling coefficient k. However, k cannot be made so small that the SQUID has

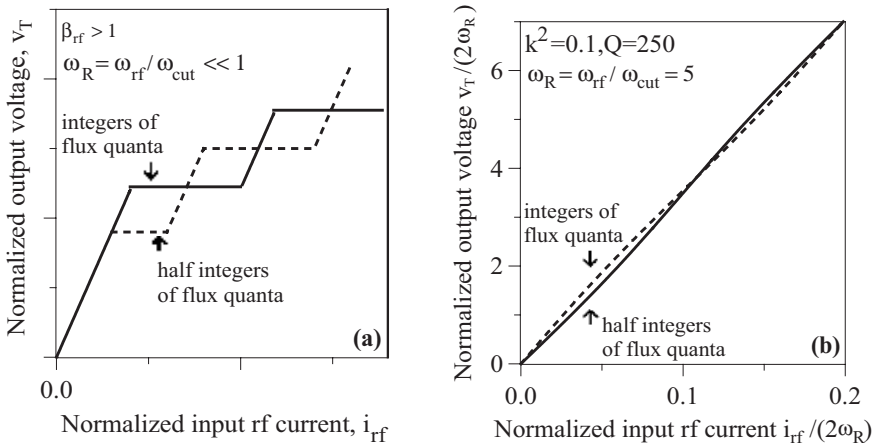

Fig. 2.28 Rf SQUID output voltage-current characteristics for integer of flux quanta (solid line) and half-integers of flux quanta (dashed line) for (a) adiabatic operation with $\beta_{rf} > 1$ and (b) non-adiabatic operation.

no influence on the tank circuit. Indeed, it can be shown that the energy transfer between SQUID and tank circuit and thus the modulation voltage is maximum, when $k^2Q \approx \pi/4$. Unlike all the other regimes of operation (see 2.3.3.), the SQUID transfer function $\partial V_T/\partial \Phi_a = (L_T/L)^{1/2}\omega_{rf}/k$ is independent of interferometer parameters I_0, and R or tank circuit parameters as ac drive amplitude i_{rf} and detuning ξ.

For practical applications, the equivalent flux noise of a SQUID system and thus its sensitivity to magnetic flux is the most important parameter. For the hysteretic SQUID, a theory of intrinsic noise has been developed in [123,124]. Intrinsic noise in the rf SQUID originates from current fluctuations in the weak link shunt resistor R. The ratio between SQUID response to the flux to be measured and to these current fluctuations, determines its maximum achievable sensitivity. The current fluctuations lead to a nonzero probability of making quantum transitions at fluxes smaller than the critical values determined from the phase diagram Fig. 2.24(b) in the absence of thermal fluctuations. If the applied rf flux is increased slowly ($\omega_{rf} << \omega_{cut}$), a quantum transition will take place before the height of the barrier between two adjacent quantum states has been reduced to below k_BT. This problem is similar to the case of a classical particle with a mean energy k_BT, which tries to overcome a barrier with a height large compared to k_BT. The attempt frequency here is of the order of the SQUID ring frequency R/L. The equivalent flux noise generated by this mechanism has been calculated [123,124]

$$S_\Phi^{1/2} \approx 1.16\,(1/\omega_{rf})^{1/2}\,LI_0^{1/3}\,(k_BT/\Phi_0)^{2/3}. \tag{2.87}$$

One notices that the rf SQUID intrinsic noise is inversely proportional to the square-root of the operating frequency. The sensitivity of rf SQUIDs can thus be enhanced by operating them at very high frequencies (the non-adiabatic case will be summarized in the next section). From (2.87) it also follows that in the hysteretic mode the input energy of the thermal noise k_BT in the SQUID loop is amplified by the flux transitions that characterize this mode of operation, so that the SQUID intrinsic noise drastically deteriorates its measuring performances. The rf SQUID energy sensitivity will therefore considerably increase over the classical limit k_BTL/R. In addition, it has been shown [113] that the intrinsic noise leads to an increase in the tank circuit voltage with increasing bias current, and thus in a tilting of the (without noise) horizontal steps in the output current–voltage characteristic of the tank circuit. The tilt angle α is related to the SQUID noise by $S_\Phi^{1/2} = (2/\omega_{rf})^{1/2}\alpha\Phi_0/(1-\alpha)$. Additionally, the step tilting reduces the modulation voltage by a factor of $1-\alpha$.

There are two further noise sources in rf SQUID systems, which, at low thermal fluctuations, turn out to have a larger influence on the system noise than the intrinsic SQUID noise: tank circuit noise and preamplifier noise. In practice the tank circuit inductance L_T is not ideal and therefore includes also a series resistance R_T which imposes a thermal noise current through L_T. This current causes the bias point of the SQUID to fluctuate, which in turn leads to a fluctuation of the output voltage V_T, since $\partial V_T/\partial i_{rf}$ is non-zero ($\partial V_T/\partial i_{rf} \approx \alpha$). In [113] this noise contribution has been calculated to be:

$$S_{\Phi}^{(tc)} = 4\pi\alpha^2/(1-\alpha^2) \cdot k_B T_{eff} L/\omega_{rf}. \tag{2.88}$$

It is important to emphasize that the effective temperature of the tank circuit T_{eff} when the preamplifier is at room temperature, is generally much higher than 4.2 K. Thus, the T_{eff} in (2.88) is not the bath temperature [51]. Since the SQUID modulation voltage $\partial V_T/\partial \Phi_0$ is relatively small, e.g., 10 μV/Φ_0 for a 30 MHz rf SQUID, the noise in the preamplifier usually limits the SQUID system noise that uses a conventional room-temperature readout electronics. The equivalent flux noise of the preamplifier is:

$$S_{\Phi}^{1/2\ (pa)} = S_V^{1/2\ (pa)} \times \partial\ \Phi_0/\partial V_T = S_V^{1/2\ (pa)} \cdot M/[\omega_{rf} L_T\ (1-\alpha)]. \tag{2.89}$$

For conventional room-temperature preamplifiers, $S_V^{1/2\ (pa)}$ is of the order of 2nV/√Hz for high (≈ 10 kΩ), and 0.5 nV/√Hz for low (50 Ω) input impedance amplifiers.

2.3.4.3 Non-adiabatic Regime

The model discussed in the previous section assumes that the times associated with the various superconducting processes in the SQUID (like flux transitions, relaxation processes) are short compared to the period of the rf cycle. At high bias frequencies, this is no longer the case. Both the L/R time of the SQUID ring response, as well as the quasiparticle relaxation time, can be of the order of the rf cycle period or higher, if the SQUID is operated at microwave frequencies. Simulations [125–126] and analytical calculations [116,127] have shown that even at bias frequencies above R/L, SQUID modulation can be observed. To obtain the highest possible modulation voltage, $k^2 Q\beta_{rf}$ should, however, be much larger than one.

To obtain an idea of what is happening at such high frequencies it is useful to introduce the analytical approach developed in [114,141]. One writes the phase δ inside the interferometer in the form

$$\delta = \widetilde{\delta}_{\omega=0} + (\widetilde{\delta})_{\omega,1} + (\widetilde{\delta})_{\omega,2} + \ldots \tag{2.90}$$

where $\widetilde{\delta}_{\omega=0}$ is the low-frequency component ($\omega << \omega_{rf}$), while $(\widetilde{\delta})_{\omega,n}$ ($n = 1,2,3,\ldots$) is the correction of the n-th order for the high-frequency component ($\omega \approx \omega_{rf}$). Introducing (2.90) into the equation of motion (2.78) one gets instead, a set of two coupled equations of motion for both low and high-frequency components which may be solved analytically by the successive approximation method. The solution of such a problem may be summarized as follows:

1) qualitatively, the low-frequency component of the phase δ versus the applied dc flux characteristic looks similar to the plot in Fig. 2.24(b), while;
2) the high-frequency component versus the applied rf flux characteristic again, qualitatively, has the shape represented in Fig. 2.25(a).

These solutions tell us that in the non-adiabatic regime no flux transitions occur, and as consequence, the major source of intrinsic noise in rf SQUIDs is eliminated.

For that reason, it is also reasonable to think of optimizing the other two sources of noise in an rf SQUID: the tank circuit noise and the preamplifier noise. In addition, the solutions for the phase δ form the basis for calculating the rf SQUID output current–voltage characteristic and it has the form represented in Fig. 2.28(b). Qualitatively, the characteristic of voltage modulation versus the detuning parameter ξ appears as shown in Fig. 2.26(b). Finally, the energy sensitivity approaches the classical limit, in this case:

$$\varepsilon = k_B T L / R. \tag{2.91}$$

which is comparable to the best dc SQUIDs.

A modified version of an rf SQUID operated in the non-adiabatic mode has been proposed in [141]. It differs from the traditional configuration in that the SQUID inductance L does not close via a single Josephson junction but via two identical junctions in parallel, symmetrically connected in a second loop. Analytical calculations [141,142] show that when the new configuration (also called rf double SQUID) is symmetric it has optimal intrinsic noise properties due to minimization of the back reaction (tank circuit → interferometer). For that reason, unlike the case of a traditional system, one can take advantage of the very high transfer function that non-adiabatic rf SQUIDs usually have, a condition interesting to confirm in practice.

References

1 Josephson, B. D. (1962) Possible new effects in superconductive tunneling, *Phys. Lett.* **1**, 251–253.

2 Josephson, B. D. (1965) Supercurrents through barriers, *Adv. Phys.* **14**, 419–451.

3 Barone, A., Paterno, G. (1982) *Physics and Applications of the Josephson Effect*. New York: John Wiley & Sons.

4 Likharev, K. K. (1986) *Dynamics of Josephson Junctions and Circuits*. New York: Gordon and Breach.

5 Stewart, W.C. (1968) Current-voltage characteristics of Josephson junctions, *Appl. Phys. Lett.* **12**, 277–280.

6 McCumber, D.E. (1968) Effect of ac impedance on dc voltage-current characteristics of Josephson junctions, *J. Appl. Phys.* **39**, 3113–3118.

7 Zappe, H. (1973) Minimum current and related topics in Josephson tunnel junction devices, *J. Appl. Phys.* **44**, 1371–1377.

8 Gross, R., Mayer B. (1991) Transport processes and noise in $YBa_2Cu_3O_{7-\delta}$ grain boundary junctions, *Physica C* **180**, 235–241.

9 Gross, R. (1994) *Grain boundary Josephson junctions in the high temperature superconductors,* in *Interfaces in High-T_c Superconducting Systems*. Edited by S.L. Shinde and D. A. Rudman, New York: Springer-Verlag, p.176–209.

10 Shapiro, S. (1963) Josephson currents in superconducting tunneling: The effect of microwaves and other observations, *Phys. Rev. Lett.* **11**, 80–82.

11 Kautz, R. L., Monaco, R. (1985) Survey of chaos in the rf-biased Josephson junction, *J. Appl. Phys.* **57**, 875–889.

12 Likharev, K. K. (1979) Superconducting weak links, *Rev. Mod. Phys.* **51**, 101–159.

13 Auracher, F., Van Duzer, T. (1972) Influence of the current-phase relationship on the I–V characteristic of superconducting weak links, *Appl. Phys. Lett.* **21**, 515–518.

14 Tsuei, C. C., Kirtley, J. R. (2000) Pairing symmetry in cuprate superconductors, *Rev. Mod. Phys.* **72**, 969–1016.

15 Kashiwaya, S., Tanaka, Y. (2000) Tunnelling effects on surface bound states in unconventional superconductors, *Rep. Prog. Phys.* **63**, 1641–1724.

16 Hilgenkamp, H, Mannhart, J. (2002) Grain boundaries in high-T_c superconductors, *Rev. Mod. Phys.* **74**, 485–549.

17 Rifkin, R., Deaver, B. S. (1976) Current-phase relation and phase-dependent conductance of superconducting point contacts from rf impedance measurements, *Phys. Rev. B* **13**, 3894–3901.

18 Il'ichev, E., Zakosarenko, V., IJsselsteijn, R. P. J., Schultze, V., Meyer, H.-G., Hoenig, H. E., Hilgenkamp, H., Mannhart, J. (1998) Nonsinusoidal current-phase relationship of grain boundary Josephson junctions in high-T_c superconductors, *Phys. Rev. Lett.* **81**, 894–897; Il'ichev, E., Zakosarenko, V., IJsselsteijn, R. P. J., Hoenig, H. E., Schultze, V., Meyer, H.-G., Grajcar, M., Hlubina, R. (1999) Anomalous periodicity of the current-phase relationship of grain-boundary Josephson junctions in high-T_c superconductors, *Phys. Rev. B* **60**, 3096–3099.

19 Il'ichev, E., Zakosarenko, V., IJsselsteijn, R. P. J., Hoenig, H. E., Meyer, H.-G., Fistul, M. V., Müller, P. (1999) Phase dependence of the Josephson current in inhomogeneous high-T_c grain-boundary junctions, *Phys. Rev. B* **59**, 11502–11505.

20 Mannhart, J., Hilgenkamp, H., Mayer, B., Gerber, Ch., Kirtley, J. R., Moler, K. A., Sigrist, M. (1996) Generation of magnetic flux by single grain boundaries of $YBa_2Cu_3O_{7-x}$, *Phys. Rev. Lett.* **77**, 2782–2785.

21 Hilgenkamp, H., Mannhart, J., Mayer, B. (1996) Implications of $d_{x^2-y^2}$ symmetry and faceting for the transport properties of grain boundaries in high-T_c superconductors, *Phys. Rev. B* **53**, 14586–14593.

22 Deutscher ,G., Müller, K. A. (1987) Origin of superconductive glassy state and extrinsic critical currents in high-T_c oxides, *Phys. Rev. Lett.* **59**, 1745–1747.

23 Tesche, C., Clarke, J. (1977) DC SQUID: noise and optimization, J. *Low. Temp. Phys.* **29**, 301–331.

24 Ivanchenko, Yu. M., Zilberman, L. A. (1968) Destruction of Josephson current by fluctuations, *Sov. Phys. – JETP Lett.* **8**, 113–115.

25 Ambegaokar, V., Halperin, B. I. (1969) Voltage due to thermal noise in the dc Josephson effect, *Phys. Rev. Lett.* **22**, 1364–1366.

26 van Kampen, N. G. (1992) *Stochastic Processes in Physics and Chemistry.* Amsterdam: North-Holland, revised and enlarged edition.

27 Risken, H. (1984) *The Fokker–Planck Equation*. Berlin: Springer-Verlag.

28 Dutta, P., Horn, P. M. (1981) Low-frequency fluctuations in solids: 1/f noise, *Rev. Mod. Phys.* **53**, 497–516.

29 Weissman, M. B. (1988) 1/f noise and other slow, nonexponential kinetics in condensed matter, *Rev. Mod. Phys.* **60**, 537–571.

30 Rogers, C. T., Buhrman, R. A. (1984) Composition of 1/f noise in metal-insulator-metal tunnel junctions, *Phys. Rev. Lett.* **53**, 1272–1275.

31 Savo, B., Wellstood, F.C., Clarke, J. (1987) Low-frequency excess noise in Nb-Al_2O_3-Nb Josephson tunnel junctions, *Appl. Phys. Lett.* **50**, 1757–1759.

32 Kawasaki, M., Chaudhari, P., Gupta, A. (1992) 1/f Noise in $YBa_2Cu_3O_{7-\delta}$ superconducting bicrystal grain-boundary junctions, *Phys. Rev. Lett.* **68**, 1065–1063.

33 Miklich, A.H., Clarke, J., Colclough, M.S., Char, K. (1992) Flicker (1/f) noise in biepitaxial grain boundary junctions of $YBa_2Cu_3O_{7-x}$, *Appl. Phys. Lett.* **60**, 1899–1901.

34 Marx, A., Fath, U., Ludwig, W., Gross, R., Amrein, T. (1995) 1/f noise in $Bi_2Sr_2Ca-Cu_2O_{8+x}$ bicrystal grain-boundary Josephson junctions, *Phys. Rev. B* **51**, 6735–6738.

35 Marx, A., Gross, R. (1997) Scaling behavior of 1/f noise in high-temperature superconductor Josephson junctions, *Appl. Phys. Lett.* **70**, 120–122.

36 Foglietti, V., Gallagher, W.J., Ketchen, M.B., Kleinsasser, A.W., Koch, R.H., Raider, S.I., Sandstrom, R.L. (1986) Low-frequency noise in low 1/f noise dc SQUIDs, *Appl. Phys. Lett.* **49**, 1393–1395.

37 Gross, R., Alff, L., Beck, A., Froehlich, O.M., Koelle, D., Marx, A. (1997) Physics and technology of high temperature superconducting Josephson junctions, *IEEE Trans. Appl. Supercond.* **7**, 2929–2935.

38 Marx, A., Alff, L., Gross, R. (1995) Correlation of critical current and resistance fluctuations in bicrystal grain boundary Josephson junctions, *Appl. Phys. Lett.* **67**, 1929–1931.

39 Gershenson, M., Hastings, R., Schneider, R., Sweeny, M., Sorensen, E. (1983) SQUID Linear Amplifier Circuit Simulations, *IEEE Trans. Magn.* **MAG-19** 2058–2060.

40 Hilbert, C., Clarke, J. (1983) Radio-frequency amplifier based on a dc superconducting quantum interference device, *Appl. Phys. Lett.* **43**, 694–696.

41 McDonald, D. G. (1984) Power gain of a SQUID amplifier, *Appl.Phys. Lett*. **44**, 556–558.

42 Hilbert, C., Clarke, J. (1985) DC SQUIDs as radiofrequency amplifiers, J. *Low Temp. Phys.* **61**, 263–280.

43 Hilbert, C. Clarke, J. (1985) Measurements of the dynamic input impedance of a DC SQUID, *J. Low Temp. Phys.* **61**, 237–262.

44 Martinis, J. M., Clarke, J. (1985) Signal and noise theory for a DC SQUID amplifier, *J. Low Temp. Phys*. **61**, 227–235.

45 Mück, M., Andre, M.-O., Clarke, J., Gail, J., Heiden, C. (1999) Microstrip superconducting quantum interference device radio-frequency amplifier: tuning and cascading, *Appl. Phys. Lett*. **75**, 3545–3547.

46 Andre, M.-O., Mück, M. A., Clarke, J., Gail, J., Heiden, C. (1999) Radio-frequency amplifier with tenth-kelvin noise temperature based on a microstrip direct current superconducting quantum interference device, *Appl. Phys. Lett*. **75**, 698–700.

47 Mück ,M., Andre, M.-O., Clarke, J., Gail, J., Heiden, C. (1998) Radio-frequency amplifier based on a niobium dc superconducting quantum interference device with microstrip input coupling, *Appl. Phys. Lett*. **72**, 2885–2887.

48 Ketchen, M. B. (1981) Dc SQUIDs 1980: The state of the art, *IEEE Trans. Magn*. **MAG-17**, 387–394.

49 Clarke, J. (1980) Advances in SQUID magnetometers, *IEEE Trans. El. Dev.* **ED-27**, 1896–1908.

50 Clarke, J. (1989) Principles and applications of SQUIDs, *Proc. IEE*E **77**, 1208–1223.

51 Clarke, J. (1996) SQUID fundamentals, in *SQUID Sensors: Fundamentals, Fabrication and Application, NATO ASI Series E: Applied Sciences*-Vol. 329, H. Weinstock (ed.). Dordrecht: Kluwer Academic Publishers, p.1–62.

52 Ryhänen, T., Seppa, H., Illimoniemi, R., Knuutila, J. (1989) SQUID magnetometers for low-frequency applications, *J. Low Temp. Phys.* **76**, 287–386.

53 Ketchen, M. B., Jaycox, J. M. (1982) Ultra low noise tunnel junction dc SQUID with a tightly coupled planar input coil, *Appl. Phys. Lett*. **40**, 736–738.

54 Jaycox, J. M., Ketchen, M. B. (1981) Planar coupling scheme for ultra low noise dc SQUIDs, *IEEE Trans. Magn*. **MAG-17**, 400–403.

55 Meservey, R., Tedrow, P. M. (1969) Measurements of the kinetic inductance of superconducting linear structures, *J. Appl. Phys.* **40**, 2028–2034.

56 Chang, W. H. (1981) Numerical calculation of the inductance of a multi-superconductor transmission line sytem, *IEEE Trans. Magn*. **MAG-17**, 764–766.

57 Hosoya, M., Goto, E., Shimizu, N., Harada, Y. (1989) Inductance calculation system for superconducting circuits, *IEEE Trans. Magn*. **MAG-25**, 1111–114.

58 Sheen, D. M., Ali, S. M., Oates, D. E., Withers, R. S., Kong, J. A. (1991) Current distribution, resistance and inductance for superconducting transmission lines, *IEEE Trans. Appl. Supercond*. **1**, 108–115.

59 Töpfer, H. (1991) Inductance determination in superconducting structures, in *Superconductivity and Cryoelectronics*. W. Krech, P. Seidel, and H. G. Meyer (eds.). Singapore: World Scientific, p.170–177.

60 Uhlmann, H., Töpfer, H., Verwiebe, F., Uhlig, J (1992) Accurate determination of electrical parameters of thin film SQUID structures and simulation of DC-SQUIDs with coupling coils. In *Superconducting Devices and their Application*, H. Koch, H. Lübbig (eds.). Berlin Heidelberg: Springer Verlag, p. 292–296.

61 Hildebrand, G., Uhlmann, F. H. (1995) Inductance calculation for integrated superconducting structures by minimizing free energy, *IEEE Trans. Appl. Supercond*. **5**, 2766–2769.

62 De Waele, A. Th. A. M., de Bruyn Qouboter, R. (1969) Quantum-interference phenomena in point contacts between two superconductors, *Physica* **41**, 225–254.

63 De Waele, A. Th. A. M., de Bruyn Qouboter, R. (1969) On the critical current through a symmetrical double contact between two superconductors as a function of the applied magnetic field, *Physica* **42**, 626–632.

64 Clarke J., Paterson, J. L. (1971) Josephson-Junction Amplifier, *Appl. Phys. Lett*. **19**, 469–471.

65 Fulton, T. A., Dunkleberger, L. N., Dynes, R. C. (1972) Quantum interference properties of double Josephson junctions, *Phys. Rev. B* **6**, 855–875.

66 Tsang, W.-T., Van Duzer, T. (1975) Dc analysis of parallel arrays of two and three Josephson junctions, *J. Appl. Phys.* **46**, 4573–4586.

67 Tsang, W.-T., Van Duzer, T. (1976) Influence of the current-phase relation on the critical-current-applied-magnetic-flux dependence in parallel-connected Josephson junctions, *J. Appl. Phys.* **47**, 2656–2661.

68 Peterson, R. L., McDonald, D. G. (1983) Voltage and current expressions for a two-junction superconducting interferometer, *J. Appl. Phys.* **54**, 992–996.

69 de Bruyn Ouboter, R. (1977) Macroscopic quantum phenomena in superconductors. In "*Superconductor Applications: SQUIDs and Machines*", B. Schwartz, S. Foner (eds.). New York: Plenum Press, p. 21–65.

70 de Waal, V. J., Schrijner, P., Llurba, R. (1984) Simulation and optimization of a DC squid with finite capacitance, *J. Low Temp. Phys.* **54**, 215–232.

71 Zappe, H.H., Landman, B.S. (1978) Analysis of resonance phenomena in Josephson interferometer devices, *J. Appl. Phys.* **49**, 344–350.

72 Zappe, H.H., Landman, B.S. (1978) Experimental investigation of resonances in low-Q interferometer devices, *J. Appl. Phys.* **49**, 4149–4154.

73 Gueret, P. *A* (1979) Simple theory of resonance amplitudes in Josephson interferometers, *Appl. Phys. Lett.* **35**, 889–891.

74 Tuckerman, D.B., Magerlein, J.H. (1980) Resonances in symmetric Josephson interferometers, *Appl. Phys. Lett.* **37**, 241–243.

75 Faris, S.M., Valsamakis, E.A. (1981) Resonances in superconducting quantum interference devices-SQUIDs, *J. Appl. Phys.* **52**, 915–920.

76 Paterno, G., Cucolo, A.M., Modestino, G. (1985) Resonant modes in Nb baselayer interferometers with two Josephson junctions, *J. Appl. Phys.* **57**, 1680–1685.

77 Enpuku, K., Sueoka, K., Yoshida, K., Irie, F. (1985) Effect of damping resistance on voltage versus flux relation of a dc SQUID with large inductance and critical current, *J. Appl. Phys.* **57**, 1691–1697.

78 Ben-Jacob, E., Imry, Y. (1981) Dynamics of the dc-SQUID, *J. Appl. Phys.* **52**, 6806–6815.

79 Ketoja, J.A., Kurkijärvi, J., Ritala, R.K. (1984) Instabilities and chaotic solutions of the current biased dc superconducting quantum interference device, *Phys. Rev. B* **30**, 3757–3764.

80 Bruines, J. J. P., de Waal, V. J., Mooij, J. E. (1982) Comment on: 'DC SQUID: noise and optimization' by Tesche and Clarke, *J. Low Temp. Phys.* **46**, 383–386.

81 Tesche, C. D., Clarke, J. (1979) DC SQUID: current noise, *J. Low Temp. Phys.* **37**, 397–403.

82 Chesca, B. (1998) Analytical theory of DC SQUIDS operating in the presence of thermal fluctuations, *J. Low.Temp.Phys.* **112**, 165–196.

83 Chesca, B. (1999) The effect of thermal noise on the I–V curves of high inductance dc SQUIDs in the presence of microwave radiation, *J. Low.Temp.Phys.* **116**, 167–186.

84 Chesca, B. (1999) The effect of thermal fluctuations on the operation of DC SQUIDs at 77 K – a fundamental analytical approach, *IEEE Trans. Appl. Supercond.* **9**, 2955–2960.

85 Chesca, B. (1998) Theory of RF SQUIDS operating in the presence of large thermal fluctuations, *J. Low.Temp.Phys.* **110**, 963–1002; *Applied Superconductivity* **6**, 829–835.

86 Enpuku, K., Shimomura, Y., Kisu, T. (1993) Effect of thermal noise on the characteristics of a high-T_c superconducting quantum interference device, *J. Appl. Phys.* **73**, 7929–7934.

87 Enpuku, K., Muta, T., Yoshida, K., Irie, F. (1985) Noise characteristics of a dc SQUID with a resistively shunted inductance, *J. Appl. Phys.* **58**, 1916–1923.

88 Enpuku, K. (1993) Voltage versus flux relation of high-T_c DC superconducting quantum interference device with different inductances, *Jpn. J. Appl. Phys.* **32**, L1407–L1409.

89 Enpuku, K., Tokita, G., Maruo, T. (1994) Inductance dependence of noise properties of a high-T_c dc superconducting quantum interference device, *J. Appl. Phys.* **76**, 8180–8185.

90 Enpuku, K., Doi, H. (1994) Voltage versus flux relation of DC superconducting quantum interference device using three Josephson junctions, *Jpn. J. Appl. Phys.* **33**, 1856–1862.

91 Enpuku, K., Doi, H., Tokita, G., Maruo, T. (1995) Method for improving voltage modulation depth of high-T_c dc SQUID with large inductance, *IEEE Trans. Appl. Supercond.* **5**, 2762–2765.

92 Enpuku, K., Tokita, G., Maruo, T., Minotani, T. (1995) Parameter dependencies of characteristics of a high-T_c dc superconducting quantum interference device, *J. Appl. Phys.* **78**, 3498–3503.

93 Foglietti, V., Koch, R. H., Sun, J. Z., Laibowitz, R. B., Gallagher, W. J. (1995) Characteriz-

ing, modeling, and optimizing high-T_c superconducting quantum interference devices, *J. Appl. Phys.* **77**, 378–381.

94 Koelle, D., Kleiner, R., Ludwig, F., Dantsker, E., Clarke, J. (1999) High-transition-temperature superconducting quantum interference devices, *Rev. Mod. Phys.* **71**, 631–686.

95 Clarke, J., Tesche, C. D., Giffard, R. P. (1979) Optimization of dc SQUID Voltmeter and Magnetometer Circuits, *J. Low. Temp. Phys.* **37**, 405–420.

96 Voss, R. F. (1981) Noise characteristics of an ideal shunted Josephson junction, *J. Low. Temp. Phys.* **42**, 151–163.

97 Voss, R. F., Laibowitz, R. B., Broers, A. N., Raider, S. I., Knoedler, C. M., Viggiano J. M., (1981) *IEEE Trans. Magn.* **MAG-17**, 395–399.

98 Tesche, C. D. (1982) Analysis of a double-loop DC SQUID, *J. Low Temp. Phys.* **47**, 385–410.

99 Kleiner, R., Koelle, D., Ludwig, F., Dantsker, E., Miklich, A. H., Clarke, J. (1996) Current amplification with asymmetric direct current superconducting quantum interference devices at 77K, *J. Appl. Phys.* **79**, 1129–1142.

100 Engeln-Müllges, G., Reutter, F. (1987) *Formelsammlung zur Numerischen Mathematik mit C-Programmen*. Mannheim/Wien/Zürich: BI Wissenschaftsverlag in German.

101 Drung, D. (1996) Advanced SQUID read-out electronics, in *SQUID Sensors: Fundamentals, Fabrication and Application, NATO ASI Series E: Applied Sciences*-Vol. 329, H. Weinstock (ed.). Dordrecht: Kluwer Academic Publishers, p.63–116.

102 Kramers, H. A. (1940) Brownian motion in a field of force and the diffusion model of chemical reactions, *Physica* **7**, 284–304.

103 Barthel, K., Koelle, D., Chesca, B., Braginski, A. I., Marx, A., Gross, R., Kleiner, R. (1999) Transfer function and thermal noise of $YBa_2Cu_3O_{7-\delta}$ dc SQUIDs operated under large thermal fluctuations, *Appl. Phys. Lett.* **74**, 2209–2211.

104 Braginski, A.I., Barthel, K., Chesca, B., Greenberg, Y., Kleiner, R., Koelle, D., Zhang, Y., Zheng, X. (2000) Progress in understanding of high-transition-temperature SQUIDs, *Physica C*, **341–348**, 2555–2559.

105 Reimann, P. (2002) Brownian motors: noisy transport far from equilibrium, *Phys. Rep.* **361**, 57–265.

106 Weiss, S., Koelle, D., Müller, J., Gross, R., Barthel, K. (2000) Ratchet effect in dc SQUIDs, *Europhys. Lett.* **51**, 305–499.

107 Sterck, A., Weiss, S., Koelle, D. (2002) SQUID ratchets: basics and experiments, *Appl. Phys. A* **75**, 253–262.

108 Müller, J., Weiss, S., Gross, R., Kleiner, R., Koelle, D. (2001) Voltage-flux-characteristics of asymmetric dc SQUIDs, *IEEE Trans. Appl. Supercond.* **11**, 912–915.

109 Testa, G., Sarnelli, E., Pagano, S., Calidonna, C. R., Furnari, M. M. (2001) Characteristics of asymmetric superconducting quantum interference devices, *J. Appl. Phys.* **89**, 5145–5150.

110 Testa, G., Pagano, S., Sarnelli, E., Calidonna, C. R., Furnari, M. M., Russo, M. (2001) Properties of asymmetric high critical temperature dc SQUIDs, *IEEE Trans. Appl. Supercond.* **11**, 908–911.

111 Silver, A.H., Zimmerman, J.E. (1967) Quantum states and transitions in weakly connected superconducting rings, *Phys. Rev.* **157**, 317–341.

112 Giffard, R. P., Webb, R.A. Wheatly, J. C. (1972) Principles and methods of low frequency electric and magnetic measurements using an rf-biased point-contact superconducting device, *J. Low Temp. Phys.* **6**, 533–611.

113 Jackel, L. D., Buhrman, R. A. (1975) Noise in the rf SQUIDs, *J. Low Temp. Phys.* **19**, 201–246.

114 Likharev, K. K, Ulrich, B. T. (1978) *Dynamics of Josephson Junctions Circuits: Basic Theory.* Moscow: Moscow Univ., (in Russian).

115 Gallop, J. C. (1991) *SQUIDs, the Josephson Effects and Superconducting Electronics.* Bristol: Adam Hilger.

116 Danilov ,V. V., Likharev, K. K. (1975) Limiting characteristics of a superconducting quantum magnetometer, *Zh.Tekhn. Fiz.* **45**, 1110–1115; (1976) *Sov. Phys. – Techn. Phys.* **20**, 697–700.

117 Danilov, V. V., Likharev, K. K., Snigirev, O. V. (1980) Signal and noise parameters of SQUIDs. In *SQUID'80, Superconducting Quantum Interference Devices and Their Applications,* H. D. Hahlbohm and H. Lübbig, (eds.). Berlin: Walter de Gruyter, p. 473–507.

118 Hansma, P.K (1973) Superconducting single-junction interferometers with small critical currents, *J. Appl. Phys.* **44**, 4191–4194.

119 Hansma, P. K. (1975) Observability of Josephson pair-quasiparticle interference in superconducting interferometers, *Phys. Rev. B* **12**, 1707–1710.

120 Rifkin, R., Vincent, D. A., Deaver Jr., B. S., Hansma, P. K. (1976) rf SQUID's in the non-hysteretic mode: detailed comparison of theory and experiment, *J. Appl. Phys.* **47**, 2645–2650.

121 Soerensen, O. H. (1976) Analysis of the ac SQUID with low inductance and low critical current, *J. Appl. Phys.* **47**, 5030–5037.

122 Buhrman, R. A. (1977) Noise limitations in rf SQUIDs. In: *Superconducting Quantum Interference Devices and Their Applications*, Eds. H.D. Hahlbohm and H. Lübbig. Berlin: de Gruyter, p. 395–431.

123 Kurkijarvi, J. (1972) Intrinsic fluctuations in a superconducting ring closed with a Josephson junction, *Phys. Rev. B* **6**, 832–835.

124 Kurkijarvi, J., Web, W. W. (1972) *Thermal Fluctuation Noise in a Superconducting Flux Detector.* New York: Proc. ASC *IEEE*, 581–587.

125 Buhrman, R.A., Jackel, L.D. (1977) Performance factors in rf SQUIDs – high frequency limit, *IEEE Tran. Magn.*, **MAG-13**, 879–882.

126 Keranen, R.I., Kurkijarvi, J. (1986) Dependence on the pump frequency of the sensitivity of the rf SQUID, *J.Low Temp.Phys.* **65**, 279–288.

127 Snigirev, O.V. (1981) High frequency characteristics of a single-junction SQUID, *Radiotek. Elektron.* **26**, (in Russian), 2178–2186.

128 Kornev, V.K., Snigirev, O.V. (1981) Theory of microwave SQUIDs with no resonators, *Radiotek. Elektron.* **26**, (in Russian), 2187–2195.

129 Kanter, H., Vernon Jr., F.L. (1977) Millimeter wave behavior of superconducting point contact SQUID, *IEEE Trans. Magn.*, **MAG-13**, 389–391.

130 Kuzmin, L. S., Likharev, K. K., Migulin, V. V., Polunin, E. A,. Simonov, N. A. (1985) X-band parametric amplifier and microwave SQUID using single-tunnel-junction superconducting interferometer. In *SQUID'85, Superconducting Quantum Interference Devices and Their Applications*, H. D.Hahlbohm and H. Lübbig, (eds.). Berlin: Walter de Gruyter, p. 1029–1034.

131 Falko, C.M., Parker, W.H. (1975) Operating characteristics of thin-film rf-biased SQUID's, *J. Appl. Phys.* **46**, 3238–3243.

132 Zhang, Y., Mück, M., Braginski, A. I., Töpfer, H. (1994) High-sensitivity microwave rf SQUID operating at 77 K, *Supercond. Sci. Techn.***7**, 269–272.

133 Zhang, Y. unpublished experimental data.

134 Zhang, Y., Mück, M., Herrmann, K., Schubert, J., Zander, W., Braginski A. I., Heiden, C. (1993) Sensitive rf SQUIDs and magnetometers operating at 77 K, *IEEE Trans. Appl. Supercond.* **3**, 2465–2468.

135 Zakosarenko, V.M., Il'ichev, E.V., Tulin, V. A. (1990) Superconducting quantum interferometer based on metal-oxide ceramic in hysteresis-free operation at 77 K, *ZhETF Pis. Red.* **51**, 275–279; (1990) *JETP Letters* **51**, 315–319.

136 Il'ichev, E.V., Zakosarenko, V.M., Ijsselsteijn, R. P. J., Schultze, V. (1997) Inductive reply of high-T_c rf SQUID in the presence of large thermal fluctuations, *J. Low Temp. Phys.* **106**, 503–508.

137 Chesca, B. (1994) On the theoretical study of an rf-SQUID operation taking into account the noise influence, *J. Low Temp. Phys.* **94**, 515–538.

138 Zeng, X. H., Zhang, Y., Chesca, B., Barthel, K., Greenberg, Ya. S., Braginski, A. I. (2000) Experimental study of amplitude-frequency characteristics of high-transition-temperature radio frequency superconducting quantum interference device, *J. Appl. Phys.* **88**, 6781–6787.

139 Mück, M., Chesca, B., Zhang, Y. (2001) Radio frequency SQUIDs and their applications. In *Proc. NATO ASI on Microwave Superconductivity*, eds. H. Weinstock and M. Nisenoff. Dordrecht: Kluwer Academic Publisher, p. 505–540.

140 Greenberg, Ya. (1998) Signal characteristics for high Tc rf SQUID from its small signal voltage-frequency characteristics, *J. Low Temp. Phys.* **114** , 297–316.

141 Chesca, B. (1996) Theory of a UHF pumped double SQUID, *Physica C* **270**, 1–20.

142 Chesca, B. (1998) A D-SQUID as a possible solution for approaching the classical sensitivity limit. Proc. EUCAS '97, July 1997, Univ. of Twente, the Netherlands, *Applied Superconductivity*, eds. H. Rogalla and D. H. A. Blank. Bristol and Philadelphia: Institute of Physics Publishing, p. 671–674.

3
SQUID Fabrication Technology

Robin Cantor and Frank Ludwig

3.1 Junction Electrode Materials and Tunnel Barriers

Thin-film tunnel junctions are the only practical Josephson devices of modern SQUID technology. Other types of Josephson junctions, from bulk point-contact devices to thin-film proximity or constriction microbridges mentioned in Chapter 1, have mostly historical significance. Therefore, in this chapter we present only the thin-film fabrication technology of low- and high-temperature Josephson tunnel devices, beginning with an overview of electrode materials and tunnel barrier properties. Similarly, other components of SQUIDs, from the SQUID loop to the input coil or the whole flux transformer, are at present fabricated from thin films of the junction electrode material, while incorporating also the required insulating, resistive, conductive, etc., films. Their fabrication is addressed in the following sections. The only optional bulk components of modern SQUIDs are wire-wound pickup coils discussed in Chapter 7.

More than 20 of the metallic elements can become superconducting, while certain semiconductors can be made superconducting under suitable conditions (e.g., by the application of pressure, or in very thin film samples). In addition, thousands of alloys and compounds have been found to exhibit superconductivity [1], but only very few of these are of interest for practical Josephson junctions and devices. The soft metallic elements such as Al, Sn, Pb, and In were commonly used to fabricate many of the first tunnel junctions in the 1960s. These metals have low melting temperatures, can easily be evaporated in simple vacuum systems, and tunnel barriers readily form by exposing the base electrode to oxygen or oxygen glow discharge. However, such junctions are unstable with respect to repeated thermal cycling and are susceptible to chemical corrosion. Junctions made using Pb-Au-In alloy films, for example, had a tendency to fail owing to a change of the film microstructure after repeated thermal cycling that caused the thin tunnel barrier to rupture [2,3].

The material parameters that are important for practical Josephson junction applications include the critical temperature T_c, superconducting energy gap Δ, the superconducting coherence length ξ, and the penetration depth λ_L of the electrode material. A high energy gap is desirable for all applications. The maximum device operating temperature, which optimally is around $2T_c/3$ or lower in order for the superconducting energy gap to be reasonably developed and relatively temperature-independent, may be determined not by the T_c of the bulk material but rather by the T_c of the material within one coherence length from the interface with the barrier.

This is a consequence of the fact that superconducting tunneling probes a distance of about one coherence length into the superconducting electrode. Thus, a long coherence length is desirable in order to minimize the effects of surface damage near the superconductor–insulator interface. The magnetic penetration depth should be low in order to minimize flux trapping.

Note that the above requirements imply that Type II superconductors which intrinsically have $\xi<\lambda_L$ are less attractive for Josephson junction applications because of their low ξ and high λ_L. According to the Ginzburg–Landau theory, in the dirty limit, $\xi(0) \propto (\rho_n T_c)^{-1/2}$ and $\lambda(0) \propto (\rho_n T_c)^{1/2}$, where ρ_n is the normal-state resistivity. This implies that the only way to optimize the ratio of ξ/λ_L is to fabricate the electrode films such that they are close to the clean limit with long electron mean free path. This is very difficult in low-temperature superconducting (LTS) Type II materials, given the impurities, defects and disorder inherent to deposited thin films, especially for the counter-electrode deposited last. In all high-temperature superconductors (HTS), which are extreme Type II materials, even atomic-scale defects may reduce the local energy gap sufficiently to result in weak (Josephson) coupling across, e.g., a high-angle grain boundary. This difficulty makes it mandatory to fabricate junction electrodes from epitaxial, nearly single-crystalline films free of high-angle grain boundaries. Fortunately, sensitivity to atomic defects can also be turned into a major advantage, by permitting technologists to use controllable grain boundaries as HTS junction tunnel barriers.

The key barrier parameters that determine any tunnel junction performance include the average height ϕ and effective width s of the barrier and the junction capacitance per unit area $c_J = C/A_J$, where C is the total capacitance and A_J is the junction area. Junction quality is further quantified by the amount of sub-gap leakage current and low-frequency $1/f$ noise. The latter is particularly important for many low-frequency SQUID applications and typically is around 1 to 2 $\mu\Phi_0 Hz^{-1/2}$ at 1 Hz for many LTS junction technologies. Sub-gap leakage current may arise from non-superconducting microshorts in the barrier or excess tunneling current via electron states localized within the barrier. Savo *et al.* [4] have shown that $1/f$ noise in LTS junctions scales roughly as $I_0 A_J^{-1/2}$. Based on this observation, very small junctions with high critical current density are less attractive for low-frequency SQUID applications. The origins of $1/f$ noise are discussed in detail in Chapter 2.

For a given barrier width, the average tunneling height determines the tunneling resistance R above the energy gap, while for a given barrier height, the junction critical current I_0 depends exponentially on the barrier width s. The effective width generally is comparable to the physical thickness of the barrier, which for oxides ranges from 1 to 10 nm. In order to obtain tight I_0 tolerances, one therefore needs to carefully control the barrier height and especially the effective barrier width s. An advantage of low barrier height materials is that control of the barrier thickness is less critical.

If the tunnel barrier is assumed to be rectangular, the average barrier height and effective width may be obtained by fitting the experimental I–V characteristic to a theoretical expression derived by Simmons [5],

$$I = \frac{3.16\times10^{31}}{s} V\sqrt{\phi}\exp(-0.1025s\sqrt{\phi})A_J,$$

where I is the junction current in μA, V is the voltage across the junction in μV, A_J is the area of the junction in μm^2, and the barrier height ϕ and width s are expressed in volts and nanometers, respectively. The junction capacitance c_J may be determined from junction resonances (Fiske modes) [6].

3.2 Low-temperature SQUID Devices

3.2.1 Refractory Junction Electrodes

Based on the considerations presented above, elemental, polycrystalline Nb is an attractive material for Josephson junction electrodes. As borderline Type II superconductor, it has a reasonable coherence length $\xi = 40$ nm, a moderate penetration depth $\lambda_L = 85$ nm, while the relatively high $T_c \approx 9.2$ K and energy gap $\Delta \approx 1.5$ mV permit one a comfortable temperature margin for junction operation at liquid helium temperatures. In addition, Nb is a refractory metal, and mechanically very stable. High-quality Nb films can be fabricated using electron-beam or ion-beam evaporation or by sputtering, and films of Nb readily form a surface oxide, Nb_2O_5. Such Nb/Nb-oxide junctions were studied extensively in the late 1970s [7,8], but the junctions exhibited excessive sub-gap leakage current, which is typically described by the parameter $V_m = I_0R$. Here, I_0 is the maximum supercurrent through each junction (assumed to be identical) and R is the resistance below the sum of the energy gaps of both electrodes, i.e., usually determined at 2 mV. Latta [9] found that Nb counter-electrodes deposited onto Nb_2O_5 barriers tend to react with the Nb_2O_5 to form NbO and NbO_2, which are metallic and semiconducting, respectively, thereby producing microshorts and excess leakage. In addition, Nb_2O_5 has a high dielectric constant, 29, resulting in a high specific capacitance of typically 0.14 $pF/\mu m^2$ [8]. The only way to effectively reduce the junction capacitance in this case is to form the tunnel junction on a sloped film edge, as reported by Sandstrom *et al.* [10]. This edge (or ramp) junction geometry later became widely used for the fabrication of HTS junctions, as described in Section 3.3.

The only strongly Type II low-temperature superconducting material, for which a usable junction technology has been developed, is the refractory metal niobium nitride, NbN (or carbonitride NbCN) having $\xi = 4$ nm and $\lambda_L = 300$ nm (Appendix A.1). Although some experimental SQUIDs have been fabricated in this technology, it did not gain broader acceptance since the junction parameters are much more difficult to control with narrow parameter spreads. The most viable, broadly used modern technology for fabricating low-temperature SQUIDs uses niobium superconducting films and AlO_x barriers discussed in the next Section.

3.2.2
Tunnel Barrier Technology

In addition to native Nb_2O_5 barriers mentioned above, artificial (deposited) low-height barriers, such as amorphous and hydrogenated silicon or germanium, were investigated in the late 1970s, and even used in junctions of some hybrid rf SQUIDs manufactured in the early 1980s [11]. However, the excessively high $1/f$ noise and subgap leakage current made all these barriers unattractive once the nearly ideal Al-AlO_x barrier technology emerged in early 1980.

The most important discovery in the development of all-refractory Josephson junctions was reported by Rowell *et al.* [12] in 1981. They observed that a very thin film (a few monolayers) of Al is sufficient to "wet" and completely cover the surface of clean Nb. Gurvitch *et al.* [13–15] subsequently demonstrated that high-quality junctions can be fabricated on Nb by depositing a very thin Al film (typically, 2 to 4 nm) onto a clean Nb surface and then oxidizing the Al layer. Interestingly, Laibowitz and Mayadas [16] also fabricated tunnel junctions on Nb using an oxidized Al barrier nine years earlier, but the Al films used were much thicker, >40 nm, presumably in order to cover the Nb film edges in their cross-strip geometry, and were leaky.

Following the initial work of Gurvitch *et al.*, tunnel junctions fabricated using Nb and oxidized Al barriers (usually denoted as Nb/Al-AlO_x/Nb or Nb/Al_2O_3/Nb structures) were largely perfected during the remainder of the 1980s. Kwo *et al.* [17] first studied the surface oxidation of Nb with thin Al overlayers using X-ray photoemission spectroscopy (EPS). They observed that an Al overlayer as thin as 1 nm is sufficient to protect the underlying Nb from oxidation owing to the stronger oxygen affinity of Al as compared with Nb. Thicker Al overlayers, subsequently oxidized in air, were observed to form self-limiting oxides not more than 2 nm thick, regardless of the deposited Al thickness. An oxidation time of up to 30 minutes was sufficient to allow most but not all of the exposed Al to become oxidized. The excess Al tends to diffuse into the underlying Nb grain boundaries depending on the process conditions and microstructure of the Nb film. In particular, if the Nb film consists of very large grains, the residual unoxidized aluminum will form a proximity layer and reduce the sum gap [18]. Thus, in order to avoid this proximity effect and also to enhance surface smoothness, the Nb films should be microcrystalline with the smallest possible grain size.

The grain boundary diffusion of Al into the underlying Nb is an important mechanism that can affect junction quality. As reported by Huggins and Gurvitch [19], the diffusion of Al into Nb depends on substrate temperature. Improved junctions were obtained by effective heat sinking of the substrate during Nb deposition, both for the deposition of the base electrode as well as the deposition of the counter electrode on top of the oxidized Al. Further improvements were reported by Morohashi *et al.* [20,21], following optimization of the Nb films and Al thickness. Since substrate heating owing to electron bombardment is larger with rf sputtering than with dc sputtering, the potentially higher temperature of rf sputter deposited films and the grain boundary diffusion mechanism help explain the degradation of tunnel junctions fabricated using rf sputter deposited Nb films [21]. The enhancement of

the grain boundary diffusion mechanism with increasing substrate temperature was also reported by Tanabe *et al.* [22] and by Chang *et al.* [23].

Huggins and Gurvitch confirmed the effect of substrate temperature on the sharpness of the Nb/Al interface using anodization spectroscopy [19]. They defined the area to be anodized using photoresist and placed the sample in an electrolyte consisting of 156 g ammonium pentaborate, 1120 ml ethelyne glycol, and 760 ml H_2O. One electrode contacted the Nb/Al film, a second electrode was placed in the solution, and the exposed film was anodized at a constant current density of 0.4 mA/cm^2 with a compliance voltage of 85–90 V. Using an *RC* differentiating circuit, *dV/dt* could be measured as a function of the voltage across the anodization cell. As the anodic oxide moves through the Al and into the Nb, the slope of the *dV/dt* versus *V* curve changes, thereby providing a qualitative measure of the sharpness of the Nb/Al interface. This technique was further refined by Blamire *et al.* [24] and by Imamura and Hasuo [25,26] for Al overlayers on sputtered Nb and by Kohlstedt *et al.* [27] for Al overlayers on electron beam evaporated Nb. Imamura and Hasuo [28] further correlated the anodization profiles with the microstructure of Nb/Al bilayers determined using cross-sectional transmission electron microscopy (TEM). They observed that the Al planarizes the Nb base electrode, resulting in good crystalline structure of the Nb counter electrode just above the AlO_x.

A key issue in all variants of the Al-AlO_x barrier technology discussed above is the thermal stability of the barrier during subsequent processing. The stability of Nb/Al-AlO_x/Nb junctions was investigated by Hikada *et al.* [29] who found that the junction critical current decreases linearly with increasing temperature while V_m remained unchanged up to 250 °C. Note that the temperature dependence of the critical current offers a means of adjusting the critical current after patterning by annealing at elevated temperatures.

In closing, we mention only that the current NbN technology of refractory junction fabrication has been employing barriers of MgO, and lately also nitrides of Si or Al. Neither metallic aluminum, nor any of these barrier materials can wet the NbN surface as Al wets Nb, which would be conducive to barrier integrity and narrow parameter spreads.

3.2.3
Deposition Techniques

SQUID process development has benefited from the rapid advance of semiconductor process technology. Whole-wafer processes for SQUID fabrication are largely analogous to those of silicon device and integrated circuit manufacturing. The most commonly used substrates include quartz (e.g., glass microscope slides) and especially Si wafers, as they are readily available at low cost. Bare Si and oxidized Si wafers (for junctions fabricated using an anodization step) are generally used, with diameters of 50 mm to 150 mm. In order to keep the substrates cool during film deposition, the wafers are often greased (e.g., using Apiezon® L-Grease, which is soluble in tetrafluoroethane), on to Cu pucks that are in contact with a water-cooled platen during deposition.

A simple and straightforward means of depositing thin films of low melting temperature materials is by thermal evaporation. Typically a vapor pressure of 1 Pa (10^{-2} mbar) must be achieved in order to obtain useful film condensation rates, corresponding to temperatures in the range of 1000 to 2000 °C for most materials of practical interest. To avoid contamination, the evaporation source, which may be in the form of a wire filament (which the evaporant will coat or "wet" upon melting), a boat or a crucible, must have a low vapor and dissociation pressure at the operating temperature. For this reason, refractory metals and oxides are generally used for evaporation sources. Most advantageous are vessel-free sources shaped as wires of the material to be evaporated.

Suitable thermal evaporation sources and conditions for a variety of elements and compounds may be found in thin film handbooks (see, for example, [30–33]). The evaporation of compounds and dielectrics can be complex, since few inorganic compounds evaporate congruently owing to different vapor pressures of the constituent elements. Thus, the composition of the thin film may be quite different from that of the source. For example, SiO is often used to define the junction area or as interlayer insulation. The deposition temperature must be carefully controlled, as above 1250 °C the dissociation into Si and O_2 begins, which may lead to oxygen-deficient films.

Instead of resistively or inductively heating the evaporant, electron bombardment may be used. By focusing an electron beam accelerated by a field of 5 to 10 kV onto the evaporant surface, temperatures in excess of 3000 °C can be reached. Using a focused source, the beam energy can be localized in a small region, such that the rest of the evaporant remains at a lower temperature. This helps reduce potential interactions between the evaporant and supporting material. Inoue *et al.* [34] described an electron beam evaporation process used to fabricate Josephson junctions using Nb electrodes.

Sputtered films are deposited by bombarding the target material with energetic ions (typically Ar^+). As the kinetic energy of the incident ions exceeds roughly 4H, where H is the heat of sublimation of the target material, the incident ions begin to dislodge and eject target atoms into the gas phase. Typically, sputter yields do not vary more than a factor of 10 for a wide variety of materials. Advantages of sputtering are several. It is possible to sputter deposit not only elements but also more complex alloys and compounds without significant compositional changes if the deposition conditions are properly configured. Film thickness control is fairly simple – the deposition rate may be calibrated for a certain set of conditions, after which the thickness is determined solely by the deposition time, and there are fewer problems with "spitting", i.e., the ejection of clumps of evaporant, which often occurs with vacuum evaporation processes. The plasma present during sputtering also provides a means of manipulating film growth to achieve desired film properties. The main disadvantage of sputtering is that the deposition rates are relatively slow, ranging from around 5 to 300 nm/min.

Many compounds can be synthesized by sputtering elemental or alloy targets in reactive gases instead of sputtering directly from compound targets. Mixing reactive gases such as oxygen or nitrogen with the inert sputter gas, for example, it is possi-

ble to deposit oxide or nitride films such as SiO_2, TiO_2, Si_3N_4, and NbN directly from metallic or semiconducting target materials.

Bias sputtering is a variant of conventional sputtering in which the substrates are ion bombarded during deposition by the application of a bias voltage to the substrate to sputter away loosely bonded species (deposited film or trapped gases such as oxygen) during film growth or to improve conformal coverage over contoured surfaces. For example, Hoko *et al.* [35] used bias sputtering to improve conformal coverage of SiO_2 films used to fabricate Josephson junction circuits.

An important parameter that can affect thin-film device performance is film stress. Evaporated Nb films typically are under a large tensile stress [36,37], which is difficult to control experimentally. The stress in sputtered Nb films, however, varies from compressive to tensile depending on the sputtering conditions such as the sputter gas pressure [38]. In the worst case, tensile stress can lead to film peeling, while excessive compressive stress can cause the film to wrinkle. Less dramatic but equally damaging, the properties of junctions made on stressed films can seriously degrade following stress relaxation after patterning.

Nearly stress-free Nb films may be sputter deposited by properly adjusting the deposition conditions. Partly for this reason, sputter deposition has become the preferred method for the fabrication of Nb/Al-AlO_x/Nb Josephson junctions for SQUID applications. Typically, sputtered Nb films have a columnar structure with polycrystalline grains [28]. In order to cover the Nb base electrode without using an exceedingly thick layer of Al, the Nb films should be smooth and stress free. The substrate also should be cooled in order to reduce grain boundary diffusion of the deposited Al into the Nb, leaving microscopic areas of the Nb base electrode exposed during the oxidation step, which can lead to microshorts. If the Al layer becomes too thick, the critical current density j_0 and the energy gap will be reduced by the proximity effect. SQUIDs fabricated using Josephson junctions with excess unoxidized Al near the barrier also exhibit increased $1/f$ noise.

The stress of sputter-deposited films has been studied and characterized by several groups [39–45]. Kuroda *et al.* [40] found that small, square junctions (<5 μm per side) fabricated from Nb films having tensile or compressive stress exceeding roughly 1×10^8 N/m^2 exhibited higher sub-gap leakage and reduced energy gaps. This demonstrated the importance of optimizing the sputter conditions to minimize film stress. Kuroda *et al.* [40] also demonstrated that similar junctions fabricated using a lift-off process exhibited performance parameters comparable to those of junctions patterned from stress-free films (see Section 3.2.6).

Original studies of the effects of stress in sputter deposited Nb films were carried out using a fixed cathode voltage and varying the Ar pressure during deposition. In these studies, the sputter conditions could be adjusted to obtain zero-stress films by adjusting the Ar pressure for a given cathode voltage. Since the cathode voltage drops as the target erodes, however, the optimal sputter conditions change and must be monitored and adjusted over time. The zero-stress conditions also tend to be system dependent [42,44,46,47] and therefore must be mapped out empirically, and they also depend on the type of substrate used [48]. In consequence, no general recipe can be recommended.

Aside from the importance of obtaining stress-free films, it is also important that the films be clean and free of impurities or defects. For example, Nb films are particularly sensitive to oxygen content, which can reduce T_c by 0.93 K per at. % O [49]. The Nb films are usually sputter-deposited in cryo-pumped UHV systems having a base pressure of the order of 10^{-5} Pa and at rates of the order of 100 nm/min. High-quality films may be obtained, with room-temperature resistivities around 15.2 $\mu\Omega$-cm, which is very close to the value of 14 $\mu\Omega$-cm for bulk Nb, and residual resistivity ratios (RRR, the resistivity at 300K divided by the residual resistivity at 10K) of 4 to 8.

3.2.4
Junction Definition

Early thin-film Josephson junctions were fabricated by depositing the metal electrodes through shadow masks made from carefully machined metal plates. Similarly deposited oxides or hand-painted insulating layers (e.g., Formvar) were used to define tunnel junction "windows" on the base electrode.

One of the first breakthroughs for the fabrication of Josephson junctions with reproducible parameters and narrow parameter spreads was the whole-wafer process described by Kroger *et al.* in 1981 [50]. First a superconductor–barrier–superconductor trilayer is deposited over an entire Si wafer in one deposition sequence without breaking vacuum. By avoiding any intermediate patterning steps, the entire trilayer can be fabricated with great cleanliness. Individual Josephson junctions (mesas) are then patterned, isolated and defined by completely anodizing the top superconducting layer down to the barrier layer using a photoresist stencil as discussed in Section 3.2.6. The junction is completed by depositing and patterning a superconducting wiring layer with or without an auxiliary insulator layer. Smith *et al.* [51] later used a thin, sputter-deposited film of SiO_2 as the anodization mask, which improved junction uniformity and anodization undercut. The Selective Niobium Anodization Process (SNAP) developed by Kroger *et al.* greatly simplified the fabrication of Josephson junctions with refractory Nb thin-film electrodes, and resulted in improved reproducibility and narrow spreads of the junction parameters over an entire wafer.

Following the pioneering work of Kroger *et al.*, several other whole-wafer processes for the fabrication of Josephson junctions were developed in the 1980s. These processes differ in the way in which the Josephson junctions are defined and isolated, but they are all based on the fabrication in one vacuum sequence of a trilayer over an entire Si wafer. These include the Selective Niobium Etch Process (SNEP) [15] and the Selective Niobium Etch and Anodization Process (SNEAP) [52], which, together with SNAP, are the most widely used Josephson junction processes. The basic process steps are shown in Figure 3.1. The SNEP junctions are defined by patterning the top Nb layer using a reactive ion etch (RIE; see Section 3.2.6) rather than anodization, while the SNEAP junctions include a light anodization step following the removal of the top Nb layer. Other whole-wafer techniques include the Selective Niobium Isolation Process (SNIP) [53] and the Self-Aligned Contact (SAC) process [54].

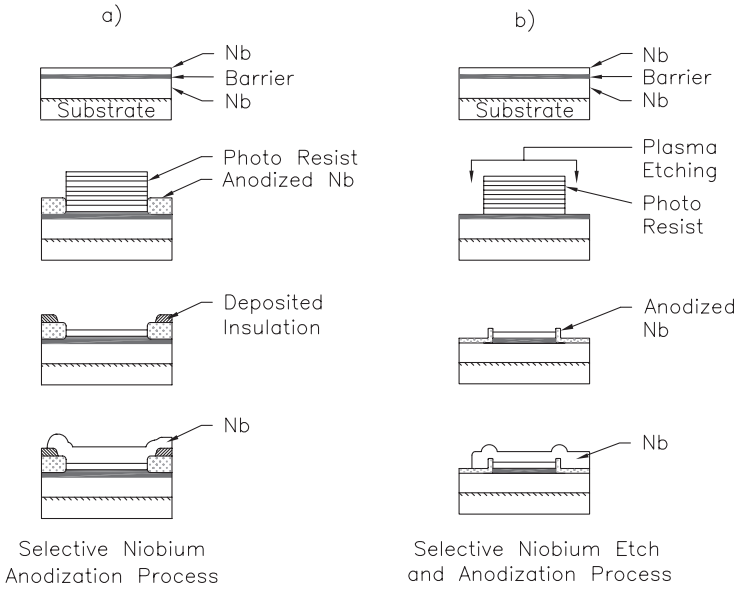

Fig. 3.1 Schematic representations of (a) the Selective Niobium Anodization Process (SNAP) with additional deposited insulation, and (b) the Selective Niobium Etch and Anodization Process (SNEAP). The Selective Niobium Etch Process (SNEP) is the same as shown in (b) except the anodization step is deleted.

By the mid-1990s, several groups had developed and optimized whole-wafer Nb/Al-AlO_x/Nb junction processes for SQUID fabrication. Most practical and nearly all commercial LTS thin-film SQUIDs and SQUID-based sensors are now fabricated using this junction technology and one of the whole-wafer processes described above. These wafer-scale processes have resulted in improved junction reproducibility with narrow parameter spreads, both of which are important in improving device yield (number of chips with acceptable parameters) and throughput. Wafer-scale processes also are important for cost-effective production of large-area devices, such as integrated thin-film magnetometer and gradiometer chips that can have side lengths of around 1 cm or 2 cm, respectively.

3.2.5 Dielectric Insulation

Owing to the high dielectric constant of Nb_2O_5, the capacitance of SNAP Josephson junctions can be dominated by the overlap between the counter-electrode wiring and base electrode. This parasitic junction capacitance can lead to resonances that degrade performance and complicate proper operation of the SQUID. This in part motivated the development of alternate junction definition techniques, such as SNEP and SNEAP discussed above. SQUIDs fabricated with integrated, thin-film input circuits also require a low dielectric constant insulator between the SQUID

and the input coil (see Chapter 5) in order to avoid introducing a large parasitic capacitance across the SQUID inductance, which also can degrade performance and complicate operation.

In view of these considerations, other oxides and nitrides with lower dielectric constants are generally used for Josephson device fabrication. Commonly used dielectrics include SiO, SiO_2 and Si_3N_4. Films of SiO are generally evaporated using specially designed resistive sources with baffles to minimize particulate ejection. Careful control of the source temperature and background pressure is required to deposit optimal films. For most wafer scale processes, SiO_2 is preferred, owing to its low dielectric constant, and ease of deposition and patterning. High-quality SiO_2 films may be rf sputter deposited using a quartz target or reactively sputtered using a Si target and an Ar-O_2 gas mixture, but the deposition rates tend to be low. Similarly, Si_3N_4 films may be reactively sputtered using a Si target and Ar-N_2 gas mixture.

More commonly, SiO_2 films are deposited using Plasma-Enhanced Chemical Vapor Deposition (PECVD) via the chemical decomposition of silane. The PECVD process is capable of much higher deposition rates, but the optimal processing temperature is 350 °C [55]. Several groups successfully developed low-temperature (<200 °C) PECVD processes for the deposition of SiO_2 [56–58], but the refractive index and density of films deposited at these reduced temperatures are degraded. Using Electron Cyclotron Resonance (ECR) enhancement, the plasma efficiency is greatly increased making it possible to deposit high-quality SiO_2 films at temperatures below 150 °C. Meng *et al.* [59] reported a significant improvement in junction uniformity and quality using low-stress SiO_2 films deposited at low temperatures with ECR-enhanced PECVD.

Recently, there has been interest in spin-on glass (SOG) dielectrics for interlayer insulation and planarization. Pavolotsky *et al.* [60] described a process that uses a 300 nm SOG film (Accuglas® 314) prepared by spin coating at 3000 rpm with a low-temperature cure at 90 °C for 3 minutes followed by electron beam curing at a dose of 3000 $\mu C/cm^2$. Advantages of such SOG films are the comparatively low dielectric constants (2 to 4) and their ability to planarize the wafer topology. These are important considerations for SQUID designs that include integrated, multi-turn input circuits.

3.2.6
Patterning Techniques

Early Josephson junctions were fabricated using shadow masks, but most circuits are now fabricated using one of the whole-wafer processes described above. The junction trilayer, wiring and dielectric layers are patterned using photomask stencils created by etching the desired pattern in a thin chrome or iron oxide film on a quartz or glass plate, which is then transferred lithographically to a UV-sensitive photoresist layer spun onto the wafer. The patterned photoresist stencil is then transferred to the underlying film or films using various dry or wet etching techniques. The desired pattern may also be obtained by depositing the film through the resist stencil and then dissolving the resist away along with the excess film depos-

ited on the photoresist. This so-called "lift-off" technique is very useful for patterning films that are otherwise difficult to etch. In order to avoid tearing along the film edges, however, the resist stencil must be carefully prepared with an overhang or negative edge profile. Special photoresists such as the nLOF™ series from Clariant have recently been developed specifically for lift-off processes and offer improved resolution and reproducibility.

Typically, dry etch techniques are used to pattern thin films, such as ion milling (e.g., using Ar^+) or Reactive Ion Etch (RIE) plasmas (e.g., CF_4, SF_6). Although Ar ion milling can be used to pattern practically any film, etch selectivity is limited, which can be a problem for multi-layer structures, and for this reason ion milling is rarely used for LTS Josephson junction fabrication. In contrast, depending on the reactive gas or gas mixture used, RIE can be very selective and can produce very steep or gradual edge profiles in etched films. Fluorine-based etch chemistries for Nb junction and device fabrication include CF_4 and $CF_4 + O_2$ mixtures developed in the early 1980s [61,62] and SF_6 developed in the early 1990s [45,47,63]. Ref. [45] also describes a CHF_3-based RIE etch process for patterning SiO_2 films. Chlorine-based chemistries also have been used to pattern Nb films, such as CCl_2F_2 [64–66], $SiCl_4$ [67], Cl_2 [68], and $Cl_2 + BCl_3 + CHCl_3$ [47], but the fluorine-based chemistries tend to be more widely used. Typical etch rates for Nb and SiO are 75 nm/min and 22 nm/min, respectively, using CF_4+10%O_2 (300 mTorr, 100 W, 100 V), while using SF_6 (30 mTorr, 85 W, 140 V), typical etch rates for Nb and SiO_2 are 140 nm/min and 30 nm/min, respectively [69].

A disadvantage of CF_4 based RIE is that Nb is isotropically etched leading to severe undercutting and poor linewidth control unless low pressure and high rf power are used, but these conditions are difficult to achieve using conventional RIE. As shown by Aoyagi *et al.* [70], however, electron cyclotron resonance (ECR) enhanced RIE may be used to develop a highly anisotropic CF_4 etch process. A similar ECR enhanced RIE process using SF_6 was described by Numata *et al.* [71].

Wet etchants generally are not used to pattern thin films, because they are less selective than dry etches and difficult to control. Some materials, however, notably Al and noble metals such as Au and Pd used for contact pads or resistors, cannot be patterned using RIE[1)]. To pattern these films, wet etches, ion milling, or lift-off stencils are typically used. Standard wet etchants include 1 HCl : 20 HNO_3 : 60 CH_3COOH [72] for Pd, PAN (Phosphoric/Acetic/Nitric acid solution) for Al, and Buffered Oxide Etch (BOE, NH_4F/HF solution) for SiO_2. The etch rate for SiO_2 may be adjusted an order of magnitude by varying the NH_4F/HF ratio.

Regardless of the patterning method used, the edge profile of the patterned film should be slightly tapered (beveled) in order to improve conformal coverage at crossovers by subsequently deposited films. The thickness of subsequently deposited films should also be higher than that of the underlying film(s) in order to improve conformal coverage. If conformal coverage is poor, isotropic wet or dry etches can undercut the photoresist at crossovers and lead to disconnects. Alternately, if the

1) For this reason these materials may be used as etch stop layers for RIE.

RIE process conditions are not properly adjusted, the trenches, for example, between finely pitched wires in transformer coils may not etch completely at crossovers, leading to shorts between the coil windings.

Both wet and dry etches are used to open contact vias through insulating layers in order to make electrical contact to the underlying metal layer. Contact vias usually are small openings, typically 2 μm to 5 μm in diameter, and must have slightly tapered edge profiles in order to avoid disconnects at the edges as discussed above. Vias to Nb films usually are Ar^+ ion etched before subsequent film deposition in order to remove surface oxides on the exposed Nb surface and prevent the formation of additional Josephson junctions in the circuit.

3.2.7
Passive Components for Device Fabrication

In order to fabricate Josephson junctions for practical SQUID applications, additional passive thin-film components such as resistors and capacitors for *RC* filter networks are usually required. Thin films of Ta, $AuIn_2$, Ti/Au and especially Mo have been used as resistors in Josephson junction integrated circuits, but all of these materials are superconductors below about 0.5 K and therefore are not suitable for devices that must be operated below this temperature. Furthermore, although Ta and Mo films are straightforward to pattern reactively, they must be buried under a dielectric layer in order to prevent corrosion. Non-superconducting films of Au and Cu also have been used to fabricate resistors, but the resistivities of these materials are low and film adhesion is generally poor. Films of Pd, PdAu [10,45] and Pt [73,74], on the other hand, also are non-superconducting and it is fairly easy to obtain reasonable sheet resistances of around 1 $\Omega/\square$ using films that are a few to several tens of nm thick.

To fabricate capacitors, a high dielectric constant material is desirable in order to keep the size of the capacitors from becoming too large. For this reason, Nb_2O_5 with its high dielectric constant of 29 is an attractive choice [73]. High-quality Nb_2O_5 films may be formed by anodic oxidation during the anodization step, when using SNAP or SNEAP.

3.2.8
Integrated SQUID Fabrication Process

A typical process suitable for the fabrication of integrated SQUIDs based on SNAP junctions consists of six mask levels (see also [75]). The mask levels, film layers and typical thicknesses are summarized in Table 3.1 and shown schematically in Figure 3.2. Minimum linewidths and spaces of 2 μm to 3 μm are sufficient and readily achievable. To begin, a Nb/Al-AlO_x/Nb trilayer is deposited over an entire wafer in a single vacuum sequence. The trilayer is patterned using a wet or dry etch to define the base electrode, contact pads, interconnects, and capacitors (if required). The Josephson junctions are then defined using photoresist (mask level two) and the top Nb layer is anodized. The shunt resistors and filter resistors (if required) are depos-

Table 3.1 Six mask level process for integrated SQUID fabrication based on SNAP.

Mask Level	Layer	Description	Thickness [nm]	Function
1	Nb	Trilayer base electrode	200 – 300	JJ's, Pads,
	Al	Trilayer barrier metal	5 – 7	Wiring, Capacitors
	AlO_x	Oxidation	1	
	Nb	Trilayer top electrode	30 – 60	
2	Al_2O_3/	Anodization		JJ Isolation
	Nb_2O_5		70 – 100	
3	Pd	Resistor	300 – 800	Shunts, Filters
4	Nb	1st Wiring Layer	300	SQUID Washer, Wiring
5	SiO_2	Interlayer Dielectric	300 – 500	Transformer Insulation
6	Nb	2nd Wiring Layer	400 – 600	Input/Feedback Coils, Wiring

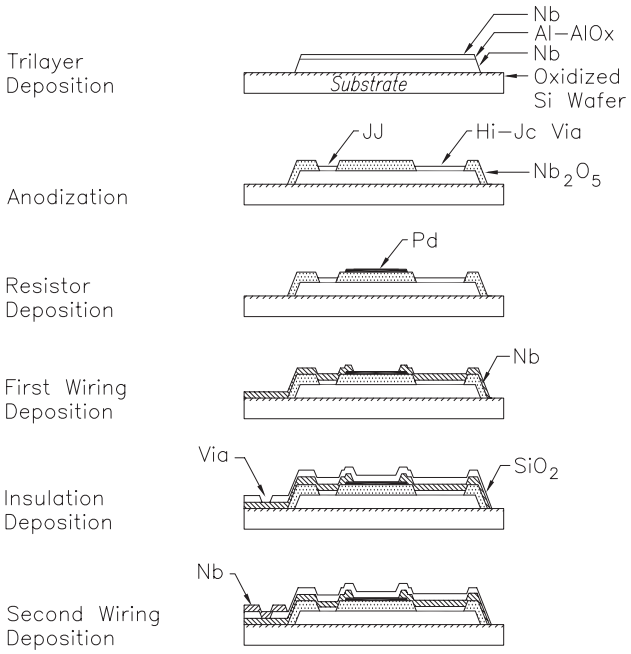

Fig. 3.2 Cross-sectional view of the layer sequence for a six mask level process for integrated SQUID fabrication based on SNAP.

ited next and patterned using mask level three and lift-off or a wet etchant. A blanket Nb wiring layer is deposited and patterned using mask level four and RIE to define the SQUID washer, counter-electrode, and interconnects. Next, an insulating layer, typically SiO_2, is deposited over the entire wafer and vias are opened to the first wiring layer or the base electrode of the trilayer using mask level five and a wet or dry

etch. The SQUIDs are completed by the deposition of the last Nb wiring layer, which is pattered using mask level six and a lift-off process or RIE to define the input and feedback coils and remaining interconnects.

If the Nb and insulator deposition conditions are properly adjusted to achieve stress-free films, the wafers are properly heat sunk as discussed in Section 3.2.3, and the film edge profiles are tapered to promote conformal coverage as discussed in Section 3.2.6, the key remaining challenges are to optimize the process conditions to reproducibly obtain the desired critical current and shunt resistor parameters with minimal spreads over the entire wafer. Critical current reproducibility and uniformity depend on good control of the oxidation conditions (pressure, time, temperature), tight control of the lithography and etch or anodization conditions used to define the junction areas, and the reduction of film stress. Shunt resistor reproducibility and uniformity depend on the stability of the deposition conditions, tight control of the photolithography, and, if a wet etchant is used to pattern the films, tight control of resist undercutting during the etch step. In any case, the uniformity of as-deposited films typically is not better than 90% unless special deposition techniques or large area targets are used. With good control over the optimized process conditions, device yield can be as high as 80% [76].

3.3
High-temperature SQUID Devices

3.3.1
General Requirements and Problems

Initially, high-T_c (HTS) SQUIDs were fabricated from polycrystalline bulk or thin films of the high-temperature superconductor $YBa_2Cu_3O_{7-x}$ (YBCO). The naturally occurring grain-boundary weak links in machined bulk constrictions or microbridges patterned in thin films served as junctions [77,78]. Despite successful operation at 77 K, the boiling temperature of liquid nitrogen, these polycrystalline devices exhibited extremely high levels of $1/f$ noise caused by the thermally activated hopping of flux vortices at grain boundaries and among intra-grain pinning sites. Whereas $1/f$ noise due to flux motion rarely is a problem for LTS thin films, it is a major issue in HTS films since the operating temperature is higher and pinning energies are much lower.

Epitaxial, nearly single-crystalline thin films exhibit much lower $1/f$ noise than polycrystalline films. As shown by Ferrari *et al.* [79], the level of $1/f$ noise in such films is correlated with their microstructural quality. Although SQUIDs were also fabricated from epitaxial thin films of other HTS compounds, high-quality SQUIDs are almost exclusively fabricated from epitaxial YBCO films with their c axis normal to the substrate ("c-axis films"). The reason for this is mainly that c-axis YBCO films have been shown to have sufficiently strong flux pinning at 77 K to ensure both high critical current densities in the ab plane (several 10^6 Acm^{-2}) and acceptably low levels of $1/f$ noise, and that worldwide efforts resulted in a readily attainable YBCO

film quality higher than that of films of other materials. It should be emphasized that the necessity to use epitaxial films with sufficiently strong flux pinning is even more stringent for SQUID devices operated in the ambient magnetic field of the Earth, which may induce vortices when the film is cooled to below its T_c.

For some structures, for example, ramp-type junctions (see Section 3.3.4), multiturn flux transformers, integrated Ketchen-type or multiloop magnetometers (see Chapter 5) one requires two or more superconducting layers separated by an insulating or metallic layer. To achieve high crystalline quality of all layers, heteroepitaxial growth is required which means that the various films must have comparable lattice constants and thermal expansion coefficients, and that they must be chemically compatible at the relatively high deposition temperature, typically 700–800 °C. Furthermore, it is essential that the films can be deposited with sufficiently smooth surfaces to allow subsequent layers to grow with high structural and electrical integrity and without electrical shorts between them. Consequently, the material used for the insulating layer is generally one of the substrate materials listed in Section 3.3.2. As an alternative to the various insulating materials, semiconducting, but sufficiently resistive $PrBa_2Cu_3O_{7-x}$ (PBCO) has been used for the fabrication of YBCO trilayer structures [80].

3.3.2 Thin-film Deposition

Thin films of YBCO for SQUIDs are most typically deposited on commercial $SrTiO_3$ (STO) substrates with (100) orientation and an epitaxial-quality polished surface. Other substrates used for SQUID fabrication are MgO, $LaAlO_3$ (LAO), $NdGaO_3$, and yttria-stabilized zirconia (YSZ). In most cases, substrates have a standard size of 10 mm × 10 mm and a thickness of 0.5 to 1.0 mm. The only disadvantage of STO is its high dielectric constant ($\varepsilon_r \approx 1900$ at 77 K), leading to potentially high parasitic capacitances and resonances that have to be taken into account in the SQUID design. Furthermore, the high dielectric losses of STO prevent its use as substrate for planar superconducting resonator tank circuits in rf SQUIDs. For such rf tank circuits, LAO has mostly been used. However, LAO twinning when cooling from the deposition temperature to below the transformation point of about 500 °C causes uncontrollable displacement of patterned features, which can be a problem for fine multilayered structures where lower and upper layers need to remain well aligned. SQUIDs were also fabricated from YBCO films grown on Si [81], but crack-free films with reasonable superconducting properties could only be obtained for thicknesses up to about 50 nm. Kinetic inductances of such thin patterned structures are undesirably large. Generally, all of these commercial substrates are of adequate quality so that only standard cleaning methods are required, involving ultrasonic rinsing, e.g., in acetone and isopropanol, and blow-off with dry nitrogen. For a more comprehensive discussion of suitable substrates see [82–85].

Among the many different techniques used to deposit YBCO, pulsed laser deposition (PLD) and sputtering are most commonly applied to SQUID fabrication; in a few cases coevaporation was successfully used. For comprehensive reviews of HTS

deposition techniques and growth-related problems see [83–87]. For the fabrication of SQUID devices only *in situ* processes are used, i.e., the material crystallizes on the substrate surface as it is deposited. At the high temperatures that are necessary to ensure a high crystallographic perfection of the YBCO film, an oxygen depleted, tetragonal phase is formed. Thus, to obtain the metallic orthorhombic phase, the YBCO is loaded with oxygen at lower temperatures after growth. Generally, it is sufficient to vent the deposition chamber with (0.5–1) $\times$ 10^5 Pa (0.5–1 bar) O_2 and to cool the sample from the deposition temperature to room temperature in about 30 min. For multilayer structures with extremely dense insulating layers in between the YBCO films it may be necessary to modify the annealing procedure to allow the lower YBCO layer to be re-oxygenated (see Section 3.3.6).

PLD was the first technique to produce *in situ* YBCO films with high transition temperatures [88–91], and is well suited to the deposition of insulators such as STO, MgO, YSZ, and normal metals such as Ag. Usually, the substrate surface is parallel to the rotating target and YBCO deposition rates well above 10 nm/min can be achieved. Targets are usually not more than 25 mm in diameter and are therefore relatively inexpensive. With the aid of a carousel with typically six targets, one can easily fabricate multilayer structures *in situ*. One disadvantage is that only a relatively small substrate area is covered uniformly, typically 10–20 mm. At the early stage, PLD YBCO films exhibited numerous particulates at the surface, which was argued to be a problem especially for multilayer structures. However, this could be solved primarily by the use of high-density targets and by carefully cleaning the heater/substrate holder prior to the next deposition.

Conventional sputtering techniques have the major disadvantage that the oxygen necessary for the *in situ* deposition of YBCO causes negative oxygen ions to bombard the substrate. This results in preferential re-sputtering of Ba and deviations from the correct stoichiometry [92–94]. This problem can be ameliorated either by using off-axis sputtering [93,95] in which the substrate is placed to one side of and perpendicular to the sputtering gun, or by using high gas pressures [96] at which the negatively-charged oxygen ions are thermalized. The disadvantage of both solutions, however, is that the deposition rates are low, typically a few tens of nanometers per hour. Important alternative sputtering techniques are the inverted cylindrical magnetron [94,97] and linear hollow cathode discharge sputtering [98,99]. Both configurations are off-axis, with the ionization and deposition rate enhanced by means of a magnetic field and the hollow cathode effect, respectively. Alternatively, a magnetron sputtering source can be used in the on-axis configuration without re-sputtering effects if it is operated unbalanced [100]. A disadvantage of sputtering multilayer structures is the need for separate sources for each material, requiring large and expensive vacuum chambers, and the high cost of targets that are usually much bigger than for laser deposition.

All of the deposition techniques mentioned above can produce – after thoroughly optimizing the deposition process – smooth YBCO films with excellent electrical properties. Typical YBCO films, 150–200 nm thick, grown on lattice-matched substrates such as STO have transition temperatures T_c = 88–91 K and critical current densities at 77 K of (2–5) $\times$ 10^6 A/cm^2. The surface roughness, usually determined

by atomic force microscopy, is below 10 nm and the half-width of the X-ray rocking curve is typically 0.1–0.3°, depending on the lattice mismatch between YBCO and substrate. It should be emphasized that there is no general recipe for the fabrication of YBCO thin films with excellent superconducting and structural properties. The optimum deposition parameters vary from deposition system to deposition system and are strongly dependent on the YBCO target properties including its history. Considering, for example, PLD, there is a variety of deposition parameters which influence the film properties: substrate temperature, oxygen partial pressure, gas flow rate, target-substrate distance, laser intensity on the target, size of the laser spot on the target, repetition rate etc. To optimize such a complex system with numerous input parameters, the design-of-experiment method, which is standard in semiconductor technology, has been successfully applied [101,102]. This statistical instrument provides a maximum of information for a minimum number of trials and can give insight into the physics of the process.

To deposit Ag or Au layers for contact pads or shunt resistors, one can use thermal evaporation, electron-beam evaporation, sputtering, or ion-beam assisted deposition, usually with the substrate at room temperature. Especially when using thermal evaporation one should take into account that any heating of the sample in vacuum can lead to oxygen loss and thus to a degradation of the superconducting properties (see next section). To achieve a low metal/YBCO contact resistance ($< 10^{-6}\ \Omega\text{cm}^2$) one should deposit the metal either *in situ* or after only a brief exposure to air. If the YBCO film is stored in air for any length of time or exposed to photoresist, either low-energy Ar ion beam cleaning of the surface, or sputter cleaning and/or post-annealing at 400–500 °C in oxygen or oxygen plasma is necessary to achieve a sufficiently low contact resistance.

3.3.3 Patterning Techniques

Patterning techniques that are well established in semiconductor and LTS technology are not necessarily applicable to YBCO thin films. One immediate problem is that contact of YBCO with water or water-soluble chemicals deteriorates the superconducting properties of the YBCO. Second, the use of dry-etching methods in vacuum such as Ar ion beam etching can lead to a significant heating of the sample and thus to oxygen loss at the patterned edges. Third, as a consequence of the complex, anisotropic crystal structure of YBCO, smooth patterned edges with well-defined slope are required as a prerequisite for the epitaxial growth of subsequent layers. Given these limitations, however, a number of techniques have been successfully used to pattern YBCO films down to sub-micrometer dimensions without degrading their properties. Braginski [84] and Wellstood *et al.* [85] have reviewed these techniques.

Conventional photomasking followed by dry etching is the most widely used technique for patterning SQUID devices based on YBCO films or multilayers. For the photolithography, one generally uses conventional photoresists, for example, Hoechst AZ 5214E or Shipley 1400-31. However, special masks are sometimes used,

especially for step-edge and ramp-type junctions (Section 3.3.4) and for patterning submicrometer structures. To obtain the edge definition essential for step-edge junctions, one often uses metal, for example Nb [103], or diamond-like carbon (DLC) masks grown by plasma-enhanced chemical vapor deposition [104].

Among dry-etching methods, an Ar-ion beam, bombarding the sample surface at an angle between 90° (normal incidence) and 0°, is the most widely used to pattern YBCO thin films and multilayers. To minimize damage of the YBCO, one restricts the beam energies to between 350 and 500 eV, the latter being the most common value, and the beam current density to below 1 mA/cm^2. To reduce heating of the sample, which can lead to significant oxygen loss from the film, it is also important to cool the sample stage, either with water or, especially for submicrometer dimensions, with liquid nitrogen. As demonstrated by Alff *et al.* [105] and Schneidewind *et al.* [106], high-quality c-axis YBCO films are damaged near edges over a distance from the edge of much less than 1 μm, provided the sample is water-cooled and the beam energy and current density do not exceed the values given above. In order to minimize the heat damage it is also recommended to use filament-free plasma sources (e.g., rf sources) and plasma bridge neutralizers rather than conventional Kaufman sources and tungsten wire neutralizers. Although microbridges in YBCO films with widths down to a few 100 nm were fabricated without significantly deteriorating the superconducting properties, linewidths below 1 μm were rarely used in SQUID structures. Typically HTS junctions are the narrowest structures of a SQUID layout, with linewidths between 1 and 5 μm, depending on the critical current density of the particular junction and the SQUID design parameters.

An alternative dry etch which has been successfully utilized by a few groups is an Ar plasma [107]. In contrast to an Ar ion beam, the ions are multi-directional; nonetheless, as for ion-beam etching with a rotating sample, the edge profiles of the etched films are determined by the shape and angle of the mask edges and the ratio of mask and film etching rates. In contrast to LTS, reactive ion etching (RIE) cannot be used for HTS materials due to the nonvolatility of Ba and (to a lesser extent) Y or another rare-earth compound such as a chloride or a fluoride.

Both Ar ion beam and plasma etching have the disadvantage of being non-selective. To detect the end-point of an etching process, secondary-ion mass spectroscopy (SIMS) of the ion-sputtered species [108], the observation of the material-dependent plasma color near the sample surface [109] and optical reflectivity measurements of the etched surface [110] have all been successfully used. If none of these methods is available, one relies on the knowledge of etching rates and film thicknesses to control the etching depth by the etching time.

Especially in the early days of HTS SQUID development, wet etching in combination with standard photolithography was widely used to pattern the individual layers since it is relatively simple and fast (etching rates are typically of the order of 100 nm/min). Wet etching has the advantages of being selective, as long as the proper etchant is used, and the sample is not exposed to heat. A comprehensive overview of wet-etching recipes is given in [84]. To etch YBCO, water-diluted HNO_3, H_3PO_4 or EDTA can be used. As a consequence of the typically isotropic etching rate, undercutting restricts the linewidth to a few μm. If exposure of YBCO to water

has to be avoided, e.g., for etch cleaning of the surface, a solution of Br in ethanol can be used. The latter etchant has been also successfully used for the fabrication of quasi-planar ramp-type junctions [111] (see also Section 3.3.4). Wet etching is suitable only for not-too-small linewidths, and the shape of the patterned edges depends crucially on the perfection of the YBCO film. A selective etchant for STO is water-diluted HF. An Au etchant, suitable for patterning metallization overlayers and not attacking YBCO, is the water-diluted mixture of potassium iodide and iodine [112].

There is a variety of alternative patterning techniques that have been developed and used for fabricating YBCO SQUID devices, including the use of shadow masks [113,114], high-temperature lift-off [115], inhibit patterning [116] and focused laser beam writing [117,118]. However, none of these reached the status of a "standard" patterning method for YBCO SQUID devices. Many of these techniques are restricted to single-layer structures or they are not suited for patterning structures with dimensions below 10 μm, and methods like ion implantation and laser-writing are unlikely to be suitable for mass production.

3.3.4
Junction Fabrication

The general requirements for a successful HTS junction technology for making SQUIDs are basically the same as for LTS devices: nonhysteretic RSJ-like *I–V* characteristics, high I_0R_n products, controllable and reproducible junction parameters (I_0, R_n, C), high stability under room temperature storage and thermal cycling, and low $1/f$ noise. Unfortunately, as a result of the short coherence length ($\xi_c \approx 0.2$ nm, $\xi_{ab} \approx 2$ nm), a trilayer "sandwich" junction technology, analogous to that described in Section 3.2, does not exist. Of the many types of internally shunted HTS junctions that have been investigated over the past decade, only a few are suited for use in SQUIDs. A comprehensive overview of fabrication issues for these junctions can be found in [119,120]. The four standard HTS junction types that are used to fabricate SQUIDs are schematically depicted in Figure 3.3.

The bicrystal grain boundary junction (GBJ) (Figure 3.3(a)) is basically a patterned microbridge crossing the grain boundary of a bicrystal substrate. Due to the epitaxial growth of YBCO on a lattice-matched substrate such as (100) STO, the a and b axes of the YBCO film are aligned along the a and b axes of the substrate. Consequently, using a bicrystal substrate (the most frequently used is the [001] tilt grain boundary), a grain boundary forms in the YBCO film. As a consequence of the complicated growth mechanisms, the YBCO grain boundary only generally follows the straight path defined by the grain boundary of the substrate and meanders around it. The faceting of the YBCO grain boundary is responsible for the experimentally observed spread of junction parameters I_0 and R_n (20–30% in the best cases), and generally the spread increases with decreasing junction width due to averaging for wider junctions. The degree of meandering depends on the deposition conditions (PLD YBCO films are generally stronger faceted than sputtered ones) [121]. Until now, bicrystal junctions have been most widely used by experimenters as well as commercial vendors to make low-noise HTS SQUIDs. The reasons are the simplicity of fabrication

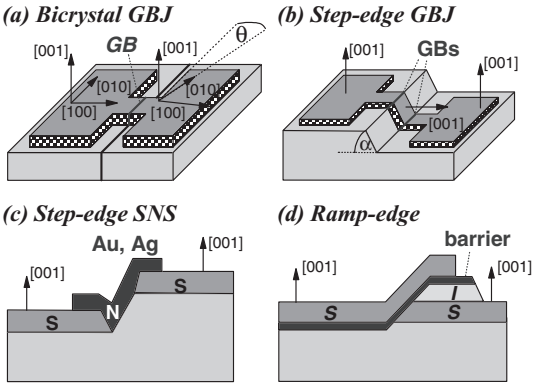

Fig. 3.3 Schematic drawing of four standard types of HTS Josephson junctions used in SQUIDs.

– a single deposition and patterning step –, the RSJ-like I–V characteristics, the comparably high I_0R_n values (typically 150–250 μV at 77 K) with a reasonable spread of their I_0 and R_n values, and the high yield of such junctions.

Commercially available are bicrystal substrates with misorientation angles of 24°, 30° or 36.8° in any material that is used to deposit *in situ* YBCO films; the most widely used material is again STO. As a good compromise between high I_0R_n values and not too high critical current densities, 30° bicrystal substrates are being increasingly used. A disadvantage of bicrystal junctions is – besides the high price of bicrystal substrates – that the grain boundary extends across the whole substrate and imposes a limitation on the SQUID layout design. If other parts of the superconducting layout intersect the substrate bicrystal line, additional $1/f$ flux noise is likely to be generated in the film grain boundaries.

Inspired by bicrystal junctions, Char *et al.* [122] developed for first commercial SQUIDs the so-called biepitaxial junctions which are, in contrast to bicrystal GBJs, free of topological limitations. The fabrication process is basically simple: an extremely thin epitaxial film with its major crystal axes rotated against those of the underlying substrate is deposited on part of the substrate, thus forming a grain boundary. The main disadvantage is that so far only processes yielding 45° grain boundaries exist, which are known to result in GBJs with low j_c and I_0R_n values. As a consequence, SQUIDs with sub-optimum junction and noise properties were obtained, eventually banishing biepitaxial GBJs from device fabrication. Only recently, Tafuri *et al.* [123] proposed an improved concept of biepitaxial junctions which, however, has not been widely tested.

Another quite frequently used type of a GBJ is the so-called step-edge junction (Figure 3.3(b)). It is based on the fact that an epitaxially grown c-axis YBCO film changes its orientation at a steep step in the substrate. As for biepitaxial junctions, step-edge GBJs do not suffer from topological limitations, except that the step edge should be aligned along the major cubic axes of the substrate. Another advantage over bicrystal GBJs is that the substrate costs are much lower. However, the addi-

tional fabrication step to define the step edge in the substrate is more expensive in terms of labor investment. The understanding of the step-edge GBJs is mainly based on the high-resolution transmission electron microscopy (HRTEM) work by Jia *et al.* [124]. The detailed microstructural investigations of YBCO films grown on steep steps (> 45°) in lattice-matched cubic single-crystal substrates, like STO and LAO, show that two nearly identical 90° tilt grain boundaries occur in the YBCO. If the step is steep enough (≥ 70°), the microstructure at the upper and lower is dissimilar, the lower exhibiting a much smaller j_c than the upper one. Consequently, for SQUID device fabrication, very steep steps are required so that only the lower grain boundary is active. Careful process optimization by numerous groups indicated that the step height h should exceed the film thickness d for optimum junction properties: $h/d = 2/3$ to 1 for PLD-grown YBCO films and about 1/2 for sputtered ones.

There is much evidence that 90° grain boundaries in planar YBCO thin films do not act as weak links. Therefore, the weak-link behavior observed for step-edge junctions is presumably a consequence of the high defect density at the grain boundary which in turn is extremely sensitive to fabrication process variations. Although I_0R_n products comparable to those of bicrystal junctions, i.e., approximately 100 μV at 77 K, were obtained for step-edge junctions, the critical parameters j_c and ρ_n are less well defined as a result of variations in the defect density at the grain boundary. The most crucial process step is the fabrication of the step edge (see Section 3.3.3).

A third type of HTS junction that is used for SQUID fabrication is the step-edge SNS junction (Figure 3.3(c)) which combines the topological freedom with excellent long-term stability and reasonable spreads in I_0 and R_n. The fabrication of such SNS step-edge junctions, originally introduced by DiIorio *et al.* [125], is more complicated than the step-edge GBJ process: One cuts a steep step into a substrate and deposits a YBCO film directionally so that the film does not grow over the step. Without breaking the vacuum in the deposition chamber, i.e., *in situ*, one fills the gap by directional deposition of an Au or Ag layer which makes contact to the a-b plane of the YBCO films. Although I_0R_n products of up to 1 mV at 77 K and R_n above 10 Ω were achieved by certain process refinements [126], the typical parameters are less optimum than those of bicrystal junctions. The major problem is the lack of control of the properties of the resistive interfaces between YBCO and the noble metal. These interfaces are responsible for the fact that the junctions are SINIS rather than SNS junctions and appear to dominate the normal resistance R_n. This has hindered the widespread application of this junction technology.

Edge- or ramp-type junctions (Figure 3.3(d)) represent the fourth type of HTS junctions that are used in SQUIDs. Similar to SNS step-edge junctions, excellent long-term stability, large freedom of positioning and acceptable I_0 and R_n spreads are claimed for these junctions. The price for these benefits is a complicated fabrication process. Unlike the other HTS junctions mentioned above, ramp-type junctions require the fabrication of an epitaxial trilayer with two superconducting electrodes separated by a thin insulating or resistive layer. As for the SNS step-edge junctions, the current transport is along the ab planes. Generally, resistive PBCO is used for the barrier material although other barrier materials, such as STO, $NdGaO_3$, Ca- or Co-doped YBCO and Ga-doped PBCO, have been tested as well. In practice, one

starts with the deposition of a bilayer YBCO/PBCO. Next, a ramp with a shallow angle (typically 10–20° to prevent the formation of any grain boundaries in the top electrode) is patterned. This patterning can be done combining conventional photolithography with ion beam etching or wet etching (e.g., Br in ethanol [111]). A principal advantage of such quasi-planar ramp-type junctions over planar GBJs is that the top electrode effectively shields the magnetic field component normal to the film surface. As for the SNS step-edge junctions, the interfaces between YBCO and barrier determine the junction characteristics and parameters. Special care has to be taken in the patterning of the ramp. Argon ion beam etching can damage the surface or the ramp, either destroying the crystallographic structure or leading to oxygen depletion; wet etching in bromine solution requires extremely smooth films, otherwise very inhomogeneous surfaces can result [127]. In spite of all these difficulties SQUIDs with ramp junctions are commercially available [128] and, with further improvements, are likely to represent the future of HTS SQUID technology .

There are other types of HTS junctions, like interface-engineered edge junctions and c-axis microbridges, but their parameters do not fulfill the requirements for making low-noise SQUIDs.

3.3.5 Fabrication of Single-layer Devices

Due to the simplicity of the fabrication process and consequently the relatively high yield of properly functioning devices, in recent years most practical HTS SQUID devices were fabricated from single YBCO layers. Examples of complete SQUID devices that can be patterned from a single YBCO film are large washer and direct-coupled SQUID magnetometers (see Chapter 5). Direct-coupled SQUID magnetometers are mostly fabricated using bicrystal junctions, although devices based on grain boundary step-edge and SNS step-edge junctions were also reported. Fabrication yields are to a large extent determined by the YBCO film quality and the spread of junction parameters. If the junction parameters are not optimum, for GB junctions they can be adjusted by a proper annealing or trimming process. For a carefully optimized deposition and patterning process, yields of "good" devices of 50 % or more are not uncommon.

Sometimes complete devices are built by mounting and pressing two single-layer devices together in a flip-chip configuration, with a very thin insulation layer (e.g., Mylar foil) in between. These two devices can be a SQUID washer or a direct-coupled SQUID magnetometer on the one side and a single-layer flux transformer or a flux concentrator on the other.

To fabricate a single-layer SQUID device on a bicrystal substrate, one has to be able to see the grain boundary at the substrate edges to exactly align the mask with respect to the substrate grain boundary. For STO, this is usually done by etching the substrate for a few seconds in diluted HF: a trench clearly visible under an optical microscope forms owing to the higher etching rate at the grain boundary.

3.3.6
Fabrication of Multilayer Devices

Most sensitive SQUID devices including spiral input coils inductively coupled to a washer SQUID or multiloop structures (see Chapter 5) as well as ramp-type junctions require fabrication of multilayer structures. In the simplest case such a multilayer structure consists of a YBCO/insulator/YBCO trilayer. Although additional layers might be advantageous, e.g., to incorporate a superconducting ground plane, almost all HTS multilayer development work has been restricted to such trilayers. The reason for this is that with an increasing number of layers it becomes more and more difficult to maintain high crystalline quality of all YBCO layers as is required for low levels of $1/f$ noise and to preserve the integrity of the thin insulating layers between the YBCO films. Thus, we will only address issues related to the fabrication of trilayer structures. As stated in Section 3.3.2, the insulator is generally one of the substrate materials, especially STO, or PBCO.

In an actual multilayer device, each layer has to be patterned separately, usually with photolithographic processing, which greatly complicates matters. Furthermore, devices with spiral input coils or multiloops all contain crossover structures where a line in the upper YBCO film crosses one patterned in the lower one, both electrically insulated against each other, and vias permitting one to make contact between the upper and lower YBCO films through the insulating layer. As an example, Figure 3.4 depicts the input coil region of a multiturn flux transformer. The crucial requirement is that the upper films have to grow over the patterned edges of the lower layers with high crystalline perfection. Another key issue is that the surface of the lower YBCO film has to be protected since the photoresist attacks it, thus degrading the growth of the subsequent layers. A third important issue related to the integrity of the insulating layer is the oxygen content in the lower YBCO film. In a multilayer process, the subsequent high-temperature deposition of an epitaxial insulating layer, typically 150–300 nm thick, leads to a loss of oxygen in the lower YBCO film. The better the crystalline perfection and thus the integrity of the insulating layer, the more it inhibits the necessary oxygen diffusion into the lower YBCO film, resulting in a reduced transition temperature. To re-oxygenate the lower YBCO film fully, one

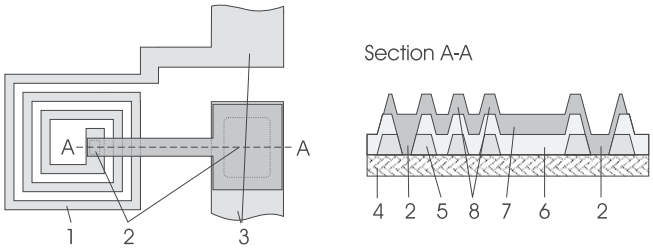

Fig. 3.4 Simplified planar view and cross-section of input coil region of multiturn flux transformer. The planar view shows the A-A cross-section position. 1 – input coil; 2 – vias; 3 – pickup loop; 4 – substrate; 5 – lower epitaxial YBCO film; 6 – epitaxial insulation layer; 7 – upper epitaxial YBCO film; 8 – crossovers.

has either to considerably increase the annealing time or perform the annealing in an oxygen plasma rather than in molecular oxygen [127,129,130].

Taking into account the issues evoked above, the following process, schematically depicted in Figure 3.5, has been successfully used to fabricate multilayer SQUID devices with white magnetic field noise levels slightly below 10 fTHz$^{-1/2}$ and $1/f$ corner frequencies around 1 Hz. After the deposition of a typically 150 nm thick, very smooth YBCO film, a 10–30 nm thin epitaxial insulating layer is deposited *in situ,* i.e., without breaking the vacuum, on the YBCO layer to protect it during the *ex situ* patterning. The patterning of the "capped" YBCO film as well as of the subsequently deposited layers is done using conventional photolithography and Ar ion beam etching. To obtain gently sloped edges of the lower layers (as stated in Section 3.3.4, to prevent nucleation of grain boundaries in the subsequent epitaxially deposited layers, the angle should not exceed 30°), one usually bakes the resist after development, at a temperature which causes it to flow at the edges (130–150 °C depending on the resist). The subsequent Ar ion-beam etching is performed with substrate holder rotation and at an ion-beam incident angle of 45–60°, the latter to prevent accumulation of milling debris at edges. With this process, one obtains beveled edges with ramp angles below 20° in all directions in the plane. After the deposition

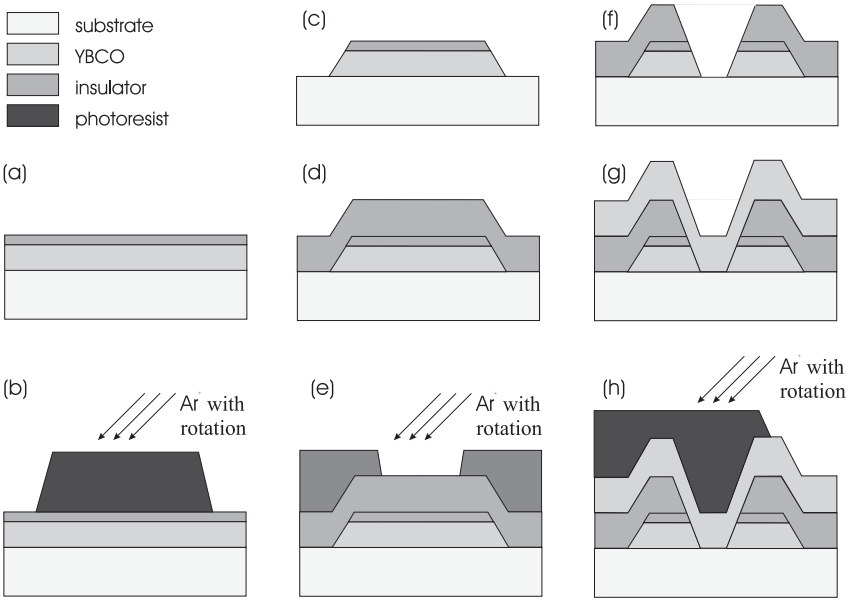

Fig. 3.5 Cross-sectional view of the fabrication step sequence for a HTS multilayer SQUID device (fabrication of contact pads not shown). (a) Deposition of YBCO film with a thin cap layer, (b) patterning of the YBCO/insulator bilayer using photolithography and Ar ion-beam etching, (c) the patterned bilayer after removing the photomask, (d) deposition of the insulating layer, (e) patterning vias using photolithography and Ar ion-beam etching, (f) a patterned via after removing the photomask, (g) deposition of the top YBCO film, (h) patterning of the upper YBCO film using photolithography and Ar ion-beam etching.

of the insulating layer and the subsequent annealing step(s), vias are opened, again using photolithography with resist postbaking and ion-beam etching. Since the lower and upper YBCO films make contact in the ab plane, one generally etches all the way through the lower YBCO film so that the upper YBCO film in the via area is deposited on ion-beam-etched substrate rather than etched YBCO. The last step is the deposition and patterning of a typically 200–300 nm thick upper YBCO film. For integrated and multiloop magnetometers the upper YBCO film deposition is followed by a Ag or Au metallization and patterning of contact pads.

The simplified description of the fabrication process of multilayer HTS SQUID devices omits many details and alternate methods which are reviewed in [84,119,127]. The processing of HTS multilayer structures is much more complicated than that of HTS single-layer devices. Due to the complicated fabrication process, the comparably low yield and the fact that – in contrast to LTS devices where 3″ or 4″ wafers are processed so that quite a number of devices can be fabricated simultaneously – only one device can be processed at a time, the fabrication of multilayer devices has been almost exclusively limited to demonstrations of feasibility by the very few laboratories capable of this technology, and to one commercial source [128] which has been offering multilayer magnetometers and gradiometers for about five years[2)]. In any case, with continuing progress in processing, the highest sensitivity SQUIDs will eventually be fabricated in multilayer technology.

3.3.7
Device Passivation and Encapsulation

One of the problems that restricts the application of HTS SQUID devices is that the superconducting properties of YBCO films deteriorate when in contact with water. There are two general ways to protect the device from moisture: one can either cover the device with a passivation/protection layer or encapsulate the device hermetically. As passivation layers, amorphous or insulating YBCO, deposited at room temperature, STO, either amorphous or crystalline, Teflon or polyamide have been used. Alternatively, the devices are sealed in a housing made, e.g., from alumina or reinforced fiberglass. The advantage of the latter approach is that other sensor components, like a heater, feedback or compensation coils can be integrated in the housing. In spite of numerous promising approaches, no standard protection method insuring long-term stability of HTS devices is presently known.

3.4
Future Trends

Fabrication of planar, thin-film low-temperature SQUIDs using the Nb/Al-AlO_x/Nb processes is already a mature technology, in which only incremental progress can be expected, aimed mostly at optimizing yields and reducing the manufacturing costs.

2) SQUID structures fabricated at the Research Center Jülich (FZJ), Germany.

An example is a possible wider introduction of less expensive lift-off processing, which can partially replace dry etching. The future of the technology is linked to the demand for most sensitive SQUID sensors and amplifiers. The former find use, for example, in some biomagnetic research and diagnostic applications, the latter are irreplaceable in scientific instrumentation and as detector readout devices.

It is possible that the demand for mechanically cryocooled LTS instruments (see Chapter 7) will provide a sufficient incentive for perfecting and using the NbN junction and circuit technology capable of providing devices operating at about 10 K. In this case, it is likely that the MgO barriers will eventually be replaced by insulating nitride barriers, and that some form of heteroepitaxial, reactive *in situ* film deposition process will be introduced to minimize the NbN λ_L/ξ ratio and reduce junction parameter spreads.

Despite the enormous progress that has been made over the last decade in terms of device performance, the numerous practical applications of HTS SQUIDs and the availability of a few commercial products, there are still a number of problems that need to be solved to turn HTS fabrication into a mature technology. This requires the development of a reproducible and reliable junction technology that combines topological freedom, long-term stability, high I_0R_n products, high R_n, and adjustable I_0s. Further improvements in the quality of YBCO thin films and patterned structures, especially in flux-pinning capability are needed, since there will be a market for HTS SQUID systems only if they can be operated in magnetically unshielded or moderately shielded environments. The noise level at 1 Hz of about 30 to 50 $fTHz^{-1/2}$, which is attainable in simple single-layer and flip-chip structures is sufficient for most anticipated HTS SQUID applications. However, to reduce that level to 10 $fTHz^{-1/2}$ or less, which might be advantageous for biomagnetic applications such as magnetocardiography, one will need multilayer devices. Here, it seems to be essential to develop a reproducible process that will allow one to fabricate many devices in a wafer batch process, not just one device per week. Also, as long as there is no junction technology ensuring high I_0R_n products, with a much lower spread of junction parameters, the best philosophy is probably to fabricate relatively large numbers of separate washer SQUIDs and multilayered input circuits, in order to select those meeting specifications for coupling in the flip-chip configuration. Last but not least, a reliable housing/protection technology is urgently needed to improve the long-term stability of the devices.

References

1 Roberts, B. W. (1976) Survey of superconductive materials and critical evaluation of selected properties, *J. Phys. Chem. Ref. Data* **5**, 581–821.

2 Murakami, M. (1978) Thermal strain in lead thin films II: Strain relaxation, *Thin Solid Films* **55**, 101–111.

3 Huang, H.-C. W., Basavaiah, S., Kircher, C. J., Harris, E. P., Murakami, M., Klepner, S. P., and Greiner, J. H. (1980) High-reliability Pb-alloy Josephson junctions for integrated circuits, *IEEE Trans. Electron Dev.* **ED-27**, 1979–1987.

4 Savo, B., Wellstood, F. C., and Clarke, J. (1987) Low-frequency excess noise in Nb-Al_2O_3-Nb Josephson tunnel junctions, *Appl. Phys. Lett.* **50**, 1757–1759.

5 Simmons, J. G. (1963) Generalized formula for the electric tunnel effect between similar electrodes separated by a thin insulating layer, *J. Appl. Phys.* **34**, 1793–1803.

6 Coon, D. D., and. Fiske, M. D. (1965) Josephson ac and step structure in the supercurrent tunneling characteristics, *Phys. Rev.* **138**, A744–A746.

7 Broom, R. F., Laibowitz, R. B., Mohr, T. O., and Walter, W. (1980) Fabrication and properties of Nb Josephson tunnel junctions, *IBM J. Res. Dev.* **24**, 212–222.

8 Broom, R. F., Raider, S. I., Oosenbrug, A., Drake, R. E., and Walter, W. (1980) Niobium oxide-barrier tunnel junctions, *IEEE Trans. Electron. Dev.* **ED-27**, 1998–2008.

9 Latta, E. E., and Gasser, M. (1983) Barrier composition and electrical properties of high-quality all-niobium Josephson tunnel junctions, *J. Appl. Phys.* **54**, 1115–1119.

10 Sandstrom, R. L., Kleinsasser, A. W., Gallagher, W. J., and Raider, S. I. (1987) Josephson integrated circuit process for scientific applications, *IEEE Trans. Magn.* **MAG23**, 1484–1488.

11 Paulson, D, formerly SHE and BTI, private information (unpublished).

12 Rowell, J. M., Gurvitch, M., and Geerk, J. (1981) Modification of tunneling barriers on Nb by a few monolayers of Al, *Phys. Rev. B* **24**, 2278–2281.

13 Gurvitch, M., Rowell, J. M., Huggins, H. A., Washington, A. M., and Fulton, T. A. (1981) Nb Josephson tunnel junctions with thin layers of Al near the barrier, in *Proceedings of the 1981 International Electron Devices Meeting* **IEDM-81**, New York: IEEE, 115–117.

14 Gurvitch, M., Washington, M. A., Huggins, H. A., and Rowell, J. M. (1983) Preparation and properties of Nb Josephson junctions with thin Al layers, *IEEE Trans. Magn.* **MAG-19**, 791–794.

15 Gurvitch, M., Washington, M. A., and Huggins, H. A. (1983) High quality refractory Josephson tunnel junctions utilizing thin aluminum layers, *Appl. Phys. Lett.* **42**, 472–474.

16 Laibowitz, R. B., and Mayadas, A. F. (1972) Josephson junctions with Nb/Al composite electrodes, *Appl. Phys. Lett.* **20**, 254–256.

17 Kwo, J., Wertheim, G., Gurvitch, K. M., and Buchanan, D. N. E. (1982) X-ray photoemission spectroscopy study of surface oxidation of Nb/Al overlayer structures, *Appl. Phys. Lett.* **40**, 675–677.

18 Wolf, E. L., Zasadzinski, J., Osmun, J. W., and Arnold, G. B. (1980) Proximity Electron Tunneling Spectroscopy I: Experiments on Nb, *J. Low Temp. Phys.* **40**, 19–50.

19 Huggins, H. A., and Gurvitch, M. (1985) Preparation and characteristics of Nb/Al-oxide-Nb tunnel junctions, *J. Appl. Phys.* **57**, 2103–2109.

20 Morohashi, S., Shinoki, F., Shoji, A., Aoyagi, M., and Hayakawa, H. (1985) High quality Nb/Al-AlO_x/Nb Josephson junction, *Appl. Phys. Lett.* **46**, 1179–1181.

21 Morohashi, S., and Hasuo, S. (1987) Experimental investigations and analysis for high-quality Nb/Al-AlO_x/Nb Josephson junctions, *J. Appl. Phys.* **61**, 4835–4849.

22 Tanabe, K., Asano, K. H., and Michikami, O. (1986) Ellipsometric study of Nb-Al-AlO_x layered structure for all-refractory Josephson junctions, *Jpn. J. Appl. Phys.* **25**, 183–188.

23 Chang, C. C., Gurvitch, M., Hwang, D. M., and Blonder, C. W. (1987) Auger electron spectroscopy, transition electron microscopy, and scanning electron microscopy studies of Nb/Al/Nb Josephson junction structures, *J. Appl. Phys.* **61**, 5089–5097.

24 Blamire, M. G, Somekh, R. E. Barber, Z. H., Morris, G. W., and Evetts, J. E. (1988) Microstructure effects on electronic properties of

$Nb/Al_2O_3/Nb$ tunnel junctions, *J. Appl. Phys.* **64**, 6396–6405.

25 Imamura, T., and. Hasuo, S. (1989) Characterization of Nb/AlO_x-Al/Nb junction structures by anodization spectroscopy, *IEEE Trans. Magn.* **MAG-25**, 1131–1134.

26 Imamura, T., and Hasuo, S. (1989) Analysis of thin AlO_x-Al Barriers in Nb Josephson junctions, in *Extended Abstracts of 1989 International Superconductive Electronics Conference*, Tokyo, 367–370.

27 Kohlstedt, H., Gundlach, K. H., and Schneider, A. (1991) Investigation of the tunnel barrier in Nb-based junctions prepared by sputtering and electron beam evaporation, *IEEE Trans. Magn.* **MAG-27**, 3149–3152.

28 Imamura, T., and Hasuo, S. (1991) Cross-sectional TEM observations of Nb/AlOx-Al/Nb junction structures, *IEEE Trans. Magn.* **MAG-27**, 3172–3175.

29 Hikada, M., Tsuge, H., and Wada, Y. (1987) Thermal stability of Nb/AlOx/Nb Josephson junctions, in *Advances in Cryogenic Engineering Materials*, A. F. Clark and R. P. Reed (Eds.), New York: Plenum Press, 765–772.

30 Maisell, L. I., and Glang, R. (Eds.) (1970) *Thin Film Handbook*, New York: McGraw-Hill.

31 Vossen, J. L., and Kern, W. (Eds.) (1978) *Thin Film Processes*, New York: Academic Press.

32 Bunshah, R. F. (Ed.) (1982) *Deposition Technologies for Films and Coatings: Developments and Applications*, Park Ridge, NJ: Noyes Publications.

33 Seshan, K. (Ed.) (2002) *Handbook of Thin-Film Deposition Processes and Techniques*, Norwich, NY: Noyes Publication.

34 Inoue, A., Nakayama, A., and Okabe, Y. (1988) $Nb/AlO_x/Nb$ Josephson tunnel-junctions using electron-beam evaporation, *Jpn. J. Appl. Phys.* **27**, 1234–1239.

35 Hoko, H., Imamura, T., and Hasuo, S. (1987) Integration of $Nb/AlO_x/Nb$ junctions planarized with bias-sputtered SiO_2 films, in *Advances in Cryogenic Engineering Materials*, A. F. Clark and R. P. Reed, (Eds.), New York: Plenum Press, 773–780.

36 Murakami, M., and Yogi, T. (1985) Strain in evaporated Nb thin films, *J. Appl. Phys.* **57**, 211–215.

37 Raider, S. I. (1985) Josephson tunnel junctions with refractory electrodes, *IEEE Trans. Magn.* **MAG-21**, 110–117.

38 Wu, C. T. (1979) Intrinsic stress of magnetron-sputtered niobium films, *Thin Solid Films* **64**, 103–110.

39 Yuda, M., Kuroda, K., and Nakano, J. (1987) Small Nb/Al-oxide/Nb Josephson junction fabrication using lift-off processes, *Jpn. J. Appl. Phys.* **26**, L166–L168.

40 Kuroda, K., and Yuda, M. (1988) Niobium-stress influence on Nb/Al-oxide/Nb Josephson junctions, *J. Appl. Phys.* **63**, 2352–2357.

41 Imamura, T., and Hasuo, S. (1989) Effects of intrinsic stress on submicrometer Nb/AlO_x/Nb Josephson junctions, *IEEE Trans. Magn.* **MAG-25**, 1119–1122.

42 Booi, P. A. A., Livingston, C. A., and Benz, S. P. (1993) Intrinsic stress in dc sputtered niobium, *IEEE Trans. Appl. Supercond.* **3**, 3029–3031.

43 Sukuda, K., Kawai, J., Uehara, G., and Kado, H. (1993) Relationship of Nb surface morphology and Al coverage to the intrinsic stress of magnetron-sputtered Nb films, *IEEE Trans. Appl. Supercond.* **3**, 2944–2946.

44 Amos, R. S., Breyer, P. E., Huang, H. H., and Lichtenberger, A. W. (1995) Stress and source conditions of DC magnetron sputtered Nb films, *IEEE Trans. Appl. Supercond.* **5**, 2326–2329.

45 Sauvageau, J. E., Burroughs, C. J., Booi, P. A. A., Cromar, M. W., Benz, S. P., and, Koch, J. A (1995) Superconducting integrated circuit fabrication with low temperature ECR-based PECVD SiO_2 dielectric films, *IEEE Trans. Appl. Supercond.* **5**, 2303–2309.

46 Imamura, T., Shiota, T., and Hasuo, S. (1992) Fabrication of high quality Nb/AlOx-Al/Nb Josephson junctions; I-Sputtered Nb films for junction electrodes, *IEEE Trans. Appl. Supercond.* **2**, 1–14.

47 Kerr, A. R., Pan, S. K., Lichtenberger, A. W., and Lea, D. M. (1992) Progress on tunerless SIS mixers for the 200–300 GHz band, *IEEE Microwave and Guided Wave Lett.* **2**, 454–456.

48 Clark IV, W. W., Beatrice, J. M, and Lichtenberger, A. W. (2001) Effects of geometry and hardware on the stress of Nb thin films, *IEEE Trans. Appl. Supercond.* **11**, 3824–3827.

49 DeSorbo, W. (1963) Effect of dissolved gases on some superconducting properties of niobium, *Phys Rev.* **132**, 107–121.

50 Kroger, H., Smith, L. N., and Jillie, D. W. (1981) Selective niobium anodization process

for fabricating Josephson tunnel junctions, *Appl. Phys. Lett.* **39**, 280–282.

51 Smith, L. N., Thaxter, J. B., Jillie, D. W, and Kroger, H. (1982) Sputtered a-silicon tunneling barriers for Nb-Nb Josephson junctions, *IEEE Trans. Magn.* **MAG-18**, 1571–1576.

52 Yu, L. S., Berry, C. J., Drake, R. E., Li, K., Patt, R., Radparvar, M., Whiteley, S. R., and Faris, S. M. (1987) An all-niobium eight level process for small and medium scale applications, *IEEE Trans. Magn.* **MAG-23**, 1476–1479.

53 Shoji, A., Shinoki, F., Kosaka, S., Aoyagi, M., and Hayakawa, H. (1982) New fabrication process for Josephson tunnel junctions with (niobium nitride, niobium) double-layered electrodes, *Appl. Phys. Lett.* **41**, 1097–1099.

54 Morohashi, S., Hasuo, S., and Yamaoka, T. (1986) Self-aligned contact process for Nb/Al-AlO_x/Nb Josephson junctions, *Appl. Phys. Lett.* **48**, 254–256.

55 Barfknecht, A. T, Ruby, R. C., Ko, H., and Lee, G. S. (1993) Josephson junction integrated circuit process with planarized PECVD SiO_2 dielectric, *IEEE Trans. Appl. Supercond.* **3**, 2201–2203.

56 Barfknecht, A. T., Ruby, R. C., and Ko, H. (1991) A simple and robust niobium Josephson junction integrated circuit process, *IEEE Trans. Magn.* **MAG-27**, 3125–3128.

57 Grönberg, L., Seppä, H., Cantor, R., Kivinanta, M., Ryhänen, T., Salmi, J., and Suni, I. (1992) A low noise DC-SQUID based on Nb/Al-AlO_x/Nb Josephson junctions, in *Superconducting Devices and their Applications*, H. Koch and H. Lübbig, (Eds.), Berlin: Springer-Verlag, 281–285.

58 Ketchen, M. B. (1992) Sub-μm linewidth input coils for low T_c integrated thin-film dc superconducting quantum interference devices, *Appl. Phys. Lett.* **61**, 336–338.

59 Meng, X., Bhat, A., and Van Duzer, T. (1999) Very small critical current spreads in Nb/Al-AlOx/Nb integrated circuits using low-temperature and low-stress ECR PECVD silicon oxide films, *IEEE Trans. Appl. Supercond.* **9**, 3208–3211.

60 Pavolotsky, A. B., Weimann, T., Scherer, H., Niemeyer, J., and Zorin, A. (1999) Novel method for fabricating deep submicron Nb/AlO_x/Nb tunnel junctions based on spin-on glass planarization, *IEEE Trans. Appl. Supercond.* **9**, 3251–3254.

61 Daetwyler, K. and Oosenburg, A. (1980) Accurate control of the edge slope of thin films, *IBM Technical Disclosure Bulletin* **23**, 3371.

62 Chen, M. and Wang, R. H. (1983) Plasma etching of niobium with CF_4/O_2 gases, *J. Vac. Sci. Technol.* **A1**, 708–711.

63 Adelerhof, D. J., Bijlsma, M. E., Fransen, P. B. M., Weimann, T., Flokstra, J., and Rogalla, H. (1993) Fabrication of Nb/Al,AlO_x/Al/Nb Josephson tunnel junctions using reactive ion etching in SF_6, *Physica C*, **209**, 477–485.

64 Reible, S. A. (1981) Reactive ion etching in the fabrication of niobium tunnel junctions, *IEEE Trans. Magn.* **MAG-17**, 303–306.

65 Worsham, A. H., Prober, D. E, Kang, J. H., Przybysz, J. X., and Rooks, M. J. (1991) High quality sub-micron Nb trilayer tunnel junctions for a 100 GHz SIS mixer, *IEEE Trans. Magn.* **MAG-27**, 3165–3167.

66 Stern, J. A., LeDuc, H. G., and Judas, A. J. (1992) Fabrication and characterization of high current-density, submicron, NbN/MgO/NbN tunnel junctions, in *Proc. Third Int. Symp. Space Terahertz Tech.*, 420–438.

67 Amin, H., Blamire, M. G., Page, K., and Evetts, J. E. (1991) Fabrication of three terminal devices via a whole-wafer processing route, *IEEE Trans. Magn.* **MAG-27**, 3145–3152.

68 Hu, C. K., Mazzeo, N., Wind, S. J., Pearson, D. J., and Ketchen, M. B. (1991) Reactive ion etching of Nb/AlO_x/Nb for Josephson technology, *Thin Solid Films* **206**, 151–155.

69 Lichtenberger, A. W., Lea, D. M., and Lloyd, F. L. (1993) Investigation of etching techniques for superconductive Nb/Al-Al_2O_3/Nb fabrication process, *IEEE Trans. Appl. Supercond.* **3**, 2191–2196.

70 Aoyagi, M., Maezawa, M., Nakagawa, H., and Kurosawa, I. (1997) Fabrication of submicron Nb/AlO_x/Nb Josephson junctions using ECR plasma etching technique, *IEEE Trans. Appl. Supercond.* **7**, 2644–2648.

71 Numata, H., Nagasawa, S., Koike, M., and Tahara, S. (1995) Fabrication technology for a high-density Josephson LSI using an electron cyclotron etching technique and a bias-sputtering planarization, in *Extended Abstracts of the 1995 International Superconductive Electronics Conference*, 201–203.

72 Shivaraman, M. S., and Svensson, C. M. (1976) Control of palladium adherence to sili-

con dioxide for photolithographic etching, *J. Electrochem. Soc.* **123**, 1258.

73 Bhushan, M., Green, J. B., and Anderson, A. C. (1989) Low-loss lumped element capacitors for integrated circuits, *IEEE Trans. Magn.* **MAG-25**, 1143–1146.

74 Berggren, K. K., Macedo, E. M., Feld, D. A., and Sage, J. P. (1999) Low T_c superconductive circuits fabricated on 150-mm-diameter wafers using a doubly planarized Nb/AlO_x/Nb process, *IEEE Trans. Appl. Supercond.* **9**, 3271–3274.

75 Niemeyer, J. and Hayakawa, H. (2002) Processing and manufacture of Josephson junctions: low T_c, in *Handbook of Superconducting Materials*, edited by David Cardwell and David Ginley (Institute of Physics Publishing, Bristol, UK) p. 833–842.

76 Granata, C., DiRusso, C., Monaco, A., and Russo, M. (2001) Integrated LTc-SQUID magnetometers for multichannel systems, *IEEE Trans. Appl. Supercond.* **11**, 95–98.

77 Koch, R.H., Umbach, C.P., Clark, G.J., Chaudhari, P., Laibowitz, R.B. (1987) Quantum interference devices made from superconducting oxide thin films, *Appl. Phys. Lett.* **51**, 200–202.

78 Zimmerman, J.E., Beall, J.A., Cromar, M.W., Ono, R.H. (1987) Operation of a Y-Ba-Cu-O rf SQUID at 81 K, *Appl. Phys. Lett.* **51**, 617–619.

79 Ferrari, M.J., Johnson, M., Wellstood, F.C., Clarke, J., Rosenthal, P.A., Hammond, R.H., Beasley, M.R. (1988) Magnetic flux noise in thin-film rings of $YBa_2Cu_3O_{7-\delta}$, *Appl. Phys. Lett.* **53**, 695–697.

80 Keene, M.N., Goodyear, S.W., Satchell, J.S., Edwards, J.A., Chew, N.G., Humphreys, R.G. (1993) Thin film HTc SQUIID construction and characterization, *IEEE Trans. Appl. Supercond.* **3**, 2430–2433.

81 Schmidl, F., Linzen, S., Wunderlich, S., Seidel, P. (1998) High-T_c direct current SQUIDs on silicon bicrystal substrates operating at 77 K, *Appl. Phys. Lett.* **72**, 602–604.

82 Scheel, H.J., Berkowski, M., Chabot, B. (1991) Problems in epitaxial growth of high-T_c superconductors, *J. Cryst. Growth* **115**, 19–30.

83 Somekh, R.E., Barber, Z.H. (1992) The deposition of ceramic superconductors, in *Physics and Materials Science of High Temperature Superconductors, II*, edited by R. Kossowsky, B. Raveau, D. Wohlleben and S. K. Patapis (Kluwer Academic Publishers, Dordrecht), p. 443–469.

84 Braginski, A.I. (1993) Thin film structures, in *The New Superconducting Electronics*, NATO ASI series, edited by H. Weinstock and R.W. Ralston (Kluwer Academic Publishers, Dordrecht), p. 89–122.

85 Wellstood, F.C., Kingston, J.J., Clarke, J. (1994) Thin-film multilayer interconnect technology for $YBa_2Cu_3O_{7-x}$, *J. Appl. Phys.* **75**, 683–702.

86 Phillips, J. (1996) High temperature superconducting thin films, *J. Appl. Phys.* **79**, 1829–1848.

87 Phillips, J. (1993) Materials issues affecting the new superconducting electronics, in *The New Superconducting Electronics,* NATO ASI series, edited by H. Weinstock and R.W. Ralston (Kluwer Academic Publishers, Dordrecht), p. 59–88.

88 Roas, B., Schultz, L., Endres, G. (1988) Epitaxial growth of $YBa_2Cu_3O_{7-x}$ thin films by a laser evaporation process, *Appl. Phys. Lett.* **53**, 1557–1559.

89 Koren, G., Polturak, E., Fisher, B., Cohen, D., Kimel, G. (1988) Highly oriented as-deposited superconducting laser ablated thin films of $Y_1Ba_2Cu_3O_{7-\delta}$ on $SrTiO_3$, zirconia, and Si substrates, *Appl. Phys. Lett.* **53**, 2330–2332.

90 Singh, R.K., Narayan, J., Singh, A.K., Krishnaswamy, J. (1988) *In situ* processing of epitaxial Y-Ba-Cu-O high T_c superconducting films on (100) $SrTiO_3$ and (100) YS-ZrO_2 substrates at 500–650 °C, *Appl. Phys. Lett.* **54**, 2271–2273.

91 Venkatesan, T., Wu, X.D., Dutta, B., Inam, A., Hegde, M.S., Hwang, D.M., Chang, C.C., Nazar, L., Wilkens, B. (1989) High-temperature superconductivity in ultrathin films of $Y_1Ba_2Cu_3O_{7-x}$, *Appl. Phys. Lett.* **54**, 581–583.

92 Selinder, T.L., Larsson, G., Helmersson, U., Rudner, S. (1991) Resputtering effects on the stoichiometry of $YBa_2Cu_3O_x$ thin films, *J. Appl. Phys.* **69**, 390–395.

93 Eom, C.B., Sun, J.Z., Larsson, B.M., Streiffer, S.K., Marshall, A.F., Yanamoto, K., Anlage, S.M., Braveman, J.C., Geballe, T.H., Laderman, S.S., Taber, R.C., Jacowitz, R.D. (1990) Synthesis and properties of $YBa_2Cu_3O_7$ thin films grown in situ by 90° off-axis single magnetron sputtering, *Physica C* **171**, 354–382.

94 Geerk, J., Linker, G., Meyer, O. (1989) Epitaxial growth and properties of YBaCuO thin films, *Materials Science Reports* **4**, 195–258.

95 Gavaler, J.R., Talvacchio, J., Braggins, T.T., Forrester, M.G., Greggi, J. (1991) Critical parameters in the single-target sputtering of $YBa_2Cu_3O_7$, *J. Appl. Phys.* **70**, 4383–4391.

96 Poppe, U., Schubert, J., Arons, R.R., Evers, W., Freiburg, C.H., Reichert, W., Schmidt, K., Sybertz, W., Urban, K. (1988) Direct production of crystalline superconducting thin films of $YBa_2Cu_3O_7$ by high-pressure oxygen sputtering, *Solid State Commun.* **66**, 661–665.

97 Xi, X.X., Geerk, J., Linker, G., Li, Q., Meyer, O. (1990) Preparation and superconducting properties of ultrathin $YBa_2Cu_3O_{7-x}$ films, *Appl. Phys. Lett.* **54**, 2367–2369.

98 Koch, H., Friedrich, L.J., Hinkel, V., Ludwig, F., Politt, B., Schurig, T. (1991) Hollow cathode discharge sputtering device for uniform large area thin film deposition, *J. Vac. Sci. Technol.* **A9**, 2374–2377.

99 Schurig, Th., Menkel, S., Quan, Z., Beyer, J., Güttler, B., Knappe, S., Koch, H. (1996) Large-area YBCO thin film deposition using linear hollow cathode discharge sputtering, *Physica C* **262**, 89–97.

100 Savvides N., Katsaros, A. (1993) In-situ growth of epitaxial $YBa_2Cu_3O_7$ thin films by on-axis unbalanced d.c. magnetron sputtering, *Thin Solid Films* **228**, 182–185.

101 Heinsohn, J.-K., Reimer, D., Richter, A., Subke, K.-O., Schilling, M. (1998) Interaction of process parameters in the laser deposition of $YBa_2Cu_3O_7$ films, *Physica C* **299**, 99–112.

102 Eulenburg, A., Romans, E.J., Fan, Y.C., Pegrum, C.M. (1999) Pulsed laser deposition of $YBa_2Cu_3O_{7-x}$ and $NdBa_2Cu_3O_{7-x}$ thin films: a comparative study, *Physica C* **312**, 91–104.

103 Luine, J., Bulman, J., Burch, J., Daly, K., Pettiette-Hall, C., Schwarzbek, S. (1992) Characteristics of high performance $YBa_2Cu_3O_7$ step-edge junctions, *Appl. Phys. Lett.* **61**, 1128–1130.

104 Sun, J.Z., Gallagher, W.J., Callegari, A.C., Foglietti, V., Koch, R.H. (1993) Improved process for high-T_c superconducting step-edge junctions, *Appl. Phys. Lett.* **63**, 1561–1563.

105 Alff, L., Fischer, G.M., Gross, R., Kober, F., Beck, A., Husemann, K.D., Nissel, T., Schmidl, F., Burckhardt, C. (1992) Dry-etching processes for high-temperature superconductors, *Physica C* **200**, 277–286.

106 Schneidewind, H., Schmidl, F., Linzen, S., Seidel, P., (1995) The possibilities and limitations of ion-beam etching of $YBa_2Cu_3O_{7-x}$ thin films and microbridges, *Physica C* **250**, 191–201.

107 Schilling, M. (1999) Heteroepitaxy and noise in integrated HTS dc-SQUID magnetometers, in *Advances in Solid State Physics 38*, edited by B. Kramer (Vieweg & Sohn Verlagsgesellschaft mbH, Braunschweig/Wiesbaden), p. 485–496.

108 Humphreys, R.G., Chew, N.G., Morgan, S.F., Satchell, J.S., Cullis, A.G., Smith, P.W. (1992) End point detection in ion beam milling of $YBa_2Cu_3O_7$ thin films, *Appl. Phys. Lett.* **61**, 228–230.

109 David, B., Grundler, D., Eckart, R., Fanghänel, K., Krumme, J.-P., Doormann, V., Dössel, O., (1994) A multi-layer process for the fabrication of HTSC flux transformers and SQUIDs, *Supercond. Sci. Technol.* **7**, 287–289.

110 Dolata, R., Fischer, M., Jutzi, W. (1992) Optical end point detection of etched YBCO films, *Physica C* **191**, 525–529.

111 Faley, M.I., Poppe, U., Urban, K., Hilgenkamp, H., Hennes, H., Aarnink, W., Flokstra, J., Rogalla, H. (1995) Noise properties of direct current SQUIDs with quasiplanar $YBa_2Cu_3O_7$ Josephson junctions, *Appl. Phys. Lett.* **67**, 2087–2089.

112 Eidelloth W., Sandstrom, R.L. (1991) Wet etching of gold films compatible with high T_c superconducting thin films, *Appl. Phys. Lett.* **59**, 1632–1634.

113 Kingston, J.J., Wellstood, F.C., Lerch, P., Miklich, A.H., Clarke, J. (1990) Multilayer $YBa_2Cu_3O_x$-$SrTiO_3$-$YBa_2Cu_3O_x$ films for insulating crossovers, *Appl. Phys. Lett.* **56**, 189–191.

114 Strikovski, M.D., Kahlmann, F., Schubert, J., Zander, W., Glyantsev, V., Ockenfuß, G., Jia, C.L. (1995) Fabrication of $YBa_2Cu_3O_x$ thin-film flux transformers using a novel microshadow mask technique for *in situ* patterning, *Appl. Phys. Lett.* **66**, 3521–3523.

115 Roas, B. (1991) Patterning of epitaxial $YBa_2Cu_3O_x$ insulator multilayers with a high-temperature-resistant lift-off mask, *Appl. Phys. Lett.* **59**, 2594–2596.

116 Ma., Y.Q., Wong, A., Dosanjh, P., Carolan, J.F., Hardy, W. (1994) A planar method for patterning of high-temperature supercon-

ducting films and multilayers, *Appl. Phys. Lett.* **65**, 240–242; Ma, Y.Q., Hong, S.H., Miller, J.R., Sun, J.Z., Gallagher, W.J., Laibowitz, R.B. (1996) High-T_c SQUIDs fabricated by inhibiting ion implantation, *Supercond. Sci. Technol.* **9**, A92–A95.

117 Shen, Y.Q., Freltoft, T., Vase, P. (1991) Laser writing and rewriting on $YBa_2Cu_3O_7$ films, *Appl. Phys. Lett.* **59**, 1365–1367.

118 Sobolewski, R., Xiong, W., Kula, W. (1993) Patterning of thin-film high-T_c circuits by the laser-writing method, *IEEE Trans Appl. Supercond.* **3**, 2986–2989; Sobolewski, R., Xiong, W., Kula, W., Maung, W.N., Buttler, D.P. (1994) Monolithic Y-Ba-Cu-O electronic devices fabricated using the laser-writing patterning technique, *Supercond. Sci. Technol.* **7**, 300–303.

119 Braginski, A.I. (1996) Fabrication of high-temperature SQUID magnetometers, in *SQUID Sensors: Fundamentals, Fabrication and Applications,* NATO ASI Series, edited by H. Weinstock (Kluwer Academic Publishers, Dordrecht), p. 235–288.

120 Dittmann, R., Braginski, A.I. (2002) Processing and manufacture of Josephson junctions, in *Handbook of Superconducting Materials*, edited by D. Cardwell and D. Ginley (Institute of Physics Publishing, Bristol, UK) p. 843–854.

121 Zhang, X.F., Miller, D.J., Talvacchio, J. (1996) Control of meandering grain boundary configurations in $YBa_2Cu_3O_y$ bicrystal thin films based on deposition rate, *J. Mater. Res.* **11**, 2440–2449.

122 Char, K., Colclough, M.S., Lee, L.P., Zaharchuk, G. (1991) Extension of the bi-epitaxial Josephson junction process to various substrates, *Appl. Phys. Lett.* **59**, 2177–2179.

123 Tafuri, F., Miletto Granzio, F., Carillo, F., Di Chiara, A., Verbist, K., Van Tendeloo, G. (1999) Microstructure and Josephson phenomenology in 45° tilt and twist $YBa_2Cu_3O_{7-\delta}$ artificial grain boundaries, *Phys. Rev. B* **59**, 11523–11531.

124 Jia, C.L., Kabius, B., Urban, K., Herrmann, K., Cui, G.J., Schubert, J., Zander, W., Braginski, A.I., Heiden, C. (1991) Microstructure of epitaxial YBCO films on step-edge $SrTiO_3$ substrates, *Physica C* **175**, 545–554; Jia, C.L., Kabius, B., Urban, K., Herrmann, K., Schubert, J., Zander, W., Braginski, A.I. (1992) The microstructure of epitaxial YBCO films on steep steps in $LaAlO_3$ substrates, *Physica C* **196**, 211–226.

125 DiIorio, M.S., Yoshizumi, S., Yang, K.-Y., Zhang, J., Maung, M. (1991) Practical high T_c Josephson junctions and dc SQUIDs operating above 85 K, *Appl. Phys. Lett.* **58**, 2552–2554.

126 Rosenthal, P.A., Grossman, E.N., Ono, R.H., Vale, L.R. (1993) High temperature superconductor-normal metal-superconductor Josephson junctions with high characteristic voltages, *Appl. Phys. Lett.* **63**, 1984–1986.

127 Ludwig, F., Dantsker, E., Koelle, D., Kleiner, R., Miklich, A.H., Clarke, J. (1995) Multilayer magnetometers based on high-T_c SQUIDs, *Appl. Supercond.* **3**, 383–398.

128 Tristan Technologies, Inc., San Diego, California, http://www.tristantech.com

129 Humphreys, R.G., Satchell, J.S., Chew, N.G., Edwards, J.A., Goodyear, S.W., Keene, M.N. (1991) Evaporated $YBa_2Cu_3O_{7-x}$ thin films and device technology, *Mater. Sci. Eng.* **B10**, 293–303.

130 Ockenfuß, G., Wördenweber, R., Scherer, T.A., Unger, R., Jutzi, W. (1995) In-situ low pressure oxygen annealing of $YBa_2Cu_3O_{7-x}$ single- and multilayer systems, *Physica C* **243**, 24–28.

4
SQUID Electronics

Dietmar Drung and Michael Mück

4.1
General

In this chapter we describe the electronics needed to read out the information of a SQUID used as a flux sensor, i.e., to quantitatively determine the amount of applied flux signal threading the SQUID loop, and also to control the device's settings in order to attain the optimum sensitivity and accuracy of the flux measurement.

The simplified general description of readout principles suitable for dc and rf SQUIDs is included in Chapter 1. The dc SQUID is a flux-to-voltage converter with a nonlinear, periodic V–Φ_a characteristic where V is the voltage across the SQUID and Φ_a is the applied flux (Figure 4.1(a)). The peak-to-peak voltage swing V_{pp} (modulation of the total voltage drop across the SQUID by the flux change) which is to be measured is rather small, typically a few tens of μV. The period is equal to one flux quantum Φ_0. The rf SQUID has a similar characteristic, but V is replaced by changes in the rf voltage amplitude across a resonant circuit inductively coupled to the rf SQUID loop and energized from an rf source. In the following general discussion of readout electronics, the dc SQUID is referred to, but the discussion is applicable to the rf SQUID as well.

4.2
Basic Principle of a Flux-locked Loop

4.2.1
Linearization of the Transfer Function

In principle, a SQUID can be operated in a small-signal mode around the optimum working point W which is typically located near the steepest part of the V–Φ_a characteristic. A small change in the applied flux $\delta\Phi_a$ will produce a proportional change in the voltage $\delta V = V_\Phi\, \delta\Phi_a$ where $V_\Phi = \partial V/\partial\Phi_a$ is the transfer coefficient at the working point (cf. Figure 4.1(a)).

However, the proportionality between voltage and flux is maintained only for very small $\delta\Phi_a$, and the output becomes strongly distorted if the peak-to-peak flux amplitude exceeds the linear flux range

$$\Phi_{lin} = V_{pp} / |V_\Phi| \lesssim \Phi_0/\pi\,. \tag{4.1}$$

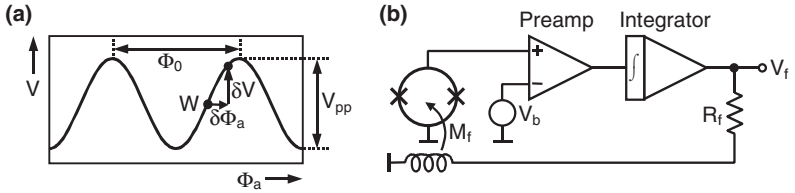

Fig. 4.1 Fundamentals of SQUID readout: (a) V–Φ_a characteristic with working point W; (b) basic direct-coupled FLL circuit. The dc SQUID is drawn (circle with two crosses indicating the Josephson junctions), but any type of SQUID with nonhysteretic V–Φ_a characteristic can be used. In the case of the rf SQUID, the voltage V has to be replaced by the rf voltage amplitude at the preamplifier input.

The expression on the right-hand side of (4.1) is valid for a sinusoidal V–Φ_a characteristic which is often a useful first approximation. In order to keep the nonlinearity low and to avoid excess noise at large excursions from the working point, the signal flux range $\delta\Phi_{pp}$ has to be made sufficiently small compared to Φ_{lin}. To discuss the nonlinearity in the small-signal readout quantitatively, we define the nonlinear error flux Φ_{nl} as the *largest* deviation of the V–Φ_a characteristic from a straight line over the full signal flux range. This straight line is defined by two parameters, the offset voltage V_0^* at the working point ($\delta\Phi_a = 0$) and the slope V_Φ^*, which are selected such that the amplitudes of the positive and negative deviations are equal. To simplify the discussion, we assume a sinusoidal V–Φ_a characteristic with the working point W located at its steepest part and a symmetric signal flux range of $\pm\delta\Phi_{pp}/2$ around it. Obviously, for this symmetric case, $V_0^* = 0$. Approximating the sine function by the two leading terms of its Taylor expansion, we find $V_\Phi^* \approx V_\Phi\,[1-(\delta\Phi_{pp}/\Phi_{lin})^2/8]$. The corresponding nonlinear error flux is given by

$$\Phi_{nl} = \pm\left|\,\delta V - (V_0^* + V_\Phi^*\,\delta\Phi_a)\,\right|_{max}/V_\Phi^* \approx \pm\delta\Phi_{pp}^3/48\;\Phi_{lin}^2. \tag{4.2}$$

For small flux ranges $\delta\Phi_{pp} \le \Phi_{lin}/2$, (4.2) deviates from the exact solution by less than 1.6%. According to (4.2), the relative nonlinearity $\Phi_{nl}/\delta\Phi_{pp}$ scales with the square of the reduced signal frequency range $\delta\Phi_{pp}/\Phi_{lin}$. Assuming a tolerable nonlinearity $\Phi_{nl}/\delta\Phi_{pp}$ of ±1% or ±0.1%, (4.2) predicts a maximum signal flux range of $\pm 0.11\;\Phi_0$ or $\pm 0.035\;\Phi_0$, respectively. In the case of rf SQUIDs, a higher linearity is expected because the V–Φ_a characteristic of rf SQUIDs is typically triangular rather than sinusoidal, and sufficient linearity might be obtained within the linear flux range of $\pm\Phi_0/4$. We see that, for a typical SQUID magnetometer with a sensitivity of 1 nT/Φ_0, the weak signal of the human heart (peak amplitude typically 50 pT) would be small enough for a small-signal readout. However, environmental interferences (e.g., a power line) commonly exhibit much larger amplitudes. Therefore, small-signal readout is rarely used.

The dynamic range can be considerably increased by using a flux-locked loop (FLL) as shown in Figure 4.1(b). The SQUID is biased at working point W as in the small-signal readout. The deviation of the SQUID voltage V from that at the working

point V_b is amplified, integrated, and fed back into the SQUID via a feedback resistor R_f and a feedback coil which is magnetically coupled to the SQUID via a mutual inductance M_f. Commonly, feedback resistances in the kΩ range are used, making the impedance of the feedback coil negligible in the frequency range of interest. For infinite integrator gain, the flux in the SQUID is kept constant by the negative feedback, and the voltage V_f across the feedback resistor depends linearly on the applied flux. For finite integrator gain, the peak-to-peak flux in the SQUID $\delta\Phi_{pp}$ is reduced by the gain of the open feedback loop (compared to the small-signal readout). For example, assuming a signal flux range of 100 Φ_0 and an open-loop gain of 1000, we obtain $\delta\Phi_{pp}$ = 0.1 Φ_0. For a sinusoidal V–Φ_a characteristic, the corresponding nonlinear error flux Φ_{nl} according to (4.2) is $\pm 2\times10^{-4}$ Φ_0 resulting in a system nonlinearity of $\pm 2\times10^{-6}$ relative to the signal flux range of 100 Φ_0. In practice, the nonlinearity of SQUID systems is characterized by applying sinusoidal test signals and investigating the generation of harmonics. In our example, a full-scale (100 Φ_0 peak-to-peak) sinusoidal signal flux at frequency f will cause a harmonic distortion flux at 3f (including higher-order harmonics at 5f, 7f, ...) with a peak-to-peak value of 4×10^{-4} Φ_0 or –108 dB below the fundamental. Experimentally, very low levels of nonlinearity have been attained for both high-T_c and low-T_c SQUIDs (harmonic distortions down to about –120 dB at low signal frequencies), which is adequate for virtually all applications [1–3].

In contrast to the small-signal readout, the FLL transfer coefficient does not depend on the working point of the SQUID but only on constant circuit parameters (feedback resistance R_f and feedback coil mutual inductance M_f). The dynamic range can easily be made very large by decreasing R_f and/or increasing M_f. However, the dynamic range is commonly not limited by the FLL but rather by the analog-to-digital converter (ADC) in the data acquisition system following the FLL. For example, a SQUID with a low noise level of 1×10^{-6} $\Phi_0/\sqrt{\text{Hz}}$ will exhibit a peak-to-peak noise flux of about 2×10^{-4} Φ_0 in a 1-kHz band (assuming that the peak-to-peak noise is about 6 times the rms noise). A feedback range of 100 Φ_0 thus requires a ≥19-bit ADC to make the least-significant bit (LSB) smaller than the noise flux. Furthermore, as discussed above, for an open-loop gain of 1000 and a sinusoidal V–Φ_a characteristic, the nonlinearity at the FLL output is $\pm 2\times10^{-6}$ relative to a 100 Φ_0 feedback range which corresponds to an integral nonlinearity of ±1 LSB for a 19-bit ADC.

The demands on the ADC can be lowered by taking advantage of the periodicity of the V–Φ_a characteristic. For this, the feedback range and the corresponding ADC input range are set to ±1 Φ_0 (or an integer multiple of it). Each time the feedback flux exceeds this range, the integrator is reset and the corresponding Φ_0 steps are counted. By combining the ADC output with the flux-quanta counted, one obtains a digital data word with substantially increased resolution [4–7]. A dynamic range of 8×10^4 Φ_0 was experimentally verified [6]. A short integrator reset time is essential to allow a high system slew rate (see Section 4.2.2) [8]. Flux-quanta counting can be conveniently implemented in a digital feedback electronics. Here, the analog output of the preamplifier is digitized, integrated digitally (e.g., using a digital signal processor (DSP)), and fed back into the SQUID via a digital-to-analog converter (DAC) [4–6]. The digital integrator can easily be reset and yields the digitized feedback sig-

nal with an accuracy given by the DAC. However, the system bandwidth is limited by the digital loop delay (e.g., ≈200 ns in a fast system [7]). Analog and digital FLLs may be combined together in a hybrid version [6]. For both analog and digital FLL, the flux-quanta counting method implies that only a small fraction of the applied magnetic field is cancelled out, i.e., that the SQUID "sees" almost all of the field. Therefore, the upper limit of the dynamic range is given by the maximum field the device can withstand without producing magnetic hysteresis or excess noise. This may be a severe limitation in the case of high-T_c SQUIDs (cf. Section 5.4).

4.2.2 Noise and Dynamic Behavior

We turn now to a brief discussion of noise and dynamic behavior of the basic FLL circuit in Figure 4.1(b). The total flux noise density of a dc SQUID operated in such a FLL is given by

$$S_{\Phi,\mathrm{FLL}} = S_\Phi + S_{V,\mathrm{amp}} / V_\Phi^2 \tag{4.3}$$

where S_Φ is the intrinsic flux noise density of the SQUID and $S_{V,\mathrm{amp}}$ is the preamplifier voltage noise density, respectively. The effect of preamplifier current noise is neglected in (4.3) because of the low dynamic resistance R_{dyn} of the SQUID. If necessary, it may be included by adding a current noise contribution $S_{I,\mathrm{amp}}\, R_{dyn}^2$ to the voltage noise density $S_{V,\mathrm{amp}}$. For typical values of preamplifier noise and transfer coefficient (1 nV/$\sqrt{\mathrm{Hz}}$ and 100 μV/Φ_0, respectively) the preamplifier flux noise contribution amounts to $\sqrt{S_{\Phi,\mathrm{amp}}} = \sqrt{S_{V,\mathrm{amp}}} / |V_\Phi| = 1{\times}10^{-5}\ \Phi_0/\sqrt{\mathrm{Hz}}$ which is substantially higher than the intrinsic dc SQUID noise level of typically a few $10^{-6}\ \Phi_0/\sqrt{\mathrm{Hz}}$. Therefore, the transfer coefficient has to be enhanced by about one order of magnitude to make the preamplifier noise negligible. In the standard dc SQUID readout involving flux modulation [9], this is done without a reduction of the linear flux range Φ_{lin} by using a step-up transformer between the SQUID and preamplifier. In contrast to this, most of the direct readout schemes without flux modulation increase $|V_\Phi| = V_{\mathrm{pp}} / \Phi_{\mathrm{lin}}$ mainly by reducing Φ_{lin} which degrades the dynamic performance [10]. The various ways to enhance the transfer coefficient of dc SQUIDs will be described in Section 4.3. In the case of traditional rf SQUIDs with bias frequencies around 30 MHz, the preamplifier usually determines the system noise due to a low transfer coefficient $\partial V_{\mathrm{T}}/\partial \Phi_{\mathrm{a}}$. The system noise can be improved by increasing the bias frequency which enlarges $\partial V_{\mathrm{T}}/\partial \Phi_{\mathrm{a}}$ without a reduction in Φ_{lin} (see Section 4.4).

The dynamic performance of the FLL in Figure 4.1(b) is estimated using the simplified FLL model depicted in Figure 4.2. This model involves three basic components: the SQUID, an ideal one-pole integrator, and a delay element. Input and output quantities are flux values: the applied flux Φ_{a} and the feedback flux Φ_{f}. The SQUID is assumed to be an infinitely fast but nonlinear flux-to-voltage converter with a linear characteristic in the flux range $\pm\Phi_{\mathrm{lin}}/2$ around the working point W. The idealized SQUID behaves as a linear element as long as the error flux

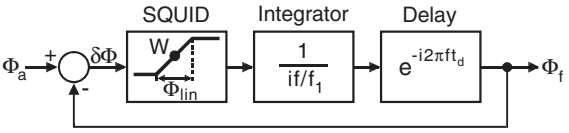

Fig. 4.2 Simplified FLL model.

$\delta\Phi = \Phi_a - \Phi_f$ remains within $\pm\Phi_{lin}/2$ but its output signal saturates for $|\delta\Phi| > \Phi_{lin}/2$. The integrator gain f_1/if represents the total gain of the open feedback loop including the gains of SQUID, preamplifier and integrator. Here, i is the imaginary unit and f_1 is the unity-gain frequency of the open feedback loop. To determine f_1, it is convenient to split the loop gain into two parts: the SQUID gain

$$G_{SQUID} = V_\Phi M_f / R_f \tag{4.4}$$

and the electronics gain $G_{Electronics} = f_{GBW}/if$, where f_{GBW} is the gain-bandwidth product of the feedback electronics (preamplifier plus integrator). G_{SQUID} represents the total gain between the system output (integrator voltage V_f in Figure 4.1(b)) and the preamplifier input. To give an example, assuming realistic parameters V_Φ = 100 μV/Φ_0, $1/M_f$ = 10 μA/Φ_0, and R_f = 10 kΩ, we obtain $G_{SQUID} = 1\times10^{-3}$. Thus, the unity-gain frequency f_1 is found from the condition $|G_{Electronics}| = 1/G_{SQUID}$ = 1000, i.e., to realize f_1 = 100 kHz with the assumed SQUID parameters, a high gain-bandwidth product f_{GBW} = 100 MHz is required. Note that in the case of flux-modulated systems (Section 4.3.2.1), the gains of the lock-in detector and of the step-up transformer between SQUID and preamplifier have to be included in the calculation.

The delay element takes into account dynamic errors and phase shifts in the circuit components. Ideally, the loop delay t_d represents the total delay time in the transmission lines between SQUID and readout electronics. In practice, however, the delay is dominated by other effects. In the case of flux-modulated SQUIDs, t_d represents phase shifts caused by the step-up transformer between SQUID and preamplifier, and by the demodulator (mixer). For a wideband electronics with 16–MHz flux modulation, t_d = 100 ns can be deduced from the measured phase response [11]. Direct-coupled readout electronics allow for much shorter loop delays, e.g., about 15 ns for a 15-MHz bandwidth system [8]. Here, the preamplifier bandwidth and *LC* resonance effects in the lines between SQUID and readout electronics are limiting factors. For rf SQUIDs, t_d is expected to be comparable to that of flux-modulated dc SQUIDs because the bandwidth limitations imposed by the step-up transformer of flux-modulated dc SQUIDs are similar to those resulting from the tank circuit of rf SQUIDs. Finally, we note that the described dynamic model can be used for digital SQUIDs with on-chip feedback (Section 4.3.4.4) as well. In this case Φ_{lin} is given by the narrow transition width of the switching probability, which is typically of the order 10^{-2} Φ_0 [12]. The loop delay is minimized due to the on-chip feedback. It is determined by the finite clock period and time constants in the sensor

design. With practical single-chip SQUIDs, $t_d \lesssim 1$ ns may be achieved for clock frequencies in the GHz range.

The closed-loop gain of the FLL with delay time is obtained from a small-signal analysis around the working point W [10]:

$$|G_{FLL}(f)| = 1/\sqrt{1 + \frac{f}{f_1}\left(\frac{f}{f_1} - 2\sin(2\pi f t_d)\right)} \,. \tag{4.5}$$

It depends on the unity-gain frequency f_1 and on the delay time t_d. In practice, the delay time is fixed for a given system, and f_1 is used to adjust the system bandwidth. The FLL gain according to (4.5) is plotted in Figure 4.3 versus the reduced frequency ft_d for various values of the reduced unity-gain frequency $f_1 t_d$.

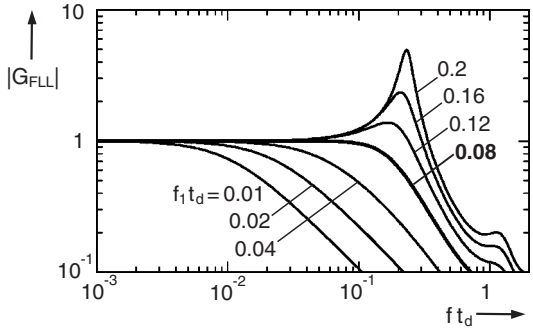

Fig. 4.3 Closed-loop frequency response of the FLL with one-pole integrator and finite loop delay for various values of the reduced unity-gain frequency $f_1 t_d$.

At low values of $f_1 t_d << 0.08$, the loop delay is negligible and the FLL exhibits a first-order low-pass response with a 3-dB bandwidth $f_{3dB} = f_1$. If $f_1 t_d$ is increased, the loop delay causes significant phase lag and a peak appears in the frequency response indicating that the system stability is impaired (cf. Figure 4.3). For $f_{1,max} = 1/4\pi t_d = 0.08/t_d$, the frequency response is optimally flat just without a peak and the bandwidth is increased to

$$f_{3dB,max} = 2.25\, f_{1,max} = 0.18/t_d \,. \tag{4.6}$$

Equation (4.6) is a realistic estimate for the achievable bandwidth of a SQUID system. A higher bandwidth is possible but results in a degraded frequency response. For room temperature readout electronics, the bandwidth is limited to about 20 MHz due to the distance between SQUID and electronics (typically 1 m).

The system slew rate is defined as $\dot{\Phi}_f \equiv |\partial \Phi_f / \partial t|_{max}$. It is commonly measured by applying a sinusoidal signal flux, the amplitude of which is increased until the system becomes unstable or the output saturates. Here, we discuss the slew rate at

high signal frequencies where it is not limited by the static feedback range. With a one-pole integrator one obtains [10]

$$\dot{\Phi}_f = \pi \, \Phi_{\mathrm{lin}} f_1 \leq \Phi_0 f_1 \, . \tag{4.7}$$

The slew rate with a one-pole integrator is frequency independent, but increases with the linear flux range Φ_{lin} and the unity-gain frequency f_1. Thus, with respect to slew rate it is not desirable to increase $\left| V_\Phi \right|$ at the expense of a reduced Φ_{lin} as is often the case in direct readout schemes. Flux-modulated SQUIDs and series SQUID arrays (Section 4.3.4.2) do not show a reduced Φ_{lin}. Assuming a sinusoidal V–Φ_{a} characteristic, one obtains for these SQUIDs the expression on the right-hand side of (4.7), i.e., a slew rate of 1 Φ_0/μs per MHz of unity-gain frequency.

Although in most cases bandwidth and slew rate requirements imposed by the measured signals are modest, the readout electronics often has to be very fast to track interference signals superimposed on the measured signals without producing nonlinear distortions or causing flux jumps by integer multiples of a flux quantum. This is particularly crucial in the case of magnetically unshielded systems where the interference signals can be orders of magnitudes larger than the signals of interest. In order to achieve the highest possible slew rate, one has to maximize the FLL bandwidth even if the measured signals exhibit a low bandwidth. The upper slew rate limit with a one-pole integrator

$$\dot{\Phi}_{f,\mathrm{max}} = \Phi_{\mathrm{lin}}/4t_{\mathrm{d}} \leq \Phi_0/4\pi t_{\mathrm{d}} \tag{4.8}$$

is obtained from (4.7) by setting $f_1 = f_{1,\mathrm{max}} = 1/4\pi t_{\mathrm{d}}$ [13]. A slew rate above $\dot{\Phi}_{f,\mathrm{max}}$ is possible by choosing $f_1 > f_{1,\mathrm{max}}$ but at too high values of f_1 the noise performance degrades due to broadband noise which is fed back into the SQUID and mixed down into the signal frequency range. Assuming realistic values for Φ_{lin} and t_{d} one obtains maximum slew rates between about 1 Φ_0/μs and 10 Φ_0/μs for the various readout schemes. Digital SQUIDs with on-chip feedback may achieve even higher slew rates if very high clock frequencies in the GHz range are used and the linear flux range is made sufficiently large.

This section is closed by a short discussion of broadband noise effects. In the FLL mode, the voltage noise across the SQUID S_V as well as the preamplifier voltage noise $S_{V,\mathrm{amp}}$ is amplified, integrated and fed back into the SQUID as a noise flux with a power spectral density $S_{\Phi,\mathrm{FLL}} = (S_V + S_{V,\mathrm{amp}})/V_\Phi^2$. The rms value of this noise flux is found by multiplying $\sqrt{S_{\Phi,\mathrm{FLL}}}$ with the square-root of the effective noise bandwidth of the FLL which (for a first-order low-pass response) is equal to $(\pi/2)$ $f_{3\mathrm{dB}}$. The corresponding peak value is obtained by multiplying the rms value with the crest factor. For a periodic signal, the crest factor is a constant depending on the shape of the signal (e.g., $\sqrt{2}$ for a sine function). For Gaussian-distributed noise, however, the crest factor depends on the probability that the noise exceeds the quoted peak value. Assuming a realistic crest factor of 4 (which means a probability of 6.3×10^{-5} for exceeding the peak value), we obtain an approximation for the peak-to-peak noise flux coupled back into the SQUID:

$$\Phi_{n,pp}/\Phi_{lin} \approx 10\sqrt{f_{3dB}(S_V + S_{V,amp})}/V_{pp} \lesssim 1\,. \tag{4.9}$$

The broadband noise flux $\Phi_{n,pp}$ increases with the square-root of the FLL bandwidth f_{3dB}. Obviously, if $\Phi_{n,pp}$ approaches Φ_{lin} at high values of f_{3dB}, the broadband noise will start to round the V–Φ_a characteristic and to correspondingly reduce the transfer coefficient $|V_\Phi|$, thereby increasing the system noise level. Furthermore, the system might become unstable (i.e., frequent unlocking events might occur) if $\Phi_{n,pp}$ becomes too large compared to Φ_{lin}. Therefore, the FLL bandwidth should be chosen such that $\Phi_{n,pp}/\Phi_{lin} \lesssim 1$ as indicated on the right-hand side of (4.9). To give an example, for $\sqrt{S_V + S_{V,amp}}$ = 1 nV/$\sqrt{\text{Hz}}$ and f_{3dB} = 10 MHz, the peak-to-peak voltage swing of the V–Φ_a characteristic should be larger than about 30 μV according to (4.9). Thus, using a low-noise preamplifier and a SQUID with a large voltage swing, a high system bandwidth can be achieved, which is limited by the loop delay rather than by broadband flux noise.

4.2.3
Integrator Types

To obtain the highest possible slew rate, one selects the highest open-loop gain (bandwidth) for which the SQUID system remains stable and no intolerably high excess noise is observed [14]. At low frequencies, the loop gain and hence the slew rate can be further increased by introducing a second pole in open-loop response at a frequency f_2 [15]. In Figure 4.4, the frequency dependence of the open-loop gain $|G_{OL}(f)|$ and phase $\varphi_{OL}(f)$ of the two-pole integrator is compared with that of the one-pole integrator for negligible loop delay (t_d = 0) and corner frequencies $f_2 = f_1/4$ and $f_2' = f_2/400$. Equations for the complex frequency response $G_{OL}(f)$ and examples of integrator circuits are also shown in Figure 4.4(a).

At high frequencies $f >> f_2$, the behavior of the two-pole integrator is identical to that of the one-pole integrator. At low frequencies $f << f_2$, however, the gain vs. frequency curve of the two-pole integrator has a slope of –40 dB/decade instead of –20 dB/decade obtained with a one-pole integrator. Therefore, the two-pole integrator gain and hence the slew rate is higher by a factor of f_2/f at low frequencies compared to that of the one-pole integrator, but the phase margin is reduced (cf. Figure 4.4). At very low frequencies $f < f_2'$, a zero in the frequency response shifts the phase back to –90°, and the enhancement factor of gain and slew rate approaches its maximum value f_2/f_2'.

The reduced phase margin of the two-pole integrator leads to a peak in the closed-loop frequency response. For t_d = 0 and $f_2' << f_2$, the peak gain is obtained from a small-signal analysis of the FLL:

$$|G_{FLL}(f_{peak})| = 1/\sqrt{1 - \frac{f_2}{f_1}\left(\sqrt{2 + f_2/f_1} - \sqrt{f_2/f_1}\right)^2} \quad \text{with}$$

$$f_{peak} = f_2\sqrt{\sqrt{1 + 2f_1/f_2} - 1}\,. \tag{4.10}$$

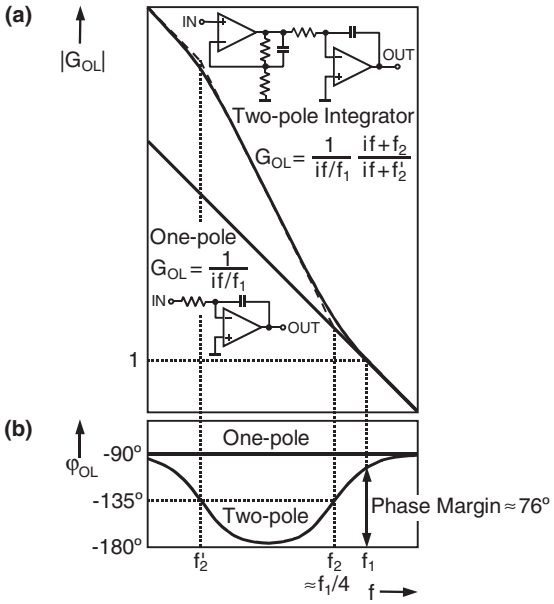

Fig. 4.4 Open-loop frequency response of (a) gain and (b) phase of the feedback loop with one-pole or two-pole integrator and negligible loop delay. Insets in (a) show examples of electrical circuits providing the respective frequency response.

To keep the peak low, the pole frequency f_2 should be made small compared to the unity-gain frequency f_1. A maximum pole frequency $f_2 = f_1/4$ was recommended in [15]. In this case, the phase margin is reduced by 14° to 76° (cf. Figure 4.4), and the closed-loop frequency response exhibits a peak of 1.25 dB according to (4.10). In the time domain, the step response has a 13.5% overshoot. In contrast, the one-pole FLL with $t_d = 0$ has a first-order low-pass response (i.e., no peak) and a step response without overshoot. With finite loop delay, the peak in the closed-loop frequency response of a two-pole FLL has a minimum value of $|G_{FLL}(f_{peak})|_{min} \approx 1/(1-f_2/2f_1)^2$ for the optimum unity-gain frequency $f_1 \approx f_{1,max} = 1/4\pi t_d$ [10]. For the recommended pole frequency $f_2 = f_1/4$, the minimum peak height with loop delay is 2.3 dB, i.e., about 1 dB larger than without loop delay. Note that the FLL with one-pole integrator has just no peak in the frequency response for the optimum $f_1 = f_{1,max}$ as discussed in Section 4.2.2.

In summary, the two-pole integrator improves the slew rate and reduces the harmonic distortion at low frequencies, but it deteriorates the high-frequency performance of the SQUID system. In most cases the deterioration of the high-frequency performance will be tolerable so that the two-pole integrator is a good choice in applications where large low-frequency signals have to be tracked with low distortions, e.g., the power-line interference in unshielded magnetometer systems. Seppä and Sipola developed a so-called $PI^{3/2}$ controller (i.e., a 1½-pole integrator), which

provides a phase of –135° and a gain slope of –30 dB/decade over five frequency decades [16]. Compared to the two-pole integrator, the $PI^{3/2}$ controller has an improved phase behavior, but a reduced low-frequency gain. It is rarely used, perhaps because the realization of –30 dB/decade requires a relatively complicated *R*–*C* network, and the dimensioning is not as simple as for a one-pole or two-pole integrator.

4.3 The dc SQUID Readout

4.3.1 Fundamentals

The main challenge in SQUID readout is to perform the linearization of the transfer function without adding noise. In the case of dc SQUIDs operated at liquid helium or nitrogen temperatures, it is relatively easy to keep the preamplifier noise contribution below the intrinsic SQUID noise. Furthermore, low-frequency excess noise arising from critical-current fluctuations in the SQUID can be removed by using bias current reversal. Here we address the fundamentals, while in the following sections we review standard dc SQUID readout schemes (both with static bias and bias reversal), as well as recently developed alternative readout concepts.

There are different ways to bias a dc SQUID, which can be understood with the help of the following small-signal description at the working point W [10]:

$$\delta V = V_\Phi \, \delta\Phi_a + R_{dyn} \, \delta I = V_\Phi \, (\delta\Phi_a + M_{dyn} \, \delta I) \, . \tag{4.11}$$

Here, δV, $\delta\Phi_a$ and δI are small deviations of the voltage across the SQUID, the applied flux and the current through the SQUID from the values V_b, Φ_b and I_b defining the working point. The transfer coefficient $V_\Phi = (\partial V/\partial\Phi_a)_{I_b}$ describes the voltage-flux dependence at constant current $I = I_b$. The dynamic resistance $R_{dyn} = (\partial V/\partial I)_{\Phi_b}$ represents the voltage–current dependence at constant flux $\Phi_a = \Phi_b$. Note that R_{dyn} might include effects not directly related to dissipative elements in the SQUID such as, e.g., a magnetic coupling between the bias current leads and the SQUID ring, which produces a contribution to $\partial V/\partial I$ via V_Φ. On the right-hand side of (4.11), the current sensitivity M_{dyn} is used, which is defined as [10]

$$M_{dyn} = -(\partial\Phi_a/\partial I)_{Vb} = R_{dyn} \, / V_\Phi \approx \pm(1...2) \, L \, . \tag{4.12}$$

It is often convenient to describe current effects in the SQUID by M_{dyn} rather than R_{dyn} for the following reason: R_{dyn} depends strongly on the working point and on parasitic effects in the SQUID structure, e.g., resonances in the input coil. In contrast to this, $M_{dyn} = R_{dyn}/V_\Phi$ is reasonably constant because the scaling of R_{dyn} and V_Φ is similar [17]. Approximately, M_{dyn} scales with the SQUID inductance *L*. One obtains values of $|M_{dyn}|$ between *L* and 2*L* for low-T_c SQUIDs covering a wide range of SQUID inductances between 7 pH and 400 pH [17–20]. For high-T_c

SQUIDs with L between 30 pH and 145 pH, a typical current sensitivity $|M_{\mathrm{dyn}}| \approx 2L$ was measured [21,22]. High-T_c SQUIDs with strongly rounded V–Φ_a characteristic are expected to exhibit a higher $|M_{\mathrm{dyn}}|$ because, in the limit of strong noise-rounding, R_{dyn} approaches the normal resistance $R/2$ but V_Φ falls to zero, and thus $|M_{\mathrm{dyn}}| = |R_{\mathrm{dyn}}/V_\Phi|$ rises.

The two basic bias modes of a dc SQUID, current bias and voltage bias, are depicted in Figure 4.5(a) and (b).

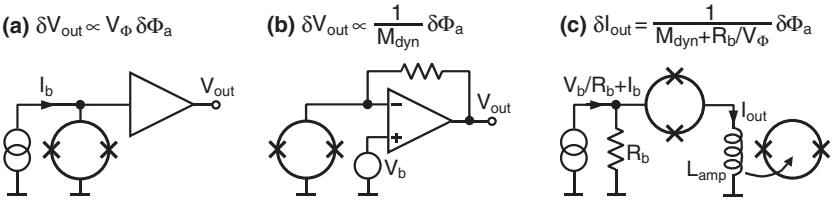

Fig. 4.5 The dc SQUID bias modes: (a) current bias with voltage amplifier, (b) voltage bias with transimpedance amplifier [23], and (c) voltage bias with inductive load.

In the current bias mode, a constant current I_b is passed through the SQUID and the voltage V across it is sensed, i.e., the SQUID acts as a flux-to-voltage converter. The transfer coefficient $\delta V/\delta\Phi_a = V_\Phi$ is obtained from (4.11) by setting $\delta I = 0$. In contrast, in the voltage bias mode, the voltage across the SQUID is kept constant and the current I through the SQUID is detected. Here, the SQUID acts as a flux-to-current converter with a transfer coefficient $\delta I/\delta\Phi_a = -1/M_{\mathrm{dyn}}$ obtained from (4.11) by setting $\delta V = 0$.

The bias voltage V_b is maintained in Figure 4.5(b) by configuring the preamplifier as a transimpedance amplifier (i.e., current-to-voltage converter) and connecting a room-temperature bias voltage source to the noninverting preamplifier input [23]. Alternatively, the bias source may be realized by sending a current through a resistor $R_b << R_{\mathrm{dyn}}$ connected in series with the SQUID and operated at the SQUID temperature T [24]. Both current and voltage bias can be used to operate a SQUID in a FLL. With respect to noise, there is no difference between the two bias modes, i.e., the total noise, including the contribution of the preamplifier voltage and the current noise, is identical [10]:

$$S_{\Phi,\mathrm{FLL}} = S_\Phi + S_{V,\mathrm{amp}}/V_\Phi^2 + S_{I,\mathrm{amp}}M_{\mathrm{dyn}}^2 \,. \tag{4.13}$$

Note that the preamplifier noise $S_{V,\mathrm{amp}}$ or $S_{I,\mathrm{amp}}$ might include contributions from noise in the bias voltage or current source, respectively.

Voltage bias has the advantage compared with current bias that it can be used for SQUIDs with unshunted Josephson junctions as well [25]. Furthermore, a higher linearity and slew rate might be obtained because the linear flux range of the I–Φ_a characteristic is somewhat larger than that of the V–Φ_a characteristic. For fast SQUID systems, however, voltage bias has the disadvantage that broadband pream-

plifier noise is fed directly back into the SQUID [24], i.e., the achievable system bandwidth is lower than with current bias. Voltage bias is particularly useful when the SQUID is connected to an inductive load, e.g., the input coil of a second SQUID (see Section 4.3.4.1 and Figure 4.5(c)). In this case, a small bias resistance $R_b << R_{dyn}$ is connected in series with the SQUID, and a current is sent through R_b in order to produce the bias voltage V_b across it. The series connection of a bias resistor (i.e., bias voltage source) and SQUID is shunted by the load (i.e., the input coil of the second SQUID). The bias resistance should be made as small as possible in order to minimize the spectral density of its flux noise contribution $4k_BTR_b/V_\Phi^2$.

4.3.2 Methods to Suppress Preamplifier Noise

4.3.2.1 Flux Modulation

In this section, we discuss the two basic readout schemes for resistively-shunted dc SQUIDs, the flux modulation and direct readout. In both cases, preamplifier noise must be suppressed by enlarging the transfer coefficient of the SQUID using extra components at cryogenic temperature.

The widely-used flux modulation readout [9] is depicted in Figure 4.6. A square-wave modulation flux Φ_{mod} of typically 100 kHz is applied to the SQUID such that it is periodically switched between two working points W^+ and W^- placed at adjacent slopes of its V–Φ_a characteristic. Using square-wave modulation, the SQUID is always biased at points with minimum noise. Sinusoidal modulation (introduced in Chapter 1) minimizes the detrimental effect of switching transients but increases the noise because the SQUID passes through points with reduced or even no sensitivity. Assume there is zero alternating voltage across the SQUID without applied flux ($\delta\Phi_a = 0$). A positive change in flux $\delta\Phi_a > 0$ leads to a square-wave SQUID voltage which is out of phase with the modulation flux (see signals $\Phi_{mod}(t)$ and $V(t)$ in

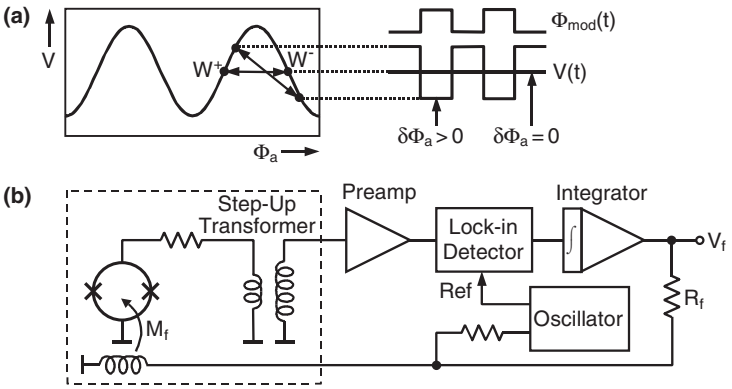

Fig. 4.6 SQUID readout with flux modulation: (a) the V–Φ_a characteristic and (b) the FLL circuit. A square-wave modulation flux Φ_{mod} switches the SQUID periodically between the working points W^+ and W^-. Components inside the dashed box are at cryogenic temperature.

Figure 4.6(a)). For a negative flux $\delta\Phi_a < 0$, the alternating SQUID voltage will be in phase with the modulation flux. Thus, the applied flux can be sensed by synchronously detecting the SQUID voltage at the modulation frequency.

In the FLL with flux modulation, the alternating voltage across the SQUID is increased by a cooled step-up transformer (or an *LC* series-resonant circuit [26]), further amplified at room temperature, and lock-in detected at the modulation frequency. A small resistance is placed between the SQUID and the transformer primary to avoid the SQUID being shorted by the transformer (i.e., the SQUID is operated with voltage bias rather than current bias). The turn ratio (i.e., the voltage "gain") of the step-up transformer is commonly chosen to transform the dynamic resistance of the SQUID to the value required to optimize the noise temperature of the preamplifier [27]. At typical modulation frequencies of some 100 kHz, field-effect transistor (FET) preamplifiers achieve noise temperatures down to a few K. Since the theoretical equivalent output noise temperature of the SQUID is about four times its operating temperature (bear in mind that for practical SQUID parameters the simulated dynamic resistance at the operating point $R_{dyn} \approx R$ and the voltage noise density across the SQUID $S_V \approx 16k_BTR \approx 4{\times}4k_BTR_{dyn}$ [18]), the preamplifier noise is negligible for SQUID temperatures above a few K. The lock-in detector involves an analog multiplier [26], a synchronous switch [28], or (in the case of wideband systems) a mixer [11]. Its output signal, which is an image of the V–Φ_a characteristic, is integrated and fed back as a current into a feedback coil in order to counterbalance the flux applied to the SQUID. The voltage V_f across the feedback resistor R_f is the linearized output signal.

Flux-modulation is an efficient way to read out SQUIDs with smooth, well-behaved V–Φ_a characteristics. Due to the cooled transformer, the preamplifier noise contribution can be made negligible for SQUIDs operated above a few K. However, the system noise may increase considerably if the SQUID exhibits strongly resonance-distorted V–Φ_a characteristics, e.g., with a high degree of asymmetry or narrow linear flux ranges around W^+ and W^- [28,29]. Preamplifier low-frequency noise and in-phase critical-current fluctuations (Section 5.4.1) are suppressed by flux modulation because they only produce a dc offset across the SQUID but no ac component at the modulation frequency (it is implied that the modulation frequency is chosen well above the respective $1/f$ corner frequencies).

The SQUID voltage is increased by the step-up transformer without reducing the linear flux range Φ_{lin} thus providing maximum slew rate for a given system bandwidth. However, with the commonly-used modulation frequency of 100 kHz to 500 kHz, the system bandwidth is severely limited by the transformer. It may be increased by using two transformers, one cooled and the other at room temperature [14]. Wideband SQUID electronics with 16-MHz flux modulation were developed, involving a resonant superconducting thin-film transformer [11] or a non-resonant terminated transmission-line transformer [30]. Using a commercial low-T_c SQUID with non-resonant transformer, a FLL bandwidth of 5 MHz, a slew rate of 1.9 $\Phi_0/\mu s$ and a noise level of $5.5{\times}10^{-6}$ $\Phi_0/\sqrt{Hz}$, were measured. Recently, a high-T_c system with a 33-MHz flux modulation and a two-pole integrator was reported which allows a FLL bandwidth of 10 MHz and a slew rate of about 10 $\Phi_0/\mu s$ [31]. Note that for

low-T_c SQUIDs the system noise tends to degrade at high modulation frequencies because the noise temperature of FET preamplifiers increases with frequency. At modulation frequencies above about 10 MHz it might even be advantageous to use a preamplifier with low-noise bipolar transistors which achieve noise temperatures around 100 K [30].

4.3.2.2 **Additional Positive Feedback**

Direct readout with additional positive feedback (APF) was developed to simplify the readout electronics of biomagnetic multichannel systems [32]. The APF circuit consists of a resistor R_{APF} and a coil L_{APF} in series, the latter being magnetically coupled to the SQUID via a mutual inductance M_{APF}. The APF circuit is connected in parallel with the SQUID (Figure 4.7(a)). Assume the SQUID is biased at a working point W at the positive slope of the V–Φ_a characteristic. A (say) positive change in flux $\delta\Phi_a$ will cause a positive voltage change δV. The resulting increase of the current in the APF coil induces an additional, positive flux in the SQUID via M_{APF}, which increases the SQUID voltage further and leads to an enhanced flux-to-voltage coefficient. Similarly, the transfer coefficient is lowered when W is at the negative slope of the V–Φ_a characteristic, i.e., the V–Φ_a characteristic becomes strongly asymmetric (cf. Figure 4.7(c)). The peak-to-peak voltage swing is somewhat reduced due to the APF resistor which acts as an extra shunt at low frequencies. The I–Φ_a characteristic, however, is not affected by APF because it is measured at constant SQUID voltage and thus at constant current through the APF coil [23]. Recently, it was demonstrated that an effect similar to APF can be obtained by making the shunt resistors of the SQUID strongly asymmetric [33].

The behavior of a SQUID with APF can be understood using the low-frequency equivalent circuit in Figure 4.7(b) which describes the behavior for small deviations from the working point W. A more detailed model including frequency dependencies is given in [10]. According to Figure 4.7(b), a SQUID with APF behaves like the same SQUID with disconnected APF circuit followed by a voltage amplifier having a gain

$$G_{APF} = 1 \,/\, (1 - \beta_{APF}) \quad \text{with} \quad \beta_{APF} = V_\Phi \,(M_{APF} - M_{dyn}) \,/ R_{APF} \lesssim 1 \,. \tag{4.14}$$

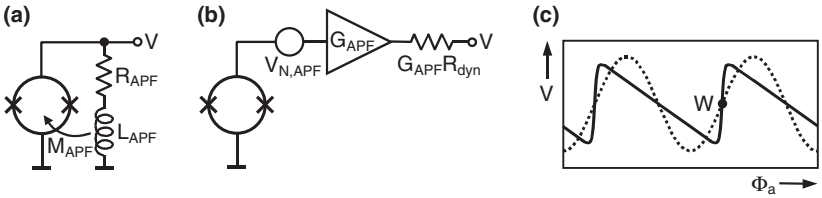

Fig. 4.7 SQUID with APF: (a) basic circuit, (b) low-frequency small-signal equivalent circuit at working point W, and (c) V–Φ_a characteristic. With APF (solid line), the V–Φ_a characteristic is steepened at the working point W by the factor G_{APF} but the peak-to-peak voltage swing is reduced compared to the case without APF (dotted line).

Here, β_{APF} is the feedback coefficient and V_Φ is the transfer coefficient of the SQUID with the APF circuit disconnected. The amplifier gain G_{APF} describes the increase of the flux-to-voltage coefficient. It becomes infinite for $\beta_{APF} = 1$. The output resistance of the amplifier $G_{APF}R_{dyn}$ represent the dynamic resistance of the SQUID with APF. Both the dynamic resistance and the flux-to-voltage coefficient increase by the same factor, and thus the current sensitivity M_{dyn} remains unchanged (reflecting the fact that the I–Φ_a characteristic is not affected by APF). The noise contribution of the APF resistor is taken into account by a voltage noise source at the amplifier input with a spectral density

$$S_{V,APF} = 4k_B T\, R_{APF}\, \beta_{APF}^2 \approx 8k_B T\, R\,. \tag{4.15}$$

For minimum noise, R_{APF} should be made as small as possible; however, $R_{APF} >> R/2$ (the normal resistance of the SQUID) should be fulfilled to avoid a serious reduction of V_{pp}. The approximation on the right-hand side of (4.15) is obtained using realistic APF parameters: $G_{APF} = 10$ and $R_{APF} = 2.5R$. For low-T_c SQUIDs, the APF noise contribution of $\approx 8k_BTR$ is well below the voltage noise across the SQUID of $\approx 16k_BTR$ [18]. For high-T_c devices, the APF noise contribution increases because, in the limit of extreme thermal noise-rounding, the voltage noise across the SQUID approaches the Nyquist noise of its normal resistance, $2k_BTR$. Therefore, for high-T_c SQUIDs the correct choice of APF parameters is crucial to achieve low overall noise.

A SQUID with APF can be operated in a direct-coupled FLL without flux modulation using either current or voltage bias. In the latter case, APF is also called the noise cancellation (NC) method [24]. With current bias, a feedback coefficient $\beta_{APF} \leq 1$ is required to avoid hysteresis in the V–Φ_a characteristic. In contrast, with voltage bias, $\beta_{APF} > 1$ does not lead to instability [23]. Furthermore, the linear flux range with voltage bias is not reduced by APF and thus the slew rate at a given system bandwidth is higher than with current bias. As β_{APF} is proportional to the intrinsic transfer coefficient V_Φ, it may be fine-tuned via the bias current [34]. The use of a cooled field-effect transistor (FET) as a tunable APF resistor [23] is an elegant method of adjusting the APF gain manually or even automatically [35]. It is important to note that the bandwidth of the enlarged flux-to-voltage coefficient is *not* equal to that of the APF circuit $f_{APF} = R_{APF}/2\pi L_{APF}$ but rather to f_{APF}/G_{APF} [10]. Therefore, for large G_{APF} the frequency range over which the system noise is low becomes small, independent of the SQUID bias mode (with current bias, the system bandwidth is also affected). The limited APF bandwidth may be critical when using bias reversal (Section 4.3.3) because it increases the settling time after each polarity change of the bias current/voltage. Therefore, the APF gain should not be made unnecessarily high, but just high enough to achieve an overall noise close to the intrinsic SQUID noise.

APF reduces the effect of preamplifier voltage noise which is commonly the dominant noise source in a direct-coupled FLL. Preamplifier current noise, which is often only of significance at low frequencies [10], is not suppressed because the current sensitivity M_{dyn} remains constant (cf. (4.13)). If required, the effect of current noise can be removed using a technique called bias current feedback (BCF) [10,19].

For this, a BCF coil is connected in series to the SQUID which is magnetically coupled to the SQUID loop via a mutual inductance $M_{BCF} \approx |M_{dyn}|$. For correct polarity of the BCF coil, any voltage change caused by a current change δI via the dynamic resistance of the SQUID is (partially) cancelled by the flux change $M_{BCF}\,\delta I$ resulting from the magnetic coupling between the BCF coil and the SQUID loop. Consequently, with BCF the net current sensitivity is $M_{dyn} \pm M_{BCF}$, and the dynamic resistance of the SQUID can be made zero in the vicinity of the working point so that preamplifier current noise no longer causes excess voltage noise across the SQUID. An effect similar to BCF is obtained if the bias current is fed asymmetrically into one of the Josephson junctions instead of symmetrically into the SQUID inductance. In this case, for a SQUID with identical Josephson junctions, half the bias current (and also half the preamplifier noise current) flows through the SQUID loop thereby producing a flux change, as in the case of BCF. Thus, asymmetric bias current feed may be applied to reduce $|M_{dyn}|$ by $L/2$ without using an extra coil [36].

Direct readout has the advantage, compared with flux modulation, that the feedback electronics is less complex. A low FLL noise level close to the intrinsic SQUID noise can be achieved even with strongly resonance-distorted, asymmetric V–Φ_a characteristics [22]. Noise levels down to 0.9 fT/$\sqrt{\text{Hz}}$ with a $1/f$ corner at 2 Hz were obtained using 7.2×7.2 mm^2 multiloop low-T_c magnetometers [37]. Biomagnetic multichannel systems with up to 256 SQUIDs were realized [38]. Furthermore, a high bandwidth can easily be obtained. The degradation of the slew rate of current-biased SQUIDs with APF (caused by their reduced Φ_{lin}) is often more than compensated by a high bandwidth. Several wideband systems were developed [1,39–41]; the fastest achieved a FLL bandwidth of 15 MHz, a slew rate of 2 Φ_0/μs and a noise level of 1.45×10^{-6} $\Phi_0/\sqrt{\text{Hz}}$ using a 100–pH low-T_c SQUID and a one-pole integrator [8]. APF was also applied to read out high-T_c magnetometers [21,22]; however, due to the higher noise level of high-T_c devices, a direct readout can often be performed even without APF if a low-noise ($\lesssim$0.4 nV/$\sqrt{\text{Hz}}$) bipolar preamplifier is used [7,37,42]. Furthermore, bipolar preamplifiers for operation at 77 K were reported exhibiting even lower noise levels of $\lesssim$0.2 nV/$\sqrt{\text{Hz}}$ [43].

4.3.3
Methods to Suppress 1/*f* Noise

Critical-current fluctuations are of minor importance for low-T_c SQUIDs with state-of-the-art tunnel junctions [44] but are a dominant source of low-frequency excess noise in high-T_c SQUIDs [45]. To understand their influence on the SQUID noise, we define two contributions: in-phase and out-of-phase fluctuations (Section 5.4.1). The first appear as a voltage across the SQUID ("vertical" shift of the V–Φ_a characteristic) whereas the latter appear as a flux in the SQUID ("horizontal" shift of the V–Φ_a characteristic). Resistance fluctuations (also those of the APF resistance) may contribute in the same way to the SQUID noise, but are commonly less important. Obviously, using flux modulation readout with static bias current, the effect of in-phase fluctuations is suppressed but that of out-of-phase fluctuations remains because it cannot be distinguished from a "real" flux applied to the SQUID. In the

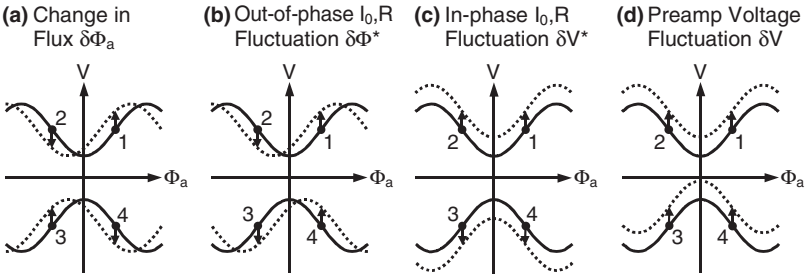

Fig. 4.8 Effect of (a) change in flux, (b),(c) out-of-phase and in-phase I_0,R fluctuations, and (d) preamplifier voltage fluctuation on the V–Φ_a characteristics for positive (upper traces) and negative (lower traces) bias current. Arbitrarily, in all cases the resulting voltage change at working point 1 is assumed to be positive.

case of direct readout with static bias, both in-phase and out-of-phase fluctuations contribute to the SQUID noise.

The effect of critical-current or resistance fluctuations (abbreviated I_0,R fluctuations) is compared in Figure 4.8 with that of a change in flux $\delta\Phi_a$.

The in-phase and out-of-phase fluctuations are labeled δV^* and $\delta\Phi^*$ because they appear as voltage or flux fluctuations, respectively. In addition, in Figure 4.8(d), the effect of preamplifier low-frequency noise is shown, which corresponds to a fluctuation in the SQUID voltage δV. The V–Φ_a characteristics for positive and negative bias current are shown both without (solid lines) and with (dotted lines) fluctuations. The optimum working points are marked in the four quadrants as 1 to 4. The effect of $\delta\Phi_a$, $\delta\Phi^*$, δV^* and δV at the four working points is indicated by vertical arrows. We see that $\delta\Phi_a$ and $\delta\Phi^*$ have the same effect for positive bias current (working points 1 and 2), but opposite effects if the bias current is reversed (working points 3 and 4). Therefore, to suppress the effect of I_0,R fluctuations, one has to apply a bias current reversal scheme that makes the net effect of the I_0,R fluctuations zero over one period of the bias reversal, but preserves the sensitivity of the SQUID for magnetic flux.

Various bias reversal schemes are described in the literature [46–54]. Their function principle is depicted in Figure 4.9. A square-wave bias current I_b and bias flux Φ_b are applied in order to switch the SQUID periodically between different sets of working points. The frequency of the bias current f_b must be chosen well above the $1/f$ corner frequency f_c that one would obtain with static bias (for typical high-T_c SQUIDs, $f_c \approx 1$ kHz with flux modulation and $f_c \approx 10$ kHz with direct readout). The switching sequences in Figure 4.9 are illustrated by arrows in the V–Φ_a characteristics and by time sequences (one bias reversal period).

The basic FLL circuit for the bias reversal schemes involving lock-in detection (Figures 4.9(a)–(c)) is depicted in Figure 4.10(a). As with static bias current, the signal of the SQUID is stepped up by a cooled transformer, amplified at room temperature, lock-in detected using the reference signal "Ref", integrated, and sent back into the SQUID via the feedback coil. In the case of direct readout (Figures 4.9(d) and

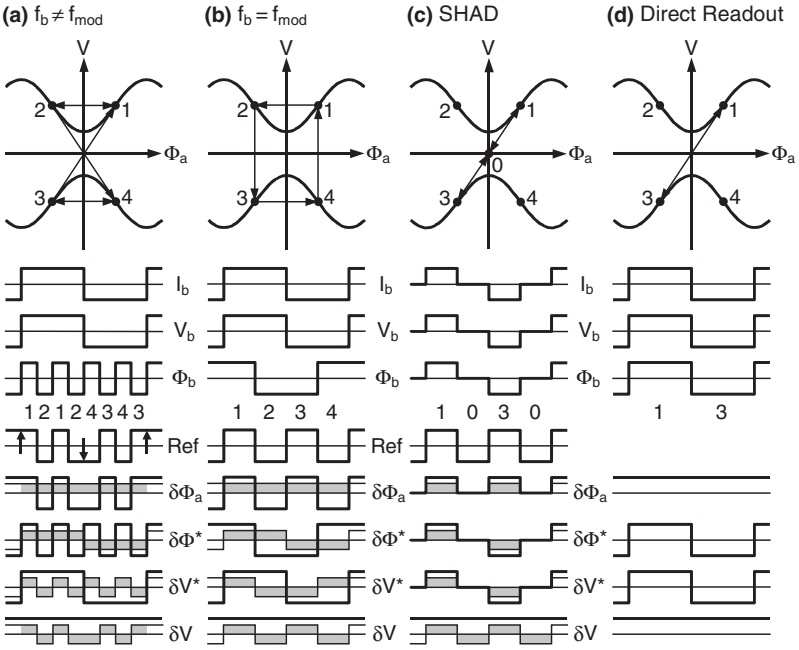

Fig. 4.9 Bias reversal schemes: (a),(b) flux modulation with $f_b \neq f_{mod}$ [46,50] and $f_b = f_{mod}$ [52], (c) SHAD scheme [48,49], and (d) direct readout [53]. The superposition of square-wave bias current I_b and bias flux Φ_b switches the SQUID periodically between the working points 0 to 4 according to the arrows in the V–Φ_a characteristics. A bias voltage V_b is subtracted from the SQUID voltage in order to provide zero output signal without applied flux. Bold lines in the bottom four rows show the preamplifier output for a change in flux $\delta\Phi_a$, for an out-of-phase or in-phase I_0,R fluctuation $\delta\Phi^*$ or δV^*, and for a voltage fluctuation δV, respectively. The lock-in detector output (thin lines) is obtained by multiplying the preamplifier output with the lock-in reference "Ref". A change in the FLL output only occurs if the lock-in detector output has a nonzero time average over one bias reversal period (shaded regions) except for direct readout where the FLL output results directly from the averaged SQUID signal.

4.10(b)), the output of the SQUID is directly connected with the preamplifier and integrated to generate the linearized system output.

With bias reversal, a large, parasitic ac voltage appears across the SQUID with a peak-to-peak value of twice the bias voltage V_b. This oscillating voltage does not contain useful information about the applied flux, but leads to switching transients in the step-up transformer of flux-modulated systems. Their effect can be minimized by connecting a resistor in series to the transformer primary, and passing a current synchronously with I_b through this resistor such that the alternating voltages across the SQUID and the resistor are equal (cf. Figure 4.10(a)) [46,47]. Recently, an alternative compensation scheme with a non-constant bias current was proposed [55].

In Figure 4.9, it is assumed for clarity that in all cases the bias voltage V_b is subtracted from the SQUID voltage such that *zero* output signal appears without

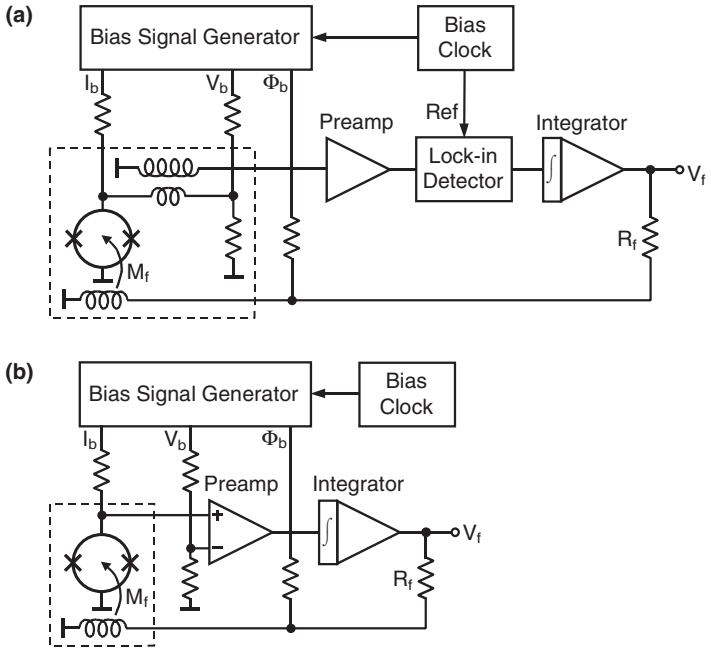

Fig. 4.10 FLL circuits with bias reversal: (a) scheme with lock-in detection and (b) direct readout. Components inside the dashed boxes are at cryogenic temperature.

applied flux. Under this condition and with the help of Figure 4.8, the corresponding preamplifier output signals for a change in flux $\delta\Phi_a$ as well as for fluctuations $\delta\Phi^*$, δV^* and δV, can easily be determined (bold traces in the four bottom rows of Figure 4.9). In the schemes involving lock-in detection, the signals at the lock-in detector output are obtained by multiplying the preamplifier output signals with the lock-in reference "Ref" (thin lines in the four bottom rows of Figure 4.9). The effect of a fluctuation is suppressed if the time average of the lock-in detector output is zero over one bias reversal period (i.e., for zero net area of the shaded regions in Figure 4.9). In contrast, a nonzero time average means that a fluctuation will cause a response at the FLL output. In the scheme with direct readout, the averaged preamplifier output signal is the measure for a change in the FLL output signal. Analyzing the time traces in Figure 4.9, one can easily verify that the presented bias reversal schemes indeed suppress I_0,R fluctuations while preserving sensitivity for magnetic flux.

We now briefly discuss the individual bias reversal schemes. Figure 4.9(a) shows a standard bias reversal scheme with flux modulation where the frequency of the bias current f_b is different from that of the modulation flux f_{mod} [46,50]. The ratio of both frequencies must be an integer. Here we discuss the widely used case $f_b < f_{mod}$ (in Figure 4.9(a), $f_b = f_{mod}/4$ is arbitrarily chosen). From Figure 4.8 we see that the flux-to-voltage coefficient changes its sign if the bias current is reversed (working point pairs 1↔4 or 2↔3). Therefore, to preserve the flux sensitivity with bias rever-

sal, the signal polarity must be changed each time the bias current is reversed. This can easily be done by reversing the phase of the lock-in reference signal at each change of the bias current (see arrows in the row "Ref" in Figure 4.9(a)). Alternatively, an extra ac flux may be applied simultaneously with the bias current in order to shift the V–Φ_a characteristics at reverse bias current polarities by $\Phi_0/2$ against each other [47].

Another bias reversal scheme is shown in Figure 4.9(b) [52]. Here, bias current and modulation flux have the same frequency ($f_b = f_{mod}$) but are shifted by 90° against each other (quadrature modulation). The demodulation is performed at twice the bias frequency. The third scheme called second harmonic detection (SHAD) involves only three working points: the pair 1,3 and a point 0 at zero bias current and voltage [48,49]. With the SHAD scheme, the white flux noise density S_Φ increases by a factor of two because the SQUID is biased half the time at the point 0 without flux sensitivity. The last scheme, direct readout, involves switching between only two working points 1↔3 [53]. Recently, another bias reversal scheme with only two working points (1↔4) was proposed, but this does not suppress in-phase I_0,R fluctuations [54]. From Figure 4.9 one sees that all bias reversal schemes using lock-in detection, suppress preamplifier low-frequency voltage noise, but direct readout does not. The described bias reversal schemes may be applied to both current-biased and voltage-biased SQUIDs. A comparative study of bias reversal schemes including noise considerations is given in [56]. Finally, we note that with bias reversal it is even possible to adjust the bias current or voltage automatically by synchronously detecting the bias frequency component at the preamplifier output and removing it via an extra feedback loop [37,46].

In Figure 4.9, ideal V–Φ_a characteristics of a symmetric SQUID have been assumed with an optimum bias flux at $\pm\Phi_0/4$. In practice, however, this assumption is not always fulfilled, which can cause problems in bias reversal schemes involving all four working points 1 to 4. For example, the V–Φ_a characteristics for positive and negative I_b might be shifted against each other due to an asymmetric bias current feed or a mutual inductance between the bias current leads and the SQUID loop. This would increase the noise level for the bias reversal schemes in Figure 4.9(a) and (b) unless an extra ac flux is applied simultaneously with the bias current in order to compensate the flux shift (the scheme in [47] already uses such an extra ac flux). Furthermore, the optimum working points might not be located at a bias flux of $\pm\Phi_0/4$ [49]. This is no problem for the schemes in Figure 4.9(a) and (b) where the modulation flux amplitude can be chosen freely, but it would increase the noise with the scheme in [47] where the modulation amplitude is fixed to a peak-to-peak value around $\Phi_0/2$. In contrast to this, the SHAD scheme and direct readout do not have any problems with the above-mentioned nonideal V–Φ_a characteristics. Low-noise SQUID operation may even be possible in the case of strongly resonance-distorted V–Φ_a characteristics.

4.3.4 Further Readout Concepts

4.3.4.1 Two–stage Configuration

In the previous sections, readout techniques for single, resistively-shunted dc SQUIDs were reviewed. Now we briefly describe alternative SQUID concepts which involve more than one SQUID per sensing channel or which require alternative SQUID designs.

A simple method of increasing the transfer coefficient of a SQUID is to use another SQUID as a low-noise preamplifier. An example of such a two-stage configuration is shown in Figure 4.5(c). Configurations with more than two stages are also possible, but are not discussed here. The front-end SQUID determines the overall system noise, so it is inevitably a standard dc SQUID with resistively-shunted junctions. It is coupled to the amplifier SQUID via a resistor R_b and the amplifier input coil. R_b should be made as small as possible to minimize its flux noise contribution $4k_BTR_b/V_\Phi^2$, i.e., voltage bias with $R_b << R_{dyn}$ gives the minimum overall noise (V_Φ and R_{dyn} are intrinsic parameters of the front-end SQUID with disconnected amplifier SQUID) [10]. A variety of amplifier SQUIDs is described in the literature: SQUIDs with hysteretic junctions being operated either digitally [51] or in an analog mode [57,58], SQUIDs with resistively-shunted junctions readout either with flux modulation [59] or directly [60,61], and series SQUID arrays [62].

To enhance the effective transfer coefficient of a two-stage configuration, a gain $G_\Phi > 1$ between the applied flux in the front-end SQUID Φ_a and that in the amplifier SQUID Φ_{amp} must be provided. The low-frequency small-signal flux gain is given by

$$G_\Phi = \partial\Phi_{amp}/\partial\Phi_a = M_{amp} / (M_{dyn} + R_b/V_\Phi) \approx M_{amp} / M_{dyn} , \tag{4.16}$$

where $M_{dyn} = R_{dyn}/V_\Phi$ is the intrinsic current sensitivity of the front-end SQUID and M_{amp} is the mutual inductance between the amplifier SQUID and its input coil, respectively. The expression on the right-hand side of (4.16) is valid for voltage bias $R_b << R_{dyn}$. The amplifier input coil inductance L_{amp} and the total loop resistance $R_{dyn}+R_b$ form a first-order lowpass which leads to a reduction in flux gain above the cut-off frequency $(R_{dyn}+R_b)/2\pi L_{amp}$.

The two-stage SQUID can be operated in a FLL as a single SQUID with enhanced transfer coefficient $G_\Phi V_\Phi$. For sufficiently high flux gain, the effect of both flux noise in the amplifier SQUID and room-temperature preamplifier noise is suppressed [10]. However, the linear flux range of a two-stage configuration shrinks to Φ_{lin}/G_Φ (Φ_{lin} is the intrinsic linear flux range of the front-end SQUID). Thus, one has to compromise between low noise and high slew rate. The reduction of the linear flux range can be avoided by using an alternative readout scheme with two feedback loops: an "inner" loop with feedback into the amplifier SQUID to linearize the transfer characteristic of the amplifier SQUID, and an "outer" loop with feedback into the front-end SQUID to provide the desired linear relation between the applied flux Φ_a and the system output [63]. With two feedback loops, however, the achievable

system bandwidth is lower because the system bandwidth (i.e., the bandwidth of the "outer" feedback loop) must be kept well below the bandwidth of the "inner" amplifier feedback loop which is limited by the loop delay as shown in Section 4.2.2.

A two-stage configuration needs more wires between the cryogenic region and room temperature than a single-stage design. Furthermore, it is more complicated to adjust the working point. For large flux gains $G_\Phi \gtrsim \Phi_0/\Phi_{\mathrm{lin}}$ (or $G_\Phi \gtrsim 2\Phi_0/\Phi_{\mathrm{lin}}$ in the scheme with two feedback loops), a locking to multiple working points is possible [10]. Therefore, this configuration is not very tempting in systems with very many channels. On the other hand, in systems with only few channels, it is an efficient method of achieving very low noise levels, in particular if the front-end SQUID is cooled at low temperatures T << 4.2 K and thus exhibits a very low voltage noise. In such cases, a two-stage configuration is often the only way to take full advantage of the low SQUID noise.

4.3.4.2 Series SQUID Arrays

The relatively small voltage signal of a single dc SQUID can be enlarged considerably by connecting many identical SQUIDs in series [64]. Provided that all SQUIDs of such a series array are biased at the same working point and that the same flux Φ_a is coupled into each of the SQUIDs, the array behaves as a single SQUID with an enlarged voltage signal. Series SQUID arrays are ideal in terms of slew rate because the linear flux range is not decreased. Arrays with 100 SQUIDs are quite common, yielding output signals of a few mV. As the voltage noise density S_V across the array rises linearly with the number of SQUIDs, 100-SQUID arrays can be connected directly to a room-temperature preamplifier with only a minor increase in system noise compared to the intrinsic noise of the SQUID array [65]. All SQUIDs of the array are equipped with input coils, which are also connected in series thus having a large input inductance (e.g., $L_i = 150$ nH [66]). Both flux noise density S_Φ and input current noise density S_I, scale inversely with the number of SQUIDs, but the coupled energy resolution $\varepsilon_c = L_i S_I/2$ should remain constant. In principle, one could couple a pickup coil to the input coil in order to build a magnetometer, but series SQUID arrays are commonly used as transimpedance amplifiers, e.g., in two-stage SQUID configurations or as readout devices for cryogenic particle detectors. A very high bandwidth of $\gtrsim$100 MHz was experimentally demonstrated with 100-SQUID arrays [64,66].

Series SQUID arrays suffer from parasitic resonances in the input coils. Improved array designs with intracoil damping were developed to solve this problem, yielding smooth V–Φ_a characteristics and input current-noise levels of $\approx$2.5 pA/$\sqrt{\mathrm{Hz}}$ at 4.2 K [66]. Recently, a low-T_c transimpedance amplifier was reported involving a three-stage configuration (two single SQUIDs followed by a 100-SQUID series array) and on-chip negative feedback to linearize the transfer function [67]. Such amplifiers might allow one to read out SQUIDs without room temperature feedback loop if the required dynamic range is not too high. An undesirable feature of large SQUID arrays is that their V–Φ_a characteristics may be distorted by variations in the bias of the individual SQUIDs, e.g., due to trapped flux or variations in the junction critical currents or SQUID geometries [64]. Recently, a

novel type of SQUID array was proposed for which the elementary dc SQUID loops vary in size according to an arithmetic relation [68,69]. These devices exhibit a V–Φ_a characteristic which is *not* periodic in Φ_0 but has a single minimum of V at zero magnetic field. Low-T_c prototypes were fabricated to demonstrate the usefulness of this concept. More recently, high-T_c versions consisting of 30 SQUIDs were reported, which were designed such that they can be coupled to a large pickup coil using a flip-chip configuration [70].

4.3.4.3 Relaxation Oscillation SQUIDs

The I–V characteristic of a hysteretic Josephson junction without a shunt resistor in parallel, exhibits stable and unstable branches, indicated in Figure 4.11 by solid and dotted lines, respectively.

If the current I through the junction is initially zero and then increased, the junction will first stay in the zero-voltage (superconducting) state. If the critical current I_0 is exceeded, the junction will switch within a few ps along the dotted line in Figure 4.11 into the voltage state, and the voltage V across the junction will rise from zero to the gap voltage (≈2.8 mV for Nb-Al_2O_3-Nb junctions at 4.2 K). The junction will remain in the voltage state even for $I < I_0$ and not switch back into the zero-voltage state until the current is lowered below the return current I_r. Both the critical and the return current are influenced by noise. Typically, the spread in the critical current, given by the full width at half-maximum value of the switching probability distribution, is of the order of 1 μA at 4.2 K [71]. The return current I_r and voltage V_r depend strongly on the damping of the junction, i.e., on the subgap leakage current, and thus on the junction quality.

The I–V characteristic of a dc SQUID with hysteretic junctions resembles that of a single junction because a dc SQUID is basically a parallel connection of two junctions via the SQUID inductance L. The major difference is that the critical current of the SQUID I_c depends sensitively on the applied magnetic field, but that of a small (point contact) junction does not. In the voltage state, only the subgap branches differ somewhat, e.g., due to parasitic L–C resonance effects. The dependence of the SQUID return current on the applied flux is of secondary importance and will not be considered here. Therefore, to understand the function of a circuit based on a dc SQUID with hysteretic junctions, it is convenient to consider the SQUID as a single junction with a critical current controlled by the current in the input coil or directly by the applied magnetic field.

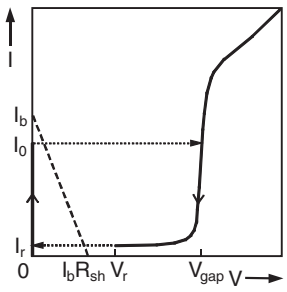

Fig. 4.11 I–V characteristic of a hysteretic Josephson junction (solid line) with load line of a shunt resistor R_{sh} in parallel to the junction (dashed line).

A relaxation oscillation SQUID (ROS) consists of a dc SQUID with hysteretic junctions, which is shunted by a resistor R_{sh} and an inductor L_{sh} in series [71–74]. The shunt circuit is similar to the APF circuit shown in Figure 4.7, except that the inductor should not be magnetically coupled to the SQUID. Relaxation oscillations can occur if the ROS is biased with a constant current I_b above the critical current I_c. This is illustrated in Figure 4.11 by the dashed load line of the shunt resistor. If the load line does not intersect the stable subgap voltage branch, a stable working point in the voltage state is not possible, and the circuit will oscillate permanently. Thus, relaxation oscillations will always appear for $(I_b - I_r)\ R_{sh} < V_r$. If this condition is not fulfilled, either the relaxation oscillations stop and the SQUID settles to a stable working point with finite voltage or, if the shunt inductance L_{sh} is within a certain range, the relaxation oscillations persist. The conditions for the occurrence of relaxation oscillations have been determined by numerical simulation of a single junction with realistic values of I_0, C and R_{sh} [71].

During the relaxation oscillations, the voltage across the ROS oscillates between zero and the gap voltage. Both the frequency f_{RO} and the duty cycle (and hence the average voltage across the ROS) depend on the bias current I_b and on the critical current I_c. As the critical current is a function of the applied flux Φ_a, both the frequency f_{RO} and the average voltage across the ROS depend on Φ_a. Therefore, a ROS can be used as a flux-to-frequency or a flux-to-voltage converter. In the first case, a simple frequency-modulated readout is possible [75,76], whereas in the second case, conventional electronics with flux modulation [74] or direct readout [71] may be used.

The flux power noise of a ROS decreases with increasing relaxation frequency: $S_\Phi \propto 1/f_{RO}$. Above about 1 GHz, there is usually no further improvement (or even an increase) in noise due to the plasma oscillation decay time [77] or resonances between the shunt inductance L_{sh} and the SQUID capacitance $2C$ [78]. By adding a damping resistor in parallel to the ROS, a higher f_{RO} can be used and a correspondingly lower noise is obtained. The need for frequencies in the GHz range explains why ROSs are commonly operated as flux-to-voltage converters. Large voltage swings V_{pp} well above those of standard resistively-shunted dc SQUIDs and transfer coefficients $|V_\Phi| > 1\ \mathrm{mV}/\Phi_0$ can easily be obtained with ROSs, thus simplifying direct readout. However, the noise level is commonly somewhat higher than for comparable resistively-shunted dc SQUIDs. Recently, a 5×5 mm^2 multiloop ROS magnetometer with a high SQUID inductance $L \approx 1$ nH and $f_{RO} \approx 2.5$ GHz was reported, which exhibited a large voltage swing $V_{pp} \approx 70\ \mu\mathrm{V}$, an exceptionally high transfer coefficient $|V_\Phi| \gtrsim 10\ \mathrm{mV}/\Phi_0$, and a typical noise level of 4.4 fT/$\sqrt{\mathrm{Hz}}$ with a 1/f corner around 1 Hz [79].

A double relaxation oscillation SQUID (DROS) consists of two hysteretic dc SQUIDs in series, shunted by an L_{sh}–R_{sh} circuit. In the original version, named balanced ROS [74,77], the signal flux is applied to both SQUIDs. In the simplified version discussed here [71], Φ_a is applied only to one of the SQUIDs, the sensor SQUID (see Figure 4.12(a)). The other one, the reference SQUID, is biased at a *constant* flux to adjust its critical current to a value that lies typically in the middle between the maximum critical current $2I_0$ and the minimum critical current (e.g.,

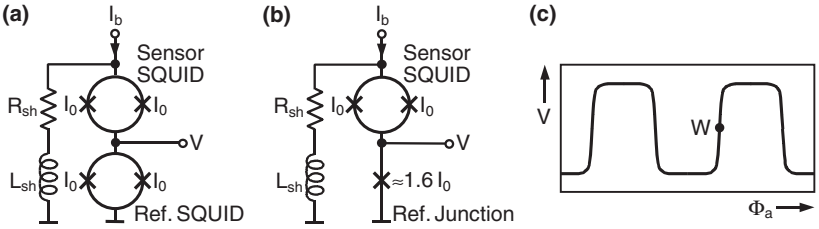

Fig. 4.12 Basic DROS circuits (a) with reference SQUID, and (b) with reference junction. An example of the step-like DROS V–Φ_a characteristic is given in (c).

$1.05 I_0$ for $\beta_L = 1$). A constant bias current I_b is passed through the DROS to start relaxation oscillations. The output voltage V is tapped across the reference SQUID. During relaxation oscillations, only the SQUID with the smaller critical current will oscillate between zero and gap voltage; the other SQUID always will stay at zero voltage. Thus, a DROS behaves as a critical-current comparator. The output voltage of the DROS will be zero if the critical current of the reference SQUID is larger than that of the sensor SQUID; otherwise, the voltage will be nonzero with an average value depending on I_b. The transition between these two states is very sharp, leading to step-like V–Φ_a characteristics with extremely high transfer coefficients $|V_\Phi|$ (cf. Figure 4.12(c)). To simplify the structure and to lower the number of wires between the cryogenic region and room temperature, the reference SQUID may be replaced by a single Josephson junction with an appropriate critical current as shown in Figure 4.12(b) [80].

DROSs need relaxation oscillation frequencies $f_{RO} \gtrsim 1$ GHz and proper damping of resonances to achieve a low noise level [78,81]. Their voltage swings V_{pp} and transfer coefficients $|V_\Phi|$ are typically higher than those of ROSs with comparable noise, and thus direct readout is relatively simple. The minimum of five wires per independent DROS unit is larger than the minimum of four wires needed to operate ROSs or dc SQUIDs with APF. Practical systems involving DROSs were developed, e.g., two low-noise biomagnetic multichannel systems (a 37-channel magnetometer and a 40-channel planar gradiometer) [81]. Furthermore, DROSs may be used to build simplified digital single-chip SQUIDs as will be discussed in the following section.

4.3.4.4 **Digital SQUIDs**

Digital SQUIDs are devices in which the sensor itself or, in multistage configurations, at least one of the following stages is operated in a digital mode. There are various digital SQUID concepts reported in the literature: concepts involving room-temperature feedback electronics [51,82], latching Josephson logic [12,83–89], rapid single-flux-quantum (RSFQ) logic [90,91], or DROSs [92,93]. A key element in digital SQUIDs is a sensitive current comparator which oversamples the input signal at a high rate. Driven by an external bipolar clock current I_{clk}, the comparator produces a sequence of voltage pulses if the signal current is above a certain threshold; otherwise, it produces pulses of inverse polarity. In the case of a unipolar clock, it pro-

duces pulses or remains in the zero-voltage state (missing pulses). The use of a DROS for the comparator avoids the need of an external clock.

The comparator pulses represent the digitized error flux. They are integrated digitally using an up/down counter. In superconducting logic, the counter function can be realized by writing flux quanta into a superconducting loop, i.e., increasing or decreasing the flux in this loop by Φ_0 at each positive or negative (missing) comparator pulse, respectively. To close the digital feedback loop, the flux in the counter loop is magnetically coupled to the comparator SQUID. For a bipolar clock, the digital feedback loop automatically locks at a state with equal probability for positive and negative pulses; with a unipolar clock, a state with 50% pulse probability is maintained. The comparator output pulses are transmitted to room temperature and counted to obtain the digital sensor output. A low bit error rate is required to avoid drift and low-frequency excess noise [87]. The minimum flux change Φ_{LSB} in the comparator SQUID (corresponding to 1 Φ_0 in the counter loop) determines the slew rate and quantization noise. A useful compromise is to make Φ_{LSB} approximately equal to the broadband rms noise flux in the comparator [87], which is typically of the order of 10^{-2} Φ_0. For an optimized digital DROS, $\Phi_{\mathrm{LSB}} \approx \sqrt{S_\Phi f_{\mathrm{RO}}}$ should be chosen [93].

In order to achieve a high current sensitivity, a low-inductance SQUID is used for the comparator involving up to 16 washers in parallel, each equipped with a multiturn coil on top [12]. These coils are connected in series to obtain an input coil with a large inductance. A pickup coil might be connected directly to it in order to build a magnetometer. However, as with (D)ROSs, a high clock frequency $f_{\mathrm{clk}} \gtrsim 1$ GHz is needed to obtain a low noise level comparable to that of standard dc SQUIDs. In contrast, an output frequency of $\lesssim$10 MHz is desirable for a convenient transmission and further processing of the comparator output pulses. A simple solution is the use of a multistage design with a low-noise resistively-shunted dc SQUID as the first stage and a ≈10 MHz comparator SQUID as the last stage, but this reduces the slew rate and bandwidth. Alternatively, the output pulse frequency might be reduced digitally from the GHz range to $\lesssim$10 MHz by using a decimation filter involving Josephson logic, but this increases the circuit complexity considerably.

We turn now to a brief discussion of practical digital SQUIDs. Three representative devices are depicted in Figure 4.13.

The first single-chip SQUID was developed at Fujitsu by Fujimaki *et al.* [12,83] – see Figure 4.13(a). In this device, an asymmetric, hysteretic dc SQUID is used as a comparator. Driven by a sinusoidal bias current, it produces positive or negative voltage pulses which increase or decrease the flux in the superconducting storage loop (the counter loop) in steps of Φ_0 via a second asymmetric SQUID, the write gate. Flux in the storage loop is equivalent to a nonzero circulating current I_{f} that couples magnetically into the input circuit consisting of a pickup coil and a comparator input coil such that the input current I_{in} is kept at zero. Some buffer gates and several damping resistors (not shown in Figure 4.13) are required for optimum performance. A 35-pH comparator with a 0.5-μH input coil and the complete feedback electronics were integrated on a single 4×10 mm^2 chip [12]. The maximum clock frequency of 10 MHz resulted in a noise level of 6.2×10^{-6} $\Phi_0/\sqrt{\mathrm{Hz}}$. The noise was

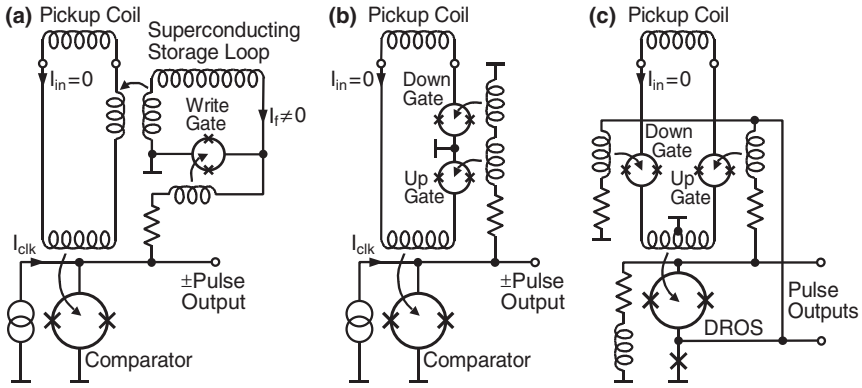

Fig. 4.13 Digital single-chip SQUIDs: (a) latching comparator with feedback via a superconducting storage loop [12], (b) latching comparator with direct feedback into the input circuit [84], and (c) digital DROS with direct feedback into the input circuit [92,93]. In (a,b) a bipolar clock current I_{clk} has to be applied externally, whereas in (c) a self-oscillating DROS involving a reference SQUID or junction is used for the comparator. Circuit details are omitted for clarity (e.g., dc bias current sources, additional buffer gates and shunt resistors).

white down to 0.2 Hz, probably because the effect of critical-current fluctuations is suppressed by using a bipolar clock (i.e., bias current reversal). The slew rate, however, was only 170 Φ_0/s due to a too small $\Phi_{LSB} = 1.7\times10^{-5}\ \Phi_0$.

The dynamic range of the Fujitsu single-chip SQUID was limited in principle, because the input flux was cancelled via a nonzero feedback current I_f flowing in the superconducting storage loop. A virtually infinite dynamic range can be obtained if the comparator output pulses are directly used to cancel the input flux without an intermediate storage loop (Figure 4.13(b)). This feedback concept was first proposed for RSFQ logic [90] and demonstrated using latching Josephson logic [84]. The input circuit consists of the pickup coil, the comparator input coil and two write gates forming a superconducting loop (the counter loop). The bipolar comparator pulses control the write (up/down) gates which keep the average flux in the input circuit constant. A prototype single-chip SQUID was fabricated and proper operation experimentally verified [84]. Subsequently, a three-stage version with bipolar clock [85] and a two-stage version with a unipolar two-phase clock [88] were developed. For the latter, a noise level of $2\times10^{-5}\ \Phi_0/\sqrt{\text{Hz}}$ and a slew rate of 0.035 Φ_0/μs were reported. The noise was probably dominated by Nyquist noise in a 1-Ω damping resistor connected in parallel to the 0.4-μH input coil.

An external clock is not needed if a self-oscillating DROS is used for the comparator. The basic circuit of such a digital DROS is depicted in Figure 4.13(c). Its feedback loop is similar to that in Figure 4.13(b). The counter loop involves two write gates: the up gate driven by the voltage pulses across the sensor SQUID, and the down gate driven by the pulses across the reference junction shown in Figure 13(c) or reference SQUID. The feedback loop automatically locks at a state with equal pulse probability for sensor and reference. Prototypes of an optimized 100-MHz

digital DROS with a 280-pH SQUID inductance were fabricated [93] but do not yet operate fully due to fabrication problems. A noise level of 6×10^{-6} $\Phi_0/\sqrt{\text{Hz}}$ and slew rate of 5 Φ_0/μs a are expected for these devices.

An extremely high slew rate can be obtained with digital SQUIDs based on RSFQ logic. A prototype of such a device was reported involving a decimation filter with a serial output and a 2^{18} over-sampling ratio to match the internal ≈20-GHz clock to the desired cut-off frequency of ≈40 kHz [91]. The basic function was experimentally demonstrated, but a fully operational chip could not be fabricated due to a high chip complexity (2700 Josephson junctions).

4.4 The rf SQUID Readout

4.4.1 General

In the case of a dispersive (non-dissipative) rf SQUID flux sensor, the readout electronics has to convert the flux-dependent change in the SQUID inductance into a voltage (usually proportional to the flux signal) of sufficient magnitude (several volts) for further information processing. In the case of the hysteretic rf SQUID, the readout must detect small changes in the rf energy dissipated by the SQUID and convert these into a voltage. In rf SQUID systems, the readout plays a key role in achieving optimum performance of the system. Unlike dc SQUID systems, where the sensitivity of the entire system is mainly determined by intrinsic SQUID noise (and thus optimum performance can still be achieved with simple electronics), in many cases rf SQUID system noise is limited by the readout. Therefore, it is important that the preamplifier noise should be minimized and that the coupling between SQUID and tank circuit, as well as between tank circuit and readout, should be optimized.

4.4.2 Basic Building Blocks of rf SQUID Readout Electronics

Zimmerman and Silver first investigated rf SQUIDs with the SQUID loop directly coupled to the rf source, a method not used today [94]. Rather, to read out the rf SQUID, one is coupling it inductively to a parallel tuned L_TC_T circuit shown in Figure 1.7. The tuned circuit, often called a tank circuit, is excited at its resonant frequency by an rf current with amplitude I_{rf} and the corresponding rf voltage across the tank circuit V_T is amplified and the amplitude detected. If the SQUID is operated in the dispersive mode ($\beta_{rf} < 1$), the flux-dependent change in SQUID inductance leads to a change in the tank circuit resonant frequency $\Delta\omega_0$, and thus to a change in the rf voltage V_T across the tank circuit. The frequency of the readout ω_{rf} is chosen such that it differs slightly from the resonant frequency of the tank circuit ω_0 in order to obtain maximum $\partial V_T/\partial\omega_{rf}$ (see Chapters 2 and 6 for more details). If

$\omega_{rf} = \omega_0$, positive and negative flux changes lead to a reduction in V_T. If the flux changes periodically by, say $\Phi_0/2$, the case for which $\omega_{rf} = \omega_0$ leads to a period doubling, which can conveniently be used to identify operation in the dispersive mode.

In the hysteretic mode, the magnitude of the rf current flowing through the tank circuit coil is chosen such that it induces periodic quantum transitions in the SQUID. A change in the (static) flux threading the SQUID causes the screening current in the SQUID to change and thus changes the frequency with which the quantum transitions occur. This in turn leads to a flux-dependent damping of the tank circuit and to a flux-dependent change in the rf voltage which develops across the tank circuit.

Figure 4.14 shows a diagram of all the components needed to operate rf SQUIDs. An rf oscillator generates the rf current I_{rf} at the chosen bias frequency ω_{rf}. The amplitude of I_{rf} can be controlled by an attenuator over a range of 20 to 30 dB. In the case of a hysteretic SQUID, the attenuator is used to adjust the rf current in the tunable tank circuit so that the SQUID is operated at the first step of the $V_T(I_{rf})$ curve. An adjustment range of 20 dB allows for the use of SQUIDs with a spread in critical currents of a factor of ten. The rf voltage drop across the tank circuit is amplified by a factor of several thousand and then amplitude demodulated, usually by an envelope detector. When using a semiconductor diode as an amplitude detector, the voltage level at the output of the rf amplifier must be sufficient to overcome the diode diffusion voltage ($\geq$100 mV_{pp}). For flux-locked-loop operation, a lock-in amplifier is provided, together with a low-frequency generator, which sweeps the flux through the SQUID by a fraction of a flux quantum. A flux-locked loop similar to the ones described for dc SQUIDs is used.

A readout system for SQUIDs operated at microwave frequencies (e.g., 3 GHz, [95]) is similar to conventional electronics used for lower radio frequency (20 to 30 MHz) SQUIDs. There are, however, a few details which differ from the conventional configuration. If the tank circuit is in the form of a microstrip or other planar resonator, its resonant frequency is fixed. This requires tuning of the rf bias current generator. Microwave preamplifiers have a relatively wide bandwidth of hundreds of MHz. In order to decrease the bandwidth to the frequency range needed, a synchronous detector (usually an analog multiplier) should be used instead of the usual en-

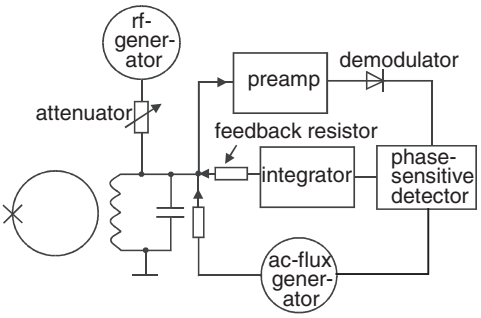

Fig. 4.14 Block diagram of rf SQUID readout electronics.

velope demodulator. The following lock-in amplifier can be a standard version, as used in lower rf systems, although a much higher modulation frequency and thus a higher slew rate are possible because of the high bias frequency.

It is also possible to operate an rf SQUID in a flux-locked-loop mode without ac modulation. As in dc SQUID electronics, Simacek *et al.*, and later others, have measured the demodulated tank-circuit voltage and compared it to an adjustable dc voltage, so that the SQUID was always biased at the steepest part of its $\partial V_T/\partial \Phi_a$ transfer function [96].

4.4.3
Construction of the Tank Circuit

At lower bias frequencies, such as the 30 MHz historically used in commercial rf SQUIDs, the tank circuit usually consisted of a wire-wound inductor and a variable capacitor, connected in parallel. For high bias frequencies, permitting one to minimize the intrinsic noise of the SQUID, the high resonant frequency of the tank circuit requires a corresponding decrease in its capacitance and inductance. However, because of stray and parasitic capacitance and inductance of the discrete components, it is not practical to use such components at frequencies above 1 GHz. Several alternatives have been studied: for very high bias frequencies, a cavity [97], or a mismatched transmission line [98] were used. For thin-film SQUIDs, a planar transmission-line resonator (e.g. a half-wavelength ($\lambda/2$) microstrip resonator) is a suitable replacement for a discrete *LC* circuit – see Figure 4.15.

In order to obtain a reasonable coupling between the SQUID and the resonator, the SQUID should be placed in the vicinity of a current anti-node. For simplicity, the SQUID can also be integrated into the resonator – see Figure 4.15. Coupling the SQUID to the room-temperature electronics can be accomplished by a second microstrip on the substrate (coupling microstrip, Figure 4.15), which runs in parallel to one end of the resonator, or by a small wire antenna.

In order for a superconducting film to form a transmission line resonator, dielectric material is required between the resonator and a metallic ground plane. The

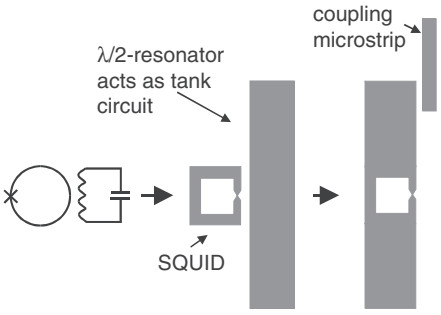

Fig. 4.15 Metamorphosis of a conventional washer-type rf SQUID with discrete tank circuit into a planar microwave SQUID integrated into a $\lambda/2$ microstrip resonator.

dielectric layer can be the substrate itself, and the ground plane can be a piece of copper-clad printed-circuit material, which at the same time can serve as the sample holder. To avoid thermal magnetic noise from the normal-conducting ground plane, it should be very thin. The presence of the ground plane lowers the SQUID inductance by a few percent.

An important requirement to be met by rf SQUIDs is that $k^2Q \approx 1$, where k is the coupling coefficient between the resonator and the SQUID loop, and Q the quality factor of the resonator. The coupling between SQUID and resonator is determined by how much rf flux threads the SQUID ring if a given rf current flows in the resonator. Planar superconducting resonators can exhibit quality factors of several thousands to tens of thousands, if dielectric and radiation losses are small.

Both low-T_c [99] and high-T_c [100,101] rf SQUIDs integrated into a half-wavelength superconducting microstrip resonator have been demonstrated. Here, we describe only the representative layout for a low-T_c SQUID integrated into a $\lambda/2$ microstrip resonator, which is shown in Figure 4.15. Resonators which are most suitable for high-T_c rf SQUIDs are described in Chapter 6.

Low-T_c microstrip resonator SQUIDs were fabricated from thin niobium films sputtered onto 1-mm-thick sapphire substrates. Microstrip resonators made of 200 μm wide niobium strips with a resonator length of 20 mm exhibited a resonant frequency of about 3 GHz [99]. With a microstrip impedance of 80 Ω, unloaded Q's of up to 4500 were measured, reflecting mainly radiation losses and losses in the normal-conducting ground plane. Loading by the readout electronics reduced the Q to 1000–3000. The 100×100 μm^2 SQUID ring was integrated into the center of the resonator – see Figure 4.15. The optimum SQUID signal voltage was obtained when the bias frequency equaled the microstrip resonant frequency. Signal voltages of up to 160 μV/Φ_0 and a white noise of about $4{\times}10^{-6}$ $\Phi_0/\sqrt{\text{Hz}}$ could be measured for tunnel-junction SQUIDs. The calculated tank circuit noise was $6{\times}10^{-7}$ $\Phi_0/\sqrt{\text{Hz}}$ and the intrinsic SQUID noise was $1{\times}10^{-6}$ $\Phi_0/\sqrt{\text{Hz}}$.

Yet another possibility of realizing a tank circuit at higher frequencies is the use of a dielectric resonator. This usually consists of a cube or cylinder of dielectric material with high ε_r and low losses. It resembles a cavity resonator filled with dielectric, but with the outer conducting walls removed. The high ε_r keeps the electric field confined to the dielectric, but since the permeability μ_r of the dielectric is low, the magnetic field also penetrates the space outside of the resonator, so that it can couple to the SQUID. Dielectric resonators are commercially available and usually used to stabilize oscillators at ultra-high frequencies, or are used in bandpass filters. They have a high Q of up to 10^4, especially when cooled to lower temperatures. Such resonators were first used as tank circuits by Kornev *et al.* [102], who deposited a niobium rf SQUID directly onto a rutile cylinder of 3-mm diameter and 1-mm height. This rutile dielectric resonator had a resonant frequency of 10 GHz and was coupled to the readout electronics by placing it into a waveguide. One can also use $SrTiO_3$ substrates as dielectric resonators for high-T_c rf SQUIDs, as discussed in Chapter 6.

4.4.4
Coupling of the Tank Circuit to the Transmission Line

For rf SQUIDs operating at 30 MHz or below, the tank circuit can be coupled directly to the room temperature preamplifier by a low-capacitance coaxial cable. As already pointed out by Jackel *et al.* [103], with increasing bias frequency it becomes increasingly difficult to maintain high tank-circuit impedance, which is desirable for high sensitivity. This is mainly due to a relative increase in parasitic capacitances, and to a reduced real part R_{in} of the input impedance of the preamplifier used. A realistic value for R_{in} for FET amplifiers at 150 MHz is of the order of 5 kΩ, compared to an obtainable tank-circuit impedance of typically 30 kΩ. The low amplifier R_{in} reduces the tank circuit voltage V_T significantly when the amplifier is directly connected to the tank circuit. Additionally, an unmatched transmission line between tank circuit and amplifier introduces a high parasitic capacitance. For this reason, several additional coupling schemes have been proposed in the literature.

The use of a low-impedance coaxial cable ("coax") between the tank circuit and the amplifier, shown in Figure 4.16(a), is a popular approach. In order to reduce its parasitic capacitance and the loading of the tank circuit, the coax is given an electrical length of $\lambda/2$. In this case, the high impedance of the tank circuit is transferred to a high-impedance amplifier. Since, however, in most cases the amplifier R_{in} is smaller than that of the tank circuit, a somewhat shorter coax would lead to a better impedance match. We note that the use of an unmatched coaxial cable leads to a high standing-wave ratio along it. This leads to higher losses in the coaxial cable as compared to a coaxial cable with matched input and output, which increase with increasing intrinsic cable loss. This is usually relatively high, since in most cases a thin coax is used to minimize thermal input. For a coax with 1-dB intrinsic loss (measured with matched input and output), a total attenuation of 6 dB can result, which leads to a reduction in sensitivity by a factor of four! Also, for tank circuits of very high impedance $Z_T \approx R_T$ near resonance, the length of the coaxial cable has to be exactly $\lambda/2$ ($\pm$ a few ppm), which is very difficult to achieve. It seems advisable, therefore, to use additional coupling schemes which include a matched transmission line, rather than to connect it to the tank circuit directly. The coupling schemes

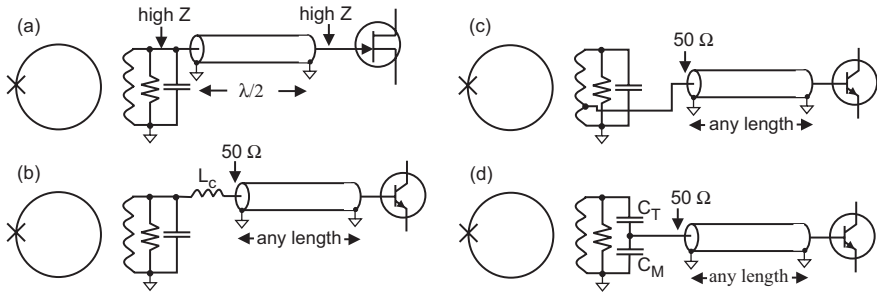

Fig. 4.16 Four variations of coupling the tank circuit via a coaxial cable to a room temperature preamplifier. See text for description.

can help in optimizing the condition $k^2Q \approx 1$ and provide matching to the line, while the virtue of the matched line itself is that all available signal power from this scheme is transferred to the amplifier. Matching can be achieved by several different schemes: Robbes *et al.* [104] have used a coil in series with the transmission line (Figure 4.16(b)), which can transform the high tank-circuit impedance to lower values. For optimum results, the inductance of the tank circuit coil must be adjusted, which is difficult, since it is at low temperature. Jackel *et al.* [103] used a tapped tank-circuit coil – see Figure 4.16(c) – which transforms the high tank-circuit impedance to a value of 50 Ω at the tap. Since it is difficult to tap the tank-circuit inductor used for a planar rf SQUID, He *et al.* avoided connecting the tank circuit galvanically to the transmission line [105]. Instead, they coupled L_T inductively to an additional low-inductance matching coil connected galvanically to the transmission line, so that only the high inductance tank coil was coupled to the SQUID.

The disadvantage of a tapped tank-circuit coil is that, with increasing bias frequency, stray inductances move the tap to higher inductance values, so that a 50-Ω impedance can no longer be obtained. For this reason, Duret *et al.* [106] developed a matching scheme using a capacitive voltage divider – see Figure 4.16(d). The capacitor C_T, in conjunction with the tank circuit inductance L_T, determines the resonant frequency of the circuit, whereas C_M determines the output impedance. One could achieve a nearly perfect impedance match (return loss > 20 dB) by choosing the proper ratio between C_T and C_M [107]. It was found that the actual value of C_M is not very critical. A return loss of >10 dB, which is sufficient, can be obtained for C_M varying by about 20%. For 150-MHz tank circuits with copper-wire coils, a ratio $C_M/C_T \approx 15$ gave optimum results. It should be noted that for quality factors of $Q > 200$ (e.g., when using a niobium coil with a low-T_c SQUID), matching by this technique becomes difficult. For tank circuits with superconducting coils, a resistor in parallel to the tank circuit can be used to reduce Q, although at the expense of increased tank-circuit noise.

An example of the coupling of a microwave SQUID with a microstrip resonator to the room-temperature electronics by a second microstrip on the substrate, or by a small wire antenna, was given in Section 4.4.3. Other examples of matching high-Q UHF and microwave resonators to the transmission line are given in Chapter 6.

4.4.5
Cryogenic Preamplifiers

The noise performance of rf SQUIDs can be improved by increasing their bias frequency, as discussed in Chapter 2. The intrinsic noise amplitude of the SQUID is proportional to $1/\sqrt{\omega_{rf}}$, whereas the transfer coefficient of the SQUID $\partial V_T/\partial \Phi_a$ is proportional to $\sqrt{\omega_{rf}}$. However, even at microwave frequencies, $\partial V_T/\partial \Phi_a$ is so small that the noise of the entire SQUID system is still likely to be limited by the noise of the room temperature preamplifier, at least in the case of a hysteretic mode of operation (for a dispersive mode, slight detuning of the tank circuit from resonance can provide very high $\partial V_T/\partial \Phi_a$, see Figure 2.26). In order to decrease this contribution to the overall noise, the preamplifier can be operated at cryogenic temperatures

[108–111]. At a temperature of 4.2 K or less (used for low-T_c SQUIDs) and for microwave amplification, only III–V semiconductor devices (made of, e.g., GaAs or InP) are suitable. Additionally, they offer the advantage of very low noise. Since a cooled preamplifier can be placed close to the SQUID, losses in the transmission line between SQUID and room-temperature electronics do not contribute to the system noise. This is particularly important at microwave frequencies, where thin coaxial cables can have considerable losses.

As an example we show in Figure 4.17 the circuit diagram of a cryogenic preamplifier developed by Mezzena *et al.* [112,113] for thin-film low-T_c rf SQUIDs operated at 1.7 GHz and 3 GHz. In order to achieve sufficient amplifier gain and to have the possibility of noise matching the amplifier, a two-stage version was used, where the input circuit could be tuned by two GaAs varactors. The power dissipation of this cryogenic preamplifier was of the order of 5 mW, which resulted in an additional helium evaporation of about 150 ml per day.

The active elements of the preamplifier were arranged in a cascade configuration and included a microwave hetero-junction FET and a dual-gate MESFET. The design was based on a cryogenic amplifier used in a 300-MHz SQUID system [111]. The cascade configuration was employed to reduce power dissipation and thus the junction temperature of the transistors. The gain of the preamplifer was 15 dB with input and output loaded with 50 Ω. A careful determination of the amplifier noise temperature led to a value of about 5 K. With this low preamplifier noise, the noise of the SQUID system was dominated only by intrinsic SQUID noise. Since the noise temperature of the rf SQUID is about four times its bath temperature, a cooled preamplifier noise temperature of about 20 K should be sufficient for rf SQUID systems operating at liquid helium temperatures.

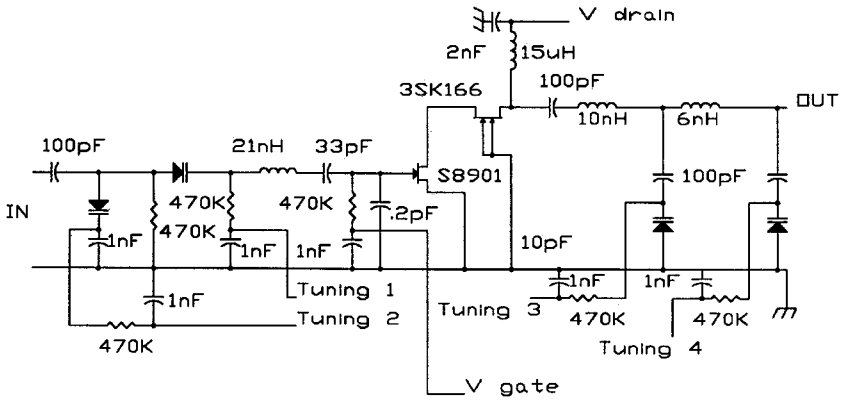

Fig. 4.17 Circuit diagram of a two-stage cryogenic preamplifier for use in rf SQUID systems with tunable input matching [from 112].

4.4.6 Optimization for Maximum Sensitivity

The sensitivity of an rf SQUID, in the absence of external noise, is limited by the sum of intrinsic noise, tank-circuit noise (inclusive transmission line) and preamplifier noise. In systems with low bias frequencies (e.g., 30 MHz) the system noise is limited by preamplifier and transmission-line noise. In order to reduce this noise contribution, the transfer coefficient $\partial V_T/\partial \Phi_a$ should be maximized. Here, we emphasize the hysteretic mode, where $\partial V_T/\partial \Phi_a$ cannot be maximized by detuning. Since $\partial V_T/\partial \Phi_a = (1-\alpha)\ \omega_{rf} L_T/(2M)$, where α is the rf I–V curve step tilting parameter [114] (see Chapter 6), it can be maximized by using the highest possible tank-circuit inductance and the lowest possible mutual inductance between SQUID and tank circuit, but without reducing k^2Q to below unity. To achieve a large L_T, the parasitic capacitance, e.g., of the transmission line to the room-temperature electronics, must be made as small as possible. A rather ingenious way to achieve this is to use a cooled field-effect transistor [115], which is employed as an impedance match between the tank circuit and a coaxial cable, rather than as an amplifier. A large L_T and small C_T additionally lead to a high tank-circuit Q in the case of a superconducting tank-circuit coil, which permits a reduction of M and a decrease in the tank-circuit noise. For low-T_c SQUIDs, the use of superconducting wire for the tank-circuit coil is advisable because of its intrinsic high Q and the absence of thermal magnetic noise. For high-T_c SQUIDs either planar superconducting tank-circuit coils, thin film resonators or dielectric substrate resonators should be used.

To give examples, we discuss two tank-circuit layouts, one with a 30 MHz bias frequency using discrete tank-circuit components, and a second where a 3-GHz microstrip resonator with an integrated SQUID is used.

In 30-MHz systems, widely used in the past, usually only the tank-circuit coil was at cryogenic temperatures. Since the bias frequency oscillator was crystal controlled, the tank-circuit capacitor was made variable to tune the resonant frequency of the tank circuit to the desired value. A low-capacitance coaxial cable connected the inductor and the room-temperature electronics. The tank-circuit was directly connected to a high-input-impedance rf amplifier. We assume that a thin-film rf SQUID with a loop size of 200 × 200 μm^2 (L = 400 pH) was used and the tank-circuit coil inductance $L_T \approx 500$ nH. This inductance required a capacitance of about 50 pF for a resonance frequency of 30 MHz and permitted the use of a coaxial cable with relatively high capacitance (say, 20 pF/m). Because of losses in the coaxial cable and the variable capacitor and of damping by the rf amplifier, the loaded quality factor of the tank circuit Q thus obtained is usually less than 100. In this example, we assume Q = 60. To obtain $k^2Q \approx 1$, the coupling between SQUID and tank-circuit coil should be chosen such that the mutual inductance, $M \approx 230$ pH. If pressing the wire-wound coil directly onto the SQUID gave too large a value of M, thin teflon pieces were inserted between the coil and the SQUID to adjust the coupling. With the parameters used, the SQUID transfer coefficient $\partial V_T/\partial \Phi_a = \omega_{rf} L_T/2M \approx 20\ \mu V/\Phi_0$ (we assume $\alpha \approx 0$). High input impedance amplifiers at 30 MHz have a typical input

voltage noise of $\sqrt{S_V} \approx 2$ nV/$\sqrt{\text{Hz}}$. Thus, the flux noise was about 10^{-4} $\Phi_0/\sqrt{\text{Hz}}$, a typical value for this type of rf SQUID system.

One might argue that by using a greater L_T, the modulation voltage could be increased and the resulting flux noise decreased, when operating in the hysteretic mode. There are, however, some limitations. If the rf amplifier is directly coupled to the tank circuit, the resistance of the tank circuit at resonance R_T must be much smaller than the input resistance of the amplifier R_{in} to avoid loading of the tank circuit by the amplifier. Also, thermal noise generated by the input resistance of the amplifier is coupled into the tank circuit, if $R_T \geq R_{in}$. In the example above, $R_T = Q\omega_{rf}L_T \approx 6$ kΩ. This is still lower than R_{in}, which is of the order of some tens of kΩ. Increasing L_T from 0.5 to 5 μH would increase V_T by a factor of about 3, since in order to keep $k^2Q \approx 1$, M is increased by a factor of three as well. At the same time, R_T will now be 60 kΩ, so that if $R_{in} = 30$ kΩ, only a fraction of V_T really develops across the tank circuit. It is not likely, therefore, that this system will have a lower flux noise than the one using $L_T = 500$ nH.

As a second example, we discuss a system with a 3-GHz rf SQUID integrated into a microstrip resonator. We assume that the resonator is a 100-μm wide, 20-mm long niobium strip on a 1-mm thick sapphire substrate ($\varepsilon_r \approx 10$, $L_T \approx 16$ nH). The loaded Q of such a resonator is assumed to be 1000. For $k^2Q \approx 1$, $M \approx 75$ pH. Thus, $\partial V_T/\partial \Phi_a \approx 9$ mV/Φ_0 across the tank circuit with $R_T \approx 320$ kΩ. This very high impedance has to be transformed to the input impedance of the rf amplifier, e.g., by using a coupling microstrip, such as the one shown in Figure 4.15. For a typical hetero-junction FET, at 3 GHz the real part of its input impedance $R_{in} \approx 200$ Ω. The resistance ratio thus is 320 kΩ/200 Ω = 1600 resulting in a voltage ratio of 40. The transfer coefficient of the SQUID at the preamplifier input is then 225 μV/Φ_0, and, assuming a noise temperature of the preamplifier of 70 K ($\sqrt{S_V} \approx 0.9$ nV/$\sqrt{\text{Hz}}$ at 200 Ω), a white flux noise of 4×10^{-6} $\Phi_0/\sqrt{\text{Hz}}$ results; a typical value measured in low-T_c rf SQUID systems at 3 GHz. We note that this flux-noise value is quite similar to that of a dc SQUID.

In the example above, there are two parameters which could be varied, Q and L_T. We could increase Q further by reducing losses in the substrate and radiation losses, and vary L_T by changing the width of the resonator or the thickness of the dielectric between resonator and ground plane. Assuming that k^2Q should be unity for maximum modulation voltage, we can write $\partial V_T/\partial \Phi_a \approx \omega_{rf}\sqrt{L_T Q}/(2\sqrt{L})$, again assuming $\alpha \approx 0$. This equation seems to imply $\partial V_T/\partial \Phi_a \propto \sqrt{L_T Q}$, but, on the other hand, $R_T \propto L_T Q$, and thus the voltage transformation ratio $V_{in}/V_T \propto \sqrt{R_{in}/R_T} \propto 1/\sqrt{L_T Q}$. So in principle the transformed transfer coefficient at the preamplifier input $\partial V_{in}/\partial \Phi_a$ is not dependent on the quality factor or the inductance of the tank circuit. One also would not expect this, because the signal energy at the input of the preamplifier V_{in}^2/R_{in} is a function only of the flux-dependent change in the energy dissipated in the SQUID, which should not depend on Q and L_T, but only on ω_{rf}.

We note that the above calculations assume that the optimum energy transfer from the SQUID to the amplifier occurs if $k^2Q = 1$. Although in some cases a larger k^2Q can lead to a larger V_T, usually the peaks of the triangular transfer coefficient are truncated, which might lead to an unstable operation of the flux-locked loop. It

was also assumed above, that the system noise is dominated by the preamplifier and transmission line, which is usually the case for rf SQUID systems using room-temperature preamplifiers, independent of the SQUID mode of operation, which may be hysteretic or dispersive.

4.4.7 Multiplexed Readouts for Multichannel rf SQUID Systems

With a growing number of channels in multichannel SQUID systems, some efforts have been made to reduce their size and complexity. Using discrete readout electronics for each channel can lead to a complex and expensive system, and to a troublesome alignment of each channel. In addition, the large number of wires between SQUIDs and the room-temperature electronics, up to four in the case of the dc SQUID (and two more if SQUID heaters are included), can lead to increased heat input and thus increased coolant loss. The individual wires of each channel must be properly screened to prevent cross-talk between channels.

In principle, some parts of the readout system, such as the amplifier and the phase detector, could be shared by all channels, if the signals from the individual SQUIDs can be distinguished from each other. However, nonlinearities in the amplifier, and especially in the detector, can give rise to mutual mixing, which makes the resulting output signals useless. Some interesting ideas have been published regarding this problem. Furukawa and Shirae [116] suggested a multichannel system where the sum of all channels modulates yet another SQUID, which then requires only one transmission line and amplifier to be read out. The response of the individual channels can be separated by individual phase detectors, but each SQUID still requires discrete wires to feed its feedback coil.

Another solution to this problem, readily applicable to a limited number of rf SQUID channels, is a serial readout of the channels instead of a parallel one [117]. Each SQUID is given a certain time window for operation, during which all other SQUIDs are switched off. Under these circumstances, only one readout and one transmission line are needed (theoretically) with the addition of a logic circuit which controls the on-off switching of the SQUIDs. Using LTS rf SQUIDs biased at around 100 MHz, a three-channel multiplexed system was demonstrated. The SQUIDs were biased at widely spaced frequencies (100, 121 and 140 MHz), and the SQUIDs turned on and off by switching the individual oscillators. The flux noise of the individual channels did not increase as a result of the multiplexed readout, and the slew rate of the system was sufficient to operate it in a low-interference unshielded environment.

Recently, Krause *et al.* have demonstrated a simplified three-channel rf SQUID system using serially-multiplexed readout suitable for applications in non-destructive evaluation [118]. For each HTS SQUID, they used higher individual bias frequencies (700 to 900 MHz), differing by 5 to 15 %. The relatively close spacing of channels was possible since the HTS coplanar tank circuits had high Qs.

4.5 Trends in SQUID Electronics

In the past decade, both rf and dc SQUID electronics have been improved considerably. Stimulated by the success of early high-T_c rf SQUIDs, practical techniques were developed to increase the bias frequency from the traditional values near 30 MHz up to $\gtrsim$1 GHz. Today, high-T_c rf SQUIDs with well-designed readout electronics can achieve noise levels comparable to those of their dc SQUID counterparts. For dc SQUIDs, the research and development activities concentrated on simplifying the readout electronics for multichannel applications and improving the dynamic performance for unshielded or high-frequency applications. Considerable increases in the slew rate and bandwidth were achieved by raising the modulation frequency from the traditional 100 kHz range up to some 10 MHz or by using direct readout without flux modulation. Today, the maximum FLL bandwidth of around 10 MHz is close to the limit given by the loop delay with room-temperature readout electronics. SQUIDs with cryogenic readout electronics or digital single-chip SQUIDs might achieve superior dynamic performance, but such devices are not yet ready for practical applications, representing a challenge and prospect for the future.

Another issue of growing importance is user friendliness. Until recently, many versions of readout electronics had to be controlled manually by operating a number of mechanical knobs. In order to obtain the best performance, a certain knowledge of the operational principle of the SQUID and the readout is then required. Efforts have been made recently to enable non-scientists to operate a SQUID successfully by performing all the necessary adjustments by means of a personal computer, DSP or microcontroller. The extensive use of digital circuits in the readout electronics allows one also a substantial increase in the dynamic range by using the flux-quanta counting method. The implementation of digital components, however, must be made in such a way as to prevent electromagnetic interference from coupling into the SQUID.

Many sets of SQUID electronics have been quite bulky. Particularly in the case of a multichannel system, the readout electronics should be as small as possible, and also should consume little electrical power. Nowadays, the use of surface-mounted electronic components makes possible a remarkable miniaturization, and – at the same time – can lead to a reduced power consumption and improved high-frequency behavior. The use of both digital circuits and surface-mounted components results in compact, fully automated, SQUID electronics which adjust the bias point of the SQUID even in a magnetically noisy environment without compromising the sensitivity.

References

1 Drung, D., Matz, H., Koch, H. (1995) A 5-MHz bandwidth SQUID magnetometer with additional positive feedback, *Rev. Sci. Instrum.* **66**, 3008–3015.

2 Nichols, D.G., Dantsker, E., Kleiner, R., Mück, M., Clarke, J. (1996) Linearity of high-T_c dc superconducting quantum interference device operated in a flux-locked loop, *J. Appl. Phys.* **80**, 6032–6038.

3 Beyer, J., Drung, D., Ludwig, F., Schurig, Th. (1999) Linearity of sensitive $YBa_2Cu_3O_{7-x}$ dc superconducting quantum interference device magnetometers, *J. Appl. Phys.* **86**, 3382–3386.

4 Kung, P.J., Bracht, R.R., Flynn, E.R., Lewis, P.S. (1996) A direct current superconducting quantum interference device gradiometer with a digital signal processor controlled flux-locked loop and comparison with a conventional analog feedback scheme, *Rev. Sci. Instrum.* **67**, 222–229.

5 Vrba, J. (1996) SQUID gradiometers in real environments, in Weinstock, H. (Ed.) *SQUID Sensors: Fundamentals, Fabrication and Applications*, NATO ASI Series E329. Dordrecht: Kluwer, pp. 117–178.

6 Zimmermann, E., Brandenburg, G., Clemens, U., Rongen, H., Halling, H., Krause, H.-J., Hohmann, R., Soltner, H., Lomparski, D., Grüneklee, M., Husemann, K.-D., Bousack, H., Braginski, A.I. (1997) HTS-SQUID magnetometer with digital feedback control for NDE applications, in Thompson, D.O., Chimenti, D.E. (Eds.) *Review of Progress in Quantitative Nondestructive Evaluation*, Vol. 16B. New York: Plenum, pp. 2129–2135.

7 Ludwig, C., Kessler, C., Steinfort, A.J., Ludwig, W. (2001) Versatile high performance digital SQUID electronics, *IEEE Trans Appl. Supercond.* **11**, 1122–1125.

8 Drung, D. (1997) Improved dc SQUID readout electronics with low 1/*f* noise preamplifier, *Rev. Sci. Instrum.* **68**, 4066–4074.

9 Forgacs, R.L., Warnick, A. (1967) Digital-analog magnetometer utilizing superconducting sensor, *Rev. Sci. Instrum.* **38**, 214–220.

10 Drung, D. (1996) Advanced SQUID read-out electronics, in Weinstock, H. (Ed.) *SQUID Sensors: Fundamentals, Fabrication and Applications*, NATO ASI Series E329. Dordrecht: Kluwer, pp. 63–116.

11 Koch, R.H., Rozen, J.R., Wöltgens, P., Picunko, T., Goss, W.J., Gambrel, D., Lathrop, D., Wiegert, R., Overway, D. (1996) High performance superconducting quantum interference device feedback electronics, *Rev. Sci. Instrum.* **67**, 2968–2976.

12 Fujimaki, N., Gotoh, K., Imamura, T., Hasuo, S. (1992) Thermal-noise-limited performance in single-chip superconducting quantum interference devices, *J. Appl. Phys.* **71**, 6182–6188.

13 Drung, D. (2002) High-performance dc SQUID read-out electronics, *Physica C* **368**, 134–140.

14 Wellstood, F., Heiden, C., Clarke, J. (1984) Integrated dc SQUID magnetometer with a high slew rate, *Rev. Sci. Instrum.* **55**, 952–957.

15 Giffard, R.P. (1980) Fundamentals for SQUID applications, in Hahlbohm, H.D., Lübbig, H. (Eds.) *Superconducting Quantum Interference Devices and their Applications*. Berlin: de Gruyter, pp. 445–471.

16 Seppä, H., Sipola, H. (1990) A high open-loop gain controller, *Rev. Sci. Instrum.* **61**, 2449–2451.

17 Ryhänen, T., Seppä, H., Cantor, R., Drung, D., Koch, H., Veldhuis, D. (1992) Noise studies of uncoupled dc SQUIDs, in Koch, H., Lübbig, H. (Eds.) *Superconducting Devices and Their Applications*. Berlin: Springer, pp. 321–325.

18 Tesche, C.D., Clarke, J. (1977) dc SQUID: noise and optimization, *J. Low Temp. Phys.* **27**, 301–331; Bruines, J.J.P., de Waal, V.J., Mooij, J.E. (1982) Comment on: "dc SQUID: noise and optimization" by Tesche and Clarke, *J. Low Temp. Phys.* **46**, 383–386.

19 Drung, D., Koch, H. (1993) An electronic second-order gradiometer for biomagnetic applications in clinical shielded rooms, *IEEE Trans. Appl. Supercond.* **3**, 2594–2597.

20 Seppä, H., Kiviranta, M., Satrapinski, A., Grönberg, L., Salmi, J., Suni, I. (1993) A coupled dc SQUID with low 1/*f* noise, *IEEE Trans. Appl. Supercond.* **3**, 1816–1819.

21 Drung, D., Dantsker, E., Ludwig, F., Koch, H., Kleiner, R., Clarke, J., Krey, S., Reimer, D., David, B., Doessel, O. (1996) Low noise $YBa_2Cu_3O_{7-x}$ SQUID magnetometers operated with additional positive feedback, *Appl. Phys. Lett.* **68**, 1856–1858.

22 Drung, D., Ludwig, F., Müller, W., Steinhoff, U., Trahms, L., Koch, H., Shen, Y.Q., Jensen, M.B., Vase, P., Holst, T., Freltoft, T., Curio, G. (1996) Integrated $YBa_2Cu_3O_{7-x}$ magnetometers for biomagnetic measurements, *Appl. Phys. Lett.* **68**, 1421–1423.

23 Seppä, H., Ahonen, A., Knuutila, J., Simola, J., Vilkman, V. (1991) dc-SQUID electronics based on adaptive positive feedback: experiments, *IEEE Trans. Magn.* **27**, 2488–2490.

24 Kiviranta, M., Seppä, H. (1995) dc SQUID electronics based on the noise cancellation scheme, *IEEE Trans. Appl. Supercond.* **5**, 2146–2148.

25 Seppä, H., Kiviranta, M., Grönberg, L. (1995) dc SQUID based on unshunted Josephson junctions: experimental results, *IEEE Trans. Appl. Supercond.* **5**, 3248–3251.

26 Clarke, J., Goubau, W.M., Ketchen, M.B. (1976) Tunnel junction dc SQUID: fabrication, operation, and performance, *J. Low Temp. Phys.* **25**, 99–144.

27 Ryhänen, T., Seppä, H., Ilmoniemi, R., Knuutila, J. (1989) SQUID magnetometers for low-frequency applications, *J. Low Temp. Phys.* **76**, 287–386.

28 Carelli, P., Foglietti, V. (1982) Behavior of a dc superconducting quantum interference device, *J. Appl. Phys.* **53**, 7592–7598.

29 Knuutila, J., Ahonen, A., Tesche, C. (1987) Effects on dc SQUID characteristics of damping of input coil resonances, *J. Low Temp. Phys.* **68**, 269–284.

30 Penny, R.D., Lathrop, D.K., Thorson, B.D., Whitecotton, B.R., Koch, R.H., Rosen, J.R. (1997) Wideband front end for high-frequency SQUID electronics, *IEEE Trans. Appl. Supercond.* **7**, 2323–2326.

31 Matlashov, A., Espy, M., Kraus, R.H., Ganther, K.R., Snapp, L.D. (2001) Electronic gradiometer using HTc SQUIDs with fast feedback electronics, *IEEE Trans Appl. Supercond.* **11**, 876–879.

32 Drung, D., Cantor, R., Peters, M., Scheer, H.J., Koch, H. (1990) Low-noise high-speed dc superconducting quantum interference device magnetometer with simplified feedback electronics, *Appl. Phys. Lett.* **57**, 406–408.

33 Testa, G., Pagano, S., Sarnelli, E., Calidonna, C.R., Mango Furnari, M. (2001) Improved superconducting quantum interference devices by resistance asymmetry, *Appl. Phys. Lett.* **79**, 2943–2945.

34 Drung, D., Koch, H. (1994) An integrated dc SQUID magnetometer with variable additional positive feedback, *Supercond. Sci. Technol.* **7**, 242–245.

35 Seppä, H. (1992) dc SQUID electronics based on adaptive noise cancellation and a high open-loop gain controller, in Koch, H., Lübbig, H. (Eds.) *Superconducting Devices and Their Applications.* Berlin: Springer, pp. 346–350.

36 Uehara, G., Matsuda, N., Kazami, K., Takada, Y., Kado, H. (1993) Asymmetric bias injection technique for Drung-type superconducting quantum interference devices, *Jpn. J. Appl. Phys.* **32**, L1735–L1738.

37 Drung, D., Bechstein, S., Franke, K.-P., Scheiner, M., Schurig, Th. (2001) Improved direct-coupled dc SQUID read-out electronics with automatic bias voltage tuning, *IEEE Trans Appl. Supercond.* **11**, 880–883.

38 Pizzella, V., Della Penna, S., Del Gratta, C., Romani, G.L. (2001) SQUID systems for biomagnetic imaging, *Supercond. Sci. Technol.* **14**, R79–R114.

39 Thomasson, S.L., Gould, C.M. (1995) 1 MHz bandwidth true NMR SQUID amplifier, *J. Low Temp. Phys.* **101**, 243–248.

40 TonThat, D.M., Clarke, J. (1996) Direct current superconducting quantum interference device spectrometer for pulsed nuclear magnetic resonance and nuclear quadrupole resonance at frequencies up to 5 MHz, *Rev. Sci. Instrum.* **67**, 2890–2893.

41 Seton, H.C., Hutchison, J.M.S., Bussell, D.M. (1997) A tuned SQUID amplifier for MRI based on a DOIT flux locked loop, *IEEE Trans Appl. Supercond.* **7**, 3213–3216.

42 Oukhanski, N., Stolz, R., Zakosarenko, V., Meyer, H.-G. (2002) Low-drift broadband directly coupled dc SQUID read-out electronics, *Physica C* **368**, 166–170.

43 Ukhansky, N.N., Gudoshnikov, S.A., Weidl, R., Dörrer, L., Seidel, P. (1997) A liquid-nitrogen-cooled preamplifier in connection with a high-T_c SQUID: direct readout and flux-locked loop with ac bias, in *Extended Abstracts of 6th International Superconductive Electronics Conference*, Vol. 3, Berlin, Germany, pp. 80–82.

44 Savo, B., Wellstood, F.C., Clarke, J. (1987) Low-frequency excess noise in Nb-Al_2O_3-Nb

Josephson tunnel junctions, *Appl. Phys. Lett.* **50**, 1757–1759.

45 Koelle, D., Kleiner, R., Ludwig, F., Dantsker, E., Clarke, J. (1999) High-transition-temperature superconducting quantum interference devices, *Rev. Mod. Phys.* **71**, 631–686.

46 Simmonds, M. B., Giffard, R. P. (1983) Apparatus for reducing low frequency noise in dc biased SQUIDs, U. S. Patent No. 4 389 612.

47 Koch, R.H., Clarke, J., Goubau, W.M., Martinis, J.M., Pegrum, C.M., Van Harlingen, D.J. (1983) Flicker (1/*f*) noise in tunnel junction dc SQUIDs, *J. Low Temp. Phys.* **51**, 207–224.

48 Foglietti, V., Gallagher, W.J., Ketchen, M.B., Kleinsasser, A.W., Koch, R.H., Raider, S.I., Sandstrom, R.L. (1986) Low-frequency noise in low 1/*f* noise dc SQUIDs, *Appl. Phys. Lett.* **49**, 1393–1395.

49 Foglietti, V., Gallagher, W.J., Koch, R.H. (1987) A novel modulation technique for 1/*f* noise reduction in dc SQUIDs, *IEEE Trans. Magn.* **23**, 1150–1153.

50 Kuriki, S., Matsuda, M., Matachi, A. (1988) Effects of alternating bias current on the low-frequency noise in dc SQUIDs, *J. Appl. Phys.* **64**, 239–241.

51 Drung, D., Crocoll, E., Herwig, R., Neuhaus, M., Jutzi, W. (1989) Measured performance parameters of gradiometers with digital output, *IEEE Trans. Magn.* **25**, 1034–1037.

52 Dössel, O., David, B., Fuchs, M., Kullmann, W.H., Lüdeke, K.-M. (1991) A modular low noise 7-channel SQUID-magnetometer, *IEEE Trans. Magn.* **27**, 2797–2800.

53 Drung, D. (1995) Low-frequency noise in low-T_c multiloop magnetometers with additional positive feedback, *Appl. Phys. Lett.* **67**, 1474–1476.

54 Higuchi, M., Kawai, J., Adachi, Y., Uehara, G., Kado, H. (2001) A new-type flux locked loop circuit with bias current modulation scheme, in *Extended Abstracts of 8th International Superconductive Electronics Conference*, Osaka, Japan, pp. 189–190.

55 Zhang, Y., Wolters, N., Otto, R., Krause, H.-J. (2002) Non-constant bias current for dc SQUID operation, *Physica C* **368**, 181–184.

56 Lam Chok Sing, M., Dolabdjian, C., Gunther, C., Bloyet, D., Certenais, J. (1996) A formal presentation and comparative study of low-frequency noise reduction techniques for direct current superconducting quantum interference devices, *Rev. Sci. Instrum.* **67**, 796–804.

57 Gershenson, M. (1991) Design of a hysteretic SQUID as the readout for a dc SQUID, *IEEE Trans. Magn.* **27**, 2910–2912.

58 Podt, M., van Duuren, M.J., Hamster, A.W., Flokstra, J., Rogalla, H. (1999) Two-stage amplifier based on a double relaxation oscillation superconducting quantum interference device, *Appl. Phys. Lett.* **75**, 2316–2318.

59 Wellstood, F.C., Urbina, C., Clarke, J. (1987) Low-frequency noise in dc superconducting quantum interference devices below 1 K, *Appl. Phys. Lett.* **50**, 772–774.

60 Foglietti, V. (1991) Double dc SQUID for flux-locked-loop operation, *Appl. Phys. Lett.* **59**, 476–478.

61 Maslennikov, Yu.V., Beljaev, A.V., Snigirev, O.V., Kaplunenko, O.V., Mezzena, R. (1995) A double dc SQUID based magnetometer, *IEEE Trans. Appl. Supercond.* **5**, 3241–3243.

62 Welty, R.P., Martinis, J.M. (1993) Two-stage integrated SQUID amplifier with series array output, *IEEE Trans. Appl. Supercond.* **3**, 2605–2608.

63 Foglietti, V., Giannini, M.E., Petrocco, G. (1991) A double dc SQUID device for flux locked loop operation, *IEEE Trans. Magn.* **27**, 2989–2992.

64 Welty, R.P., Martinis, J.M. (1991) A series array of dc SQUIDs, *IEEE Trans. Magn.* **27**, 2924–2926.

65 Stawiasz, K.G., Ketchen, M.B. (1993) Noise measurements of series SQUID arrays, *IEEE Trans. Appl. Supercond.* **3**, 1808–1811.

66 Huber, M.E., Neil, P.A., Benson, R.G., Burns, D.A., Corey, A.M., Flynn, C.S., Kitaygorodskaya, Y., Massihzadeh, O., Martinis, J.M., Hilton, G.C. (2001) dc SQUID series array amplifiers with 120 MHz bandwidth, *IEEE Trans. Appl. Supercond.* **11**, 1251–1256.

67 Irwin, K.D., Huber, M.E. (2001) SQUID operational amplifier, *IEEE Trans. Appl. Supercond.* **11**, 1265–1270.

68 Carelli, P., Castellano, M.G., Flacco, K., Leoni, R., Torrioli, G. (1997) An absolute magnetometer based on dc superconducting quantum interference devices, *Europhys. Lett.* **39**, 569–574.

69 Häussler, Ch., Oppenländer, J., Schopohl, N. (2001) Nonperiodic flux to voltage conversion of series arrays of dc superconducting quan-

tum interference devices, *J. Appl. Phys.* **89**, 1875–1879.

70 Schultze, V., IJsselsteijn, R., Meyer, H.-G., Oppenländer, J., Häussler, Ch., Schopohl, N. (2003) High-T_c superconducting quantum interference filters for sensitive magnetometers, to appear in *IEEE Trans. Appl. Supercond.* **13**.

71 Adelerhof, D.J., Nijstad, H., Flokstra, J., Rogalla, H. (1994) (Double) relaxation oscillation SQUIDs with high flux-to-voltage transfer: simulations and experiments, *J. Appl. Phys.* **76**, 3875–3886.

72 Vernon, F.L., Pedersen, R.P. (1968) Relaxation oscillations in Josephson junctions, *J. Appl. Phys.* **39**, 2661–2664.

73 Gutmann, P. (1979) dc SQUID with high energy resolution, *Electr. Lett.* **15**, 372–373.

74 Gudoshnikov, S.A., Maslennikov, Yu.V., Semenov, V.K., Snigirev, O.V., Vasiliev, A.V. (1989) Relaxation-oscillation-driven dc SQUIDs, *IEEE Trans. Magn.* **25**, 1178–1181.

75 Mück, M., Rogalla, H., Heiden, C. (1988) A frequency-modulated read-out system for dc SQUIDs, *Appl. Phys. A* **47**, 285–289.

76 Mück, M., Heiden, C. (1989) Simple dc SQUID system based on a frequency modulated relaxation oscillator, *IEEE Trans. Magn.* **25**, 1151–1153.

77 Gudoshnikov, S.A., Kaplunenko, O.V., Maslennikov, Yu.V., Snigirev, O.V. (1991) Noise in relaxation-oscillation-driven dc SQUIDs, *IEEE Trans. Magn.* **27**, 2439–2441.

78 Adelerhof, D.J., Kawai, J., Uehara, G., Kado, H. (1995) High sensitivity double relaxation oscillation superconducting quantum interference devices with large transfer from flux to voltage, *Rev. Sci. Instrum.* **66**, 2631–2637.

79 Kawai, J., Uehara, G., Higuchi, M., Ogata, H., Kado, H. (2001) Multi-loop relaxation oscillation SQUID magnetometers with large flux-to-voltage transfer functions, *IEEE Trans. Appl. Supercond.* **11**, 1247–1250.

80 Lee, Y.H., Kim, J.M., Kwon, H.C., Park, Y.K., Park, J.C., van Duuren, M.J., Adelerhof, D.J., Flokstra, J., Rogalla, H. (1995) 3-channel double relaxation oscillation SQUID magnetometer system with simple readout electronics, *IEEE Trans. Appl. Supercond.* **5**, 2156–2159.

81 Lee, Y.-H., Kwon, H., Kim, J.-M., Park, Y.-K. (2001) Multichannel applications of double relaxation oscillation SQUIDs, *Supercond. Sci. Technol.* **14**, 1022–1026.

82 Drung, D. (1986) Digital feedback loops for dc SQUIDs, *Cryogenics* **26**, 623–627.

83 Fujimaki, N., Tamura, H., Imamura, T., Hasuo, S. (1988) A single-chip SQUID magnetometer, *IEEE Trans. Electron Devices* **35**, 2412–2418.

84 Radparvar, M. (1994) A wide dynamic range single-chip SQUID magnetometer, *IEEE Trans. Appl. Supercond.* **4**, 87–91.

85 Radparvar, M., Rylov, S. (1995) An integrated digital SQUID magnetometer with high sensitivity input, *IEEE Trans. Appl. Supercond.* **5**, 2142–2145.

86 Yuh, P.-F., Rylov, S.V. (1995) An experimental digital SQUID with large dynamic range and low noise, *IEEE Trans. Appl. Supercond.* **5**, 2129–2132.

87 Fath, U., Hundhausen, R., Fregin, T., Gerigk, P., Eschner, W., Schindler, A., Uhlmann, F.H. (1997) Experimental digital SQUID with integrated feedback circuit, *IEEE Trans. Appl. Supercond.* **7**, 2747–2751.

88 Radparvar, M., Rylov, S.V. (1997) High sensitivity digital SQUID magnetometers, *IEEE Trans. Appl. Supercond.* **7**, 3682–3685.

89 Gupta, D., Radparvar, M. (2001) Subranging digital SQUID ammeter, *IEEE Trans. Appl. Supercond.* **11**, 1261–1264.

90 Likharev, K.K., Semenov, V.K. (1991) RSFQ logic/memory family: A new Josephson-junction technology for sub-THz-clock-frequency digital systems, *IEEE Trans. Appl. Supercond.* **1**, 3–28.

91 Semenov, V.K., Polyakov, Yu.A. (1997) Fully integrated digital SQUID, in *Extended Abstracts of 6th International Superconductive Electronics Conference*, Vol. 2, Berlin, Germany, pp. 329–331.

92 Podt, M., Mieog, A.J., Flokstra, J., Rogalla, H. (2001) Numerical analysis of the smart DROS, *Physica C* **350**, 193–200.

93 Podt, M., Mieog, A.J., Flokstra, J., Rogalla, H. (2001) Design of a fast digital double relaxation oscillation SQUID, *IEEE Trans. Appl. Supercond.* **11**, 1235–1238.

94 Zimmerman, J.E., Silver, A.H. (1966) Macroscopic quantum interference effects through superconducting point contacts, *Phys. Rev.* **141**, 367–375.

95 Mück, M. (1992) A readout electronics for 3 GHz rf SQUIDs, *Rev. Sci. Instrum.* **63**, 2268–2273.

96 Simacek, I., Zrubec, V., Skakala, M. (1993) rf SQUID magnetometer with simplified circuitry, *Rev. Sci. Instrum.* **64**, 2401–2402.

97 Kamper, R.A., Simmonds, M.B. (1972) Broadband superconducting quantum magnetometer, *Appl. Phys. Lett.* **20**, 270–272.

98 Hollenhorst, J.N., Giffard, R.P (1979) High sensitivity microwave SQUID, *IEEE Trans. Magn.* **15**, 474–477.

99 Mück, M., Heiden, C. (1992) Planar microwave biased rf SQUIDS, *Appl. Phys.* **A54**, 475–479.

100 Zhang, Y., Mück, M., Bode, M., Herrmann, K., Schubert, J., Zander, W., Braginski, A.I., Heiden, C. (1992) Microwave SQUIDs with integrated YBCO resonator, *Appl. Phys. Lett.* **60**, 2303–2305.

101 Fontana, G., Mezzena, R., Vitale, S., Cerdonio, M., Mück, M., Hallmanns, G., Heiden, C. (1993) rf SQUIDs for application in a gravitational wave detector, in *Proceedings of the Workshop on Cryogenic Gravitational Wave Antennae, Legnaro* (unpublished).

102 Kornev, V.K., Likharev, K.K., Snigirev, O.V., Soldatov, Ye.S., Khanin, V.V. (1980) Microwave SQUID with a high-Q dielectric resonator, *Radio Engineering and Electronic Physics* **25**, 2647–2655 (in Russian).

103 Jackel, L.D., Stoeckenius, J.W.H., Epworth, R.W. (1978) Analysis and operation of UHF SQUID with tapped tank circuit, *J. Appl. Phys.* **49**, 471–472.

104 Robbes, D., Dubuc, C., Lepaisant, J., Bloyet D., Duret, D. (1985) Impedance matching of an rf SQUID to a standard transmission line, *IEEE Trans. Magn.* **21**, 892–895.

105 He, D.F., Zeng, X.H., Krause, H.-J., Soltner, H., Rüders, F., Zhang, Y. (1998), Radio frequency SQUIDs operating at 77 K with 1 GHz lumped-element tank circuits, *Appl. Phys. Lett.* **72**, 969–971.

106 Duret, D., Bernard, P., Zenatti, D. (1975) A UHF superconducting magnetometer utilizing a new thin film sensor, *Rev. Sci. Instrum.* **46**, 474–480.

107 Zhang, Y., Mück, M., Herrmann, K., Schubert, J., Zander, W., Braginski, A.I., Heiden, C. (1992) Low noise $YBa_2Cu_3O_7$ rf SQUID magnetometer, *Appl. Phys. Lett.* **60**, 645–647.

108 Gaerttner, M.R. (1974) in *Int. Mag. Conf. Toronto, Publ. No. 74 CHO 852-4-MAG*. New York: IEEE.

109 Long, A.P., Prance, R.J., Clark, T.D., Mutton, J.E., Potts, M.W., Widom, A., Goodall, F. (1980) Quantum limited ac-biased SQUID magnetometer, in Hahlbohm, H.D., Lübbig, H. (Eds.) *Superconducting Quantum Interference Devices and their Applications*. Berlin: de Gruyter, pp. 207–211.

110 Ahola, H., Ehnholm, G.J., Östman, P., Rantala, B. (1979) Cryogenic GaAs-FET amplifiers for SQUIDs, *J. Low Temp. Phys.* **35**, 313–328.

111 Cavalleri, A., Cerdonio, M., Fontana, G., Jung, G., Machietta, R., Mezzena, R., Vitale S., Zendri, J.P. (1992) UHF thin film rf SQUID magnetometer with a cryogenic preamplifier employing a high-electron mobility transistor, *Rev. Sci. Instrum.* **63**, 5403–5407.

112 Mück, M., Hallmanns, G., Heiden, C., Cerdonio, M., Fontana, G., Mezzena, R., Vitale, S. (1992) Planar microwave biased rf SQUIDs with a cryogenic preamplifier, *Appl. Phys. Lett.* **61**, 1231–1233.

113 Fontana, G., Mezzena, R., Vitale, S., Cerdonio, M., Mück, M., Hallmanns, G., Heiden, C. (1993) Improved sensitivity of planar microwave biased rf SQUIDs using a cryogenic HEMT amplifier, *IEEE Trans. Appl. Supercond.* **3**, 1820–1823.

114 Jackel, L.D., Buhrman, R.A. (1975) Noise in the rf SQUID, *J. Low Temp. Phys.* **19**, 201–246.

115 Goodkind, J.M., Stolfa, D.L. (1970) The superconducting magnetic flux detector, *Rev. Sci. Instrum.* **41**, 799–807.

116 Furukawa, H., Shirae, K. (1989) Multichannel dc SQUID system, *Jpn. J. Appl. Phys.* **28**, L456–458.

117 Mück, M. (1991) A Three-channel SQUID-system with multiplexed readout, *IEEE Trans. Magn.* **27**, 2986–2989.

118 Krause, H.J., Gärtner, S., Wolters, J., Hohmann, R., Wolf, W., Schubert, J., Zander, W., Zhang, Y., Kreutzbruck, M., Mück, M. (2001) Multiplexed SQUID array for non-destructive evaluation of aircraft structures, *IEEE Trans. Appl. Supercond.* **11**, 1168–1171.

5
Practical DC SQUIDS: Configuration and Performance

Robin Cantor and Dieter Koelle

5.1 Introduction

Jaklevic *et al.* [1] first observed quantum interference in a dc SQUID made of films of Pb and Sn. Since tunnel junctions made of soft superconductors tend to be short-lived, shortly afterwards, there were attempts to develop alternative technologies that were perceived as being less fragile. The point contact junction [2] was an early invention that was used for many years, and is found even today in undergraduate laboratories. This junction involves pressing the sharpened end of a piece of niobium wire or a niobium screw against a niobium surface, and adjusting the force to achieve the desired critical current. An early dc SQUID made in this way is shown in Figure 5.1.

Shortly afterwards came the invention of the SLUG (Superconducting Low-Inductance Undulatory Galvanometer), shown in Figure 5.2 [3]. The SLUG consisted of a bead of PbSn solder frozen around a length of Nb wire. The *I–V* characteristic, measured between the solder and the wire, showed Josephson-like behavior; in addition,

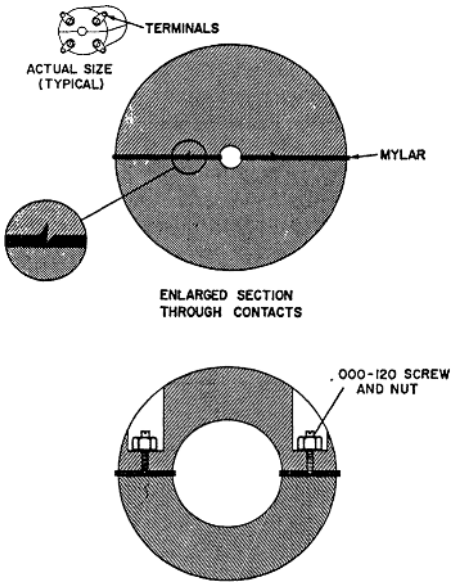

Fig. 5.1 Drawing of point contact dc SQUID (reprinted with permission from ref. [2].)

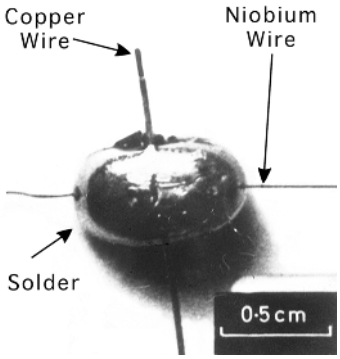

Fig. 5.2 SLUG (courtesy of John Clarke).

the critical current was periodic in a current passed along the Nb wire, often with more than one periodicity. This behavior implied that the Josephson current was carried by a small number of contacts between the solder and the wire. The current along the wire produced a magnetic field within the penetration depths of the wire and the solder, thus modulating the critical current. This device was used chiefly as a voltmeter, with a noise level as low as $10\,\mathrm{fV} \cdot \mathrm{Hz}^{-1/2}$. Connecting the ends of the Nb wire to make a superconducting loop produced a magnetometer – and demonstrated the great utility of the flux transformer [4].

These early devices were far from being ideally coupled to the readout electronics, which in retrospect meant that they did not realize their full potential. The introduction of the rf SQUID [5] – requiring only a single junction – led to the first commercially available SQUIDs, and in the early 1970's these were much more widely used than their dc counterparts. The scene shifted again, however, with the introduction of the cylindrical dc SQUID [6], shown in Figure 5.3. This device consisted of a 3-mm diameter fused quartz tube on which Nb-NbO_x-PbIn junctions were grown – patterned with shadow masks – and connected to a thin-film PbIn cylinder. The SQUID was optimally coupled to the room temperature amplifier via a cold resonant circuit. The flux noise, $3.5 \times 10^{-5}\ \Phi_0\text{-Hz}^{-1/2}$, was not strikingly low by today's standards, but the large area of the SQUID loop corresponded to a magnetic field noise of $10\,\mathrm{fT} \cdot \mathrm{Hz}^{-1/2}$ – that was white at frequencies down to 0.02 Hz. This development was followed shortly afterwards by the theory for noise in the dc SQUID [7] which showed that the intrinsic noise was much lower than that of rf SQUIDs operated at tens of megahertz. The next step in the development of thin-film dc SQUIDs was the planar square washer design with an integrated, multi-turn input coil (Figure 5.6) [8]. Combined with the Nb-AlO_x-Nb tunnel junction [9], this configuration is the dc SQUID of choice today, and is manufactured on Si wafers in batches of hundreds. The essential features of this device have changed little over the past two decades.

The appearance of high-T_c superconductivity focused attention on the development of dc SQUIDs based on YBCO. The first such device [10] involved grain boundary junctions formed between randomly oriented grains in the film. Most subsequent devices have relied on rather more controlled grain boundary junctions

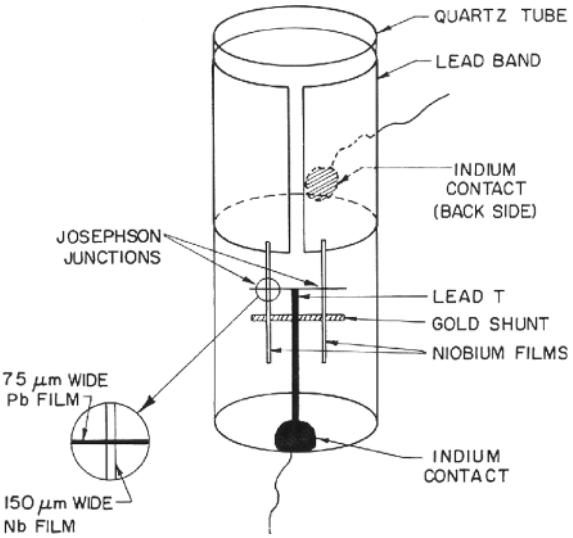

Fig. 5.3 Schematic representation of cylindrical dc SQUID (reprinted with kind permission of Kluwer Academic Publishers from ref. [6]).

formed by growing YBCO epitaxially on either a bicrystal [11] or a step-edge patterned in the substrate [12]. However, devices have been made successfully with ramp-edge junctions, too [13]. Another early development was the YBCO-$SrTiO_3$-YBCO multilayer technology [14] – with insulating crossovers and superconducting vias – required to make integrated high-T_c SQUIDs. As with low-T_c SQUIDs, it is necessary to couple a superconducting flux transformer to the SQUID to increase its effective area and thus achieve low-noise magnetometers. There are two basic approaches. The lowest magnetic field noise is achieved with a planar, multilayer flux transformer in which a single-turn pickup loop is connected to a multi-turn coil that is either integrated with the SQUID – as with low-T_c devices – or alternatively made on a separate substrate that is pressed against the SQUID in a flip-chip arrangement. The second approach involves a single-layer technology in which a relatively large pickup loop – say 10 mm across – injects current into the body of the SQUID. This "directly coupled magnetometer" is considerably simpler to fabricate than the multilayer devices, but its white magnetic field noise is high because of the inductive mismatch between the pickup loop and the SQUID. On the other hand, the multilayer devices have a higher level of $1/f$ noise at low frequencies, so that at 1 Hz the difference in performance of the two kinds of device may not be very significant.

In the remainder of this chapter, the basic elements of dc SQUID design for practical applications are discussed. Both LTS and HTS design considerations and practical examples are presented. The discussion starts with a brief review of basic dc SQUID operation and the optimization of a simple, uncoupled or "bare" dc SQUID design. This discussion forms the foundation for the subsequent overview of the key design issues and optimization procedures for coupled dc SQUIDs. Several practical

examples are described, including thin-film magnetometers and gradiometers as well as the design of wire-wound pickup coils for magnetometer and gradiometer applications. The chapter concludes with two sections on special effects that can cause a deterioration of the performance of practical dc SQUIDs. We focus on the discussion of low-frequency $1/f$ noise and operation in an ambient magnetic field, which is a much bigger problem for high-T_c than for low-T_c SQUIDs. In addition, we give a brief discussion of hysteresis, the effects of rf interference, and finally, of the effect of temperature fluctuations and drift.

5.2
Basic dc SQUID Design

5.2.1
Uncoupled SQUIDs

For the reader's convenience, we first summarize the basics of dc SQUIDs discussed in Chapters 1 and 2. An uncoupled or "bare" dc SQUID consists of two resistively-shunted Josephson junctions connected in parallel within a superconducting loop and biased by an external dc source, as shown in Figure 5.4. The SQUID may be current biased or voltage biased depending on the readout technique used (see Chapter 4). Each Josephson junction may be represented by the resistively-shunted-junction (RSJ) model, consisting of an ideal Josephson junction with maximum supercurrent I_0, capacitance C and shunt resistance R. The inductance of the SQUID loop is L. A lumped circuit element model (equivalent circuit) of the dc SQUID is shown in Figure 5.5.

An important figure of merit for dc SQUIDs is the noise energy per unit bandwidth, commonly referred to as the energy resolution, defined as $\varepsilon = S_\Phi(f)/(2L)$, where the flux power spectral density is given by $S_\Phi(f) = S_V(f)/(\partial V/\partial \Phi_a)^2$. Here, $S_V(f)$ is the spectral density of the voltage noise power across the SQUID and $\partial V/\partial \Phi_a$ is the flux-to-voltage transfer function. Its optimum value is $|\partial V/\partial \Phi_a|_{max} = V_\Phi$.

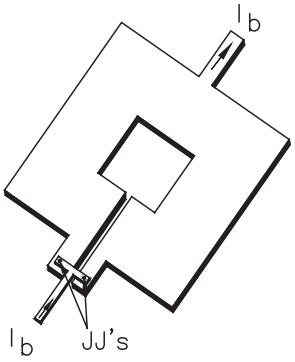

Fig. 5.4 Model layout of a dc SQUID. The SQUID inductance is shaped in the form of a square washer with a hole in the center and slit to the outer edge where the two Josephson junctions (JJ's) are located. The SQUID is biased using a dc current I_b.

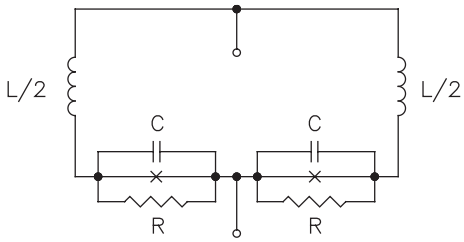

Fig. 5.5 A lumped circuit element representation of a dc SQUID.

As discussed in Chapters 1 and 2, the dynamics of the SQUID are determined by two key parameters. The modulation parameter $\beta_L = 2LI_0/\Phi_0$ is a measure of the modulation depth of the maximum zero-voltage current as a function of the applied flux. For $\beta_L >> 1$, the modulation depth is very much smaller than $2I_0$, while for $\beta_L << 1$, the modulation depth approaches the limit $2I_0$. The Stewart-McCumber parameter $\beta_c = (2\pi/\Phi_0)\, I_0 R^2\, C$ is a measure of the damping of the Josephson junctions. For $\beta_c \leq 0.7$, the SQUID current-voltage (I–V) characteristics are non-hysteretic and the average voltage across the SQUID for a given applied flux is single valued. For $\beta_c > 0.7$, the I–V characteristics are hysteretic, although the experimentally measured characteristics may appear to be single-valued owing to smearing caused by thermal noise [15]. Hysteresis leads to excess noise and a degradation of the energy resolution. Based on simulations [15], the optimal energy resolution in the low-fluctuation limit is obtained roughly for $\beta_c \sim 1$, in which case $\varepsilon \approx 12 k_B T \sqrt{LC}$. This is about 25 % less than that predicted by simulations carried out assuming that the junctions are over-damped with $\beta_c << 1$, where the nearly unlimited bandwidth increases the mixing-down effect of noise and $\varepsilon \approx 16 k_B T \sqrt{LC}$.

Based on the above considerations, the design of an uncoupled dc SQUID for a given operating temperature T is, in principle, straightforward: the SQUID inductance and junction capacitance should be made as small as possible, consistent with the available process technology. In practice, neither may be made arbitrarily small, however. It is difficult to make the SQUID inductance much smaller than 10 pH, and LTS fabrication technology limits the minimum junction capacitance that can be achieved typically to 0.5 to 1 pF. Once L is chosen, the condition that $\beta_L = 1$ determines the critical current. This value along with the junction capacitance and the condition that $\beta_c \leq 0.7$ determines the shunt resistance R. Thus, all of the SQUID parameters are defined.

One complication is the possibility of a strong LC resonance in the SQUID dynamics [15]. Resistive damping may be used to improve performance in situations where the LC resonance is too strong or unavoidable (see Section 5.2.2). Also, excess $1/f$ noise may be observed if very small junctions are used, as shown by Savo *et al.* [16]. They noted that $1/f$ noise scales as $I_0/A_J^{1/2}$, where A_J is the junction area, suggesting that larger junction sizes should be preferable for low-frequency SQUID applications. Increasing the junction size in order to reduce excess $1/f$ noise necessarily requires a junction fabrication process with low j_0, typically of the order of

100 A/cm^2 for SQUID applications. The low j_0 requirement is contrary to what one would expect based on the expression for the energy resolution, since, for $\beta_L = \beta_c = 1$, it can be shown that $\varepsilon \propto \sqrt{L/j_0}$.

Although the small inductance of uncoupled SQUIDs leads to a small effective flux capture area and poor magnetic field resolution, the spatial resolution can be very good. For example, bare SQUIDs have been used to build SQUID-based microscopes capable of producing high-resolution magnetic images of a variety of samples. Configured as a two-loop gradiometer (see Section 5.4.2), miniature susceptometers have been developed to study the behavior of minute magnetic particles. Aside from these specialized applications, which are discussed in more detail in Section 5.3.2 and Section 5.4.2, a means of coupling the external signal to the SQUID inductance is generally required. For a bare SQUID, the simplest approach is to extend the area of the loop without increasing the inductance, and to use the flux-focusing properties of a large washer structure such as is shown in Figure 5.4 [17]. This approach has been used to fabricate HTS devices, for example. However, it is much less effective than the flux transformer discussed in the next section.

5.2.2 Coupled SQUIDs

To improve the magnetic field resolution, a separate pickup loop, having a much larger flux capture area than the bare SQUID, may be flux-transformer-coupled to the SQUID inductance via a multi-turn spiral input coil. Tight coupling is obtained by patterning the SQUID inductance in the shape of a washer with a multi-turn input coil integrated on top, as shown in Figure 5.6 [18]. Useful expressions to calculate the inductance of the input coil, L_i, and the mutual inductance of the input coil with respect to the SQUID, M_i, are given in Table 5.1. If the input flux transformer circuit (e.g., the input coil and pickup loop) forms a closed superconducting circuit,

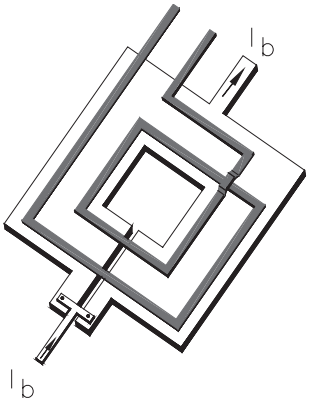

Fig. 5.6 Model layout of a dc SQUID with integrated input coil. For simplicity, only two turns of the coil are drawn ($N = 2$); practical N values are much higher.

the effective SQUID inductance will be smaller (typically 40 % to 50 %) than the inductance calculated using the SQUID washer dimensions owing to screening effects by the flux transformer circuit. The effective or "screened" SQUID inductance is often denoted by L_{dc}; an expression for the screened inductance is given in Table 5.1. Similarly, the SQUID inductance screens the input coil, resulting in an effective input coil inductance, $L_{i,eff}$, that is somewhat smaller (typically around 10 % to 20 %) than L_i (see Table 5.1).

Although excellent coupling can be achieved, the integrated thin-film coil introduces a parasitic capacitance C_p across the SQUID inductance that can lead to a degradation of the energy resolution [19]. Furthermore, the input coil and SQUID washer as groundplane form a microwave transmission line (a microstrip) that can have high-Q resonances near the frequency corresponding to the optimal SQUID working point. The transmission line resonance is either a half-wavelength or quarter-wavelength resonance depending on whether the inner end of the input coil is floating or grounded to the washer. Note that, as the frequency of the input signal becomes greater than the transmission line resonant frequency (typically a few GHz), the phase of the input signal between consecutive turns in the input coil eventually reverses, thereby decoupling the input circuit from the SQUID [20,21].

The Q-value of the half-wavelength resonance of the washer is also enhanced by the groundplane effect of the multi-turn input coil [19]. These high-Q resonances affect the SQUID dynamics and produce strong irregularities in the I–V and V–Φ characteristics, leading to increased noise and making it difficult to find a suitable working point for the SQUID [19,22]. Thus, it is essential that the microwave resonances and parasitic capacitance be properly taken into account in designing SQUIDs with integrated coupling circuits.

It has been demonstrated that the input circuit resonance can be damped in a nearly noise-free manner by the insertion of a series R_xC_x shunt across the input coil [23]. The resonance of the microstrip line is suppressed by preventing reflections at the "open" end of the line as it leaves the washer. The reflection coefficient is given by $\Gamma_r = (Z_L - Z) / (Z_L + Z)$, where Z_L is the impedance of the termination at the end of the stripline and Z is the nominal impedance of the transmission line. The shunt resistor R_x is matched to the nominal transmission line impedance, which properly terminates the stripline and inhibits the microstripline resonance, and the shunt capacitor C_x fixes the resonant frequency of the input circuit at 10 to 100 MHz. In addition, C_x effectively blocks the injection of low-frequency noise currents due to R_x into the SQUID input circuit. The Q-value of the input circuit resonance is determined by the R_xC_x shunt. In practice, typical values for R_x (a few Ohms) and C_x (of the order of 100 pF) lead to a moderate Q (2 to 4), which ensures that the resonance is well damped but not over-damped to prevent the Josephson oscillations from mixing noise due to R_x down to low frequencies.

It has also been shown that the insertion of a damping resistor R_d across the SQUID inductance can improve noise performance [24,25]. For $R_d = R$, the additional resistor effectively damps the washer resonance and smoothes the SQUID characteristics, leading to an enhancement of the transfer function and reduced noise [15]. The microstripline resonances, however, will still be present. The

improvement is also partially offset by the additional flux noise arising from the current noise of the damping resistor R_d. Alternatively, the damping resistor may be placed across the turns of the input coil [26]. This intra-coil damping technique has proven to be quite effective in smoothing the I–V characteristics of series SQUID array amplifiers [27] but can lead to some additional noise owing to the noise currents of the resistive links that are directly injected into the input circuit. Thus, this additional noise contribution must be taken into account if intra-coil damping is used.

The resonances described above may be studied using expanded models fabricated from standard, two-sided Cu-clad printed circuit boards, where scaled layouts (e.g., 500×) of the SQUID input coil and SQUID washer are patterned on the top and bottom layers of the printed circuit board [28,29]. For frequencies greater than 20 MHz, the skin depth of the Cu in the expanded printed circuit board model is less than 14 μm, which is less than the thickness of the Cu layers, while the separation of the Cu layers (i.e., board thickness) is much greater than twice the skin depth. The behavior of the electromagnetic fields in the expanded model therefore provides a reliable representation of the electromagnetic field behavior of the SQUID. For example, Enpuku *et al.* [29] used expanded models to investigate the properties of gradiometric dual-washer configurations connected either in series or in parallel, as shown in Figure 5.7. Each washer was coupled to a multi-turn input coil connected in series. Based on the expanded model studies, no significant rf interaction between the two washers for either gradiometer configuration was found. Furthermore, the impedance seen by the Josephson junctions in the series gradiometer configuration is simply twice the impedance of a single washer, while the

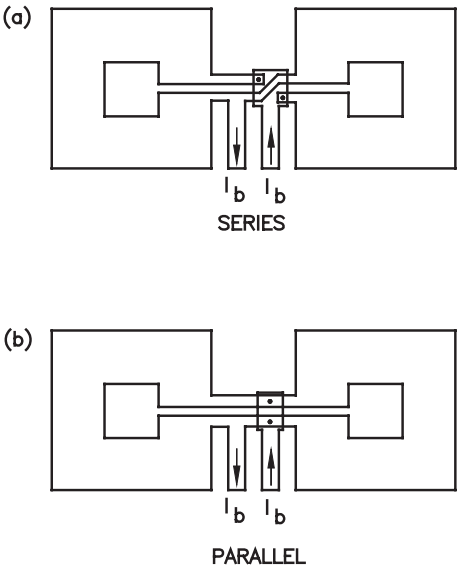

Fig. 5.7 Series- and parallel-configured double washer SQUID layouts. For clarity, the integrated input coils are not shown.

impedance seen by the Josephson junctions in the parallel gradiometer configuration is one-half the impedance of a single washer. These results are useful in designing dual-washer gradiometric SQUID layouts.

As noted above, the thin-film input coil deposited on top of the SQUID washer introduces a potentially large parasitic capacitance C_p across the SQUID inductance. If $C_p > C$, simulations and experiments by Ryhänen *et al.* suggest that the parasitic capacitance leads to a degradation of the energy resolution [30]. In particular, for large SQUID inductances $L \sim 300\,\text{pH}$, Ryhänen *et al.* found that $\varepsilon \propto \sqrt{1 + 2C_p/C}$ for $C_p / C \leq 2$, while for $C_p / C > 2$, ε saturates and becomes roughly twice the value for $C_p / C \approx 0$ in the limit $C_p / C >> 1$. A large parasitic capacitance can also lead to a strong LC_p resonance, complicating SQUID operation and resulting in increased noise caused by thermally activated hopping between the zero-voltage state and the resonant state, for example.

Based on these observations, the parasitic capacitance should be minimized such that $C_p << C$. Various design approaches have been developed to either reduce the parasitic capacitance or use it to advantage in order to define a low-noise point of operation. One way to eliminate the parasitic capacitance is to locate the Josephson junctions near the hole in the slotted SQUID washer rather than at the outer edge (as shown in Figure 5.4). The first tightly coupled SQUIDs built by Jaycox and Ketchen [18] were designed with the junctions located at the outer edge of the washer in order to avoid the magnetic field region inside the washer hole. Later, Seppä *et al.* [31] successfully built a low-noise SQUID with junctions located near the inner hole, which largely eliminates the parasitic capacitance and associated parasitic effects. No adverse affects owing to the close proximity to the inner hole were observed. Alternatively, the SQUID may be designed using a small washer and input coil with only a few turns, which requires coupling the SQUID to the load using an intermediate coupling transformer [22,32]. Although attractive for very high load inductances, the energy transfer function from the load inductance to the SQUID is in practice a factor of two lower than without the transformer, if ideal inductance matching is achieved in both cases [22].

Instead of choosing a layout that minimizes the parasitic capacitance, one may use the parasitic capacitance to define a specific resonance where the SQUID may be operated, often with low noise. For example, the double-loop SQUID shown schematically in Figure 5.8 will have a high frequency resonance above the normal range of operating frequencies [15]. For this structure, the total SQUID inductance is given by $L_{\text{tot}} = L + L_{Jp}$, where the parasitic inductance L_{Jp} is much smaller than the inductance L (for practical designs L_{Jp} can be difficult to calculate exactly, but an approximate value can be determined using the inductance formula for the structure that most resembles the actual layout; e.g., using the coplanar stripline formula for the two, long and narrow, junction bridges in an HTS SQUID). Also shown in the figure are the parasitic capacitance C_p and damping resistor R_d. Since the large parasitic capacitance C_p is effectively a short at high frequencies, a resonance occurs at the frequency $f_r = (1/2\pi)\,(L_{Jp}\,C/2)^{-1/2}$. Inside this high-frequency resonance, the SQUID characteristics are very smooth, and the energy resolution is nearly the same as that for a SQUID having the same total inductance but with $C_p = 0$. This is an interesting

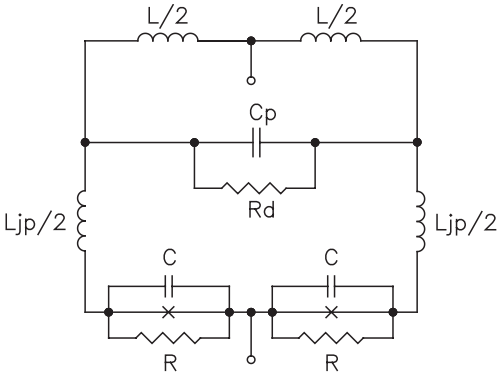

Fig. 5.8 A lumped circuit element representation of a double-loop dc SQUID.

design alternative for devices with high parasitic capacitance (e.g., when $C_p \gg C$), provided sufficient space is available for a double-loop layout. An example of such a device is the multi-loop SQUID magnetometer described by Drung *et al.* [33] (see Section 5.3.3).

In a hybrid approach first described by Cromar and Carelli [34] and subsequently improved by Carelli *et al.*, [35] a low-noise multi-loop SQUID is placed inside the core of an integral thin-film multi-turn input coil of a flux transformer, as shown in Figure 5.9. They were able to achieve a very low SQUID inductance of 28 pH with

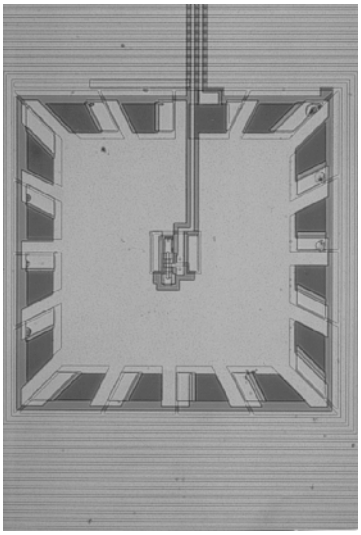

Fig. 5.9 A photograph of a hybrid SQUID design with multi-turn input coil surrounding a multi-loop dc SQUID (courtesy of P. Carelli).

minimal capacitive coupling between the SQUID and 1 μH input coil, thereby pushing the parasitic resonances to very high frequencies, well away from the intended SQUID working point. The coupling constant k_i was 0.42, however, which is about two times less than can be achieved using a washer-shaped SQUID inductance with integral input coil on top, and consequently the mutual inductance of the input coil with respect to the SQUID was only 2.1 nH (corresponding to approximately 1 μA/Φ_0). Designs based on conventional flux transformers with integrated input coils typically have much higher input mutual inductances of around 10 nH.

Several years ago, Knuutila *et al.* [22] introduced an optimization procedure for the design of thin-film dc SQUIDs with integrated coupling circuits that includes the parasitic effects associated with the input coil. This procedure was further developed to build integrated SQUID magnetometers and gradiometers [36,37]. The general design guidelines are as follows. For typical layouts, the operating frequency f_{op} corresponding to the optimal SQUID working point lies below the resonant frequency of the washer f_w and above the stripline resonant frequency f_s. According to simulations [20], the optimal operating frequency $f_{op} = 0.3 I_0 R/\Phi_0$. The frequency f_{op} corresponds to the voltage at which the noise performance of a current- or dc flux-biased SQUID is optimal. For designs requiring an input coil with many turns, the long length of the input coil pushes the stripline resonance to frequencies well below f_{op}, but the large size of the washer usually causes the washer resonance to move towards f_{op}. A reasonable compromise is to choose the SQUID layout such that $4f_s < f_{op} < f_w / 4$. The resonances are also damped using an $R_x C_x$ shunt in parallel with the input circuit as discussed above. Based on these guidelines, design optimization models were developed [22,31,36] to express the energy resolution in design-dependent parameters only (e.g., β_L and β_c, the SQUID inductance, the junction capacitance, the input coil coupling constant, etc.). A summary of useful expressions to calculate the relevant junction parameters, inductances and resonant frequencies is given in Table 5.1 and in [38]. Once the energy resolution (or other application-specific parameter) is expressed in design-dependent parameters only, it can be optimized using conventional multi-variable minimization algorithms.

Table 5.1 Summary of expressions used to calculate SQUID design parameters.

	Description	Ref.
Total Junction Capacitance		
$C = -c_J A_J + C_{Jp} + C_R,$	Junction Capacitance	
$1/(c_J A_J) = a - b\ln j_0$	A_J = junction area a, b are process-dependent parameters	
$C_{Jp} = \varepsilon_0 \varepsilon_r A_{Jp} / h$	Parasitic Junction Capacitance A_{Jp} = parasitic area (overlap with base-electrode) ε_r, h are permittivity, thickness of dielectric	
$C_R = \varepsilon_0 \varepsilon_r A_R / 2h$	Parasitic Capacitance from Shunt Resistors A_R = area of shunt resistor	
SQUID Inductance		
$L = L_h + L_{sl} + L_{Jp}$	Geometric inductance of the washer:	
$L_h = 1.25\,\mu_0 d$	square washer with square hole	[18]
$L_h = 1.05\,\mu_0 d$	octagonal washer with octagonal hole	[39]
$L_h = \mu_0 d$	circular washer with circular hole (d = inner side length or diameter of washer hole)	[40]
$L_{sl} \approx 0.3$ pH/μm	Slit Inductance (without groundplane)	[41]
L_{Jp}	Parasitic Junction Inductance (usually negligible)	
$L_{dc} = (1 - k_i s_{in}) L$	Screened SQUID Inductance k_i = input coil coupling constant $s_{in} = L_i / (L_i + L_p)$, L_i = input coil inductance L_p = pickup loop inductance	
Input Circuit		
$\ell = 4N_i[d + (N_i + 1)s_i + N_i w_i]$	Input Coil Length, Square Coil N_i = Number of turns w_i and s_i are linewidth and spacing, respectively	
$\ell = 2\pi N_i (d + w_i)/2 + \frac{w_i + s_i}{2}\sqrt{\frac{N_i}{2\pi}}$	Input Coil Length, Circular Coil	
$C'_{strip} = \frac{\varepsilon_0 \varepsilon_r w_i}{h} K(w_i, h, t_i)$	Microstripline Capacitance $K(w_i, h, t_i)$ = field fringe factor (typically 1.1 to 1.6)	[42]
$L'_{strip} \approx \mu_0 \frac{h + \lambda_{L,w} + \lambda_{L,i}}{w_i + 2(h + \lambda_{L,w} + \lambda_{L,i})}$	Stripline Inductance $\lambda_{L,w}$ and $\lambda_{L,i}$ are London penetration depths of the washer and input coil, respectively	[42]

Table 5.1 continued

	Description	Ref.
$Z = \sqrt{L_{strip} \Big/ C_{strip}}$	Input Coil Stripline Impedance	
$L_i = N_i^2 \left(L_h + L_{sl}/3\right) + \ell L'_{strip}$	Input Coil Inductance (single washer)	[41]
$L_i = 2\left[N_i^2 \left(L_h + L_{sl}/3\right) + \ell L'_{strip}\right]$	Input Coil Inductance (dual washers, series or parallel)	[41]
$M_i = N_i \left(L_h + L_{sl}/2\right)$	Input Coil Mutual Inductance (single washer or dual washers, parallel)	[41]
$M_i = 2N_i \left(L_h + L_{sl}/2\right)$	Input Coil Mutual Inductance (dual washers, series)	[41]
$k_i = M_i \sqrt{LL_i}$	Input Coil Coupling Constant	
$L_{i,\text{eff}} = \left(1 - k_i^2 s\right) L_i,$ $s = \dfrac{\beta_L s_{in} k_i^2}{6 + 2\beta_L + \beta_L s_{in} k_i^2}$	Screened Input Inductance	[22]
	Stripline Resonance	
$f_s = v/4\ell,\ v = \left(L'_{strip} C'_{strip}\right)^{-1/2}$	input coil grounded to washer	
$f_s = v/2\ell$	input coil floating	
$f_w = \dfrac{c}{2\ell_{\text{eff}} \sqrt{\varepsilon_r (1 + (\lambda_{L,w} + \lambda_{L,i})/h)}}$	Washer Resonance (without groundplane) $\ell_{\text{eff}} = 4(d + 4b_{\text{sl}}/3)$, b_{sl} is slit length	[43]
Parasitic Capacitance		
$C_p = \ell C'_{strip}/8 + 0.5 C_{gp}$	Input Coil Parasitic Capacitance (single washer) Groundplane Capacitance C_{gp} may be calculated using expression for stripline	[43]
$C_p = \ell C'_{strip}/16 + 0.25 C_{gp}$	Input Coil Parasitic Capacitance (dual washers, series)	[43]
$C_p = \ell C'_{strip}/4 + C_{gp}$	Input Coil Parasitic Capacitance (dual washers, parallel)	[43]

For most instrument applications, a SQUID is operated as a null detector using negative feedback electronics in order to linearize the periodic SQUID output. The SQUID may be operated using two different negative feedback modes, [44] which are referred to as flux-lock and current-lock modes. In the flux-lock mode, the feedback signal is coupled to the SQUID: a flux applied to the SQUID by an external signal in the input coil is cancelled by an opposing flux in the feedback coil that is coupled to the SQUID inductance. In this case, if the feedback and input coils are

not sufficiently isolated, the feedback signal (and modulation signal if conventional readout electronics are used) may couple to the input circuit and interact with the load. Similarly, for experiments where the (superconducting) load inductance is not fixed, the feedback coupling changes as the load is varied because of screening effects. For these applications, it is desirable to design the SQUID such that there is negligible coupling of the feedback and modulation signals to the input circuit. This may be accomplished, for example, by designing the SQUID layout such that separate secondaries are used for the input and feedback flux transformers, as shown in Figure 5.10 and schematically in Figure 5.11. A more elegant design due to Simmonds [45] uses a four-hole, symmetric washer configuration rather than a two-hole configuration.

In the current-lock mode, the feedback signal is coupled to the SQUID input, either directly or using transformer coupling. In this case, the feedback signal opposes any change of the current in the input circuit. If the load consists of a superconducting pickup loop, for example, this feedback mode maintains constant cur-

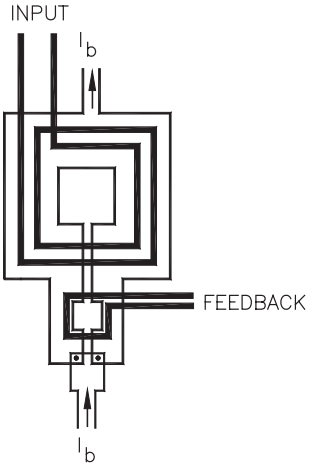

Fig. 5.10 A model of a dc SQUID layout with separate input and feedback secondaries.

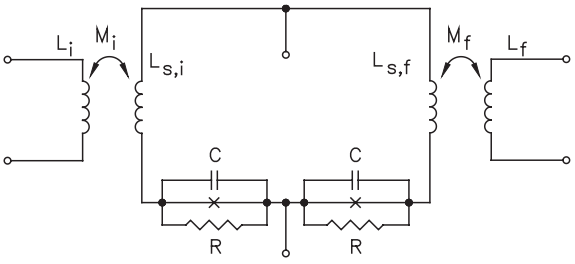

Fig. 5.11 Lumped circuit element representation of a dc SQUID with separate input and feedback secondaries.

rent (e.g., zero) in the pickup loop and input coil circuit, and offers the advantages that very little distortion of the field being measured is introduced and cross-talk in multi-channel applications is greatly reduced. If the feedback is transformer-coupled to the input circuit, note that this feedback mode *requires* that the load be superconducting.

In addition to provisions for coupling the feedback to the SQUID, the electrical connections for the bias current and feedback should be routed such that the magnetic fields arising from these currents do not couple to the SQUID, as substantial self-coupling may complicate proper operation of the SQUID.

5.3 Magnetometers

5.3.1 Overview

In the following sub-sections, magnetometers designed for high spatial resolution and high magnetic field resolution are discussed. These are predominantly thin-film devices, as in many cases it is easier and more cost effective to integrate the pickup loop and SQUID on the same chip, or, especially for HTS, the SQUID and the pickup loop with flux transformer may be fabricated on separate substrates which are then pressed together face-to-face in a "flip-chip" configuration. For some applications, however, it may be desirable to locate the pickup loop remotely from the SQUID. In such cases, the pickup loop is usually made from superconducting wire and connected to the SQUID input using superconducting screw terminals. At present, such configurations can only be realized using LTS SQUIDs. A photograph of a packaged dc SQUID with superconducting screw terminal inputs and detachable superconducting shield is shown in Figure 5.12.

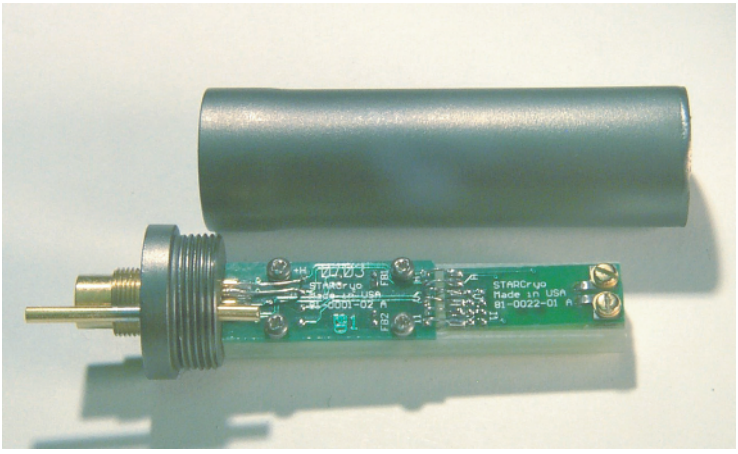

Fig. 5.12 A photograph of a packaged dc SQUID assembly with niobium shield.

5.3.2 Magnetometers for High Spatial Resolution

Beginning in the early 1990's, several groups developed scanning SQUID-based magnetic microscopes to record magnetic images of a variety of samples [46,47,48]. Most of these microscopes are based on HTS SQUIDs and measure only a single component of the sample's magnetic field. Spatial resolutions as low as 15 μm for room-temperature samples have been achieved [49]. Microscopes based on LTS SQUIDs include the miniature LTS vector magnetometer developed by Ketchen *et al.* [50] consisting of three orthogonal magnetometers used to measure the three orthogonal components of the magnetic field, and the self-oscillating LTS micro-SQUID (see Chapter 4) developed by Dechert *et al.* [51].

To obtain high spatial resolution, a small pickup loop is required (e.g., of the order of 10 μm diameter). Given the small size, the pickup loop is often formed from part of the SQUID inductance, or the SQUID loop itself is used as the pickup loop; that is, the SQUID is uncoupled. If a large magnetic polarizing field is needed to image the sample, the junctions may be located well away from the pickup loop using coplanar transmission lines. In such cases, it is usually necessary to use superconducting groundplanes under the lines to prevent stray pickup and to reduce the transmission line inductance, which is desirable in order to keep the total SQUID inductance low. Groundplanes under the junctions may also be needed to protect them from potentially high magnetic fields. The use of groundplanes is much more difficult to implement in HTS, and consequently the SQUID loop is generally used as the pickup loop for high spatial resolution HTS magnetometers. Feedback may be inductively coupled to the pickup loop or to the leads to the pickup loop, as shown in Figures 5.13(a) and (b). Again, the design of the feedback circuit is easier to implement with LTS SQUIDs, since high yield in HTS SQUID processing is generally obtained only for single-layer designs. For HTS SQUIDs, it may be simpler to galvanically couple the feedback to the SQUID, as shown in Figure 5.13(c). Given the small geometries and narrow linewidths typically used, kinetic inductance contributions also play a more important role for HTS than for LTS designs. If the HTS film thickness is less than the London penetration depth λ_L and the film width w is much greater than the film thickness t, the kinetic inductance per unit length is approximately given by $L_k' = \mu_0 \lambda_L^2 / wt$ [52].

For LTS applications in high magnetizing fields or in the presence of electromagnetic interference (EMI), a miniature pickup loop may be made from superconducting wire and located well away from the SQUID, which may be further protected by a superconducting shield assembly (see Figure 5.12). Spatial resolution may be improved by mounting the coils inside the dewar (cryostat) vacuum space in order to reduce the distance between the sample and pick up loop. Pickup coils generally are wound on fiber-glass epoxy (G-10) or Macor™ ceramic forms, and may require several turns in order to minimize the effect of the parasitic inductance of the leads going to the SQUID. To reduce pickup, the twisted-pair leads to the SQUID are usually routed through superconducting Pb or Nb tubing. Useful expressions to calculate loop inductances for wire-wound coils are given in Section 5.3.3.

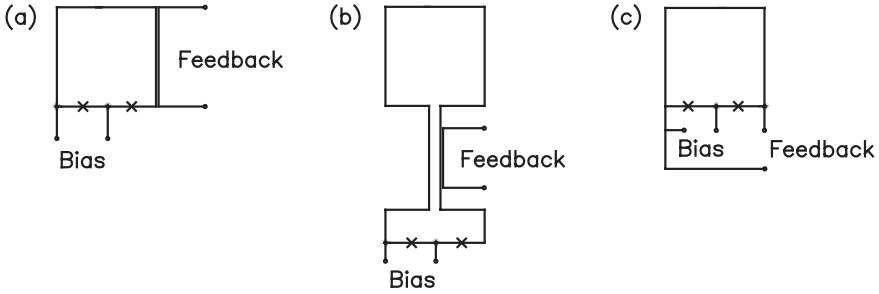

Fig. 5.13 Feedback coupling schemes for miniature dc SQUIDs: (a) feedback coupling to the pickup loop, (b) feedback coupling to the leads to the pickup loop, and (c) direct coupling of the feedback to the SQUID.

5.3.3 Magnetometers for High Field Resolution

In order to enhance magnetic field resolution, a pickup loop with large effective flux capture area is required. This loop may be a thin-film or wire-wound coil that is transformer-coupled to the SQUID via an input coil, or (as above) the SQUID inductance itself may be used to directly sense the magnetic field. In the latter case, as the size of the SQUID loop is increased in order to improve the effective area and magnetic field sensitivity, the SQUID inductance increases as well and quickly becomes excessively high. If the inner dimension of the SQUID washer is kept small, however (wide linewidth design), the SQUID inductance will not increase as significantly as may be seen from the expressions in Table 5.1 for the SQUID washer inductance and pickup loop effective area. On the other hand, the effective area will be much lower than that for a layout where the outer and inner dimensions of the SQUID washer are more comparable (narrow linewidth design). According to the optimization condition that $\beta_L = 2LI_0/\Phi_0 = 1$, an excessively high SQUID inductance can lead to a critical current that is comparable to or less than the current noise at the given operating temperature.

The LTS thin-film pickup loop designs usually are integrated with the SQUID on a single chip. Assuming that the parasitic capacitance can be kept small, the discussion in Section 5.2.2 describes a design optimization procedure where the energy resolution is expressed in design-dependent parameters and then minimized using multi-variable minimization algorithms, subject to the constraints on the microwave resonances. For magnetometers, the relevant application-specific figure of merit is the rms magnetic field noise $S_B^{1/2}(f) = S_\Phi^{1/2}(f) / A_{\text{eff}}$, where A_{eff} is the effective flux capture area of the magnetometer. The rms magnetic field noise is often referred to simply as the magnetic field resolution $B_n(f) \equiv S_B^{1/2}(f)$. In practice, the design parameters that minimize the application-specific figure of merit are often different from those which minimize the energy resolution, although the two minima generally are broad and do not differ by more than a factor of 10. In this case, mag-

netometer designs may be optimized by minimizing the magnetic field noise calculated from the energy resolution using the expression $S_B^{1/2}(f) = \sqrt{2\varepsilon L}/A_{\text{eff}} \equiv \sqrt{2\varepsilon L} B_\Phi / \Phi_0$, where the magnetic field sensitivity B_Φ is given by

$$B_\Phi = \Phi_0 \frac{L_p + L_{i,\text{eff}}}{M_i A_{p,\text{eff}}}. \tag{5.1}$$

Here, L_p is the inductance of the pickup loop, M_i is the mutual inductance of the input coil, $L_{i,\text{eff}}$ is the effective inductance of the input coil including the effects of screening by the SQUID inductance, and $A_{p,\text{eff}}$ is the effective area of the pickup loop including flux-focusing effects [17]. For a square pickup loop with linewidth w_p, inner side length d and outer side length a, the inductance and effective area are given by

$$L_p = \frac{2}{\pi} \mu_0 (d + w_p) \left[\ln(1 + d/w_p) + 0.5 \right] \qquad (\text{d/wp} > 10), [53] \tag{5.2}$$

$$L_p = \frac{2}{\pi} \mu_0 d \left[\ln(5 + d/w_p) + 0.25 \right] \qquad (1 < d/w_p < 10), [57] \tag{5.3}$$

$$L_p = 1.25 \mu_0 d \qquad (d/w_p < 1), [18] \tag{5.4}$$

$$A_{p,\text{eff}} = ad [17]. \tag{5.5}$$

For a circular pickup loop, the inductance and effective area are given by

$$L_p = \mu_0 \frac{d}{2} \left[\ln(8d/w_p) - 2 \right] \qquad (\text{d/wp} > 10), [53] \tag{5.6}$$

$$L_p = \mu_0 d \qquad (\text{d/wp} < 1), [40] \tag{5.7}$$

$$A_{\text{p,eff}} = (2/\pi) ad [17]. \tag{5.8}$$

The first integrated LTS thin-film magnetometers designed using this optimization procedure were fabricated on 4-mm × 4-mm chips [36,37]. The magnetometers exhibited smooth characteristics over the entire operating range of the SQUID with a broad noise minimum (<5 $\text{fT/Hz}^{1/2}$ at 1 kHz), even though the SQUID was near the hysteretic limit with $\beta_c = 0.6$. The smooth characteristics and broad noise minimum help to simplify operation in flux-locked loop mode using standard feedback electronics. Although these magnetometers exhibited a very low white rms flux noise of $0.61 \mu\Phi_0/\text{Hz}^{1/2}$, the small chip size and low mutual inductance of the input circuit resulted in a magnetic field sensitivity of $5.6\ \text{nT}/\Phi_0$, corresponding to a magnetic field noise at 1 kHz of $3.4\ \text{fT/Hz}^{1/2}$. For optimal performance, the total noise of the SQUID magnetometer and room-temperature readout electronics should be

dominated by the SQUID noise. The low intrinsic flux noise of the above magnetometer, however, places stringent demands on the noise performance of the room-temperature electronics, especially if conventional flux-modulation readout electronics are used. In addition, the flux noise increases at low frequencies, becoming about $2\,\mu\Phi_0/\mathrm{Hz}^{1/2}$ at 1 Hz, a typical value independent of the junction technology used, corresponding to a magnetic field noise at 1 Hz of over $10\,\mathrm{fT/Hz}^{1/2}$. The reduced field resolution at low frequencies makes these small magnetometers less attractive for applications such as biomedical imaging.

To improve magnetometer field resolution, a larger chip size may be used, which increases the flux capture area of the pickup loop, along with a higher SQUID inductance, in order to increase the mutual inductance of the input circuit. For example, magnetometers fabricated using a 7.75-mm × 7.75-mm pickup loop and a relatively high SQUID inductance of $L = 190\,\mathrm{pH}$ (in order to increase the mutual inductance to $M_i = 1.7\,\mathrm{nH}$) exhibited a high field-to-flux conversion efficiency (magnetic field sensitivity) of $0.83\,\mathrm{nT}/\Phi_0$ [54]. For these magnetometers, an integral R_xC_x shunt installed in the input circuit resulted in very smooth I–V and V–Φ characteristics. The intrinsic rms white flux noise of this magnetometer was measured to be $1.6\,\mu\Phi_0/\mathrm{Hz}^{1/2}$ at 1 kHz, corresponding to an rms magnetic field noise of better than $1.4\,\mathrm{fT/Hz}^{1/2}$. More recently, Granata *et al.* [55] described a similar thin-film magnetometer with 8.2-mm × 8.2-mm pickup loop coupled to a 260 pH SQUID inductance via a 12-turn input coil with 2.9 nH mutual inductance, giving a magnetic field sensitivity of $0.7\,\mathrm{nT}/\Phi_0$. Using directly-coupled readout electronics with Additional Positive Feedback (APF) (see Chapter 4) [33], a magnetic field noise of $1.5\,\mathrm{fT/Hz}^{1/2}$ was obtained.

As shown by Zimmerman, an effective way to increase the effective area of the SQUID, while at the same time keeping the total SQUID inductance at a tolerable level in order to keep the SQUID noise low, is to use a layout consisting of several pickup loops connected in parallel [56]. Drung *et al.* [33] were first to demonstrate a planar version of this concept, reminiscent of a wheel with spokes (often called "Drung's wheel"), which is shown in Figure 5.14. For n loops connected in parallel, the total SQUID inductance is $L = L_\mathrm{p}/n^2 + L_\mathrm{spoke}/n$ and the total effective area is given by $A_\mathrm{eff} = A_\mathrm{p}/n - A_\mathrm{spoke}$, where L_p and A_p are the inductance and effective area, respectively, of an equivalent pickup loop without spokes and L_spoke and A_spoke are the average parasitic inductance and average parasitic effective area associated with the pair of "spokes" between neighboring loops that form coplanar transmission lines. If w_c and s_c are the linewidth and separation of the spokes, the coplanar line inductance L_{cop} is given by [57]

$$L_{cop} = \frac{\mu_0}{\pi}\ln\left[\frac{4(w_c + s_c)}{w_c} - \frac{w_c}{w_c + s_c}\right]. \tag{5.9}$$

For the special case that $w_c = s_c$, the coplanar transmission line inductance $L_{cop} = 0.8\,\mathrm{pH}/\mu\mathrm{m}$.

Drung *et al.* [58] have recently demonstrated a multi-loop LTS magnetometer with a field sensitivity $B_\Phi = \Phi_0/A_\mathrm{eff} = 0.46\,\mathrm{nT}/\Phi_0$ and rms magnetic field noise

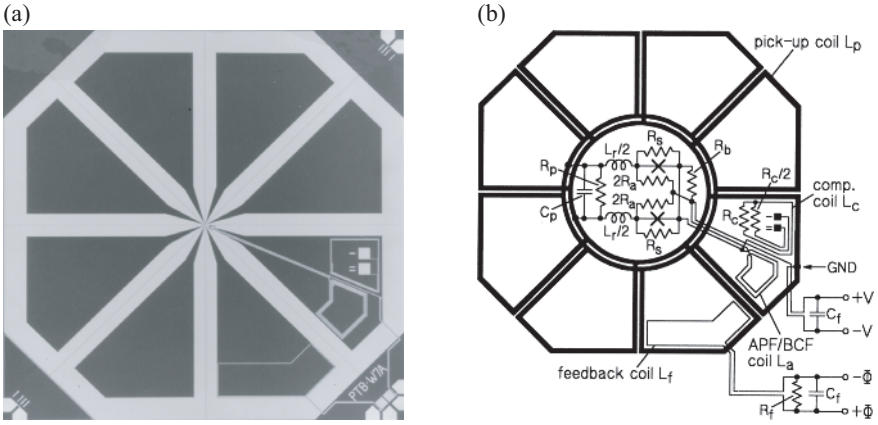

Fig. 5.14 (a) Photograph and (b) schematic diagram of the PTB multi-loop magnetometer type W7A (reprinted with permission from D. Drung and H. Koch, "An integrated DC SQUID magnetometer with variable additional positive feedback," *Supercond. Sci. Technol.* ***7***, 242–245 (1994)).

$S_B^{1/2}(f) = 0.9\,\mathrm{fT/Hz^{1/2}}$. Similar designs have been successfully fabricated in HTS as well [59], but twice as many loops were required in order to further reduce the SQUID inductance and allow the use of a higher critical current per junction, owing to the stronger effects of thermal noise at 77 K.

Magnetometers based on HTS SQUIDs for operation at 77 K generally require a SQUID inductance of about 100 pH or less. Since the flux capture area of a SQUID loop with such a low inductance is generally very small as well, a pickup coil with much larger flux capture area may be flux-transformer-coupled to the SQUID inductance via a multi-turn input coil as described above for LTS magnetometers. Owing to difficulties in fabricating the multi-layer structures necessary to pattern designs of this type, however, early HTS magnetometers were fabricated using a much simpler approach, whereby the signal from the pickup loop is coupled to the SQUID by direct injection, as shown in Figure 5.15 [60, 61]. Although connecting the pickup loop in parallel with the SQUID inductance results in a substantial inductance mismatch, reasonable coupling and a significant enhancement of the effective area can be achieved. For example, in 1993 Koelle *et al.* reported a field noise of $93\,\mathrm{fT/Hz^{1/2}}$ at 1 Hz for a 1-cm × 1-cm direct-coupled dc SQUID magnetometer at 77 K. A noteworthy advantage of this approach is that a complete device can be fabricated from a single layer of high-T_c superconducting film.

Multi-layer HTS magnetometers may be fabricated with the pickup loop, input coil and SQUID integrated on the same chip as described above for LTS magnetometers, or the flux transformer and SQUID may be fabricated on separate chips and then pressed together in a "flip-chip" configuration. Shen *et al.* [62,63] reported the first fully integrated magnetometer for operation at 77 K with a white rms magnetic field noise below $10\,\mathrm{fT/Hz^{1/2}}$ at 1 kHz, but the noise increased to $53\,\mathrm{fT/Hz^{1/2}}$ at

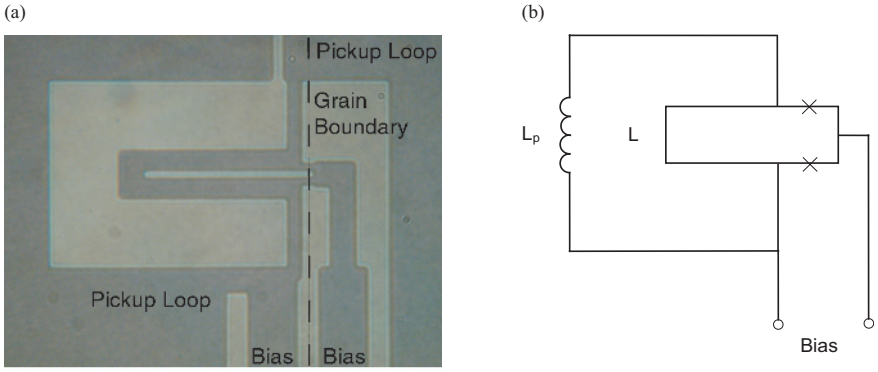

Fig. 5.15 (a) Photograph and (b) schematic diagram of a high-T_c dc SQUID fabricated on a bicrystal substrate. The two vertical strips in (a) are the bias leads, one of which is connected to the signal injection lead from the pickup loop. The dashed line in (a) shows the location of the bicrystal grain boundary.

1 Hz for reasons discussed in Section 5.5. In another approach, Scharnweber *et al.* [64] described a multi-loop pickup coil that is transformer-coupled to a washer-shaped SQUID using an integrated thin-film input coil and reported a magnetic field sensitivity B_Φ of 1.34 nT/Φ_0, which is quite good, but the relatively high rms flux noise observed resulted in a field noise of 100 fT/Hz$^{1/2}$ at 1 Hz. This approach can significantly reduce the inductance of the load coupled to the SQUID, thereby reducing the number of turns required in the input coil and simplifying the design of the input circuit such that the parasitic resonances are well away from the intended working point.

Excess $1/f$ noise in multi-layer flux transformers is often observed for frequencies f below 1 kHz [65,66] owing to a degradation of the critical current density of the top HTS film particularly at crossovers. Dantsker *et al.* [67] improved the low-frequency noise performance using a 9-mm × 9-mm multi-layer pickup loop and flux transformer flip-chip coupled to a separate SQUID chip and achieved noise levels of 27 fT/Hz$^{1/2}$ at 1 Hz and 8.5 fT/Hz$^{1/2}$ at 1 kHz. Faley *et al.* [68] reported 6 fT/Hz$^{1/2}$ at 1 kHz also for a flip-chip magnetometer using a larger, 16-mm × 16-mm multi-layer pickup loop and flux transformer. An important advantage of the flip-chip approach is that one may select the lowest noise HTS SQUIDs from several made on a single substrate in a separate run.

As discussed in Section 5.3.2, magnetometer applications in the presence of high background magnetic fields generally require the use of wire-wound pickup coils so that the SQUID can be located remotely from the high-field region. At the present time, this applies to LTS SQUID sensors only, as suitable HTS wire and superconducting contact technologies currently do not exist. In designing systems where the LTS SQUID is a large distance from the pickup loop, it is important to consider the effects of the parasitic inductance of the superconducting twisted pair leads connected to the SQUID input.

For a single-turn pickup loop of mean diameter D made from wire having diameter d such that $D/d > 10$, the loop inductance is given by [53]

$$L_{loop} = \frac{\mu_0 D}{2}[\ln(8D/d) - 1.75]. \tag{5.10}$$

The parasitic inductance of the leads connecting the pickup loop to the SQUID, which should be twisted to avoid picking up stray signals, adds to this inductance. Typically, twisted pair leads have an inductance per unit length of $L_{leads} \approx 0.5$ nH/mm. Then, $L_p = L_{loop} + L_{leads}$ and (5.1) becomes

$$B_\Phi = \Phi_0 \cdot \frac{(L_{loop} + L_{leads}) + L_i}{M_i A_p}. \tag{5.11}$$

Since the parasitic inductance of the leads can be comparable to the inductance of a single-turn pickup loop, an improvement in performance may be achieved by increasing the number of turns in the pickup loop. In general, the inductance of an N-turn pickup loop is approximately given by [69]

$$L_{loop}(N) = F \cdot D[\text{cm}] \cdot N^2 \text{ nH}, \tag{5.12}$$

where F is a function [70] of the coil diameter D and length ℓ. The coil length ℓ is determined by the winding pitch p and the diameter of the wire d; that is, $\ell = (N-1)p + d$. Over the useful range $0.01 < \ell/D < 0.40$, F is given by [71] $F = 5.87 - 14.25\text{Log}(\ell/D)$ with an accuracy of better than 1 %. This expression for F may be used with (5.12) to calculate the loop inductance as a function of the number of turns N. As shown in ref. [71] for a typical coil with $D = 16$ mm, $L_{loop}(N) = 58.98N^{1.56}$ with an accuracy of better than 4 % for $N \geq 2$ (better than 2.2 % for $N \geq 3$).

The effective area of an N-turn pickup loop $A_p(N)$ is simply N times the area A_p of a single-turn loop, or $A_p(N) = NA_p$. Since the inductance of an N-turn pickup loop $L_{loop}(N) \propto N^{1.56}$ and $A_p(N) \propto N$, it is clear from (5.11) that B_Φ will initially improve for $N > 1$, but then get worse as the effect of L_{leads} becomes negligible with respect to $L_{loop}(N)$.

5.4 Gradiometers

5.4.1 Overview

For many applications of practical interest (e.g., biomedical imaging, non-destructive testing of materials, geophysical prospecting), it may not be possible to place the sample or magnetic field source very close to the SQUID or to locate the source in a sufficiently quiet environment to allow one to use SQUID magnetometers. In such

cases it is more desirable and more cost effective to use gradiometric sensors that strongly discriminate against distant sources.

Schematic representations of several gradiometric pickup loop configurations are shown in Figure 1.10. In each case, the pickup loop is transformer-coupled to the SQUID, which is operated in locked-loop mode. Two loops separated axially by a distance b and connected in series opposition form a first-order axial gradiometer. The coil separation b is referred to as the gradiometer baseline. By properly balancing the two loops, a uniform axial field B_z will couple zero net flux to the SQUID, while a field gradient $\partial B_z/\partial z$ in the z-direction will couple a non-zero net flux to the SQUID. In practice, however, some response is always observed owing to imperfections and asymmetries in the coil windings. The ratio of the gradiometer response in a uniform field gradient to that in a uniform gradient field is referred to as the gradiometer balance. A thorough discussion of gradiometer balance can be found in Section 7.7. Achieving a balance of 1 %–0.1 % is straightforward, while achieving a balance of 0.1 %–0.01 % or better, is more difficult, requiring very high-precision fabrication and post-assembly balancing. Aside from asymmetries in the coils, the presence of nearby objects (such as the superconducting enclosure surrounding the SQUID) may, in response to a changing uniform background field, distort the local field seen by the pickup loop and also lead to a degradation of the gradiometer balance. Similarly, connecting together two first-order gradiometers of opposite polarity results in a second-order axial gradiometer (see Figure 1.10), and two second-order gradiometers of opposite polarity connected together form a third-order axial gradiometer. Gradiometers may also be fabricated using thin-film pickup loops, but for practical reasons such devices are planar and measure off-diagonal gradients, such as $\partial B_z/\partial x$ or $\partial^2 B_z/\partial x \partial y$ (see Figure 1.10). Wire-wound or thin-film SQUID gradiometers are referred to as hardware gradiometers since the corresponding gradient signal is coupled to the SQUID by the pickup loop.

As discussed in Chapter 4, it is also possible to form first-order gradiometers by subtracting the outputs of two magnetometers either electronically or in software [72], a technique that is attractive in order to achieve high baselines using HTS SQUIDs [73,74]. Similarly, a second-order gradiometer can be formed by subtracting the outputs of two first-order hardware gradiometers. Although it is often simpler to build electronic or software first-order gradiometers in situations where the number of channels required is small (especially when using HTS SQUIDs), the magnetometers and associated readout electronics must be capable of operating without losing lock in potentially high ambient magnetic fields.

An elegant solution that addresses this issue is the three-SQUID gradiometer (TSG) devised by Koch *et al.* [75]. The axial TSG consists of a reference SQUID located between two sensor SQUIDs, all of which are operated in locked-loop mode. The feedback to the reference SQUID, however, is coupled also to the two sensor SQUIDs using three identical coils connected in series that produce the same magnetic field at each of the three SQUID locations. Any change of the uniform magnetic field along the TSG axis is therefore nulled at all three SQUIDs, while a non-uniform field will produce a difference in the outputs of the two sensor SQUIDs. The average gradient is then simply the difference of the sensor SQUID outputs

divided by their axial distance. Note that, to first order, the noise associated with the reference (which actually need not be a SQUID) does not appear at the output since this noise is added coherently to both sensor SQUIDs and is subtracted out by the electronic differencing to form the gradient.

5.4.2 Thin-Film Planar Gradiometers

The first thin-film planar gradiometers were reported by Donaldson *et al.* [76] and Ketchen *et al.* [77] in the late 1970's. Although the two-dimensional nature of thin-film gradiometers limits these devices to measurements of off-diagonal magnetic field gradient components, planar gradiometers of this type are nevertheless very attractive for practical applications, such as to study the magnetic properties of microscopic materials, to build x-ray detectors based on magnetic calorimeters, and to map the magnetic fields generated by neuronal activity in the human brain or muscle activity in the heart.

Similar to the thin-film magnetometers for high spatial resolution discussed in Section 5.3.2, Ketchen *et al.* [78] and Narasimhan *et al.* [79] described gradiometric thin-film miniature susceptometers that may be used to study magnetic properties of very small particles and thin-film samples. The gradiometer consists of two series-configured pickup loops remotely located from the two Josephson junctions, similar to the two-washer layouts shown in Figure 5.7. An integral magnetizing field coil around each pickup loop, along with a center tap, can be used to apply a balanced magnetic field to both loops. If a sample of magnetic material is placed inside one of the pickup loops, a change of the current through the field coils will lead to an imbalance signal, depending on the susceptibility of the magnetic material. Using such devices, the magnetic properties of extremely small particles of the order of 10-μm diameter can be studied. Since a change in temperature will also lead to an imbalance signal, thin-film susceptometers can also be used as readout devices for magnetic calorimeter x-ray detectors [80]. The energy dissipated by x-rays incident upon a magnetic calorimeter located in one of the gradiometric pickup loops produces a proportional temperature change and consequently a magnetization change that is sensed by the susceptometer.

Applications in biomagnetism require gradient sensitivity much higher than that used in other applications. Similar to the magnetometers for high field resolution discussed in Section 5.3.3, a gradiometric thin-film or wire-wound pickup loop having a high flux capture area is generally used, which is transformer coupled to the SQUID via an integrated input coil, as in the case of high-sensitivity magnetometers. Following the discussion in Section 5.3.3, the application-specific functional form to be minimized for a first-order gradiometer is the magnetic field gradient noise, $S_B^{1/2}(f)/b$, where $S_B^{1/2}(f)$ is the rms magnetic field noise associated with signals coupled to one of the gradiometer loops and b is the baseline of the gradiometer. Several integrated first-order and second-order LTS thin-film gradiometers have been developed specifically for applications in biomagnetism [22,36,81–84].

These devices typically have a gradient noise of 0.01 to 0.3 fT/cm · $Hz^{1/2}$ with baselines of around 1 cm.

Although the first HTS thin-film planar gradiometer was fabricated using a multi-layer process [85], most HTS planar gradiometers are based on single-layer, directly-coupled designs or flip-chip designs owing to the complexity of fabricating multi-layer HTS structures with high-quality junctions, vias and crossovers (see Chapter 3). First-order planar gradiometers were first reported by Knappe *et al.* [86] and Zakosarenko *et al.* [87]. The performance of such gradiometer has improved considerably over the past 10 years. For example, Eulenburg *et al.* [88] achieved a magnetic field gradient noise of 50 ft/cm · $Hz^{1/2}$ at 1 kHz with a baseline of 1.3 cm using a longer, 30-mm × 10-mm substrate and single layer design, while a flip-chip gradiometer with 24-mm diameter pickup loop described by Faley *et al.* [68] achieved a gradient noise level of 30 ft/cm · $Hz^{1/2}$ at 1 kHz with an approximate baseline of 1 cm.

Aside from the intrinsic noise performance, of particular interest are the gradiometer balance and noise performance in ambient magnetic fields. Since the SQUID used to build the gradiometer is sensitive to uniform magnetic fields, the SQUID effective area can be a limiting factor in optimizing the balance of single-layer and multi-layer gradiometers. In order to reduce the SQUID sensitivity to uniform fields, a gradiometric SQUID design [89] or single-layer, anti-parallel two-SQUID design may be used [88]. The gradiometric HTS SQUIDs shown in Figure 5.16 and fabricated by Millar *et al.* [90] using step edge junctions (see Chapter 3) had sensitivities to uniform magnetic fields about two orders of magnitude lower than single-loop SQUIDs with comparable inductance. Using two pairs of anti-parallel configured SQUIDs as shown in Figure 5.17 to reduce the sensitivity to uniform fields, Eulenburg *et al.* [88] and Carr *et al.* [91] achieved roughly an order of magnitude balance enhancement over similar designs with a single-loop SQUID, resulting in a balance of 3×10^{-5} for their single-layer gradiometer.

As shown by Dantsker *et al.*, [92] one may alternatively exploit the sensitivity of the SQUID to uniform fields to build a flip-chip asymmetric gradiometer with a balance of 1 part in 3000 and 4.8 cm baseline simply by adjusting the coupling of the flux transformer with respect to the SQUID as shown in Figure 5.18. Kittel *et al.* [93] used a similar approach to build a second-order gradiometer by flip-chip coupling a symmetric flux transformer with 3.1 cm baseline to a directly-coupled SQUID magnetometer as shown in Figure 5.19. By mechanically adjusting the mutual inductance between the magnetometer and flux transformer, the response to uniform magnetic fields was reduced to 50 ppm. Single-layer second-order gradiometers have also been developed, consisting of three symmetrically designed, parallel-configured pickup loops that are directly coupled to the SQUID inductance [94]. Thus far, however, these devices have much smaller baselines than the flip-chip designs owing to the limited size of available substrates to fabricate the SQUID and integral pickup loop layout. Dantsker *et al.* also demonstrated that SQUIDs made using narrow linewidths w (e.g., $w = 4\,\mu m$) or perforations in the SQUID film [92] have low excess $1/f$ noise when cooled in magnetic fields up to a threshold value of $\pi\Phi_0/4w$ [95]. The use of narrow linewidths or perforated SQUID washers is especially impor-

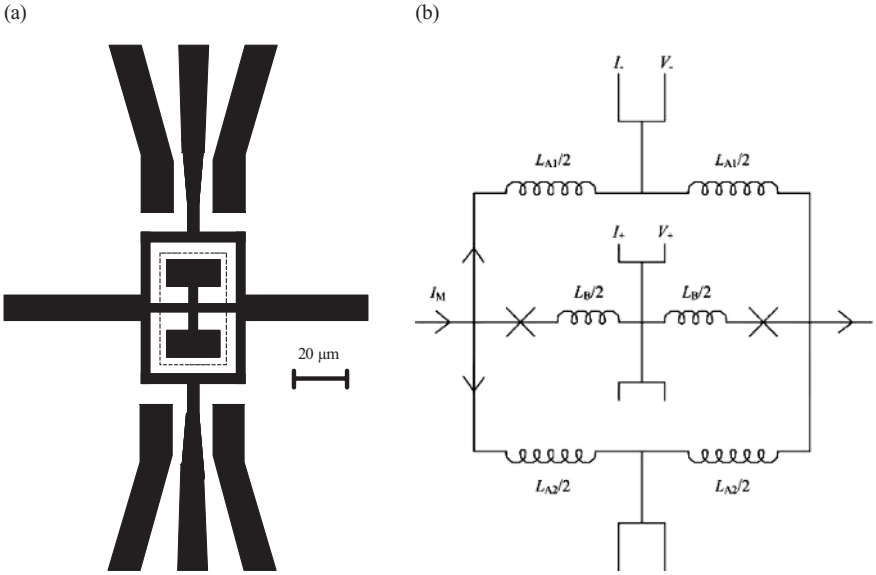

Fig. 5.16 A gradiometric SQUID layout designed by Millar *et al.* [90] (reprinted with permission from ref. [90]). The dotted line is the step used to define the step-edge Josephson junctions, and I_M is the current from the two pickup loops.

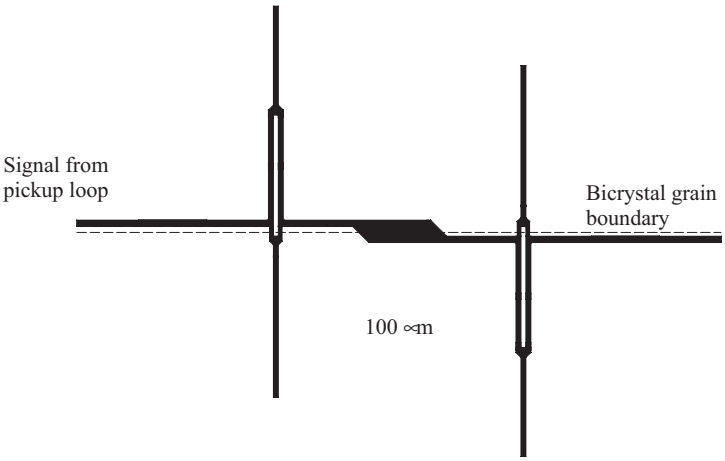

Fig. 5.17 An anti-parallel SQUID layout designed by Carr *et al.* [91] to reduce the magnetometer response of their single-layer gradiometer (reprinted with permission from ref. [91]).

tant for devices operated in ambient fields and leads to a reduction of the coupling using flip-chip flux transformers of only around 16 %. A more detailed discussion about the origins of $1/f$ noise is given in Section 5.5.1.

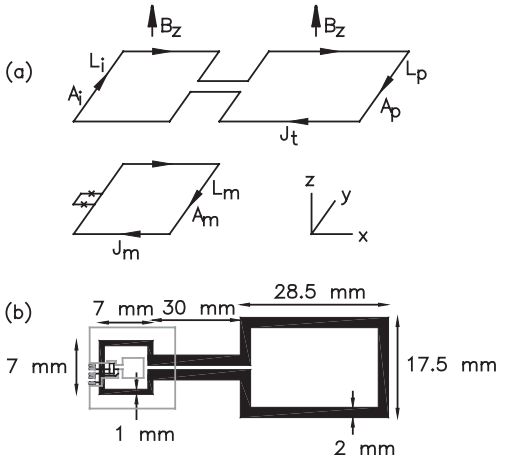

Fig. 5.18 An asymmetric first-order flip-chip gradiometer developed by Dantsker *et al*. [92] (reprinted with permission from ref. [92]).

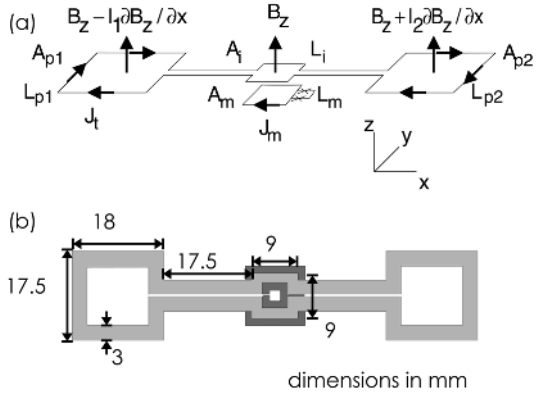

Fig. 5.19 A second-order flip-chip gradiometer developed by Kittel *et al*. [93] (reprinted with permission from ref. [93]).

5.4.3
Wire-Wound Axial Gradiometers

Long baseline axial gradiometers are usually preferred to image deep-lying sources. Axial LTS gradiometers are almost always fabricated using wire-wound pickup coils that are transformer-coupled to the SQUID. To determine the performance parameters of a first-order axial gradiometer, each loop is assumed to have the same area $A_p = \pi D^2/4$, where D is the mean diameter of the coils. The loop closest to the source is often referred to as the signal loop, while the more distant loop is referred to as the reference loop. The first-order gradient sensitivity $G_{1,\Phi}$ is given by

$$G_{1,\Phi} = \Phi_0 \cdot \frac{2L_{loop} + L_{leads} + L_i}{M_i A_p b}, \tag{5.13}$$

where L_{loop} is the inductance of each loop and L_{leads} is the total parasitic inductance of the twisted pair leads running between the two loops and to the SQUID input (typically, 0.5 nH/mm). The loop inductance may be calculated as described in Section 5.3.3. The rms field gradient noise $S_{G,1}^{1/2}(f)$ for the first-order gradiometer is then given by

$$S_{G,1}^{1/2}(f) = G_{1,\Phi} \cdot S_{\Phi}^{1/2}(f). \tag{5.14}$$

As discussed in Section 5.3.3, a significant part of the total inductance coupled to the SQUID can arise from the parasitic inductance of the leads. In such cases, one may obtain a performance improvement by decreasing the ratio of the lead inductance to the sum of the signal and reference loop inductances, e.g., by increasing the number of turns of each loop.

Gradiometer coils typically are wound on materials such as quartz, Macor, or G-10 fiberglass epoxy that have relatively small coefficients of thermal expansion, which is necessary in order to reproducibly obtain balance levels of up to 0.1 %. To further optimize the balance, the response of the gradiometer coils to uniform axial fields can be trimmed (nulled) by adjusting the position of superconducting tabs near the reference loop. In this way, balance levels of 0.01 % to 0.001 % may be achieved. More recently, electronic correction of balance employing signals from a reference vector magnetometer has been introduced to attain comparable or better balances, as discussed in Section 7.7.

To improve the rejection of background fields and field gradients, a second-order gradiometer may be built by winding (in opposition) two first-order gradiometer coils on the same coil form (see Figure 1.10). The distance between the centers of the first-order gradiometer coils is the baseline (the spacing between the coils of each first-order gradiometer need not be the same). For a single-turn configuration, there is a single turn at one end, two turns in the middle, and one turn at the other end, or the turns ratio is 1:2:1. For a two-turn configuration, the turns ratio is 2:4:2, and so on.

Assuming that any multi-turn coils used to build the gradiometer are closely wound and the spacing of the lower and upper coils from the middle coil is b, the baseline of the second-order gradiometer is also equal to b. The second-order gradient sensitivity and rms field gradient noise are then given by $G_{2,\Phi} = G_{1,\Phi}/b$ and $S_{G,2}^{1/2}(f) = G_{2,\Phi}\ S_{\Phi}^{1/2}(f)$, respectively.

5.5
1/*f* Noise and Operation in Ambient Field

5.5.1
General Remarks on 1/*f* Noise

In applications such as biomagnetism or geophysics, one requires the low level of noise to extend down to frequencies of 1 Hz or lower. In this frequency range it is often observed that the spectral density of flux noise S_Φ or of magnetic field noise $S_{B,}$ scales as $1/f$. Such a $1/f$ noise (or "flicker noise") can significantly limit the performance of practical devices at low frequencies. We note that $1/f$ noise has been observed in low-T_c SQUIDs, but is generally not a serious issue. In contrast, in high-T_c SQUIDs $1/f$ noise is a severe problem and a great deal of effort has been expended in attempting to understand its origins and reduce its magnitude. Early high-T_c dc SQUIDs made from polycrystalline YBCO films [96] exhibited large levels of $1/f$ noise, which increased the noise energy at 1 Hz to above 10^{-26} J/Hz. Since that time, there have been dramatic reductions in the level of $1/f$ noise, and the $1/f$ corner frequency f_c (the frequency at which the extrapolated values of the white noise and $1/f$ noise intersect) has been reduced from ~1 kHz to ~ 1 Hz.

There are two major sources of $1/f$ noise in dc SQUIDs [97]. One is due to fluctuations of the critical current I_0 in the Josephson junctions (as discussed in Section 2.1.3); the other is due to the motion of flux lines (vortices) trapped in the body of the SQUID or in the superconducting input circuit. The effect of both sources on dc SQUID performance is discussed below.

5.5.2
Critical Current Fluctuations

Fluctuations of the critical current of the junctions contribute in two independent ways to the dc SQUID noise. One is the "in-phase" mode, in which the critical currents of the two junctions fluctuate in phase to produce a voltage across the SQUID, and the second is the "out-of-phase" mode in which the two fluctuating critical currents produce a current circulating around the SQUID loop. Resistance fluctuations also contribute $1/f$ noise. However, at the low voltages where SQUIDs are operated, critical current fluctuations dominate, and we shall not address resistance fluctuations further. As discussed in Section 4.3.3 there exist various electronic readout schemes, based on reversing the bias current at some frequency above f_c, to reduce or eliminate $1/f$ noise from I_0 fluctuations. In practice, the reduction of $1/f$ noise with bias reversal is optimized empirically, but nonetheless, there are predictions for the magnitudes of the in-phase and out-of-phase contributions [97,98]. The in-phase mode produces a voltage noise with a spectral density $S_V \approx (\delta V^*/I_0)^2 \; S_I/2 \approx (V - IR_{dyn})^2 \times S_I/2I_0^2$, and the out-of-phase mode produces a term $S_V \approx L^2 S_I V_\Phi^2/2$. Here, R_{dyn} is the dynamic resistance and S_I is the spectral density of critical current fluctuations, as introduced in Section 2.1.3. With $S_V = S_\Phi/V_\Phi^2$ one obtains the approximate expressions for the spectral density of flux noise

$$S_{\Phi,in-phase} \cdot f \approx \frac{\Phi_0^2}{2} \frac{\zeta^2}{v_\phi^2} s_I f \tag{5.15a}$$

$$S_{\Phi,out-of-phase} \cdot f \approx \frac{\Phi_0^2}{8} \beta_L^2 s_I f, \tag{5.15b}$$

where $\zeta \equiv |V - IR_{dyn}|/I_0R$ is close to unity and $v_\phi \equiv V_\Phi \Phi_0/I_0R$ and $s_I \equiv S_I/I_0^2$ are the normalized transfer function and normalized spectral density of I_0-fluctuations, respectively. Both, the in-phase and out-of-phase contributions to S_Φ scale linearly with $s_I \cdot f$. For a variety of high-T_c junctions $s_I \cdot f$ is temperature independent and approximately equal to $10^{-8}\, R/\Omega$ [99], which is about three orders of magnitude larger than for typical Nb tunnel junctions with shunt resistances of a few ohms [16,98]. Hence, $1/f$ noise from I_0-fluctuations is orders of magnitude higher in high-T_c than in low-T_c dc SQUIDs. Assuming $\varsigma = 1$ and typical values $I_0R = 100\,\mu V$, $\Gamma = 0.2$ and $\beta_L = 1$ for high-T_c dc SQUIDs operated at 77 K, we estimate from (5.15), and from the numerical simulation results (2.47), (2.48) for v_ϕ, a flux noise of about 200 (100) $\mu\Phi_0 \cdot \mathrm{Hz}^{-1/2}$ at 1 Hz for the in-phase (out-of-phase) contribution. This is substantially above measured levels of white noise. These estimates are in reasonable agreement with experimental observations, and emphasize the need for bias reversal in any high-T_c dc SQUID used for low-frequency measurements.

5.5.3
Thermally Activated Motion of Vortices

The second major source of $1/f$ noise in SQUIDs, which cannot be reduced by any bias reversal scheme, is due to thermally activated vortex motion. A vortex, which is trapped in the body of the SQUID or in the superconducting input circuit, experiences a random pinning potential determined by the presence and nature of defects acting as pinning sites. If the thermal energy is sufficiently large, the vortex may overcome the pinning energy and hop back and forth between two or more adjacent pinning sites. Such a process can induce a change in the flux Φ_a coupled to the SQUID in two different ways [65,100]: First, the SQUID senses directly the change in magnetic stray flux coupled to the SQUID loop, as produced by a vortex moving with a spectral density of 'radial' motion $S_r(f)$. This so-called "direct noise" produces a flux noise $S_\Phi = S_r(\partial\Phi_a/\partial r)^2$, where r is the radial distance of the vortex from the SQUID hole. Second, a vortex fluctuating perpendicularly to some line which is part of the superconducting input structure (e.g., the input coil, crossover or pickup loop of a flux transformer) induces a fluctuating screening current to conserve the total magnetic flux. This process induces also a fluctuation of the magnetic flux coupled into the SQUID ("indirect noise").

Direct and indirect noise both induce a random telegraph signal (RTS) in the SQUID output if a single vortex is hopping between two pinning sites. If the hopping process is thermally activated, the lifetimes $\tau_1(T)$ and $\tau_2(T)$ in each of the potential wells labeled by 1 and 2 are given by

$$\tau_i(T) = \tau_{a,i}\, e^{U_i(T)/k_B T}, \quad (\mathrm{i}=1,2). \tag{5.16}$$

Here, $1/\tau_{a,i}$ is the attempt frequency for the i^{th} state and $U_i(T)$ is the temperature-dependent energy barrier for hopping out of that state. With the change of flux $\Delta\Phi_a$, due to the hopping process between the two states, one obtains the Lorentzian power spectrum of the RTS as [101]

$$S_\Phi(f,T) = \frac{4\Delta\Phi_a^2}{(\tau_1+\tau_2)\left\{\left(\frac{1}{\tau_1}+\frac{1}{\tau_2}\right)^2 + (2\pi f)^2\right\}}. \tag{5.17}$$

Assuming symmetric wells, so that $U_1 = U_2 \equiv U$ and $\tau_{a,1} = \tau_{a,2} \equiv 2\tau_0$, one can characterize the hopping process with a single characteristic time $\tau \equiv 1/(\tau_1^{-1} + \tau_2^{-1}) = \tau_0 \exp\{U(T)/k_B T\}$. In this case (5.17) simplifies to

$$S_\Phi(f,T) = \frac{\Delta\Phi_a^2\,\tau}{1+(2\pi f\tau)^2}. \tag{5.18}$$

Following the approach of Dutta, Dimon and Horn (DDH), [102,103] one can superimpose various uncorrelated hopping processes (see also Sec. 2.1.3), each with its own characteristic time, to obtain a $1/f$ power spectrum

$$S_\Phi(f,T) \propto \frac{k_B T}{f} D(\tilde{U}) \tag{5.19}$$

where $D(U)$ is the distribution of activation energies and $\tilde{U} \equiv -k_B T \ln(2\pi f \tau_0)$. The DDH-model was extended by Ferrari and co-workers to include a generalization of temperature-dependent activation energies [104] and a driving force which acts on the vortices [105]. This model is in good agreement with the experimentally observed dependence of the low- frequency flux noise in high-T_c thin films and single crystals, on frequency, temperature (if not too close to T_c), magnetic field and current [101]. The model allowed the authors to derive the distribution of pinning energies from flux noise measurement. They obtained a broad peak in $D(U)$ at a level below 0.1 eV in YBCO and near 0.2 eV in $Bi_2Sr_2CaCu_2O_8$. The experimentally observed linear increase in flux noise power with magnetic field, in which the sample is cooled, supports the assumption of uncorrelated hopping of vortices. We note that $1/f$ noise from vortex motion is a much bigger issue in high-T_c SQUIDs at 77 K than in low-T_c SQUIDs because of the large thermal activation at the operation temperature 77 K and the low pinning energies of defects.

5.5.4 Generation of vortices

In the following, we consider three different scenarios for the generation of vortices in thin film structures:

(i) The SQUIDs are cooled and operated in a magnetically well-shielded environment. In this case, the magnetic flux density B_0 should be small enough to avoid magnetization of the thin-film SQUID. However, vortex-antivortex pairs can be nucleated upon cooling through T_c. Such pairs may not entirely annihilate because they could be pinned while the temperature is being lowered below the Kosterlitz–Thouless transition temperature. Vortices formed that way can contribute to low-frequency flux noise, even if $B_0 = 0$. However, at present there is no clear experimental evidence that this source of noise plays an important role for SQUID operation. Measurements of flux noise and simultaneous imaging of vortices in YBCO dc SQUIDs by low- temperature scanning electron microscopy (LTSEM) never showed formation of vortex-antivortex pairs. Images taken after zero-field cooling showed that the thin film structures were free of vortices, and the flux noise was white down to the lowest measured frequency of ~1 Hz [106].

(ii) The SQUID is cooled in a static magnetic field and vortices are induced with an areal density $n_\Phi \approx B_0/\Phi_0$. Cooling in the Earth's magnetic field of $B_0 \approx 50\,\mu T$ results in approximately 250 trapped flux quanta over an area of $100\,\mu m \times 100\,\mu m$. Indeed, one requires very high magnetic shielding factors (above 25 000) to keep a $1\,mm^2$ washer free of vortices. In general, when HTS SQUIDs are cooled in a nonzero magnetic field, the additional vortices so formed can create high noise levels. In fact, the low-frequency flux noise power of most high-T_c SQUIDs increases when they are cooled in the Earth's field, by as much as a factor of 50. Figure 5.20 (a) shows the flux noise S_Φ ($f = 1$ Hz) versus cooling field, measured for a YBCO thin film which showed $S_\Phi(f) \propto 1/f$ for cooling fields B_0 above a few μT [107]. $S_\Phi(f)$ scales linearly with B_0, as expected for the uncorrelated hopping of vortices, since $S_\Phi(f)$ is expected to be proportional to the number of vortices and hence to B_0. Similar behavior was found for YBCO dc SQUIDs (see Figure 5.20(b)), directly-coupled magnetometers and planar gradiometers, although $S_\Phi(f)$ did not always scale linearly with B_0 [107–112]. The deviation from the linear increase of S_Φ could be due to sample geometry, inhomogeneous distribution of pinning sites and distribution of activation energies. Reduction of the excess $1/f$ noise in SQUIDs cooled in the static magnetic field of the Earth is clearly essential.

(iii) Below T_c, vortices may enter the superconducting thin film structures at their edges if screening currents due to (time varying) magnetic fields are strong enough. This may be the case even with proper magnetic shielding if currents in metallic parts close to the SQUIDs are generated by thermal gradients upon cooling. Vortices created that way are another possible source of

the low-frequency flux noise observed in a magnetically shielded environment. This is supported by observations that the low-frequency flux noise tends to be higher when the SQUIDs are more rapidly cooled through T_c. Careful design of SQUID probes and slow cooling from T_c down to the operation temperature can reduce such vortex generation. In SQUIDs operated without magnetic shielding, vortices can be generated by screening supercurrents induced by time-varying external field disturbances. This may occur also in unshielded mobile SQUIDs rotated in the static magnetic field of the Earth. For example, Koch *et al.* [113] investigated the effect of removal of a magnetic shield, in which a directly-coupled HTS magnetometer was first cooled. Exposure to a field of 50 μT, for example, caused a substantial increase in the level of $1/f$ noise, even when the device was subsequently placed inside the same shield. Generation of vortices is certainly a bigger problem in unshielded operation than when shielding is used.

We note that the above discussion refers to Abrikosov vortices, which are hopping in the superconducting film. Josephson vortices which can move along grain boundaries in polycrystalline high-T_c thin films have been a major source of $1/f$ noise in the early days of high-T_c superconductivity. The improvement of film quality, however, has greatly reduced this source of $1/f$ noise.

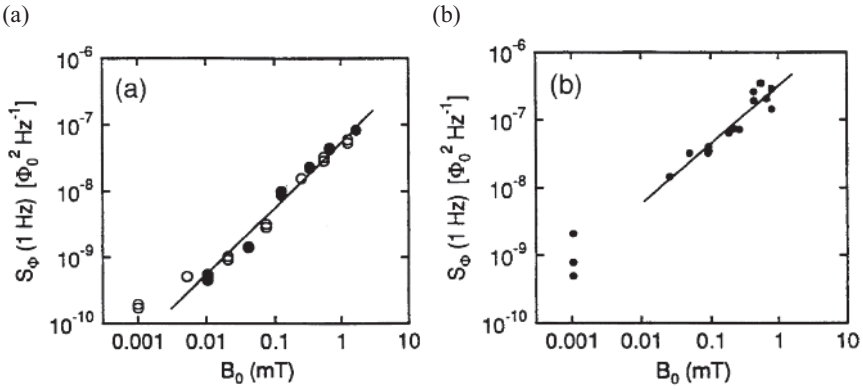

Fig. 5.20 Flux noise S_Φ (1 Hz) vs. cooling field B_0 (a) for a YBCO film at 77 K, measured with a low-T_c SQUID. Filled and open circles indicate reversed direction of B_0, the line is a least- squares fit; (b) for YBCO dc SQUID with bicrystal junctions and 250 μm washer, measured with bias reversal (reprinted with permission from ref. [107]).

5.5.5 Reduction of 1/*f* Noise Generated by Vortex Motion

5.5.5.1 Overview

There are two basically different approaches to minimizing 1/*f*-noise caused by vortex motion: (1) to improve pinning of vortices inside superconducting structures, and (2) to avoid vortex entry. The latter is more effective in HTS structures and can be done by introducing (a) an active cancellation of the external magnetic field discussed in Chapter 7, (b) narrow linewidth structures making it energetically unfavorable for vortices to enter upon cooling in a static magnetic field, (c) flux dams, which reduce screening, and (d) high quality of film edges, which avoid vortex entry *after* cooling below T_c.

5.5.5.2 Vortex pinning

The vortex hopping rate increases exponentially as the ratio of pinning energy to thermal energy k_BT is reduced. Therefore, the microstructurural quality of films and the related pinning energies play an important role in determining the level of low-frequency noise [101]. While SQUIDs made from high-quality Nb thin films usually do not show 1/*f*-noise caused by vortex motion down to frequencies around 1Hz, such noise can be dominant in high-T_c SQUIDs fabricated from YBCO thin films. Hence, much effort has been expended to improve techniques for depositing YBCO on lattice-matched single-crystal substrates (see Section 3.3.2).

To study the flux noise in high-T_c thin films and single crystals, Ferrari *et al.* [101,114,115] measured their fluctuating magnetization using a low-T_c, thin-film dc SQUID. It was inductively coupled to the high-T_c sample, the temperature of which could be raised to above T_c. Subsequently, the availability of high-T_c SQUIDs with low levels of 1/*f* noise made it possible to measure flux noise of high-T_c films more straightforwardly by mounting them directly on such a SQUID placed in liquid nitrogen [116,117,118]. In their early work, Ferrari *et al.* [114] found that the 1/*f* flux noise of a YBCO thin film decreases dramatically as the crystalline quality of the sample improves. For example, for a polycrystalline YBCO film they found a flux noise power of $3 \times 10^{-4} \Phi_0^2$/Hz at 1 Hz and 40 K, whereas values below 10^{-10} Φ_0^2/Hz at 1 Hz and 77 K were obtained for high-quality epitaxial YBCO films [119]. In YBCO single crystals, the flux noise power at 1 Hz was more than a factor of 50 higher, even after the incorporation of artificial defects by proton irradiation. This indicated that high-quality epitaxial YBCO films contain a high density of effective, intrinsic pinning sites. Unfortunately, little is known about their nature. Flux pinning studies, in which various parameters controlling sample quality are systematically and independently varied, are very much needed. In any event dc SQUIDs fabricated from carefully optimized YBCO thin films have reached noise energies close to 10^{-30} J/Hz at 1 Hz [120]. Such a performance is adequate provided the SQUIDs can be coupled to appropriate pickup loops without further increase in the 1/*f* noise. This, however, may require fabrication of low-noise multilayer thin film structures. The general tendencies observed for single YBCO films also apply to such multilayers. Through careful optimization of the multilayer fabrication process, *ex situ*

YBCO/insulator/YBCO trilayers have been fabricated [117,118] which showed low levels of $1/f$ flux noise in a magnetically shielded environment. However, since the upper YBCO film in patterned trilayers tends to be of poorer quality than a single-layer YBCO film, its flux noise is generally higher.

Overall elimination of vortex motion in high-T_c thin films via creation of strong pinning sites, proved to be very difficult. Proton or heavy ion irradiation of single crystals of YBCO increased the critical current density and reduced the $1/f$ noise substantially [119]. However, these critical current densities were still substantially lower, and the $1/f$ noise in ambient fields still substantially higher, than the values in thin films. Furthermore, heavy ion irradiation at doses up to the level at which T_c starts to degrade does not increase the critical current of thin films that already have high critical current densities [121], implying that pinning in these films as grown is already close to optimum. Thus, it seems unlikely that this approach will materially reduce the level of $1/f$ noise in thin YBCO films cooled in an ambient magnetic field.

5.5.5.3 Narrow Linewidth Device Structures

The most practical method of eliminating the excess $1/f$ noise in high-T_c SQUIDs is to design the superconducting components of the magnetometer so that vortices do not enter. Clem calculated that it is energetically unfavorable for magnetic flux to penetrate a film of width w, cooled in a perpendicular field B_0, when $w \leq (\pi\Phi_0/4B_0)^{1/2}$ [122]. This has been proved experimentally on YBCO dc SQUIDs with various film widths by measurements of flux noise vs. cooling field B_0 [95]. Figure 5.21 shows $S_\Phi^{1/2}(f)$ of a square-washer bicrystal SQUID with outer dimensions of 500 µm and a slit 100 µm long and 4 µm wide, cooled in 24 µT (upper trace). The observed $1/f$ spectrum is typical for such devices. The SQUID was subsequently re-patterned to reduce the outer dimension to 30 µm and the linewidth to 13 µm, as indicated by dotted lines in the inset. The lower trace shows that the low-frequency noise is dramatically lower, by two orders of magnitude in power at 1 Hz. Similar measurements on SQUIDs with linewidths ranging from 4 to 13 µm showed that the flux noise at 1 Hz, typically 8–20 $\mu\Phi_0 \cdot \mathrm{Hz}^{-1/2}$, was independent of the cooling field up to a threshold B_T, above which the noise increased rapidly, indicating that vortices penetrated the film. Although B_T increased with decreasing linewidth, the increase was slower than Clem's model predicts. It was suggested that poor quality edges, which contain low-energy sites where vortices tend to nucleate, were the most likely cause of the lower threshold. Indeed, subsequent work (see below) showed that threshold fields of over 100 µT could be achieved with more carefully patterned edges. We note that edges should be vertical to give the highest threshold field, a requirement opposing that of the smoothly-beveled edges needed for multilayer structures.

The concept of narrow linewidths was extended to SQUID washers with arrays of slots or holes (see Figure 5.22). Such structures showed virtually no increase in the low-frequency noise for B_0 up to above 100 µT [123] while their effective area was almost unchanged, sometimes even larger than the effective area of comparable washers without slots or holes [124,125]. Similarly, directly coupled magnetometers with narrow linewidth pickup loop structures have been investigated. Due to the

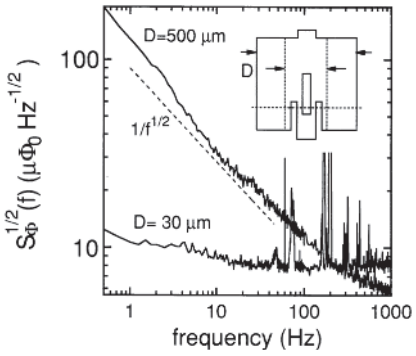

Fig. 5.21 $S_\Phi^{1/2}(f)$ for dc SQUID shown in the inset, cooled in a field of 24 μT. Upper trace is for device with outer dimension $D = 500$ μm, lower trace is after re-patterning to a width $D = 30$ μm (dotted lines). Inset not to scale. Dashed line indicates grain boundary (reprinted with permission from ref. [95]).

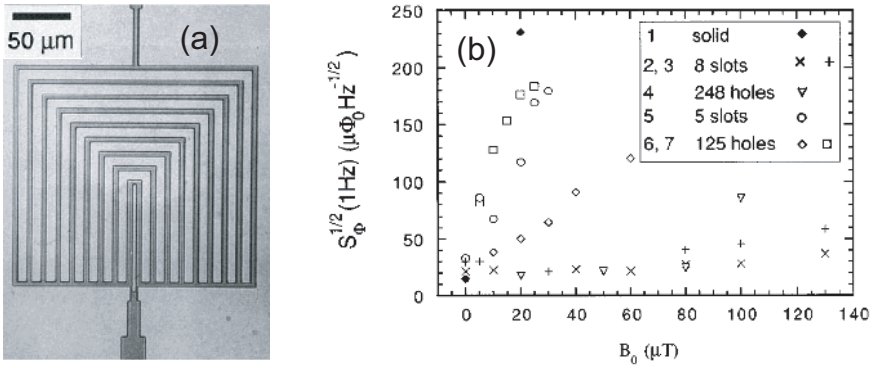

Fig. 5.22 (a) A "slotted washer" design (outer dimension 186 × 204 μm); (b) Noise at 1 Hz $S_\Phi^{1/2}(f)$ vs. cooling field B_0 for various washer SQUIDs (reprinted with permission from ref. [123]).

large mismatch of inductances of the pickup loop and the SQUID, indirect $1/f$ noise from vortices created in the pickup loop, upon cooling through T_c in a static magnetic field, is usually negligible [95,126].

Narrow linewidths can also be useful for multilayer devices. In the case of the multiloop magnetometer, at least in principle, it should be possible to reduce all the linewidths to (say) 4 μm, so that the $1/f$ noise should not increase in ambient cooling fields up to about 100 μT. For a square washer SQUID coupled to a multiturn flux transformer, one can use a washer and a pickup loop with arrays of slots or holes. Such an approach has been successfully demonstrated for YBCO flip-chip magnetometers, which showed only a slight increase of the low-frequency noise when the cooling field was increased from zero up to about 80–100 μT [127].

5.5.5.4 **Flux Dams**

When a device is moved in an ambient magnetic field, the induced supercurrents are very likely to generate vortices and increase the noise. Koch *et al.* [113] demonstrated that this flux entry and the ensuing $1/f$ noise could be prevented or reduced

by means of a "flux dam" – a weak link in the pickup loop that limits the circulating supercurrent. With the flux dam in place, exposing a directly coupled YBCO magnetometer to 50 μT after a zero-field cooling resulted in a considerably smaller increase in the $1/f$ noise than in the absence of the flux dam. Similar devices have shown no significant increase in flux noise (beyond several hundred fT $Hz^{-1/2}$ at 1 Hz, 77 K) after exposure to fields as high as 34 μT following zero-field cooling [128]. Replacing the wide pickup loop of directly coupled magnetometers by several parallel, narrow loops, each with a flux dam, resulted in further improved performance. Such devices have been shown to maintain relatively low noise levels at low-frequency, even after exposure to ac fields with amplitudes up to about 50–60 μT [129,130]. Furthermore, for multiturn flux transformers coupled to narrow linewidth SQUIDs it has been shown that the use of flux dams in the pickup loop is essential to avoid rapid increase of low-frequency flux noise if the magnetometers are subjected to changes of the applied field after cooling below T_c [127]. Thus, for mobile magnetometers the lowest levels of $1/f$ noise are likely to be achieved by combining narrow linewidths and flux dams.

5.6 Other Performance Degrading Effects

5.6.1 Hysteresis

Magnetic hysteresis in a SQUID-based instrument manifests itself as a shift of the voltage-flux characteristics along the flux axis after the magnetic field is cycled [131]. This effect is undesirable if one wishes to keep track of the absolute value of the magnetic field or to measure gradients in large fluctuating background fields. Magnetic hysteresis is observed in low-T_c and high-T_c SQUIDs and is related to vortex entry and pinning near the edges of thin films [96,111,131–135]. The degree of hysteresis is expressed by the hysteresis parameter $h = \delta\Phi/\Delta\Phi$, where $\delta\Phi$ is the flux error caused by sweeping the applied flux between $\pm\Delta\Phi$. For integrated thin film low-T_c gradiometers operated at 4.2K in the ambient magnetic field, a magnetic hysteresis as low as 10^{-9}–10^{-11} has been measured [136]. Initial studies on high-T_c dc SQUIDs made from polycrystalline films showed high levels of nonlinear hysteresis [96,137]. For grain boundary dc SQUIDs involving epitaxial YBCO films on bicrystals, Gross and Chaudhari reported $h < 10^{-6}$ at 77 K for $\Delta\Phi \leq \Phi_0$ [138].

Sun *et al.* [139] made systematic studies of the hysteresis in low-T_c and high-T_c dc SQUIDs using cycling fields ranging from 10 μT to 1 mT peak-to-peak. In each case they found both time- independent and time-dependent hysteresis. The time-independent hysteresis appeared above a threshold field of a few hundred μT. The temperature dependence of the threshold field was similar to that of the critical current density in thin films, suggesting a relationship between this hysteresis and flux pinning. Sun *et al.* developed a quantitative model involving the Lorentz force on vortices due to screening currents, the surface barrier to flux entry, and the pinning

force of defects in the superconducting film. Within this model they showed that the observed threshold field corresponds to the value at which the Lorentz force equals the sum of the surface barrier and the pinning force. Since the screening currents and thus the Lorentz force acting on a vortex are maximum at the edges of the film and decay into film, the vortices are swept into the film until the Lorentz force becomes smaller than the pinning force. The distance over which the vortices penetrate into the washer and the ensuing degree of hysteresis are predicted to depend crucially on the local pinning force near the film edges, in agreement with the dramatic reduction of the hysteresis achieved by improving the quality of the film edges [139]. Clearly, to obtain small hysteresis one requires a high average critical current density in the films and one needs to avoid the presence of grain boundaries in the case of high-T_c films, because they can increase the hysteresis by several orders of magnitude due to the motion of Josephson vortices [131]. In devices made from high-quality films, the hysteresis is dominated by the local film properties close to the edges. Keene *et al.* made measurements of hysteresis in a gradiometric, high-T_c SQUID coupled to a gradiometric flux transformer with multiturn input coils [111]. For cycling fields up to 70 μT, the hysteresis parameter averaged 10^{-9}. When the measurements were repeated on the SQUID without the flux transformer, the hysteresis was little changed for cycling fields below 40 μT but increased dramatically for higher fields. The authors attributed this behavior to the pinning of radial motion of vortices in the SQUID by the input coils. It is particularly important to note that high edge-pinning forces are the key to producing low levels of both $1/f$ noise and hysteresis, which requires steep film edges. This requirement is, unfortunately, not compatible with the need for gently sloping edges on all but the last film of a multilayer structure.

5.6.2
Radio-Frequency Interference

Environmental rf fields may have a major effect on dc SQUID operation, leading to a change in the transfer function V_Φ and to an increase in the white noise [140]. Usually the physical dimension of the SQUID is much smaller than the wavelength of the rf signal. In that case one can consider an external rf radiation applied to the SQUID via its input and output circuitry as an additional rf current bias and rf flux bias. In their simulations, Koch *et al.* [141] coupled rf signals to dc SQUIDs as both an rf flux and an rf current bias. They showed that applying either rf flux or rf current causes rounding of the V–Φ curve. This results in a reduced transfer function and hence leads to an increase in the white noise of the SQUID. However, when conventional flux modulation is used, the rf interference does not create a shift in the output of the SQUID if it is operated in the flux-locked loop. In practice, one expects an external rf signal to induce both an rf flux and rf current simultaneously; these are applied coherently to the SQUID. Simulations showed that in this case the V–Φ curve can become asymmetric about the $\Phi_0/2$ point, even if the rf-free V–Φ curve is symmetric. Such an asymmetry leads to a shift in the output of the flux-locked loop, which is proportional to the applied rf amplitude. If the applied rf sig-

nal is changing, e.g., due to low-frequency modulation, the low-frequency spectrum of the SQUID output will contain the modulated rf amplitude. Therefore, rf interference may cause a large increase in the level of low-frequency noise of the dc SQUID. Fortunately, the rf induced shift of the SQUID output changes polarity with a change in the polarity of the bias current. Therefore, the combined use of flux modulation and bias current reversal can be used to largely eliminate this problem, as has been suggested and demonstrated experimentally by Koch and coworkers [141].

One can often effectively eliminate rf interference by means of appropriate shielding. However, this may not be possible in systems that are required to move in the Earth's field since motion induces eddy currents in the shield. If operation without rf shielding is required, one should make the rf transfer function, which quantifies the coupling of the rf field to the rf bias applied to the SQUID, as small as possible. The direct coupling of the rf radiation as an rf flux bias is usually smaller than the indirect coupling of applied rf fields through rf currents and rf potentials generated in both the input and output components of the SQUID systems. Hence, the exact geometry of these structures (flux transformer, readout wires, etc.) determine the frequency-dependent rf transfer function. Koch *et al.* [141] emphasized that rf coupling is reduced by making the superconducting structures small so as to decrease their antenna gain and, especially, by making the input and output circuits and the SQUID itself as balanced as possible. A high degree of balance prevents common mode rf fields, which have no effect on the SQUID itself, from creating differential signals that could couple to the current and flux bias. Also, rf filtering at both input and output terminals of the SQUID can help in reducing rf interference. An analysis of rf interference pertinent also to the dc SQUID can be found in Chapter 6.

5.6.3 Temperature Fluctuations and Drift

The effects of temperature fluctuations or drifts on the output of a dc SQUID can be substantial [130,142–144]. When operating with liquid coolants, changes in temperature can be induced by boiling or by changes in the ambient pressure above the liquid nitrogen or helium bath. When a cryocooler is used, the temperature of the cold head can fluctuate. Depending on the application, long-term drift or short-term fluctuations will be of different importance. For measurements at low frequencies above 0.5 Hz, as in magnetocardiography, the change in SQUID output, due to drifts in temperature, may be eliminated by a simple high-pass filter. For other applications, which require measurement frequencies as low as 1 mHz, as in geophysics, drifts are a serious issue, whereas high-frequency fluctuations can be averaged.

Different mechanisms can contribute to instability of, or increased noise in, SQUIDs exposed to temperature variations. Due to the temperature dependence of the critical current I_0, the $1/f$ noise caused by critical current fluctuations may change with temperature. This effect, however, can be eliminated by using bias current reversal readout. In dc SQUIDs with critical current asymmetry α_I or inductance asymmetry α_L one may experience a flux shift proportional to $\beta_L(\alpha_I + \alpha_L)$ (see

Section 2.2.4). The temperature dependence of $I_0 \propto \beta_L$ produces a flux change associated with a non-zero coefficient $\partial\Phi/\partial T$ [142]. This effect, however, can also be eliminated by using bias current reversal readout. Furthermore, a change ΔT in temperature modifies the London penetration depth λ_L (T) and thus the effective sensing area A_{eff} (λ_L) of any SQUID or a SQUID magnetometer. This mechanism produces a flux change $\Delta\Phi = (\partial\Phi/\partial T) \cdot \Delta T = B \cdot (\partial A_{\text{eff}}/\partial T) \cdot \Delta T$ in the presence of an ambient magnetic field. With the spectral density of temperature fluctuation S_T, one finds an rms flux noise contribution given by $S_\Phi^{1/2} = B \cdot (\partial A_{\text{eff}}/\partial T) \cdot S_T^{1/2}$ or for the rms magnetic field noise $S_B^{1/2} = B \cdot \alpha_T \cdot S_T^{1/2}$, with $\alpha_T \equiv (\partial A_{\text{eff}}/\partial T)/A_{\text{eff}}$. Using the London formula $\lambda_L(T) = \lambda_L(0)[1 - (T/T_c)^4]^{-1/2}$ one finds $\partial\lambda_L/\partial T \approx 5.3\,\text{nm/K}$ for YBCO (with $\lambda_L(0) = 150\,\text{nm}$, $T_c = 92\,\text{K}$) at $T = 77\,\text{K}$ and $\partial\lambda_L/\partial T \approx 0.84\,\text{nm/K}$ for Nb (with $\lambda_L(0) = 39\,\text{nm}$, $T_c = 9.2\,\text{K}$) at $T = 4.2\,\text{K}$. Therefore, one expects a much stronger temperature fluctuation effect on noise in YBCO SQUIDs operated at 77 K than on noise in Nb SQUIDs operated at 4.2 K. The coefficient α_T depends strongly on the type and geometry of the SQUID or SQUID magnetometer. For a detailed treatment and experimental results obtained for high-T_c devices we refer to [130,143,144]. For typical devices in the earth's magnetic field, the change in flux can be as high as $0.5\,\Phi_0/\text{K}$. To achieve a noise level of (say) $10\,\mu\Phi_0\,\text{Hz}^{-1/2}$, with this temperature coefficient, would require a temperature stability of a few tens of $\mu\text{K Hz}^{-1/2}$ at frequencies above 1 Hz. The effect of temperature fluctuations can be reduced by appropriate design of the SQUID and flux transformer, by stabilizing the ambient pressure, providing a long thermal time constant between the bath and the device, and reducing the ambient field. We note that for magnetometers operated in the Earth's magnetic field, the use of flux dams can significantly reduce $\partial\Phi/\partial T$ as demonstrated by Milliken *et al.* [143].

References

[1] Jaklevic, R.C., Lambe, J., Silver, A.H. and Mercereau, J.E. (1964) Quantum interference effects in Josephson tunneling, *Phys. Rev. Lett.* **12**, 159–160.

[2] Zimmerman, J.E and Silver, A.H. (1966) Macroscopic quantum interference effects through superconducting point contacts, *Phys. Rev.* **141**, 367–375.

[3] Clarke, J. (1966) A superconducting galvanometer employing Josephson tunneling, *Phil. Mag.* **13**, 115–127.

[4] J. Clarke, Measurement of Small Voltages using a Quantum Interference Device in *Proc. Symposium on the Physics of Superconducting Devices* B.S. Deaver, Jr. and W.S. Goree (Eds.), University of Virginia, Charlottesville, 1967.

[5] Silver, A.H. and Zimmerman, J.E. (1967) Quantum states and transitions in weakly connected superconducting rings, *Phys. Rev.* **157**, 317–341.

[6] Clarke, J., Goubau, W.M. and Ketchen, M.B. (1976) Tunnel junction dc SQUID: fabrication, operation and performance, *J. Low Temp. Phys.* **25**, 99–144.

[7] Tesche, C.D. and Clarke, J. (1977) dc SQUID: noise and optimization, *J. Low Temp. Phys.* **27**, 301–331.

[8] Ketchen, M.B. and Jaycox, J.M. (1981) Planar coupling scheme for ultra low noise dc SQUIDs, *IEEE Trans. Magn.* **MAG-17**, 400–403.

[9] Gurvitch, M., Washington, M.A. and Huggins, H.A. (1983) High quality refractory Josephson tunnel junctions utilizing thin aluminum layers, *Appl. Phys. Lett.* **42**, 472–474.

[10] Koch, R.H., Umbach, C.P., Clark, G.J., Chaudhari, P. and Laibowitz, R.B. (1987) Quantum interference devices made from superconducting oxide thin films, *Appl. Phys. Lett.* **51**, 200–202.

[11] Dimos, D., Chaudhari, P., Mannhart, J. and LeGoues, F.K. (1988) Orientation dependence of grain-boundary critical currents in $Yba_2Cu_3O_{7-\delta}$, *Phys. Rev. Lett.* **61**, 219–222.

[12] Simon, R.W., Bulman, J.B., Burch, J.F., Coons, S.B., Daly, K.P., Dozier, W.D., Hu, R., Lee, A.E., Luiere, J.A., Platt, C.E., Schwarzbek, S.M., Wire, M.S. and Zani, M.J. (1991) Engineered HTS microbridges, *IEEE Trans. Magn.* **MAG-27**, 3209–3214.

[13] Gao, J., Aarnink, W.A.M., Gerritsma, G.J., and Rogalla, H. (1990) Controlled preparation of all high-T_c SNS-type edge junctions and DC SQUIDs, *Physica C* **171**, 126–130.

[14] Kingston, J.J., Wellstood, F.C., Lerch, Ph., Micklich, A.H. and Clarke, J. (1990) Multilayer $YBa_2Cu_3O_x$-$SrTiO_3$-YBa_2Cu_3Ox films for insulating crossovers, *Appl. Phys. Lett.* **56**, 189–191.

[15] Ryhänen, T., Seppä, H., and Cantor, R. (1992) Effect of parasitic capacitance and inductance on the dynamics and noise of dc superconducting quantum interference devices, *J. Appl. Phys.* **71**, 6150–6166.

[16] Savo, B., Wellstood, F. C., and Clarke, J. (1987) Low-frequency excess noise in Nb-Al_2O_3-Nb Josephson tunnel junctions, *Appl. Phys. Lett.* **50**, 1757–1759.

[17] Ketchen, M. B., Gallagher, W. J., Kleinsasser, A. W., and Murphy, S. (1985) DC SQUID flux focuser, in *SQUID'85, Superconducting Quantum Interference Devices and their Applications* H. D. Hahlbohm and H. Lübbig, (Eds.), Berlin: Walter de Gruyter, 865–871.

[18] Jaycox, J. M., and Ketchen, M. B. (1981) Planar coupling scheme for ultra low noise dc SQUIDs, *IEEE Trans. Magn.* **MAG-17**, 400–403.

[19] Knuutila, J., Ahonen, A., and Tesche, C. (1987) Effects on dc SQUID characteristics of damping of input coil resonances *J. Low Temp. Phys.* **68**, 269–284.

[20] Ryhänen, T., Seppä, H., Ilmoniemi, R., and Knuutila, J. (1989) SQUID magnetometers for low-frequency applications, *J. Low Temp. Phys.* **76**, 287–386.

[21] Hilbert, C. and Clarke, J. (1985) DC SQUIDs as Radio Frequency Amplifiers, *J. Low Temp. Phys.* **61**, 263–280.

[22] Knuutila, J., Kajola, M., Seppä, H., Mutikainen, R., and Salmi, J. (1988) Design, optimization, and construction of a dc SQUID with complete flux transformer circuits, *J. Low Temp. Phys.* **71**, 369–392.

[23] Seppä, H., and Ryhänen, T. (1987) Influence of the signal coil on the dc SQUID dynamics, *IEEE Trans. Magn.* **MAG-23**, 1083–1086.

[24] Enpuku, K., Yoshida, K., and Kohijo, S. (1986) Noise characteristics of a dc SQUID with resistively shunted inductance. II. Optimal damping, *J. Appl. Phys.* **60**, 4218–4223.

[25] Tarte, E. J., Kang, D. J., Booij, W. E., Coleman, P. D., Moya, A., Baudenbacher, F., Moon, S. H., and Blamire, M. G. (1999) Improvement of High T_c SQUID performance using an integrated resistor, *IEEE Trans. Appl. Supercond.* **9**, 4432–4435.

[26] Ono, R. H., Koch, J. A., Steinbach, A., Huber, M. E., and Cromar, M. W. (1997) Tightly coupled dc SQUIDs with resonance damping, *IEEE Trans. Appl. Supercond.* **7**, 2538–2541.

[27] Huber, M. E., Niel, P. A., Benson, R. G., Burns, D. A., Corey, A. M., Flynn, C. S, Kitaygorodskaya, Y, Massihzadeh, O J., Martinis, M., and. Hilton, G. C. (2001) DC SQUID series array amplifiers with 120 MHz bandwidth, *IEEE Trans. Appl. Supercond.* **11**, 1251–1256.

[28] Seppä, H. (1986) unpublished.

[29] Enpuku, K., Cantor, R., and. Koch, H. (1992) Modelling the dc superconducting quantum interference device coupled to the multiturn input coil. II, *J. Appl. Phys.* **71**, 2338–2346.

[30] Ryhänen, T., Cantor, R., Drung, D., Koch, H., and Seppä, H. (1990) Effect of parasitic capacitance on dc SQUID performance, *IEEE Trans. Magn.* **27**, 3013–3016.

[31] Seppä, H., Kiviranta, M., and Satrapinski, A. (1993) A coupled dc SQUID with low 1/f noise, *IEEE Trans. Appl. Supercond.* **3**, 1816–1819.

[32] Muhlfelder, B., Johnson, W., and Cromar, M W. (1983) Double transformer coupling to a very low noise SQUID, *IEEE Trans. Magn.* **19**, 303–307.

[33] Drung, D., Cantor, R., Peters, M., Ryhänen, T., and Koch, H. (1991) Integrated dc SQUID

magnetometer with high dV/dB, *IEEE Trans. Magn.* **27**, 3001–3004.

[34] Cromar, M. W., and Carelli, P. (1981) Low-noise tunnel junction dc SQUIDs, *Appl. Phys. Lett.* **38**, 723–725.

[35] Carelli, P., Foglietti, V., Leoni, R., and Pullano, M. (1989) Reliable low noise DC-SQUID, *IEEE Trans. Magn.* **25**, 1026–1029.

[36] Cantor, R., Ryhänen, T., Drung, D., Koch, H., and Seppä, H. (1991) Design and optimization of dc SQUIDs fabricated using a simplified four-level process, *IEEE Trans. Magn.* **MAG-27**, 2927–2931.

[37] Cantor, R., Enpuku, T., Ryhänen, K., and Seppä., H. (1993) A high performance integrated dc SQUID magnetometer, *IEEE Trans. Appl. Supercond.* **3**, 1800–1803.

[38] Cantor, R. (1996) DC SQUIDs: Design, optimization and practical applications, in *SQUID Sensors: Fundamentals, Fabrication, and Applications* H. Weinstock (Ed.), Dordrecht: Kluwer Academic Publishers, 179–233.

[39] Ketchen, M. B., Stawiasz, K. G., Pearson, D. J., Brunner, T. A., Hu, C. K., Jaso, M. A., Manny, M. P., Parsons, A. A., and Stein, K. J. (1992) Sub-μm linewidth input coils for low T_c integrated thin-film dc superconducting quantum interference devices, *Appl. Phys. Lett.* **61**, 336–338.

[40] Ketchen, M. B. (1987) Integrated thin-film dc SQUID sensors, *IEEE Trans. Magn.* **MAG-23**, 1650–1657.

[41] Ketchen, M. B. (1991) Design considerations for dc SQUIDs fabricated in deep sub-micron technology, *IEEE Trans. Magn.* **27**, 2916–2919.

[42] Chang, W. H. (1979) The inductance of a superconducting strip transmission line, *J. Appl. Phys.* **50**, 8129–8134.

[43] Enpuku, K., Cantor, R., and Koch, H. (1992) Modelling the dc superconducting quantum interference device coupled to the multiturn input coil. III, *J. Appl. Phys.* **72**, 1000–1006.

[44] Clarke, J., Goubau, W.M., and Ketchen, M. (1976) Tunnel junction dc SQUID: fabrication, operation, and performance, *J. Low Temp. Phys.* **25**, 99–144.

[45] Simmonds, M. B., High symmetry dc SQUID system, US Patent No. 5053834.

[46] Mathai, A., Song, D., Gim, Y., and Wellstood, F. C. (1992) One dimensional magnetic flux microscope based on the dc SQUID, *Appl. Phys. Lett.* **61**, 598–600.

[47] Black, R. C., Mathai, A., Wellstood, F. C., Dantsker, E., Miklich, A. H., Nemeth, D.T., Kingston, J. J., and Clarke, J. (1993) Magnetic microscopy using a liquid nitrogen cooled YBCO SQUID, *Appl. Phys. Lett.* **62**, 2128–2130.

[48] Kirtley, J. R., Ketchen, M. B., Stawiasz, K. G., Sun, J. Z., Gallagher, W. J., Blanton, S. H., and Wind, S. J. (1995) High-resolution scanning SQUID microscope, *Appl. Phys. Lett.* **66**, 1138–1140.

[49] Lee, T. S., Chemla, Y. R., Dantsker, E., and Clarke, J. (1997) High-Tc SQUID microscope for room temperature samples, *IEEE Trans. Appl. Supercond.*7, 3147–3150.

[50] Ketchen, M. B., Kirtley, J. R., and Bhushan, M. (1997) Miniature Vector Magnetometer for Scanning SQUID Microscopy, *IEEE Trans. Appl. Supercond.* **7**, 3139–3142.

[51] Dechert, J., Kirschker, K., Göddenhenrich, T., Mück, M., and Heiden, C. (1997) Self-oscillating micro-SQUID for application in scanning SQUID microscopy, *IEEE Trans. Appl. Supercond.* **7**, 3143–3146.

[52] Hardy, W. N., Bonn, D. A., Morgan, D. C., Liang, R. and Zhang, K. (1993) Precision measurements of the temperature dependence of λ in $YBa_2Cu_3O_{6.95}$: strong evidence for nodes in the gap function, *Phys. Rev. Lett.* **70**, 3999–4002.

[53] Grover, F. W. (1946) *Inductance calculations* New York: Dover, p. 143.

[54] Cantor, R., Vinetskiy, V., and Matlashov, A. (2000) A low-noise, integrated dc SQUID magnetometer for applications in biomagnetism, in *Biomag 96* C. J. Aine, Y. Okada, G. Stroink, S. J. Swithenby, and C. C. Wood, (Eds.), New York: Springer, 15–19.

[55] Granata, C., di Russo, C., Monaco, A., and Russo, M. (2001) Integrated LTc-SQUID magnetometers for multichannel systems, *IEEE Trans. Appl. Supercond.* **11**, 95–98.

[56] Zimmermann, J.E. (1971) Sensitivity enhancement of superconducting interference devices through the use of fractional-turn loops, *J. Appl. Phys.* **42**, 4483–4487.

[57] Drung, D. (1988) Sensor und A/D-Wandlerstufe auf einem Chip zur Präzisionsmessung von Magnetfeldgradienten mit Josephson-Kontakten, Ph.D. Thesis, Universität Fridericiana Karlsruhe, Germany.

[58] Drung, D., Bechstein, S., Franke, K. P., Scheiner, M., and Schurig, T. H. (2001) Improved direct-coupled dc SQUID readout electronics with automatic bias voltage tuning, *IEEE Trans. Appl. Supercond.* **11**, 880–883.

[59] Reimer, D., Schilling, M., Knappe, S., and Drung, D. (1995) Integrated $YBa_2Cu_3O_7$ multi-loop magnetometers at 77K, *IEEE Trans. Appl. Supercond.* **5**, 2342–2645.

[60] Matsuda, M., Murayama, Y., Kiryu, S., Kasai, N., Kashiwaya, S., Koyanagi, M. and Endo, T. (1991) Directly-coupled dc SQUID magnetometers made of Bi-Sr-Ca-Cu oxide films, *IEEE Trans. Magn.*27, 3043–3046.

[61] Koelle, D., Miklich, A.H., Ludwig, F., Dantsker, E., Nemeth, D.T. and Clarke, J. (1993) DC SQUID magnetometers from single layers of $YBa_2Cu_3O_{7-x}$, *Appl. Phys. Lett.* **63**, 2271–2273.

[62] Shen, Y. Q., Sun, Z. J., Kromann, R., Holst, T., Vase, P., and Freloft, T. (1995) Integrated high-T_c superconducting magnetometer with multiturn input coil and grain boundary junctions, *Appl. Phys. Lett.* **67**, 2081–2083.

[63] Drung, D., Ludwig, F., Müller, W., Steinhoff, U., Trahms, L., Shen, Y. Q., Jensen, M. B., Vase, P., Holst, T., Freloft, T., and Curio, G. (1996) Integrated $YBa_2Cu_3O_{7-x}$ magnetometer for biomagnetic measurements, *Appl. Phys. Lett.* **68**, 1421–1423.

[64] Scharnweber, R., and Schilling, M. (1997) A new concept for integrated $YBa_2Cu_3O_7$ magnetometers, *IEEE Trans. Appl. Supercond.* **7**, 3485–3488.

[65] Ferrari, M., Kingston, J. J., Wellstood, F. C., and Clarke, J. (1991) Flux noise from superconducting $YBa_2Cu_3O_{7-x}$ flux transformers, *Appl. Phys. Lett.* **58**, 1106–1108.

[66] Ludwig, F., Dantsker, E., Nemeth, D. T., Koelle, D., Miklich, A. H., Clarke, J., Knappe, S., Koch, H., and Thomson, R. E. (1994) Fabrication issues in optimizing $YBa_2Cu_3O_{7-x}$ flux transformers for low $1/f$ noise, *Supercond. Sci. Tech.* **7**, 273–276.

[67] Dantsker, E., Ludwig, F., Kleiner, R., Clarke, J. Teepe, M., Lee, L. P., Alford, N. M., and Button, T. (1995) Addendum: Low noise $YBa_2Cu_3O_{7-x}$-$SrTiO_3$-$YBa_2Cu_3O_{7-x}$ multilayers for improved superconducting magnetometers [*Appl. Phys. Lett.* **66**, 373], *Appl. Phys. Lett.* **67**, 725–726.

[68] Faley, M. I., Poppe, U., Urban, K., Paulson, D. N., Starr, T. N., and Fagaly, R. L. (2001) Low noise HTS dc-SQUID flip-chip magnetometers and gradiometers, *IEEE Trans. Appl. Supercond.* **11** 1383–1386.

[69] Grover, F. W., (1946) *Inductance calculations* New York: Dover, p. 153.

[70] Grover, F. W., (1946) *Inductance calculations* New York: Dover, Tables 40 and 41, pp. 152–155.

[71] Cantor, R. (2000) Inductance calculations for magnetometer and gradiometer applications, STAR Cryoelectronics Technical Report (unpublished).

[72] Drung, D. (1992) Performance of an electronic gradiometer in noisy environments, in *Superconducting Devices and their Applications* H. Koch and H. Lübbig, (Eds.), Berlin: Springer-Verlag, 542–546.

[73] Espy, M. A., Flynn, E. R., Kraus, R. H., Jr., and Matlashov, A. N. (1999). Two methods for a first order hardware gradiometer using two HTS SQUIDs, *IEEE Trans. Appl. Supercond.* **9**, 3302–3305.

[74] Matlashov, A., Espy, M., Kraus, R. H., Jr., Ganther, K. R., Jr., and Snapp, L. (2001) Electronic gradiometer using HTc SQUIDs with fast feedback electronics, *IEEE Trans. Appl. Supercond.* **11**, 876–879.

[75] Koch, R. H., Rozen, J. R., Sun., J. Z., and Gallagher., W. J. (1993) Three SQUID gradiometer, *Appl. Phys. Lett.* **63**, 403–405.

[76] Donaldson, G. B, Ketchen, M. B, Clarke, J., and Goubau, W. (1976) An integrated thin film gradiometer based on a dc SQUID, in *SQUID'76, Superconducting Quantum Interference Devices and their Applications* H. D. Hahlbohm and H. Lübbig, (Eds.), Berlin, Walter de Gruyter, 303–309.

[77] Ketchen, M. B., Goubau, W., Clarke, J., and Donaldson, G. B. (1978) Superconducting thin-film gradiometer, *J. Appl. Phys.* **49**, 4111–4116.

[78] Ketchen, M. B., Kopley, T., and Ling, H. (1984) Miniature SQUID susceptometer, *Appl. Phys. Lett.* **44**, 1008–1010.

[79] Narasimhan, L. R., Patel, C. K. N., and Ketchen, M. B. (1999) SQUID microsusceptometry in applied magnetic fields, *IEEE Trans. Appl. Supercond.* **9**, 3503–3506.

[80] Enss, C. (2002) Magnetic sensors for x-ray and gamma-ray detection, in *Low Temperature Detectors* F. S. Porter, D. McCammon, M. Gal-

leazzi, and C. Stahle, (Eds.), Melville, NY: American Institute of Physics, 5–10.

[81] de Waal, V. J., van Nieuwenhuyzen, G. J., and Klapwijk, T. M. (1983) Design and optimization of integrated dc SQUID gradiometers, *IEEE Trans. Magn.* **19**, 648–651.

[82] Carelli, P., and Foglietti, V. (1983) A second derivative gradiometer integrated with a dc superconducting interferometer, *J. Appl. Phys.* **54**, 6065–6067.

[83] Kuriki, S., Isobe, Y., and Mizutani, Y. (1987) A second-order planar gradiometer composed of concentric superconductive loops, *J. Appl. Phys.* **61**, 781–784.

[84] Chinone, K., Kasai, N., Kiryu, S., Koyanagi, M., Kado, H., Nakanishi, M., and Kosaka, S. (1991) An integrated dc SQUID gradiometer for biomagnetic applications, *Systems and Computers in Japan* **22**, 88–97.

[85] Eidelloth, W., Oh, B., Robertazzi, R. P., Gallagher, W. J., and Koch, R. H. (1991) $YBa_2C_3uO_7$ thin-film gradiometers: Fabrication and performance, *Appl. Phys. Lett.* **59**, 3473–3475.

[86] Knappe, S., Drung, D., Schurig, T., Koch, H., Klinger, M., and Hinken, J. (1992) A planar $YBa_2Cu_3O_7$ gradiometer operating at 77 K, *Cryogenics* **32**, 881–884.

[87] Zakosarenko, V., Schmidl, F., Schneidewind, H., Dörrer, L., and Seidel, P. (1994) Thin-film dc SQUID gradiometer using a single $YBa_2Cu_3O_{7-x}$ layer, *Appl. Phys. Lett.* **65**, 779–780.

[88] Eulenburg, A., Romans, E. J., Carr, C., Millar, A. J., Donaldson, G. B., and Pegrum, C. M. (1999) Highly balanced long-baseline single-layer high-T_c superconducting quantum interference device gradiometer, *Appl. Phys. Lett.* **75**, 2301–2303.

[89] Millar, A. J., Romans, E. J., Carr, C., Eulenburg, A., Donaldson, G. B., Maas, P., and Pegrum, C. M. (2000) High-T_c gradiometric superconducting quantum interference device and its incorporation into a single-layer gradiometer, *Appl. Phys. Lett.* **76** 2445–2447.

[90] Millar, A. J., Romans, E. J., Carr, C., Eulenburg, A., Donaldson, G. B., and Pegrum, C. M. (2001) Step-edge Josephson junctions and their use in HTS single-layer gradiometers, *IEEE Trans. Appl. Supercond.* **11**, 1351–1354.

[91] Carr, C., Romans, E. J., Millar, A. J., Eulenburg, A., Donaldson, G. B., and Pegrum, C. M., (2001) First-order high-T_c single-layer gradiometers: parasitic effective area compensation and system balance, *IEEE Trans. Appl. Supercond.* **11**, 1367–1370.

[92] Dantsker, E., Tanaka, S., Froehlich, O., Kouznetzov, K., and Clarke, J. (1997) High-T_c SQUIDs with slots and holes and a long-baseline asymmetric gradiometer, in *ISEC '97, 6th International Superconductive Electronics Conference Extended Abstracts*, Vol. 1, H. Koch and S. Knappe, (Eds.), Braunschweig, Germany: Physikalisch-Technische Bundesanstalt, 60–62.

[93] Kittel, A., Kouznetzov, K. A., McDermott, R., Oh, B., and Clarke, J. (1998) High T_c superconducting second-order gradiometer, *Appl. Phys. Lett.* **69**, 2197–2199.

[94] Hwang, Y., Ahn, J. R., Lee, S. G., Kim, J. T., Kim, I. S., and Park, Y. K. (2001) Balancing of the single-layer second-order high-T_c SQUID gradiometer, *IEEE Trans. Appl. Supercond.* **11**, 1343–1346.

[95] Dantsker, E., Tanaka, S., Nilsson, P.-Å., Kleiner, R., Clarke, J. (1996) Reduction of 1/f noise in high-T_c dc superconducting quantum interference devices cooled in an ambient magnetic field, *Appl. Phys. Lett.* **69**, 4099–4101.

[96] Koch, R.H., Gallagher, W.J., Bumble, B., Lee, W.Y. (1989) Low-noise thin-film TlBaCaCuO dc SQUIDs operated at 77 K, *Appl. Phys. Lett.* **54**, 951–953.

[97] Koch, R.H., Clarke J., Goubau W.M., Martinis J.M., Pegrum C.M., Van Harlingen D.J. (1983) Flicker (1/*f*) noise in tunnel junction dc SQUIDs, *J. Low Temp. Phys.* **51**, 207–224.

[98] Foglietti V., Gallagher W.J., Ketchen M.B., Kleinsasser A.W., Koch R.H., Raider S.I., Sandstrom R.L.(1986) Low-frequency noise in low 1/*f* noise dc SQUIDs, *Appl. Phys. Lett.* **49**, 1393–1395.

[99] Marx A., Gross R. (1997) Scaling behavior of 1/*f* noise in high-temperature superconductor Josephson junctions, *Appl. Phys. Lett.* **70**, 120–122.

[100] Wellstood F.C., Kingston J.J., Ferrari M.J., Clarke J. (1991) Thin-film flux transformers of $YBa_2Cu_3O_{7-x}$, *IEEE Trans Magn.* **27**, 2569–2572.

[101] Ferrari M.J., Johnson M., Wellstood F.C., Kingston J.J., Shaw T.J., Clarke J. (1994) Magnetic flux noise in copper oxide superconductors, *J. Low Temp. Phys.* **94**, 15–61.

[102] Dutta P., Dimon P., Horn P. M. (1979) Energy Scales for Noise Processes in Metals, *Phys. Rev. Lett.* **43** 646–649.

[103] Dutta P., Horn P. M. (1981) Low-frequency fluctuations in solids: $1/f$ noise, *Rev. Mod. Phys.* **53**, 497–516.

[104] Ferrari M. J., Johnson M., Wellstood F.C., Clarke J., Mitzi D., Rosenthal P.A., Eom C.B., Geballe T.H., Kapitulnik A., Beasley M.R (1990). Distribution of flux-pinning energies in $YBa_2Cu_3O_{7-x}$ and $Bi_2Sr_2CaCu_2O_{8+x}$ from flux noise, *Phys. Rev. Lett.* **64**, 72–75.

[105] Ferrari M.J., Wellstood F.C., Kingston J.J., Clarke J. (1991) Suppression of magnetic-flux noise in $YBa_2Cu_3O_{7-x}$ by a supercurrent, *Phys. Rev. Lett.* **67**, 1346–1349.

[106] Straub R., Keil S., Kleiner R., Koelle D. (2001). Low-frequncy flux noise and visualization of vortices in a $YBa_2Cu_3O_7$ dc SQUID washer with an integrated input coil, *Appl. Phys. Lett.* **78**, 3645–3648.

[107] Miklich A.H., Koelle D., Shaw T.J., Ludwig F., Nemeth D.T., Dantsker E., Clarke J. (1994) Low frequency excess noise in $YBa_2Cu_3O_{7-x}$ dc superconducting quantum interference devices cooled in static magnetic fields, *Appl. Phys. Lett.* **64**, 3494–3496.

[108] Tanaka S., Itozaki H., Kado H. (1995) Flux trapping of high Tc SQUID, in *Proc. of the 7th Int. Symposium on Superconductivity (ISS '94)*, Advances in Superconductivity VII, Tokyo: Springer-Verlag, edited by Yamafuji K., Morishita T., pp. 1117–1120.

[109] Glyantsev V.N., Tavrin Y., Zander W., Schubert J., Siegel M. (1996) The stability of dc and rf SQUIDs in static ambient fields, *Supercond. Sci. Technol.* **9**, A105–A108.

[110] Faley M.I., U. Poppe M.I., Urban K., Hilgenkamp H., Hennes H., Aarnink W., Flokstra J., Rogalla H. (1995) Noise properties of direct current SQUIDs with quasiplanar YBCO Josephson junctions, *Appl. Phys. Lett.* **67**, 2087–2089.

[111] Keene M.N., Exon N.J., Humphreys R.G., Chew N.G. (1996) The influence of ambient magnetic environments on high-Tc superconducting quantum interference device gradiometers, *J. Appl. Phys.* **79**, 8783–8791.

[112] Dönitz, D., Straub R., Kleiner R., Koelle D. (2001) unpublished.

[113] Koch R.H., Sun J.Z., Foglietti V., Gallagher W.J. (1995) Flux dam, a method to reduce extra low frequency noise when a superconducting magnetometer is exposed to a magnetic field, *Appl. Phys. Lett.* **67**, 709–711.

[114] Ferrari M.J., Johnson M., Wellstood F.C., Clarke J, Rosenthal P.A., Hammond R.H., Beasley M.R. (1988) Magnetic flux noise in thin-film rings of $YBa_2Cu_3O_{7-x}$, *Appl. Phys. Lett.* **53**, 695–697.

[115] Ferrari M.J., Johnson M., Wellstood F.C, Clarke J., Inam A., Wu X.D., Nazar L., Venkatesan T. (1989) Low magnetic flux noise observed in laser-deposited in situ films of $YBa_2Cu_3O_y$ and implications for high-Tc SQUIDs, *Nature* **341**, 723–725.

[116] Koelle D., Miklich A.H., Dantsker E., Ludwig F., Nemeth D.T., Clarke J., Ruby W., Char K. (1993) High performance dc SQUID magnetometers with single layer $YBa_2Cu_3O_{7-x}$ flux transformers, *Appl. Phys. Lett.* **63**, 3630–3632.

[117] Ludwig F., Koelle D., Dantsker E., Nemeth D.T., Miklich A.H., Clarke J., Thomson R.E. (1995) Low noise $YBa_2Cu_3O_{7-x}$-$SrTiO_3$ -$YBa_2Cu_3O_{7-x}$ multilayers for improved magnetometers, *Appl. Phys. Lett.* **66**, 373–375.

[118] Ludwig F., Dantsker E., Koelle D., Kleiner R., Miklich A.H., Clarke J. (1995) Multilayer magnetometers based on high-T_cSQUIDs, *Appl. Supercond.* **3**, 383–398.

[119] Shaw T.J., Clarke J., van Dover R.B., Schneemeyer L.F., White A.E. (1996) Effects of 3.1 MeV proton and 1 GeV Au ion irradiation on the magnetic flux noise and critical current of $YBa_2Cu_3O_{7-x}$, *Phys. Rev B* **54**, 15411–15416.

[120] Koelle D., Kleiner R., Ludwig F., Dantsker E., Clarke J. (1999) High-transition-temperature superconducting quantum interference devices, *Rev. Mod. Phys.* **71**, 631–686.

[121] Barbour J.C., Venturini E.L,. Ginley D.S, Kwak J.F. (1992) Irradiation effects in high temperature superconductors, *Nucl. Instrum. Methods* B **65**, 531–538.

[122] Clem J. (1996) unpublished.

[123] Dantsker, E., Tanaka S., Clarke J. (1997) High-T_c SQUIDs with slots or holes: low 1/f noise in ambient magnetic fields, *Appl. Phys. Lett.* **70**, 2037–2039.

[124] Jansman A.B.M., Izquierdo M., Eiguren A., Flokstra J., Rogalla H. (1998) Effective area in slotted high T_c dc washer superconducting quantum interference devices, *Appl. Phys. Lett.* **72**, 3515–3517.

[125] Jansman A.B.M., Izquierdo M., Flokstra J., Rogalla H. (1999) Slotted high-T_c dc SQUID

magnetometers, *IEEE Trans. Appl. Supercond.* **9**, 3290–3293.

[126] Cho H.-M., McDermott R., Oh B., Kousnetzov K.A., Kittel A., Miller J.H. Jr.. Clarke J. (1999) Low-frequency noise in field-cooled, directly coupled magnetometers, *IEEE Trans. Appl. Supercond.* **9**, 3294–3297.

[127] Cho H.-M., Andresen Y. T., Clarke J. (2001) Low-frequency noise in high-transition-temperature superconducting multilayer magnetometers in ambient magnetic fields, *Appl. Phys. Lett.* **79**, 2483–2485.

[128] Milliken F.P., Brown S.L., Koch R.H. (1997) Magnetic field-induced noise in directly coupled high-T_c superconducting quantum interference device magnetometers, *Appl. Phys. Lett.* **71**, 1857–1859.

[129] DiIorio M.S., Yang K.-Y., Yoshizumi S., Haupt S.G, Haran D., Koch R.H., Milliken F.P., Rozen J.R, Lathrop D.K., Kumar S., Trammell H.S. III (1999) Sensitive high-T_c SQUID magnetometers for unshielded operation, *IEEE Trans. Appl. Supercond.* **9**, 4428–4431.

[130] Ludwig F., Drung D. (1999) Low-frequency noise of improved direct-coupled high-T_c superconducting quantum interference device magnetometers in ac and dc magnetic fields, *Appl. Phys. Lett.* **75**, 2821–2823.

[131] Sun J.Z., Gallagher W.J., Koch R. H. (1994) Initial-vortex-entry-related magnetic hysteresis in thin-film SQUID magnetometers, *Phys. Rev. B* **50**, 13664–13673.

[132] Sun J.Z., Gallagher W.J, Koch R.H. (1992) Magnetic hysteresis in thin film dc SQUID magnetometers, *Appl. Phys. Lett.* **61**, 3190–3192.

[133] Sun, J.Z., Gallagher W.J., Koch R.H. (1993) Non-linear hysteresis in thin film SQUID magnetometers, *IEEE Trans. Appl. Supercond.*, **3** 2022–2025.

[134] Clem T.R., Purpura J.W., Wiegert R.F., Goodman W.L. (1993) Nonlinear response of low temperature superconducting thin film gradiometer sense loops, *IEEE Trans. Appl. Supercond.* **3**, 1848–1851.

[135] Purpura J.W., Clem T.R., Wiegert R.F. (1993) Nonlinear response in thin film high temperature superconducting magnetometer sense loops, *IEEE Trans. Appl. Supercond.* **3**, 2445–2448.

[136] Koch R.H., Ketchen M.B., Gallagher W.J., Sandstrom R.L., Kleinsasser A.W., Gambrel D.R., Field T.H., Matz H. (1991) Magnetic hysteresis in integrated low-Tc SQUID gradiometers, *Appl. Phys. Lett.* **58**, 1786–1788.

[137] Foglietti V., Koch R.H., Gallagher W.J., Oh B., Bumble B., Lee W.Y. (1989) Noise and hysteresis in flux-locked TlBaCaCuO SQUIDs, *Appl. Phys. Lett.* **54**, 2259–2261.

[138] Gross, R., Chaudhari P. (1992) SQUIDs employing high-T_c Superconductors in *Principles and Applications of Superconducting Quantum Interference Devices* edited by Barone A. (Singapore: World Scientific) pp. 419–479.

[139] Sun J.Z., Gallagher W.J., Callegari A.C., Foglietti V., Koch R.H. (1993) Improved process for high-Tc superconducting step-edge junctions, *Appl. Phys. Lett.* **63**, *1561–1563.*

[140] Ishikawa N., Nagata K., Sata H., Nasai N., Kiryu S. (1993) *IEEE Trans. Appl. Supercond.* **3**, 1910–1913.

[141] Koch R. H., Foglietti V., Rozen J.R., Stawiasz K.G., Ketchen M.B., Lathrop D.K., Sun J.Z., Gallagher W.J. (1994) Effects of radio frequency radiation on the dc SQUID, *Appl. Phys. Lett.* **65**, 100–102.

[142] Schöne S., Mück M., Thummes G., Heiden C. (1997) Investigation of the response of superconducting quantum interference devices to temperature variation, *Rev. Sci. Instr.* **68**, 85–88.

[143] Milliken F.P., Koch R.H., Brown S.L., Altman R.A., Gallagher W.J., Haupt S.G., Lathrop D.K. (1997) The response of high-T_c SQUID magnetometers to small changes in temperature, *J. Appl. Phys.* **82**, 6301–6305.

[144] ter Brake H.J.M., Aarnink W.A.M., van den Bosch P.J., Hilgenkamp J.W.M., Flokstra J., Rogalla H. (1997) Temperature dependence of the effective sensing area of high-T_c dc SQUIDs, *Supercond. Sci. Technol.* **10**, 512–515.

6
Practical RF SQUIDs: Configuration and Performance

Alex Braginski and Yi Zhang

6.1 Introduction

A simplified description of rf SQUIDs is given in Chapter 1, their theory is presented in Chapter 2 and the readout electronics in Chapter 4. Given this background, we concentrate here on presenting in historical perspective the more important examples of practical embodiments of rf SQUIDs, and their performance as magnetic flux and field sensors. Indeed, since the ground breaking work and initial instrument demonstrations in the 1960s [1,2], rf SQUIDs were used as magnetic field sensors for applications requiring high sensitivity. With no reproducible thin-film junction technology at hand, this was a natural consequence of the relatively easy set-up and operation of rf SQUIDs, which required only a single adjustable point contact junction,. Later on, in the 1980s, they were gradually replaced by thin-film dc SQUIDs, which then offered sensitivity much higher than that of the first commercially available lower radio frequency SQUIDs of the 1970s.

The discovery of high-T_c superconductors (HTS) in 1986 rekindled interest in rf SQUIDs. Indeed, sensitivity comparable to that of high-T_c dc SQUIDs was immediately achieved. Also, at the end of that decade, very high bias frequency (above 1 GHz, microwave) low-T_c (LTS) rf SQUIDs, in a practical thin-film (microstrip resonator) embodiment, were also shown to offer flux noise and energy resolution comparable to those of good low-T_c dc SQUIDs [3].

Operation of high-T_c and low-T_c rf SQUIDs at very high bias frequencies is currently a standard approach, and such devices continue to be attractive as magnetic field sensors. However, with low-T_c dc SQUIDs well entrenched in most existing applications involving liquid helium, only high-T_c rf SQUIDs have viable application prospects. For that reason, in this chapter we emphasize practical HTS rf SQUIDs.

6.2 Rf SQUID Magnetometers

6.2.1 Practical Device Optimization

In the following sections, we review earlier and recent practical rf SQUID magnetometers and gradiometers. Most of the essential parameters characterizing the per-

formance of such practical devices are the same as those introduced in Chapter 5. To calculate and optimize rf SQUID parameters such as inductance and coupling between the input coil and the SQUID loop, one should proceed as described there. However, additional parameters specific only to rf SQUIDs, which are most important for practical device optimization, need to be introduced and emphasized here. We restrict our attention to rf SQUIDs operating in the adiabatic regime, where the angular bias frequency ω_{rf} is sufficiently below the cutoff frequency $\omega_{cut} = 2\pi f_{cut} = R/L$; here R is the junction resistance and L the rf SQUID loop inductance.

It was shown in Sections 1.4 and 2.3 that rf SQUIDs can operate either in the hysteretic (dissipative) or nonhysteretic (dispersive) regime, depending on the value of the hysteresis or screening parameter $\beta_{rf} = 2\pi LI_0/\Phi_0$; here I_0 is the junction critical current and Φ_0 is the flux quantum. Early analog simulations and experiments indicated that in the case of dissipative low-T_c SQUIDs operating at liquid helium (LHe) temperatures, the rf SQUID output (modulation) signal V_T and the transfer coefficient $\partial V_T/\partial \Phi_a$ are maximum and the white noise intrinsic energy $\varepsilon(f)$ is a minimum when $\beta_{rf} \approx 1$, i.e., near the transition from the dissipative to dispersive mode of operation [4,5].

Another equally essential requirement for the best performance is the optimization of inductive coupling between the rf SQUID loop and the tank circuit. It was shown in Chapter 2 that, while the coupling needs to be *weak* in the dissipative mode, it should not be weaker than some necessary minimum. At low thermal fluctuations, simulations and experiments lead to the requirement $k^2Q \approx 1$, where k is the coupling coefficient and Q is the loaded quality factor of the tank circuit [5].

Indeed, hysteretic rf SQUIDs designed using these two optimization criteria were prevalently in use until the 1990s, while the attainable superior performance of nonhysteretic rf SQUIDs remained largely ignored. Even today, highly sensitive microwave LTS SQUIDs are usually hysteretic. Yet, it was analytically shown [6,7] and also confirmed by experiments, that in the dispersive mode a very high transfer coefficient [8] and superior energy resolution [9] can be attained, provided that $\beta_{rf}k^2Q > 1$. This condition can be fulfilled when Q, and thus the impedance of the tank circuit is sufficiently high.[1)] Nonhysteretic rf SQUIDs operate with bias frequency ω_{rf} off resonance (which occurs at ω_0), while the resonance curve of their tank circuit $V_T(\xi)$ is nonlinearly dependent on the applied flux Φ_a; here $\xi = (\omega_{rf} - \omega_0)/\omega_0$ is the detuning coefficient. When Φ_a deviates from $(n + 1/4)\Phi_0$, the usual bias point, the resonance curve becomes asymmetrical and even multivalued as shown in Figure 2.27(a). With the bias frequency set off-resonance, near an infinite slope point, the transfer coefficient can be arbitrarily high, but at the cost of reduced bandwidth and strong dependence on SQUID parameters, especially on the bias current amplitude and frequency [7]. Hence, the requirement for optimal performance is an appropriate value of ξ set so that the transfer coefficient will be very high, but not exceedingly

1) Since the impedance of the semiconductor preamplifier is rather low at very high (microwave) frequencies, operation in this regime can be advantageous only when impedance matching of the preamplifier and the tank circuit is possible in spite of the high impedance of a high-Q resonator, as it was done in [9], for example. This is discussed in Subsection 6.2.2.2.

so – to safeguard the stability of flux locking and the required signal bandwidth. In any given system, one needs to adjust ξ empirically.

The analyses and simulations cited above were performed for practical values of the critical current and SQUID loop inductance, and are valid in the low-thermal-fluctuation limit $\beta_{rf}\Gamma << 1$; here $\Gamma = 2\pi k_B T/I_0\Phi_0$. However, in the case of rf SQUIDs operating at liquid nitrogen (LN_2) temperatures, practical values of I_0 and L often result in the high thermal fluctuation limit, $\beta_{rf}\Gamma \geq 1$. The unitary theory (Section 2.3.3) and experiments to date [10] suggest that in this limit, and with $\beta_{rf}k^2Q > 1$, the output signal is maximum and the white noise minimum at $\beta_{rf} < 3$. The transition from dispersive to hysteretic mode of operation occurs at $\beta_{rf} \approx 3$ (in [10] the transition was observed at $\beta_{rf} = 3.6$). In experimental practice, the optimum value of β_{rf} is usually attained or approached by adjusting the junction's critical current I_0, usually by appropriate annealing processes.

The general requirement for optimum performance of all rf SQUIDs, dissipative and dispersive, is a high bias frequency ω_{rf}. According to the low thermal fluctuation hysteretic noise theory (see Section 2.3.4.2), the energy resolution scales as $1/\omega_{rf}$ up to about 0.1 ω_{cut}, although even at $\omega_{rf} > R/L$ the SQUID can still operate. This scaling is the cause of the already mentioned high sensitivity of microwave hysteretic rf SQUIDs [3]. In nonhysteretic SQUIDs, high $\omega_{rf} << \omega_{cut}$ minimizes the contribution of the tank circuit to the noise and thus helps to optimize the system's energy resolution. To take full advantage of the low noise and energy resolution of all sensitive rf SQUIDs, cryocooled preamplifiers are usually required, as pointed out in Sections 2.3 and 4.4.

Theoretical predictions in the high thermal fluctuations limit apply only when $\omega_{rf} << \omega_{cut}$ (Section 2.3.3). For high-T_c rf SQUIDs, the attainable HTS junction resistances lead to practical optimum bias frequencies in the UHF and low microwave range, between, say, 0.6 and 3 GHz. In practice, the exact frequency choice is not very critical, and depends also on tank circuit layout design and size considerations. For example, when the tank circuit resonator is integrated with a SQUID single-layer flux focuser, the resonator's size, and thus its resonant frequency ω_0, may depend on the required magnetic field resolution.

We note that, in contrast to dc SQUID magnetometers, quantitative optimization (numerical simulation), which incorporates all high-frequency effects, and also parasitic couplings between the low-frequency (input) and rf (tank) circuits, has not been applied extensively to rf SQUIDs. Especially, the high-T_c rf SQUID device optimization has been mostly empirical. Hopefully, numerical analysis of practical high-T_c rf SQUIDs, which will include both the tank circuit resonator design and the input circuit optimization, analogous to that discussed in Chapter 5, will be performed in the future and will lead to a more precise determination of layouts and parameters for optimized performance.

6.2.2
Low-Temperature rf SQUID Magnetometers

6.2.2.1 Low-Temperature Bulk Magnetometers

Historically, the first practical rf SQUIDs were made from pieces of machined bulk niobium cylinder, in which a hole with a diameter of a few mm was drilled and a slit machined, as shown in Figure 6.1(a). An adjustable point contact between two anodized niobium screws across the slit, served as the Josephson junction. A more inherently stable symmetrical mechanical design, less sensitive to mechanical vibrations, is shown in Figure 6.1(b) [2]. The niobium cylinder had two identical holes drilled parallel to the cylinder axis with a slit between them, which was bridged by the point contact. The tank circuit was wound from niobium wire and placed inside one SQUID hole. A superconducting wire coil permitted one to attain a high quality factor of the tank circuit, thus minimizing its noise (normal conducting wire, e.g., of copper, generates Nyquist noise currents and resulting magnetic noise, which was thus avoided). This structure was suitable as a magnetometer in cases where the bare SQUID was not used as a field sensor, but rather as a current sensor measuring the current flowing in the input coil of a flux transformer. That coil could be placed in the other hole of the symmetrical SQUID structure. A major advantage of that structure was also its insensitivity to an external uniform magnetic field.

The disadvantage of such open-hole bulk SQUID structures was their high loop inductance, which could reach or exceed 1 nH, depending on the hole diameter and length. A high SQUID loop inductance, of the order of nH, leads to low I_0, comparable with noise current, and thus high flux noise, low modulation voltage and low transfer coefficient. To minimize the loop inductance, Zimmerman proposed and demonstrated the so-called fractional turn rf SQUID, which essentially consisted of a number of SQUID loops connected in parallel [11]. This reduced the total loop inductance to L/n, where n is the number of loops, all having equal areas. Since all

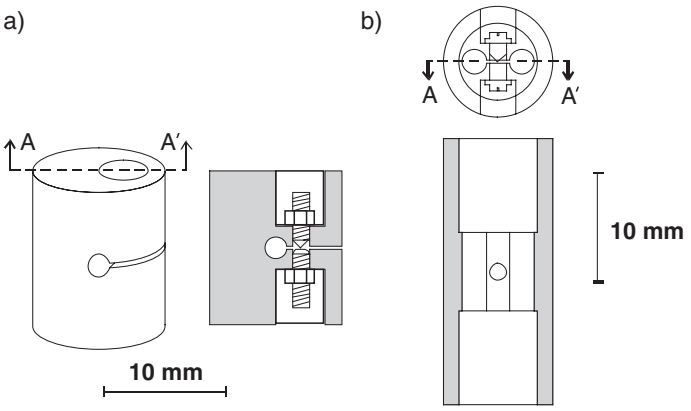

Fig. 6.1 Bulk niobium rf SQUID point-contact devices: (a) an early asymmetrical configuration, (b) an inherently more stable symmetrical structure. Drawn following [2] (*with permission, © J. Appl. Phys.*)

loops are threaded by magnetic flux, the magnetic field sensitivity (field-to-flux coefficient $\partial B/\partial \Phi$) is the same as for one single loop. As discussed in Chapter 5, a planar version of this concept, shown in Fig. 5.14, became quite useful and widely used in LTS thin-film dc SQUIDs.

A different approach to attaining a sufficiently small loop inductance was the toroidal cavity rf SQUID. A cut-away schematic drawing is shown in Figure 6.2(a). A major advantage of the toroidal cavity was its long length and, therefore, a loop inductance that was much lower than that of the open two-hole structure. This made the rather complicated bulk multi-loop structure unnecessary. Furthermore, the toroidal SQUID permitted to attain tight coupling between the wire-wound input coil and the SQUID loop, while at the same time providing an excellent superconducting self-shield for the SQUID, especially helpful in preventing direct rf interference coupling into the structure and also reducing flux trapping. The first demonstrated device had one cavity, common for the input and tank coils [12]. Soon thereafter, a design with two concentric toroidal cavities shown in Figure 6.2(a), a smaller one for the tank circuit coil and a slightly larger for the input coil, was introduced [13] and used also in commercial designs. An additional advantage was that the mutual inductance between these coils was zero. The loop inductance of such structures could be rather low, down to below 100 pH. Such toroidal SQUIDs (with factory-adjusted, fixed point contacts, or early thin film junctions) became work horses in early commercial magnetometer systems. Table 6.1 contains a performance summary of a typical magnetometer, which used to be manufactured by BTi and is shown in Figure 6.3 [14]. The values of typical design parameters such as the input inductance, input and feedback coupling, etc., are rather typical also for more recent thin-film magnetometers (compare Tables 6.1 and 6.2). With an appropriate flux transformer pickup coil, the magnetic field resolution B_N of this magnetometer was of the order of 10 fT/√Hz.

It was recognized very early that the SQUID sensitivity should increase with tank resonant frequency (see Table 6.1) and several demonstrations of bulk microwave SQUID operation were made at frequencies up to 10 GHz [15,16]. A significantly improved energy resolution of $\varepsilon = 7 \times 10^{-31}$ J/Hz was obtained at 9 GHz for a point-

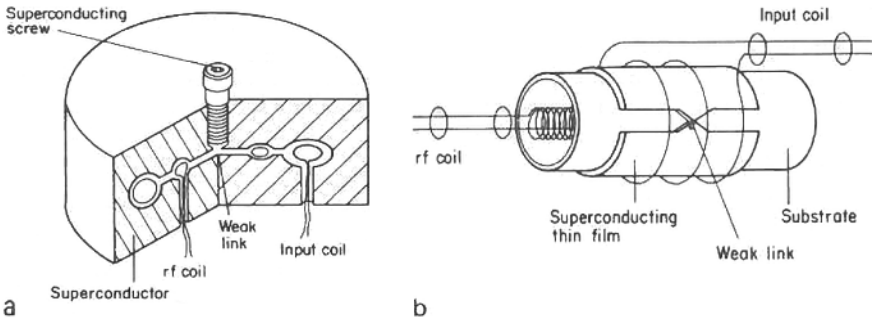

Fig. 6.2 The early rf SQUIDs: (a) toroidal SQUID (a cut-away) with point contact, (b) a cylindrical thin-film SQUID with Dayem bridge weak link. Courtesy D. Paulson, Tristan Technologies.

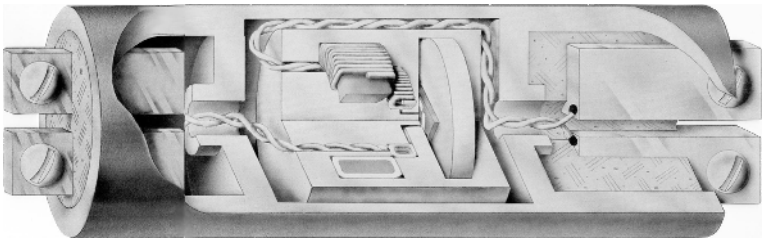

Fig. 6.3 Cut-away drawing of a commercial toroidal rf SQUID with two cavities (BTI, courtesy D. Paulson, Tristan Technologies).

contact toroidal SQUID adjusted to operate in the hysteretic mode [16]. A low-Q resonant annular cavity was used as a tank circuit, which constituted a mismatched low-impedance transmission line having an electrical length of $\lambda/2$ at 9 GHz. The complex *reflected* signal was monitored rather than the signal being *transmitted* through the cavity. The matched $\lambda/2$ resonator and the readout in the reflection mode were later emulated in the development of modern planar microwave rf SQUIDs described below. At the time, that important laboratory demonstration did not result in any practical devices.

Tab. 6.1 Characteristics of a commercial (BTi) toroidal rf SQUID (1975) [14]

Parameter	Symbol	Unit	Value
Overall dimensions (in housing, with screw terminals for input and tank coils, see Fig. 6.3)	–	mm	20 diam. × 75 long
Toroidal capsule dimensions	–	mm	11.9 diam. × 39 long
Josephson junction: thin-film, Nb-based			
SQUID loop inductance	L	pH	60
Input coil inductance	L_i	μH	1.7–2.0
Input coil coupling (current sensitivity)	$1/M_{dyn}$	$\mu A/\Phi_0$	0.1
Feedback coupling (current-lock), separate modulation coil	–	$\mu A/\Phi_0$	1 to 2
Flux noise	$S_\Phi{}^{1/2}$	$\mu\Phi_0/\sqrt{Hz}$	80–200 ($f_0 = 20$ MHz) 20 ($f_0 = 200$ MHz)
Corner frequency (to 1/f noise)	f_c	Hz	0.01 to 1
Energy resolution ($f_0 = 20$ MHz)	ε	J/Hz	$0.6–1.5 \times 10^{-28}$

6.2.2.2 Low-Temperature Thin-Film Magnetometers

Even at the beginning of research on rf SQUIDs, and into the 1970's, some devices had been made entirely by thin-film technology [12,17], using the cylindrical geometry shown in Fig. 6.2(b). In the early 1980's, Ketchen *et al.* proposed a wide thin-film dc SQUID loop (a planar washer, see Figures 5.4 and 5.6) to maximize coupling between the SQUID and an integrated input coil [18]. At about the same time, emerged the reliable technology of the trilayer Nb-AlO_x-Nb refractory tunnel junction. As a consequence of these two milestone achievements, refractory washer-type rf SQUID magnetometers were promptly demonstrated by a number of research groups. Shortly thereafter, such devices became commercially available from several sources [BTi, Quantum Design, Cryogenic Consultants (later Oxford Instruments)]. These rf SQUIDs operated at bias frequencies between 20 and 200 MHz. Their main advantage over the bulk devices was ruggedness, exemplified by unlimited shelf-life and immunity to thermal cycling failures. At higher bias frequencies, the thin-film devices were also more sensitive than at 20- or 30-MHz. Shielding was assured by a niobium cylinder, inside which the SQUID chip was mounted on a printed circuit board or encapsulated in an appropriate epoxy – in analogy to dc SQUIDs, see Figure 5.12. The rf SQUID chip was typically a two-hole gradiometric washer (see Section 6.3), with an integrated input coil coupled to one hole and either an integrated or a wire-wound tank coil coupled to the other (within the polymer capsule). As representative examples, we summarize in Table 6.2 the performance of two such commercial refractory devices fabricated on sapphire or quartz substrates [19,20]. Such devices, even if still available commercially, are a dying breed, since their flux noise and energy resolution are significantly worse than those of modern LTS dc SQUIDs.

Tab. 6.2 Performance of commercial thin-film rf SQUID magnetometers [19,20]

Parameter	Symbol	Unit	Oxford Instruments SQS6C Values (1992)	Quantum Design 20 RF Values (2002)
Overall dimensions (in Nb cylindrical shield)	–	mm	12.7 diam. × 70 long	46 or 76 long
SQUID loop inductance	L	pH	150	NA*
Input coil inductance	L_i	μH	1.5	2.0
Input coil coupling (current sensitivity)	$1/M_{dyn}$	μA/Φ_0	< 1.0	0.2
Feedback/modulation coil inductance	–	μH	NA	0.3
Feedback/mod. coupling (current-lock)	–	μA/Φ_0	1.0	1.5
Flux noise	$S_\Phi^{1/2}$	$\mu\Phi_0/\sqrt{\text{Hz}}$	70 (f_0 = 20 MHz) 30 (f_0 = 200 MHz)	30–35 (f_0 = 150 MHz)
Corner frequency	f_c	Hz	NA	0.01–0.2
Energy resolution	ε	J/Hz	0.7×10^{-28} (f_0 = 20 MHz) 0.2×10^{-28} (f_0 = 200 MHz)	NA

* NA = information not available to us

The flux noise and noise energy of uncoupled thin-film hysteretic rf SQUIDs can be made comparable to those of typical dc SQUIDs by adopting a sufficiently high bias frequency and emulating the approach of [16]. A practical and relatively simple planar tank circuit was demonstrated as a half-wavelength ($\lambda/2$) narrow microstrip niobium resonator into which the SQUID loop could be integrated [21]. The conceptual transition from a SQUID with discrete *LC* elements tank circuit to a microstrip rf SQUID, is schematically illustrated in Figure 4.15. Optimized coupling to the microwave oscillator and readout electronics was provided by a thin-film coupling microstrip (also shown in the Figure)[2)], which permitted readout in the reflection mode.

At the tank frequency of 3 GHz, the Nb resonator with copper or Nb ground plane had a loaded Q of 500 to 1000. The coupling coefficient between the SQUID and microstrip inductances was calculated to be $k^2 = 1 \times 10^{-3}$ to 3×10^{-3} for SQUID inductances between 80 and 240 pH, with the effective microstrip inductance estimated at 8 nH for an assumed sinusoidal current distribution. The I_0 of the tunnel junction was set to obtain $\beta_{rf} \geq 1$. Consequently, optimum coupling of the rf SQUID to the resonator ($k^2 Q \approx 1$) and thus optimum performance could be attained. The signal amplitude and transfer coefficient were reasonably high, for example, $V_T = 80\,\mu V$ and $\partial V_T / \partial \Phi_a = 160\,\mu V/\Phi_0$ at a SQUID inductance $L = 100$ pH. The best measured rms white noise level was $\sqrt{S_\Phi} = 3 \times 10^{-6}\ \Phi_0/\sqrt{\text{Hz}}$ down to 0.1 Hz and reflected the dominating room-temperature preamplifier noise rather than the intrinsic noise of the SQUID. In the best case, the white noise energy resolution was $\varepsilon = 2 \times 10^{-31}$ J/Hz for a SQUID inductance of 240 pH [21,3]. A further improvement of noise, down to $1.2 \times 10^{-6}\ \Phi_0/\sqrt{\text{Hz}}$, was experimentally recorded in flux-locked loop when using a cooled GaAs HEMT preamplifier. In this case, the lowest energy resolution was approximately 3×10^{-32} J/Hz or about $300\hbar$ [22,23]. Optimization considerations for the microstrip rf SQUID can be found in Section 4.4.6. Such SQUIDs, with room-temperature preamplifiers, have been used in successful demonstrations of various practical applications.

The possibility of designing thin-film rf SQUID magnetometers with an input coil, which would have a magnetic field or current resolution comparable to that of modern dc SQUIDs was also shown in [21]. Superconducting input coils of various designs could be integrated on the microstrip rf SQUID. Depending upon the design, no increase of noise or only a moderate increase was observed.

An important demonstration of an even more sensitive nonhysteretic thin-film rf SQUID actually preceded the work [21] described above. A washer SQUID with a PbAuIn-PbSb tunnel junction was flip-chip mounted with a larger thin-film flux concentrator (2 mm in diameter) and a rutile (TiO_2) substrate ($4 \times 3 \times 0.7$ mm) high-Q dielectric resonator serving as the tank circuit and oscillating in the distorted H_{11} mode at about 9.5 GHz [9]. Coupling between the SQUID, the flux concentrator and the resonator was easily adjustable by spacers in the flip-chip assembly. The H_{11}

2) In ref. [21] the coupling microstrip was actually a small piece of thin brass plate, which could be positioned to adjust coupling. Since the position was found not critical, in subsequent experiments the microstrip was included into the photolithographic design.

mode has maximum field perpendicular to the main surface of resonator and SQUID loop. In this configuration, the maximum field corresponds to maximum current, the resonator and SQUID can be seen as connected in series, and the equivalent resistance of the resonator is Q times less than its high wave impedance. Hence, good matching to a relatively low-impedance microwave amplifier is possible.

The whole assembly was placed inside a microwave cavity (near its shorted end) attached to the end of a coaxial cable connected to the 9.5 GHz oscillator and readout electronics (readout was in reflection mode), with a preamplifier at room temperature. An open coupling loop was formed of the internal coax conductor end. It could be rotated from outside the cryostat to adjust the coupling to the tank resonator. Importantly, in this experimental setup it was possible to compare directly the performance of hysteretic and nonhysteretic SQUIDs using the same evaluation method. Measured with a 10 kHz output bandwidth, with $k^2Q \approx 0.9$ and $\beta_{rf} \approx 3.2$, an energy resolution of $\varepsilon = 1.5 \times 10^{-31}$ J/Hz was recorded [24], similar to that in [21], but with a much lower loop inductance of only 30 pH. Yet, when $\beta_{rf} < 1$ was obtained by reducing I_0 of an otherwise identical SQUID junction, and $\beta_{rf} k^2 Q > 1$ ($k^2 Q \approx 6$, with $k^2 \approx 1 \times 10^{-3}$), the reported energy resolution was $(2.5 \pm 0.7) \times 10^{-33}$ J/Hz or about $24\hbar$ [9], nearly two orders of magnitude better than for the hysteretic SQUID. One can question how such resolution could be attained without cooling the amplifier, which at room temperature had a noise temperature of 2000 K. According to the authors, this is possible because the rf SQUID in nonhysteretic mode is a parametric amplifier, using the rf bias "pumping" to boost the energy of low-frequency input signals [9,25]. Hence, the noise temperature of the system can be well below that of the amplifier to which the SQUID output (the tank resonator) is connected.

The results described in [9] to our knowledge have not been duplicated by others. However, the design approach demonstrated in [9] was later successfully emulated in high-performance high-T_c rf SQUIDs with dielectric resonators, which are described below.

6.2.3
High-Temperature rf SQUID Magnetometers

6.2.3.1 Technological Limitations

As in the case of dc SQUIDs, the lack of HTS wire suitable for making pickup coils and of a bonding technology for high-T_c superconducting contacts, restrict high-T_c rf SQUIDs to planar structures, usually mounted in flip-chip configuration. Typically, two single-layer HTS film structures are used, one including the SQUID itself, and the other a flux focuser, possibly integrated with a superconducting tank circuit resonator. The reported high-T_c flux transformers, which were suitable for rf SQUIDs (see Section 6.2.3.6), and were fabricated using the multilayer fabrication technology, represented feasibility demonstrations rather than production devices.

6.2.3.2 Bulk High-T_c Magnetometers

Usable SQUIDs were made initially from HTS bulk samples [26-30]. At first, unstructured pieces of HTS material were used, but soon thereafter more suitable geometries were tested, which already had been proven in bulk LTS rf SQUIDs. Simple one-hole SQUIDs or fractional turn SQUIDs were fabricated. White noise levels between 10^{-3} and 10^{-4} $\Phi_0/\sqrt{\text{Hz}}$ were obtained in some cases, with field-noise levels down to about 1 pT/$\sqrt{\text{Hz}}$. Toroidal rf SQUIDs were also demonstrated [31], but, in the absence of suitable HTS wire for winding a flux transformer, such devices have not been used in any application demonstrations.

The weak links in high-T_c bulk rf SQUIDs consist of natural grain boundaries and their critical current was usually trimmed by some procedure to obtain the value required at 77 K. These procedures included heating [28], squeezing [30] or spark erosion [32] of a small bridge machined into the superconductor. Notably, in the first demonstration by Zimmerman *et al.* [27], the use of a break junction made it possible to reversibly adjust the junction's critical current, and thus the SQUID parameter β_{rf}. However, no solution could be found to the main problem of bulk polycrystalline high-T_c SQUIDs – the pronounced low-frequency excess noise – which was attributed mainly to thermally-activated hopping of vortices in the bulk material and its grain boundaries (see Section 5.5). Nevertheless, given the large hole (loop) diameter of up to several mm, magnetic field resolutions of the order of 1pT/$\sqrt{\text{Hz}}$ were obtained, sufficient even to demonstrate rudimentary biomagnetic measurements [29,32].

It is unlikely that the performance of bulk SQUIDs could have been improved further, unless single crystals or nearly single-crystalline bulk materials were introduced. Most of these early devices were operated at or near 20 MHz, and a slight decrease in white noise was achieved using higher bias frequencies [33].

6.2.3.3 Early Thin-Film High-T_c Magnetometers

From 1990 onwards, with steady advances in cuprate [mostly $YBa_2Cu_3O_{7-x}$ (YBCO)] epitaxial thin film and junction fabrication technology, single-layer high-T_c thin-film rf SQUIDs were investigated and developed. Most substrates were single crystal $SrTiO_3$ (STO) or $LaAlO_3$ (LAO), 0.5 to 1 mm thick, but Y:ZrO_2 (YSZ) and MgO substrates were also used. Many research groups reported early washer-type devices [34–40] utilizing various HTS junction types. Compared to high-T_c dc SQUIDs, all of these rf devices had a relatively large SQUID loop size, up to $0.4 \times 0.4\ \text{mm}^2$, corresponding to an inductance of over 500 pH, and an external lump-element tank circuit with a wire-wound coil providing only suboptimal coupling to the SQUID, $k^2Q << 1$. At tank frequencies of 20 to 30 MHz, such devices exhibited a rather high level of white noise, $\sqrt{S_\Phi} = 2\text{–}3 \times 10^{-4}\ \Phi_0/\sqrt{\text{Hz}}$ at best. A somewhat lower white noise level could be achieved using a higher bias frequency of 150–160 MHz [38,39]. There was no observable 1/f noise at frequencies above 1 Hz (as it was submerged by the high white noise), and the absolute value of the noise at a specified low frequency, typically 1 Hz, was usually lower than that of early thin-film HTS dc SQUIDs. An example was a 150-MHz rf SQUID utilizing step-edge junctions [41]. With loop inductance of $L = 125$ pH it exhibited a white noise of about $\sqrt{S_\Phi} = 1 \times 10^{-4}$

$\Phi_0/\sqrt{\text{Hz}}$ down to 0.3 Hz, an energy resolution of 1.4×10^{-28} J/Hz, and a magnetic field resolution of $B_N = 0.9$ pT/$\sqrt{\text{Hz}}$ at 1 Hz, for a washer size of only 1.4×1.4 mm^2 [38]. Similar single-layer magnetometers having much larger washer size and loop inductance were then developed to optimize flux capture and focusing, and thus improve the field sensitivity ($\partial B/\partial\Phi$) and resolution. With a washer size close to 10×10 mm^2, and a loop inductance $L\approx300$ pH (still below the critical L value, beyond which $\partial V_T/\partial\Phi_a$ degrades) these simple magnetometers attained a B_N close to 100 fT/$\sqrt{\text{Hz}}$, sufficient for many applications [42]. A 4×4 cm^2 thin-film flux focuser in flip-chip configuration with such a SQUID, exhibited a B_N of 24 fT/$\sqrt{\text{Hz}}$. Large bulk focusers were also demonstrated to improve B_N significantly. One should note that, due to the higher loop inductances, the magnetic field noise without flip-chip concentrators could be made comparable to that of direct-coupled high-T_c dc SQUIDs of the same size, in spite of the flux noise levels much exceeding those of dc SQUIDs (see data in Chapter 5).

The possibility of obtaining lower levels of flux noise in planar rf SQUIDs, by using bias frequencies in the microwave range, was pursued from the beginning of the HTS thin-film rf SQUID investigations. Daly *et al.* reported the first microwave YBCO SQUIDs, which had been coupled to a 10-GHz TE_{011} cylindrical cavity and operated at temperatures up to 55 K [43]. Instead of using a cavity, Zhang *et al.* used a superconducting microstrip $\lambda/2$ resonator as a 3-GHz tank circuit for a step-edge junction rf SQUID integrated into the microstrip [44], in direct analogy to the LTS microwave rf SQUIDs [3,21]. For a SQUID inductance of 140 pH, the best reported white flux noise was, approximately, $\sqrt{S_\Phi} = 3\times10^{-5}\ \Phi_0/\sqrt{\text{Hz}}$, and the corresponding noise energy resolution $\varepsilon = 1.9\times10^{-29}$ J/Hz [45]. That value of flux noise was one order of magnitude higher than that of the LTS microstrip rf SQUID [21], and the energy resolution was two orders of magnitude higher. One of the reasons for such rather substandard performance was the weak coupling of the SQUID to the microstrip resonator, caused by the loaded Q of the resonator being too low.

Afterwards, over several years, a largely empirical development process continued, aimed at: (1) designs with sufficiently high k^2Q at high, but not too high, tank frequencies, say, between 0.5 and about 1 GHz, and (2) flip-chip high-Q resonators integrated with a thin-film flux concentrator (focuser). This made it possible to optimize $\partial B/\partial\Phi$ and B_N for substrate sizes not exceeding 10×10 to 15×15 mm^2. Eventually, two relatively mature and simple rf SQUID types emerged, which are described in the following two sections. We note that initially the nominal optimization criteria were $\beta_{rf}\geq1$ and $k^2Q\approx1$, and only later, after the experimental confirmation [10] of the unitary noise theory [46], was it fully understood why the tank circuit I–V characteristics (discussed in Section 6.6) suggested a nonhysteretic behavior even when $\beta_{rf}>1$. A more conscious effort was then made to maintain $\beta_{rf}\,k^2Q>1$.

6.2.3.4 **Magnetometers with Coplanar Resonators**

The superconducting coplanar resonator tank circuit consists of two concentric stripes surrounding a flux-focusing large washer, both patterned from the same YBCO thin film. The motivation for the coplanar rather than microstrip configuration with a high-ε_r dielectric (e.g., LAO) spacer (substrate) was to eliminate eddy

current losses originating in the large-area normal ground plane under the focuser. Two typical layouts, circular and square, are shown in Figure 6.4 [47,48]. The resonant frequency f_o can be controlled (reduced) by increasing the angle $\theta > 0$ between the resonator slits, i.e., by relative rotation of open ends of the two resonator stripes. For the circular layout, the dependence of f_0 on θ was calculated to be

$$f_{o,th}(\theta) = f_0(0) / \left[1 + 2\frac{\theta}{\pi} - \left(\frac{\theta}{\pi}\right)^2 \right]^{1/2}, \tag{6.1}$$

where $f_0(0)$ is experimentally determined at $\theta = 0$ [49]. The experimental dependence on θ is in reasonable agreement with Eq. (6.1). An additional degree of $f_0(\theta)$ control can be achieved by introducing a small short between the resonator stripes positioned at an angle ξ relative to the inner slit, as also shown in Figure 6.4. For washer outer dimensions of 8.0 to 8.5 mm on a 10×10 mm substrate, and with stripe widths and separation of 0.1 to 0.2 mm, the experimental values of $f_0(\theta,\xi)$ can be varied from approximately 1.5 GHz at $\theta = 0$ and no short in the circular layout, down to ≈ 0.6 GHz at $(\theta,\xi) = 90°$, in the square layout [48]. With increasing size of each layout the resonant frequency decreases. For example, for the circular layout of Figure 6.4 with $(\theta,\xi) = 0$, the measured frequency decreases from $f_0 \approx 1.5$ GHz at $D_1 = 8.1$ mm to ≈ 0.8 GHz at 13.4 mm, and 0.6 GHz at 23 mm. The unloaded Q_0 of such coplanar YBCO resonators at 77 K is typically a few thousand, without any electromagnetic shielding.

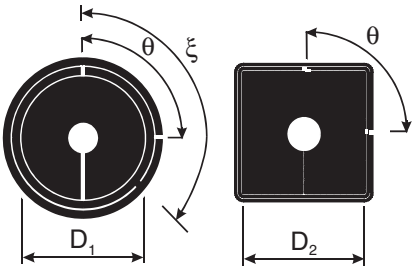

Fig. 6.4 Two layouts of flux concentrator surrounded by coplanar resonator [48]. Resonance frequency depends on θ, the angle between stripe slits, and ξ, the angle between the position of the optional short between stripes and of the inner slit.

The resonator is coupled inductively (indirectly, via the flux concentrator), to a concentrically positioned small washer rf SQUID, 2 to 3 mm in diameter, with a trimmed step-edge junction. The SQUID and the resonator are assembled in a flip-chip configuration. Typical SQUID inductances are $L = 150$ to 300 pH, with $1 < \beta_{rf} < 3$ at 77 K so that the SQUID operates in the dispersive mode. Slit hole inductances providing effective field sensitivity (low $\partial B/\partial \Phi$) are calculated using an empirical formula [50], which does not account for the kinetic inductance L_{kin}. For better accuracy, numerical calculations incorporating L_{kin} were also used [51].

The coupling coefficient k can be roughly estimated from

$$k^2 = A_{\text{eff}}/A_{\text{t,c}} \tag{6.2}$$

where A_{eff} is the effective area [52] of the small SQUID and $A_{\text{t,c}}$ is the geometric area of the flux concentrator with the surrounding resonator. The loaded Q of the resonator coupled to the SQUID and the electronics is 200 to 300 in the L range indicated above, so that $\beta_{\text{rf}} k^2 Q > 1$ is attained with $\beta_{\text{rf}} \geq 2$ and $k^2 \geq 7 \times 10^{-3}$ [53]. A single-turn coupling coil (readout loop), fabricated as a printed circuit positioned close to the other side of the resonator substrate, provides matching between the high-impedance tank circuit and the 50 Ω coaxial cable, which connects to the electronics. The coil provides rf biasing, flux modulation (if used) and feedback to the SQUID, and also picks up the readout signal, so that, in the reflection measurement mode, only one coaxial cable connects the SQUID with the room-temperature electronics. A complete SQUID probe thus consists of at least three planar flip-chip-mounted elements: the SQUID, the resonator with flux focuser and the coupling (readout) coil, all shown in Figure 6.5(a). Additionally, a planar heater can be incorporated into an encapsulated package, as shown. Mylar® foil spacers between these elements permit one to adjust coupling and matching.

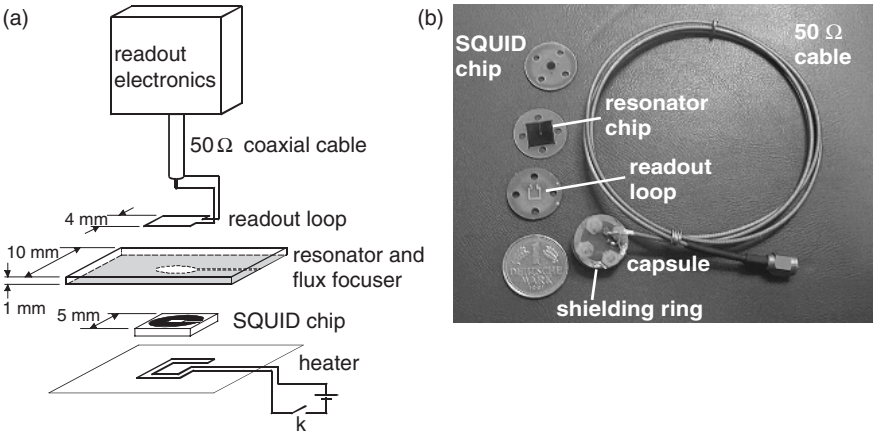

Fig. 6.5 Elements of encapsulated rf SQUID probe: (a) schematic representation, (b) a photograph of probe components with cable (adapted from [57]).

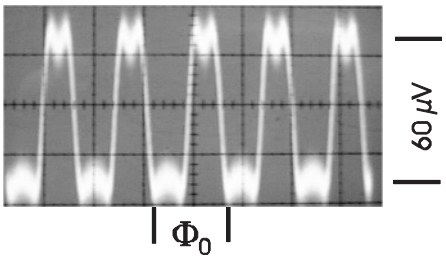

Fig. 6.6 An oscilloscope trace of typical V_T-Φ_a function of a dispersive optimized rf SQUID with coplanar or dielectric resonator.

In the nonhysteretic mode, and when $\beta_{rf}k^2Q>1$, the V–Φ function is nearly rectangular at a proper detuning from resonance, as discussed in Chapter 2.3 and shown in Fig. 6.6, so that $\partial V_T/\partial \Phi_a$ is high, up to 0.5 mV/Φ_o. At 77 K the preamplifier noise contribution is thus small and optimal performance is approached.

A few examples of best performance reported for coplanar resonator magnetometers are presented in Table 6.3. The noise spectrum, compared to that of an optimized rf SQUID with tank circuit made of normal discrete elements, is shown in Figure 6.7(a).

A rms white flux noise level of slightly less than 1×10^{-5} $\Phi_0/\sqrt{\text{Hz}}$, and a corresponding noise energy resolution of about 1×10^{-30} J/Hz at signal frequencies f > 100 Hz were attained. Accordingly, the white magnetic field noise of 23 to 35 fT/$\sqrt{\text{Hz}}$ for the square washer size of 8.5 mm and 16 fT/$\sqrt{\text{Hz}}$ at $D_1 = 13.4$ mm are among the lowest attained in the absence of a planar flux transformer. However, one should note that the low-frequency (LF) flux noise remains rather high, e.g., $\sqrt{S_\Phi}(1\text{ Hz}) \approx 6\times10^{-5}$ $\Phi_0/\sqrt{\text{Hz}}$. It turns out that lack of effective rf shielding permits the modulated electromagnetic interference (EMI) disturbances to mix down and contribute to LF noise (see Section 6.6). Also, the stability of the SQUID's operating point can be adversely affected by slowly varying external fields, and this contributes

Tab. 6.3 Reported performance of planar HTS magnetometers with flux focusers [48,57]

Parameter → Resonator Type ↓	Washer Size	f_0	Loop Size	L	$\partial B/\partial\Phi$	$S_\Phi^{1/2}$ $\mu\Phi_0/\sqrt{\text{Hz}}$		ε 10^{-30}J/Hz	B_N fT/$\sqrt{\text{Hz}}$	
	mm	MHz	μm	pH	nT/ Φ_0	100 Hz	1 Hz	100 Hz	100 Hz	1 Hz
Coplanar	8.5×8.5	910	100×100	≈150	3.87	6.5	NR*	≈0.6	26	NR
	8.5×8.5	810	10×500	≈260	2.54	9.0	NR	≈0.7	23	NR
	8.5×8.5	810	15×500	≈270	2.42	14.4	60	≈1.6	35	≈150
	13.4 dia.	650	10×500	≈260	1.85	8.5	55	≈0.6	16	≈105
Dielectric, STO	10×10	650	100×100	≈150	3.2	7.3	25	≈0.8	24	≈83

* NR = not recorded

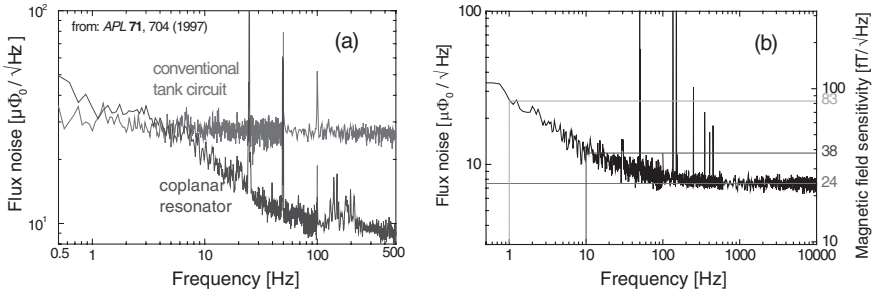

Fig. 6.7 Noise spectra of HTS rf SQUIDs: (a) with coplanar resonator and an optimized rf SQUID with discrete *LC* tank circuit, $L = 150$ pH, $D_1 = 13.4$ mm; (b) with dielectric substrate resonator, $L = 150$ pH, $D_2 = 10$ mm.

to LF noise as well. Attempts to reduce these effects consisted of two approaches: (1) to shield the SQUID and resonator partially by introducing the, so-called, planar toroidal design [54], inspired by the bulk toroidal SQUID [12,13]; and (2) to concentrate the rf field of the resonator and SQUID by replacing the coplanar resonator with a suitable dielectric resonator with high ε_r, as described below, and depositing the SQUID washer on the same high-ε_r substrate material.

In closing, to emphasize that the described properties of magnetometers with coplanar resonators were consistently attained using nonhysteretic SQUIDs operating in the high fluctuation limit, we give the example of another 8.5×8.5 mm SQUID with loop inductance $L \geq 260$ pH[3)], similar to the two included in Table 6.3. At about 77 K, this sample had the following properties, determined in part by direct, destructive measurement (of I_0 and R) [10]: $k^2 \approx 8 \times 10^{-3}$, $\beta_{rf} \approx 1.8$, $k^2 Q \beta_{rf} \geq 3$, $I_0 \approx 2\,\mu$A, $R \approx 11\,\Omega$ (low $V_0 = I_0 R$ of only 22 μV), $\Gamma \approx 1.4$, $\varepsilon \approx 0.9 \times 10^{-30}$ J/Hz.

6.2.3.5 Magnetometers with Dielectric Resonators

The use of a bulk high-Q dielectric resonator as a microwave tank circuit was first proposed and demonstrated for a low-T_c thin-film rf SQUID [55]. The rf SQUID loop was deposited directly on a rutile disc 3 mm in diameter and 1 mm thick, serving as a resonator at about 10 GHz. Subsequently, the flip-chip flux concentrator was added as described in [9] (Section 6.2.2.2). This approach was adapted to nonhysteretic high-T_c rf SQUIDs [56] and eventually empirically optimized by using a standard $10 \times 10 \times 1$ mm STO substrate as a resonator with the flux concentrator deposited on it [57]. While the bare substrate resonates at about 1.6 GHz, the YBCO thin-film flux focuser, deposited on this substrate, reduces f_0 to only 0.65 GHz, a convenient value. With YBCO coating, the unshielded Q_0 is still of the order of several thousand at 77 K. Hence, a loaded Q of a few hundred and $k^2 Q \beta_{rf} > 1$ can easily be attained. The same layout of SQUID washer is used as with the coplanar resonator, but deposited on STO rather than LAO. In fact, all the components of the encapsulated probe package shown in Figure 6.5(b) are fully analogous to those of the coplanar resonator package, except that the coplanar stripes are now absent. The essential motivation for replacing the coplanar resonator with the dielectric one is the much improved stability of the rf SQUID operating point. The SQUID and resonator are sandwiched between high-ε_r STO substrate plates, which confine the operating electromagnetic fields to a small electrically shielded volume. As already mentioned in Section 6.2.3.4, such field confinement and shielding should reduce the LF noise.

The reported properties are included in Table 6.3, and the noise spectrum is shown in Figure 6.7(b). One can see that the white noise is virtually identical with that of coplanar devices, while the LF noise at 1 Hz is reduced. Nevertheless, it is still higher than in the best direct-coupled dc SQUIDs operating with bias reversal.

3) The inductance was determined without accounting for the kinetic inductance contribution, which at 77 K can represent 10 to 20 % of the geometric inductance.

6.2.3.6 Thin-Film HTS Magnetometers with Flux Transformers

To enhance the field sensitivity of rf SQUIDs further, planar flux transformers with a multi-turn input coil are desirable. For YBCO rf SQUIDs, attempts to use flux transformers remained unsuccessful until it was shown that the multi-turn input coil must be rf-decoupled from the planar tank-circuit resonator to prevent damping of the latter [58]. The feasibility of such decoupling was demonstrated using a coplanar resonator design, and a flip-chip two-hole planar gradiometric rf SQUID shown in Figure 6.8(a) and (b). A thin-film normal shunt shorts the pickup coil for the rf bias only, while the low-frequency signal current flows through the trilayer multi-turn input coil (Figure 6.8(a)). The input coil is coupled to one hole of the gradiometric SQUID, while the rf bias is coupled to the other hole by a single-turn loop shaped within the contour of the pickup coil. The separate equivalent layouts for rf- and low-frequency currents are shown in Fig. 6.8(c) and (d). Simulations of current distribution and Q_0 of the resonator versus the substrate loss tangent, were performed for various resonator and flux transformer layouts and showed that it is possible to test various layouts numerically for effective rf decoupling without resorting to experiments [53]. With a somewhat optimized design using a modified coplanar resonator on the 10 mm × 10 mm substrate, a $\partial B/\partial \Phi = 0.9\,\mathrm{nT}/\Phi_o$ and $B_N \approx 12\,\mathrm{fT}/\sqrt{\mathrm{Hz}}$ were demonstrated, an improvement by a factor of 2 compared with the best data of Table 6.3 (for devices of nearly the same size) [59]. The 1/f noise for this structure was, unfortunately, very high, about $S_\Phi{}^{1/2}(10\,\mathrm{Hz}) = 300\,\mu\Phi_0/\sqrt{\mathrm{Hz}}$, with a corner frequency of about 2000 Hz. The results to date should be considered only as a demonstration of feasibility since a reliable technology for input coil fabrication, a prerequisite for any 1/f noise reduction effort, has not been implemented.

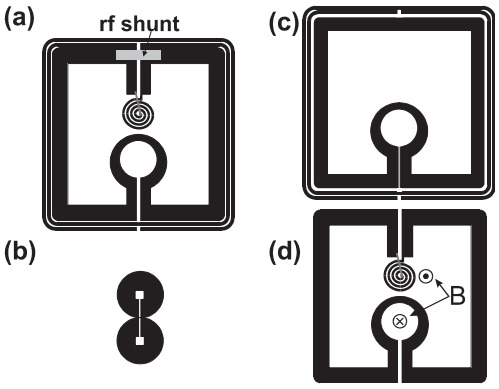

Fig. 6.8 Experimental and equivalent layouts illustrating the decoupling of HF and LF circuits in a flip-chip transformer operating in a flip-chip configuration with a two-hole gradiometric rf SQUID: (a) layout of the complete flip-chip transformer with an rf shunt; (b) layout of the gradiometric two-hole SQUID; its baseline equals the separation between the centers of the input and tank coupling coils; (c) equivalent layout for rf currents; (d) equivalent layout for LF currents [58].

6.3 Rf SQUID Gradiometers

6.3.1 Low-Temperature Gradiometers

In an unshielded environment, one can use gradiometers of first or higher order to reduce interference by distant undesired external signal sources within the measuring signal bandwidth. The conventional solution for low-T_c rf SQUID gradiometers has been to use superconducting (niobium) wire-wound pickup gradiometric coils in an axial (radial) configuration (see Figure 1.10(b,c)). These coils are attached to the thin-film input coil of the SQUID so that a superconducting contact is obtained. These gradiometric coils are the same as those of the dc SQUID gradiometers described in Chapter 5. Planar low-T_c rf SQUID gradiometers, again similar to those of the dc SQUID, can be fabricated, but are rarely used in practice, in contrast to planar dc SQUID gradiometers, which are used, for example, in some commercial biomagnetic systems.

6.3.2 High-Temperature Gradiometers

6.3.2.1 Hardware rf SQUID Gradiometers

No HTS wire is available to wind the pickup coils and the input coil of a SQUID gradiometer. The technology of superconductive connections between HTS wire and an HTS thin-film input coil also does not exist. First-order high-T_c gradiometers can be shaped (machined) from bulk material as two-hole structures, fully analogous to the early bulk LTS designs, but with a weak-link bridge trimmed as in bulk HTS magnetometers (see 6.2.2.1).

Thin-film two-hole gradiometer structures with short baselines were developed and implemented in various nondestructive evaluation (NDE) applications. The equivalent circuit and an example of a practical layout are shown in Figure 6.9. This layout, which measures the off-diagonal field component $\partial B_z/\partial x$, is equivalent to two washer SQUIDs, connected in parallel and sharing the common junction, in which currents induced by the signals captured by the two washers subtract. The

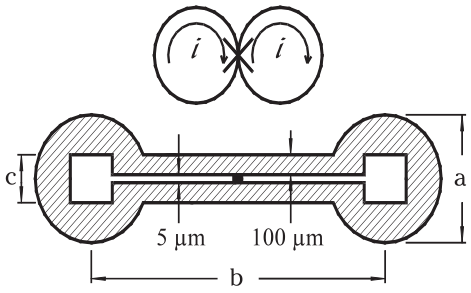

Fig. 6.9 The equivalent circuit and an example of a two-hole planar gradiometer layout, where *b* is the baseline and *a* the outer diameter of the washer [61].

geometrical symmetry of such a layout permits one to attain easily a gradiometer imbalance on the order of 0.1 % (common mode suppression by a factor of over 1000). The wire-wound tank coil can be coupled to one of the holes without significantly affecting the balance.

Tinchev was first to report a thin-film YBCO rf SQUID gradiometer with a baseline of 1.4 mm [60]. It operated at 20 MHz and its flux noise was about 1×10^{-4} $\Phi_0/\sqrt{\text{Hz}}$ in a flux-locked loop. Subsequently, thin-film YBCO two-hole gradiometers were developed with somewhat longer baselines, up to 5 mm, and similar noise levels [61]. Their gradient sensitivity has been typically of the order of 1 pT/cm$\sqrt{\text{Hz}}$.

Baselines exceeding a few millimeters are impractical since the parasitic inductance of the slit dominates, and may exceed the washer inductance of 100 ± 50 pH by an order of magnitude [62]. Consequently, the total inductance is likely to exceed 0.5 nH and thus fall in the range where $\partial V_T/\partial \Phi_a$ is depressed and the flux noise increased. The inductance of slits can be reduced by a factor of roughly two with a flip-chip YBCO film cover shield, and possibly by a higher factor when introducing a shield patterned in a trilayer structure, but this is likely to be at the price of deteriorated balance. Much longer baselines, up to about 30 mm, were attained by adapting to rf SQUID [63] the asymmetric first-order gradiometer concept demonstrated by Dantsker *et al.* for dc SQUID gradiometers [64]. A gradiometer balance of better than 0.1 % was measured in the rf SQUID version. To date, a similar second-order asymmetric gradiometer [65] has not been demonstrated for rf SQUIDs. Higher order thin-film rf SQUID gradiometers requiring multilayer fabrication technology have not been developed to date.

6.3.2.2 Electronic rf SQUID gradiometers

An alternative to a wire-wound axial gradiometer is an electronic gradiometer, where two or more magnetometers are separated by the required baseline, typically of the order of some tens of millimeters, and their output signals are subtracted. As discussed in Chapter 4, subtracting the signals can be done by analog as well as by digital (software) techniques. The requirements for the dynamic range, slew rate and stability of the individual (magnetometer) channels of such a gradiometer, are substantially more severe than for a system with a gradiometric pickup coil because such a well-balanced pickup coil can reduce the response to homogeneous fields by a factor of 10^2 to 10^4. Also the electronics is more cumbersome, since the number of individual channels is n + 1 or more for a gradiometer of n^{th} order, and their output phases need to be identical. Nevertheless, the electronic high-T_c rf SQUID gradiometers have been successfully used in applications, especially in various biomagnetic demonstrations.

6.4 Low-Frequency Excess Noise in rf SQUIDs

Certain applications of SQUIDs require high sensitivity at relatively low frequencies, often 1 Hz or lower. However, excess noise, typically with a spectral density scaling

inversely with the frequency f, can substantially reduce the sensitivity of SQUIDs at low frequencies. Although this $1/f$ noise has been known for many years in LTS SQUIDs, it is particularly severe in high-T_c devices. The reader is referred to Section 5.5 for an in-depth discussion of the origins of $1/f$ noise in both low- and high-T_c devices. One major source of this noise is fluctuations in the junction critical current I_0. In the rf SQUID, the combination of rf bias and flux modulation eliminates that noise. This fact was recognized long ago by Giffard, who gave a correct, albeit concise, discussion of the theory [66]. The second source of $1/f$ noise involves thermally-activated hopping of flux vortices between pinning sites in the body of the SQUID. Noise from this source cannot be reduced by any bias modulation scheme. The magnitude of such noise depends strongly on the quality of the superconducting material.

Here, we reproduce a description of how the operation of the rf SQUID in an ac flux-modulated (at frequency ω_m) flux-locked loop suppresses $1/f$ noise due to critical current fluctuations – as given by Mück *et al.* [67][4]. First, we consider the effect on the tank circuit voltage V_T of a fluctuation δI_0 in I_0 at a frequency $f << \omega_{rf}$ for a SQUID operated in the hysteretic mode. Fluctuations in I_0 lead to a fluctuation of the critical flux Φ_c, for which a quantum transition takes place. We note that Φ_c fluctuates in any case due to white noise in the SQUID. However, fluctuations due to $1/f$ noise are slow compared to the frequency of quantum transitions. An increase in I_0 increases the value of Φ_c to $L(I_0 + \delta I_0)$, and thus the transitions from the k= 0 state to the +1 and –1 states occur at the flux values $L(I_0 + \delta I_0)$ and $-L(I_0 + \delta I_0)$, respectively. As a result, V_T ($\Phi_a = 0$) is increased to

$$\tilde{V}_T\,(\Phi_a = 0) = \omega_{rf}\, L_T\,(\Phi_c + L\delta I_0)\ /\ M. \tag{6.3}$$

We can see that $1/f$ noise in the critical current will result in a $1/f$ noise component in the demodulated rf voltage.

However, when the SQUID is flux modulated and operated in a flux-locked loop, the effect of critical-current fluctuations is reduced. The effect of a (say) positive fluctuation δI_0 is to increase V_T uniformly for all values of applied flux. The effect on the demodulated voltage versus flux is as follows: the demodulated output consists of a "rectified" sine wave with no Fourier components at a frequency ω_m, and a peak value $\omega_{rf} L_T \Phi_0 / 4M$ for critical currents of I_0 and $I_0 + \delta I_0$. When this signal is mixed with the fundamental frequency ω_m, the output of the mixer is zero, regardless of the voltage offset of the signal produced by the critical current fluctuations at frequencies $f << \omega_m$. In this way, the effect of low-frequency fluctuations in the critical current on the output of the flux-locked loop is substantially reduced. We note that any slow fluctuation of the rf driving current will be similarly suppressed.

The discussion above has neglected the effects of thermal noise, that is, white noise that adds a random component to the value of Φ_c, at which each transition between quantum states occurs. The effect of this noise is to tilt the plateaus in the

4) We gratefully acknowledge M. Mück's draft of this section.

$V_T(I_{rf})$-curve, but it does not affect the mechanism for $1/f$ noise reduction. Furthermore, we have neglected the fluctuations in the resistance of the junction. Resistance fluctuations will, in turn, produce fluctuations in the quality factor Q of the tank circuit. Fortunately, the magnitude of V_T does not depend on Q, at least for $k^2Q \approx 1$, so that, to first order, resistance fluctuations will not give rise to noise at the output of the flux-locked loop.

We extend the discussion to the dispersive mode: a calculation of the tank-circuit voltage V_T shows that, in this case, V_T is also proportional to δI_0. Here, however, the transfer function $\partial V_T/\partial \Phi_a$ is nonlinear and dependent on I_0. This not only leads to fluctuations of the static component of V_T, but also to amplitude fluctuation of the oscillating component generated by flux modulation. Since an ideal feedback loop is sensitive only to the phase of the flux modulation, amplitude fluctuations will not change the output voltage at the phase-sensitive detector. Noise produced by critical-current fluctuations will thus be suppressed as in the hysteretic mode.

The effects of $1/f$ noise in the rf SQUID had not been investigated extensively before the advent of HTS. This may be due to the fact that preamplifier noise usually dominated the rf SQUID-system noise and any low-frequency excess noise of the SQUID was thus buried in the preamplifier noise. Mück *et al.* investigated $1/f$ noise in niobium rf SQUIDs operated at 3 GHz while using a cold preamplifier to minimize the electronics noise [67]. They found that the measured $1/f$ noise of their LTS rf SQUIDs was in good agreement with the model described above. In their Josephson junctions, the rms current noise was $\delta I_0 \approx 1\,\text{nA}/\sqrt{\text{Hz}}$ at 1 Hz. The corresponding flux noise measured in open loop $\delta\Phi = L\delta I_0$ was about $1.5 \times 10^{-4}\ \Phi_0/\sqrt{\text{Hz}}$ for a 300 pH SQUID. By operating the rf SQUID in an ac flux-modulated loop, no $1/f$ noise was observed down to frequencies below 0.1 Hz. We note that, although the current noise of their Josephson junctions was large compared to that of others [68,69], the large reduction in the $1/f$ noise engendered by the standard read-out scheme implies that one can achieve very good low-frequency performance without using junctions with the lowest possible critical current fluctuations.

As in dc SQUIDs, the $1/f$ noise depends strongly on the external magnetic field, in which the device was cooled, or which was applied to a cold device. The discussion of this effect, presented in Section 5.5, applies also to rf SQUIDs.

6.5
Response of rf SQUIDs to High-Frequency Electromagnetic Interference

It has long been known that SQUIDs are very sensitive to high-frequency electromagnetic interference (EMI). EMI can severely degrade the performance of SQUID systems operated in an unshielded environment. Normal-conducting foil shields, placed around each individual SQUID, substantially reduce EMI, but at the expense of increased thermal magnetic noise, reduced bandwidth and a frequency-dependent phase shift due to eddy currents in the shield. Ishikawa *et al.* [70] and Koch *et al.* [71] investigated the effects of EMI on dc SQUIDs, and Mück *et al.* [72], on rf SQUIDs. They all found that EMI of sufficient intensity can reduce the modulation

depth of SQUIDs, as well as induce low-frequency excess noise, especially if the EMI has an amplitude-modulated component. We reproduce Mück's explanation of why high-frequency interference can decrease the modulation depth for (slowly varying) magnetic fields.[5)] This explanation is applicable also to dc SQUIDs.

In most cases, the physical dimensions of SQUIDs are small compared to the wavelength of the EMI. Radiation applied to the SQUIDs can then be considered to be a pure rf flux bias [70], i.e., the SQUID senses only the magnetic component of the electromagnetic field. Indirect (electric or magnetic) coupling can occur by pickup of EMI in the tank circuit, and by the leads between SQUID and readout electronics. It is believed, however, that proper shielding of the transmission line between the SQUID and the readout, e.g., by using a semi-rigid coaxial cable, can minimize these effects. Besides, since the tank circuit is a resonant structure, substantial pickup of the electrical EMI component will take place only at frequencies at or close to its resonant frequency.

For this reason, one can primarily consider effects of EMI magnetic flux Φ_{EMI} on SQUID operation. For a quantitative treatment of the effect of EMI on the modulation depth of a SQUID, we assume that only EMI at a single frequency $\omega_{\mathrm{rf}} = \omega_{EMI}$ is present. The rf flux induced by EMI generates an additional screening current in the SQUID loop, which adds to that of the rf bias flux generated by the tank circuit. The tank-circuit voltage will then be the result of a superposition of the SQUID response to Φ_{a} and the interference signal. The time-dependent modulation voltage of the SQUID $V(t)$ can be then written as

$$V(t) = \Delta V_m \cos\left[\frac{2\pi\Phi_{rf}}{\Phi_0}\cos\omega_{rf}t + \frac{2\pi\Phi_a}{\Phi_0}\right]$$

$$= \Delta V_m \cos\left(\frac{2\pi\Phi_a}{\Phi_0}\right)\cos\left(\frac{2\pi\Phi_{rf}}{\Phi_0}\cos\omega_{rf}t\right) - \sin\left(\frac{2\pi\Phi_a}{\Phi_0}\right)\sin\left(\frac{2\pi\Phi_{rf}}{\Phi_0}\sin\omega_{rf}t\right) \tag{6.4}$$

For $\Phi_{\mathrm{a}} << \Phi_0$, $\sin(2\pi\Phi_{\mathrm{a}}/\Phi_0) \approx 0$, so that

$$V(t) = \Delta V_m \cos\left(\frac{2\pi\Phi_a}{\Phi_0}\right)\sum_{n=-\infty}^{\infty} J_n\left(\frac{2\pi\Phi_{rf}}{\Phi_0}\right)\cos n\omega_{rf}t. \tag{6.5}$$

The "low-frequency" EMI, of the order of several hundred kHz, may be sensed by the flux-locked loop, and thus will be present at the loop output. Higher frequencies will not appear at the detector output, since both the bandwidth of the detector circuit used in rf SQUID electronics and the bandwidth of the tank circuit, limit the frequency response of the system to a few MHz. Nevertheless, the SQUID itself will respond to much faster flux changes, since its response time is given only by the

5) We gratefully acknowledge M. Mück's permission to adopt his unpublished description of the problem.

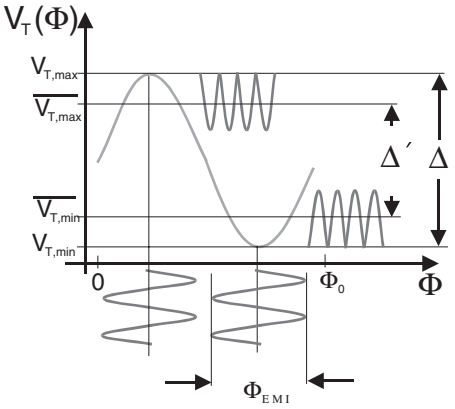

Fig. 6.10 Effects of EMI on the transfer function of an rf SQUID for $\Phi_{EMI} = \Phi_0/4$.

switching time of its Josephson junction and the L/R time constant of the SQUID ring, which, for conventional thin film SQUIDs, is of the order of 50 ps. Thus, the only component of the indefinite sum in (6.5), which will be present at the output of the detector (or the preamplifier in the case of a dc SQUID), is $J_0(2\pi\Phi_a/\Phi_0)$, leading to

$$V(t) = \Delta V_m \cos\left(\frac{2\pi\Phi_a}{\Phi_0}\right) J_0\left(\frac{2\pi\Phi_{rf}}{\Phi_0}\right). \tag{6.6}$$

We see that as $\Phi_{rf} = \Phi_{EMI}$ is increased, the modulation voltage V is decreased as $J_0(2\pi\Phi_{rf}/\Phi_0)$. This is illustrated in Figure 6.10 for $\Phi_{rf} = 0.25\Phi_0$, where Δ is the modulation depth of the undisturbed $V(\Phi_a)$ curve and Δ' the disturbed depth, which is the difference between the averaged tank circuit voltages $\overline{V_{T,max}}$ and $\overline{V_{T,min}}$. For a peak rf flux of $\Phi_{rf} = 0.38\ \Phi_0$, $V = 0$, independent of a change in Φ_a. For larger rf fluxes, the SQUID modulates again, but the modulation depth is much smaller than for $\Phi_{rf} = 0$.

In summary, high-frequency electromagnetic interference leads to a reduction of the SQUID modulation voltage, even if the EMI flux is only a fraction of a flux quantum. The only way to ameliorate this problem would be by using a flux-locked loop with very high bandwidth (larger than ω_{rf}, which in most cases is impossible), or to prevent EMI flux from leaking into the SQUID by proper rf shielding and filtering of both sensors and electronics.

6.6 Characterization and Adjustment of rf SQUIDs

For optimal performance, the rf SQUIDs require a careful adjustment of β_{rf} and k^2Q, and of detuning from resonance when in the dispersive mode; these require-

ments necessitate convenient characterization techniques. We provide here a brief outline of such techniques, based in part on the evaluation of the rf *I–V* characteristics such as those shown in Figures 6.11 and 6.12. When the measured rf *I–V* traces for $n\Phi_0$ and $(n+1)\ \Phi_0/2$ intersect at the origin $I_{rf} = V_{rf} = 0$, the SQUID is nonhysteretic (dispersive), with $\beta_{rf} < 1$ at low levels of thermal fluctuations (the case of low-T_c rf SQUID operating in LHe), and $\beta_{rf} \leq 3$ when thermal fluctuations are high (the case of high-T_c rf SQUID operating in LN_2). In the hysteretic (dissipative) mode, the first intersection point occurs at finite values of I_{rf} and V_{rf}, i.e., to the right and above the origin of coordinates [73]. With some experience, it is possible to estimate semi-quantitatively the hysteretic β_{rf} value from this shift.

As discussed in Sections 1.4 and 6.2.1, one obtains the lowest white flux noise in hysteretic low-T_c rf SQUIDs at the transition from dispersive to dissipative mode, i.e., when $\beta_{rf} \approx 1$. In this case, the optimum value of the junction critical current I_0 can be chosen in the design process, since LTS tunnel junction parameters are reproducible with a narrow spread. The noise performance of the hysteretic rf SQUID can be roughly estimated from the rf *I–V* characteristics, if the current-phase relationship in the junction is sinusoidal, which is usually the case. Jackel and Buhrman have shown that the step slope (tilt) in the rf *I–V* curve is directly proportional to the intrinsic flux noise of the SQUID, regardless of the form of the fluxoid transition distribution [74]. They verified experimentally that the ratio α of the voltage rise along a step ΔV_s, to the voltage difference ΔV_o between steps (the step tilting parameter), shown in Figure 6.12, is given by

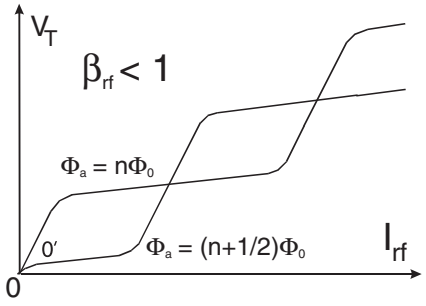

Fig. 6.11 The rf current-voltage characteristics of a dispersive rf SQUID.

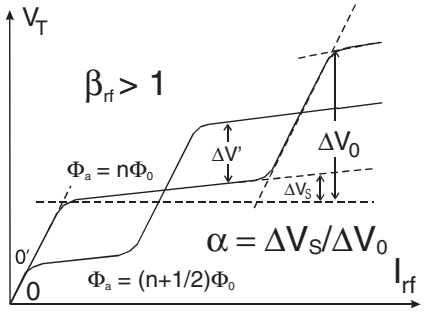

Fig. 6.12 The rf current-voltage characteristics of a hysteretic rf SQUID, and the determination of α [74].

$$\alpha \approx \frac{1}{0.7\Phi_0}\left(\frac{\omega_{rf}}{2\pi}\right)^{1/2}\frac{\langle S_\Phi\rangle^{1/2}}{\sqrt{Hz}}. \tag{6.7}$$

Hence, one can determine the intrinsic noise from the measured α. The nonintrinsic component of the flux noise is also proportional to α. Therefore, for the total noise energy resolution, one finds

$$\varepsilon(f) = \frac{1}{\omega_{rf}}\left(\frac{\alpha\pi^2\Phi_0^2}{2L} + 2\pi\alpha k_B T_{\text{eff}}\right) \tag{6.8}$$

Here, T_{eff} is the effective noise temperature of the tank circuit, transmission line and preamplifier, all lumped together. The value of T can be estimated from room-temperature noise data of the amplifier and the transmission line can contribute about 100 K if the amplifier is at room temperature. The noise in the tank circuit can be neglected in modern hysteretic SQUIDs since the resonator is integrated and thus cooled [21].

In nonhysteretic low-T_c SQUIDs with $k^2Q\beta_{\text{rf}} > 1$, the value of I_0 can be set in the design, but the lowest flux noise is obtained at the maximum practical value of the transfer coefficient, which still provides the required bandwidth and operation stability. This value is found empirically, by adjusting the detuning from resonance, that is, by varying the frequency of the rf bias oscillator.

As shown in Section 6.2.3, the best high-T_c rf SQUIDs are always operated in the nonhysteretic regime with $k^2Q\beta_{\text{rf}} > 1$. Unfortunately, in the case of HTS junctions the reproducibility of I_0 is inadequate, and β_{rf} may be outside the range of the nonhysteretic mode or too low to ensure $k^2Q\beta_{\text{rf}} > 1$. Therefore, it is usually necessary to trim I_0 iteratively by the methods described in Chapter 3, while verifying the result of trimming by inspecting the V–Φ characteristic and the rf I–V curves for $n\Phi_0$ and $(n + 1)\ \Phi_0/2$. Obviously, such iterative trimming may significantly increase the cost of high-T_c rf SQUID fabrication.

It is essential to have $k^2Q\beta_{\text{rf}} > 1$ to attain the optimum performance of high-T_c dispersive SQUIDs. In the HTS flip-chip designs presented in Subsections 6.2.3.4 and 6.2.3.5, the value of k^2 is determined by the layout and spacing between the SQUID and the flux focuser, coupled to the tank circuit resonator. This spacing is usually kept as small as possible by pressing the two parts against each other. Similarly, the unloaded Q_0 of the tank circuit resonator (coplanar or dielectric substrate) is always kept at the maximum value permitted by the resonator's dimensions (layout) and the material of which it is made, so that k^2Q remains as high as possible. The matching to the preamplifier via the 50 Ω coax is done by varying the size of the matching loop and its distance from the resonator. Once found, these geometric parameters can be fixed in the matching loop printed circuit and assembly design, such as that shown in Figure 6.5.

It was shown theoretically that, for a nonhysteretic SQUID operating in the high fluctuation limit, the I_0 and R of the junction and also k^2 and Q, can be inferred from the experimental amplitude-frequency characteristics (AFC), i.e., from $V_T(\xi)$

curves measured for $\Phi_a = n\Phi_0$ (with resonance at ω_1) and $\Phi_a = (n+1)\,\Phi_0/2$ (with resonance at ω_2) using weak rf bias [75]. With I_0 known, β_{rf} and Γ can be determined. Experiments confirmed a good agreement with I_0 and R determined directly (destructively) by opening the SQUID loop and measuring the junction characteristics [10].

6.7 The rf SQUID versus the dc SQUID

Due to their different loop geometry and readout, rf SQUIDs offer some interesting advantages when compared to dc SQUIDs fabricated using a similar technology. The rf SQUID requires no dc electrical connection between the SQUID itself and the readout electronics. Due to the low impedance of the dc SQUID, a contact resistance of only a few ohms (which is quite common for contacts to HTS films) can significantly reduce its modulation voltage. In contrast, it is rather easy to obtain relatively high modulation voltages across the tank circuit of an rf SQUID. The inductance of the rf SQUID, and thus its loop area, can be made larger than that of the dc SQUID, before a significant reduction in signal (modulation) voltage is observed. This leads to a higher field sensitivity of the uncoupled rf SQUID (compared to the uncoupled dc SQUID), so that for many applications a complex flux transformer is not needed. Furthermore, when a transformer is used, the absence of Josephson oscillations in the SQUID loop eliminates resonances in its integrated input coil, which in the dc SQUID can lead to a reduction in signal voltage and sensitivity.

The comparison of noise performance of the two kinds of SQUIDs is a complex issue. When rf SQUIDs are operated at UHF or microwave frequencies, their *intrinsic* flux noise is on the same order as that of dc SQUIDs.[6)] However, at liquid helium temperatures, the *system* flux noise of rf SQUIDs may be truly comparable to that of dc SQUIDs only when a cold rf preamplifier is used. Otherwise, the effective noise temperatures of the transmission line connecting the tank circuit to the room-temperature preamplifier and of the preamplifier itself will likely exceed 100 K, and thus submerge the intrinsic SQUID noise. Hence, the rf SQUID *system* noise energy will be much higher than that of a dc SQUID. A possible exception is the dispersive SQUID with $k^2 Q \beta_{rf} > 1$ when it acts as a (rf bias pumped) parametric amplifier such that the system noise can be lower than the amplifier noise (see 6.2.2.2. and [9]) In contrast, at liquid nitrogen temperatures, where the intrinsic noise energy of any SQUID is a factor of about 20 higher than at 4.2 K, the relative noise contribution of the transmission line and the preamplifier may be less significant. Therefore, the system noise of dc and rf SQUIDS can be truly comparable even when using room-temperature preamplifiers. Furthermore, at 77 K the dispersive rf SQUIDs are likely to be preferable to hysteretic SQUIDs since the intrinsic flux noise is much lower.

6) The rather common belief that rf SQUIDs exhibit mediocre sensitivity originated in the past, when 30 MHz electronics had been widely used.

When operated in an ac-modulated flux-locked loop, usually no $1/f$ noise is observed in low-T_c rf SQUIDs down to frequencies below 1 Hz, as is also the case for low-T_c dc SQUIDs without any bias reversal. Unfortunately, high-T_c rf SQUIDs exhibit higher $1/f$ noise than the direct-coupled high-T_c dc SQUIDs operating with bias reversal. The origin of the higher noise is only partially explained by the effects of external disturbing fields on the working point of the rf SQUID [54], and requires further investigation. A systematic comparison of $1/f$ noise in the two kinds of SQUIDs is still missing.

Of course, in an unshielded or weakly shielded environment the flux noise of any SQUID may increase drastically due to the nonintrinsic noise caused either by vortex hopping or by electromagnetic interference. The broadband environmental signals can be high and regarded as extra noise, as discussed in Chapter 7. Ultimately, therefore, in the absence of good magnetic shielding the difference in overall noise performance between typical dc and rf SQUID systems may be rather insignificant.

The readout electronics of the rf SQUID are more complex and bulky than those of the dc SQUID, although differences in the number and price of electronic components used may be negligible in commercial production on a larger scale, especially if the chosen bias frequency permits one to use the inexpensive electronic components of wireless communication. The absence of any galvanic connection between rf SQUID and readout electronics simplifies manufacturing for a large number of devices, prevents aging (contact corrosion effects), and, most importantly, eliminates the possibility of rf SQUID destruction by accidental electrical discharge (junction burnout).

In principle, it is even possible to separate the rf SQUID from the conventional tank circuit by a thin thermally insulating wall, so that, for example, the SQUID could be mounted in a cold vacuum space, whereas the tank circuit and the wires leading to the room-temperature electronics could be at atmospheric pressure and room temperature. At a price of extrinsic noise higher than that with an integrated tank circuit, this can minimize the thermal load of the cryostat or cryocooler, which otherwise is much higher in the case of rf SQUIDs. This is because the rf coaxial cables to the room-temperature electronics, even miniature versions, have higher thermal losses than the extremely thin twisted wire pairs used in the case of dc SQUIDs. Cryogenic preamplifiers further increase the thermal load of rf SQUIDs so that systems with many such channels may be entirely impractical.

We note that there are a few applications where rf SQUIDs either cannot be used, or are inferior to dc SQUIDs. These applications include low-T_c high-frequency amplifiers, and low-T_c scanning SQUID microscopes where SQUIDs with the smallest possible loop area must be used and brought into very close proximity of the sample under test.

To complement the comparisons made above, Table 6.4 summarizes typical and some best properties of dc and rf SQUIDs [76]. This Table is intended to provide a quick and convenient comparison, but SQUIDs may exist with parameters well outside the indicated value ranges.

Tab. 6.4. Comparison of typical properties of thin-film dc and rf SQUIDs; preamplifier at 300 K

Kind of SQUID at Temperature →	dc SQUID	Hysteretic rf SQUID	Nonhysteretic rf SQUID	dc SQUID	Nonhysteretic rf SQUID
Parameter, Property↓	**4.2 K**	**4.2 K**	**4.2 K**	**77 K**	**77 K**
Inductance range, L, pH	500–10*	500–100*	500–100*	150–20*	300–100*
Output signal range, (peak-to-peak) μV	10–100	<20–100	<20–100	10–50	10–50
Transfer coefficient, μV/Φ_0	30–1000	60–200	300–1000	30–150	< 200–500
(lower line: dc SQUID with APF)	up to 1000			up to 1000	
White flux noise, $S_\Phi{}^{1/2}(f)$,					
$\mu\Phi_0/\sqrt{\text{Hz}}$	0.3–5	1–6	20 (best) 0.3	3–10; best 1.5	8–20
at 1 Hz	1.5–3	1–6	– –	3–10; best 2.3?	25–50
Best energy resolution reported, ε(f), J/Hz	3.6×10^{-33}	1.5×10^{-31}	2.5×10^{-33}	2×10^{-31}	7×10^{-31}
Magnetometer field resolution (white), B_N, fT//$\sqrt{\text{Hz}}$					
Single layer/flip-chip	not used	not reported	not reported	15–50	25–50
Multilayer flux transformer,	1–5	not reported	not reported	6–20	12–20
Bias frequency, GHz	–	3	9.5	–	0.5–1

* Better values of parameters below correspond to lower inductance

6.8 Concluding Remarks and Outlook

The performance of planar low-T_c rf SQUID magnetometers can be competitive with planar dc SQUID magnetometer performance only when a sufficiently high bias frequency, an optimized tank resonator and a cryocooled preamplifier are used.[7)] Such optimized low-T_c SQUIDs are rarely used since they emerged when the technology of high-performance dc SQUIDs was already mature and firmly entrenched in applications. We do not see clear incentives for the use of low-temperature rf SQUID sensors, except possibly in special scientific applications.

In the past decade, progress in the understanding and development of high-T_c rf SQUIDs has been remarkable, so that the demonstrated performance of practical rf-biased sensors (operated in the optimal dispersive mode) is today largely competitive with that of their dc-biased counterparts, except at very low frequencies. Nevertheless, as in the case of high-T_c dc SQUIDs, the poor reliability of HTS fabrication technology was limiting progress. The main difficulty has been to fabricate multilayered flux transformers and fully integrated sensor structures reproducibly and economically. Further significant improvements in field noise (resolution) to attain $B_N \leq 10\,\text{fT}/\sqrt{\text{Hz}}$ reproducibly (on $10\times10\,\text{mm}^2$ substrates) and down to very low fre-

7) Amplifier cryocooling may be avoidable in the case of nonhysteretic rf SQUIDs acting as parametric amplifiers [9,25].

quencies (and also to improve the sensitivity, extend the baseline, balance and order of planar gradiometers) will be paced by progress in understanding the cause of excess low-frequency noise and in fabrication technology of patterned multilayered structures. As for dc SQUIDs, there is a need for better parameter control, reproducibility and long-term stability of viable types of high-T_c Josephson junctions.

The development of sensitive high-T_c rf SQUIDs, although qualitatively guided by the new unitary theory, has been largely empirical. In contrast to dc SQUIDs, only few simulations of rf SQUIDs, rf-compatible flux transformers and tank circuit resonators have been performed to aid the design. It is important to have this gap filled to generate quantitative guidelines for optimized designs.

One may expect high-T_c rf SQUIDs to find an increasing use in applications such as NDE and geomagnetic prospecting, where simplicity, ruggedness and performance of today's rf SQUIDs are crucial. The prospect of implementing high-T_c rf SQUIDs into biomagnetic applications is less certain since the evolutionary introduction of high-T_c systems will most likely benefit from the existing low-T_c dc SQUID electronics and the know-how accumulated for low-T_c dc SQUID multichannel systems. Also, the heat influx into the cryostat via multiple concentric cables is likely to be excessive.

References

[1] Silver, A.H. and Zimmerman, J.E. (1967) Quantum states and transitions in weakly connected superconducting rings, *Phys. Rev.* **157**, 317–341.

[2] Zimmerman, J.E., Thiene, P., Harding, J.T. (1970) Design and operation of stable rf-biased superconducting point-contact quantum devices, and note on the properties of perfectly clean metal contacts, *J. Appl. Phys.* **41**, 1572–1580.

[3] Mück, M. (1993) Progress in rf SQUIDS, *IEEE Trans. Appl. Supercond.* **3**, 2003–2010, and references therein.

[4] Simmonds, M.B. and Parker, W.H. (1971) Analog computer simulation of weakly coupled superconducting rings, *J. Appl. Phys.* **42**, 38–45.

[5] Pascal, D. and Sauzade, M. (1974) Experimental determination of optimum operating conditions of a superconducting interferometer, *J. Appl. Phys.* **45**, 3085–3090.

[6] Danilov, V.V. and Likharev, K.K. and Snigirev, O.V. (1980) Signal and noise parameters of SQUIDs. In H.D. Hahlbohm and H. Lübbig (eds.) *SQUID'80, Superconducting Quantum Interference Devices and their Applications*, Walter de Gruyter, Berlin, pp. 473–507.

[7] Likharev, K.K. (1986) *Dynamics of Josephson Junctions and Circuits*, Gordon and Breach Science Publ., New York, pp. 492–494.

[8] Dmitrenko, I.M., Tsoi, G.M., Shnyrkov, V.I. and Kartsovnik, V.V. (1982) Rf SQUID in the nonhysteretic regime with $k^2Ql > 1$, *J. Low Temp. Phys.* **46**, 417–433.

[9] Kuzmin, L. S., Likharev, K. K., Migulin, V. V., et al. (1985) X-band parametric amplifier and microwave SQUID using single-tunnel-junction superconducting interferometer. In H.D.Hahlbohm and H. Lübbig, (eds.), *SQUID'85, Superconducting Quantum Interference Devices and Their Applications*, Walter de Gruyter, Berlin, pp. 1029–1034; and private communication by K.K. Likharev.

[10] Zeng, X.H., Zhang, Y., Chesca, B., et al. (2000) Experimental study of amplitude-frequency characteristics of high-transition-temperature radio frequency superconducting quantum interference device, *J. Appl. Phys.* **88**, 6781–6787.

[11] Zimmermann, J.E. (1971) Sensitivity enhancement of superconducting interference devices through the use of fractional-turn loops, *J. Appl. Phys.* **42**, 4483–4487.

[12] Goodman, W.L., Hesterman, V.W., Rorden, L.H. and Goree, W.S. (1973) Superconducting instrument systems, *Proceedings of the IEEE* **61**, 20–27.

[13] Rifkin, R. and Deaver Jr, B.S. (1976) Current-phase relation and phase-dependent conductance of superconducting point contacts from rf impedance measurements, *Phys. Rev. B* **13**, 3896–3901.

[14] Courtesy of D. Paulson, Tristan Technologies.

[15] Kamper, R.A. and Simmonds, M.B. (1972) Broadband superconducting quantum magnetometer, *Appl. Phys. Lett.* **20**, 270–272.

[16] Hollenhorst, J.N. and Giffard, R.P. (1979) High sensitivity microwave SQUID, *IEEE Trans. Magn.* **MAG-15**, 474–477; and references therein.

[17] Duret, D., Bernard, P. and Zenatti, D. (1975) A UHF superconducting magnetometer utilizing a new thin-film sensor, *Rev. Sci. Technol.* **46**, 474–480.

[18] Ketchen, M.B., and Jaycox, J.M. (1982) Ultra-low noise tunnel junction dc SQUID with a tightly coupled planar input coil, *Appl. Phys. Lett.* **40**, 736–738.

[19] Sensors SQS5C, SQS6C, Oxford Instruments, Scientific Research Division., Eynsham, Witney Oxon, OX8 1TL, UK (1992).

[20] Model 20 rf SQUID Sensor of Quantum Design, 11578 Sorrento Valley Rd., San Diego, CA 92121-1311, USA (2002).

[21] Mück, M. and Heiden, C. (1992) Planar microwave biased rf-SQUIDs in niobium technology, *Appl. Phys.* (A) **54**, 475–480.

[22] Mück, M., Hallmanns, G., Heiden, et al. (1992) Planar microwave biased rf SQUIDs with a cryogenic preamplifier, *Appl. Phys. Lett.* **61**, 1231–1233.

[23] Fontana, G., Mezzena, R., Vitale, S., Cerdonio, M., Mück, M., Hallmanns, G., Heiden, C. (1993) Improved sensitivity of planar microwave biased rf SQUIDs using a cryogenic HEMT amplifier, *IEEE Trans. Appl. Supercond.* **3**, 1820–1823.

[24] Butusov, D.A., Kornev, V.K., Kuzmin, L. S. and Likharev, K. K. (1985) Hysteretic AC SQUIDs using tunnel Josephson junctions. In H.D.Hahlbohm and H. Lübbig, (eds.), *SQUID'85, Superconducting Quantum Interference Devices and Their Applications*, Walter de Gruyter, Berlin, pp. 791–796.

[25] Likharev, K. K. (2003) Private communication.

[26] Colclough, M.S., Gough, C.E., Keene, et al. (1987) Radio frequency SQUID operation using a ceramic high-temperature superconductor, *Nature* **328**, 47–48.

[27] Zimmerman, J.E., Beall, J.A., Cromar, M.W. and Ono, R.H. (1987) Operation of YBCuO rf SQUID at 81 K, *Appl. Phys. Lett.* **51**, 617–619.

[28] Tinchev, S.S. and Hinken, J.H. (1989) 77 K rf SQUID with 1/f noise only below 5 Hz, *Electronics. Lett.* **25**, 1579–1580.

[29] Likhachev, A.G., Polushkin, V.N., Uchaikin, S.V. and Vasiliev, B.V. (1990) Magnetocardiometer based on a single-hole high-Tc SQUID, *Supercond. Sci. Technol.* **3**, 148–151.

[30] Zhang, Y., Xu, Y.H. and Heiden, C. (1990) Bulk BiPbSrCaCuO rf SQUIDs operating up to 101 K, *Appl. Phys. Lett.* **56**, 1597–1599.

[31] Zhang, Y., Diegel, M. and Heiden, C., (1989) Preparation and performance of toroidal YBCO rf SQUIDs, *IEEE Trans. Mag.* **MAG-25**, 869–871.

[32] Tavrin, Y. (formerly at FITM, Germany), private information (unpublished).

[33] Shnyrkov, V.I., Timofeev, V., Khvostov, S. and Tsoi, G. (1991) UHF high-Tc SQUID, *Mod. Phys. Lett.* **B5**, 1281–1286.

[34] Tinchev, S.S. (1990) Investigations of rf SQUIDs made from epitaxial YBCO films, *Supercond. Sci. Technol.* **3**, 500–502.

[35] Zani, M.Z., Luine, J.A., Lee, G.S. et al. (1991) Focused ion beam high-Tc superconducting SQUIDs, *IEEE Trans. Mag.* **MAG-27**, 2557–2560.

[36] Daly, K.P., Dozier, W.D., Burch, J.F., et al. (1991) Substrate step-edge YBCO rf SQUIDs, *Appl. Phys. Lett.* **58**, 543–545.

[37] Cui, G., Zhang, Y., Herrmann, et al. (1991) Properties of rf SQUIDs fabricated from epitaxial $YBa_2Cu_3O_7$ films, *Supercond. Sci. Technol.* **4**, S130–S133.

[38] Zhang, Y., Mück, M., Herrmann, K., et al. (1992) Low noise $YBa_2Cu_3O_7$ rf SQUID magnetometer, *Appl. Phys. Lett.* **60**, 645–647.

[39] Wang, S.G., formerly Peking University, private communication (unpublished).

[40] Sloggett, J., Dart, D.L., Foley, C.P., et al. (1994) Noise in thin-film $YBa_2Cu_3O_7$ step-edge junction SQUIDs, *Supercond. Sci. Technol.* **7**, 260–264.

[41] The junctions were fabricated by patterning a narrow film microbridge across a rectangular pocket (pit) etched in the substrate. This created up to four step-edge junctions in series, of which the weakest served as the SQUID

weak link, and the other contributed only some additional kinetic inductance.

[42] Zhang, Y., Krüger, U., Kutzner, R., et al. (1994) Single layer YBCO rf SQUID magnetometer with direct-coupled pickup coil and flip-chip flux transformers, *Appl. Phys. Lett.* **65**, 3380–3382.

[43] Daly, K.P., Burch, J.F., Coons, S.B. and Hu, R. (1991) YBCO step-edge rf SQUID biased at 10 GHz, *IEEE Trans. Mag.* **MAG-27**, 3066–3069.

[44] Zhang, Y., Mück, M., Bode, M., et al. (1992) Microwave SQUIDs with integrated YBCO resonator, *Appl. Phys. Lett.* **60**, 2303–2305.

[45] Zhang, Y., Mück, M., Braginski, A.I. and Toepfer, H. (1994) High-sensitivity microwave rf SQUID operating at 77 K, *Supercond. Sci. Technol.* **7**, 269–272.

[46] Chesca, B. (1998) Theory of RF SQUIDS operating in the presence of large thermal fluctuations, *J. Low. Temp. Phys.* **110**, 963–1002.

[47] Zhang, Y., Zander, W., Schubert, J., et al. (1997) Operation of high-sensitivity radio-frequency SQUID magnetometers with superconducting coplanar resonators at 77 K, *Appl. Phys. Lett.* **71**, 704–706.

[48] Zhang, Y., Wolters, N., Zeng, X.H., et al. (1998) Washer rf SQUID magnetometers with coplanar resonators at 77 K, *Appl. Supercond.* **6**, 385–388.

[49] Kurin, V.V., Levichev, M.Yu. and Pankratov, A.L. (1997, IPM-RAS, Nishnyi Novgorod), unpublished.

[50] Fuke, H., Saitoh, K., Utagawa, T. and Enomoto, Y. (1996) Estimation of inductance for high-Tc dc SQUIDs in coplanar waveguide, *Jpn. J. Appl. Phys.* **35**, L1582–L1584.

[51] Toepfer, H. (1991) Inductance determination of superconducting structures, in W. Krech, P. Seidel and H.-G. Meyer (eds.) *Superconductivity and Cryoelectronics*, World Scientific, Singapore, pp. 170–177.

[52] Ketchen, M.B., Gallagher, W.J., Kleinsasser, et al. (1985) dc SQUID flux focuser, in H.D. Hahlbohm and H. Lübbig (eds.) *SQUID '85: Superconducting Quantum Interference Devices and their Applications*, Walter de Gruyter, Berlin, pp. 865–871.

[53] Yi, H.R., Zhang, Y., Schubert, J., et al. (2000) Superconducting multiturn transformers for radio frequency SQUIDs, *J. Appl. Phys.* **88**, 5966–5974.

[54] Zhang, Y. (2001) Evolution of HTS rf SQUIDs, *IEEE Trans. Supercond.* **11**, 1038–1042.

[55] Kornev, V.K., Likharev, K.K., Snigirev, O.V., et al. (1980) Microwave-frequency SQUID with a high-Q dielectric resonator, *Radio Eng. Electronic Phys.* **25**, 122–129.

[56] Zhang, Y., Gottschlich, M., Soltner, H., et al. (1995) Operation of high-temperature rf SQUID magnetometers using dielectric $SrTiO_3$ resonators, *Appl. Phys. Lett.* **67**, 3183–3185.

[57] Zhang, Y., Schubert, J., Wolters, N., et al. (2002) Substrate resonator for HTS rf SQUID operations, *Physica C* **372-376**, part 1, 282–286.

[58] Zhang, Y., Yi, H.R., Schubert, J., Zander, W., et al. (1998), A design of planar multi-turn flux transformers for radio frequency SQUID magnetometers, *Appl. Phys. Lett.* **72**, 2029–2031.

[59] Zhang, Y., Yi, H.R., Schubert, J., et al. (1999) Operation of rf SQUID magnetometers with a multi-turn flux transformer integrated with a superconducting labyrinth resonator, *IEEE Trans. Appl. Supercond.* **9**, 3396–3400.

[60] Tinchev, S.S. (1994) YBCO thin film gradiometer, in H.C.Freyhardt (ed.) *Proceedings of the 1st European Conference on Applied Superconductivity (EUCAS)* Göttingen, pp. 1435–1437.

[61] Zhang, Y., Soltner, H., Krause, H.-J., et al. (1997) Planar HTS gradiometer with large baseline, *IEEE Trans. Appl. Supercond.* **7**, 2866–2869.

[62] Slit inductances can be calculated using the formula in Table 5.1 or the code from [51].

[63] Panaitov, G.I., Zhang, Y., Krause, H.-J., et al. (2003) Long baseline hardware gradiometer based on HTS rf SQUIDs with substrate resonators, *Trans.Appl. Supercond.* **13,** 841–844.

[64] Dantsker, E., Froehlich, O., Tanaka, S., et al. (1997) High-T_c superconducting gradiometer with a long baseline asymmetric flux transformer, *Appl. Phys. Lett.* **71**, 1712–1714.

[65] Kittel, A., Kousnetsov, K.A., McDermott, R., et al. (1998) High-Tc superconducting second-order gradiometer, *Appl. Phys. Lett.* **73**, 2197–2199.

[66] Giffard, R.P. (1980) Fundamentals for SQUID Applications, in H.D.Hahlbohm and H.Lübbig (eds.) *SQUID'80 'Superconducting Quantum Interference Devices and Their Applications'*, W. de Gruyter, Berlin pp. 445–471.

[67] Mück, M., Heiden, C. and Clarke, J. (1994) Investigation and reduction of low frequency excess noise in rf SQUIDs, *J. Appl. Phys.* **75**, 4588–4592 (and unpublished manuscript by Mück, M., 2001).

[68] Folglietti, V., Gallagher, W.J., Ketchen, M.B., et al. (1986) Low-frequency noise in low 1/f noise dc SQUIDs, *Appl. Phys. Lett.* **49**, 1393–1395.

[69] Savo, B., Wellstood, F.C. and Clarke, J. (1987) Low frequency excess noise in Nb Al_2O_3-Nb Josephson tunnel junctions, *Appl. Phys. Lett.* **50**, 1757–1759.

[70] Ishikawa, N., Nagata, K., Sato, H., et al. (1993) Effect of rf interference on characteristics of dc SQUID system, *IEEE Trans. Appl. Supercond.* **3**, 1910–1913.

[71] Koch, R.H., Foglietti, V., Rozen, J.R., et al. (1994) Radio Frequency Interference in dc SQUIDs, *Appl. Phys. Lett.* **65**, 100–102.

[72] Mück, M., Dechert, J., Gail, J., et al. (1995) Response of Radio Frequency SQUIDs to Electromagnetic Interference, *Rev. Sci. Instrum.* **66**, 4690–4694 (and unpublished manuscript by Mück, M., 2001).

[73] Zhang, Y., Heiden, C. (1992) A Compact High-TC rf-SQUID-System with Reduced Tank Circuit Damping, in H. Koch and H. Luebbig (eds.) *Superconducting Devices and their Applications*, Springer-Verlag, Berlin, Germany, pp. 87–91.

[74] Jackel, L.D. and Buhrman, R.A. (1975) Noise in the rf SQUID, *J. Low Temp. Phys.* **19**, 201–246.

[75] Greenberg, Ya.S. (1999) determination of the parameters of high-T_c rf SQUID from its small signal voltage-frequency characteristics, *J. Low. Temp. Phys.* **114**, 297–315.

[76] Cantor, R. and Koelle, D. (2003) the authors of Chapter 5, kindly provided the data for dc SQUIDs.

7
SQUID System Issues

C.P. Foley, M.N. Keene, H.J.M. ter Brake and J. Vrba

7.1 Introduction

A SQUID system contains various building blocks in addition to the SQUID itself. In this chapter, we consider the issues relating to these components in several system configurations; for example, shielded and unshielded, static or mobile. We provide practical information derived from our knowledge and experience with LTS and HTS magnetometers and gradiometers for various applications such as biomedical, nondestructive evaluation (NDE), geophysics and defense, for magnetically shielded and unshielded environments, and in remote or urban areas. Much of this practical information is not described in existing publications.

A SQUID system, in order to be suitable for implementation, must be considered holistically. It is not sufficient merely to use good SQUIDs or low-noise electronics. Rather, all components of the system must be integrated together, with each component being developed and optimized to eliminate noise and interference while meeting the specifications for the current application.

The SQUID system can be separated into the following components:

- SQUIDs
- Signal pickup and noise-cancellation circuits
- Housings and cryogenics
- Shielding
- Electronics, connectors and cables and
- Data-acquisition hardware and software.

The SQUID itself (which is not discussed in this chapter), and the signal pickup coils, together form a sensor. Various configurations of pickup coils and possibly additional reference sensors are required for external noise cancellation. When the system is constructed, it is necessary to integrate all the components listed above, methodically, to minimize external noise and interference. It is also necessary to characterize, calibrate and test the system to ensure that it can achieve the desired specifications. Accordingly, we address the integration of SQUID systems and provide the information required to bring these most sensitive detectors of magnetic fields into the realm of useful applications.

7.2 Cryogenics

7.2.1 Introduction

SQUID magnetometers can be cooled by two methods: either by a cryogenic liquid or by a cooler. In this section, both methods are considered and compared. In this comparison, noise contributions arising from a cooler are shown to be important and the reduction of this cooler interference is considered separately. Material properties at cryogenic temperatures, relevant to both cooling methods, are also discussed.

As discussed in Chapters 3, 5, and 6, high-T_c SQUIDs are much more difficult to fabricate with desired parameters and harder to work with than low-T_c SQUIDs. However, cooling is much simpler and cheaper. The heat of evaporation per unit volume of liquid nitrogen is a factor of 60 higher than that of liquid helium, and in addition, it is cheaper by a factor of about 15 [1]. Also, coolers for the HTS range are much smaller, lighter and less expensive than those for 4 K. The differences in mass, volume and cost between 80 K and 4 K systems may range up to 3 orders of magnitude [1–4]. This big difference is the driving force behind the worldwide research aimed at overcoming the material-related disadvantages of HTS.

This section provides an introduction to SQUID cooling, and the discussion is valid both for high-T_c and low-T_c SQUIDs. For more information on cryogenics, the reader is referred to [1, 5–10] and, for coolers, to [1, 2, 11–16]. Furthermore, in the literature, valuable information on specific cryogenic topics is available in the journal *Cryogenics* and in proceedings of various conferences, such as the International Cryocooler Conferences (published by Kluwer Academic/Plenum Publishers under *Cryocoolers*); the Cryogenic Engineering Conferences (published as *Advances in Cryogenic Engineering* by the same publishers); and the International Cryogenic Engineering Conferences.

In order to find the best method for cooling the SQUID, a number of requirements need to be considered. The most important parameter is the contribution of the cryogenic system to the noise level of the magnetometer. Electromagnetic interference should be below the targeted noise level of the system; vibrations in the environmental-background field (especially tilting) should be avoided and temperature fluctuations should be limited, since the SQUID operating parameters may be affected, and their variation may add to the system noise. Other parameters, such as cost and reliability, may also be relevant in the selection of the cryogenic system (see also Section 7.2.4). However, these requirements will depend strongly on the specific application and cannot be generalized in a simple manner.

7.2.2
Liquid Cryogen Cooling (Cryostats)

A simple method of cooling is to immerse the SQUID in a cryogenic liquid that is contained in a cryostat using liquid helium for low-T_c and liquid nitrogen for high-T_c SQUIDs. The properties of cryogenic liquids are discussed in numerous contributions to the open literature [e.g., 1, 9, 10]. A typical liquid-helium cryostat for a SQUID magnetometer is depicted in Figure 7.1. Depending on the desired hold-time, the helium reservoir can be from a few liters to a hundred liters or even more. By surrounding the reservoir with an outer casing, and evacuating the space in between, rapid boil-off due to convective heat exchange with the 300 K environment can be prevented. In order to maintain the vacuum despite outgassing, a getter material, such as carbon or a zeolite can be attached to the helium reservoir. Residual gases in the vacuum space would thus be cryotrapped in a very effective way [17, 18]. To withstand the atmospheric pressure, the bottom and top plates of the cryostat should be relatively thick compared to the cylindrical walls. After evacuation, the main heat load to the reservoir is thermal radiation, but placing superinsulation in the vacuum space will reduce this radiative heat flow. Superinsulation, or multilayer insulation (MLI), consists of alternating layers of highly reflective material such as aluminized Mylar, and a low-conductivity spacer material such as nylon net [5, 6, 10, 19–21]. The superinsulation known as NRC-2 is crinkled so that successive layers make occasional point contact and no spacer material is needed [22]. The optimum layer density of MLI is about 30 layers per 10 mm [5, 19]. Usually, in SQUID cryostats, two blankets of MLI are applied: one blanket wrapped around the reservoir, the other around a radiation shield. This is a thin shield of good conducting material that is positioned in the vacuum space and is attached to the neck of

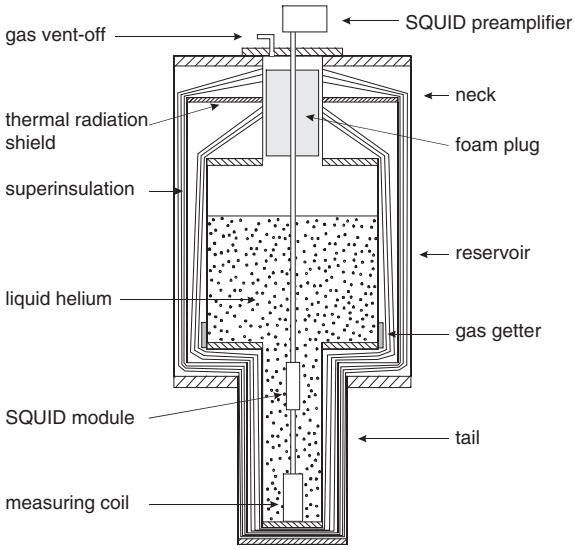

Fig. 7.1 Standard liquid-helium cryostat with SQUID system.

the cryostat. A large proportion of thermal radiation that is emitted by the 300 K outside wall is reflected by the MLI blanket on this shield. The small amount of heat that is absorbed by the shield is partly emitted from its inside surface, and partly conducted to the cryostat neck. The radiative heat flow from the shield to the reservoir can be reduced to a negligible level by the MLI blanket on the reservoir. Thus the heat flow to the helium bath of the bare cryostat (i.e. without the SQUID installed) is determined by conductive heat flow through its neck. This includes conduction from 300 K plus the conductive load coming from the radiation shield. For this reason, the neck is made of a low-conductivity material that, also needs to be sufficiently strong. Usually, glass-fiber reinforced epoxies are used for this purpose [17]. The conductive heat flow through the neck is further reduced by enforcing a good heat exchange of the neck with the boil-off helium gas: the conductive flow is used to warm up the gas, or in other words the vented helium gas cools the neck. In SQUID cryostats, usually, a plug (e.g. a foam material) is placed in the neck of the cryostat, leaving an annular gap of a few mm. The evaporated helium is forced to flow along the neck, thus establishing a good thermal contact between the neck and the gas. In helium cryostats, this utilization of the gas enthalpy change is extremely important. If the available enthalpy change is fully used, the conductive heat load coming from 300 K is reduced by a factor of 80!

By incorporating these insulating techniques, the boil-off of commercial helium containers can be reduced to a level as low as 1 % of the reservoir volume per day. Hence, hold times of a few months can be realized. However, SQUID systems which are used for measuring magnetic-field sources outside the cryostat (e.g., in biomagnetism, NDE, and geomagnetism) have significantly higher boil-off rates due to two effects. First, the thermal radiation shielding in the vacuum space requires metallic sheets. These affect the measuring field because of eddy currents and, furthermore, their thermal noise adds to the system noise. Because low-T_c SQUIDs have magnetic field resolutions of only a few $\mathrm{fT\,Hz^{-1/2}}$, the thermal noise of cryostats may be a limiting factor [23–25]. Therefore, a compromise has to be found between the unwanted interference effects and a minimum boil-off: the price for lower interference is higher boil-off. Second, in many applications, the distance of the sensing coil to the source should be minimized (e.g., in biomagnetism and NDE). Again, a trade-off results: a smaller distance means higher boil-off. Usually, commercial SQUID cryostats are designed to have hold times of roughly one week with a daily boil-off of around 15 % of the reservoir volume. When installing a SQUID in the cryostat, the boil-off increases because of the additional conductive heat load. The increase depends on how the SQUID insert is configured (e.g., how many channels are installed). Low-conductivity materials should be used as much as possible. For instance, the dc SQUID lines can be made from high-ohmic wires (apart from the voltage output lines). Another consideration is that the insert material forming the thermal contact between the 300 K outside and the helium bath, should be well cooled by the vented helium. For this reason, it may be advantageous to anchor cables and leads thermally on plates that are in good contact with the helium gas. Despite these measures, an increase in the evaporation rate of 30 to 40 % is not uncommon.

Obviously, the situation is significantly different for nitrogen cryostats, where, as previously mentioned, the heat of evaporation per unit volume is a factor of 60 higher. Insulation is, therefore, not that critical. Usually, merely vacuum insulation is applied, with highly reflective walls (as in Dewar bottles) or with a simple MLI blanket. Even non-evacuated containers may be used which are made of materials such as polystyrene. Also, the gas enthalpy change is not that relevant. The maximum conductive heat load reduction that is attainable is merely a factor of 2.

The specific SQUID application may put specific constraints on both the design and materials of the cryostat. As stated above, systems for measuring sources outside the cryostat, should contain a minimum amount of metal. Therefore, engineering composites such as glass-fiber reinforced epoxies are used, and the measuring section may have a specific shape. A typical example in this respect is the concave-tail cryostat bottom used for MEG experiments. Another example is SQUID microscopy. Here, the separation between the sensing element and the source should be minimized to an extremely low value (order of magnitude 0.1 mm). For this purpose, the sensors are placed in the vacuum space and thermally linked to the helium bath by a non-metallic good conducting material (usually sapphire). The tail contains a very thin window and the separation between the vacuum wall and the 4 K part can be mechanically controlled.

A cryostat is usually filled by siphoning the liquid cryogen from a transport and storage container. For this purpose, a tube is immersed in the liquid in the container and the other end of the tube is inserted into the cryostat. Then, by building up a small overpressure in the container, the liquid cryogen is siphoned from the container into the cryostat. For helium cryostats, the siphoning tube has to be vacuum-insulated. Usually, the filling procedure is monitored by means of liquid-level indicators. For both helium and nitrogen, special safety precautions have to be taken (e.g., face protection and gloves). The filling of the liquid-cryogen reservoirs can also be automated by means of valves. Automated transfer of liquid nitrogen is now standard and available from a number of suppliers, automated transfer of helium is also possible but it is difficult to restrict the transfer losses in this case [26].

7.2.3 Cryogenic Refrigerators (Cryocoolers)

7.2.3.1 Introduction

Conventional coolers for the cryogenic temperature range (i.e., < 120 K), all consist of a mechanical compressor, that compresses a working gas at about ambient temperature, and an expansion space at a low temperature. In the expansion space, the compressed fluid is allowed to expand, thus causing refrigeration. This section focuses on four representative types of mechanical cooler: the Joule–Thomson, the Stirling, the Gifford–McMahon, and pulse-tube coolers. Alternative cooling techniques and trends in cooling will also be discussed.

7.2.3.2 Joule–Thomson Coolers

In the early 1850s, two British scientists J.P. Joule and William Thomson (later Lord Kelvin) performed experiments on the expansion of gases. They expanded gases from a high pressure, through a porous plug, under adiabatic conditions. Under these conditions, the expansion is isenthalpic and the temperature of the gas increases or decreases depending on the sign of the Joule–Thomson coefficient $\mu = (\partial T/\partial P)_H$ [1, 27]. Below the so-called inversion temperature, μ is positive and cooling can be obtained as the result of expansion. This inversion temperature depends on the pressure, the maximum value of which (i.e., at $P = 0$) for helium is 40 K, for hydrogen it is 205 K, for neon, 250 K, and for nitrogen, 621 K. A cooler which utilizes this effect, consists of a compressor, a control and filter unit, a counter-flow heat exchanger (CFHX), and a Joule–Thomson expansion stage, including a porous plug or another type of flow restriction (the JT-valve). For an ideal CFHX, the cooling power of a JT cooler is given by the product of the mass-flow rate and the difference in specific enthalpy between the high and low-pressure sides at the warm end of the CFHX [1, 13]. Lowering the warm-end temperature, i.e., by pre-cooling the fluid before it enters the CFHX can increase this enthalpy difference, and thus the cooling power. Very large enthalpy changes can be obtained by pre-cooling to a level such that the fluid is liquefied before the expansion. In this case, the expansion valve is usually referred to as a throttling valve rather than a JT-valve [28]. Another way of obtaining large enthalpy differences is to mix hydrocarbons, with higher boiling points, into the working fluid [1, 12, 28, 29]. The much higher enthalpy difference then allows for a one-order-of-magnitude lower pressure ratio and, as a result, straightforward air-conditioning-type compressors can be used. An example of this is the "Cryotiger", a commercial cooler developed by APD cryogenics, [30] and shown in Figure 7.4(a). A refrigerant mixture is used here in a single flow stream.

The advantage of these JT-type coolers with regard to SQUID cooling is the absence of cold moving parts, which helps to attain a low level of interference. Furthermore, the cold stage can be constructed in a very simple and straightforward way [e.g., 13, 31] and is very suitable for miniaturization [32, 33]. The biggest problem with these JT-type coolers is clogging of the cold stage caused by moisture and contamination. The lower the operating temperature, the bigger the problem. In the case of 4 K cooling, a further disadvantage is that a helium-based JT cooler has to be pre-cooled to, typically, 20 K, because of the inversion temperature. As a result, a three-stage cooler is configured using a two-stage Gifford–McMahon pre-cooler. Three-stage coolers consisting of helium JT loops pre-cooled by two-stage GM coolers were used to cool low-T_c SQUIDs by Biomagnetic Technologies Inc [34] and by Daikin [35]. To cool high-T_c SQUIDs (from 300 K to below 80 K) nitrogen can be applied in a single stage, but this is very inefficient [1, 13]. As an alternative, gas-mixture coolers can be used in spite of problems caused by de-mixing and clogging. The cooling of high-T_c SQUIDs by a "Cryotiger" was investigated at the Research Center Jülich [36, 37] and at the University of Twente [38, 39].

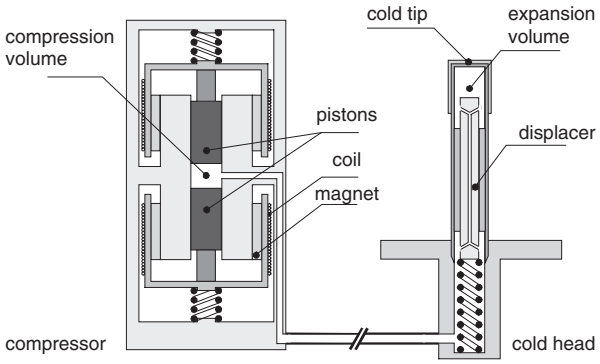

Fig. 7.2 Cross-section of compressor and cold head of split-Stirling cryocooler, compressor height typically 12 cm (Courtesy of Thales Cryogenics).

7.2.3.3 **Stirling Coolers**

A schematic diagram of the so-called split-type Stirling cooler is presented in Figure 7.2. In the compressor, two pistons are driven by linear motors. The motion of each piston is produced by the time-varying magnetic field of a coil that interacts with a permanent magnetic field around the coil. The permanent magnets are fixed to the compressor housing. Because the coil is connected to the piston, a pressure wave is established in the gas that acts on the spring-loaded displacer in the cold head. In order to establish high compressor efficiency, the pistons are operated close to mechanical resonance (50/60 Hz). First, by moving the compressor pistons towards one another, the gas is compressed isothermally and the heat of compression is passed to the environment. After the compression, the displacer moves down and displaces gas from the compression space to the expansion space. The motion of the displacer is discussed in more detail at the end of this paragraph. In this process, the gas is forced to flow through the interior of the displacer, which is filled with a regenerator material. This is a material with a large specific heat (e.g., copper screens or lead spheres). Along the regenerator, a temperature gradient is established from the compression space at ambient temperature to the expansion space at low temperature. The gas exchanges heat with the regenerator material and is thus cooled to a temperature close to that of the cold tip. Then, the compressor pistons move apart and the gas is allowed to expand at the cold tip. Because the gas is in good thermal contact with the environment, the heat of expansion is absorbed from the environment. This is the actual cooling step in the cycle. After the expansion, the gas is returned to the compression space by an upward motion of the displacer. Passing the regenerator, the gas warms up to the compression space temperature. In this cooling cycle, the phase of the displacer motion with respect to that of the compressor pistons, is very important. In general, the required phase difference can be obtained by attaching the compressor piston(s) and the displacer to a kinetic drive mechanism resulting in a disciplined piston/displacer Stirling cooler. In the example given in Figure 7.2, a free displacer is used. Here, the dynamic gas forces

acting on it, together with the mechanical spring, cause the movement of the displacer. The effective spring constant and the mass of the displacer determine the resonance frequency of this displacer motion. By adjusting the latter two parameters, the phase of the displacer motion can be tuned to that of the compressor pistons. Thus, at a given compressor operating frequency, the cooling performance can be optimized.

Since the late 1950s, small Stirling coolers with helium as the working gas were especially developed for cooling infrared detectors in military applications. Currently, thousands of units a month are produced worldwide for cooling these detectors in night-vision equipment and missile guidance systems [15]. Coolers for this market are manufactured with more or less standard dimensions: cold tip diameter, 5–10 mm, length of the cold finger, typically 6 cm, compressor diameter, 55 mm and length, 120 mm (see also Figure 7.4). Their cooling powers range from 0.2 W to 2 W at 80 K, with the environment at 20 °C and an input power of typically 50 W. They are usually operated at 50/60 Hz. Larger Stirling coolers are, for instance, applied for cooling superconducting filters in telecommunication systems (5–10 W of cooling power [16]).

At the end of the 1970s, the cooling of low-T_c SQUIDs by means of custom-made multi-stage plastic Stirling coolers was investigated by Zimmerman et al. at NIST in Boulder, NBS [40, 41]. The advent of high-T_c SQUIDs made possible the use of commercially available Stirling coolers [42, 43]. By means of various measures (see 7.2.5.), the cooler noise contribution can be reduced to below that of the high-T_c SQUID measuring system (range 0.1–0.2 pT $Hz^{-1/2}$, < 100 Hz, except for the power-line interference peak, e.g., [43]).

7.2.3.4 **Gifford–McMahon Coolers**

One disadvantage of the Stirling cooler was the inability to separate the compression and expansion sections by a large distance thus limiting the flexibility of the cooler [44]. At the end of the 1950s, Gifford and McMahon developed a method of separating the compressor and expander [45]. In their approach, the compressor is just a high-pressure generator connected to the expansion unit by flexible gas lines that can be up to several meters long, with an active-valve unit that generates the pressure wave. As well as the advantage of separation, the compressor can be a standard oil-lubricated air-conditioning type compressor, involving a much lower cost. Of course, provisions are included for filtering the compressor oil out of the working fluid. The cold head is similar to that of a Stirling cooler. The phasing of the displacer movement with respect to the pressure wave is set and controlled by means of the mechanics that drive the valve unit and the displacer/regenerator. In contrast, the Stirling cooler of Figure 7.2 is a mechanically resonant system in which the proper phasing has to be tuned in the design.

GM-coolers with helium gas as the working fluid were primarily developed for cryopumping and are now available from a large number of suppliers, amongst whom are the biggest suppliers of vacuum equipment. Cryopumps constitute the largest commercial application of cryocoolers (roughly 20 000 units per year [46]). In addition, GM-coolers are installed in MRI systems for reducing the boil-off rate of

the liquid helium bath. These coolers are commonly manufactured in single-stage and double-stage versions. The latter type has cooling powers of several watts at the coldest stage (typically at 20 K) and several tens of watts at the other stage (at 80 K) with an input of a few kilowatts [1], see Figure 7.4. Two-stage GM coolers are also available, which can cool down to 4 K by using rare-earth regenerator materials. These materials have magnetic phase transitions in the temperature range 4 K – 10 K, and thus a high latent heat in that temperature range [47, 48]. The operating frequency of the displacer and the valves is relatively low, in the range of a few Hz.

A two-stage GM cooler equipped with an Er_3Ni regenerator, was used to cool two low-T_c SQUIDs by researchers from SSL and ETL in Japan [49, 50]. At the University of Twente, a helium-gas circulation was used to cool a high-T_c SQUID by means of a "normal" two-stage GM cooler [51, 52].

7.2.3.5 **Pulse-tube Coolers**

An important drawback of both Stirling and GM coolers is the presence of a moving displacer in the cold part of the cooler. This displacer limits the lifetime (due to wear) and, because of its movement, it can generate noise (vibrations and EMI [1]). In 1963, Gifford and Longsworth invented a regenerative refrigeration technique that did not need a displacer [53]. They called their invention a pulse-tube refrigerator. An improved concept of it was introduced by Mikulin et al. in 1984 [54] and later refined by Radebaugh and co-workers [55]. In this concept, an orifice was inserted at the warm end of the pulse tube to allow some gas to flow into a relatively large reservoir volume. The ideal operation of the orifice pulse-tube refrigerator is explained in Figure 7.3. Here, both ends are at environmental (high) temperature T_H, whereas the cold spot in the middle is at a low temperature T_L. The dense vertical lines in the figure symbolize heat exchangers (HX). In a similar way to the Stirling cycle, gas is compressed in step a → b with release of heat Q_{H1} to the environment, followed by a regenerative step b → c. In this step, the gas is forced to flow through the regenerator and is thus cooled from T_H to T_L. The expansion of the working gas (c → d) is not against a piston, as is the case in a Stirling cooler, but against a compressible gas volume in the pulse tube. This gas volume can be considered as a freely moving

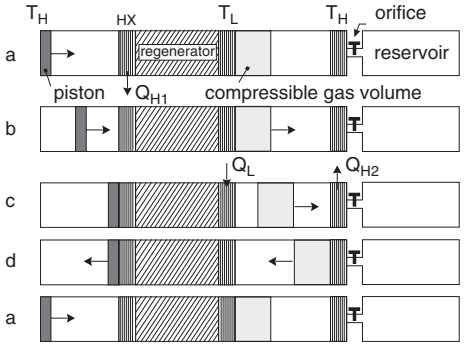

Fig. 7.3 Schematic representation of an ideal orifice pulse-tube refrigerator.

piston. The heat of expansion, Q_L, is absorbed at the cold heat exchanger. The mechanical work of expansion is transferred to the warm end of the tube by means of the gas piston. The associated heat Q_{H2} (which equals Q_L) is released to the warm environment. The cycle is closed with the regenerative step d → a. The orifice and the reservoir are needed to establish the proper phasing between the gas movement in the tube and the pressure wave imposed by the compressor.

In an electronic circuit analogy, the pressure and gas flow can be seen as the voltage and current respectively, whereas the orifice and reservoir act as an RC load. The schematic diagram of Figure 7.3 depicts a so-called in-line arrangement, in which the regenerator and pulse tube are in line. Because this implies two warm ends and a cold spot in the middle, this arrangement is difficult to integrate within a device. A more compact design is possible by reversing the gas flow at the cold heat exchanger in a U-shape (the regenerator and pulse tube are side by side, connected by the cold heat exchanger) or in a coaxial arrangement (the regenerator is coaxially outside the pulse tube). The advantage of these arrangements is a more compact design with a single warm end and a cold end, similar to the other coolers. The advantage is a slightly lower power efficiency compared to the in-line configuration, because of losses in the flow reversal.

In the last few years, pulse-tube coolers have been improved to such a level that their efficiencies at cryogenic temperatures are comparable to those of Stirling coolers. The most important improvement was a so-called double inlet that was introduced by Zhu et al. in 1990 [56]. They added a by-pass from the warm end of the pulse tube to the inlet of the regenerator, in which a second orifice was placed. The benefit of this by-pass plus second orifice is two-fold: first, it provides an extra parameter in optimizing the phasing between mass flow in the tube and pressure wave at the inlet; second, part of the gas flow that is required for expansion and compression at the warm end of the pulse tube is taken directly from the inlet, instead of passing through the regenerator and the pulse tube. A reduction in mass flow through the regenerator means lower regenerator losses, and thus a higher efficiency, especially at higher operating frequencies. The disadvantage of pulse-tube coolers is that they may exhibit temperature stability problems because of unwanted gas flows. This may be a dc flow through the double inlet [57–59] or gravity-induced secondary streaming in the tube [60]. Apart from these problems, it is clear that the pulse-tube cooler has great advantages over the Stirling or the GM cooler: the absence of moving parts in the cold results in longer life, lower interference, and lower cost. Moreover, a pulse-tube cooler is less sensitive to side loads (i.e., forces in the radial direction) and less sensitive to contamination coming from the compressor.

Two types of pulse-tube cryocoolers can be distinguished: A Stirling-type pulse tube is directly connected to the pressure-wave generating compressor, whereas a GM-type pulse tube is connected to an active-valve unit connected to a compressor. In terms of cooling power, input power, size, operating temperature and frequency, these pulse-tube coolers resemble their Stirling and GM-type counterparts. GM-type pulse-tube coolers are also available for the 4 K range [61].

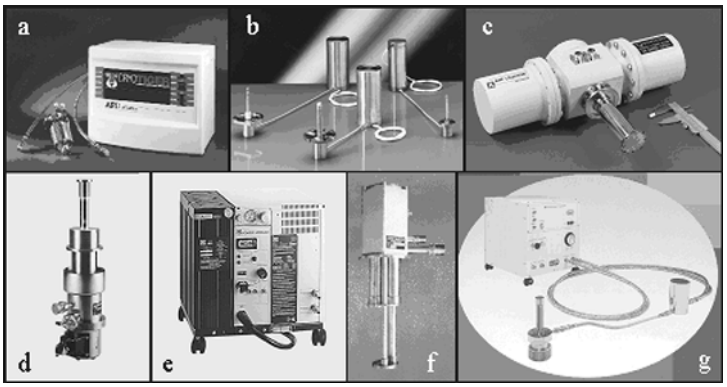

Fig. 7.4 Examples of commercially available cryocoolers. Indicative values for cooling power/operating temperature/input power/size are given in brackets. (a) APD Cryotiger Joule–Thomson gas-mixture cooler (3 W/80 K/300 W/compressor 40 cm); (b) Thales Cryogenics Stirling coolers UP series (1 W/80 K/50 W/10 cm); (c) AirLiquide/Ricor K535 Stirling cooler (6 W/80 K/200 W/30 cm); (d) Leybold cold head of RGD 5-100 2-stage GM cooler (5 W/20 K/4 kW/60 cm), also available in (1 W/4.2 K/6 kW/60 cm); (e) Leybold 4 kW compressor to be combined with cold head under d; (f) Cryomech cold head of PT 405 pulse tube cooler (0.5 W/4.2 K/5 kW/60 cm); (g) Iwatani P301 pulse tube cooler (2 W/77 K/700 W/compressor 40 cm).

The application of pulse-tube coolers for cooling SQUIDs has so far been restricted to high-T_c SQUIDs. These investigations were carried out in Germany at the Universities of Giessen [62, 63] and Jena [64]. Research was also conducted by a collaborative effort of CNRS with Air Liquide in France [65].

7.2.3.6 **Comparison of Cryocoolers**

The operating temperature of low-T_c SQUIDs can be attained with GM coolers and GM-type pulse-tube coolers. Joule–Thomson coolers with two-stage precooling are available but are more complex and more expensive. GM coolers have higher cooling capacities than pulse-tube coolers and correspondingly higher efficiencies; GM coolers are available in the range 0.5 W to 1.5 W at 4 K with efficiencies of typically 1 % of Carnot (e.g., 1 W of cooling power at about 7 kW of input power), whereas GM-type pulse-tube coolers have cooling powers below 1 W at a Carnot efficiency of about 0.7 % (e.g., 0.5 W at about 5 kW input) [16]. Despite the lower efficiency, the pulse-tube cooler is more attractive for SQUID cooling then a GM cooler because of the much lower level of vibration. In this respect, a pulse-tube pre-cooled Joule–Thomson cooler may also be attractive.

In the temperature range of high-T_c SQUIDs, a large variety of coolers can be used, as discussed in [16]. Below 1 W of cooling power, Stirling coolers are the most efficient with Carnot efficiencies of up to 15 %. Between 1 W and 10 W, Stirling-type pulse-tube coolers perform almost as well as Stirling coolers with typical Carnot efficiencies of between 10 % and 20 %. Cooling powers well above 10 W can be attained with GM coolers and GM-type pulse tubes. Carnot efficiencies are about 5 % at a

few tens of watts, approaching 20 % for cooling powers around 300 W. Since a SQUID system shows hardly any power dissipation, the required cooling power will be below 10 W and, therefore, Stirling-type pulse-tube coolers and Stirling coolers are the most attractive in terms of cooling performance. However, the compressor in these coolers is usually close to the cold head and generates a lot of noise (electromagnetic noise and vibrations). Special measures are therefore required (see Section 7.2.5). Joule–Thomson coolers are much less noisy but have a far lower efficiency and, as a result, require relatively big compressors.

7.2.3.7 Trends in Cryocooling

High Reliability. In the second half of the 1990s, the most important issue in the development of coolers, was reliability. Available coolers had specified lifetimes of the order of one year, whereas the requirement for civil applications was more than five years. Since then, considerable developmental work has been done on the compressor and on the gas-expansion unit. Concerning the latter, the main attention has been on eliminating the moving parts in the cold. Typical examples are the pulse-tube refrigerator and the developments in Joule–Thomson cooling. In the case of the compressor, the key issue was the rubbing contact between the compressor piston and the cylinder. The wearing of the rubbing seals was the limiting factor in the lifetime of the compressor. Nowadays, using flexure bearings that support the piston and the displacer inside their respective cylinders, without any contact, can eliminate these rubbing contacts. Accurate machining can reduce the gap between piston and cylinder to a few μm. The flow impedance of this clearance gap is so high that it acts as a dynamic seal for the helium gas. The "mean-time-to-failure" (MTTF) of these compressors can exceed 50 000 hours, whereas Stirling compressors without flexure bearings have MTTF levels of less than 10 000 hours [16, 66]. Another approach is to eliminate the moving parts of the compressor by means of a so-called sorption compressor. In such a compressor, a number of cells with adsorber material (for instance charcoal) are alternately cooled, to adsorb a working gas (e.g. nitrogen), and heated to desorb it. In this way gas flow can be established from a heated desorbing sorption cell to a cooled adsorbing cell. This flow can be used in a Linde–Hampson cycle to obtain cooling from a JT-valve. By far the largest amount of research in this field has been carried out at the Jet Propulsion Laboratory, mainly on metal hydrides with a hydrogen cycle [67]. More recently, work has also been performed at the University of Twente [33, 68].

Low Cost. Another challenge is to manufacture highly reliable coolers at a sufficiently low price. Cooler manufacturers are continuously improving their designs and manufacturing processes, with cost reduction being the main concern. Descriptions of such processes were presented by Superconductor Technologies Inc. [69, 70] and by Sunpower [71]. The US DARPA program that sponsored research aiming at $ 1,000 coolers, largely stimulated these efforts towards lower cryocooler cost. Nowadays (2002), the cost of a single unit sub-1W cryocooler ranges roughly from 20 k$ to 40 k$ for low T_c (~ 4 K), and from 5 k$ to 15 K$ for high T_c (~ 70 K) [16]. The

production volume is an important cost-determining parameter. As a rough indication, the price per cooler goes down by a factor of two when the number of coolers produced is increased by one order of magnitude [16].

Small Size. Increasing attention has been paid to the size of the cooler. Since electronic devices become smaller and smaller in terms of size and dissipation, there is need for extremely small coolers (with the dimensions of centimeters) with small cold heads (of the order of mm) and low cooling powers (of the order of mWs). Extreme miniaturization is possible by using micromechanical techniques. Walker first suggested this in 1990 [72], and by the mid-90s, patents were already being filed on a micro-pulse-tube cooler [73] and on a micro-Stirling-cooler [74]. Actual micro-cooling research was performed at the University of Twente [33, 68, 75].

7.2.4 Cryostat or Cryocooler?

In order to compare cryostats with cryocoolers, it is important to note that the cryostat with the liquid cryogen is only a small part of a rather complex cryogenic system. It just serves as a thermal buffer in the total system. First, gas has to be liquefied in a large cooler that produces relatively large amounts of liquid in big storage dewars. This liquefaction is performed industrially. The liquid cryogen is then shipped in large transport/storage dewars to a customer, who transfers the liquid into smaller (e.g., SQUID system) dewars and vents it to air. This is the standard procedure with liquid nitrogen, but helium is so expensive that it is often worthwhile to recover the vented gas. In this case, it is captured in large inflatable gasbags or gas tanks, and, after filtering and purification, is re-pressurized by a compressor to be re-liquefied through expansion.

The main drawback of liquid cryogens is that periodical replenishment of the cryostat is required for long-term operation. In particular with liquid helium, expertise and cryogenic facilities are required. It is necessary to have available the service of a skilled technician who can safely transfer the liquid from a storage dewar with comparatively little transfer losses. This is especially relevant for applications outside the cryogenic laboratory (e.g., in hospitals). In addition, not all spaces are suitable for transfer; low ceilings, for instance, make transfer difficult. The most attractive feature of a cryocooler is, in general terms, its turn-key operation. No expertise or cryogenic facility is required. This dramatically lowers the barrier preventing the application of superconducting devices outside cryogenic laboratories. A very important requirement in this respect is reliability. The cooler should be a 'black box' to the user, who should not need to worry about it at all. A qualitative comparison between liquid-cryogen cooling and cryocoolers is given in Table 7.1.

The operating temperature of any liquid cryogen is fixed by its boiling point and a temperature variation is only possible by changing the vapor pressure, e.g., by pumping the space above the bath. Practical cryocoolers are available for cryogenic temperatures down to well below 4 K. Within some range, changing the input power to the cooler can simply vary the temperature. Temperature stability and low inter-

Tab. 7.1 Qualitative comparison between liquid-cryogen cooling and cryocoolers.

	Liquid cryogen	Cryocooler
Operating temperature	+ / −	+
Temperature stability	+	−
Interference	+	−
"User friendliness"	−	+
"Maker friendliness" (= costs)	+	−
Reliability	+	+ / −
World-wide availability	−	+
Weight (long-term operation)	−	+
Operating orientations	+ / −	+

ference are clear advantages of cryogens, although methods are available to control the cryocooler temperature fluctuations and reduce interference (see Section 7.2.5). As mentioned above, cryocoolers are very "friendly" to the user because of their turn-key operation. On the other hand, they are rather "unfriendly" to the manufacturer because of their constructional complexity. The latter aspect directly translates into higher costs.

Liquid-cryogen cooling is quite reliable. Once the cryostat is filled, it will operate for a predictable period of time and is not vulnerable to unscheduled interruptions of the electric power. However, availability may be the problem of cryogens. These fluids, particularly helium, are not widely available in some parts of the world. A further point related to the reliability of cryostats is the availability of a good clean vacuum. The necessary periodical re-pumping may be problematic in some places.

A big advantage of cryocoolers compared with liquid cryogens, is the weight required for long-term operation, which is especially relevant in space applications. The possibility of operating the cryogenic systems in all orientations is another clear advantage of cryocoolers. For earth applications, a liquid cryogen clearly has its limitations, although special constructions can be used to keep the liquid inside the cryostat at all orientations [76].

7.2.5 Cryocooler-interference Reduction

7.2.5.1 Interference Mechanisms

As mentioned in the previous section, one main disadvantage of cryocoolers is their interference with the SQUID operation. This interference can be electromagnetic interference (EMI), mechanical vibrations, and/or temperature fluctuations. EMI can be caused by currents flowing through the compressor coils or the motors that drive the valves or the displacer, and also by moving magnetic material. The movement of pistons, displacers and valves causes mechanical vibrations, as also can gas flow or pressure oscillations. The cold-tip temperature may fluctuate with a characteristic frequency (in regenerative coolers, this is the operating frequency), or it may

exhibit a low-frequency drift. In addition, cryocoolers usually contain metallic parts and, therefore, thermal noise and eddy-currents may cause problems, as in the case of cryostats. In this section, methods are discussed to reduce the effect of these interference mechanisms. A more detailed review was presented elsewhere [1].

7.2.5.2 **Time Separation**

The simplest approach for the suppression of cooler interference is to switch off the cooler when the SQUID is to be used. There are two problems with this separation in time: first, the cooler should not be switched off too frequently because that can seriously limit its lifetime, and, second, the temperature of the device will slowly increase while the cooler is switched off (thermal drift). Incorporating a sufficiently large thermal buffer, i.e., a thermal storage unit, can solve both problems. To stabilize the temperature most efficiently, it is best to provide a buffer or thermal storage unit with a phase change material (e.g., a boiling liquid). Using this approach, Longsworth et al., for instance, equipped a Linde-Hampson cooler with a 1.4-liter helium reservoir [77]. After switching off the cooler, this buffer maintained a temperature of 4.2 K for a period of 10 hours.

7.2.5.3 **Space Separation**

Coolers and SQUIDs can also be separated in space. The problem to be solved in this case is how to transport the heat from the SQUID to the cooler. Three possible interfaces can be used: a heat pipe, a forced gas circulation and a thermal strap.

Heat Pipe. A standard heat pipe is a tube with axial grooves along the inside wall. The closed tube is filled with a fluid such as ammonia or, for lower temperatures, nitrogen or oxygen. It is connected at one end to a cold station (i.e., a cryocooler) where the fluid condenses. Capillary action moves the fluid into the grooves, thus transporting it to the other end of the tube, where it makes contact with the device (e.g., a SQUID). Heat is absorbed from the device and the fluid evaporates. Due to the pressure increase, the vapor can return via the center part of the tube to the cold condenser side [78]. The attractive aspect of the heat pipe is the, more or less, isothermal behavior, i.e., the high heat fluxes that can be obtained over relatively large distances with very small temperature drops. Furthermore, it has no moving parts, is highly reliable and has a relatively low mass. Therefore, heat pipes have been specially developed for applications in space. In ground applications, gravity will affect the fluid motion and, in general, special configurations must be used. Either gravity needs to be applied as an extra driving force [e.g., 79], or larger capillary forces must be established.

Forced Gas Circulation. A gas that is circulated in a closed-cycle system can also transfer heat. This method was investigated by Van den Bosch et al., who used helium gas circulated by a diaphragm pump and cooled by a two-stage GM-cooler [51, 52]. Using a 2.5 m long gas line, a heat exchanger, on which a superconducting device could be mounted, was cooled. A temperature of 31 K was established [see also 80, 81].

Thermal Strap. If the separation between the cooler and the superconducting device is relatively small (roughly 0.5 m or less) a thermally conductive strap interface, made, e.g., of a copper braid, is a reasonable option [43].

7.2.5.4 Low-noise Coolers

Most of the noise that a cooler generates, arises from the moving parts, as discussed in 7.2.5.1. Therefore, the elimination of moving parts in the cold stage is needed for lower-noise cold heads. This is attained in JT-coolers and pulse-tube refrigerators, although mechanical vibrations transmitted from the compressor via gas tubing may often require additional damping. Alternatively, non-magnetic or even non-metallic components should be used to reduce EMI [82–84]. It is therefore obvious that, besides the cold heads, it is also useful to develop compressors without moving parts. The main effort in this respect has been the development of sorption compressors (see Section 7.2.4).

7.2.5.5 Noise Suppression Techniques

Direct EMI. Coolers usually operate at a well-defined frequency and generate periodic EMI signals. Therefore, various filtering techniques can be applied. As well as commutative filters [41], digital signal processing can be applied in which templates of the cryocooler noise are subtracted from the signal [35, 49, 50]. One disadvantage of filtering techniques is that all information, including the desired data, is lost at the cooler operating frequency and its higher harmonics. When the relative configuration of the cooler and SQUIDs is fixed, the following alternative procedure suggested by Van den Bosch et al. can be applied [85]. Prior to the actual experiments, the transfer functions of the compressor currents to the SQUID outputs should be determined. Then, during the experiments, the compressor currents are monitored and, because the transfer functions are known, the compressor field contributions can be subtracted from all SQUID outputs in a simple manner.

Mechanical Vibrations. The correct mechanical design and both passive and active damping, can reduce mechanical vibrations in various ways. The design of the system should be such that the cooler is mechanically uncoupled from the SQUID device as well as possible. Since a cooler usually operates at a fixed frequency, the vibrations of a system element can be damped in a passive way by connecting a mass-spring system to it that vibrates in anti-phase at that specific frequency. Vibrations can also be minimized in an active way by applying compensating forces e.g., [86–89].

Temperature Fluctuations. The simplest way to reduce temperature fluctuations is to use a passive thermal filter, which is a piece of material placed between the cold tip of the cooler and the SQUIDs. This material conducts the heat but it also damps the thermal oscillations as a first-order low-pass filter. For example, Hohmann et al. attenuated the 0.08 Hz oscillations of their cooler by a factor of 50 using a 5 mm-

thick piece of PMMA (Polymethylmethacrylate) [90]. The temperature can also be stabilized and controlled by incorporating an active feedback loop, e.g., [1].

7.2.6 Material Properties

Mechanical and thermal properties of materials are important in cryogenic design. Specifically for SQUID applications, electrical properties are also relevant. Material properties at cryogenic temperatures can be found in much of the literature in the form of tables and graphs, and are, to some extent, also available in software. Data is also included in handbooks such as in reference [10]. The reader is particularly referred to [91] and the software that is available from Cryodata [92] and from JAHM Software [93]. This section focuses on the relevance of the various properties and the general tendencies of their temperature dependence. The most important properties of some of the materials that are commonly used in cryogenic constructions are given in Table 7.2 at temperatures of 300 K, 80 K, and 4 K, the data being mostly based on [91–93].

Mechanical Properties. The mechanical properties, especially Young's modulus and the yield strength, are important in the design of vacuum casings. Metals and polymer composites show a monotonic increase in stiffness with decreasing temperature. However, the overall effect is small. When cooling from 300 K to 77 K, the increase in Young's modulus for metals is of the order of 10 %, whereas, for composites, this increase may reach 50 %. The temperature effect is much bigger for polymers (by a factor of 5 or even more).

Thermal Conductivity. The most important thermal property of a material is its thermal conductivity, since this often determines the heat flow into the cryostat and thus the boil-off rate. There is quite a wide range of values. At 300 K, for instance, the thermal conductivity of copper is typically 400 $Wm^{-1}K^{-1}$, whereas that of stainless steel is 15 $Wm^{-1}K^{-1}$ and that of glass only 1 Wm^{-1}. From 300 K down to 150 K, the conductivity decreases but not very dramatically. Below about 100 K, however, the conductivity roughly scales with temperature. Important in this cryogenic temperature range is the purity of the material. At around 10 K, for instance, the conductivity of copper may vary by more than one order of magnitude, depending on its purity.

Specific Heat. The specific heat C_p is of relevance in dynamic effects, such as cool-down time, damping of temperature oscillations, regenerator performance, etc. This property is even more temperature dependent than the thermal conductivity. In most of the cryogenic temperature range, C_p scales with T^3 because of the lattice contribution. Below about 10 K, the C_p of metals scales with T, because the electron contribution is dominant. For temperatures around the ambient temperature, the heat capacity levels off to the Dulong–Petit limit. All in all, from 300 K to 4 K, the specific heat of a material may drop by more than four orders of magnitude!

Tab. 7.2 Properties of materials commonly used in cryogenic constructions.

	T (K)	Copper	Aluminum	Stainless steel 304	Niobium	G10 [A]	Nylon	Pyrex [B]	Teflon	Al_2O_3
Young's	300	128	70.0	194	102	38	2.9	62.6	0.38	–
modulus	80	140	76.8	208	–	41	7.6	–	5.4	–
(GPa)	4	143	79.1	204	–	–	–	–	–	–
Stress at	300	350	110	1.1×10^3	–	1.2×10^3	59	–	7.5	–
0.2% strain	80	420	150	1.5×10^3	–	1.7×10^3	21	–	83	–
(MPa)	4	–	–	–	–	–	–	–	–	–
Thermal	300	397	236	15.2	53.7	0.80[C]	0.30	1.13	0.25	40
conductivity	80	571	415	8.33	57.9	0.50[C]	0.22	0.52	0.22	900[D]
($Wm^{-1}K^{-1}$)	4	11370[E]	1576	0.252	99.7	0.18[C]	0.012	0.11	0.04	110[D]
Specific	300	384	904	378	257	810	1700	732	1000	760
heat	80	201	340	179	155	230	580	220	320	63
($Jkg^{-1}K^{-1}$)	4	0.0914	0.22	1.67	~0.8	1.6	1.3	0.20	1.3	0.09
$(L_{293}-L_T)/L_{293}$	300	–0.011	–0.016	–0.01	–0.01	–	–	0.00	–	–
	80	0.29	0.376	0.28	0.129	0.22[F]	1.21	0.051	1.88	0.08
(%)	4	0.33	0.418	0.34	0.143	0.26[F]	1.39	0.054	2.14	–
Electrical	300	0.0583	0.0363	0.00138	0.00635	–	–	–	–	–
conductivity	80	0.463	0.398	0.00181	0.0169[G]	–	–	–	–	–
($10^9\ \Omega^{-1}m^{-1}$)	4	50	920	0.00196	–	–	–	–	–	–

A: Glass-fibre reinforced epoxy
B: Corning 7740
C: Warp direction (normal direction: about 40 % of these values)
D: Single-crystal; polycrystalline 80K: 120 $Wm^{-1}K^{-1}$; 4K: ~1 $Wm^{-1}K^{-1}$
E: High-purity copper (better than 99.9 %), lower purity: value down to 300 $Wm^{-1}K^{-1}$
F: Warp direction (normal direction: 0.66 % @ 80 K; 0.72 % @ 4 K)
G: Value at 100 K

Thermal Expansion. Thermal expansion (or shrinkage) is of importance in constructions with accurate fittings. It also affects the distance from the sensing coil to the outside (as discussed in 7.2.2), since the inner parts of the cryostat shrink when it is filled. Coefficients exist for the volumetric expansion (β) of a material, and of its linear expansion (α, for an isotropic material $\beta = 3\alpha$). Above about 100 K, these coefficients are roughly constant, and below this they decrease to zero at the absolute zero. The integral expansion is even more important than the coefficients. In one dimension, this integral expansion (or shrinkage) is given with respect to a reference temperature, e.g., 293 K, by $(L_{293}-L_T)/L_{293}$ expressed as percentages. Following the temperature dependence of the coefficients, the integral expansion scales with T above about 100 K, and levels off to a constant for lower temperatures. Metals shrink by about 0.2–0.5 % from 300 K to 4 K, whereas non-metals, such as epoxies and nylon, shrink up to 1.5 %.

Electrical conductivity. Metal in the vicinity of a SQUID magnetometer generates noise, not only because of magnetic impurities, but also because of eddy-currents and thermal noise, the latter originating from the thermally activated motion of electrons. For the determination of noise due to both eddy-currents and thermal noise, the electrical conductivity of the material is an important parameter. For temperatures below ambient down to about 100 K, the conductivity scales roughly with $1/T$. At lower temperatures, the electrical conductivity levels off to a constant value that is determined by the purity of the material. Combining this temperature dependence with that of the thermal conductivity, it follows that, for metals, the ratio of the thermal and electrical conductivities is linear with temperature. This is the so-called Wiedemann–Franz–Lorenz law. At a specific temperature, this means that a high thermal conductivity also automatically implies a high electrical conductivity. In cryogenic SQUID magnetometer design, this may present some problems. For instance, when a SQUID has to be thermally anchored to a cold plate, a thermally, good-conducting interface is required. However, an electrically good conducting surface would produce a high thermal-noise contribution. To overcome this problem, non-metals are used such as sapphire (single crystalline Al_2O_3). Single-crystalline materials can have a very high thermal conductivity and be electrically insulating at the same time.

7.3 Cabling and Electronics

7.3.1 Shielding and Filtering of Noise Sources

7.3.1.1 Introduction to Shielding Effectiveness

SQUID operation can be disturbed by stray low-frequency and rf electromagnetic fields from a range of sources such as permanent magnets, power cables, transformers, motors, television or communication transmission towers, radar and railways.

This interference, which has contributed to many unsuccessful SQUID system trials, can also originate from the system's own electronics or computers as well as other electronics in the vicinity.

Inadequate shielding of cables and electronics is a common problem and can lead to the failure of the system to meet the specifications required for the anticipated operating environment. This section discusses ways of providing adequate low-frequency and rf screening, and gives a method of determining the level of low-frequency shielding and filtering required.

Shielding is one of the most effective methods for controlling radiated electromagnetic interference (EMI) effects on all components of a system. The performance of a shield is a function of the characteristics of the incident electromagnetic fields. The terms "shield" and "screen" are used synonymously in the EMI context and refer to the use of conducting panels and enclosures to prevent or minimize the access of electromagnetic fields to the system. There are two shielding mechanisms: field absorption and reflection. The combination of these mechanisms reduces the level of electromagnetic fields in the protected space (volume). The total shielding effectiveness (S) is usually expressed as either a dimensionless ratio or, as shown below, in decibels as [94–96]:

$$S = 20 \log_{10} E_0/E \text{ [dB] (for electric fields) and} \tag{7.1}$$

$$S = 20 \log_{10} B_0/B \text{ [dB] (for magnetic fields)} \tag{7.2}$$

where E_0 (or B_0) is the intensity of the electric (or magnetic) field outside and E (or B) is the intensity inside the screen.

7.3.1.2 **Absorption**

When an electromagnetic wave encounters a shield, a portion of this wave penetrates and experiences an exponential decay of amplitude, $\exp(-d/\delta)$. Here, d is the distance the wave has traveled into the shield, and δ is the penetration depth. In the case of conductors, δ can be extremely small. The resulting confinement of the field close to the surface is known as the skin effect, and δ is called the skin depth. This skin depth can be expressed as [96, 97]:

$$\delta = \left(\frac{1}{\pi\mu\sigma f}\right)^{1/2} \text{ [m]}. \tag{7.3}$$

Here, $\mu = \mu_0\mu_r$ where μ_0 is the permeability of free space ($4\pi \times 10^{-7}$ Hm^{-1}), μ_r is the dimensionless relative permeability, σ is the electrical conductivity (S m^{-1}) and f is the frequency of the wave (Hz). The resulting EMI absorption, A, expressed in dB for a metal sheet of thickness, t, is approximated by [94–96]:

$$A = 8.686\, t/\delta \qquad \text{[dB]}. \tag{7.4}$$

In this equation, t and δ must be expressed in the same length units. Some typical values of absorption and skin depths at various frequencies are given in Tables

Tab. 7.3 Typical absorption losses for possible shielding materials.

Metal	Conductivity relative to copper	Permeability relative to copper	Absorption loss, A, dB/mm
Silver	1.05	1	52
Copper–annealed	1.00	1	51
Copper–hard drawn	0.97	1	50
Gold	0.70	1	42
Aluminum	0.61	1	40
Brass	0.26	1	26
Nickel	0.20	1	23
Phosphor-bronze	0.18	1	22
Mu-metal	0.03	80000	2500[a]

a) assuming the material is not saturated.

Tab. 7.4 The skin depth of various common shielding materials over a range of frequencies [97].

			t (mm)	
Frequency *f* (Hz)	**Cu**	**Al**	**Fe μ_r=200**	**Fe μ_r=20**
25	13.40	17.40	2.54	8.10
50	9.44	12.30	1.80	5.69
100	6.67	8.70	1.30	4.11
1000	2.11	2.75	0.41	1.29
10 k	0.667	0.87	0.13	0.41
100 k	0.211	0.275	0.041	0.13
1 M	0.0667	0.087	0.013	0.04

7.3 and 7.4. If the shield material is thick compared to the skin depth (i.e., about equivalent to three skin depths), then absorption is significantly greater than the reflection at the surface. This is particularly true for high-frequency EMI waves.

7.3.1.3 Reflection

When an electromagnetic wave strikes a conducting surface, some of the incident energy is reflected at the air–conductor interface and some is transmitted into the metal. If the metal is thick compared to the skin depth then the absorption is significant as discussed in Section 7.3.1.2. The reflection mechanism is similar to that which occurs in a mismatched transmission line where an incident voltage is reflected at a mismatched termination as determined by a reflection coefficient. By determining this reflection coefficient at various interfaces, the amount of energy transmitted through the shield can be calculated. Using this approach, an expression for attenuation due to reflection in dB is given as [96]:

$$R\,20\log_{10}\frac{(Z_W+Z_S)}{4Z_WZ_S}\,[\mathrm{dB}] \tag{7.5}$$

where Z_W is the wave impedance of the incident energy and Z_S is the intrinsic impedance of the shield, which can be written as:

$$Z_S = \sqrt{\frac{2\pi f\mu_0}{\sigma}}\,[\mathrm{dB}]. \tag{7.6}$$

Z_S is very small for good conductors. At 3 GHz, for example, copper has $Z_S = 0.02\,\Omega$ and less for lower frequencies. The value for Z_W is not as easily defined as it depends on two factors: the type of electromagnetic source and the distance between the source and the shield. Figure 7.5 shows the variation in wave impedance, Z_W, with distance, r, from the source, expressed in units of $r = \lambda/2\pi$ where λ is the EMI wavelength. This figure shows that when $r \gg \lambda/2\pi$, then $Z_W = 377\,\Omega$ (the intrinsic impedance of free space). When $r < \lambda/2\pi$, the wave impedance depends on whether the source emits predominantly an E-field or a B-field component. Predominant E-field components have a Z_{WE} given by:

$$Z_{WE} = 377\frac{\lambda}{2\pi r}\,[\mathrm{dB}]. \tag{7.7}$$

A dominant B-field component source has a wave impedance of

$$Z_{WB} = 377\frac{2\pi r}{\lambda}\,[\mathrm{dB}]. \tag{7.8}$$

A correction factor for multiple reflections between the two surfaces of the shield can usually be ignored. This is possible because the electric field sources are more easily shielded. This is due to the large difference between Z_{WE} and Z_S and more than 90 dB of shielding effectiveness can easily be achieved. However, the typical

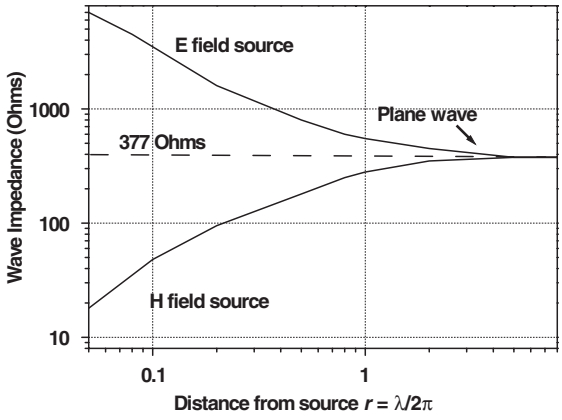

Fig. 7.5 Variation in wave impedance versus distance from the source, r, in units of $\lambda/2\pi$.

low impedance magnetic field penetrates the shield more effectively and undergoes multiple reflections, making inclusion of a correction factor necessary. As a general rule, if absorption is less than 15 dB then the correction factor, C, must be added and can be estimated by:

$$C = 20\log_{10}(1 - e^{(-2t/\delta)}) \text{ [dB]}. \tag{7.9}$$

Note that C is usually a negative number, indicating that the shielding effectiveness is reduced due to the presence of multiple reflections. If the correction factor is significant (i.e., greater than 15 dB), the shield design may need to be modified. This is particularly relevant for magnetic shielding as discussed in Section 7.3.1.5. A detailed description of absorption and reflection mechanisms can be found in references [94–96, 98].

For SQUID systems, there are two main external electromagnetic-noise frequency ranges, which require different shielding approaches. These are: high (radio) frequency (rf) signals in the range of 10 kHz to GHz and the low-frequency signals in the range of dc to 10 kHz. The two corresponding shielding approaches are considered separately below.

7.3.1.4 **High-frequency Shielding**

Rf interference is the common cause of output drift, higher noise levels and the failure of a system to lock up in a flux-locked loop, particularly for operation outside an rf-screened laboratory. To screen out rf interference, the SQUID system must be surrounded by well rf-screened housings or shields around the dewar and the electronics, with appropriately rf-screened cables connecting various electronic components. This is discussed in Section 7.3.2.

Whenever the rf EMI screening is placed around the dewar or located in the vicinity of the SQUID sensors, it may increase the noise due to eddy currents induced in the rf screen by the external changing fields. The minimization of these eddy currents was first achieved in the development of Magnetic Resonance Imaging (MRI) systems, which operate at about 100 MHz [99–102]. The approach was to provide effective rf shielding by copper [101], but with eddy currents minimized by sufficiently thin layered copper shields separated by a thin dielectric material [102]. To achieve successful rf shielding, the total copper thickness must be three or more times the skin depth at the frequency of the EMI source, while each individual copper layer should be less than a skin depth in thickness to minimize eddy currents. The amplitude of the interference decays by 37 % of its incident value within one skin depth [96]. Data from Table 7.4 can be used to design optimal shielding.

It is also possible to model the eddy currents in a shield by finite-element analysis (FEA) using one of the various FEA computer packages available commercially [103]. Successful computation needs a programmer with sufficient expertise to run the program. FEA requires the modeling of the source field that induces the eddy current by using an estimation of the field-source strength, the frequency and the orientation. An example of the calculation results using the FEMLAB program is shown in Figure 7.6. At an operating frequency of 1 MHz, calculated surface plots of

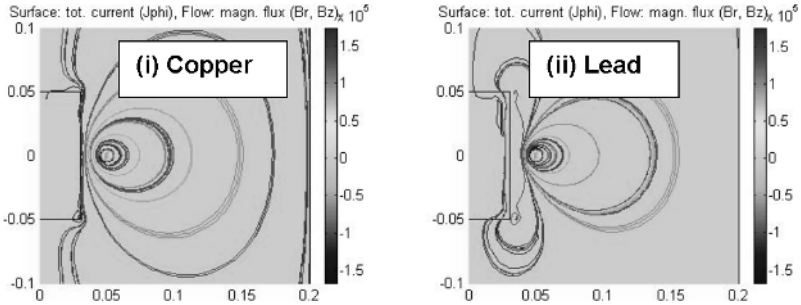

Fig. 7.6 Surface plots of eddy currents with field flow lines calculated using FEMLAB [103] for a (i) copper and (ii) lead, cylinder. The magnetic field in this example is from a single coil of diameter 0.01 m with a 100 kA current at 1 MHz, with the skin effect taken into account. The current and frequency have exaggerated values to enhance the visualization of the difference between the two materials.

eddy currents induced in copper and lead cylinders, each surrounded by a current-carrying excitation coil, are compared. The calculation shows that, with identical excitation, the rf screening achieved by copper is higher than that achieved in a lead cylinder, which has a higher resistance.

Overall, the rf EMI shielding can be summarized as follows.

- The absorption losses predominate above about 10 MHz.
- The reflection effects are more significant below 10 MHz.
- The total-shielding effectiveness of a 0.5 mm thick aluminum panel without orifices exceeds 200 dB at 10 MHz.
- Below 10 MHz, electric fields are still attenuated by more than 100 dB, while the attenuation of magnetic fields decreases with frequency and is less than 10 dB at 100 Hz.
- For low-frequency magnetic fields, the best attenuation is achieved by using high-permeability materials as discussed below.
- As shown by (7.3), shielding material with high permeability may have such a small-skin depth that the shield structure would be impractically thin, even at low frequencies.

7.3.1.5 **Low-frequency Shielding**

Power lines or moving magnetic objects generate low-frequency noise. Three methods can be used to reduce these disturbances: magnetic shielding, signal filtering and noise cancellation techniques. For low-frequency or dc fields, it is usually necessary to use a high-permeability soft magnetic material, which provides a low-resistance path for the magnetic flux to move around, rather than to penetrate the device to be shielded. This type of shield is referred to as a "magnetic shield". Magnetic shielding is the most straightforward, but relatively costly and cumbersome, method for the reduction of environmental noise. A thick layer of high-conductivity metal, as shown in Figure 7.7(a) curve 1 [104, 105], can provide the simplest shielding tech-

nique achieved by the presence of eddy currents. The effectiveness of such eddy current shielding increases with the thickness of the conducting layer. Magnetic shields are constructed of high-permeability alloys such as mu-metal (a trade name for an alloy composed mostly of nickel and iron [106]). A list of possible soft magnetic high-permeability materials is given in Table 7.5. Magnetic shield design is complex and a detailed discussion can be found in references [107–109]. When the shield is required to operate in a magnetic field of high intensity, the design complexity increases. If the operating flux level in the shield wall approaches 0.6 T, it may become necessary to use lower permeability materials such as iron or 50 % Ni–50 % Fe as these materials also have high saturation flux densities. To optimize the design, it may be necessary to use a multiple shield construction combining higher permeability material, e.g., mu-metal inside and higher magnetic saturation materials such as iron outside [109].

Generally, the following factors need to be considered in magnetic shield design: the required size and shape of the shield, the thickness and permeability of the shield material and the intensity of the field to be screened. The shielding factor can be estimated for various shapes from the dimensionless ratios given below:

$$S_{\text{sphere}}=4\mu t/3D \tag{7.10}$$

$$S_{\text{cube}}=0.7\mu t/a \tag{7.11}$$

$$S_{\text{cyclinder}}=\mu t/D \tag{7.12}$$

where μ is the sheet permeability (Hm^{-1}), t is the sheet thickness, D is the screen diameter and a is the side length. All dimensions are in the same units.

For open-ended cylindrical shields, the length should exceed twice the radius. End caps should be used if the length is less than this. Ideally, the magnetic dc field should be perpendicular to the shield axis. When this is not possible and the mag-

Tab. 7.5 High-permeability alloys suitable for magnetic shields and their properties [94, 107].

Material	Composition	Initial permeability	Maximum permeability	Saturation flux density (T)	Coercive force (Am^{-1})
	Ni_{77} $Fe_{14}Cu_5Mo_4$	50000	200000	0.8	1.0
Hypernik	$Ni_{50}Fe_{50}$	6000	40000	1.6	8
Iron	Commercial 99 Fe	300	5000	2.15	70
Iron	Pure 99.9 Fe	25000	350000	2.16	0.8
Mild Steel	$FeC_{0.1}Si_{0.1}Mn_{0.4}$	800	1100		200
78 Permalloy	$Ni_{78}Fe_{22}$	4000	100000	1.05	4
Supermalloy	$Ni_{79}Fe_{16}Cu_5Cr_{0.5}$	100000	1000000	0.79	0.15
Mu-metal	$Ni_{77}Fe_{16}Cu_5Cr_2$	20000	100000	0.75	4
Alfenol (Alperm)	$Fe_{84}Al_{16}$	3000	55000	0.8	3.2
Sendust	$Fe_{85}Si_{10}Al_5$	36000	120000	0.89	1.6

netic field can impinge directly into the open end of a cylinder, the shielding factor may be only 20 % of that for the perpendicular field. For ac fields, induced eddy currents can reduce field penetration, but this can be compromised as the magnetic permeability decreases with increasing frequency. Thick conductors with high permeability (e.g., mu-metal) are advantageous.

The design of mu-metal shields can be summarized as follows: The magnetic shield must operate at magnetic induction levels well below the saturation level of the shield material. The permeability of the material and hence also the shielding factor, decrease when approaching saturation. The magnetic induction in a cylindrical shield wall, B_{SW} (T), in a magnetic field strength of $H_{outside}$ (Am^{-1}) can be approximated by [107]:

$$B_{SW} = \mu_0 \mu_r H_{outside} D/t \tag{7.13}$$

where D is the diameter and t is the thickness of the shield. Saturation is avoided by the use of thicker shielding material or multiple concentric shields [109]. In general, the use of multiple shields is more effective than the use of increased shield-wall thickness. For example, the shielding factor for two shields can be calculated using the equations below, which give a dimensionless shielding ratio [107]:

$$S_{sphere} = S_1 + S_2 + S_1 S_2 (1 - D_1^3 / D_2^3) \tag{7.14}$$

$$S_{cyclinder} = S_1 + S_2 + S_1 S_2 (1 - D_1^2 / D_2^3) \tag{7.15}$$

$$S_{cube} = S_1 + S_2 + 0.8 S_1 S_2 (1 - a_1^3 / a_2^3) \tag{7.16}$$

where S_i and D_i are the dimensionless shielding factors and the diameters of each shield are given in the same units. For very sensitive scientific or medical measurements, shielding can be enhanced by a technique known as "shaking" [110]. This involves applying a continuous high-frequency field to the shield wall.

The fabrication of a mechanically hard metal shield as can be made from mu-metal, requires welding with the parent alloy being used as a filler rod. Subsequently, the shield must be heat-treated to restore the material's high permeability. This requires the, suitably supported, shield to be annealed at a temperature of 1050 °C and cooled for a period of 2–4 hours in a dry hydrogen atmosphere. This process requires special safety precautions and is best left to expert manufacturing companies who specialize in fabricating finished shields according to customers' engineering drawings.

For research and development, design evaluation or small production runs, the cost of a fully fabricated, mechanically rigid magnetic shield may be too expensive. However, pre-annealed foils made from high-permeability materials, may possibly achieve sufficient magnetic shielding. The foils can be wrapped around the device with the number of wraps adjusted to provide the thickness necessary to achieve the required attenuation.

An often forgotten requirement is the need for magnetic-shield demagnetization to achieve low-remnant fields. This is accomplished by toroidally winding a number of turns around the shield. A current at power-line frequency, which is sufficient to saturate the shield, is passed through the coil and then slowly reduced to zero.

The discussion above merely gives an overview of the complexity of magnetic shielding design, fabrication and use. The reader may seek detailed information in the references listed earlier.

For practical applications, such as, e.g., magnetoencephalography (MEG) or paleomagnetometry, mu-metal shielded rooms are usually used [106]. The typical attenuation of such rooms is shown in Figure 7.7(a) curve (2). Even though their low-frequency attenuation is relatively modest, the attenuation below 1 Hz is in a range of less than 100 to about 1000. Low-frequency attenuation in excess of 10^4 can be achieved with multilayer mu-metal rooms and examples are shown in Figure 7.7(a), curves (3) and (4) [106, 111–113]. The overall field attenuation of the shielded room can be enhanced by active shielding, as discussed in Section 7.7.3 and shown by curve (5) [117]. High attenuation can also be provided by the use of a superconducting shield. An example is the whole-body high-T_c superconducting shield [119], which provides a low-frequency shielding factor of nearly 10^8 (see curve (6)).

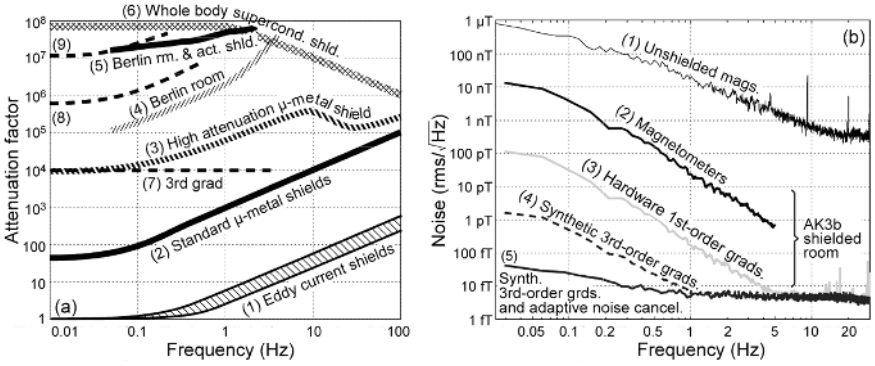

Fig. 7.7 Noise attenuation methods. (a) Noise attenuation by shielded rooms. (1) Eddy-current shields [104, 105]. (2) Modestly shielded mu-metal rooms with low-frequency attenuation of < 100, e.g., [106, 111–113]. (3, 4) High shielding ratio mu-metal rooms with low-frequency attenuation > 10^4 [114–116]. (5) High attenuation mu-metal room with active shielding [117]. (6) Whole-body high-T_C superconducting shield with low-frequency attenuation of nearly 10^8 [119]. (7) Typical attenuation by third-order synthetic gradiometers [120]. (8) Combined attenuation of modestly shielded mu-metal rooms as in (2) and third-order synthetic gradiometers as in (7) [121]. (9) Combined attenuation of modestly shielded mu-metal rooms, third-order synthetic gradiometers, and adaptive noise cancellation, see part (b). (b) Noise cancellation, MEG site in Toronto, AK3b-shielded room [106], channel MLF43, 151 channel MEG system [122]. Primary sensors are radial gradiometers with 5 cm baseline, frequency spectra were averaged over 20 trials. (1) Unshielded magnetometers. (2) Shielded magnetometers, the different noise slope is due to the presence of a thick Al layer in the shielded room wall. (3) Hardware first-order gradiometer. (4) Synthetic third-order gradiometer. (5) Synthetic third-order gradiometer and adaptive noise cancellation.

7.3.1.6 Filtering in an Unshielded Urban Environment

Mains power is a source of strong noise at the fundamental and harmonic frequencies. When a very effective magnetic shield is not available, noise from power lines is best removed by filtering.

The noise levels due to mains power at 50/60 Hz and computer monitor frequencies ("lines") at about 67 to 75 Hz, are usually much higher than the intrinsic-noise levels of the sensors and are best removed by the use of electronic filters. Figure 7.8 shows an idealized filter response for the various filter classes in use. There are many references [123–126] that provide assistance in the design of filters. SQUID systems are often used for measurements in the low-frequency range, where they show a significant advantage over other magnetic field sensors. In this case, the use of a high-order low-pass filter with a cut-off frequency of about 30 Hz can minimize the influence of power-line interference [124]. It is also possible to use specially designed comb filters described in [127]. These filters combine several notch filters to block out a particular noise source of a certain frequency and its harmonics. This is particularly useful for the removal of power-line noise especially if the SQUID system is being used in a broadband application. However, the use of notch filters may significantly distort the signal spectrum, by also removing useful signals at filtered out frequencies.

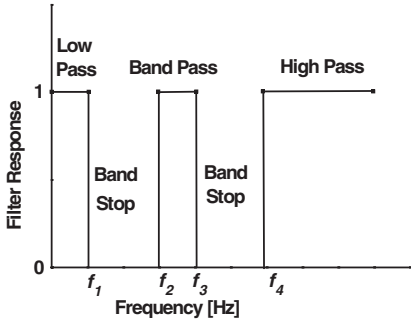

Fig. 7.8 Idealized filter responses

7.3.1.7 Determination of Low-frequency Shielding, Filtering or Noise Cancellation Requirements

In order to design sufficient low-frequency shielding and filtering, it is necessary to measure the background field level at the point of application with no magnetic shielding present and then to determine the system sensitivity required for the intended application. Measurement of background electromagnetic fields for frequencies less than 1000 Hz can be simply achieved by using a fluxgate magnetometer with a spectrum analyzer and measuring a noise spectrum over a wide frequency range. For example, Figure 7.9 shows noise spectra obtained with a well rf-shielded SQUID and a flux gate. The spectra (i) and (ii) correspond to magnetically unshielded measurements undertaken in a factory, and the spectrum (iii) indicates the noise measured in a double mu-metal shield. The 50 Hz mains power and its

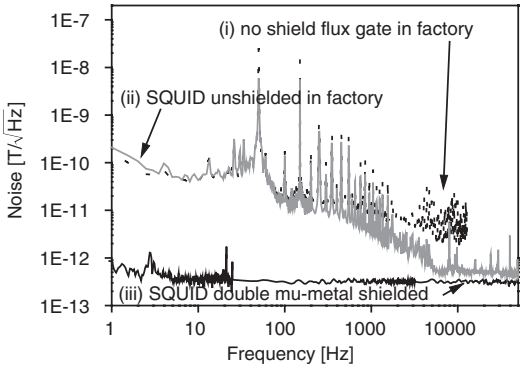

Fig. 7.9 An example of noise spectra taken in a factory using (i) a flux gate and (ii) an rf-shielded SQUID both magnetically unshielded and (iii) the same SQUID with two layers of mu-metal shielding.

harmonics cause peaks in the unshielded spectrum. The ratio of the unshielded environmental noise to the desirable resolution required, gives the shielding effectiveness needed. In this example, if the sensitivity required for a specific application were 400 fT $Hz^{-1/2}$ at 1 Hz, then to reduce the noise level at 1 Hz to 200 pT $Hz^{-1/2}$, a shielding effectiveness of 500 is required. This is achievable by the use of a three-layer mu-metal shield, which would have a shielding factor of about 1000 at 1 Hz. Another method of achieving lower noise is the use of noise cancellation techniques.

Noise reduction by various noise-cancellation techniques can provide an alternative to, or a significant enhancement of the magnetically shielded performance. An example of such a method is a synthetic higher-order gradiometer, discussed in Section 7.7.4.2. Depending on the spatial characteristics of the noise, the synthetic third-order gradiometer can provide noise attenuation of several times 10^3 to more than 10^4 (the 10^4 level is shown in Figure 7.7(a), curve (7)) [120]. Such attenuation also works within shielded rooms and is added to that of the shielded rooms [121]. The combined attenuation of a third-order gradiometer and a modestly shielded room is shown in Figure 7.7(a), curve (8). At low frequencies, where the residual noise is larger than the SQUID noise, an additional, adaptive noise cancellation (discussed in Section 7.7.4.1) can increase the attenuation by a factor of 10 or more, Figure 7.7(a) curve (9). The combined attenuation using modestly shielded rooms and the synthetic methods, is illustrated in greater detail in Figure 7.7(b), for a specific measurement site. At low frequencies, the shielded room attenuates the unshielded magnetic field by a factor of about 50. The primary hardware first-order gradiometers, provide an additional attenuation of about 100, and the synthetic third-order gradiometers increase the attenuation by another factor of nearly 100. Below about 0.1 Hz, an additional attenuation of about 30 is achieved by adaptive-noise minimization. Thus at low frequencies, the combined noise attenuation of the modestly shielded rooms and the synthetic methods, is greater than 10^7 and is compar-

able to that of expensive high-attenuation rooms with active shielding (compare curves (5) and (9) in Figure 7.7(a)).

7.3.2 Electronics and Cables

7.3.2.1 RF Screening of Electronics

Chapter 4 gives information on SQUID electronics. This section considers some of the issues necessary to transfer the electronics from an ideal laboratory environment to a non-ideal environment while still meeting the specifications for a specific application.

The electronics require adequate rf shielding to prevent their stray fields from contributing to the noise of the SQUID sensor. As discussed in Section 7.3.1, in order to obtain shielding effectiveness for electric fields, one should use a good conductor such as copper or aluminum of sufficient thickness. Any mechanically rigid metal box will usually provide effective shielding. However, in some applications, where it is necessary to have the SQUID and the electronics close to each other, there is a need to optimize the shielding of the electronics (i.e., the amount of metal present in the electronics housing required to achieve sufficient shielding effectiveness) while minimizing the amount of metal present to prevent eddy-current noise contributions, as discussed above.

Optimized construction of the electronic housings (casings) and cables should follow the general guidelines below:

- Use materials of high conductivity (see Table 7.3).
- Choose a suitable wall thickness in order that the EMI frequency is shielded out: the higher the frequency, the thinner it can be for a given material (see Table 7.4).
- At high frequencies ($f > 1$ MHz), non-ferrous materials such as copper and aluminum will be sufficient for both electric and magnetic fields.
- Holes, gaps and apertures in the shield must be kept as small as possible. A general rule is that the largest dimension of the hole is more critical than its area. The maximum permissible length is $\lambda/10$ where λ is the EMI wavelength.
- Avoid gaps between panels.
- A large number of small round holes is better than one long hole.

To achieve the desired shielding effectiveness, all the seams and joints in the housings of the dewar and the electronics, need to be welded or sealed with overlapping joints providing intimate contact between mating surfaces [128]. Screened cables that penetrate a case should be terminated "shield-to-shield" in a peripheral bond at the point of entry or around the barrel of the plug or connector by soldering around the full 360°. If a "pigtail" connection is used, then the current is no longer confined within the cable and a common-mode component (discussed in detail below) will flow along the outer surface of the shield from where it can be conducted to other susceptible points in the system or produce radiated energy causing deleter-

ious effects on the system performance. Soldering the shield peripherally around the complete circumference of the cable may result in a reduction of the common-mode current by as much as 65 dB. Multiple shielding of cables may be necessary in application areas where high-rf fields are present. In some cases, it may be necessary to construct cables with extra sleeves of shielding, such as double silver-coated copper-braided sheaths, to obtain the desired shielding effectiveness. It is not uncommon to see SQUID systems with extra layers of aluminum foil (Alfoil) crimped onto the cables to enhance rf shielding during the development phases, or a system testing where system drift or failure to lock is apparent. If this is necessary, the eventual use of multiple-shielded cables, as described below, is recommended.

7.3.2.2 **Cables and Conductors**

A major source of EMI is radiation from the cable or conductor network. There are two modes of current flow along the conductor: the common mode and the differential mode. Differential-mode conduction is the usual conduction mechanism. Here, the functional currents flow within any electrical circuit and are of equal amplitude but in the opposite direction. If the distance between these conductors is small, the radiation is negligible. This can be easily achieved by twisted pairs, for example. Common-mode conditions exist when currents of equal amplitudes flow in a multiwired system in the same direction in all of the conductors. The return path is provided by nearby conducting objects. The dimensionless ratio of the differential-mode to common-mode currents can be estimated by:

$$I_d/I_c = cl/2\pi fA \tag{7.17}$$

where c is the speed of light (ms^{-1}), l the length of the conductor carrying the common-mode current (m), A is the area of the small loop carrying the differential-mode current (m^2) and f is the frequency (Hz). For example, if l is 1 m and A is 1000 mm^2, then at 30 MHz, I_d is about 1500 times greater than I_c, while at 1000 MHz, the ratio is about 50, suggesting that the common mode will have a greater effect.

The source of common-mode current is frequently a voltage drop within the ground system. If a long, thin conduction wire is used to provide a connection to ground, the voltage drop will be greater than if a conductor with a large cross-section were used. Ground planes are needed for high-frequency applications. As a general rule, the more copper used, the better the ground. However, compromise is necessary to avoid excessive eddy currents causing a "self-field" noise source. More details on grounding are given in Section 7.3.2.3.

The following suggestions can minimize the radiation from cables:

For common-mode:

- Use the shortest possible length of cable within or between the various system components.
- To the maximum possible extent, eliminate independent-ground connections and minimize the common-mode spurious voltage-to-ground connections.

- Use common-mode filters, such as ferrite rings, on all cables but do not position them so that they create a magnetic noise source for the SQUID.
- Screen the cable while keeping the area of the resulting loop as small as possible.

For differential-modes:

- Minimize the area of all current-carrying loops, particularly high-frequency signals.
- Operate the system at the lowest possible frequency.
- Reduce the current amplitudes as much as possible.
- Screen the cable, while keeping the loop as small as possible.

7.3.2.3 Cable Junctions, Terminations, Connectors and Grounding

As a general rule, there are two types of basic conductor configurations: the balanced, parallel or twin-wire cable and the co-axial or shielded cable. The twin-wire cable is a balanced and symmetric system, where equal and opposite (differential) currents flow. The co-axial cable is unsymmetrical because of the dissimilar conductor geometries. If these two cables are interconnected, then the symmetrical current flow on the twin cables is converted into two modes along a co-axial cable. One flows conventionally within the cable and returns via the inner surface of the outer conductor or screen. The second mode causes current to flow along the outer surface of the cable screen and to return via the surrounding conductors or the earth. Because of this, the mating of balanced with unbalanced conductors, will introduce significant EMI and must therefore be avoided.

The choice of connectors involves balancing the need to provide user friendliness with suitability for a specific application. In all cases, the connector material needs to be checked. Many connectors are made of gold or chrome-coated nickel, which is ferromagnetic and can contribute to system noise due to “self-field” effects. Bayonet and military style connectors are useful for rugged applications in the field, such as for geophysical exploration and defense applications. BNC and SMA connectors are suitable for laboratory or stationary applications but are not suitable for setups where frequent connecting and disconnecting may be anticipated, as they can be fragile.

A ground is an equipotential point to which all other potentials in the system are referenced. In practice, grounds are rarely at the same potential and care must be taken to ensure that unwanted coupling of various signals does not take place since the ground system includes a “loop”. The ground system should provide the low impedance route for a signal to its return path.

Effective grounding can reduce noise pickup very significantly while inadequate grounding can exacerbate interference. The ground system must be designed and not left as an afterthought. Safety grounding is also necessary to prevent shock hazards.

There are three grounding techniques: floating, single-point and multiple-point. Floating points should be avoided as static charges can build up and may cause

SQUID failure when discharged. Static discharges can also create increased noise. Bleeder resistors are recommended when an application requires a floating earth. A single-point earth is preferred for low frequencies (below 1 MHz). When all the earth leads are connected to a common point, no interference will be produced, if sufficiently large cross-sections of conductors are used. However, at frequencies above 1 MHz, prevention of capacitive coupling is necessary to avoid interference, and multi-point grounds may be required. Such grounds are made by the most direct route to the nearest low-impedance ground. The wire length must be kept to a minimum to reduce self-inductance and high-frequency resistance. Multi-point grounding can lead to ground loops which are a common cause of malfunctioning electronics. Cable-shield grounding must also be designed to take into account the frequency range in use [128].

7.3.2.4 **Crosstalk**

Performance degradation due to the interference between the various system components is a serious issue in the design of multi-component magnetometers and gradiometers. In this discussion, crosstalk is defined as the interaction between devices where any signal current flowing in one device induces error currents in other devices. Crosstalk is a consequence of various contributions:

Self-field Effects. The interference between SQUIDs and adjacent low-temperature electronic components in the probe is referred to as "self-field" effects, which can be mitigated by the appropriate use of shielding and an increased distance between interacting components in order to provide satisfactory isolation.

Electronic Component Interactions. Crosstalk can also be introduced into the SQUID system via the electronics by poorly mounted connectors which can cause capacitive coupling between the leads which are carrying different signals. The choice of electronic components and their position is important in the control of crosstalk. For example, a circuit containing an inductor can interact with nearby circuits, due to mutual inductance. Shielding and separating such components is essential [129]. Inductive crosstalk occurs when poorly designed circuits create a mutual inductance between neighboring wires whether on a circuit board or in a poorly designed connector. A general discussion of crosstalk is given in ref [129].

Crosstalk in Multichannel SQUID Magnetometers. Crosstalk is caused by the mutual inductances between individual sensing coils, where the sensing current of one coil induces an error current in a nearby coil. For example, estimation of the crosstalk signals can be obtained by considering two second-order gradiometers (diameter 20 mm, baseline 40 mm) placed parallel to one another with a distance of 41 mm between the gradiometer axes. Here, the crosstalk between the sensing coils is 5 % [130]. When these coils are part of a multi-channel system, the crosstalk is even larger. For example, in a hexagonal configuration, a coil can have six neighbors resulting in a crosstalk of about 30 % [130].

Crosstalk Mitigation for Arrays. Crosstalk can be minimized be separating the pickup coil structures, but this is often impractical, especially in multi-channel systems. Another option is to apply "external" feedback directly to each input circuit rather than to the SQUID, such that the flux transformers carry zero current and thus do not interact [130]. Since the inductive crosstalk is directly proportional to the current in the coupled inductors, nulling of the flux transformer current will eliminate the crosstalk. It should be emphasized that this procedure is applicable only to analogue SQUID electronics and is not effective in systems with digital electronics, where different methods must be used.

Crosstalk Mitigation for Orthogonal SQUIDs. In systems with orthogonal SQUIDs, the feedback operates in order to keep the currents flowing in the SQUID constant and hence the SQUID itself will not be a source of indirect crosstalk. However, the feedback also produces a fringing field, which can couple to orthogonally oriented SQUIDs. This form of coupling is linear and will give rise to direct crosstalk between channels. Ideally devices need to be located at null points of the fields of orthogonal feedback coils as the coupling, which is causing the direct crosstalk between channels, is geometry and frequency dependent. The positioning of orthogonal components requires trial and error to find the null positions, or crosstalk removal by means of signal processing.

The orthogonality–crosstalk error correction, along with gradiometer and magnetometer calibration, is all necessary in order to make an accurate analysis of measurements possible. If crosstalk is present between the components, the error will add linearly to the true response. Crosstalk can be measured by using a set of three calibrated orthogonal calibration coils, which are accurately orthogonal and also accurately oriented with respect to the SQUID system. For example, to achieve an error correction to an accuracy of 1 %, the orientation of the calibration coils would need to be aligned to better than $\sin^{-1}(0.01) = 0.06°$. Moreover, the required accuracy of the field orientation needs to be sustained over the entire volume occupied by the sensors, and all components which may contribute to crosstalk. Typical systems would have an orthogonality accuracy of 1 % with a crosstalk of less than 3 % in each channel, when measured in a calibrated Helmholtz coil. More details of calibration methods are given in Section 7.5.

7.3.2.5 Power Consumption and Supply

A range of power consumption levels for various SQUID electronics, is currently available commercially. For laboratory or static use, mains power is available and power consumption is not an issue unless power-line harmonics cause excessive noise and filtering is not sufficient to obtain the desired signal-to-noise ratio. Battery-operated systems are necessary for remote and mobile applications. When operation is by battery, power consumption is then an important parameter. Choosing the correct type of battery requires consideration of the space and weight that is allowable, and also the rating of the battery to ensure that it holds enough charge to provide operation without the need for a recharge over the required measurement period. Information needed for choice of battery is current rating, tolerable weight,

Tab. 7.6 A list of various rechargeable batteries and their characteristics.

Type of battery	Typical battery voltage (V)	Typical ampere-hour rating (A · hour)	Typical life (years)	Volts per cell	Advantages	Disadvantages
Lead acid	6–12 (sealed)	5–12	1–4	2.14 initial; 2.1 to 1.46 under discharge	Cheap Can be obtained as a gel-cell	Deteriorates quickly under neglect Cells not uniform unless carefully maintained
Nickel-cadium	6–12 (sealed)	To 15+	15+	1.34 initial; 1.3 to 0.75 under discharge	Holds charge for years Withstands vibration	2–3 times as expensive as lead acid More cells required for same load as lead acid Charger characteristics are critical on sealed cells.
Silver-Zinc	6–12	3–8+	1–2	1.86; 1.55 to 1.1	Very high energy per unit volume	May cost 10 times that of lead acid Heavy
Silver-cad-mium	6–12	3–8+	2–3	1.34; 1.3 to 0.8	High energy per unit volume. Withstands frequent cycling	Very expensive and limited life-time

voltage (and hence the number of cells required), the relative costs of the batteries, their operating time and their performance at different temperatures, if they are to be used in external locations. For example, lead-acid gel-cell batteries are heavy, but offer good lifetimes, are easily recharged and are relatively cheap. However, gel-cell battery capacity is severely compromised in low-temperature environments. The rating of the battery at different environmental temperatures should be noted from the battery specification sheets or measured in environmental chambers when extreme variations of temperature are to be experienced. Table 7.6 gives the battery characteristics for a range of rechargeable batteries. It is also important to verify that the electronics powered by the batteries are able to cope with the voltage fall-off during operation as the battery charge drops. Otherwise, one needs to provide appropriate compensating electronics. Sufficient shielding and filtering, as outlined in Sections 7.3.1.4 and 7.3.1.5, must be implemented if AC-DC converters or other switched-mode power supplies are used, because of the generation of high-frequency noise.

7.3.2.6 Choice of SQUIDs and Electronics

As outlined in previous chapters, alternative choices of dc versus rf SQUID and analog versus digital electronics, can be made. When designing a SQUID system, it is necessary to determine what the specification requires. For example, the enormous dynamic range offered by digital electronics (192 dB with 32 bit converters) is needed for unshielded stationary or mobile magnetometers and unshielded mobile gradiometers (Tables 7.11 and 7.13). In the opposite extreme of a well shielded environment with a background-noise level as shown in Figure 7.13(a), such a large dynamic range is not necessary because the signal plus noise has only a small dynamic range of about 26 dB (about 4.3 bits). Generally, diverse magnetometry applications span the whole range between the two indicated extremes.

7.4 Data Acquisition and Rudimentary Signal Processing

7.4.1 Introduction

For the vast majority of SQUID systems, a computer interface is required so that the sensor's signals may be processed by algorithms, then stored and presented. This section overviews some guidelines for designing data-acquisition systems for analog-output SQUID systems. (Digital-SQUID systems are usually directly interfaced to computers). We assume that the most common situation is where the SQUID's output is a voltage proportional to the feedback current in the flux-locked loop, although the same data acquisition principles are applicable to other situations. Several manufacturers of SQUID systems offer good data acquisition products, but many researchers prefer to configure their own, tailored to their specific systems.

7.4.2 Hardware Considerations

Analog-to-Digital Converters, ADCs, are required to make the computer interface. The hardware required may vary, but the most flexible approach is to use an ordinary personal computer with plug-in data acquisition cards. It is important to ensure that there are suitable software drivers for the cards that work well with the computer's operating system and the programming language of choice. Some companies offer acquisition hardware and software programming environments that are guaranteed to work properly together. Irrespective of the hardware choice, due consideration must be given to the key issues of dynamic range, sampling frequency and analog signal conditioning.

7.4.3 Dynamic Range, Accuracy and Linearity

ADCs have a finite dynamic range. The output resolution of a single sample is one least significant bit, LSB, and the digital-output range is 2^n where n is the number of bits that the ADC can convert. It is usual to match the voltage output range of the SQUID electronics to the input range of the ADC.

One key requirement for matching a SQUID channel to an ADC is that the voltage noise on the SQUID output must exceed the resolution of the ADC, usually several LSBs in magnitude. If this is not met, then the ADC rather than the SQUID, will dominate the system's overall noise performance. A second key requirement is that the ADC's input voltage range must exceed the maximum expected signal size, otherwise, information will be lost where the ADC saturates. The practical example below illustrates a selection process for an ADC with suitable resolution.

Example. A SQUID has a flux noise of 10 $\mu\Phi_{0\ \mathrm{rms}}/\sqrt{\mathrm{Hz}}$, a FLL bandwidth of 10 kHz and a range in flux, up to a maximum of +/– 4 Φ_0. (The FLL is not of the automatic reset variety described in Section 4.2) The feedback electronics has selectable FLL feedback resistors, but a voltage range limited to +/–10 V. To make best use of the voltage range, an ADC with a +/–10 V input range, should be selected. The FLL feedback resistor is chosen to provide 10 V for 4 Φ_0 at the SQUID, i.e., 2.5 V/Φ_0. This satisfies the range requirement, so now the resolution requirement can be calculated. The voltage noise on the FLL output is $2.5\ \mathrm{V}/\Phi_0 \times 10\ \mu\Phi_{0\,\mathrm{rms}}/\sqrt{\mathrm{Hz}}$ i.e., $25\ \mu\mathrm{V_{rms}}/\sqrt{\mathrm{Hz}}$, and this is equivalent to 2.5 $\mathrm{mV_{rms}}$ over the full bandwidth. The voltage noise is equated to, say, 10 LSBs, to be on the safe side, so the required LSB is equivalent to 250 μV at the input. The ADC resolution, calculated from the formula 2^n = Voltage range/LSB equivalent voltage, i.e. 20V/250 μV, is $n = 16.3$. For this example, a 16-bit ADC would be just sufficient while an 18-bit ADC would provide a better safety margin. If the bandwidth of the SQUID output is subsequently likely to be reduced, then the resolution limit may be reached, so it is best to base the calculation upon the lowest bandwidth that is likely to be used in practice.

It is also important to be aware that most ADCs have self-noise at the one to two LSBs for 20 bits or less and more noise for higher-resolution ones. For example, many 24-bit ADCs have a useable resolution of only 21 or 22 bits because of their self-noise. Where the ADC's self-noise exceeds one or two LSBs and the noise has a gaussian distribution, then extra voltage resolution may be obtained by over-sampling the data and decimating. For example, sampling four times faster and averaging the results over four samples increases the resolution $\sqrt{4}$ times.

ADCs can vary considerably in their linearity and in the accuracy with which they can reproduce a digital representation of an analog signal. Where a SQUID is being used for simple measurements with a low signal-to-noise ratio, the accuracy and linearity requirements are modest and most modern ADCs are more than good enough. For systems that use software algorithms to cancel high levels of noise using reference SQUIDs, poor accuracy and linearity can compromise system performance so these factors should be considered at the selection stage.

7.4.4 Sampling Rate and Signal Conditioning

The maximum frequency that an ADC can resolve is one-half of its sampling rate. It is therefore easy to calculate the minimum sampling rate required for a system of given bandwidth. As a general principle, it is good to sample at the maximum rate that the ADCs can manage (providing the software can handle it) and use the largest SQUID bandwidth that can be accommodated. In this way the maximum information is captured from the SQUID. It is important to avoid conditions under which aliasing occurs, i.e., when noise that is above the maximum resolvable frequency is reflected down into the bandwidth of interest and adds to the noise there. This is usually avoided with "anti-aliasing" low-pass filters between the SQUID outputs and ADCs that cut off the signals below the maximum-resolvable frequency, so the aliased noise makes no significant contribution. If the FLL electronics has a lower cut-off frequency than the ADCs, then filters are not needed.

It is important to be cautious with low-pass filters on SQUID outputs – particularly in multi-channel systems. The problem is that the filters induce phase shifts in the signals at frequencies well below the cut-off (pole) frequency. The phase shift is proportional to the frequency well below the pole, which is equivalent to a constant time delay on the signal. In many multi-channel SQUID systems, the accurate time alignment of signals from channel to channel is crucial for effective noise cancellation, so different delays on each channel are not acceptable. A high degree of matching of the filters is thus required to keep the delays equal. If the use of analog filters is unavoidable, then implementing the highest practical pole frequency, and careful matching of high-stability resistors and capacitors in the filters, will help.

Many ADCs inject noise onto the wires joining them to the SQUID electronics. This is mostly in the form of spikes originating from the digital electronics behind the ADCs that are picked up on the wires and carried towards the SQUIDs. If this is a problem, then RF filters should be placed in the lines to prevent the spikes from passing. Otherwise these could easily knock SQUIDs 'off lock'. If the physical dis-

tance between the SQUID outputs and the ADCs is long or there is a strong likelihood of interference pickup on the wires, then it is better to use balanced differential pairs to convey the signals. Many ADCs have differential inputs so it is straightforward to generate a balanced pair of signals using an accurate buffer and an inverter (there are also good analog ICs available especially for this purpose, such as Analog Devices SSM2142, a balanced line driver, and the SSM2141, a complementary receiver). In this case the cables used should be a shielded twisted pair of wires to connect to the differential ADCs. High-quality commercial microphone cable is excellent for this as it well shielded and has no microphonic pickup, which can be a problem with some cables. For multi-channel systems, cables with several individually shielded twisted pairs within an overall shield could be used.

7.4.5
Digital Signal Conditioning and Storage

When the signals from the SQUID channels have entered the digital domain, they should each be SQUID-noise limited in range, accurately time-aligned from channel to channel, and preferably have a higher bandwidth than is required for subsequent processing. The extra bandwidth is useful because it can then be reduced using decimation and digital filters that are perfectly matched channel to channel. The system should also be checked to ensure that the data is continuous, with no time gaps. This is particularly important for "event driven" software used, for example, in many graphical programming environments.

Many researchers prefer to stream data to a hard disk before undertaking any digital processing. This ensures that it is preserved and can be re-processed in other ways if, for example, a bug is subsequently found. For large numbers of channels or slow computers, the streaming to disk may not be quick enough for the raw data so this function is performed after filtering. The signals from the multiple channels may then be passed to the subsequent signal-processing stages. If quality ADCs were selected with high linearity and very low bit error rates, then the signals can be passed to the processing algorithms with practically the same integrity as the analog outputs from the SQUID's electronics.

7.5
Characterization, Calibration and Testing

7.5.1
Introduction

The previous sections of this chapter and Chapters 4, 5 and 6 have provided information on how to construct a SQUID-based system with appropriate cryogenics, SQUIDs, electronics, cables, connectors, shielding, filters, and data acquisition suitable for the intended application and specification. This section will consider the measurements that are necessary in order to characterize and calibrate the system.

Various measurements are recommended to test both the individual SQUID sensor and the whole system in a low-noise environment, such as in a laboratory with an rf and low-frequency shielded-measurement set-up, to check that the system is operating as ideally as possible and in the manner desired. Issues related to the operation of the system under the conditions imposed by the environment of an application, will be discussed in Sections 7.6–7.8.

7.5.2 Characterizing SQUIDs

7.5.2.1 Introduction

The standard measurements necessary to characterize the performance of a SQUID are: optimized-transfer coefficient, noise floor over a range of frequencies, bandwidth, slew rate, dynamic range and SQUID effective area. The following methods assume an rf or dc SQUID with electronics optimized for maximum transfer function as outlined in Chapters 4 to 6. These initial measurements should be undertaken in a two or three-layer mu-metal shield, achieving a magnetic-field attenuation of at least 500 in the required frequency band. The suggested test equipment required for characterization of a SQUID is given in Table 7.7. SQUID manufacturers usually provide some information on the device characterization in their manuals and websites and these are recommended reading.

Tab. 7.7 Test equipment required for characterization of a SQUID system.

Equipment	Comments
SQUID system	Assuming SQUID, dewar, cryogen, electronics, cables, flux-locked loop setup.
Mu-metal shield	Double or triple layer
Magnetic field calibration coil	For example, 2 mT/A with high (10 kΩ) or low (330 Ω) input resistance
Signal generator	Sine and triangular waveform with symmetry adjustment
Oscilloscope	Analog, dual channel, 50–200 MHz bandwidth
Spectrum analyzer	
Appropriate cables and connectors	Well shielded, non-magnetic connections

7.5.2.2 Transfer Coefficient

The performance of a SQUID is usually first evaluated by determining the transfer coefficient, $\partial V/\partial \Phi_a$ for the dc SQUID or $\partial V_T/\partial \Phi_a$ for the rf SQUID, in volts per flux quantum. This can be achieved by displaying the SQUID voltage against the applied flux on an oscilloscope (FLL off), measuring the peak-to-peak voltage and dividing by $\Phi_0/2$. The displayed waveform is ideally sinusoidal for dc SQUIDs and nearly triangular (with possible noise rounding) for rf SQUIDs. For dc SQUIDs, a peak-to-peak measurement is only indicative as the maximum value of $\partial V/\partial \Phi_a$ is $\pi/2$ times

larger if the function is a true sinusoid. If it is not sinusoidal, then the maximum slope should be measured directly from the oscilloscope trace. This is particularly important where the characteristic is distorted, e.g., when a direct readout scheme with additional positive feedback is used.

Typical dc SQUIDs should have $\partial V/\partial \Phi_a \cong 10\text{–}100\,\mu V/\Phi_0$ while the transfer coefficient of rf SQUIDs depends greatly on the frequency and mode of operation, as discussed in Chapters 1, 2 and 6. Under most circumstances, the SQUID biasing is adjusted to maximize $\partial V/\partial \Phi_a$, so it is useful to record the biasing conditions as well. These are important measurements because they provide an easy benchmark to monitor long-term changes in a device (e.g., in HTS SQUIDs where I_0 may change slowly due to oxygen migration within the junctions). In addition, $\partial V/\partial \Phi_a$ may be depressed under operational conditions due to rf interference, so knowledge of the transfer function and its optimized biasing under shielded conditions (both high and low-frequency shielding) can be used to indicate how the environment is effecting the SQUID in later measurements.

If a wire-wound gradiometer is connected to a SQUID, it is crucial that the flux-transformer circuit is superconducting (or else a high-pass transfer results). After cool-down, this can simply be tested by generating a change in the environmental dc field (e.g., by moving a chair in the vicinity of the system). The SQUID output should respond by changing along with the environmental field change, but after that it should remain at a constant level. A small resistance in the flux transformer circuit will give a slow decay.

7.5.2.3 Effective Area of a Magnetometer

The effective area, $A_{eff,}$ is an indication of the efficiency of the SQUID at capturing magnetic flux, and is sometimes referred to as the responsivity. The effective area is defined as $A_{eff} = \Phi_s/\Delta B$, where Φ_s is the magnetic flux produced in the SQUID by a change in the externally applied magnetic field, ΔB (in the direction of highest SQUID sensitivity). The higher the value of A_{eff}, the more flux that is coupled to the SQUID for a given external field and thus the higher the field sensitivity of the device. A_{eff} depends only on the geometry of the superconducting structures and is independent of the junction properties in the limit when the junction inductance is negligible compared with that of the SQUID. For thin-film structures, A_{eff} should therefore never change and one initial measurement will be sufficient. For structures where the geometry may change over time, as in the case of flip-chip devices, it is prudent to measure it periodically. One may determine A_{eff} by placing the SQUID at the midpoint of the axis of a calibrated Helmholtz pair, or solenoid with its plane parallel to the coils, and then counting the number of flux quanta induced by a given change in field. The procedure for setting up and using calibrated coils to make this measurement is described in detail in Section 7.5.4.

7.5.2.4 Effective Volume of a Gradiometer

For first-order gradiometers, the effective volume (responsivity), R_g, is defined by $R_g = \Phi_s/\Delta G$ and relates an externally-applied change in gradient ΔG to the flux coupled to the SQUID, Φ_s. (For higher-order gradiometers, the responsivity has

units of length^{2+n} where n is the order of the gradiometer.) It is also important to measure A_{eff} for a first-order gradiometer because, unless the coils are perfectly balanced, there will also be a response to the magnetic field, thus:

$$\Phi_s = R_g \Delta G + A_{\text{eff}} \Delta B. \tag{7.18}$$

This also extends to higher-order gradiometers. One may use $(A_{\text{eff}}\, b)/R_g$ as a measure of imbalance where b is the baseline of the gradiometer. Practical details on measuring responsivity and calibrating gradiometers are given in Section 7.5.4.

7.5.2.5 SQUID Noise and Bandwidth Measurements

The spectral voltage noise power density at the output of the FLL, S_V, should be measured while the SQUID is operating within a well-shielded environment, in order to determine the intrinsic noise of the SQUID and its associated electronics. From this, the spectral-power density of the flux noise in FLL mode, S_Φ, can be calculated from:

$$S_\Phi(f) = S_V(f) \,/\, V_{\Phi,\text{FLL}}^2 \; [\Phi_0{}^2/\text{Hz}] \tag{7.19}$$

where $V_{\Phi,\text{FLL}} = \partial V_{\text{out}}/\partial \Phi_a$ is the ratio of the FLL output to the flux applied to the SQUID set within the FLL. In the white noise region, carefully designed dc and rf SQUIDs have values for S_Φ in the region of about $10^{-12}\ \Phi_0{}^2\,\text{Hz}^{-1}$, for LTS devices. An alternative figure of merit is the noise energy per unit bandwidth:

$$\varepsilon(f) = S_\Phi(f)/(2L)\ [\text{Joules/Hz}]. \tag{7.20}$$

This parameter takes into account the SQUID inductance and gives a better basis for comparing SQUIDs of different geometries.

The SQUID noise may be measured with a spectrum analyser or a Fast-Fourier Transform (FFT) algorithm included in the system's data-acquisition software. For noise measurements in the absence of signals, a Hanning window function should be used prior to the FFT. The least significant bit (LSB) of the analyser or data acquisition system should be significantly lower than the level of SQUID noise (if this is not the case, digital-quantization steps will appear in the FFT trace.) The $1/f$ noise-corner frequency and the white noise at 1 kHz can be determined from recorded noise spectra. FFT spectra can be averaged to reduce the noise on the traces. The bandwidth can be determined from the FFT spectrum as the frequency where the white noise has dropped to half its amplitude, or alternatively the frequency of a small applied field may be increased until its measured amplitude has halved. This assumes that the bandwidth starts at dc, which is not always the case.

There is generally a trade-off between wide bandwidth and low noise. As the bandwidth is increased, due to increased gain, the white noise will also increase. The bandwidth can usually be adjusted by trimming the gain of the SQUID preamplifier. When undertaking noise measurements, it is sensible to adjust the gain to optimize for the best white noise and bandwidth required for the intended application.

7.5.2.6 Dynamic Range

The task of the experimenter is to measure magnetic fields with a specified resolution. Invariably, the detection system is exposed not only to the desired signal, but also to environmental magnetic noise, which may be many orders of magnitude larger than the signal of interest. The SQUID and its associated electronics must be designed to handle all applied magnetic fields (signal and noise) and still provide the resolution appropriate for the specific measurement task.

The ratio between the total applied signal and the noise amplitude, determined to the desired resolution, is called the dynamic range of the applied fields. If the required electronics resolution is ∂B and the peak magnitude of the applied quantity (field, gradient, etc.) is ΔB, then the dynamic range may be defined as a peak-to-peak amplitude divided by the resolution [132], or

$$D = \frac{2\Delta B}{\partial B} \tag{7.21}$$

The dynamic range can be expressed either as a ratio, in decibels (dB), or by the number of bits. The dynamic range is discussed in detail in Section 7.8.2.

It is clear that the applied dynamic range is often much larger than the dynamic range of the signal of interest. For example, for MEG, the magnetic fields (signal) from the brain may have peak-to-peak amplitudes of about 300 fT. We may want to resolve this signal with an accuracy of 0.5 fT, which corresponds to a signal dynamic range of only $D = 600 = 56\,\text{dB} = 9.2$ bits. However, even within shielded rooms, the environmental-noise amplitude can be as large as 40 nT, resulting in a much larger total dynamic range for magnetometers of $D_{\text{total}} = 4 \times 10^7 = 158\,\text{dB} = 26.3$ bits [132]. In contrast, rock magnetometers operate within superconducting shields where the environmental noise is negligible and the total dynamic range is small and roughly corresponds to that of the signal (85 dB or 8 bits).

Therefore, the SQUID and its associated electronics must be designed to handle the dynamic range which is relevant to the measurement problem, and this can range from negligible up to about 31 bits [132].

7.5.2.7 Slew Rate

The slew rate describes the rate of change of the applied field. The maximum slew rate of a sinusoidal signal with amplitude ΔB is:

$$\dot{B} = \omega \Delta B \tag{7.22}$$

where $\omega = 2\pi f$ is the signal frequency. The applied-field slew rate, $\dot{B}$ (T/s), and its conversion to flux slew rate, $\dot{\Phi}$ (Φ_o/s), are discussed in a detail in Section 7.8.2.

The slew rates within shielded rooms are small, typically $< 10\,\Phi_o$/s, while the slew rates for sensitive magnetometers in unshielded environments can be in excess of $10^6\,\Phi_o$/s [132]. The SQUID and its electronics must be designed to handle the slew rates which are expected to occur during the measurement.

The slew rate of a SQUID system can be measured by applying a known time-variable field or gradient and determining the slew rate as the point at which the flux-lock loop ceases to follow the applied signal. This requires that the SQUID be placed within a calibration coil, which has a known triangular signal of a few kHz, and the SQUID output monitored. The slew rate is determined from the maximum peak-to-peak applied field at which the SQUID FLL is able to remain in lock. Using this value, B_{max}, the flux slew rate can be evaluated as:

$$\dot{\Phi}_f \equiv \left| \partial \Phi_f / \partial t \right|_{max} = 2 f B_{max} \, [\mathrm{T}/\mu\mathrm{s}] \tag{7.23}$$

where f is the frequency of the triangular applied field.

7.5.2.8 Nonlinearity

Low-T_c SQUID magnetometers are among the most linear devices available in metrology. Small nonlinearities are caused by various system imperfections such as weak links in contacts, dependence of the transfer function on the applied fields, large deflections along the sinusoidal SQUID transfer function (see Section 4.2.1), penetration-depth dependence on the applied field, and also by nonlinearity of the electronics components in the SQUID circuitry (e.g., resistors). Successful noise cancellation and signal processing requires the nonlinearities to be sufficiently small [132]. The maximum allowed nonlinearity is inversely proportional to the dynamic range and is discussed in detail in Section 7.8.2. The nonlinearity of low-T_c systems has been discussed in references [133] to [137], including the use of modified feedback circuit to improve the linearity.

The nonlinearity requirements, which stem from the need to cancel high levels of environmental noise, can be relaxed by configuring the SQUID flux transformer to detect smaller levels of environmental noise. For example, in some unshielded applications, the use of a magnetometer flux transformer would require the nonlinearity to be less than –185 dB, while the same application using the first-order gradiometer flux transformer, would relax the nonlinearity requirement by about –150 to –160 dB [132]. Nonlinearity in some commercial MEG systems was measured to be $<10^{-6}$ with signal amplitudes of 1000 Φ_0 [132].

The nonlinearity can be measured either by harmonic distortion or by the intermodulation product. During the measurement of harmonic distortion, a pure sinusoidal signal is applied to a SQUID magnetometer. The presence of nonlinearities will result in harmonic generation. The total harmonic power can be measured by a spectrum analyser. The ratio of power in the generated harmonics to the power of the fundamental frequency is then related to the degree of nonlinearity. Good quality and appropriately filtered oscillators can produce sine waves with harmonics which are at least 130 dB below the fundamental.

Alternatively, if two harmonically unrelated signals are applied and the inter-modulation product measured, this can also determine the nonlinearity. The intermodulation method is less demanding on the oscillator purity than is the harmonic distortion method.

The generation of even harmonics depends crucially on the amplitude of the flux modulation. The modulation should be adjusted for minimum nonlinearity and the measurements should be performed at different constant flux biases and different open loop gains. These measurements are best made with zero magnetic field cooling. The performance can also be affected by the open-loop gain. To obtain the highest possible linearity at the highest possible frequency, it is desirable to use a SQUID with low flux noise so that the operation is possible in a FLL with the highest bandwidth, without causing loss of lock. The sensitivity of the nonlinearity to the flux modulation reflects the fact that V_Φ is linear only over a relatively narrow range of flux. Once it moves out of this range, the level of distortion grows rapidly with signal amplitude. Rf SQUIDs have a high level of linearity, and the harmonic generation is likely to be relatively independent of the level of flux modulation. However, the flux noise is usually higher than for dc SQUIDs and so rf SQUIDs must be operated with a lower-gain bandwidth to prevent the feedback loop from losing lock. High-frequency nonlinearity is not an intrinsic property of the SQUID, but rather of the electronics package. There are schemes that have been devised to reduce this nonlinearity [137].

7.5.3 Characterization in Various Magnetic Field Situations

7.5.3.1 Introduction

Section 5.5.1 has provided some details of SQUID performance in magnetic fields. However, the specific type of magnetic field history and the setup in which a SQUID is measured can affect the SQUID performance and behavior. Below is a list of different magnetic field setups that can be used. This is followed by a discussion of how these setups should be used:

- Zero-field cooled (ZFC) where the SQUID is cooled in a high-performance magnetic shield.
- Field-cooled (FC) where the SQUID is cooled in the presence of a dc magnetic field.
- Field-applied (FA) where the SQUID is ZFC and a dc magnetic field is subsequently switched on.
- Field-removed (FR) where the SQUID is stable with no creep apparent in an applied dc magnetic field, which is then turned off.
- Ac fields which were covered in Section 7.3.1.4.

Understanding the SQUID behavior in these different situations can assist in the selection of the best measurement protocols for a particular application. Indeed, in most applications, SQUIDs and gradiometers are operated in constant or varying magnetic fields, which might be much stronger than the measured signal.

For the characterization of the effects of magnetic fields on a system's performance, the SQUID should be operated in a FLL. Noise spectra should be measured as the FLL output using, e.g., a spectrum analyser, and the measurement value converted to flux in the SQUID or pickup circuit.

7.5.3.2 Field-applied (FA) Characterization

FA measurements will give direct performance data for a SQUID operating in a low magnetic field. Low-frequency excess noise arises from movement of the flux trapped during any exposure. For these measurements, it is necessary that the applied field itself should not contain significant low-frequency noise. For example, a solenoid energized using a current derived from a stable voltage reference can provide such a field. In general, the magnetic field magnitudes employed in these types of experiments should be increased step-wise until well in excess of the dynamic range of the FLL. Thus, the application of a field after ZFC, or a change of the field without a thermal cycle, causes the FLL to lose lock and the SQUID will be exposed to, essentially, the full change of the applied field. Where necessary, the FLL should be reset to the locked state giving a near-zero FLL output before noise measurements are made.

7.5.3.3 Field-removed (FR) Characterization

FR measurements rely on the fact that the SQUID retains a remnant magnetization for a period following exposure to a magnetic field. In measurements of this type, there is no requirement that the applied field itself should have low noise; hence, a simple current supply may be used. The upper limit of the applied field for FR measurements is greater than for FA measurements since the remnant field near the junction is less than the applied field. However, FR measurements are only an indirect indication of the performance of a SQUID under practical conditions, since the amount of flux present in the device and the forces to which the flux is subjected, are different from the FA case.

Both FA and FR measurements can be made under either field-cooled (FC) or zero-field cooled (ZCF) conditions. In order to determine the field dependence of the excess noise, measurements can be made for a sequence of different fields as given in references [138–140]. FR measurements are easier to perform than FA measurements because of the simpler instrumentation used and the absence of potential errors due to the effects of the applied field. FR measurements are preferable to FA measurements for routine noise characterization of the SQUIDs and can be used to determine the FR noise-corner frequency, f_c, as a convenient measure of the relative performance of the SQUID in a magnetic field.

FR noise exhibits a similar frequency and field dependence but has a lower magnitude than FA noise for a given applied field. FR noise decays with time following removal of the applied field, as shown, for example, in Figure 7.10(a). The form of the decay cannot be fitted by a single simple curve of exponential, logarithmic or power-law form, but a logarithmic function is often a reasonable fit for times earlier than a certain value, as in this case (30 minutes in Figure 7.10(a)).

For later times, the rate of decrease of noise slows markedly, and indeed, within the limits of measurement uncertainty, the noise reaches a stable "plateau" at which decay effectively ceases. For weaker fields, the plateau is reached at earlier times than for stronger fields, and is achieved within about 15 minutes for fields below $100\,\mu$T. Note that the plateau is well above the white noise floor of the device and that the noise studied in these experiments is at all times excess noise.

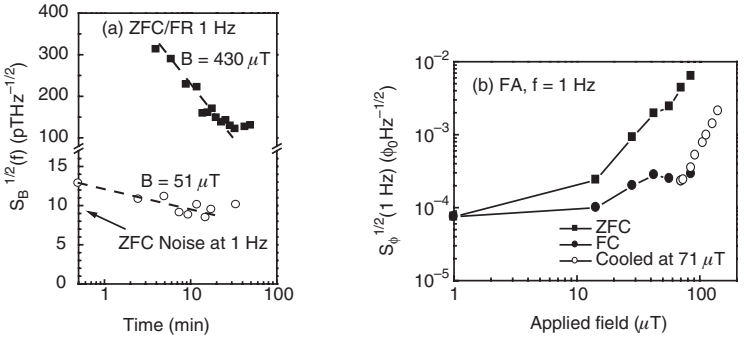

Fig. 7.10 (a) ZFC FR measurements of noise at 1 Hz as a function of time after removal of an applied field of 430 μT and 51 μT. The field was applied for a period of 3 minutes in each case. The dashed lines indicate logarithmic fits to part of the data. (b) FA noise at 1 Hz for a 2 mm rf SQUID for three different cooling modes [138].

An example of FA excess noise data for a 2 mm washer SQUID, which has been both field cooled (FC) and zero-field cooled (ZFC), is shown in Figure 7.10(b). The FC noise magnitudes are less than the ZFC noise magnitudes, typically by an order of magnitude at 1 Hz and $B = 50\,\mu$T (the Earth's field). The field-dependence exponent is also lower for a FC SQUID, which is less than 0.5 in all cases. Miklich et al. [139], in their FC/FA studies, observed exponent values of about 0.5 at 1 Hz.

After field cooling, although flux is trapped in the SQUID body, the SQUID is in magnetic equilibrium with its environment. The extremes of field concentration which occur at the device edges, and which lead to high rates of flux creep and high levels of noise in the ZFC case, are avoided in the FC case. As a practical implication, a SQUID magnetometer, operating in the earth's field, exhibits substantially lower excess noise if FC than if it is ZFC. However, it is important that, if FC, no subsequent variation in the applied field should occur to perturb the SQUID's magnetic equilibrium, a potentially quite restrictive requirement in many situations. A field variation large enough to cause a substantial increase in noise, compared with the FC case, could readily arise, for example, from reorientation of the magnetometer with respect to the direction of the Earth's field. The ability to "degauss" the SQUID by local heating to remove flux and then either field cooling or the use of active Earth field compensation, discussed in Sections 7.7.2 and 7.7.3, can overcome this. A scheme to "demagnetize" SQUIDs in order to reduce the $1/f$ noise generated by thermally activated hopping of vortices, either by removing the vortices from the SQUID body or by moving the flux to pinning sites with high pinning energy, has been described in [141]. The $1/f$ noise and, in some cases, the white noise of a SQUID can increase by two orders of magnitude due to rapid transients caused by nearby equipment being turned off and on, or by rapid changes in the applied static magnetic fields. The flux noise can be reduced by generating a high-frequency magnetic field by passing an rf current through a wire-wound coil close to the SQUID. Frequencies of the order of several hundred MHz and a maximum power of 10 mW at the generator output, are required. The rf amplitude is slowly increased to 10 mW

and then slowly decreased again over about a 15 second period. The rf generator is then disconnected. This should return the SQUID to its original noise value.

7.5.3.4 Hysteresis

Magnetic hysteresis in a SQUID system is observable as a shift of the voltage-flux characteristic along the flux axis after the magnetic field is cycled. This effect is undesirable if the absolute value of the magnetic field or measurement of the gradients in highly fluctuating background fields is required. Magnetic hysteresis is observed in both LTS and HTS SQUIDs and is related to vortex entry and pinning near the edges of thin films [140, 142]. The degree of hysteresis is expressed by the hysteresis parameter:

$$\eta = \delta\Phi/\Delta\Phi \tag{7.24}$$

where $\delta\Phi$ is the flux error caused by sweeping the applied flux between $\pm\Delta\Phi$. For LTS SQUIDs, η can be 10^{-9}–10^{-11} [142]. HTS SQUIDs show high levels of non linear hysteresis with $\eta < 10^{-6}$ for $\Delta\Phi \leq \Phi_0$. Sun et al. [143] have made systematic studies of hysteresis in LTS and HTS dc SQUIDs by cycling fields ranging from $10\,\mu$T to 1 mT peak-to-peak. In each case, they found both time independent and time dependent hysteresis. Time independent hysteresis appeared above a threshold field of a few hundred μT. This was also found for a time independent critical current density of thin films suggesting a relationship between hysteresis and flux pinning. Reduction of hysteresis by providing high pinning forces within the superconducting material and at the edges can be achieved during the device fabrication process by:

- high-film critical current density,
- reduced edge damage during device fabrication and
- steep film edges, defining the SQUID device.

7.5.4 Calibration

7.5.4.1 Setting up Calibration Fields

When using a SQUID system in a quantitative measurement, it is extremely important to calibrate the system properly. Calibration is the method used to relate the output of a magnetometer or gradiometer to the value of the external field or gradient of a known reference system. To achieve a calibration accuracy of less than one percent is non-trivial. An example of an analytical model for the calibration of a magnetometer using the relative motion of the sensor in a constant magnetic field is given in [144]. This technique parameterizes the sensor motion in terms of the elementary rotations about one axis, with the number of rotations giving the number of degrees of freedom. The general method used to establish the flux/voltage calibration factor of the SQUID system consists of measuring a known magnetic flux and then comparing the known and experimental values. The two most reliable methods for one-channel magnetometer calibration are [145]:

- A sufficiently large calibration coil is placed around a cryogenic dewar containing the SQUID system and the position of the dewar is adjusted in the coil until a maximum output voltage from the SQUID is obtained. From the geometry of the calibration coil and the magnetometer, the mutual inductance can then be calculated [146]. The product of the mutual inductance and the current in the calibration coil is the magnetic flux applied to the gradiometer. The field that corresponds to the SQUID output voltage is obtained by dividing this flux by the magnetometer area.
- A small calibration coil (about 5 mm diameter) is axially placed at about 20 cm from the magnetometer, to approximate a magnetic dipole. When the flux in the magnetometer is calculated and divided by the SQUID area, the field that corresponds to the output voltage is obtained.

Both methods can give an accuracy of about 10 %. However, if more than one sensor is to be used or if better accuracy is required, different calibration errors will correspond to different errors in different positions. Note that the calibration factor is usually quoted as field/voltage by dividing the sensor net flux by the effective area of the sensor. This is an approximation as it assumes: 1) a uniform field over the pickup loop of the sensor and; 2) that no other magnetic field is coupled in. In some applications, accurate calibration is of the utmost importance. For example, in multichannel biomagnetic measurements (such as when determining the location in the brain of the focal point causing epilepsy), a relative inaccuracy of a few percent can lead to errors of several millimetres in the location of the source [147]. However, the calibration of all channels relative to one another is crucial here, rather than the absolute calibration.

The calibration should be set up under heavily shielded conditions to avoid inaccuracies due to noise or interactions with the earth's field. Ideally, a calibration would be conducted in a magnetically shielded room or a compensated coil system as described in [148]. In the literature, various methods have been developed to calibrate a system and they are given in [149] and [150]. In most simple applications where the SQUID system and cryogenic housing are not too large, the use of a double or triple mu-metal shield, a well made coil (powered by a low-noise current supply) and accurate positioning of the sensor, will be sufficient. However, if the shields are in close proximity to the coils, distortion of the generated field may lead to errors. Another issue relating to shielding is that it is not always possible to make the field coil sufficiently large or distant from the SQUID to obtain high uniformity of the field or gradient over the volume of the sensor. (The applied signal should be highly uniform for the "order" of the sensor, e.g., for a magnetometer it should be a uniform field with no higher order terms, for a first-order gradiometer it should be a uniform gradient with no second-order terms, etc.) When it is not possible to achieve this, a calibration may still be conducted by explicitly calculating the average applied field over each input coil or loop in the flux transformer, which can be done provided that the precise geometries of the field coil and superconducting structure are known.

Multichannel systems requiring complex and large cryogenic housings such as are used in tensor gradiometry and magnetoencephalography, are more likely to require access to a high-quality magnetically shielded room or compensated Helmholtz or Rubens coils discussed in [151–153].

Calibration procedures for planar, axial and second-order gradiometers are given in reference [154]. The methods are briefly outlined below:

Planar Gradiometer. Calibration of a planar SQUID gradiometer can be achieved with the use of a spatial Fourier technique and a theoretical spatial transfer function, which is dependent on the planar gradiometer design (this procedure is valid for all planar gradiometers designs). The calibration process requires that the gradiometer is scanned over a known input-field source and the output-voltage values measured. The measured transfer function is the result of the division of the Fourier transform of the output signal by the Fourier transform of the input signal. The gradiometer spatial transfer function $G(k)$ can be expressed as:

$$G(k_s) = \sum_{i=0}^{n-1} A_i e^{-jk_s ib} \tag{7.25}$$

where n is the number of gradiometer coils, A_i is the area of the coil i, k_s is the spatial frequency and b is the gradiometer sampling period or baseline. The calibration factor is obtained by fitting the measured transfer function by the theoretical one. This calibration method provides an uncertainty of about 0.2 %. Further details are given in reference [154(c)].

First-order Axial Gradiometer. First-order axial gradiometers can be calibrated by the use of a numerical optimization technique [154(b)]. The procedure uses a dc current carrying wire of infinite length whose magnetic field spatial distribution is determined analytically as shown in Figure 7.11(a). Ampere's law gives the vertical component of the magnetic field, B_z, generated by a wire of infinite length, coincid-

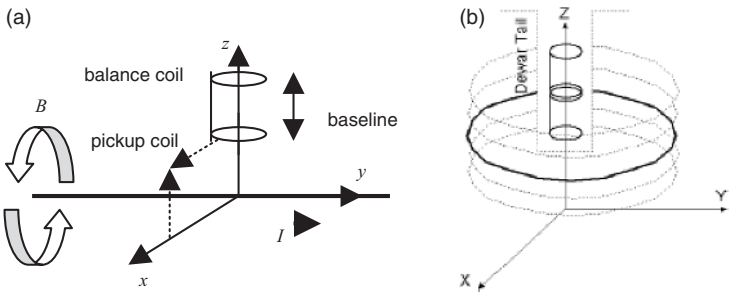

Fig. 7.11 Schematic drawing of (a) the geometry for a magnetic field calculation showing an infinite wire and first-order axial gradiometer [154(c)] and (b) large coil calibration for a second-order gradiometer [154(a)].

ing with the y-axis. In the x direction, at a distance z above the wire carrying the current I, the field is:

$$B_z(x) = \frac{\mu_0}{2\pi} I\left[\frac{x}{x^2+z^2}\right] . \tag{7.26}$$

(7.26), valid when the gradiometer axis is exactly parallel to the z-axis of the coordinate system, can be used with a numerical algorithm to integrate the magnetic field over the coil area and compute the flux over each gradiometer coil. After summing each flux, taking into account the winding directions of the coils, it is possible to obtain the simulated net flux. This technique requires an accurate knowledge of the position of the device in the dewar. However, normalizing the simulated flux and the experimental voltage values can overcome this. By using a least-squares optimization to determine the distance from the lower pickup coil to the x–y plane and determining the best match to the normalization curves, the signals can be normalized and the calibration factor, C, can be calculated through a second least-squares optimization, in order to minimize the error function, ζ, which is given by:

$$\zeta = V_{out} \cdot C \cdot A_{eff} - \Phi_{theo} \tag{7.27}$$

where V_{out} is the output SQUID voltage and Φ_{theo} is the theoretical gradiometer net flux.

The axial SQUID gradiometer output is monitored for various positions along the wire and at different heights above the wire.

Second-order Gradiometer Using a Large Coil. A large current carrying single-turn coil surrounding the dewar, which is concentric with the gradiometer axis, can be used to calibrate a second-order gradiometer. Measurements are taken at various positions along the z axis, as shown in Figure 7.11(b). In this case, the Biot–Savart Law expresses the magnetic field as:

$$B_z(x=0, y=0, z) = \frac{\mu_0 I R^2}{2\left(R^2+z^2\right)^{\frac{3}{2}}} \tag{7.28}$$

where R is the radius of the current-carrying coil and it is assumed that the center coordinates coincide with the geometrical center of the large coil. The diameter of that coil should be about 20 times the diameter of the gradiometer coils, to create a uniform field over the gradiometer. This will enable a calibration with an error of about 0.1 % in the flux calculation, which is negligible. There is no requirement to determine the vertical position of the sensor inside the dewar, using the optimization method which is needed for an infinite-wire calibration. Rather, the center of the gradiometer, and hence the z-coordinate of the center of the gradiometer in the coil, is determined as the position where the experimental signal reaches its maximum absolute value. There are various techniques for integrating the z-component of the magnetic field over the area of the gradiometer coils. A comparison of differ-

ent integration techniques is given by Ornelas et al. [154], who compare trapezoidal, adaptive recursive, Simpson's rule, seven-point Gaussian quadrature and convolution techniques. Determination of which integration technique should be used will depend on the error of the technique and the execution time.

Calibration accuracy is affected by noise and gradiometer imbalance. The gradiometer imbalance is an indication of the unwanted sensitivity of the gradiometer to homogeneous magnetic fields and gradients lower than the order of the gradiometer. For small-coil techniques discussed in [154(a)], as the sensor is moved away from the coil, discrepancies in the calibration "best-estimate" increase, because the theoretical model does not take into account the imbalance effect. This can be minimized by extrapolation to zero in a distance-calibration graph. Removal of the imbalance effect for the large-coil calibration technique requires the use of spatial Fourier techniques described in detail in [145].

7.5.4.2 Magnetometer and Gradiometer Calibration

For a magnetometer, calibration consists of measuring the flux response of the SQUID to an external field, A_{eff} (i.e. $\partial \Phi_s/\partial B_a$), and the response of the FLL output to a flux applied to the SQUID, $V_{\Phi,\ \text{FLL}}$ (i.e. $\partial V_{\text{out}}/\partial \Phi_s$). The product of these relates the voltage output of the SQUID electronics to the field applied to the SQUID. A_{eff} is measured by displaying the periodic voltage against flux (FLL off) on an oscilloscope, then increasing the calibration field until a precise-integer number of quanta has passed and noting that field change. More quanta give better precision on the field-per-quantum, i.e., $1/A_{\text{eff}}$.

$V_{\Phi,\text{FLL}}$ is measured with the FLL on, by applying a known flux to the SQUID and measuring the change in the output signal. This can be achieved by applying a triangular wave signal to the SQUID with the FLL off, and adjusting the amplitude to sweep an integer number of flux quanta. The FLL is then switched on and the same sweep signal restored. The voltage deflection divided by the number of quanta swept is $V_{\Phi,\text{FLL}}$. It is best to use most of the output range of the FLL to maximize the precision. Gradiometers may be calibrated using exactly the same method, the only experimental difference being the geometry of the calibrated signal coils used to determine the responsivity, R_g (i.e., $\partial \Phi_s/\partial \Delta G$).

7.5.5 Testing and Practical Tips

7.5.5.1 Drifts and Offsets

Drifts and offsets may be measured by observing the outputs over a long period. There is a very wide range of possible causes and remedies for them but we touch briefly upon just a few in Table 7.8.

7.5.5.2 SQUID or Flux Jumps

SQUID or flux jumps can easily be observed by viewing the SQUID output. There are two types of jump, one is where the FLL temporarily loses, and then regains, lock at another quantum level. This usually occurs in systems with poor signal-to-

Tab. 7.8 Factors that lead to drift

Effect	Test	Remedial action
Thermoelectric effects in the SQUID electronics. Usually originates in connectors.	Correlate SQUID output with thermometer at the electronics	Avoid connectors between SQUIDs and pre-amplifiers if possible. Insulate or pot connectors in thermally conductive epoxy.
Flux creep in the SQUID or flux transformer.	If the drift is large and continuous.	Thermally cycle the SQUID above T_c and re-cool.
Poor cryogenic temperature stability.	Very accurate temperature measurement. If not possible, check for air pressure changes or low cryogen levels.	Very difficult to achieve retrospectively. Requires better cryogenic design.
External effects, e.g., magnetic relaxation in an abused mu-metal shield or drift in compensation coils.	Drift characteristics are common to all SQUID channels.	De-gauss and re-anneal (if excessively abused) mu-metal. Improve compensation coil driver electronics.
Drift in application use but no drift in laboratory test	Re-test in laboratory to confirm this is an effect caused by operation in the other environment.	Use Al foil on crimped cables and around cryostat to increase rf shielding in the application use. Check for the position of other electronic gear and move as far away from SQUID as possible.

noise ratio or where there is inadequate shielding from external interference. This jumping is caused by the slew rate of the FLL being temporarily exceeded. The other type of flux jump is manifested as a very low-frequency telegraph noise. This is characterized by being smaller in amplitude than one quantum and originates from either a trapped fluxon hopping between two positions within the SQUID or flux transformer's structure, or a critical-current fluctuation in a Josephson junction. In the case of dc SQUIDs, the latter would usually be compensated for by using a bias reversal scheme as described in Chapter 4, while jumps caused by I_0 fluctuation should not occur in rf SQUIDs operated with modulation (see Section 6.4). The trapped fluxon should be removed by thermal cycling to above T_c and back. Improved shielding will help eliminate flux jumps due to any of these causes.

Koch [155] has modelled the theoretical bandwidth and slew rate of a dc SQUID feedback system. When noise appears as a signal applied to a SQUID in a feedback loop, the performance of the SQUID can be downgraded. Flux jumps can then occur. The feedback error flux is defined as the difference between the input signal flux applied to the SQUID and the feedback flux. Nominally, in a feedback circuit the error flux is zero. However, the noise due to the feedback circuit and the finite gain of the feedback loop can mean that this error flux is non-zero. When the size of the error flux exceeds a one-half flux quantum, the SQUID feedback circuit will

usually experience a flux jump or phase-slip one period along the periodic flux-to-voltage characteristic of the SQUID response curve. If the bandwidth or slew rate is increased, more error flux, and therefore more noise, will be fed back to the SQUID. This will cause the tendency for the feedback loop to jump lock.

7.5.5.3 Excess Noise

If a SQUID operates with noise that is excessively above the anticipated levels measured in heavily shielded conditions, it is important to find out the reason for this. For a high level of white noise, excess noise is usually due to the suppression of the V_Φ transfer coefficient caused by external interference or by trapped flux in a junction, which cause changes in I_0 so that the SQUID is no longer optimized or symmetrical, for d.c. SQUIDs. Excess low-frequency noise may be telegraph noise due to trapped flux moving in the device. If this noise is evident at a very low frequency, then flux hopping will be seen directly at the output and a large $1/f$ noise will be observed in the FFT spectrum. If the flux hopping is too rapid to resolve in the time domain, the FFT spectrum will take on a characteristic Lorentzian form. There are several ways of dealing with excess noise:

- Use an imbedded heater on the SQUID chip to heat-cycle the SQUID past T_c and then re-cool to expel trapped flux.
- Improve the rf shielding as outlined in Sections 7.3.1.4 and 7.3.2.1.
- Check that a high-T_c device has good YBCO film J_c, which provides good flux trapping.
- Check for unnecessary metal and other magnetic materials near the SQUID that will cause a self-field effect.
- Check that the SQUID has enough coolant and is at the required temperature.

7.5.5.4 Electronic Noise from Other Systems

If the SQUID system uses motors, both the motor and the drive amplifiers can generate substantial electromagnetic noise. Significant attention to shielding and elimination of ground loops is then necessary. The use of pneumatic motors can reduce this problem. If noise is coming from the motor control electronics, a metal chassis and routing of the motor cables through braided shields will help, also locating the stage and motors away from the SQUID system can be effective (see Section 7.3.2.1). The remaining high-frequency contributions may need to be removed by low-pass filtering of the output prior to data acquisition.

7.5.5.5 Adequate Shielding of the Cryostat

The cryogenic design of each system is different. In some cases, it is possible to have the rf shielding integral with the cryostat by using, for example, sticky aluminum foil as a layered coating on the outside of the dewar or by using super-insulation on the inside of the dewar. The FLL electronics and the control electronics must be placed in copper or aluminum boxes and may be connected by copper pipes, through which cables are fed. These boxes must be constructed using the principles

given in Section 7.3.2. The entire rf shielding must be grounded via a low resistive path to the main ground, with the electrical cables between the FFL and the SQUID threaded through toroidal filter cores.

7.5.5.6 Consequences of Cryogen Boil-off

In cryogen-cooled systems, there is the potential problem that microphonic noise, due to the bubbles from the liquid boil-off bumping the SQUID, might cause "micro" vibrations. This is an often forgotten source of noise. The use of cotton or glass wool in the dewar has been found to be highly effective at muffling the bubbles by providing a bigger surface area so that bubble size is insignificant. Use of cotton or glass wool does not cause an increase in the cryogen boil-off. Microphonic noise from bubbles can be effectively eliminated by the positioning of the SQUID so it is mechanically isolated from the bubbles. For example, mounting an HTS SQUID with the YBCO surface oriented towards the face of the SQUID holder, can eliminate the microphonic vibrations caused by bubbles knocking the surface.

7.5.5.7 Mechanical Vibration

Mechanical vibration can be caused by a cryocooler, the cantilever vibration of the SQUID on a probe or as a consequence of the SQUID being in motion, such as in airborne applications. Section 7.2.5.5 gives various options for suppression of cryocooler vibrations. When the system is operated in motion, vibrations can be damped by a suitable mechanical suspension system, the use of a gradiometer rather than a magnetometer and also by the use of digital finite-impulse response filters. Using these techniques can reduce the motion noise to below the sensor noise.

Motion noise is dominant below 25 Hz, as determined from the noise spectrum of the SQUID magnetometer in motion. An example of the noise spectrum of a system, which is stationary, and then in motion with both poor suspension and good suspension, is shown in Figure 7.12. Ideally the SQUID sensor should be mounted in a system so that it is immune from the motion-induced noise at all frequencies. There is one example of a suspension system that decreased the noise level to the SQUID noise floor at around 30–35 Hz [138]. This suspension system was developed for airborne magnetometery. It uses fluid damping with a two-stage spring mounting.

Specially designed filters can be used for noise reduction, such as a digital tapered stacking filter [127]. These comb filters are related to the *B*-spline filters which are used in wavelet transforms and have little effect on the spatial resolution of the system.

The vibration due the motion of a cantilevered probe can be removed by fixing the SQUID to the base of the dewar [138].

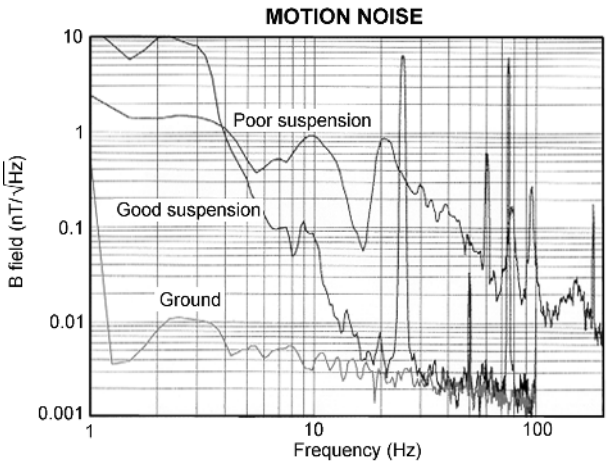

Fig. 7.12 Noise spectrum of a magnetometer with no motion (on the ground), in motion with a poor suspension system and in motion with a good suspension system.

7.5.5.8 Increase in Noise of the System Compared to a SQUID

Ideally, the SQUID sensor should limit the sensitivity of the whole system. If the system noise is higher than the SQUID noise, it is necessary to analyse the noise spectrum, step-by-step to identify the noise sources and then to undertake appropriate actions to eliminate the various sources of noise using the methods listed above. This can be a very long process but can make the difference in whether or not the system succeeds in its application.

7.6 Conditions Imposed on SQUID Systems by the Environment and Applications

7.6.1 Introduction

SQUID magnetometer or gradiometer outputs consist of two parts: (i) random instrumental noise generated within the SQUID sensors and their electronics; and (ii) SQUID-sensor response to external signals. This section will be mostly concerned with detection of external magnetic signals applied to a properly functioning SQUID magnetometer or to gradiometer systems through their flux transformers. Examples from SQUID magnetoencephalography will often be used to illustrate the concepts discussed.

In most situations, the external magnetic signals are a combination of the required signals and environmental noise. The distinction between the signal and the noise is possible only if the context of the measurement is known. What may be noise in one experiment may become signal in another. For example, the variation

in the magnetic field of the human heart will represent noise when the brain is studied, but will be a signal to a researcher who is investigating the heart; similarly, the geophysical magnetic field variations represent noise during various low-frequency measurements, while they may represent signal to a geophysicist. Thus the terms "signal" and "noise" will often be used interchangeably and their meaning will vary depending on what is being discussed. In this section we shall review typical features of the signal and the noise. These features will be used in the subsequent sections for discussion of the noise reduction methods and for determination of the SQUID system design parameters which are necessary for successful noise elimination.

SQUID systems are operated either in a stationary position or are moved during the measurement. Stationary instruments are usually employed in urban environments in the presence of high man-made magnetic noise (environmental fields and gradients). Such noise is caused by various moving objects (cars, trains and trolleys, elevators, people), power-line related sources (power-line frequencies and harmonics, rotating machinery, current fluctuations), or other sources such as computers, monitors, digital switching, etc. In addition, the static instruments are also operated in large-dc environmental fields and gradients, and small vibrations of the SQUID system will also contribute noise. The mobile systems are typically operated far from the man-made noise. However, mobile instruments are subjected to a large motion in the Earth's magnetic field and environmental gradients, which in turn impose different operational requirements. The hand-held SQUID detectors which are operated in the large gradients of urban environments represent an extreme limit of mobile instrumentation and will be briefly commented on in Section 7.7.4.3.

7.6.2
Signals Acting on SQUID Systems

A detailed description of various applications and the corresponding signal strengths are presented in the second volume of this Handbook. In this section, only the magnitudes of the observed signals will be indicated. The SQUID detector parameters are usually a compromise between the desire for the best resolution and the reality of the noisy environment. The consideration of only the signal magnitudes is not sufficient for designing SQUID systems, the environmental-noise parameters, discussed in Section 7.6.3, must also be included. In the absence of environmental noise, an arbitrarily small, spatially uniform magnetic signal could always be detected by making the flux transformer coils sufficiently large [156]. However, the presence of a large-magnitude environmental noise may make an excessively sensitive magnetometer impossible to operate.

The smallest magnetic field magnitudes, which need to be measured in stationary applications are of the order of 5–60 fT (e.g., [157–165, 174]). To obtain a meaningful measurement, the SQUID-system resolution in the required bandwidth must be better than the measured signal. In many situations, such a condition implies white noise levels of no more than several fT rms/$\sqrt{\text{Hz}}$. The resolution can often be improved by averaging if the signal is repetitive, relative to a trigger or a stimulus.

Mobile applications typically require gradient resolutions of the order of 10–1000 fT/m rms/√Hz. Since in these applications, the gradiometer baselines are of the order of 10 cm, this represents field resolutions of about 1–100 fT rms/√Hz, similar to what is needed for stationary applications.

The smallest measured signals determine the required SQUID-sensor resolution. The largest encountered field or gradient magnitudes affect other parameters, such as the dynamic range, the slew rate, and the required linearity. In most situations the latter are due to environmental noise and are the determining factors to be considered when designing the SQUID system. There are a few exceptions, e.g., susceptometers or rock magnetometers [158–161], where the sensors are operated within superconducting shields. In these instruments the measured signals dominate and can be as large as 0.1–1 μT. However, no complex signal processing is usually required (since these measurements employ only a few channels), there are no special linearity requirements, and the dynamic range can be handled by analog ranging or digital flux counting (see the second volume of this Handbook).

7.6.3 Noise Acting on a SQUID System

7.6.3.1 Environmental Noise in Stationary Applications

SQUID systems are subjected to dc fields regardless of whether they are shielded or unshielded. The dc fields will introduce noise only in the presence of small motions or vibrations (note that the vibration-induced SQUID outputs will be noise only if we are not interested in vibrations; they will be signal if we want to measure them). The dc fields are due to the earth's magnetic field and to various stationary magnetic objects. The environmental dc fields and gradients are summarized in Table 7.9; the fields and first gradients were measured, while the higher gradients were extrapolated.

Tab. 7.9 Typical dc fields and gradients at various locations. (a) In Vacuumschmelze shielded room AK3 [106], with dc field attenuation of about 1000 (modest shielding). (b) The range represents the gradient increase during the period from 1982 to 2000 [118]. (c) This value can be as large as several 100 000 nT directly above ore deposits. (d) For a dipole source, $G = 3B/r$ [169]. If $B = 50\,000$ nT, $r = 6300$ km, then $G = 2.4 \times 10^{-2}$ nT/m. (e) Extrapolated, assuming a distance from the gradient generating dipole object of $r \approx 10$ m, $G^{(2)} \approx 4G/r$, and $G^{(3)} \approx 20G/r^2$, where G, $G^{(2)}$, and $G^{(3)}$ denote the first, second and third gradients, respectively [169]. The shielding is assumed to preserve the spatial character of the fields. (f) Extrapolated by the same equations as in (e), but $r = 200$ m. (g) Extrapolated by the same equations as in (e), but $r = 6300$ km.

Parameter	Unshielded			Modest shielded urban [a]
	Urban	Rural	Earth dipole only	
field (nT)	55 000	55 000 [c]	55 000	50
First grad. (nT/m)	200 to 3000 [b]	1 to 20	2.4×10^{-2} [d]	10 to 30
Second grad (nT/m^2)	80 to 1200 [e]	0.02 to 0.4 [f]	1.5×10^{-8} [g]	4 to 12 [e]
Third grad (nT/m^3)	40 to 600 [e]	$(5 \text{ to } 100) \times 10^{-4}$ [f]	1.2×10^{-14} [g]	2 to 6 [e]

In addition to the static-field components, the earth's magnetic field is also subject to diurnal variations. The magnitude of these variations is typically 20–40 nT/day, but during magnetic storms it can be as large as about 10 % of the earth's magnetic field magnitude.

Unshielded SQUID magnetometers are also exposed to periodic fields from power lines and electrical machinery. These ac fields are especially large in urban environments, where the magnitude of the first harmonic can be as much as 500 nT. The power-line interference exists even in rural environments. Close to the ground, the magnetic fields due to the ground currents (caused by electric power system and electric trains) can dominate direct field from wires.

Gradients of the power line fields, G, can be estimated by assuming infinitely long single or parallel wires. Then $G = nB/r$, where $n = 1$ for a single wire, $n = 2$ for a parallel wire and r is the distance from the magnetometer to the power line (parallel wires carry currents in opposing directions). If $B = 500$ nT, $r = 5$ m, then $G \approx 200$ nT/m for parallel wires. Higher gradients can be computed similarly [169]. Modestly shielded rooms provide an attenuation of about 10^4–10^5 at power-line frequencies [106] and the expected magnitude of the power-line fields within shielded rooms is up to about 5–50 pT. In addition, the magnetic disturbances can be generated at frequencies related to the subharmonics of the power line frequencies, the power transmission line resonances, computer monitor frequencies, etc.

Depending on the shielding levels, the SQUID instruments may also be exposed to non-periodic man-made noise, which has mostly low-frequency character. The ranges of the observed noise can be as large as 10^4 and are shown as a function of the frequency by gray patches in Figure 7.13. For unshielded magnetometers in Figure 7.13(c), the patch covers the range of noise magnitudes reported in the literature [116, 165–168] and for shielded magnetometers and all gradiometers, the patches correspond to observations made with MEG systems at laboratories around the world [169, 177]. Specific examples of the noise spectra in various environments are shown by black lines in Figure 7.13. For gradiometers, the noise was multiplied by the baseline and is also expressed in units of field. The field noise magnitudes in rural environments were reported in [168] and [169]. The unshielded noise was not measured at the quietest site (Tu2 in Figure 7.13(b)) and therefore the shielded noise was scaled up by the room-shielding ratio – line 'Tu2 (scaled)' in Figure 7.13(c). The traces 'C^{3rd}', 'T (3^{3rd} & adapt)' will be discussed in Section 7.7.5.2.

Noise within the high-attenuation Berlin shielded room[1)] [117] was not available and therefore the data from the noisiest site, T in Figure 7.13(c), was copied into Figure 7.13(a) as a gray line and scaled by the Berlin room combined shielding and active shielding attenuations (Sections 7.7.2 and 7.7.3) and is labeled by 'T (scaled)'. Noise measured within the whole-body superconducting shield (Yokohama, [119]) is labeled by 'SC shield' and is roughly the same as the 'T (scaled)' at low frequencies.

1) The shielded room at Physikalisch-Technische Bundesanstalt in Berlin, Germany, exhibits the highest environmental noise attenuation presently available. The room consists of one aluminum and seven mu-metal layers and its low-frequency attenuation is about 3×10^4 without active shielding and more than 10^7 with active shielding.

For comparison, the noise levels corresponding to the trace T after noise suppression by shielding (AK3b room [106]), by third-order gradiometers, and with or without additional adaptive noise reduction are shown by dashed lines in Figure 7.13(a) (labeled by T (3^{rd}) and T (3^{rd} & adapt)). These noise levels are comparable to that obtained with the high-attenuation shielded rooms and illustrate that the combination of a modestly shielded room with synthetic-noise cancellation can be as effective as the high-attenuation shields.

Also shown in Figure 7.13(d) is the noise generated by the background brain activity measured in an unshielded environment (C), upper two lines. The difference between the brain activity with the eyes closed or open is largest at about 8 Hz. The bottom trace indicates the system noise with no subject in the MEG helmet. The environmental noise was cancelled by third-order synthetic gradiometers and small arrows at the bottom of the plot indicate residual noise lines due to nearby

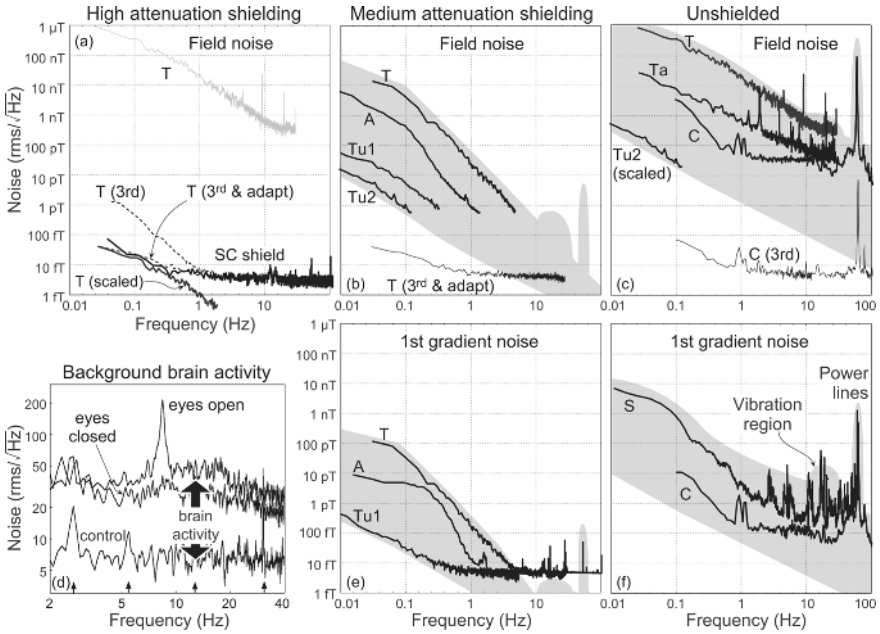

Fig. 7.13 Environmental noise measured at various locations: T – Toronto MEG site, A – Amsterdam MEG site, Tu1 and Tu2 – Tuebingen MEG site (day and night), C – CTF unshielded laboratory, S – unshielded Brain Behaviour Laboratory at SFU, Ta – Taipei site. (a) High attenuation shielding (b) – either the Berlin room [117] or the whole body, high-T_c superconducting shield [119]. Medium attenuation shielding – typically Vacuumschmelze AK3b room [106]. (c) Unshielded – no shielding. Gray patches – range of noise observed at various sites around the world, heavy black lines – examples of noise spectra, thin black lines in (b) and (c) – illustration of synthetic noise reduction, dashed lines in (a) – comparison of synthetic noise suppression with the shielded room performance, gray line in (a) – same as unshielded line T in (c). (a, b, c) Magnetic field noise; (e, f) Gradient noise measured with first-order gradiometer with 5 cm baseline; (d) Noise generated by the background brain activity measured in an unshielded environment (c).

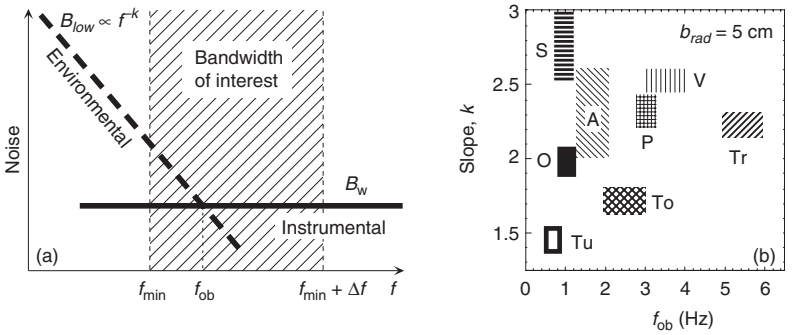

Fig. 7.14 Noise detected by gradiometers. (a) Noise detected by a SQUID sensor consists of white instrumental and low-frequency environmental noise (higher frequency noise due to power lines and various alternating sources is not considered here). The measurements extend over the bandwidth of interest, Δf, which typically spans both the low- and high-frequency noise regimes. The amplitude of the low-frequency noise depends on the gradiometer baseline. (b) Onset of low-frequency noise, f_{ob}, and the noise slope, k, measured within AK3b [106] shielded rooms at various sites. Noise slope, k, corresponds to noise amplitude vs frequency plots. Measured with hardware first-order radial gradiometers with 5 cm baseline [177], Tu – Tuebingen, O – Osaka (night), S – Sendai, A – Amsterdam, To – Tokyo, P – Paris, V – Vienna, Tr – Toronto. The parameters change with time, the results correspond to one or several measurements only.

machinery. The brain noise is only one example of noise generated by the body. The heart, muscles, eye blinks or eye motion, etc., also produce noise.

At low frequencies, the SQUID-detector noise is dominated by low-frequency noise, which for low-T_c SQUIDs is solely due to the environmental noise. At higher frequencies, the white-instrumental SQUID noise is dominant. In addition, the noise spectrum at higher frequencies also contains contributions from power-line frequencies and their harmonics. The frequency dependence of the noise spectra is shown schematically in Figure 7.14(a). The onset of the low-frequency noise is denoted by f_{ob} and the low-frequency noise amplitude slope (on a log-log scale) by k. The f_{ob} and k depend on the location and the time of the day and are shown for a number of sites in Figure 7.14(b). The measurements in Figure 7.14(b) were obtained with hardware first-order gradiometers with a 5 cm baseline inside a shielded room (AK3b[2)] [106]). The eddy-current layer within the shielded rooms increases the low-frequency noise slope by 1. Therefore, the corresponding noise slope outside the shielded rooms should be reduced by the same amount (the change in the noise slope due to the shielded-room effect is illustrated in Section 7.3.1.5 in Figure 7.7(b) lines 1 and 2). The measurement bandwidth typically spans

2) The AK3b is a shielded room produced by Vacuumschmelze in Hanau, Germany, and is used here as a typical example of a modestly shielded room, such as is frequently used in biomagnetic applications. The room's inside dimensions are 3 m × 4 m and about 2.8 m in height. The room is constructed from one aluminum and two mu-metal layers.

both the low and the high-frequency noise regions (shaded area in Figure 7.14(a)) and both noise regimes must be considered during the sensor design.

7.6.3.2 Additional Noise in Mobile Instrumentation

Mobile SQUID sensors are exposed to additional noise due to their motion relative to the earth and to geophysical and man-made fields and gradients. This motion noise can be quite large. For example, the SQUID sensor rotating in the environmental fields will be subjected to signal changes as large as twice the values shown in Table 7.9. The moving gradiometers will be exposed to geological fields and gradients, which at an altitude of, e.g., 170 m above the earth's surface, may have a magnitude of up to 1000 nT and 5 nT/m, respectively [175, 176]. Also, the moving devices are exposed to vibrations and electromagnetic interference from their supporting platform.

If hand-held SQUID detectors were constructed, they would be moved in urban environments within large higher-order gradients, as in Table 7.9. The presence of high-order gradients significantly complicates the removal of motion noise and is briefly discussed in Section 7.7.4.3.

7.7 Noise Suppression

7.7.1 Introduction

The output of a properly functioning SQUID detector contains, not only the intended signals and the SQUID noise, but also environmental noise, as discussed in Section 7.6. The signals and the environmental noise enter through the SQUID flux transformers and temporal filtering usually cannot separate them. To reduce the environmental noise, a typical SQUID system employs a combination of noise cancellation methods, including: shielding, active shielding, optimization of the flux transformer signal-to-noise ratio (SNR), reference-based noise-cancellation, and methods based on the spatial difference between the signal and the noise sources (spatial filtering). Shielding has been discussed in detail in Section 7.3.1. However, active shielding using reference magnetometers, feedback electronics and a set of compensating coils can also reduce environmental noise.

7.7.2 Active Shielding

Active shields can reduce environmental noise when employed either in unshielded environments [178, 179], or in combination with shielded rooms, e.g., [180–183, 117]. Active shielding consists of a reference magnetometer, feedback electronics, and a set of compensating coils. The references can be either SQUID magnetometers, flux-gate magnetometers, or sensing coils which are exposed to the envi-

ronment. The noise cancellation can be provided by a system of coils either surrounding the detection area or wrapped around the shielded room.

The active shielding operated in unshielded environments must cancel both the low-frequency noise as well as the power lines and their harmonics. The power-line harmonics can have significant magnitudes up to high frequencies and the active shielding must operate over the whole-frequency range (in some environments the 13^{th} harmonic of 60 Hz has been observed to be as high as 1 nT). Requirements for such broadband active shielding in unshielded environments can pose a problem, because the useful frequency range of the active shielding is limited by the phase shifts which are introduced by the large inductances of the compensation coils.

In shielded environments, SQUID magnetometers can be used as references [182, 183]. If they are located within a distance of up to 1 m from the measurement area, active shielding better than 40 dB below 50 Hz can be obtained. When the references are positioned far from the measurement area or outside the shielded rooms, smaller attenuations were found. In the recently built Berlin room (7 mu-metal layers and one 1 cm thick Al layer [117]), flux gate magnetometers were located outside the shielded room and an attenuation of about 28.5 dB at low frequencies was reported (see also the footnotes in Section 7.6.3.1).

The noise of the reference sensors, transformed through the feedback electronics, will be added to the primary sensor noise. If the SQUID sensors are magnetometers, then the transformed reference noise is simply added to the sensor noise [183]. If the sensors are gradiometers, then the reference noise contribution is more complicated and will depend on the field uniformity produced by the compensation coils.

In general, the active shielding reduces the magnetic field noise due to far field sources and is effective only for magnetometers with no noise cancellation, while it has only a small effect on well balanced first-order gradiometers or magnetometers with noise cancellation. For higher-order gradiometers, the active shielding actually degrades the noise attenuation, because the active coils produce higher-order gradients, which are larger than that of the environmental noise.

In some situations, static compensation of the earth's dc magnetic field may be provided [184, 185]. Such dc compensation reduces the effect of vibrations on the SQUID detector and is advantageous for operation of high-T_c SQUIDs, which tend to exhibit noise due to motion of trapped flux [140]. If used in combination with shielded rooms, the static compensation allows tuning of the working point of the soft magnetic material of the shielded room to its optimal shielding performance (where the magnetic permeability is at a maximum).

7.7.3
Noise Cancellation by Primary Sensors

A SQUID system consists of primary sensors and, optionally, reference sensors. The primary sensors are located in close proximity to the measured signal source(s) so that they detect the source fields and also the environmental noise. The references are designed to measure the environmental noise and are located at some distance from the signal sources so that they have low sensitivity to them. The referenc-

es are used to subtract the environmental noise from the primary sensor outputs and are discussed in Section 7.7.4.

The primary sensors can be magnetometers or low-order hardware gradiometers. The direct use of magnetometers, even within shielded rooms, is usually not possible because the environmental noise is too large (see Figure 7.7). In these situations the magnetometers must be coupled with references to reduce the noise and consequently, the magnetometers with noise cancellation behave as first- or higher-order gradiometers relative to distant noise sources (Section 7.7.4.1). The distance between the magnetometer and the references is equivalent to the gradiometer baseline. In this section, we will consider either primary magnetometers with reference vector magnetometers, or hardware first-order gradiometers, and such configurations will be called first-order detection systems. Extension to higher-order systems is possible.

The first-order systems can have either a long or short baseline, as shown in Figure 7.15(a). For the optimum detection, the baseline length should be chosen to maximize the sensor's SNR. The optimized sensor will exhibit high sensitivity to near field signals while rejecting the far field environmental noise [186]. The baseline optimization is shown schematically in Figures 7.15(b) and (c).

The magnitude of the detected near-fields (e.g., biomagnetic, non-destructive evaluation, etc.) typically increases with increasing baseline length. This is because, for short baselines, both gradiometer coils (or a magnetometer and its reference) detect the measured signal and, since they are connected in subtractive fashion, the net signal is reduced. For long baselines, the more distant gradiometer coil (or reference) will detect less signal and the overall signal reduction will be smaller. Similarly, the environmental noise usually has spatial gradients and increasing the baseline will increase the magnitude of the detected noise. Thus both signal and noise increase with increasing baseline, but their functional dependencies on the baseline are different. As a result, the SNR exhibits a peak at a certain baseline length. Since the SNR is usually the most important operational parameter, the best performance of the first-order flux transformers is obtained in the vicinity of their SNR maximum.

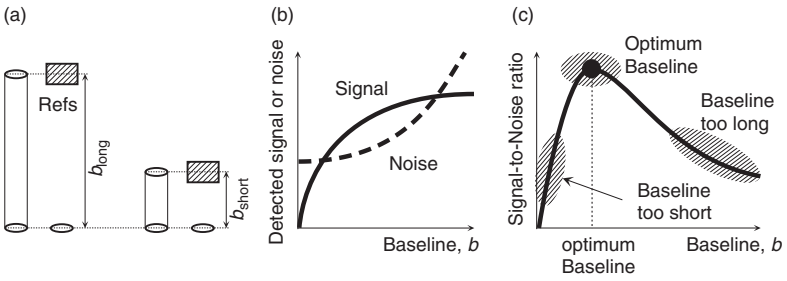

Fig. 7.15 Optimization of the radial gradiometer baseline. (a) Magnetometers with noise cancellation and gradiometers can have long or short baselines. (b) Detected signal and noise both increase with baseline but have different functional dependencies on the baseline. (c) Dependence of SNR on the baseline exhibits a maximum (region of optimum baseline) and regions where the baseline is either too short or too long.

The argument above can be developed more quantitatively. Consider first the environmental noise. Its magnitude can be approximated by $B_{\text{low}} = A/f^k$, where k is the noise slope (see Figure 7.14(b)) ranging from about $k = 1$ to more than $k = 6$ in some unshielded environments [169]. The noise amplitude A is proportional to the baseline length, $A = A_o b/b_o$, where the amplitudes A and A_o correspond to the gradiometer baselines of b and b_o, respectively [121, 186]. Denote by f_o the low-frequency noise onset measured with the baseline b_o. Then the low-frequency noise measured with baseline b can be expressed in terms of the white noise density as

$$B_{low} = B_w \frac{b}{b_o} \left(\frac{f_o}{f}\right)^k \tag{7.29}$$

where B_w is the system rms white noise per $\sqrt{\text{Hz}}$. The total noise, B_N, is the rms addition of the white and low-frequency noise, $B_N^2 = B_w^2 + B_{low}^2$. Substituting for B_{low} from (7.29) and integrating the total noise over the bandwidth of interest (as shown in Figure 7.14(a)), the detected rms noise is obtained as

$$\begin{aligned} B_{N_{rms}} &= \sqrt{\int_{f_1}^{f_1+\Delta f} B_N^2 \, df} \\ &= \frac{B_w}{\sqrt{N_{ave}}} \sqrt{\Delta f + \frac{f_{\min}}{2k-1} \left(\frac{f_o}{f_{\min}}\right)^{2k} \left(\frac{b}{b_o}\right)^2 \left[1 - \left(\frac{f_{\min}}{f_{\min}+\Delta f}\right)^{2k-1}\right]} \end{aligned} \tag{7.30}$$

where N_{ave} is the number of averages, $f_{\min}$ is the minimum frequency of interest, and Δf is the measurement bandwidth. If $f_{\min} \gg f_{\text{ob}} = f_o (b/b_o)^{1/k}$, the measurement is in the white-noise regime (see Figure 7.14(a)) and then (7.30) simplifies to the standard white noise expression for rms noise. For longer baselines, the transition to the white-noise regime occurs at higher frequencies. In general, the rms noise in (7.30) increases monotonically with increasing baseline b, as shown by the dashed line in Figure 7.15(b).

The baseline dependence of the near-field signal can be illustrated by the example of a magnetic dipole with moment M_{dip}. Let the dipole distance from the nearest gradiometer coil be r and the gradiometer baseline again be b. The field change over the gradiometer dimension is $\Delta B = (M_{dip}/r^3)\{1 - [r/(r+b)]^3\}$. This expression together with (7.30) can be used to calculate the SNR, and its maximum as a function of the baseline, can be found numerically. For $B_w = 5$ fT rms/$\sqrt{\text{Hz}}$, $N_{\text{ave}} = 1$, $f_{\min} = 1$ Hz, $\Delta f = 100$ Hz, $k = 2$, $f_o = 2$ Hz, $b_o = 5$ cm, the SNR attains a maximum for the baselines in the range 2.4–6.7 cm, when r is in the range 1–10 cm.

The optimized baseline is only weakly dependent on the character of the source. Similar computations for MEG current dipoles [186, 121] also resulted in comparable optimum baselines of 2–8 cm for noise parameters measured at a number of MEG sites shielded by AK3b, [106].

The conclusion that the optimum primary sensor baselines are short is valid in most detection situations. This is because, even in modestly shielded rooms, (curve 2

in Figure 7.7(a)), the environmental noise is still substantial (Figure 7.13(b)). Only in high-quality shielded rooms (curves 5 and 6 in Figure 7.7(a)) is the environmental noise sufficiently low that the white-noise limit, $f_{min} \gg f_{ob}$, is approached and gradiometers with long baselines or even magnetometers can be successfully employed.

The considerations in this section do not apply to far field measurements, where the dependencies of the signal and noise on the baseline are comparable.

7.7.4
Noise Cancellation Using References

7.7.4.1 Introduction

SQUID flux transformers can be configured as magnetometers or gradiometers. Hardware gradiometer flux transformers typically consist of a collection of coils at different spatial locations connected subtractively to a SQUID sensor. For example, a first-order hardware gradiometer consists of two coils wound in opposite directions. For near sources, the coil closer to the source may be considered to be a sensor, and the more distant coil, the reference.

Consider a sensor and a number of separate references located at different positions; the sensor and the references are connected to different SQUIDs. Such a system can be used for synthetic noise cancellation which will be understood to mean the subtraction of a linear combination of the reference outputs from the sensor output, using subtraction coefficients constructed to accomplish a specified task, e.g., to minimize noise, or to construct a synthetic gradiometer, etc. Synthetic noise cancellation is quite flexible because results with different characteristics can be obtained from the same sensor and reference data. This is different from the hardware-noise cancellation, where the coefficients of the subtraction are predetermined by the construction of the hardware for example, for a perfectly symmetrical first-order gradiometer, the subtraction coefficient between the sensing and reference coils is equal to 1.

References for a synthetic noise cancellation system span a wide range of complexity, from simple three-component magnetometers, to complex structures comprising magnetometers and gradiometers suitable for synthesis of higher-order gradiometers. The sensors can be either magnetometers (magnetometer-based systems as in Figure 7.16(a)), or hardware first-order gradiometers (gradiometer-based systems as in Figures 7.16(b) and (c)), or any other type of flux transformer.

The relationship between the synthetic noise cancellation designed either to minimize the environmental noise (adaptive system) or to synthesize a gradiometer response (gradiometer system) will be illustrated analytically [121]. For simplicity, a first-order system as in Figure 7.16(a) will be considered. The system consists of a magnetometer sensor and a three-component vector magnetometer reference. If the magnetometer output is denoted by $g^{(0)}$ and the reference outputs are r_i, $i = 1, 2, 3$, then both the synthetic gradiometer and the adaptive system may be described as

$$S = g^{(0)} - \sum_{i=1}^{3} \xi_i r_i \tag{7.31}$$

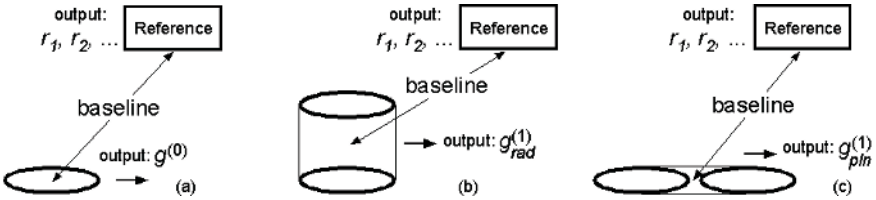

Fig. 7.16 Synthetic noise-cancellation systems. (a) Magnetometer-based system. (b) Hardware first-order radial gradiometer-based system. (c) Hardware first-order planar gradiometer-based system.

where ξ_i are subtraction coefficients, and S is the synthetic system output. Assume that the primary magnetometer is positioned at the origin as in Figure 7.17(a), only the field and first gradients are present, and the field at a position $\boldsymbol{b}$ is related to the field at the origin, $\boldsymbol{B_0}$, by $\boldsymbol{B} = \boldsymbol{B_0} + \boldsymbol{G} \cdot \boldsymbol{b}$, where $\boldsymbol{G}$ is the first gradient tensor. The coefficients ξ_i may be determined by the minimization of S.

Assume that the fields and gradients are generated by a large number of randomly positioned sources and that the random source configuration is changing with time. The variable sources will result in a time-variable output of the synthetic system, which can be described as a vector $\boldsymbol{S} = [S(t_1), S(t_2), \ldots]$. A snapshot of the system at one time instant is shown in Figure 7.17(b). If the components of the magnetic fields and gradients are independent, if the coefficients are determined by minimization of the vector $\boldsymbol{S}$ norm, and if the norm of a column vector $\boldsymbol{V}$ is defined as $\|\boldsymbol{V}\| = (\boldsymbol{V}^T\boldsymbol{V})^{1/2}$ [204], then the coefficients ξ_i can be derived as [121]

$$\xi_i = p_i \frac{\|\boldsymbol{B}_i^t\|^2}{\|\boldsymbol{B}_i^t\|^2 + \|\boldsymbol{G}_i^t\|^2} \quad i = 1, 2, 3 \tag{7.32}$$

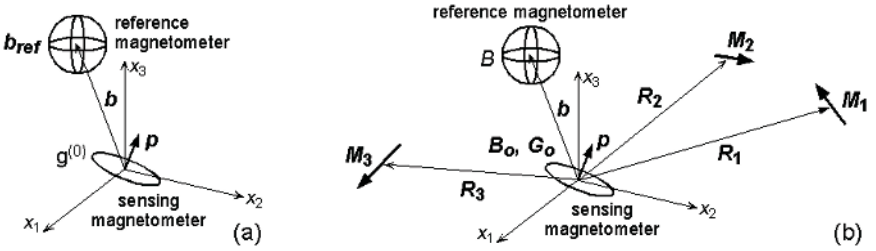

Fig. 7.17 Magnetometer-based first-order synthetic noise cancellation system with vector magnetometer as a reference. (a) General detection configuration; the magnetometer sensor is oriented along $\boldsymbol{p}$ and the three-component reference vector magnetometer is located at distance $\boldsymbol{b}$ from the magnetometer sensor. (b) System exposed to a field consisting of a number of noise sources (dipoles $\boldsymbol{M_1}$, $\boldsymbol{M_2}$, and $\boldsymbol{M_3}$ in this diagram; however, the sources are not limited to dipoles and there are typically many more than three sources present).

where $\boldsymbol{B}_i^t = \{B_{Oi}(t_1),\ B_{Oi}(t_2),\ \ldots\}$, $\boldsymbol{G}_i^t = \{(\boldsymbol{G}(t_1)\cdot\boldsymbol{b})_i,\ (\boldsymbol{G}(t_2)\cdot\boldsymbol{b})_i,\ \ldots\}$, and t_k are time samples (note that the norm defined in [121] is the square of the norm defined here).

The result in (7.32) indicates that, if the minimization is performed in a uniform field, $\boldsymbol{G}=0$, then $\boldsymbol{G}_i^t=0$, and $\xi_i = p_i$, $i=1, 2, 3$, or the coefficients are equal to the components of the magnetometer orientation vector and the synthetic system then describes a first-order gradiometer. This result is intuitive, and agrees with the concept of a first-order gradiometer consisting of two parallel coils: one coil corresponding to the magnetometer sensor, and the second coil at the position $\boldsymbol{b}$ which is emulated by the projection of the reference outputs to the orientation $\boldsymbol{p}$. The gradiometer coefficients depend only on the sensor geometry and are universal, i.e., independent of the character of the noise.

If the field during the noise minimization is non-uniform, $\boldsymbol{G}\neq 0$, then the subtraction coefficients in (7.32) do not describe a gradiometer system, they correspond to an adaptive system designed to minimize the noise. In this case, the coefficients are not universal because they depend on the fields and gradients present during the adaptation (i.e., they depend on the norms $\|\boldsymbol{B}_i^t\|$ and $\|\boldsymbol{G}_i^t\|$). If the fields and gradients change during the subsequent measurement, it is necessary to determine new adaptive coefficients.

The norms of the vector $\boldsymbol{S}$ minimized for the true gradiometer or the adaptive systems can be derived as [121]

$$\left(\|\boldsymbol{S}\|_{\min}^{adapt}\right)^2 = \sum_{i=1}^{3} p_i^2 \frac{\left\|\boldsymbol{B}_i^t\right\|^2}{\left\|\boldsymbol{B}_i^t\right\|^2 + \left\|\boldsymbol{G}_i^t\right\|^2} \tag{7.33}$$

$$\left(\|\boldsymbol{S}\|_{\min}^{grad}\right)^2 = \sum_{i=1}^{3} p_i^2 \left\|\boldsymbol{G}_i^t\right\|^2 . \tag{7.34}$$

In the gradiometer case, the coefficients were determined to cancel the field, and therefore the residual $\|\boldsymbol{S}\|^2$ contains only the gradient components. In the adaptive case, the residual contains a combination of gradients and fields. All the quantities in (7.33) and (7.34) are positive and, for a given i, the adaptive term is smaller than the corresponding gradiometer term. Thus the adaptive noise yields better cancellation, but only during the time period for which the noise character is not changing (norms $\|\boldsymbol{B}_i^t\|$ and $\|\boldsymbol{G}_i^t\|$ remain constant). Similar minimization can also be performed for higher-order gradiometers and the results will contain norms corresponding to the fields and gradients of all orders up to the investigated gradiometer order.

The above results can be illustrated graphically for a simplified case where the magnetometer is oriented along the x_3 direction and $\boldsymbol{p}=(0,\ 0,\ 1)$, as in Figure 7.18(a). In this case, (7.33) and (7.34) contain only one term each. If it is further assumed that the environmental sources are magnetic dipoles with the same magnitude and are distributed on the surface of a sphere with radius r, then it can be shown [121] that $(\|\boldsymbol{G}_i^t\|/\|\boldsymbol{B}_i^t\|)^2 = \Psi(3b/r)^2 \approx (3b/r)^2$, where $\Psi \approx 1$ and b is the baseline of the synthetic system. If a dimensionless quantity $r_b = R/(3b\sqrt{\Psi}) \approx r/(3b)$ is introduced, then (7.33) and (7.34) simplify to

$$\frac{\|\boldsymbol{S}\|_{\min}^{adapt}}{\|\boldsymbol{B}_3^t\|} = \frac{1}{\sqrt{1+r_b^2}} \tag{7.35}$$

$$\frac{\|\boldsymbol{S}\|_{\min}^{grad}}{\|\boldsymbol{B}_3^t\|} = \frac{1}{r_b}. \tag{7.36}$$

The minimized norm of the vector $\boldsymbol{S}$, i.e., the residual noise after the noise minimization or gradiometer synthesis, is shown in Figure 7.18(b). For large r_b (i.e., $r \gg 3b$, for distant sources) the performances of the adaptive and gradiometer systems are similar, and for small r_b ($r \ll 3b$), the adaptive systems produce significantly smaller noise. However, since the largest realistic gradiometer baselines are small, $b \leq 0.3$ m, the dividing point between these two limits, $r_b \approx 1$ (or $r \approx 3b \approx 1$ m) represents very near distances. Since in practical situations the environmental noise sources are located at large distances, $r \gg 3b$ ($r_b \gg 1$), the differences between the adaptive and synthetic gradiometer performances are typically small. For higher-order gradiometers (i.e., more references), the adaptive methods can perform better than indicated for the present simple first-order system. The utility of the adaptive systems, however, is not as great as that of the gradiometers, because the gradiometer coefficients are universal, while the adaptive coefficients are not.

In summary: the synthetic noise cancellation coefficients are different for the gradiometer and adaptive processes. The adaptive methods can provide better noise rejection than the synthetic gradiometers, but only during the time period for which the noise character remains constant. In practice, this time period depends on the environment and it ranges from as short as several seconds to long periods of several months [169]. On the other hand, the synthetic gradiometer coefficients are truly universal (they can be factory pre-determined and are independent of the noise character or dewar orientation), while the adaptive coefficients are not [169, 121] (the adaptive coefficients must be recomputed every time either the noise character or

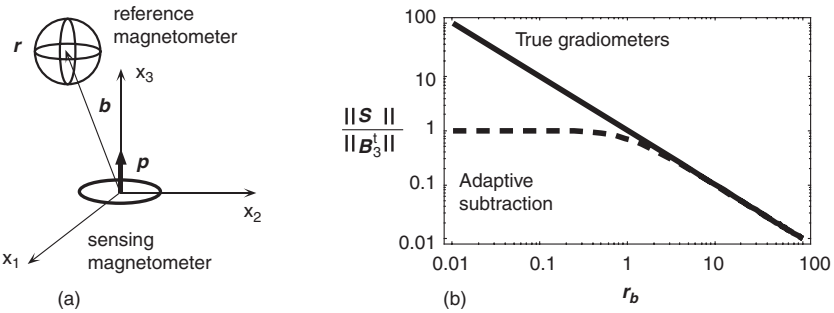

Fig. 7.18 A comparison of first-order synthetic gradiometers and adaptive systems. (a) Geometry of the sensor and the references. The magnetometer sensor is oriented along x_3 and the reference is a three-component vector magnetometer. (b) Residual noise for the gradiometer and adaptive systems. Parameter r_b is the normalized distance from the MEG system, $r_b \approx r/(3b)$, where b is the baseline length.

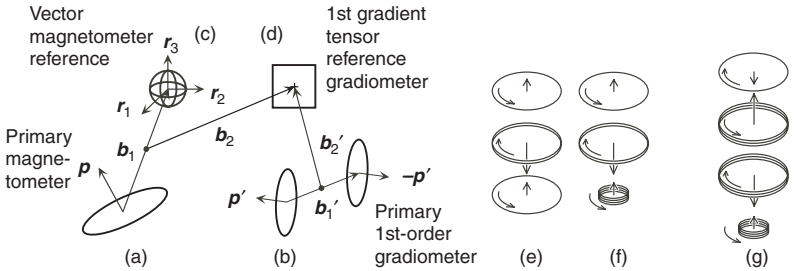

Fig. 7.19 Magnetometers and hardware and synthetic gradiometers. (a) Magnetometer oriented along vector $\boldsymbol{p}$. (b) Hardware first-order gradiometer with baseline $\boldsymbol{b}_1'$ and coil orientation $\boldsymbol{p}'$. (c) Reference vector magnetometer: three components are oriented along orthogonal directions. (d) Reference tensor gradiometer consisting of 5 components for operation in the air and 9 components for operation in conducting media. (e) Symmetric second-order hardware gradiometer. (f) Asymmetric second-order hardware gradiometer. (g) Asymmetric third-order hardware gradiometer.

the dewar orientation change). In all practical situations, the residual noise for both adaptive and gradiometer processes is proportional to the baseline.

7.7.4.2 **Static Systems**

It was shown in Section 7.7.3 that the first step towards the environmental noise reduction is to optimize the primary sensors. However, noise attenuation by first-order sensors (either gradiometers or adaptive) is usually insufficient and more effective noise cancellation must be implemented. One possibility is to use higher-order systems, usually gradiometers. For a small number of channels, the higher-order gradiometers can be constructed in hardware by connecting together a sufficient number of coils. Examples of hardware symmetric and asymmetric second-order gradiometers and an asymmetric third-order gradiometer, are shown in Figure 7.19.(e)–(g) [190]. However, the hardware gradiometers are bulky, complicated to construct, and difficult to balance and are not suitable for multichannel systems. For these reasons synthetic higher-order gradiometers (or adaptive systems) were developed. Such systems typically use low-order sensors (either magnetometers or first-order hardware gradiometers) and a system of reference magnetometers and gradiometers which are suitable for synthesis of a required-order gradiometer. The synthetic gradiometer outputs are independent of the noise character and the dewar orientation, as discussed in Section 7.7.4.1. In this section, a more direct, physically based approach to the gradiometer synthesis will be described.

Before proceeding with a more detailed discussion of the gradiometer synthesis, the gradiometer tensor properties will be briefly reviewed. The first gradient is a spatial derivative of the magnetic field. As there are three components of the magnetic field and three spatial directions, the first gradient tensor has $3 \times 3 = 9$ components. But because the first gradient tensor is traceless ($\mathrm{div}\boldsymbol{B} = 0$) and symmetrical ($\mathrm{curl}\boldsymbol{B} = 0$), it has only five linearly independent terms [169]. The second gradient tensor is the second spatial derivative of magnetic field and it has $3 \times 3 \times 3 = 27$ com-

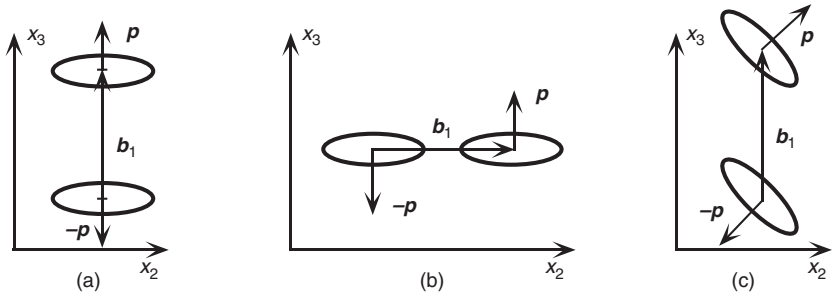

Fig. 7.20 Examples of ideal first-order gradiometers. Vector ***p*** denotes orientations of the gradiometer coils. (a) Axial (radial) gradiometer. (b) Off-axis (planar) gradiometer. (c) Gradiometer with tilted coils.

ponents. But because of the same symmetry relationships, there are only seven linearly independent terms. Similarly, the third gradient tensor has 81 components, but only 9 linearly independent terms. Generally, for every increase in the tensor gradiometer order by one, the number of linearly independent terms increases by two.

The simplest example of the gradiometer synthesis is a first-order gradiometer, based on a magnetometer sensor and a three-component vector magnetometer reference, as in Figure 7.19(a) and (c) [187–189, 169]. The primary magnetometer detects the magnetic field component along its coil normal, $\boldsymbol{p}$ (unit vector), as $g^{(0)} = a\,(\boldsymbol{p} \cdot \boldsymbol{B})$, where $\boldsymbol{B}$ is the vector of the environmental magnetic field and a is the inverse of the field-to-flux conversion coefficient, called the magnetometer gain (Φ_o/T) for brevity. For simplicity, the three reference magnetometers are assumed to be orthogonal and to have identical gains, a_r. The reference outputs are then $r_k = a_r B_k$, $k = 1, 2, 3$, where B_k are the components of $\boldsymbol{B}$. The outputs r_k form a vector of the reference output, $\boldsymbol{r}_{\text{ref}}$. Expanding the magnetic field into a Taylor series about the origin, defining the gradiometer baseline $\boldsymbol{b}_1$ as in Figure 7.19, and projecting the reference output to the direction $\boldsymbol{p}$, the first-order gradiometer, $g^{(1)}$, can be synthesized as

$$g^{(1)} = g^{(0)} - \frac{a}{a_r}\left(\boldsymbol{p} \cdot \boldsymbol{r}_{\text{ref}}\right) = a\,\boldsymbol{p}\boldsymbol{G}\boldsymbol{b}_1 \tag{7.37}$$

where $\boldsymbol{G}$ is the first gradient tensor at the coordinate origin. The synthetic first-order gradiometer output is given as a projection of the first gradient tensor to the primary magnetometer orientation, $\boldsymbol{p}$, and the baseline, $\boldsymbol{b}_1$. If the $\boldsymbol{p}$ and $\boldsymbol{b}_1$ have general orientations, the synthetic gradiometer in (7.43) is a linear combination of the first gradient tensor components. Note that the synthetic gradiometer output in (7.37) is expressed in units of Φ_o.

Examples of ideal first-order gradiometers are shown in Figure 7.20. Figure 7.20(a) corresponds to an axial gradiometer where $\boldsymbol{b}_1 = b_1(0, 0, 1)$, $\boldsymbol{p} = (0, 0, 1)$ and $g^{(1)} = a\boldsymbol{p} \cdot \boldsymbol{G} \cdot \boldsymbol{b}_1 = ab_1 G_{33}$. Figure 7.20(b) corresponds to an off-axis (planar) gradiometer where $\boldsymbol{b}_1 = b_1(0, 1, 0)$, $\boldsymbol{p} = (0, 0, 1)$ and $g^{(1)} = ab_1 G_{23}$. In Figure 7.20(c) the coils

and the baseline are not aligned, $\boldsymbol{b}_1 = b_1(0,\ 0,\ 1)$, $\boldsymbol{p} = (0,\ 1/\sqrt{2},\ 1/\sqrt{2})$ and $g^{(1)} = ab_1 (G_{23} + G_{33})/\sqrt{2}$.

The synthesis of a second-order gradiometer from a primary first-order hardware gradiometer and a first gradient tensor reference gradiometer, is illustrated in Figure 7.19(b) and (d)[121]. Assume that the primary first-order gradiometer has a baseline $\boldsymbol{b}_1'$ and coil orientation unit vector $\boldsymbol{p}'$. The second-order baseline $\boldsymbol{b}_2'$ connects the reference and the primary gradiometer centers. Similar to the first-order gradiometer, the second-order gradiometer, $g^{(2)}$, is synthesized by projecting the reference tensor gradiometer output to the vectors $\boldsymbol{p}'$ and $\boldsymbol{b}_1'$ and subtracting the projection, scaled by the gains, from the primary gradiometer output. It can be shown that $g^{(2)}$ is given by the projection of the second gradient tensor, $\boldsymbol{G}^{(2)}$, on to the vectors $\boldsymbol{p}'$, $\boldsymbol{b}_1'$, and $\boldsymbol{b}_2'$ as

$$g^{(2)} \approx a\boldsymbol{p}'\boldsymbol{G}^{(2)}\boldsymbol{b}_2'\boldsymbol{b}_1' \tag{7.38}$$

where a is the primary first-order gradiometer gain. To simplify the notation, it was assumed that the hardware gradiometer gain in Figure 7.19(b) is the same as that of the synthetic gradiometer in (7.37). In a similar way, the second-order gradiometer could be synthesized from a magnetometer primary sensor using vector magnetometer and first gradient tensor gradiometer references, as in Figures 7.19(a), (c), and (d). In this case, the first-order gradiometer is synthesized first as in (7.37), and then the second-order gradiometer is synthesized as in (7.38) using the synthetic first-order gradiometer as a primary sensor, and the relevant system vectors in Figure 7.19 are $\boldsymbol{p}$, $\boldsymbol{b}_1$, and $\boldsymbol{b}_2$. The procedure can be generalized to higher-order gradiometers. For example, a third-order gradiometer can be synthesized as $g^{(3)} = a\boldsymbol{p}\boldsymbol{G}^{(3)}\boldsymbol{b}_1\boldsymbol{b}_2\boldsymbol{b}_3$, where $\boldsymbol{b}_3$ is the third-order baseline. Synthetic third-order gradiometers are now routinely used in commercial MEG systems [133].

Examples of ideal second-order gradiometers are shown in Figure 7.21. Figure 7.21(a) corresponds to a second-order gradiometer where all three principal vectors are parallel, $\boldsymbol{p} \parallel \boldsymbol{b}_1 \parallel \boldsymbol{b}_2$, and $\boldsymbol{p} = (0,\ 0,\ 1)$. The second-order-gradiometer output is then $g^{(2)} = a\boldsymbol{p}\boldsymbol{G}^{(2)}\boldsymbol{b}_1\boldsymbol{b}_2 = ab_1b_2G_{333}$. The gradiometer in Figure 7.21(b) corresponds to the case where $\boldsymbol{p} \parallel \boldsymbol{b}_1 \perp \boldsymbol{b}_2$, and $\boldsymbol{p} = (0,\ 0,\ 1)$, $\boldsymbol{b}_2 = b_2(0,\ 1,\ 0)$ and $g^{(2)} = ab_1b_2G_{233}$. The gradi-

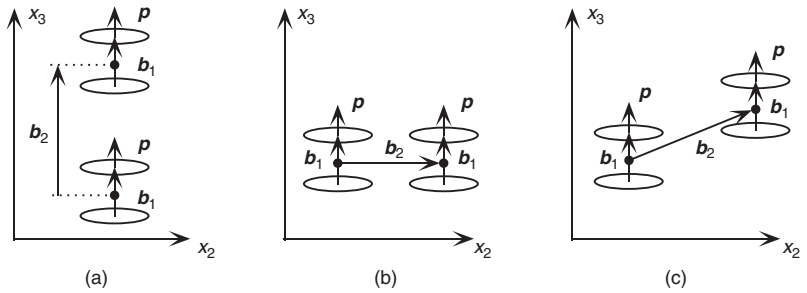

Fig 7.21 Examples of ideal second-order gradiometers. (a) Axial gradiometer G_{333}. (b) Gradiometer G_{233}. (c) Second-order gradiometer with tilted baseline.

ometer in Figure 7.21(c) has a tilted baseline $\boldsymbol{b}_2$, and $\boldsymbol{p} \parallel \boldsymbol{b}_1$, where $\boldsymbol{p}=(0,\ 0,\ 1)$, $\boldsymbol{b}_2 = b_2(0,\ 1/\sqrt{2},\ 1/\sqrt{2})$, and the second-order gradiometer output $g^{(2)} = ab_1b_2(G_{233} + G_{333})/\sqrt{2}$ is a linear combination of the second gradient tensor components.

In practice, gradiometers are not perfect, either because of manufacturing errors or due to the presence of normal conducting or superconducting objects in their vicinity. These gradiometer imperfections can be described by means of common-mode and eddy-current vectors [169].

For a simple first-order gradiometer, the field common-mode vector, $\boldsymbol{C}_B$, describes the gradiometer residual sensitivity to magnetic field. The origins of the common-mode vector can be either mechanical (imperfect construction, as in Figure 7.22(a) and (b)), or the common-mode vector can be induced by the presence of a superconducting object near the gradiometer (Figure 7.22(c)). A normal metal in the vicinity of the gradiometer can be modeled as an R–L circuit, Figure 7.22(d). The time-varying applied fields will excite currents within it, which in turn will generate magnetic fields and affect the gradiometer. This effect depends on the time derivative of the magnetic fields and can be described in terms of an eddy-current vector $\boldsymbol{E}_B$.

Generally, the presence of a normal metal in the vicinity of the gradiometer will induce not only a frequency-dependent eddy current vector, $\boldsymbol{E}_B$, but also a frequency-dependent common mode vector, $\boldsymbol{C}_B$. This will be illustrated for a first-order gradiometer [169]. If the eddy current source is modeled as an R–L circuit as in Figure 7.22(d), then it can be shown that the total field acting on a magnetometer is frequency dependent, as

$$B_T = \left(1 + \kappa \frac{\omega^2}{\omega^2 + \omega_E^2}\right) B + \kappa \frac{\omega_E}{\omega^2 + \omega_E^2} \dot{B} \tag{7.39}$$

where $\omega = 2\pi f$ is the frequency of the applied field, $\dot{B}$ is the time derivative of the applied field, ω_E is the characteristic frequency of the R–L circuit $\omega_E = R_E/L_E$, where L_E is the inductance of the normal metal inductor, and κ is the coupling constant, given by

$$\kappa = \frac{M_E A_E}{L_E A_p} \tag{7.40}$$

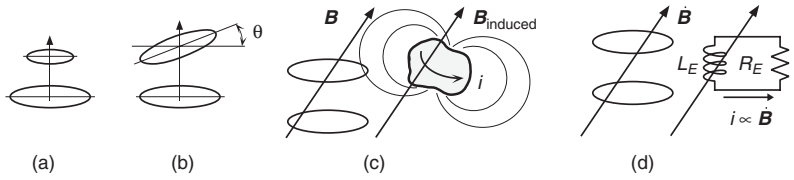

Fig. 7.22 Sources of common-mode and eddy-current vectors. (a, b, c) common-mode vector sources. (a) Inequality of coil areas. (b) Coil tilt. (c) Presence of a superconducting object near the gradiometer. (d) Eddy-current vector source represented by a normal metal object near the gradiometer.

where A_E is the area of the normal metal inductor, A_p is the magnetometer coil area, and M_E is the mutual inductance between the R–L circuit and the magnetometer coil.

Let us consider a first-order gradiometer positioned in the vicinity of a conducting object (Figure 7.23(a)). This gradiometer can be thought of as two coils coupled to the conducting object by the coupling constants κ_1 and κ_2, and exposed to total fields B_{T1} and B_{T2}. Further, assume that the gradiometer is imperfectly constructed and its common-mode vector magnitude is C_o. For simplicity, assume that the field difference detected by the gradiometer is

$$\Delta B \approx (1 + C_o) B_{T1} - B_{T2} \tag{7.41}$$

Substituting for the B_T's from (7.39) into (7.41), the signal detected by the gradiometer can be written as

$$\Delta B = C_B B + E_B \dot{B} \tag{7.42}$$

where $\Delta\kappa = \kappa_1 - \kappa_2$ and

$$C_B = C_o + \left(\Delta\kappa + C_o\kappa_1\right) \frac{\omega^2}{\omega^2 + \omega_E^2} \tag{7.43}$$

$$E_B = \left(\Delta\kappa + C_o\kappa_1\right) \frac{\omega_E}{\omega^2 + \omega_E^2}. \tag{7.44}$$

Thus, the gradiometer output consists of the common-mode term (proportional to the applied field) and the eddy-current term (proportional to the time derivative of the applied field). Both vectors C_B and E_B are frequency dependent. Examine the behavior at the high and low-frequency limits. In the high-frequency limit, when

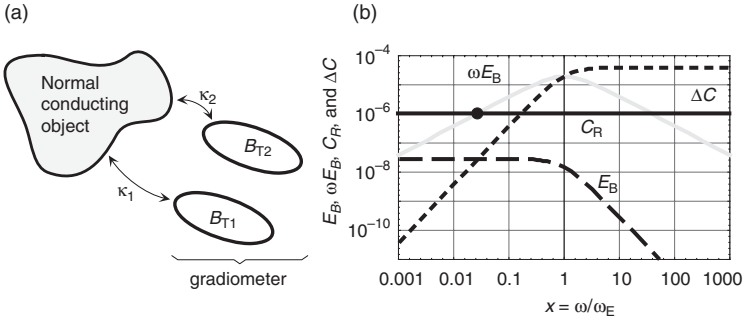

Fig. 7.23 Effect of a normal conducting object on a first-order gradiometer. (a) Geometry of the conducting object relative to the gradiometer. (b) Frequency dependence of the common-mode and eddy-current vectors induced by a brass cylinder with a radius of 2 cm, length 10 cm, and wall thickness of 0.5 cm (see the text). $C_S = 3.8 \times 10^{-5}$, $f_E = 207$ Hz, $C_o = 2 \times 10^{-3}$, $C_R = 10^{-6}$.

$\omega \gg \omega_E$ (or $\omega_E \to 0$, or $R_E \to 0$), the material behaves as a superconductor, and the vectors C_B and E_B become

$$\omega \gg \omega_E: \quad C_B = C_o + C_S \tag{7.45a}$$

$$E_B = 0 \tag{7.45b}$$

where $C_S = \Delta\kappa + C_o \cdot \kappa_1$ is the common-mode vector magnitude which would be induced if the eddy current source were superconducting. In the high-frequency limit, the conducting object affects only the C_B. The situation is opposite in the low-frequency limit, where the conducting object affects only the eddy-current vector

$$\omega \ll \omega_E: \quad C_B = C_o \tag{7.46a}$$

$$E_B = \frac{C_S}{\omega_E} \tag{7.46b}$$

An acceptable magnitude of the eddy-current vector can be estimated by requiring the eddy-current signal to be smaller than the common-mode signal when the common-mode vector is balanced to a required level C_R:

$$E_R \dot{B} < C_R B \tag{7.47}$$

Considering only the magnitudes, the condition imposed on the eddy-current vector at frequency ω is

$$E_R < \frac{C_R}{\omega}. \tag{7.48}$$

In practice, the condition in (7.48) may be difficult to achieve, and the eddy current may have to be reduced by methods similar to common-mode balancing.

As an example, consider a brass cylinder with radius 2 cm, length 10 cm, wall thickness 0.5 cm, and resistivity 6.4×10^{-8} Ωm, coupled to an axial gradiometer with baseline $b = 8$ cm and common-mode vector $C_o = 2 \times 10^{-3}$. The brass cylinder is positioned coaxially with the gradiometer such that the cylinder center is at a distance of 60 cm from the nearest gradiometer coil. Such a brass cylinder results in $C_S = 3.8 \times 10^{-5}$ and a characteristic frequency of $f_E = 207$ Hz ($\omega_E = 2\pi f_E$).

Finally, to illustrate the frequency dependent effects, the common-mode and eddy-current vector parameters induced by the brass cylinder above, are plotted as a function of the normalized frequency $x = \omega/\omega_E$ in Figure 7.23(b). The quantities plotted are E_B, see (7.44), ωE_B, $\Delta C = C_B - C_o$, see (7.43), and C_R (the level to which the common-mode vector should be balanced). The eddy-current vector E_B is frequency independent for $x \ll 1$, and its magnitude decreases as $1/\omega^2$ for $x \gg 1$. As a result, ωE_B increases as ω for $x \ll 1$, and decreases as $1/\omega$ for $x \gg 1$. The common-mode vector ΔC increases as ω^2 for $x \ll 1$ and is independent of frequency for $x \gg 1$. The C_R is frequency independent and is crossed by the ωE_B term at $x = 0.026$

(frequency $f \approx 5.6$ Hz). This implies that, for frequencies less than 5.6 Hz, the eddy-current signal due to the brass cylinder is negligible, while for frequencies greater than 5.6 Hz, it is dominant and cannot be neglected.

The common-mode and eddy-current vectors in the case of higher-order gradiometers are somewhat more complicated. An imperfect k^{th}-order gradiometer will have residual sensitivity not only to the field, but also to all gradients of order lower than k. Similarly, such a gradiometer will also have a residual eddy-current sensitivity to derivatives of field and to all gradients with order lower than k. If, for simplicity, only the eddy-current contributions due to the field derivatives are considered, the outputs of first-, second- and third-order gradiometers can be described as

$$g^{(1)} = a\left(\boldsymbol{C}_B \boldsymbol{B} + \boldsymbol{E}_B \dot{\boldsymbol{B}} + \boldsymbol{p}\boldsymbol{G}^{(1)} \boldsymbol{b}_1\right) \tag{7.49a}$$

$$g^{(2)} = a\left(\boldsymbol{C}_B \boldsymbol{B} + \boldsymbol{E}_B \dot{\boldsymbol{B}} + \boldsymbol{C}_{G1} \boldsymbol{y}_1 \boldsymbol{b}_1 + \boldsymbol{p}\boldsymbol{G}^{(2)} \boldsymbol{b}_1 \boldsymbol{b}_2\right) \tag{7.49b}$$

$$g^{(3)} = a\left(\boldsymbol{C}_B \boldsymbol{B} + \boldsymbol{E}_B \dot{\boldsymbol{B}} + \boldsymbol{C}_{G1} \boldsymbol{y}_1 \boldsymbol{b}_1 + \boldsymbol{C}_{G2} \boldsymbol{y}_2 \boldsymbol{b}_1 \boldsymbol{b}_2 + \boldsymbol{p}\boldsymbol{G}^{(3)} \boldsymbol{b}_1 \boldsymbol{b}_2 \boldsymbol{b}_3\right). \tag{7.49c}$$

For a gradiometer of order k the output can be generalized (including eddy current terms corresponding to higher gradients) as

$$g^{(k)} = a\left(\boldsymbol{C}_B \boldsymbol{B} + \boldsymbol{E}_B \dot{\boldsymbol{B}} + \sum_{i=1}^{k-1} \boldsymbol{C}_{Gi} \boldsymbol{y}_i \prod_{j=1}^{i} \boldsymbol{b}_j + \sum_{i=1}^{k-1} \boldsymbol{E}_{Gi} \dot{\boldsymbol{y}}_i \prod_{j=1}^{i} \boldsymbol{b}_j + \boldsymbol{p}\boldsymbol{G}^{(k)} \prod_{i=1}^{k} \boldsymbol{b}_i\right) \tag{7.49d}$$

where Π signifies the product, b_1, b_2, b_3, and b_i are the baselines of the first-, second-, third, and i^{th}-order gradiometer and a is the gradiometer gain equal to the inverse of the field-to-flux conversion coefficient (assumed to be the same for all gradiometer orders). The $\boldsymbol{C}_B$, $\boldsymbol{C}_{G1}$, $\boldsymbol{C}_{G2}$, and $\boldsymbol{C}_{Gi}$ are 3, 5, 7, and $(3+2i)$-component common-mode vectors, $\boldsymbol{E}_{Gi}$ is the $(3+2i)$-component eddy-current vector, $\boldsymbol{y}_1$, $\boldsymbol{y}_2$, and $\boldsymbol{y}_i$ are 5, 7, and $(3+2i)$-component vectors with elements equal to the independent components of the first, second, and i^{th}-gradient tensors, and $\boldsymbol{G}^{(1)}$, $\boldsymbol{G}^{(2)}$, $\boldsymbol{G}^{(3)}$, and $\boldsymbol{G}^{(k)}$ are the first, second, third, and k^{th}-gradient tensors. The far right-hand terms in (7.49) are the desired gradiometer responses; all other terms are undesirable and should be balanced out. The balancing is usually done synthetically by determining the coefficients between the references and the primary sensors. Only in simple systems, consisting of one or a few channels, is hardware or electronics balancing practical [191–194]. The balancing accuracy must be quite high, especially for higher-order gradiometers, and it is also necessary to construct the sensor reference system with utmost rigidity [173].

Noise cancellation by synthetic third-order gradiometers within a modestly shielded room is illustrated in Figure 7.7(b). The primary channel was a first-order hardware gradiometer with a 5 cm baseline [169]. Even within the shielded room, the synthesis of a third-order gradiometer reduces noise at low frequencies by about four orders of magnitude, relative to the magnetometers. This result is also shown in Figure 7.7(a) by the dashed line 7. The combined noise attenuation of the mod-

estly shielded rooms and gradiometers is more than 5.5 orders of magnitude at low frequencies and is shown by line 8 in Figure 7.7(a).

The environmental noise can also be removed using adaptation, as discussed in Section 7.7.4.1. To determine the adaptive coefficients, the system of primary sensors and references is observed during the application of noise and the adaptive coefficients are adjusted to minimize this noise. The frequent need for re-adaptation for every dewar orientation or change of the noise character makes the adaptive systems less desirable than the gradiometers. Furthermore, the adaptive methods may not provide linear combinations which give the lowest white noise. The adaptation can be done with constant coefficients or with frequency dependent coefficients [169].

Constant coefficient adaptive noise cancellation applied in addition to the synthetic third-order gradiometer is illustrated in Figure 7.7(b), line 5. This figure also shows that, at low frequencies, the combined shielded rooms, gradiometers, and adaptation, attenuates noise by more than seven orders of magnitude, see line 9 in Figure 7.7(a). This performance is also compared with the high-T_c superconducting shield [119] and the high-performance Berlin room [117] in Figure 7.13(a) and it indicates that combined synthetic noise cancellation with modestly shielded rooms can successfully compete with the best available shielded environments.

7.7.4.3 Mobile Systems

The mobile systems for geophysical or military applications usually operate in relatively low environmental gradients and employ first-order gradiometers. The higher-order gradiometers are not used because the distances to the targets are large and signal strengths decay with distance (characteristic of their performance). Since the mobile systems use first-order gradiometers, then (7.49a) applies and can be rewritten for gradient component k (k=11, 12, 13, 22, 23, where the pairs of indices are determined by the orientations of the vectors $\boldsymbol{p}$ and $\boldsymbol{b}_1$) as

$$g_k^{(1)} = a_k\left(\boldsymbol{C}_B\boldsymbol{B} + \boldsymbol{E}_B\dot{\boldsymbol{B}} + \boldsymbol{p}\boldsymbol{G}^{(1)}\boldsymbol{b}_1\right). \tag{7.50}$$

The mobile gradiometers and magnetometers move relative to the environment and detect motion-induced noise. If it is assumed that the environmental gradient is constant and equal to $\boldsymbol{G}_E$, then five linearly independent components of this gradient tensor (see Section 7.7.4.2) can be arranged into a five-component column vector, e.g., $\boldsymbol{y}_E = (G_{11}, G_{12}, G_{13}, G_{22}, G_{23})^T$.

To simplify the discussion, assume that the vectors $\boldsymbol{C}_B$ and $\boldsymbol{E}_B$ in (7.50) are zero (extension to nonzero vectors is straightforward). Further, assume that the gradiometer motion is described by a matrix of rotation, $\boldsymbol{a}$ (translational terms vanish for a perfectly balanced gradiometer moving in a constant first gradient). The rotated gradient tensor, as seen by the gradiometer, will be $\boldsymbol{G}_R = \boldsymbol{a}\boldsymbol{G}_E\boldsymbol{a}^T$. Since the rotated tensor depends only on the five components of $\boldsymbol{y}_E$, the matrix of rotation terms in front of each component can be collected (including the gains) and the rotated gradiometer output g_k^R can be expressed as $g_k^R = \boldsymbol{A}_k^T\boldsymbol{y}_E$, where $\boldsymbol{A}_k$ is a five component vector with elements constructed from the sensor gains and the elements of the matrix $\boldsymbol{a}$. The gradiometer outputs corresponding to the five independent components of

the gradient tensor can be arranged into a vector $\boldsymbol{g}^R = \boldsymbol{A}^T \boldsymbol{y}_E$, where the columns of the 5×5 matrix $\boldsymbol{A}$ are the vectors $\boldsymbol{A}_k$.

Assume that there is a crosstalk present and that a 5×5 matrix $\boldsymbol{X}$ describes it. Then the tensor gradiometer will measure vector $\boldsymbol{g}^m = \boldsymbol{X}^T \boldsymbol{g}^R = \boldsymbol{X}^T \boldsymbol{A}^T \boldsymbol{y}_E$. In general, the expression for each gradiometer (each element of $\boldsymbol{g}^m$) contains 25 unknown products between the elements of the matrix $\boldsymbol{X}$ and the vector $\boldsymbol{y}_E$. If the matrix $\boldsymbol{A}$ is known (through the knowledge of the matrix of rotation $\boldsymbol{a}$ and the gradiometer calibration), then the 25 unknown parameters can be determined from measurement during the gradiometer motion in a constant gradient. In the absence of crosstalk (or if the crosstalk is known), each gradiometer will depend on only five unknown components of the vector $\boldsymbol{y}_E$. In practice, additional parameters due to unknown $\boldsymbol{C}_B$ and $\boldsymbol{E}_B$ must also be added to the computational procedure.

For a hand-held device operated in high-order gradients of an urban environment, the above procedure cannot be used because the first gradients are not constant. As an example, consider a second-order tensor gradiometer, which is well balanced against three components of the magnetic field and five components of the first gradient tensor. Since the second gradient tensor has seven linearly independent components (Section 7.7.4.2), extrapolation of the above method would suggest that 49 calibration coefficients are needed. If also the second gradient was non-uniform and the third-order gradiometer was required to compensate for the motion, the number of coefficients would be 81. Presently, the values of second and third gradients in the unshielded or shielded environments have not been reported in the literature. However, they were deduced from the estimated distance to the gradient-generating objects in Table 7.9.

The motion–noise cancellation in high-gradient environments is relatively complex and can be avoided under certain conditions. For example, if the environmental third gradient was negligible, then a well balanced third-order gradiometer would be immune to motion. Such a condition is satisfied within modestly shielded rooms [106], where the immunity to small motions has been demonstrated in MEG measurements during an epileptic seizure when the patient moved and slightly shifted the dewar. The magnetometers recorded about 100 pT and the first-order gradiometers about 10 pT signals, while the third-order gradiometer output remained unperturbed [173] (to within the SQUID noise resolution, or about 1/2 of the SQUID peak-to-peak noise; the measurement was performed with $\Delta f = 70$ Hz bandwidth, $B_w = 5$ fT rms/$\sqrt{\text{Hz}}$, and $B_{p-p}/2 \approx 5 B_w \sqrt{\Delta f/2} = 105\ \text{fT}_{p-p}$). Similar results were obtained with fetal MEG where mothers actually sit on the dewar and transmit vibrations directly into it. The third-order gradiometer outputs still exhibit noise of $< 10\ \text{fT}/\sqrt{\text{Hz}}$ [174]. The results above are consistent with the third gradient values within a shielded room of $G^{(3)} \approx 4\ \text{nT/m}^3$ for $r = 10$ m, in Table 7.9. If a third-order gradiometer were to be moved by a small distance $\Delta r \approx 0.5$ cm in such a gradient field, and if the relevant baselines were $b_1 = 5$ cm, $b_2 = 20$ cm, and $b_3 = 15$ cm [169], then the signal change would be $6 G^{(3)} b_1 b_2 b_3 \Delta r / r \approx 18$ fT. Such a signal change is small in comparison with brain noise. However, the same motion in an unshielded environment where the third gradient value may be as large as 40–600 nT/m^3, would

produce unacceptably large signal changes of 180 fT–2.7 pT and motion noise cancellation would have to be implemented.

7.7.5 Noise Cancellation Without the References

Noise cancellation without the references is possible only in systems with a larger number of channels. The operations are usually performed in the so-called "signal space", a multidimensional space where the number of dimensions is equal to the number of channels, K. A single measurement is represented by a vector in the signal space, and a sequence of measurements is represented by a vector whose orientation and length are changing. Noise or signal sources occupy certain vectors in the signal space. Noise cancellation by the techniques mentioned in this section is sometimes called spatial filtering.

Gradiometers with their spatially separated coils can also be considered as spatial filters [203]. They reject sources which produce spatially uniform fields, and detect only the sources which produce large spatial variations (i.e., large spatial gradients); so they function as spatial high-pass filters. Gradiometers are usually utilized to separate, within one sensor, distant and near sources (distant sources produce only low-spatial frequencies and near sources produce high-spatial frequencies). The spatial filtering considered in this section separates the sources corresponding to different signal space vectors, where the sources do not need to be at different distances from the sensor array. The source separation is accomplished by considering signals measured simultaneously by many sensors.

The simplest spatial filtering method is Signal Space Projection (SSP) [195–197], which projects out from the measurement, those noise components that are oriented along specific spatial vectors in the signal space. Assume that the noise components (vectors) are known. Assuming that the noise is stationary during the measurement, the noise vectors can be determined, e.g., by measuring the environmental noise before the application of the required signal to the SQUID system. Denote the noise column vectors by $\boldsymbol{V}_k$, $k=1, \ldots K_N$, $K_N < K$, where K is the number of channels, and arrange them in a $K \times K_N$ matrix $\boldsymbol{V}=(\boldsymbol{V}_1, \boldsymbol{V}_2, \ldots \boldsymbol{V}_{K_N})$. The matrix $\boldsymbol{V}$ describes the "noise subspace" and it can be used to construct parallel, $\boldsymbol{P}_{\|}$, and orthogonal, $\boldsymbol{P}_{\perp}$, projection operators [199] as

$$\boldsymbol{P}_{||} = \boldsymbol{V}\left(\boldsymbol{V}^T\boldsymbol{V}\right)^{-1}\boldsymbol{V}^T \quad \text{and} \quad \boldsymbol{P}_{\perp} = \boldsymbol{I} - \boldsymbol{P}_{||} \tag{7.51}$$

where $\boldsymbol{I}$ is the identity matrix and the superscript T denotes transposition. The operator $\boldsymbol{P}_{\|}$ will project data into a subspace parallel to the noise subspace, while the operator $\boldsymbol{P}_{\perp}$ will project the data into a subspace orthogonal to the noise subspace. If a $K \times N$ matrix $\boldsymbol{m}$ describes the measured data, where N is the number of time samples, then the projection operators are applied to the measurement as $\boldsymbol{P}_{\|}\boldsymbol{m}$ and $\boldsymbol{P}_{\perp}\boldsymbol{m}$.

The functioning of the projection operators is illustrated in Figure 7.24 for a simple system of 34 axial gradiometers uniformly distributed on a hemispherical sur-

face and oriented along the local surface normal (since the gradiometer baselines are parallel to the local radius vector, they are often called radial gradiometers). The system also contains one signal and one noise source. The signal and noise are mixed at the sensors and they are in a similar bandwidth, such that they cannot be separated by temporal filtering (compare Figures 7.24(b) and (d)). Yet it is possible to project out the noise from the data to retrieve the original signal, see Figure 7.24(g). The method works best when the signal and noise subspaces are nearly orthogonal.

More insight into the mechanics of the SSP can be obtained by first considering the measurement when only the noise is present. The noise at time t_n can be modeled as [196]

$$\boldsymbol{m}_{noise}(t_n) = \boldsymbol{V}\boldsymbol{a}(t_n) + \boldsymbol{v}(t_n) \tag{7.52}$$

where $\boldsymbol{m}_{\text{noise}}(t_n)$ is the K-component vector of noise measurement at time t_n, $\boldsymbol{v}(t_n)$ is the K-component sensor noise vector, and the noise space waveforms $\boldsymbol{a}(t_n) = \{a_1(t_n), a_2(t_n), \ldots, a_{K_N}(t_n)\}^T$ describe the time dependence of the noise source magnitudes. If $\boldsymbol{v}$ is normally distributed, the unbiased estimate for $\boldsymbol{a}(t_n)$ is obtained as $\boldsymbol{a}(t_n) = \boldsymbol{w}^+\boldsymbol{m}_{noise}(t_n)$, where $\boldsymbol{w}^+ = (\boldsymbol{V}^T\boldsymbol{V})^{-1}\boldsymbol{V}^T$ is the Moore–Penrose pseudoinverse.

Let the required signal be described by a $K \times K_S$ matrix $\boldsymbol{U} = (\boldsymbol{U}_1, \boldsymbol{U}_2, \ldots \boldsymbol{U}_{K_S})$ and the corresponding signal space waveforms $\boldsymbol{u}(t_n) = \{u_1(t_n), u_2(t_n), \ldots, u_{K_S}(t_n)\}^T$. Then, in the presence of both signal and noise, the measurement is given by

$$\boldsymbol{m}(t_n) = \boldsymbol{V}\boldsymbol{a}(t_n) + \boldsymbol{U}\boldsymbol{u}(t_n) + \nu(t_n). \tag{7.53}$$

Application of the orthogonal projection operator $\boldsymbol{P}_\perp$, see (7.51), to the measurement in (7.53) will yield

$$\boldsymbol{P}_\perp\boldsymbol{m}(t_n) = \boldsymbol{P}_\perp\boldsymbol{U}\boldsymbol{u}(t_n) + \boldsymbol{P}_\perp\nu(t_n). \tag{7.54}$$

Equation (7.54) indicates that the noise has been projected out and if none of the vectors $\boldsymbol{U}_k$, $k = 1, 2, \ldots K_S$, are completely in the noise subspace then the projected measurement will preserve the required signal. (7.54) also indicates that the signal in the projected measurement will be affected by the projection operation; so instead of the spatial distribution $\boldsymbol{U}$, we shall have the spatial distribution $\boldsymbol{P}_\perp\boldsymbol{U}$. The signal will be redistributed among the channels by the action of the projection operation [200]. This can also be seen in Figure 7.24 where the signals in frames (b) and (g) have different amplitudes, indicating a redistribution of the signal among different channels. More examples of the redistribution are shown in [201]. The signal redistribution will be smallest when the signal and noise subspaces are nearly orthogonal.

Related to the SSP is the noise elimination by rotation in the signal space [198], which avoids the loss of degrees of freedom encountered in SSP. In this method, a set of virtual "compensator" channels is added to the system and the rotation is arranged such that the compensator channels contain a projection of the input sig-

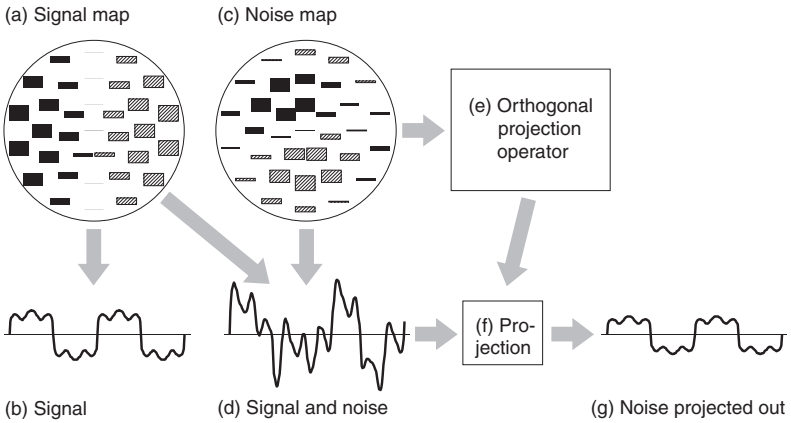

Fig. 7.24 Illustration of noise cancellation by Signal Space Projection. The signal and noise vectors are represented by block-maps in (a) and (c). The block height denotes the vector component magnitude corresponding to a particular sensor: black is positive, hatched is negative. Time courses correspond to the same selected channel and are shown on the same scale. Sensors are radial gradiometers with 5 cm baseline uniformly distributed on the surface of a hemisphere with radius 11 cm. The number of sensors is $K = 34$ and the mean distance between the sensors is about 5 cm. (a) Signal generated by a magnetic dipole positioned at the center of the sensor hemisphere, located at the coordinate origin. Dipole orientation is (0, 1, 0) and its moment M_{source} is variable in time. (b) Time course of the source waveform. (c) Noise is generated by a magnetic dipole positioned at (10, 3, 0) m and oriented along (0, 0.287, 0.958). The noise dipole is time variable with magnitude $3 \times 10^7 M_{source}$. (d) Combination of signal and noise at the selected channel. (e) Noise is used to construct an orthogonal projection operator. (f) Noise is projected out from the combination of signal and noise in 'd'. (g) The original signal waveform is retrieved.

nal into interference subspace, while the real channels are orthogonal to it. The number of compensation channels is equal to the dimensionality of the interference subspace. The interference subspace can be determined from the noise measurement by the principal component analysis.

Other array techniques, such as beamformers and MUSIC also provide efficient cancellation of the environmental noise. These techniques are mostly used for signal extraction from the region of interest and the environmental noise cancellation is their beneficial side effect. These methods will be discussed in greater detail in the second volume of this Handbook in the chapter on Biomagnetism.

7.8
Signal and Noise Implications for the SQUID System Design

7.8.1
Introduction

The operation of a high-resolution SQUID system within high environmental noise, imposes special demands on the system parameters. Such demands must be met in order to realize the high degree of noise cancellation discussed in Section 7.7. The parameters affected by these demands include environmental noise attenuations, common-mode and eddy-current vector magnitudes, slew rates, dynamic range, nonlinearity, and inter-channel matching. These parameters will be discussed in this section and their determination will be outlined for static and mobile systems.

7.8.2
Static SQUID Systems

Static systems (e.g, MEG, NDE, geophysical, etc.) have to operate in changing environmental fields (noise) and are subjected to vibrations. Assume that the electronics bit resolution in field units (T) is ∂B and $b\partial G$ for the magnetometers and first-order gradiometers, respectively, and b is the gradiometer baseline. The electronics resolution can be different from the system white noise in 1 Hz bandwidth, δB or $b\delta G$ (in this section, δB and δG represent all noise at the output and include the SQUID and electronics noise, B_N, dewar noise, etc.). For the present purposes it will be assumed that $\delta B = 2^q \partial B$ or $\delta G = 2^q \partial G$ (e.g., $q = 4$ in some commercial MEG systems [172, 121]). Denote the gradiometer common-mode and eddy-current vectors by $\boldsymbol{C}_B$ and $\boldsymbol{E}_B$ (Section 7.7.4), the amplitudes of the applied fields and gradients by ΔB and ΔG, and their angular frequency by $\omega = 2\pi f$. The ΔB and ΔG can represent either signals or environmental noise.

Let the operational parameters of the SQUID system be: ψ – the environmental noise attenuation; D – the dynamic range; $\dot{B}$ (or $\dot{G}$) – the slew rate; L – the nonlinearity; δt – the delay among channels, and subscripts '*mag*' and '*grd*' denote the magnetometer or gradiometer sensors. The noise attenuation, ψ, should reduce the environmental noise down to, or below, the instrumental white-noise level in a representative bandwidth. Since the required ψ will be largest for narrow bandwidth experiments, the representative bandwidth is arbitrarily chosen to be 1 Hz. Then the ψ is given by

$$\psi_{mag} = \Delta B/\delta B, \qquad \psi_{grd} = \Delta G/\delta G. \tag{7.55}$$

The dynamic range can be defined as the applied peak-to-peak field or gradient magnitude divided by the electronics resolution [132]. The division by the electronics resolution, rather than by the white noise in the 1 Hz bandwidth, is necessary because it determines the true dynamic range of the electronics system.

$$D_{mag} = 2\Delta B/\partial B = 2^{q+1}\Delta B/\delta B, \qquad D_{grd} = 2\Delta G/\partial G = 2^{q+1}\Delta G/\delta G. \tag{7.56}$$

The factor of $q+1$ arises because we are dividing a peak-to-peak signal which is equal to twice the magnitude. The dynamic range for low-frequency noise must be computed by integrating over the frequency range of interest [132]. The maximum-field slew rate for a sinusoidal signal with amplitude ΔB is $\dot{B} = \omega\Delta B$ (T/s). The slew rate for gradiometers is obtained, similarly, by replacing ΔB by $b\Delta G$. The slew rate can be expressed in Φ_o/s by dividing the $\dot{B}$ by the SQUID field-to-flux conversion coefficient, $B_\Phi = \delta B/\delta\Phi$ (T/Φ_o), and substituting for ΔB or ΔG from (7.56). The $\delta\Phi$ is either the magnetometer, $\delta\Phi_B$, or the gradiometer, $\delta\Phi_G$, flux resolution referenced to the system field or gradient noise. The magnetometer and gradiometer slew rates (in Φ_o/s) then become [132]

$$\dot{\Phi}_{mag} = \omega\delta\Phi_B \frac{\Delta B}{\delta B} = \omega\delta\Phi_B \frac{D_{mag}}{2^{q+1}}, \qquad \dot{\Phi}_{grd} = \omega\delta\Phi_G \frac{\Delta G}{\delta G} = \omega\delta\Phi_G \frac{D_{grd}}{2^{q+1}}. \tag{7.57}$$

The system nonlinearity, L_{mag} or L_{grd}, may be defined as a deviation from the linear input–output relationship. It is important to keep the nonlinearity small in order that large numbers may be accurately substracted during the noise cancellation (Section 7.7.4). The noise cancellation will only be as good as the nonlinearity. The required nonlinearity may be defined as the ratio of the white noise in 1 Hz bandwidth to the peak-to-peak signal amplitude [132]

$$L_{mag} = \delta B/(2\Delta B) = 2^q/D_{mag}, \qquad L_{grd} = \delta G/(2\Delta G) = 2^q/D_{grd}. \tag{7.58}$$

For example, in the presence of polynomial nonlinearity of order n, the measured field will be given as $B_{\mathrm{meas}} = \Delta B + \varphi_n\Delta B^n = \Delta B(1 + \varphi_n\Delta B^{n-1})$, where the relative deviation from linearity, $\varphi_n\Delta B^{n-1}$, should satisfy $\varphi_n\Delta B^{n-1} \le \delta B/\Delta B = 2L_{\mathrm{mag}}$. The nonlinearity discussed in Section 4.2.1 corresponds to the sinusoidal SQUID transfer function where, for small excursions around the working point, the nonlinearity order is $n = 3$.

Equation (7.58) shows that the acceptable nonlinearity is inversely proportional to the dynamic range. (7.56)–(7.58) are also valid for the gradiometer output, due to the common-mode signal, rather than the gradient variation. Equivalent expressions for the common-mode signal can be obtained by the replacement $b\Delta G \to C_B\Delta B$ in (7.56)–(7.58).

The time delay between the reference and primary sensors (Section 7.7) is manifested as an eddy-current term in the balancing equations [169]. This eddy-current term can be handled either by: (i) making the time delay sufficiently small so that the eddy-current term is negligible; or by (ii) balancing out the eddy-current term. In the following discussion, it will be assumed that the common-mode term (Section 7.7.4) is completely balanced out. The eddy-current term due to the time delay δt among the channels will be negligible if the time delay satisfies $\delta t \le \delta t^{(1)}$ [132], where

$$\delta t^{(1)} = L_{mag}/(\pi f C_B) = 2^q/\left(\pi f D_{mag} C_B\right) \tag{7.59}$$

where C_B is the gradiometer common-mode vector magnitude. If subtraction between two magnetometers is attempted, then $C_B = 1$ in (7.59) and $\delta t^{(1)}$ is much smaller than that for the gradiometers. If the field common-mode and the eddy-current vectors are both balanced out by frequency-independent coefficients, see, e.g., (7.46), then the cancellation error will be caused only by the frequency dependence of the C_B and E_B, see (7.42)–(7.44), and the delay must satisfy $\delta t \le \delta t^{(2)}$ [132], where

$$\delta t^{(2)} = \sqrt{\delta t^{(1)}/(\pi f)}. \tag{7.60}$$

In all practical situations $\delta t^{(2)} \gg \delta t^{(1)}$. The delay limit $\delta t^{(1)}$ is difficult to achieve. It is less than 100 ps for unshielded magnetometers and about 100 ns for unshielded gradiometers. The limit $\delta t^{(2)}$ is larger than several 100 ns even for unshielded magnetometers and is relatively easy to achieve, however, it requires differentiation, see (7.39) and (7.42). Simple differentiators are sufficiently accurate only if the sampling rates are high. For example, a three-point differentiator and maximum signal frequency of 60 Hz would require sample rates in excess of 17.5 kHz to achieve an eddy current subtraction error less than the SQUID sensor noise in a 1 Hz bandwidth. Such high sample rates are impractical, especially in multichannel systems, and therefore accurate but computationally more expensive, differentiators must be used [170, 202].

The delay between channels becomes completely unimportant from the gradiometer balancing point of view if the frequency-dependent balancing is implemented, e.g., using the coherence method [171]. This method provides separate common-mode and eddy-current balancing at each frequency and operates by eliminating coherent parts of the sensor and reference outputs (note, however, that the time delay between the channels must still be kept low for accurate signal analysis and interpretation).

During ordinary use, even stationary systems are subjected to small vibrations. For example, the biomedical systems are often in contact with the subjects, and breathing, heart beats, and other tremors are transmitted to the SQUID system. Similarly, the systems for non-biological measurements are subject to vibrations induced by the environment. The vibrations can either rotate or translate the SQUID system [169]. The translational vibrations produce noise through motion in environmental gradients. If the translational vibration amplitude is Δd, then the translational noise is given as

$$\Delta B_T = G\Delta d, \qquad \Delta G_T^C = C_B \Delta B_T = C_B G \Delta d, \qquad \Delta G_T^G = \Delta d G^{(2)} b, \tag{7.61}$$

where b is the gradiometer baseline and $G^{(2)}$ is the second gradient. The rotational vibrations are proportional to the angle of rotation, θ:

$$\Delta B_R = \theta B, \qquad \Delta G_R^C = C_B \Delta B_R = \theta C_B B, \qquad \Delta G_R^G = \theta G b. \tag{7.62}$$

Tab. 7.10 Vibrational noise amplitudes, $\Delta d = 10\,\mu$m, $\theta = 10^{-5}$ rad, $b = 0.1$ m, $C_B = C_o = 10^{-3}$. Urban environment (Table 7.9): unshielded, $B = 55\,\mu$T, $G = G^{(1)} = 1000$ nT/m, $G^{(2)} = 400$ nT/m^2; modestly shielded, $B = 50$ nT, $G = 20$ nT/m, $G^{(2)} = 8$ nT/m^2. Modest shielding is provided by, e.g., VAC AK3b shielded room (Section 7.3). All entries are in fT; see (7.61) and (7.62) for definitions of symbols.

Environment	ΔB_T	ΔB_R	$b\Delta G_T^C$	$b\Delta G_R^C$	$b\Delta G_T^G$	$b\Delta G_R^G$
Unshielded	10 000	550 000	10	550	400	1 000
Shielded	200	500	0.2	0.5	8	20

In the above equations, the superscripts '*C*' and '*G*' denote the vibrational noise due to either the common-mode vector or the environmental gradients. The vibrational noise amplitudes are summarized in Table 7.10 for $\Delta d = 10\,\mu$m and $\theta = 10^{-5}$ rad (this θ corresponds to $10\,\mu$m motion at 1 m arm). The results indicate that for the selected parameters, the vibrational noise is quite severe in unshielded environments even for first-order gradiometers (but it is highly attenuated by higher-order gradiometers [173]). In shielded environments, the magnetometer vibrational noise is still unacceptably high, but the first-order gradiometer noise is nearly acceptable. Generally, the rotational vibrations produce larger noise than the translational vibrations.

Finally, the noise attenuation, ψ, will be considered. The required ψ can be obtained from the noise envelopes in Figure 7.13 and by assuming that the ultimate SQUID system white noise is about 2–5 fTrms/$\sqrt{\text{Hz}}$. At low frequencies (about 0.1 Hz), the noise attenuation for unshielded magnetometer-based systems would have to be up to $\psi_{mag} \approx 10^7$ and, in modestly shielded environments, $\psi_{mag} > 10^5$. Similarly for the gradiometer-based systems, the attenuations would have to be up to $\psi_{\text{grd}} \approx 10^5$ and $\psi_{\text{grd}} > 10^3$, for unshielded and modestly shielded systems, respectively. In highly shielded environments (high-T_c superconducting [119] or high-quality mu-metal [117] rooms) the noise appears to be sufficiently low even for magnetometers without any additional noise cancellation.

The required dynamic range and slew rates corresponding to the noise envelopes in Figure 7.13 are represented graphically in Figure 7.25.

Figure 7.25(a) indicates that for magnetometers in static unshielded environments the dynamic range due to low-frequency noise can be in excess of 30 bits and the power line slew rates can be of the order of 10^6 Φ_o/s. The use of gradiometers greatly relaxes the operational requirements. Even in unshielded environments, the gradiometer dynamic range is only up to 25 bits and the power line slew rates are of the order of 10^4 Φ_o/s. The conditions in modestly or well-shielded environments are easy to achieve even for magnetometers, Figure 7.25(b).

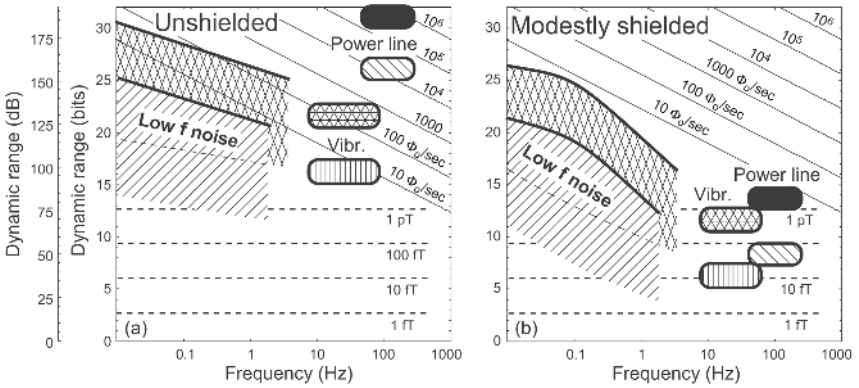

Fig. 7.25 Dynamic range as a function of frequency for the noise ranges shown in Figure 7.13, for magnetometer and gradiometer-based systems with white noise = 5 fT rms/$\sqrt{\text{Hz}}$, $q = 4$, gradiometer baseline of $b = 0.05$ m, $\Delta d = 10\,\mu$m, $\theta = 10^{-5}$, and $C_B = C_o = 10^{-2}$. Unshielded dc fields and gradients were 55 μT and 200 nT/m, and shielded, 55 nT and 10 nT/m, respectively. Field power line amplitudes were 200 nT in unshielded and 2 pT in shielded environments. Signal levels corresponding to 1 fT, 10 fT, 100 fT and 1 pT are shown by dashed lines. Modified from [132]. (a) Unshielded. (b) Shielded.

7.8.3 Mobile SQUID Systems

Mobile systems for geophysical or military applications usually use first-order SQUID tensor gradiometers and vector magnetometers. The gradiometers are employed not only because they provide more information than the magnetometers (five linearly independent components, rather than three for magnetometers, see Section 7.7.4.2), but also because they have additional advantages. Gradiometers are less sensitive to micropulsations[3)] and diurnal variations of the earth's field, because these variations originate at large distances and are spatially uniform. Gradiometers exhibit reduced sensitivity to the altitude variations. If the altitude change is small in comparison with the distance to the source, r, then the ratio of the gradient variation, ΔG, to the field variation, ΔB, is approximately $b\Delta G/\Delta B \approx nb/r \ll 1$ because $b \ll r$. The distance–decay exponent n depends on the source type and is $n = 3$ for a magnetic dipole. Gradiometers have better spatial resolution than magnetometers because the gradients decay faster with distance than the fields. For the same reason, the gradiometers also enhance the near-surface structures relative to deeply buried structures, and also enhance a local anomaly relative to large-scale regional variations, if they are at similar distances from the gradiometer (by the ratio of their

3) Micropulsations are small, almost sinusoidal fluctuations of the geomagnetic field, usually with a duration of seconds to minutes and a frequency range from mHz to Hz. Micropulsations are responses to changes in the magnetosphere. Pulsations are divided into two classes; continuous and irregular, each of which is further divided according to the period of the pulsations.

distance–decay exponents, n_{loc}/n_{reg}, where n_{loc} and n_{reg} are the distance–decay exponents for the local and the regional variations, $n_{loc} > n_{reg}$. For example, the local anomaly can be an extrusion or a dipole with $n_{loc} = 3$ or a magnetized cylinder with $n_{loc} = 2$, while the regional anomaly could be a thin magnetized dipping sheet with $n_{reg} = 1$, or a large magnetized region, or a thick polarized dipping sheet with $0 < n_{reg} < 1$).

The gradiometer motion in the environmental magnetic field (usually the earth's field) produces noise. To reduce (or eliminate) the field motion noise, the gradiometers must be well balanced. Since accurate hardware balancing is impractical, gradiometers are balanced synthetically using a reference vector magnetometer. The magnetometer gain must be designed such that the gradiometer noise is not degraded by the balancing. Let the SQUID signals corresponding to the reference magnetometers (in Φ_o) be $r_i = a_B B_i$, $i = 1, 2, 3$, where B_i is the i^{th} component of the applied magnetic field and a_B is the reference magnetometer gain, assumed to be the same for all three magnetometer components (the gain was defined in Section 7.7.4.2 as an inverse of the field-to-flux conversion coefficient and is expressed in Φ_o/T). Further, assume that the output of the gradiometer (also in Φ_o) is $g = a(\boldsymbol{C}_B \boldsymbol{B} + Gb)$, where a is the gain and G is the magnitude of the gradient tensor component to be measured. Assume that the magnetometer and gradiometer white-noise levels in the 1 Hz bandwidth are δB and δG. Then the corresponding flux noise of the magnetometer and gradiometer SQUIDs are $\delta\Phi_r = a_B \delta B$ and $\delta\Phi_G = ab\delta G$. The noise contributed by the balancing should be less than the gradiometer noise, or $C_B \delta B < b\delta G$. This condition determines the required magnetometer gain as

$$a_B > \frac{C_B \delta \Phi_r}{b\delta G} \qquad \text{or} \qquad a_B = \zeta \frac{C_B \delta \Phi_r}{b\delta G} \tag{7.63}$$

where the parameter $\zeta > 1$ describes the strength of the inequality. The "as made" gradiometer common-mode vectors are typically in the range from 10^{-2} to 10^{-4}. For illustration purposes, assume $C_B = C_o = 10^{-3}$, the gradiometer baseline $b = 0.1$ m, the reference magnetometer SQUID flux noise $\delta\Phi_r \approx 10^{-5}\ \Phi_o$ rms/$\sqrt{\text{Hz}}$, and the required gradient resolution to be about $\delta G = 20$ fT/m rms/$\sqrt{\text{Hz}}$ (corresponding to the gradiometer gain $a \approx 5 \times 10^9\ \Phi_o$/T if $\delta\Phi_G = \delta\Phi_r$). Then the required magnetometer gain is $a_B > 5 \times 10^6\ \Phi_o$/T, and for $\zeta = 4$, the magnetic field resolution should be $\delta B = 0.5$ pT rms/$\sqrt{\text{Hz}}$.

The maximum allowed common-mode vector magnitude, C_R, may be estimated from the assumed environmental field amplitude during the motion, ΔB_E. If the measurement bandwidth is Δf, and if the common-mode signal is required to be smaller than the gradiometer rms noise, then $C_R 2\Delta B_E < b\delta G\sqrt{\Delta f}$, or

$$C_R \leq \frac{b\delta G\sqrt{\Delta f}}{2\Delta B_E} \tag{7.64}$$

where a peak-to-peak environmental field variation was used. If the gradiometer resolution was $\delta G = 20$ fT/m rms/$\sqrt{\text{Hz}}$, $b = 0.1$ m, $\Delta f = 4$ Hz, and the gradiometer was

rotated by 360° in the earth's field, then $\Delta B_E = B_E \approx 55\,\mu$T, and $C_R \leq 3.6\times10^{-11}$. This is also the required common-mode stability (or system rigidity). It is an incredibly small value – if the gradiometer coils were 5 cm in diameter, then such a small C_R would be obtained by a gradiometer coil tilt corresponding to a 0.02 Å displacement of the coil rim. From the computational point of view, the common-mode vector must be improved by the magnetometer balancing by a factor of $C_R/C_o \approx 3.6\times10^{-8}$ if the "as made" gradiometer common-mode vector magnitude was $C_o = 10^{-3}$. If the motion was stabilized to, e.g., $\phi = \pm 0.5°$, then $\Delta B_E \approx B_E \sin\phi \approx 480$ nT, the required common-mode vector would be $C_R \leq 4.2\times10^{-9}$, and the required improvement of the gradiometer balance would be $C_R/C_o \approx 4.2\times10^{-6}$. The common-mode vector for the stabilized platform would correspond to coil-edge motion of ≈ 2 Å, or about one atomic distance. This example illustrates the importance of achieving the smallest possible magnitude of the "as made" common-mode vector, C_o, and the highest possible degree of rigidity.

The dynamic range is given by (7.56). The reference magnetometer dynamic range can be obtained from (7.56) by expressing the field resolution in terms of the SQUID flux noise, $\delta\Phi_r$, and substituting for gain from (7.63). The required gradiometer dynamic range is defined either by the gradient changes, D^G_{grd}, or through the common-mode vector, D^C_{grd}. The latter is obtained from (7.56) by substituting $b\Delta G_E = C_B \Delta B_E$. Then the dynamic ranges are given by

$$D_{mag} = \zeta \frac{2^{q+1} C_B \Delta B_E}{b\delta G}, \qquad D^G_{grd} = \frac{2^{q+1}\Delta G_E}{\delta G}, \qquad D^C_{grd} = \frac{D_{mag}}{\zeta}. \tag{7.65}$$

If the gradiometer was rotated by 360° in the earth's field, then $\Delta B_E = 55\,\mu$T and $\Delta G_E = 20$ nT/m (see Table 7.4 for rural environment). Then for $q = 4$, $\zeta = 4$, $b = 0.1$ m, $C_B = C_o = 10^{-3}$, and $\delta G = 20$ fT/m rms/√Hz, the dynamic ranges would be $D_{mag} = 3.5\times10^9$ (31.7 bits), $D^G_{grd} = 3.2\times10^7$ (24.9 bits), and $D^C_{grd} = 8.8\times10^8$ (29.7 bits). If the platform was again stabilized to ±0.5°, then the dynamic ranges would be reduced by a factor of $1/\sin(0.5°) \approx 114.6$ or by about 6.8 bits.

Assume that the SQUID detector is rotating in a uniform field and gradient with angular rate ω. Then expressing $\delta B = \delta\Phi_r/a_B$ from (7.63) and substituting it into (7.57) and equating $\delta\Phi_r = \delta\Phi_G = \delta\Phi$, the reference magnetometer and gradiometer slew rates are obtained as

$$\dot{\Phi}_{mag} = \omega\delta\Phi \frac{C_B\Delta B_E}{b\delta G}\zeta, \quad \dot{\Phi}^G_{grd} = \omega\delta\Phi\frac{\Delta G_E}{\delta G}, \qquad \dot{\Phi}^C_{grd} = \frac{\dot{\Phi}_{mag}}{\zeta}, \tag{7.66}$$

where the right-hand part of (7.66) was again obtained by substituting $b\Delta G_E \rightarrow C_B\Delta B_E$. Assume that $\omega = 90$ deg/s ≈ 1.57 rad/s ($f = 0.25$ Hz) and that the parameters are the same as in the example for (7.65). Then the slew rates are $\dot{\Phi}_{mag} = 1{,}728\,\Phi_o$/s, $\dot{\Phi}^G_{grd} = 15.7\,\Phi_o$/s, and $\dot{\Phi}^C_{grd} = 432\,\Phi_o$/s. Such slew rates are small and any SQUID system should be able to achieve them.

The acceptable nonlinearity, as given by (7.58) is proportional to the inverse of the dynamic range computed above. For a platform stabilized to about ±0.5°, a nonline-

arity of better than about 10^{-6} is required. Such a nonlinearity is achievable; values of 10^{-6} or less were measured in commercial MEG systems [121]. Sufficiently small nonlinearity is important for realization of the common-mode cancellation with the required accuracy.

If a system without the eddy-current cancellation was used, then the eddy-current error should be less than the system noise [169] (Section 7.7.4.2). Since the common-mode error was adjusted to be about equal to the system noise, the eddy-current contribution should be smaller than, or equal to, the common-mode signal, or $\omega E_R \leq C_R$. Consider a frequency $f = 1$ Hz, then for an unstabilized platform, the eddy-current vector magnitude should be $E_R \leq 5.8 \times 10^{-12}$ s and for a ±0.5° stabilized platform, $E_R \leq 6.7 \times 10^{-10}$ s. The eddy-current vector for a stabilized platform should be achievable. As an example, consider a relatively large eddy-current source represented by a Cu wire ring with a radius of 2.5 cm, wire diameter of 0.2 cm and resistivity of 1.75×10^{-8} Ωm at a distance of 0.75 m from a radial gradiometer with a baseline of 10 cm and a coil radius of 1 cm. Such a ring would induce $E \approx 6.5 \times 10^{-10}$ s.

Consider a SQUID tensor gradiometer moving in a constant gradient background. Such motion will introduce noise similar to that induced in magnetometers by the motion in the earth's field. It is not possible to use gradiometer references to eliminate this motion noise, because they would also eliminate the gradient signal. However, the motion noise can be cancelled using angular motion sensors as references (see Section 7.7.4.3 for discussion of the matrix of rotation). This type of noise cancellation, especially if higher-order gradients have to be accounted for as in the hand-held instruments, requires a high degree of accuracy; the nonlinearity, common-mode balancing, and stability discussed in this section then become extremely important.

7.8.4
Summary of Parameters

Examples of the SQUID system design parameters are shown in Tables 7.11–7.13. For each parameter, the difficulty of its realization is also indicated. Generally, most of the parameters in these tables can be met with low-T_c SQUIDs. The high-T_c devices are not as suitable, particularly for mobile applications, because they are too hysteretic when in motion and exposed to the earth's magnetic field [140]. However, there has been a report of an airborne HTS SQUID system for mineral exploration [138]. Issues that can cause problems are the high level of low-frequency noise and the difficulty in maintaining stable values of common-mode vectors with high-T_c devices.

Tab. 7.11 Examples of SQUID system design parameters for a static magnetometer. $q = 4$, $f_{low} = 0.1$ Hz, $\Delta B_{unshielded} = 100$ nT, $\Delta B_{shielded} = 1$ nT, $f_{power} = 60$ Hz, $\Delta B_{power\ unshielded} = 200$ nT, $\Delta B_{power\ shielded} = 2$ pT, $\delta\Phi = 10^{-5}\ \Phi_o$ rms/$\sqrt{\text{Hz}}$, and the maximum allowed inter-channel delay was computed at f_{power}.

Parameter	Unshielded Required	Difficulty	Modestly shielded Required	Difficulty
White noise δB (fT rms/$\sqrt{\text{Hz}}$)	5	Easy	5	Easy
Noise attenuation ψ_{mag}	2×10^{7}	Difficult	2×10^{5}	Possible
Dynamic range, D_{mag} (bits)	29.3	Easy	22.6	Easy
Nonlinearity, L_{mag}	2.5×10^{-8}	Not known	2.5×10^{-6}	Possible
Slew rate, $\dot{\Phi}_{mag}$ (Φ_o/s)	1.5×10^{5}	Possible	1.5	Easy
Inter-channel delay, $\delta t^{(2)}$ (ns)	593	Easy	187 566	Easy

Tab. 7.12 Examples of SQUID system design parameters for static gradiometer. $q = 4$, $b = 0.1$ m, $f_{low} = 0.1$ Hz, $b\Delta G_{unshielded} = 1$ nT, $b\Delta G_{shielded} = 50$ pT, $f_{power} = 60$ Hz, $b\Delta G_{power\ unshielded} = 5$ nT, $b\Delta G_{power\ shielded} = 200$ pT, $\delta\Phi = 10^{-5}\ \Phi_o$ rms/$\sqrt{\text{Hz}}$, $C_B = C_o = 10^{-3}$, and the maximum allowed inter-channel delay was computed at f_{power}.

Parameter	Unshielded Required	Difficulty	Modestly shielded Required	Difficulty
Noise, $b\delta G$ (fT rms/$\sqrt{\text{Hz}}$)	5	Easy	5	Easy
Noise attenuation, ψ_{grd}	2×10^{5}	Easy	1×10^{4}	Easy
Dynamic range, D_{grd} (bits)	22.6	Easy	18.3	Easy
Nonlinearity, L_{grd}	2.5×10^{-6}	Possible	5×10^{-5}	Easy
Slew rate, $\dot{\Phi}_{grd}$ (Φ_o/s)	3.8×10^{3}	Easy	0.15	Easy
Inter-channel delay, $\delta t^{(2)}$ (μs)	118.6	Easy	18 757	Easy

Tab. 7.13 Examples of SQUID system design parameters for mobile gradiometer system. $q = 4$, $\zeta = 4$, $b = 0.1$ m, $C_B = C_o = 10^{-3}$, $\delta\Phi = 10^{-5}\ \Phi_o$ rms/$\sqrt{\text{Hz}}$, $\delta G = 20$ fT/m rms/$\sqrt{\text{Hz}}$, $\Delta B_E = 55\ \mu$T, $G_E = 20$ nT/m (rural environment), $\Delta f = 4$ Hz, platform stability $\phi = \pm0.5°$, unstabilized platform is assumed to rotate with frequency of $f_{rot} = 0.25$ Hz, frequency for eddy current vector computation, $f_{eddy} = 1$ Hz. Linearity is not shown, but it is related to the dynamic range, see (7.58) and (7.65).

Parameter	Platform not stabilized Required	Difficulty	Platform stabilized Required	Difficulty
Mag. gain, a_B (Φ_o/T)	5×10^{6}	Easy	5×10^{6}	Easy
Mag. resol., δB (pT rms/$\sqrt{\text{Hz}}$)	0.5	Easy	0.5	Easy
Mag. dynamic range, D_{mag} (bits)	31.7	Easy	24.9	Easy
Mag. slew rate, $\dot{\Phi}_{mag}$ (Φ_o/s)	1728	Easy	negligible	Easy
Grad resol., δG (fT/m rms/$\sqrt{\text{Hz}}$)	20	Easy	20	Easy
Grad. dyn. range, D^{C}_{grd} (bits)	29.7	Easy	22.9	Easy
Grad. dyn. range, D^{G}_{grd} (bits)	24.9	Easy	18.1	Easy
Grad. slew rate, $\dot{\Phi}^{C}_{grd}$ (Φ_o/s)	432	Easy	negligible	Easy
Grad. slew rate, $\dot{\Phi}^{G}_{grd}$ (Φ_o/s)	15.7	Easy	negligible	Easy
C_R	3.6×10^{-11}	Not possible	4.2×10^{-9}	Very difficult
E_R (s)	5.8×10^{-12}	Very difficult	6.7×10^{-10}	Possible

7.9 Concluding Remarks and System Trends

The preceding sections provide an overview of issues relating to methods for optimizing the performance of a SQUID system. A large part of our considerations was based on practical experience gained in the development of various stationary and mobile magnetometer systems, especially those for biomagnetic and prospecting applications. However, these also remain largely valid for other SQUID-based systems, such as detector readout amplifiers, for example.

We defer the practical examples of the implementation of various precepts presented here, to the second volume of this Handbook. There, examples of developed systems will be discussed to illustrate how the specified performance can be achieved for a given application type with the help of the methods and approaches reviewed here.

Although quite complex in implementation, SQUID systems make it possible to perform extremely sensitive measurements of magnetic fluxes, fields and gradients (or physical quantities which can be related to these), which are not achievable by other means. This extreme sensitivity can be exploited even in the presence of spurious noise signals, which exceed the measured "useful" signal by orders of magnitude. Also, SQUID systems have a wide frequency response, exceeding that of most other magnetic field sensors. Finally, the extremely high dynamic range also makes SQUID systems truly unique. The various application examples described in the second volume, will illustrate the versatility of SQUID sytems and their potential for a great many practical uses. However, the complexity of SQUID systems and the necessity to cool the SQUID devices to very low temperatures are significant barriers to widespread application. It is thus appropriate to recall the important maxim of Harold Weinstock: "never use a SQUID when a simpler, cheaper device will do" [205].

Future system evolution trends will certainly aim at increased user friendliness, optimized performance, improved versatility, system simplification and the associated cost reduction. At present, we can identify the following future developments.

We expect that sufficiently quiet and relatively inexpensive cold-finger cryocoolers will gradually replace liquid cryogens, especially liquid nitrogen, in an increasing number of stationary applications. Development of "black box" cryogenics containing the sensor and cooler as an integrated, replaceable module of the SQUID system, will be necessary for high-volume applications such as stainless-steel detection in quality assurance during the manufacture of food, cosmetics and pharmaceutical products [206]. In small, mobile hand-held HTS systems, there is the perspective of eventually using so-called "cold batteries" – precooled, high thermal capacity inserts, permitting the user to operate them autonomously over a limited period of time [207, 208]. In large and extremely sensitive biomagnetic systems, liquid helium will be preferred as a cooling medium, but in a closed cooling system – in association with a subsidiary cryocooler, which may operate only during the biomagnetometer off-time, in analogy to what is now rather common in modern MRI systems – to

reduce dramatically the consumption of liquid helium and thus the operating costs, and to minimize cryogen handling.

A broader replacement of low-T_c SQUIDs by their high-T_c counterparts, will be a function of progress in HTS fabrication technology, especially with respect to improved junction reproducibility, much reduced 1/f noise in multilayer circuits, reduced cost of fabrication and electronics and the feasibility of fabricating axial gradiometer coils[4]. As pointed out in Section 1.8, these are formidable challenges. As also pointed out there, propagation delays in cables connecting the SQUID to the room-temperature electronics set the upper frequency limit of the flux-locked loop. When cryogenic, low-power semiconductor chips become available, a substantially higher frequency response and slew rate will be attained by placing the electronics package closer to the SQUID. Alternatively, one could introduce superconducting "on-chip" SQUID electronics based on RSFQ circuits [210]. This prospect is still possible, even if no fully successful implementation has been demonstrated to date. Indeed, such electronics should also have an incomparably high dynamic range, greatly facilitating the use of SQUIDs in unshielded environments.

The cost of magnetic shielding is a significant fraction of the total system price. Also, the need to operate in shielded rooms, as is the case for biomagnetic applications, greatly reduces the system flexibility in terms of accessibility and installation site. Therefore, there has been a trend towards multichannel systems which are capable of operating without any magnetic shielding but with a, still acceptable quality of recorded signals [211]. This trend is now especially discernible in MCG biomagnetometers [212]. However, the electromagnetic pollution of the environment is steadily increasing due to mobile telecommunications, and, in hospitals, due to saturation caused by electronic monitoring, diagnostics and therapy apparatus. Therefore, we believe that eventually the most viable systems will be those which operate within relatively inexpensive magnetic or electromagnetic shielding. This will improve the chances of high-T_c SQUIDs being used for biomagnetometers. A broader use of active shielding is also an option for the future. The development of absolute-value devices [213] and superconducting interference filter devices (SQIFs) [214, 215] for use as referencing sensors, will enable the implementation of "built-in" compensation instead of the, currently used, external flux gates [216].

There is a general trend towards improved user friendliness and ease of operation. Computer-controlled setting of SQUID parameters is already commonplace, while automating setting and optimization of these, using either a computer or a dedicated microprocessor, is becoming increasingly popular.

We expect that multiplexed SQUID amplifier arrays for the readout of submillimeter, infrared and X-ray detectors (see volume II) will, in the near future, be as commonplace as multichannel biomagnetometers are today. SQUID amplification and multiplexing in biomagnetometers could also greatly reduce the cost, enhance the simplicity and improve accuracy, but the speed, bandwidth and low-noise

4) First attempt to use patterned YBCO film on flexible hastelloy tape, to form an axial gradiometer, was recently reported [209].

requirements are much more formidable than in the case of detector arrays, so that such multiplexed systems are not likely in the near future.

An important trend in multichannel biomagnetometers is towards improved versatility and accuracy attained by combining SQUID magnetometry with low-field MRI imaging using SQUID amplifiers. The first steps in this direction were recently announced [217].

Finally, there is a clear development towards further optimization of portable and mobile systems for various kinds of exploration. Important steps in this direction are the recent common-feedback schemes for a mobile gradiometer [218, 219] and the recent concept of a rotating axial gradiometer [220]. With the rapid rate of progress in adaptive signal-processing algorithms, it may also become possible, in the near future, to configure an accurate total-field magnetometer from three orthogonal SQUIDs. If successfully implemented, these developments might significantly contribute to the acceptance of SQUID systems in many mobile applications.

References

1 ter Brake, H.J.M (1999) Cryogenic systems for superconducting devices, in *Applications of Superconductivity* H. Weinstock (ed.), Kluwer Academic Publ. Dordrecht, 561–639.

2 Walker , G. (1983) *Cryocoolers, part 1: Fundamentals*, Plenum Press, New York.

3 Strobridge, T.R. (1974) Cryogenic Refrigerators – An Updated Survey, National Bureau of Standards Technical Note 655 (Supt. Documents, U.S. Govt. Printing Off.).

4 Ackermann, R.A. (1993) *Superconductor Industry*, Fall , 15–24.

5 Barron, R. (1966) *Cryogenic Systems*, McGraw-Hill Book Company, New York.

6 Kurti, N. (1971) Introduction, in G.G. Haselden, *Cryogenic Fundamentals*, Academic Press, London.

7 Mendelssohn, K. (1977) *The Quest for Absolute Zero*, Taylor & Francis LTD, London.

8 Scurlock, R.G. (1992) *History and Origins of Cryogenics*, Clarendon Press, Oxford.

9 Hands, B.A. (1986) *Cryogenic Engineering*, Academic Press, London.

10 Weisend, J.G. (1998) *Handbook of Cryogenic Engineering*, Taylor & Francis, Philadelphia.

11 Collins, S.C. and Canaday, R.L. (1958) *Expansion Machines for Low Temperature Processes*, Oxford University Press, Oxford.

12 Radebaugh, R. (1995) Recent developments in cryocoolers, in *Proc. 19th International Congress of Refrigeration*, Den Haag, 973–989.

13 Walker, G. (1989) *Miniature Refrigerators for Cryogenic Sensors and Cold Electronics*, Clarendon Press, Oxford.

14 Walker , G. (1983) *Cryocoolers, part 2: Applications*, Plenum Press, New York.

15 Walker, G. and Bingham E.R. (1994) *Low-Capacity Cryogenic Refrigeration*, Clarendon Press, Oxford.

16 Ter Brake, H.J.M. and Wiegerinck, G.F.M. (2002) Low-power cryocooler survey, *Cryogenics* **42**, 705–718.

17 Ter Brake, H.J.M. (2001) Cooling and packaging of RF components, in *Microwave Superconductivity* H. Weinstock (ed.), Kluwer Academic Publ. Dordrecht.

18 Roth, A. (1990) *Vacuum Technology*, Elsevier, Amsterdam.

19 Ter Brake, H.J.M. and Flokstra, J. (1988) Computer aided cryostat design: recent developments, R.G. Scurlock and C.A. Bailey (eds.), Proceedings 12th International Cryogenic Engineering Conference, Butterworth, UK, 88–92.

20 Leung, E.M.W., Fast, R.W., Hart, H.L., and Heim, J.R. (1980) Techniques for reducing radiation heat transfer between 77 and 4.2 K, *Adv. Cryogenic Eng.* **25**, 489–499.

21 Bell, G.A., Nast, T.C., and Wedel, R.K. (1977) Thermal performance of multiplayer insulation applied to small cryogenic tankage, *Adv. Cryogenic Eng.* **22**, 272–282.

22 Superinsulation NRC-2 Oxford Instruments Ltd, Eynsham, Oxford OX8 1TL, UK.

23 Nenonen, J., Katila, T. and Montonen, J. (1989) Thermal noise of a biomagnetic measurement dewar, in *Advances in Biomagnetism*, Plenum Press, New York, 729–732.

24 Kasai, N., Sasaki, K., Kiryu, S. and Suzuki, Y. (1993) Thermal magnetic noise of dewars for biomagnetic measurements, *Cryogenics* **33**, 175–179.

25 Van Duuren, M.J. (1997) *Advanced relaxation oscillation SQUIDs*, Ph.D. thesis University of Twente, Enschede.

26 Cushman, G.M., Gummer, R.M., Buchanan, E., Jenkins, O. and Powers, T. (1999) Automated liquid helium transfer system *Rev. Sci. Instrum.* **70**, 1575–1576.

27 Callen, H.B. (1985) *Thermodynamics and an Introduction to Thermostatistics*, John Wiley & Sons, New York.

28 Longsworth, R.C., Boiarski, M.J. and Klusmier, L.A. (1995) 80 K Closed-cycle throttle refrigerator, in R.G. Ross, Jr. (ed.), *Cryocoolers* **8**, 537–541.

29 Little, W.A. and Sapozhnikov, I. (1997) Low cost cryocoolers for cryoelectronics, in R.G. Ross, Jr. (ed.), *Cryocoolers* **9**, 509–513.

30 IGC Polycold Systems Inc., 3800 Lakeville Hwy, Petaluna, CA 94954, USA (www.polycold.com).

31 Holland, H.J., Burger, J.F., Boersma, N., Ter Brake, H.J.M. and Rogalla, H. (1998), Miniature 10–150 mW Linde-Hampson cooler with glass-tube heat exchanger operating with nitrogen, *Cryogenics* **38**, 407–410.

32 Little, W.A. (1984) Microminiture refrigeration, *Rev. Sci. Instrum.* **55**, 661–680.

33 Burger, J.F. (2001) *Cryogenic Microcooling*, Ph.D. thesis University of Twente, Enschede.

34 Klemic, G.A., Buchanan, D.S., Cycowicz, Y.M. and Williamson, S.J.(1989) Sequential spatially distributed activity of the human brain detected by CryoSQUIDs, in S.J. Williamson *et al.* (eds.), *Advances in Biomagnetism*, Plenum Press, New York, 685–688.

35 Sata, K., Fujimoto, S., Fukui, N., Haraguchi, E., Kido, T., Nishiguchi, K. and Kang, Y.-M. (1997) A 61-channel SQUID system for MEG measurement cooled by a GM/JT cryocooler, *IEEE Transactions on Applied Superconductivity* **7**, 2526–2529.

36 Hohmann, R., *SQUID-System mit Joule-Thomson Kuehlung zur Wirbelstrompruefung von Flugzeugfelgen*, Ph.D. thesis Justus Liebig University Giessen, 1999.

37 Hohmann, R., Maus, M., Lomparski, D., Grüneklee, M., Zhang, Y., Krause, H.-J., Bousak, H. and Braginski, A.I. (1999) Aircraft wheel testing with machine-cooled HTS SQUID gradiometer system, *IEEE Trans. Appl. Supercond.* **9**, 3801–3804.

38 Bangma, M.R., Rijpma, A.P., De Vries, E., Reincke, H.A., Holland, H.J., Ter Brake, H.J.M. and Rogalla, H. (2001) Interference characterisation of a commercial Joule-Thomson cooler to be used in a SQUID-based heart monitor, *Cryogenics*, **41**, 657–663.

39 Rijpma, A.P., Ter Brake, H.J.M., De Vries, E., Nijhof, N., Holland, H.J. and Rogalla, H. (2002) A high-Tc SQUID-based sensor head cooled by a Joule-Thomson cryocooler, *Physica C*, **372–376**, 209–212.

40 Zimmerman, J.E. and Radebaugh, R.(1978) Operation of a SQUID in a very low-power cryocooler, in J.E. Zimmerman and T.M. Flynn (eds.) *Applications of Closed-Cycle Cryocoolers to Small Superconducting Devices*, NBS Spec. Publ. 508, 59–66.

41 Zimmerman, J.E. (1980) Cryogenics for SQUIDs, in H.D. Hahlbohm and H. Lübbig (eds.) *Proceedings of the second International Conference on Superconducting Quantum Devices*, Springer-Verlag, Berlin, 423–443.

42 Khare, N. and Chaudhari, P. (1994) Operation of bicrystal junction high-T_c direct current-SQUID in a portable microcooler *Appl. Phys. Lett.* **65**, 2353–2355.

43 Rijpma, A.P., Blom, C.J.H.A., Balena, A.P., De Vries, E., Holland, H.J., and Rogalla, H. (2000) Construction and tests of a heart scanner based on superconducting sensors cooled by small stirling cryocoolers, *Cryogenics* **40**, 821–828.

44 McMahon, H.O (1960) Recent Developments of gas cryogenics, *Cryogenics* **1**, 65–70.

45 Gifford, W.E. and Mc Mahon, H.O. (1959) A low temperature heat pump, in *Proceedings. 10th International Congress of Refrigeration* **1**.

46 Radebaugh, R. (1997) Advances in cryocoolers, in T. Haruyama, T. Mitsui and K. Yamafuji (eds.), *Proceedings 16th International Cryogenic Engineering Conference*, Kitakyushu, Japan, 20–24 May 1996, Elsevier Science, New York, 33–44.

47 Kariyama, T., Hakamada, R., Nakagome, H., Tokai, Y. *et al.* (1990) High efficient two-stage

GM refrigerator with magnetic material in the liquid helium temperature region, *Advances in Cryogenic Engineering* **35**, 1261–1269.

48 Satoh, T., Onishi, A., Li, R., Asami, H. and Kanazawa, Y. (1996) Development of a 1.5 W 4 K G.M. cryocooler with magnetic regenerator material, *Advances in Cryogenic Engineering* **41**, 1631–1637.

49 Kazami, K., Takada, Y., Fujimoto, S., *et al.* (1994) A Drung-type magnetometer mounted on a GM cryocooler, *Superconductor Science & Technology* **7**, 256–259

50 Kazami, K., Takada, Y., Yoshida, T., Ogata, H. and Kado, H. (1995) Cooling of SQUIDs using a Gifford-McMahon cryocooler containing magnetic regenerative material to measure biomagetnism, *Cryogenics* **35**, 143–148.

51 Van den Bosch, P.J. (1996) *Cryocooler-operated high-T_c SQUID system for magneto-cardiography in an unshielded environment*, Ph.D. thesis University of Twente, Enschede.

52 Van den Bosch, P.J., Holland, H.J., Ter Brake, H.J.M. and Rogalla, H. (1995) Closed –cycle gas flow system for cooling of high T_c d.c. SQUID magnetometers, *Cryogenics*, **35**, 109–116.

53 Gifford, W.E. and Longsworth, R.C. (1963) Pulse-tube refrigeration, ASME paper No. 63-WA-290 presented at Winter Annual Meeting of the American Society of Mechanical Engineers, Philadelphia, Pennsylvania, Nov. 17–22.

54 Mikulin, E.I., Tarasov, A.A. and Shkrebyonock, (1984) Temperature expansion pulse tubes, *Advances in Cryogenic Engineering* **29**, 629–637.

55 Radebaugh, R., Zimmerman, J., Smith, D.R. and Louie, B. (1986) A comparison of three types of pulse tube refrigerators: new methods for reaching 60 K, *Advances in Cryogenic Engineering* **31**, 779–789.

56 Zhu, S., Wu, P. and Chen, Z (1990) On the 410-degrees-c embrittling of n19 steel, *Cryogenics* **30**, 399–406.

57 Duband, L., Charles, I., Ravex, A., Miquet, L. and Jewell, C. (1999) Experimental results on inertance and permanent flow in pulse tube coolers, in R.G. Ross, Jr. (ed.), *Cryocoolers* **10**, 281–290.

58 Kotsubo, V., Huang, P. and Nast, T.C. (1999) Observation of DC flows in a double inlet pulse tube, in R.G. Ross, Jr. (ed.), *Cryocoolers* **10**, 299–305.

59 Wang, C., Thummes, G. and Heiden, C. (1998) Control of DC gas flow in a single-stage double-inlet pulse tube cooler, *Cryogenics* **38**, 843–847.

60 Thummes, G., Schreiber, M., Landgraf, R. and Heiden, C. (1997) Convective heat losses in pulse tube coolers: effect of pulse tube inclination, in R.G. Ross, Jr. (ed.), *Cryocoolers* **9**, 393–402.

61 Cryomech,113 Falso Drive, Syracuse, NY 13211 USA, www.cryomech.com.; Sumitomo Heavy Industries, Ltd., Res. and Development Ctr., 63–30, Yuhigaoka, Hiratsuka, Kanagawa, 254 Japan, www.shi.co.jp/english.

62 Thummes, G., Landgraf, R., Mück, M., Klundt, K. and Heiden, C. (1997) Operation of a high-T_c SQUID gradiometer by use of a pulse tube refrigerator, in T. Haruyama, T. Mitsui and K. Yamafuji (eds.) *Proceedings 16th International Cryogenic Engineering Conference*, Kitakyushu, Japan, 20–24 May 1996, Elsevier Science, New York, 283–286.

63 Lienerth, C., Thummes, G. and Heiden, C. (2001) *IEEE Trans. Appl. Supercond.* **11**, 812–815.

64 Kaiser, G., Brehm, H., Wagner, R., Gerster, J., Wunderlich, S., Thürk, M. And Seidel, P. (1997) *Cryogenics* **37**, 699–703.

65 Dolabdjian, C., Saez, S., Bloyet, D., David, M. and Maréchal, J.C. (1998) *Appl. Supercond.* **7–9**, 459–464.

66 Nast, T., Champagne, P. and Kotsubo, V. (1998) Development of a low-cost unlimited-life pulse-tube cryocooler for commercial applications, *Advances in Cryogenic Engineering* **43**, 2047–2053.

67 Wade, L.A. (1992) An overview of the development of sorption refrigeration, *Advances in Cryogenic Engineering* **37**, 1095–1106.

68 Burger, J.F. *et al.* (1999) Thermodynamic considerations on a microminiature sorption cooler, in R.G. Ross, Jr. (ed.), *Cryocoolers* **10**, 553–563.

69 Loung, V., O'Baid and Harper, S. (1997) Path to low cost and high reliability Stirling coolers, in R.G. Ross, Jr. (ed.), *Cryocoolers* **9**, 97–108.

70 Hanes, M. (2001) Performance and reliability improvements in a low-cost Stirling cycle cryocooler, in R.G. Ross Jr. (Ed.), *Cryocoolers* **11**, 87–95.

71 Unger, R.Z., Wiseman, R.B., Hummon, M.R. (2001) The advent of low cost cryocoolers, in R.G. Ross Jr. (Ed.), *Cryocoolers* **11**, 79–86.

72 Walker, G. and Bingham, E.R. (1990) Micro and nanno cryocoolers: speculation on future development, in *Proceedings of the 6th International Cryocooler Conference*, Plymouth, Mass., October, 363–375.

73 Crete, D., Cabanel, R. and Friederich, A. (1995) Refroidisseur à gaz pulsé, European patent publication 0 672 873 A1.

74 Bowman, L., Berchowitz, D.M. and Urieli, I. (1994) Microminiature Stirling cycle cryocoolers and engines, US patent 5,457,956.

75 Burger, J.F. *et al.* (1997) Microcooling: study on the application of micromechanical techniques, in R.G. Ross, Jr. (ed.), *Cryocoolers* **9**, 687–696.

76 Orientation independent cryostat, type ILK-4, Institut für Luft- und Kältetechnik, Bertolt-Brecht-Allee 20, 01309 Dresden, Germany.

77 Longsworth, R.C. (1980) Serviceable refrigerator system for small superconducting devices, in J.E. Zimmerman, D.B. Sullivan and S.E. Mc Carthy (eds.), *Refrigeration for cryogenic sensors and electronic systems*, Proc. NBS Boulder, Oct. 6–7, 82–92.

78 Dunn, P.D. and Reay, D.A. (1982) *Heat Pipes*, Pergamon Press 3rd ed., Oxford.

79 Prenger, F.C., Hill, D.D..*et al.* (1997) Heat pipes for enhanced cooldown of cryogenic systems, in R.G. Ross, Jr. (ed.), *Cryocoolers* **9**, 831–839.

80 Troell, J. and Heiden, C. (1997) Low noise gas flow cryosystem for cooling high-T_c SQUID, in T. Haruyama, *et al.* (eds.), *Proceedings 16th International Cryogenic Engineering Conference*, Kitakyushu, Japan, 20–24 May 1996, Elsevier Science, New York, 453–456.

81 Kotsubo, V. and Black, R.D. (1996) Apparatus for cooling NMR coils, U.S. patent 5,508,613.

82 Sullivan, D.B., Zimmerman, J.E. and Ives, J.T. (1980) Operation of a practical SQUID gradiometer in a low-power Stirling cryocooler, in J.E. Zimmerman, D.B. Sullivan, S.E. Mc Carthy (eds.), *Proc. Conf. Refrigeration for Cryogenic Sensors and Electronic Systems*, NBS Boulder, 6–7 October, 186–194.

83 Klundt, K., Lienerth, C., Thummes, G., Steinmeyer, F. *et al.* (1998) Use of a pulse tube refrigerator for cooling a HTS antenna for magnetic imaging, *Advances in Cryogenic Engineering*, **43**, 2085–2092.

84 Gerster, J., Kaiser, G., Reißig, Thürk, M. and Seidel, P. (1998) *Advances in Cryogenic Engineering* **43**, 2077–2084.

85 Van den Bosch, P.J., Ter Brake, H.J.M., Holland, H.J., De Boer, H.A., Verberne, J.F.C. and Rogalla, H., *Cryogenics* **1997**, *37*, 139–151.

86 Wu, Y.A. (1994) Active vibration control algorithm for cryocooled systems, *Advances in Cryogenic Engineering* **39**, 1271–1280.

87 Collins, S.A., Paduano, J.D. and Von Flotow, A.H. (1995) Active multi-axis vibration cancellation for split-Stirling cryocoolers, in R.G. Ross, Jr. (ed.), *Cryocoolers* **8**, 437–448.

88 Kieffer, M., Wu, A. and Champion S. (1997) Summary and results of Hughes improved standard spacecraft cryocooler vibration suppression experiment, in R.G. Ross, Jr. (ed.), *Cryocoolers* **9**, 705–710.

89 Rijpma, A.P., Verberne, J.F.C., Witbreuk, E.H.R., Bruins, P.C. and Ter Brake, H.J.M. (1998) Adaptive periodic disturbance cancellation in a set-up of two cryocoolers, *J. Sound and Vibration* **217**, 419–434.

90 Hohmann, R., Lucía, M.L., Soltner, H., *et al.* (1997) Integration of HTS SQUIDs with portable cooling devices for the detection of material defects in non-destructive evaluation, in R.G. Ross, Jr. (ed.), *Cryocoolers* **9**, 925–934.

91 Reed, R.P. and Clark, A.F. (1983) *Materials at Low Temperatures*, American Society of Metals.

92 Cryodata Inc., P.O.Box 558, Niwot, Colorado, USA.

93 www.jahm.com; Material Properties Data Base (MPDB).

94 Mills, J.P. (1993*) Electromagnetic Interference Reduction in Electronics Systems*, Prentice Hall, New Jersey, 42–71.

95 Ott, H.W. (1988) *Noise Reduction in Electronic Systems*, second Edition, Wiley, NY.

96 Chatterton, P.A. and Houlden, M.A. (1992) *EMC- Electromagnetic Theory to Practical Design*, Wiley, Chichester.

97 Lammeraner, J. and Stafl, M. (1966) *Eddy Currents*, ILIFFE Books Ltd, London, 18.

98 Paul, C.R. (1992*) Introduction to Electromagnetic Compatibility*, Wiley, New York.

99 Alecci, M. and Jezzard, P. (2002) Characterisation and reduction of gradient-induced eddy currents in rf shield of a TEM resonator, *Magn. Resoanance in Medic.* **48**, 404–407.

100 Burl, M. and Young, I.R. (1996) Eddy currents and their control, in *The Encyclopaedia of Nuclear Magnetic Resonance*, Wiley, NY, 1841–1846.

101 Carlsom, J.W. (1994) Apparatus and method for shielding MRI RF antennae from the effect of surrounding objects, US patent 5,304,932.

102 Hayes, C.E. and Eash, M.G. (1987) Shield for decoupling RF and gradient coils in an NMR apparatus. US patent 4,506,224 (1985).

103 There is an enormous number of both shareware and commercial finite element analysis packages available. A simple web search will find many listings. One example is FEMLAB http://www.femlab.com.

104 Zimmerman, J. E. (1977) SQUID instruments and shielding for low level magnetic measurements, *J. Appl. Phys.* **48**, 702–710.

105 Stroink, G., Blackford, B., Brown, B. and Horacek, M. (1981) Aluminum Shielded Room for Biomagnetic Measurements. *Rev. Sci. Instrum.* **52**, 463–468.

106 Vacuumschmelze GmbH, Hanau, Germany, shielded room model AK-3.

107 Evetts, J. (1992) *Concise Encyclopaedia of Magnetic and Superconducting Materials*, Peragamon Press, Oxford, 492–493.

108 Cohen D (1967) Enhancement of ferromagnetic shielding against low frequency magnetic fields, *Appl. Phys Lett*, **10**, 67–69.

109 Wadey, W.G. (1956) Magnetic shielding with multiple cylindrical shells, *Rev. Sci. Instrum.* **27**, 910–916.

110 Kelha, V. (1981) The effect of shaking on magnetic shields, *IEEE Trans. Magn.* **16**, 575–578.

111 Amuneal Manufacturing Corp., 4737 Darrah Street, Philadelphia, PA 19124, USA.

112 Tokin Corporation, 6-7-1 Koriyama Tihakuku, Sendai-City, Miyagi-pref, 982, Japan.

113 Imedco, AG., Industriestrasse West 14, CH-4614 Hagendorf, Switzerland.

114 Erne, S. N., Hahlbohm, H.-D., Scheer, H. and Trontelj, Z. (1981) The Berlin Magnetically Shielded Room (BMSR) Section B – Performances, in S.N. Erne et al (eds.), *Biomagnetism*, Walter de Gruyter, Berlin and New York, 79–87.

115 Harakwa, K., Kajiware, G., Kazami, K., Ogata, H., and Kado, H. (1996) Evaluation of high-performance magnetically shielded room for biomagnetic measurement, *IEEE Trans. Mag.* **32**, 5226–5259.

116 Kelha, V.O. (1981) Construction and performance of the Otaniemi magnetically shielded room, in S.N. Erne *et al.* (eds.), *Biomagnetism*, Walter de Gruyter, Berlin and New York, 33–50.

117 Bork, J., Hahlbohm, H.-D., Klein, R., and Schnabel, A. (2001) The 8-layered magnetically shielded room of the PTB: Design and construction, in J. Nenonen et al. (Eds.), *Biomag 2000*, Proc. 12th Int. Conf. Biomagnetism, Helsinki Univ. of Technology, Espoo, Finland, pp. 970–973.

118 CTF Systems Inc., Division of VSM MedTech Ltd., Port Coquitlam, BC, Canada.

119 Matsuba, H., Shintomi, K., Yahara, A., Irisawa, D., Imai, K., Yoshida, H., and Seike, S. (1995) Superconducting shielding enclosing a human body for biomagnetic measurement, in Baumgartner, C. et al (eds.), *Biomagnetism: Fundamental research and clinical applications*, Elsevier Science, IOS Press, 483–489.

120 Vrba, J., Angus, V., Betts, K., Burbank, M.B., Cheung, T., Fife, A.A., Haid, G., Kubik, P.R., Lee, S., Ludwig, W., McCubbin, J., McKay, J., McKenzie, D., Robinson, S.E., Smith, M., Spear, P., Taylor, B., Tillotson, M., Cheyne, D., and Weinberg, H. (1997) 143 channel whole-cortex MEG system, in C. Aine *et al.* (eds.), *Biomag96: Advances in Biomagnetism Research*, Springer-Verlag, 138–141.

121 Vrba, J. (2000) Multichannel SQUID biomagnetic systems, in H. Weinstock (ed.), *Applications of superconductivity*, Kluwer Academic Publishers, Dordrecht, 61–138.

122 Vrba, J. and Robinson, S.E. (2002) SQUID sensor array configurations for magnetoencephalography applications. *Supercond. Sci. Technol.* **15**, R51–R89.

123 Henry, O.H. (1988) *Noise Reduction Techniques in Electronics Systems*, 2nd Edition, John Wiley, NY, 51–59.

124 Leslie, K.E., Small, G.W. and Sloggett, G.J. (1995), Cancellation of periodic noise in low-level magnetic signals, *Meas. Sci. and Technol.* **6**, 1093–1098.

125 Williams, C.S. (1986) *Designing Digital Filters*, Prentice-Hall, Englewood Cliffs, NJ.

126 Horowitz, P. and Hill, W. (1980) *The Art of Electronics*, Cambridge University Press, Cambridge.

127 Macnae, J.C., Lamontagne, Y. and West, G.F. (1984) Noise Processing techniques for time domain EM systems, *Geophysics* **49**, 934–943.

128 Vance, E. F. (1978) *Coupling the Shielded Cables*, John Wiley, NY.

129 Walker, C.S. (1009) *Capacitance, Inductance and Crosstalk Analysis*, Norwood, MA., Artech House, 125–152.

130 ter Brake H.J.M., Fleuren, F.H., Ulfman, J.A. and Flokstra, J. (1986) Elimination of flux transformer crosstalk in multichannel SQUID magnetometers, *Cryogenics* **26**, 667–670.

131 Crompton, T.R. (1995) *Battery Reference Book*, Butterworth Heinemann, Oxford.

132 Vrba, J. and McKay, J. (1998) Character and acquisition of multichannel biomagnetic data, *Applied Supercond.* **5**, 431–439.

133 Vrba, J., Betts, K., Burbank, M.B., Cheung, T., Fife, A.A., Haid, G., Kubik, P.R., Lee, S., McCubbin, J., McKay, J., McKenzie, D., Spear, P., Taylor, B., Tillotson, M., Cheyne, D., and Weinberg, H. (1993) Whole Cortex, 64 Channel SQUID Biomagnetic System, *IEEE Trans. Appl. Supercond.* **3**, 1878–1882.

134 Drung, D. Matz, H. and Koch, H., (1995) A 5 MHz bandwidth SQUID magnetometer with additional positive feedback, *Rev. Sci. Instrument.* **66**, 3008–3015.

135 Drung, D., Cantor, R., Peters, M., Scheer, H.J. and Koch, H. (1990) Low-noise high-speed dc superconducting quantum interference device magnetometer with simplified feedback electronics, *Appl. Phys. Lett.* **57**, 406–408.

136 Zimmerman, J.E. and Frederick, N.V. (1971) Miniature ultra-sensitive superconducting magnetic gradiometer and its use in cardiographs and other applications, *Appl. Phys. Lett.* **19**, 16–19.

137 Nichols, D.G., Dantsker, E., Kleiner, R. and Clarke, J. (1996) Linearity of high Tc dc superconducting quantum interference device operated in a flux locked loop, *J. Appl. Phys.* **80**, 6032–6038.

138 Foley, C.P., Leslie, K.E., Binks, R.A., Lam, S.H.K, Du, J., Tilbrook, D.L., Mitchell, E.E., Macfarlane, J.C. (2002) Issues relating to airborne applications of HTS SQUIDs, *Supercond. Sci.Technol.* **15**, 1641–1645.

139 Miklich, A.H., Koelle, D., Shaw, T.J., Ludwig, F., Nemeth, D.T., Dantsker, E., Clarke, J., Alford, N.Mc.N, Button, T.W. and Colclough, M.S. (1994) Low frequency excess noise in YBCO dc superconducting devices cooled in static magnetic fields, *Appl. Phys. Lett.* **64**, 3494–3496.

140 Keene, M.N., Exon, N.J., Humphreys, R.G. and Chew, N.G. (1996) The influence of ambient magnetic environments on high T_c superconducting quantum interference device gradiometers, *Appl. Phys. Lett.* **79**, 8783–8791.

141 Mück, M., Schöne, S. and Heiden, C. (1997) Reduction of low frequency noise and temperature drift of SQUIDs by degaussing using high frequency magnetic fields , *IEEE Trans. Appl. Supercond.* **7**, 3263–3266.

142 Koelle, D., Kleiner, R., Ludwig, F., Dantsker, E. and Clarke, J. (1999) High transition temperature superconducting quantum interference devices, *Rev. Mod. Phys.* **71**, 631–686.

143 Sun, J.Z., Gallagher, W.J. and Koch, R.H. (1994) Initial-vortex-entry-related magnetic hystersis in thin film SQUID magnetometers, *Phys. Rev. B* **50**, 13664–13673.

144 Auster, H.U., Fornacon, K.H., Georgescu, E., Glassmeier, K.H. and Motschmann, U. (2002) Calibration of flux gate magnetometers using relative motion, *Meas. Sci. and Technol.* **13**, 1124–1131.

145 Bruno, A.C. and Costa Ribeiro, P. (1991) Spatial Fourier calibration method for multichannel SQUID magnetometers, *Rev. Sci. Instrum.* **62**, 1005–1009.

146 Glover, F.W. (1962) *Inductance Calculations*, Dover NY.

147 Costa Ribeiro, P., Williamson, S.J. and Kaufman, L. (1988) SQUID arrays for simultaneous magnetic measurements: calibration and source localization performance, *IEEE Trans. Biomed. Eng.* **35**, 551–560.

148 Kado J., Higuchi M., Shimogawara M., Haruta Y., Adachi Y., Kawai J., Ogala H. and Vehara G. (1999) Magnetoencephalogram System developed at KIT, *IEEE Appl. Supercond.* **9**, 4057–4062.

149 Merayo JMG, Petersen JR., Nielson OV., Primdahl F. and Braver P. (2001) A portable single axis magnetic gradiometer, *Sensors and Actuators* **A93**, 185–196.

150 Schill RA and Hoff K., Characterizing and calibrating a large Helmholtz coil at low ac magnetic field levels with peak magnitudes below the earth's magnetic field, *Rev. Sci. Instrum.* **72**, 2769–2776.

151 Boll, R. (1989) *Introduction in Sensors- A Comprehensive Survey*, Eds: Gopel, W. Hesse, J. and Zemel, J.N. Weinheim Basel and NY, 20–24.

152 Lin, S.T. and Kaufmann, A.R. (1953) Helmholtz coils for production of powerful and uniform fields and gradients, *Rev. Mod. Phys.* **25**, 182.

153 Rubens, S.M. (1945) Cube-surface coil for producing a uniform magnetic field, *Rev. Sci. Instrum.* **16**, 243–245.

154 (a) Ornelas, P.H., Bruno, A.C., Hall Barbosa, C., Andrade Lima and Costa Ribeiro, P. (2003) A survey of calibration procedures for SQUID gradiometers, *Supercond. Sci. and Technol.* **16**, 427–431 and (b) Hall Barbosa, C., Andrade Lima, E., Bruno, A.C., Ewing, A.P. and Wikswo, J.P. (1999) Flux/voltage calibration of axial SQUID gradiometers using an optimization procedure, *IEEE Trans. Appl. Supercond.*, **9**, 3523–3526 and (c) Bruno, A.C. (1997) Tesla/volt calibration method for integrated planar SQUID gradiometer, *IEEE Trans. Appl. Supercond.* **7**, 2760–2763.

155 Koch, R.H. (1997) Maximum Theoretical Bandwidth and Slewrate of a dc SQUID Feedback System, *IEEE Trans. Appl. Supercond.* **7**, 3259–3262.

156 Clarke, J. (1996) SQUID Fundamentals, in H. Weinstock (ed.), *SQUID Sensors: Fundamentals, Fabrication and Applications*, NATO ASI Series E: Applied Sciences, Vol. 329, Kluwer Academic Publishers, Dordrecht, 1–62.

157 Curio, G., Mackert, B.-M., Burghoff, M., Koetitz, R., Drung, D., and Marx, P. (1995) Neuromagnetic correlates of evoked somatosensory activity traveling through the lumbosacral cauda equina and thoracic spinal cord in man, in C. Baumgartner *et al.* (eds.), Biomagnetism: Fundamental Research and Clinical Applications, Elsevier Science, IOS Press, 723–726.

158 Goree, W.S. and Fuller, M. (1976) Magnetometers using rf-driven SQUIDs and their applications in rock magnetism and paleomagnetism, *Rev. Geophys. and Space Physics* **14**, 591–608.

159 Applied Physics Systems, Inc., 897 Independence Ave, Suite 1C, Mountain View, CA 94043, USA. Also: www.2Genterprises.com.

160 Diederichs, J., Spagna, S., and Sager, R.E. (1996) Breaking through the 10^{-8} emu sensitivity barrier in magnetometers, *Czech J. Phys.* **46**, Suppl. S5, 2803–2806.

161 Quantum Design, 11578 Sorrento Valley Road, San Diego, California, USA 92121-1311.

162 Comani, S., Basile, M., Casciardi, S., Del Gratta, C., Di Luzio, S., Erne, S.N., Macri, M., Neri, M., Peresson, M., and Romani, J.L. (1992) Extracorporeal direct magnetic measurement of gastric activity, in Biomagnetism: Clinical aspects, in Hoke, M. *et al.* (eds.), Elsevier Science, 639–642.

163 Richards, W.O., Staton, D., Golzarian, J., Friedman, R.N., and Wikswo, J.P. (1995) Non-invasive SQUID magnetometer measurement of human gastric and small bowel electrical activity, in Baumgartner, C. *et al.* (eds.), *Biomagnetism: Fundamental Research*, Elsevier Science, 743–747.

164 Carelli, P., Modena, I., and Romani, G.L. (1982) Detection coils, in S.J. Williamson, G.L. Romani, L.Kaufman, and I.Modena (eds.), *NATO ASI Biomagnetism, An Interdisciplinary Approach*, Series A: Life Sciences, **66**, Plenum Press, New York and London, 85–95.

165 Katila, T. (1989) Principles and applications of SQUID sensors, in S.J. Williamson *et al.* (eds.), *Advances in Biomagnetism*, Plenum Press, New York and London, 19–32.

166 Katila, T. (1981) Instrumentation for biomedical applications, in *Biomagnetism*, Proceedings of the Third International Workshop on Biomagnetism, in S.N. Erne *et al.* (eds.), *Biomagnetism*, Walter de Gruyter, Berlin and New York, 3–31.

167 Sullivan, G.W. and Flynn, E.R. (1987) Performance of the Los Alamos shielded room, in K. Atsumi *et al.* (eds.), *Biomagnetism'87*, Tokyo Denki University Press, Tokyo, 486–489.

168 Fraser-Smith, A.C. and Buxton, J.L. (1975) Superconducting magnetometer measurements of geomagnetic activity in the 0.1 to 14 Hz frequency range, *J. Geophys. Res.* **80**, 3141–3147.

169 Vrba, J. (1996) SQUID gradiometers in real environments, in H. Weinstock (ed.), *SQUID sensors: Fundamentals, Fabrication and Applications*, Kluwer Academic Publishers, Dordrecht, 117–178.

170 Rabiner, L.R and Gold, B. (1975) *Theory and Application of Digital Signal Processing*, Prentice-Hall Inc., Englewood Cliffs, New Jersey.

171 Bendat, J.S. and Piersol, A.G. (1986) *Random Data*, John Willey & Sons, New York.

172 McKay, J., Vrba, J., Betts, K., Burbank, M.B., Lee, S., Mori, K., Nonis, D., Spear, P., and Uriel, Y. (1993) Implementation of a Multi-Channel Biomagnetic Measurement System Using DSP Technology, *Proceedings of 1993 Canadian Conference on Electrical and Computer Engineering*, vol. II, 1090–1093.

173 Vrba, J., McCubbin, J., and Robinson, S.E. (1999) Vibration analysis of MEG systems, in T. Yoshimoto *et al.* (eds.), *Recent Advances in Biomagnetism*, Tohoku University Press, 109–112.

174 Robinson, S.E., Burbank, M.B., Fife, A.A., Haid, G., Kubik, P.R., Sekachev, I., Taylor, B., Tillotson, M., Vrba, J., Wong, G., Lowery, C., Eswaran, H., Wilson, D., Murphy, P., and Preisl, H. (2000) A biomagnetic instrument for human reproductive assessment, in J. Nenonen *et al.* (Eds.), *Biomag 2000*, Proc. 12th Int. Conf. Biomagnetism, Helsinki Univ. of Technology, Espoo, Finland, 919–922.

175 Hood, P. (1965) Gradient measurements in aeromagnetic surveying, *Geophysics*, **XXX**, 891–902; Hood, P. (1975) EMR's new geophysical tool, *Energy Mines and Resources*, Canada publication, 19–21.

176 Slack, H.A., Lynch, V.M., and Langan, L. (1967) The geomagnetic gradiometer, *Geophysics* **XXXII**, 877–892.

177 Vrba, J. and Robinson, S.E. (2000) The effect of environmental noise on magnetometer- and gradiometer-based MEG systems, in J. Nenonen *et al.* (Eds.), *Biomag 2000*, Proc. 12th Int. Conf. Biomagnetism, Helsinki Univ. of Technology, Espoo, Finland, pp. 953–956.

178 Matsumoto, K., Yamagishi, Y., Wakusawa, A., Noda, T., Fujioka, K., and Kuraoka, Y. (1992) SQUID based active shield for biomagnetic measurement, in M. Hoke *et al.* (eds.), *Biomagnetism: Clinical Aspects*, Elsevier Science Publishers B.V., Excerpta Medica, Amsterdam, London, NewYork, Tokyo, 857–861.

179 Skakala, M., Zrubec, V., and Manka, J. (1993) Active compensation for ambient magnetic noise in the unshielded environment, *Meas. Sci. Technol.* **4**, 468–472.

180 Malmivuo, J., Lekkala, J., Kontro, P., Suomaa, I., and Vihinen, H. (1987) Improvement of the properties of an eddy current magnetic shield with active compensation, *J. Phys. E: Sci. Instrum.* **20**, 151–164.

181 Kelha, V.O., Pukki, J.M., Peltonen, R.S., Penttinen, V.J., Ilmoniemi, R.J., and Heino, J.J. (1982) Design, construction, and performance of a large volume magnetic shield, *IEEE Trans. Magn.* **18**, 260–270.

182 ter Brake, H.J.M., Wieringa, H.J., and Rogalla, H. (1991) Improvement of the performance of a μ-metal magnetically shielded room by means of active compensation, *Meas. Sci. Technol.* **2**, 596–601.

183 ter Brake, H.J.M., Huonker, R., and Rogalla, H. (1993) New results in active noise compensation for magnetically shielded rooms, *Meas. Sci. Technol.* **4**, 1370–1375.

184 Pasquarelli, A., Jammrath, H., Tenner, U., and Erne, S.N. (1999) The new Ulm magnetic shielded room, in T. Yoshimoto *et al.* (eds.), *Recent advances in biomagnetism*, Tohoku University Press, pp. 55–58.

185 Rijpma, A.P., Seppenwoolde, Y., ter Brake, H.J.M., Peters, M.J., and Rogalla, H. (1997) Application of SQUID magnetometers in fetal magnetocardiography, in *Proc. EUCAS'97, Inst. Phys. Conf. Ser. No* **158**, 771–774.

186 Vrba, J. (1997) Baseline optimization for noise cancellation systems, *Proc. 19th Int. Conf. IEEE/EMBS*, Oct. 30 –Nov. 2, Chicago, Il., USA, 1240–1243.

187 Drung, D. (1991) Performance of an Electronic Gradiometer in Noisy Environments, in H. Koch and H. Lubbig (eds.), *SQUID'91, Superconducting Devices and their Applications*, Berlin, June 18–21, 1991, *Springer Proceedings in Physics* **64**, 542–546.

188 Becker, W., Dickmann, V., Jurgens, R. and Kornhuber, C. (1993) First experiences with a multichannel software gradiometer recording normal and tangential components of MEG, *Physiol. Meas.* **14**, A45–A50.

189 Dieckmann, V., Jurgens R., Becker, W., Elias, H., Ludwig, W. and Vodel,W. (1996) RF-SQUID to DC-SQUID Upgrade of a 28-Channel Magnetoencephalography (MEG) System, *Meas. Sci. Technol.* **7**, 844–852.

190 Vrba, J., Fife, A.A., and Burbank, M.B. (1982) Spatial discrimination in SQUID gradiometers and third-order gradiometer performance, *Can. J. Phys.* **60**, 1060–1073.

191 Sarwinski, R. E. (1977) Superconducting Instruments, *Cryogenics* **17**, 671–679.

192 Brenner, D., Kaufman, L. and Williamson, S. J. (1977) Application of a SQUID for Monitoring Magnetic Response of the Human Brain, *IEEE Trans. Mag.* **MAG-13**, 365–368.

193 Williamson, S. J., Pelizzone, M., Okada, Y., Kaufman, L., Crum, D. B. and Marsden, J. R. (1984) Magnetoencephalography with an Array of SQUID Sensors, in Collan, H., Berglund, P. and Krusius, M. (eds.), *Proceedings of the Tenth International Cryogenic Engineering Conference*, Butterworth, Guildford, 339–348.

194 Matlashov, A., Zhuravlev, Yu., Lipovich, A., Alexandrov, A., Mazaev, E., Slobodchikov, V. and Washiewski, O. (1989) Electronic noise suppression in multi-channel neuromagnetic system, in S.J. Williamson, M. Hoke, G. Stroink, M. Kotani (Eds.), *Advances in Biomagnetism*, Plenum Press, New York and London, 725–728.

195 Huotilainen, M., Ilmoniemi, R.J., Tiitinen, H., Lavikainen, J., Alho, K., Kajola, M., and Naatanen, R. (1995) The projection method in removing eye blink artefacts from multichannel MEG measurements, in C. Baumgartner *et al*. (eds.), *Biomagnetism: Fundamental research and clinical applications*, Elsevier Science, IOS Press, 363–367.

196 Tesche, C.D., Uusitalo, M.A., Ilmoniemi, R.J., Huotilainen, M., Kajola, M., and Salonen, O. (1995) Signal-space projections of MEG data characteristics both distributed and well-organized neuronal sources. *Electroencephalography and Clinical Neurophysiology* **95**, 189–200.

197 Uusitalo, M.A. and Ilmoniemi, R.J. (1997) Signal space projection method for separating MEG or EEG into components, *Med. Biol. Eng. Comput*. **35**, 135–140.

198 Parkkonen, L.T., Simola, J.T., Tuoriniemi, J.T., and Ahonen, A.I. (1999) An interference suppression system for multichannel magnetic field detector arrays, in T. Yoshimoto *et al*. (Eds.), *Recent Advances in Biomagnetism*, Tohoku University Press, 13–16.

199 Sorenson, H.W. (1980) *Parameter Estimation: Principles and problems*, Marcel Dekker Inc., New York and Basel.

200 Hamalainen, M.S. (1995) Functional localization based on measurements with a wholehead magnetometer system. *Brain Topography* **7**, 283–289.

201 Vrba, J., Robinson, S.E., McCubbin, J., Lowery, C.L., Preißl, H., Eswaran, H., Wilson, D., and Murphy, P. (2002) Spatial redistribution of fMEG signals by projection operators, in H. Nowak, J. Haueisen, F. Gießler, and R. Huonker (Eds.), *Biomag 2002*, Proc. 13th Int. Conf. Biomag., Jena, Germany, 1039–1041.

202 Mitra, S.K. and Kaiser, J.F. (1993) *Handbook for Digital Signal Processing*, Wiley, New York.

203 Bruno, A.C., Dolce, C.S., Soares, S.D., and Ribeiro, P.C. (1989) Spatial Fourier technique for calibrating gradiometers, in S.J. Williamson, M. Hoke, G. Stroink, M. Kotani (Eds.), *Advances in Biomagnetism*, Plenum Press, New York and London, 709–712.

204 Golub, G.H. and van Loan, C.F. (1996) *Matrix Computations*, John Hopkins University Press, Baltimore and London.

205 Weinstock H. (1996) *SQUID Sensors: Fundamentals, Fabrication and Applications*, Kluwer Academic Publishers, Dordrecht, p. xv.

206 He, D.F. and Yoshizawa, M. (2002) Metal detector based on high Tc rf SQUIDs, *Physica C* **378**, 1404–1407.

207 Podney, W. (1999) Development of an electromagnetic microscope using HTS SQUIDs, *IEEE Trans. Appl. Supercond*. **9**, 3483–3486.

208 Carr, C., Macfarlane, J.C. and Donaldson, G.B. (2003) A fully portable, cryocooler-based HTS SQUID NDE instrument, *IEEE Trans. Appl. Supercond*. **13**, 245–249.

209 Bick, M., Leslie, K.E., Tilbrook, D.L., Lam, S.K.H., Gnanarajan, S., Binks, R.A., Du, J. and Foley, C.P. (2003) Flexible superconducting tape transformer for an axial HTS SQUID gradiometer, *Extended Abstracts 9th International Superconducting Electronics Conference*, 7–11 July 2003, Sydney, PTh05.

210 Semenov, V. (2003) Digital SQUIDs: New definitions and results, *IEEE Trans. Appl. Supercond*. **13**, 747–750.

211 Vrba, J., Haid, G., Lee, S., Taylor, B., Fife, A.A., Kubik, P., McCubbin, J. and Burbank, M.B. (1991) Biomagnetometers for unshielded and well shielded environments, *Clinical Physics and Physiological Measurement* **12**, 81–86.

212 Currently manufactured by CardioMag Imaging, 450 Duane Ave., Schenectady, NY 12304, USA and by MagScan – Medizinische Technologie GmbH,Essen, Germany.

213 Carelli, P., Castellano, M.G., Flacco, K., Leoni. R., Torrioli and G. (1997) An absolute magnetometer based on dc superconducting quantum interference devices, *Europhys. Lett.* **39**, 569–574.

214 Schultze, V., Ijsselsteijn, R., Meyer, H.G., Oppenlander, J., Haussler, C. and Schopohl, N. (2003) High-Tc superconducting quantum interference filters for sensitive magnetometers, *IEEE Trans Appl. Supercond.* **13**, 775–778.

215 Oppenlander, J., Haussler, C., Trauble, T. and Schopohl, N. (2002) Highly sensitive magnetometers for absolute magnetic field measurements based on quantum interference filters, *Physica C* **368**, 119–124.

216 Clem, T.R., Overway, D.J., Purpura, J.W., Bono, J.T., Koch, R.H., Rozen, J.R., Keefe, G.A., Willen, S. and Mohling, R.A. (2001) High-T-c SQUID gradiometer for mobile magnetic anomaly detection, *IEEE Trans. Appl. Supercond.* **11**, 871–875.

217 Schlenga, K., McDermott, R., Clarke, J., de Souza, R.E., Wong-Foy, A. and Pines, A. (1999) Low-field magnetic resonance imaging with a high-T-c dc superconducting quantum interference device, *Appl. Phys. Lett.* **75**, 3695–3697.

218 Koch, R. H., Rozen, J. R., Sun, J. Z., Gallagher, W. J. (1993) Three SQUID gradiometer, *Appl. Phys. Lett.* **63**, 403–405.

219 Keene, M. N. and Satchell, J. S. (2002) Magnetic Gradiometer Incorporating Global Feedback, US Patent No. US 6,339,328.

220 Tilbrook, D.L., Foley, C.P., Leslie, K.E., Binks, R.A., Du, J., Lam, S.K.H., Bick, M., Gnanarajan, S., Clark, D. and Schmit, P. (2002) Design and development of a SQUID magnetic tensor gradiometer, *Appl. Supercond. Conf. Houston*, 4–9 Aug. 4EA01.

Appendix 1
Basic Properties of Superconductivity

Reinhold Kleiner and Dieter Koelle

A.1.1
Introductory Remarks

This appendix is intended to give a very brief introduction to some of the basic properties of superconductors used in the context of SQUIDs. For more details, we refer to some of the many excellent books on either superconductivity in general [1–6] or specifically on the Josephson effect [7,8]. Our introduction is divided into two subsections. The first focuses on the bulk properties of superconductors while the second deals with currents across interfaces weakly coupling massive superconducting electrodes.

A.1.2
Bulk Superconductors

The key quantity which we will start with is the wave function of the superconducting condensate. It has a well defined phase, being responsible for many of the properties of superconductors. While in a normal metal, charge carriers can be excited or scattered basically independent of each other, they become strongly correlated in the superconducting state existing below the critical temperature T_c. At least for the known superconductors, the charge carriers – electrons or holes – form pairs with charge $2e$, and all pairs are strongly correlated in momentum space having a common center of mass. This Cooper pairing allows one to assign the superconducting state a macroscopic wave function or order parameter $\Psi\ (\vec{r},t) = \Psi_0(\vec{r},t)\ \exp[i\varphi(\vec{r},t)]$ with Ψ_0^2 being proportional to the density of pairs in the condensate. The phase φ describes the center of mass motion of the Cooper pairs. With the possible exception of some materials, like the heavy fermion compounds or the recently discovered ruthenium oxides, the Cooper pairs form spin singlets. Thus, for symmetry reasons the relative momentum of the two electrons of the pair needs to be an even multiple of $\hbar$, for example 0 (s state) or $2\hbar$ (d state). The conventional superconductors like Pb or Nb are in the spin singlet s state, and the macroscopic wave function has an amplitude Ψ_0 which is more or less isotropic. In contrast, for high-temperature superconductors there is overwhelming evidence that the $d_{x^2-y^2}$ state prevails, with

possible admixtures of subdominant components. Ψ_0 is maximum along the Cu-O bonds of the CuO_2 layers forming the basic superconducting units of these materials and has nodes along the diagonal. Upon a 90° rotation, the wave function changes sign, or, in other words, the phase φ jumps by π when passing a node of Ψ_0. Fig. A.1.1 shows the isotropic *s* wave order parameter in comparison to the $d_{x^2-y^2}$ state.

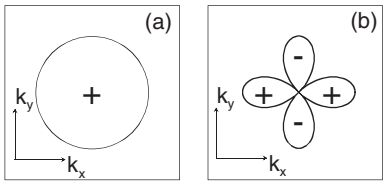

Fig. A.1.1 Superconducting order parameter in momentum space. (a) *s* wave order parameter; (b) $d_{x^2-y^2}$ wave order parameter. The *s* wave order parameter is essentially isotropic. It has the same phase for all directions. The $d_{x^2-y^2}$ wave order parameter is maximum along k_x and k_y, corresponding to current flow along the CuO_2 bonds in high-T_c superconductors. It changes sign upon a 90° rotation and has nodes along the diagonals.

The simplest excitation in a superconductor is to add an electron or hole which is not paired. It requires at least an energy Δ to have this quasiparticle, and an energy of 2Δ is required to break a Cooper pair. It can be shown that Δ is proportional to Ψ_0. Thus, for an *s* wave superconductor there is a well defined gap in the density of states for energies below Δ. At nonzero temperatures quasiparticles are thermally excited. For temperatures well below T_c, their number is exponentially small and the density of Cooper pairs is almost independent of temperature. When approaching T_c, the density of quasiparticles increases and both the Cooper pair density and Δ go to zero. For a *d* wave superconductor, quasiparticle states with wave vectors along the nodes of Ψ can be created without additional cost of energy. Thus there are quasiparticle states at any energy, although the density of states is low below the maximum value $\Delta_{max} \propto \Psi_{0,max}$. Δ also scales with T_c. For many conventional superconductors the ratio $2\Delta/k_BT_c$ is near 3.5, the value obtained from BCS theory [9]. For high-temperature superconductors, one finds values of $2\Delta_{max}/k_BT_c$ between 5 and 8.

What are the consequences of the macroscopic wave function having a well defined phase? The first consequence is the existence of persistent supercurrents, for example, flowing around a superconducting ring. Once the Cooper pair condensate is set into motion all pairs move with the same center of mass velocity and cannot lose their energy one by one, due to inelastic scattering processes. The condensate could, in principle, be slowed down as a whole. However, sufficiently below T_c the energy required is extremely large making this process completely unlikely. The second consequence is the existence of magnetic flux quantization. Let us consider a superconductor in an external magnetic field with flux density $\vec{B}$. When moving once around a closed path inside the superconductor, the phase can only vary by multiples of 2π to guarantee a unique wave function. Writing the phase gradient as

$$\vec{\nabla}\varphi = \frac{1}{\hbar}(m_p\vec{v}_p + q_p\vec{A}), \tag{A.1.1}$$

with the Cooper pair mass m_p, density n_p, velocity v_p, charge q_p and vector potential $\vec{A}$, and replacing the kinetic term $m_p\vec{v}_p$ by $(m_p/q_p n_p)\vec{j}_s$ using the supercurrent density $\vec{j}_s = q_p n_p \vec{v}_p$ we find

$$2\pi n = \oint \vec{\nabla}\varphi \, d\vec{l} = \frac{m_p}{q_p n_p \hbar} \oint \vec{j}_s \, d\vec{l} + \frac{q_p}{\hbar} \oint \vec{A} d\vec{l}; \qquad n = 0, \pm 1, \pm 2, \ldots \tag{A.1.2}$$

The second integral on the right-hand side is equivalent to the magnetic flux Φ through the closed contour. With the flux quantum $\Phi_0 = h/q_p = h/2e$ and the London penetration depth $\lambda_L = (\mu_0 q_p^2 n_p/m_p)^{-1/2}$, with the permeability μ_0 we finally get the fluxoid quantization condition

$$n\Phi_0 = \mu_0 \lambda_L^2 \oint \vec{j}_s d\vec{l} + \Phi; \qquad n = 0, \pm 1, \pm 2, \ldots \tag{A.1.3}$$

Often, the supercurrent density along the contour is exponentially small, in which case (A.1.3) reduces to the flux quantization condition $\Phi = n\Phi_0$.

Let us consider a massive superconductor where Ψ is nonzero everywhere inside the integration path. Here, (A.1.3) must hold even for a path with infinitely small radius in which case both terms on the right-hand side approach zero. Consequently, we have $n = 0$ and $\mu_0 \lambda_L^2 \oint \vec{j}_s d\vec{l} = -\Phi = -\int \vec{B} d\vec{f}$. The latter condition can also be written as $\vec{B} = -\mu_0 \lambda_L^2 curl \vec{j}_s$. The latter condition can be combined with Maxwell's equation $curl\, \vec{B} = -\mu_0 \vec{j}$ resulting in $\Delta\vec{B} = \vec{B}/\lambda_L^2$ with the Laplace operator Δ. This equation shows that magnetic fields will exponentially decrease inside an homogeneous superconductor on a length scale λ_L. Since the London penetration depth λ_L is proportional to $n_p^{-1/2}$ it diverges at T_c. Typical low-temperature values are 100–300 nm.

Nonzero values of n can be obtained if Ψ is zero somewhere inside the integration path. The simplest way to achieve this is a superconducting ring. Here n can take many values with an upper limit given by the maximum supercurrent density j_c which can flow around the ring. The case $n = \pm 1$ is realized in the mixed state of type II superconductors where the flux penetrates the superconductor in the form of Abrikosov vortices (see Fig. A.1.2). Here, circulating currents flow around an axis

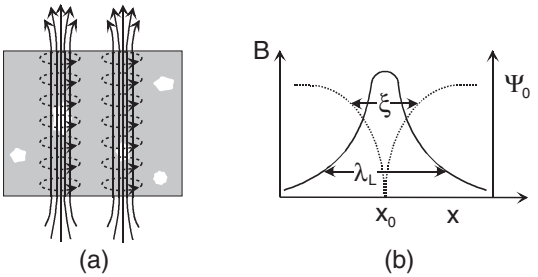

Fig. A.1.2 (a) Schematic drawing of Abrikosov vortices penetrating a type II superconductor. Solid lines symbolize magnetic field lines and dashed lines, circulating currents; (b) shows schematically the variation of Ψ_0 (dashed curve) and B (solid curve) when passing a vortex core.

where Ψ approaches zero on a length scale ξ (Ginzburg–Landau coherence length). The magnetic field inside the vortex, which is maximum on the axis, again decreases on a length scale λ_L. Like λ_L, ξ also diverges when approaching T_c, and the Ginzburg Landau parameter $\kappa = \lambda_L/\xi$ is almost temperature independent.

Under which conditions do Abrikosov vortices form in a superconductor? In type I superconductors where κ is smaller than $1/\sqrt{2}$ the formation of a vortex costs energy in any field and only the case $n = 0$ is realized. The reason is that superconductivity needs to be suppressed in a relatively large volume $\propto \xi^2$ while the magnetic field remains confined in a relatively small volume $\propto \lambda_L^2$. This energy balance becomes opposite in type II superconductors (for example, $YBa_2Cu_3O_7$ belongs to this class) where we have $\kappa > 1/\sqrt{2}$. While for external fields below the lower critical field $B_{c1} \approx (\Phi_0/4\pi\lambda_L^2)\ln\kappa$ (for $\kappa >> 1$) again the vortex-free Meissner state is thermodynamically stable, Abrikosov vortices appear in the fields between B_{c1} and the upper critical field $B_{c2} = \Phi_0/2\pi\xi^2$ above which the system returns to the normal conducting state. If the superconductor has no, or only a few, defects the Abrikosov vortices arrange themselves in the form of a triangular lattice. In most practical cases, however, a large number of defects is present, pinning a vortex and disturbing the triangular lattice. A pinning center essentially is a region of suitable size where superconductivity is weakened or absent. If the core of the vortex is located in this region, the suppression of Ψ costs less energy and thus the vortex tends to remain at the pinning site.

The consideration of vortices presented above assumes that the superconducting state is more or less isotropic. This assumption holds for many conventional superconductors. In the case of high-T_c materials, superconductivity is mostly restricted to the CuO_2 planes while the "barrier" layers in between are only weakly superconducting or even insulating. Thus Ψ not only strongly varies in k-space but is also spatially modulated, leading, for example, to a quite complex behavior of the vortices. For details, we refer the reader to the literature [10]. Here, we only mention that for magnetic fields oriented perpendicular to the layers, circulating currents flow in the CuO_2 planes almost exclusively, and the flux line consists of a stack of almost two-dimensional pancake vortices. In fields parallel to the layers, part of the circulating currents flows as a Josephson current across the layers, as discussed in the next section. In this case, flux penetrates the material in the form of Josephson vortices, being much larger in size than pancake or Abrikosov vortices.

We finish this section with some remarks on the maximum supercurrent that can flow in a superconductor. We first consider a superconducting wire thin enough for radial variations of Ψ to be neglected. In that case it turns out that, when the supercurrent flowing along the wire increases, the number of Cooper pairs decreases in proportion to their kinetic energy. The current density j_s along the wire can thus be written as $j_s = 2en_pv_p = 2en_{p0}(1 - m_pv_p^2/2\,|\,\alpha_{cp}\,|\,)v_p$. Here, n_{p0} denotes the density of Cooper pairs in the absence of a supercurrent, m_p is the Cooper pair mass, and α_{cp} is the condensation energy per Cooper pair, as given by the Ginzburg–Landau theory describing the superconducting state near T_c. The expression has a maximum at $v_p = (2\,|\,\alpha_{cp}\,|\,/3m_p)^2$ thus defining the depairing critical

current density $j_{c,p} = 2en_{p0}\frac{2}{3}\sqrt{\frac{2|\alpha_{cp}|}{3m_p}}$. The parameter α_{cp} is related to the thermodynamical critical field B_c via $B_c = \sqrt{n_{p0}|\alpha_{cp}|\mu_0}$. With B_c and the London penetration depth, $j_{c,p}$ can be expressed as $\left(\frac{2}{3}\right)^{3/2}\frac{B_c}{\mu_0\lambda_L}$, which has values of the order of 10^8 A/cm^2 for $YBa_2Cu_3O_7$ and also Nb. When the dimensions of the superconductor (a wire or a thin-film structure) are large compared to λ_L, the maximum supercurrent is actually much less than the above value. For example, consider a type II superconductor in the vortex state. The transport current imposes a Lorentz force on the vortices. Consequently, above some threshold value the vortices become depinned and a nonzero voltage appears as soon as the vortices start to move. The critical current density is thus essentially limited by pinning forces. Even in zero magnetic field, pairs of vortices with opposite polarity can be created by self-field effects also resulting in a critical current density well below the depairing current density. Another way to decrease the critical current density is to introduce a barrier region into the superconducting structure resulting in the Josephson effects discussed in the next section. To conclude this section, we give in Table A.1.1, the critical temperature, the London penetration depth, the Ginzburg–Landau coherence length, critical fields and the energy gap for some superconductors of interest.

Tab. A.1.1 The critical temperature, London penetration depth, Ginzburg–Landau coherence length, critical fields and the energy gap of some superconductors.

Material	T_c [K]	λ_L [nm]	ξ [nm]	B_{c1} [T]	B_{c2} [T]	B_c [T]	2Δ [meV]
Nb	9.25	39	38	0.2	0.27	0.21	3.0
Pb	7.20	37	83	–	–	0.08	2.7
Al	1.18	16	1600	–	–	0.01	0.34
In	3.41	21	440	–	–	0.028	1.0
NbN	17.3	300	4		47	0.19[d]	6.4
MgB_2	40	85–180	3.7–12[ab] 1.6–3.6[c]	0.027– 0.048	2–24$^{\perp}$ 14–39$^{\parallel}$		1.8–7.5
$YBa_2Cu_3O_7$	92	140$^{\perp}$ 700$^{\parallel}$	1.5[ab] ~0.3[c]	0.085$^{\perp}$ 0.025$^{\parallel}$	130$^{\perp}$	1.1[d]	50–60
$Bi_2Sr_2CaCu_2O_8$	90	200–300$^{\perp}$ >5×10^4 $^{\parallel}$	~2[ab] <0.1[c]	0.1$^{\perp}$ 6×10^{-4} $^{\parallel}$	33$^{\perp}$ 1600$^{\parallel}$	0.39[d]	80–90

$\perp$ For magnetic fields perpendicular to the layers (a–b plane)
$\parallel$ For magnetic fields parallel to the layers
ab in a–b plane
c along c-axis
d from $B_c = \frac{\Phi_0}{2\sqrt{2}\pi\lambda_L\xi}$

A.1.3
Weakly Coupled Superconductors

We consider a one-dimensional geometry where the current flows through a barrier region connecting two superconductors. The barrier can, for example, be an insulating layer allowing electrons to tunnel from one side to the other (see Fig. A.1.3). The barrier can also be a normal conducting one in which case the superconducting transport is associated with Andreev reflection processes [11]. Although quite different from a microscopic point of view, all geometries have in common that the supercurrent across the barrier (the Josephson current) has a simple sinusoidal dependence on the difference of the phase $\varphi(z)$ of the wave functions of the two superconductors near the barrier. We assume the current to flow in the z direction. From (A.1.1) we get for the z component of the Cooper pair velocity

$$v_{p,z} = \frac{1}{m_p}\left(\hbar\frac{d\varphi}{dz} - q_p A_z\right) \text{ or} \tag{A.1.4a}$$

$$j_z = \frac{q_p n_p \hbar}{m_p}\left(\frac{d\varphi}{dz} - \frac{2\pi}{\Phi_0}A_z\right) = \frac{q_p n_p \hbar}{m_p}\cdot\frac{d\delta}{dz}\ , \tag{A.1.4b}$$

where we have defined the quantity $\delta(z) = \varphi(z) - \frac{2\pi}{\Phi_0}\int_0^z A_z dz$, where A_z denotes the z component of the vector potential [see (A.1.1)].

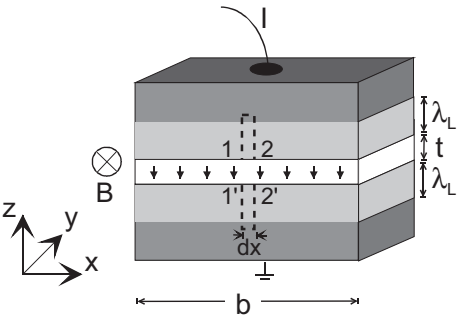

Fig. A.1.3 Geometry of a Josephson junction in an external magnetic field *B* directed along *y*. The bias current *I* is applied along *z*. The junction length along *x* is denoted *b*. The magnetic field penetrates into the superconducting electrodes by a distance λ_L. The thickness of the barrier layer is *t*. The dashed contour is an integration path used to determine the dependence of the phase difference δ on *B*.

Note that the supercurrent density can depend on z via the Cooper pair density n_p and the phase difference $\delta(z)$. Also, in the one-dimensional situation, the current conservation requires j_s to be constant in space. Thus changes in n_p have to be compensated by changes in $d\delta(z)/dz$. At the barrier layer the Cooper pair density is strongly suppressed. Thus $d\delta(z)/dz$ is large here, leading to a step-like increase of $\delta(z)$ which, inside the superconductors, is almost constant. Thus the supercurrent j_s across the barrier essentially becomes a function of $\delta \equiv \varphi_2 - \varphi_1 - \frac{2\pi}{\Phi_0}\int_1^2 A_z dz$, where '1' and '2' are positions near both sides of the barrier. This δ is often called the "gauge invariant phase difference". Since it is defined only modulo 2π, $j_s(\delta)$ can be written as a Fourier series in δ consisting of sine and cosine terms. Only the sine

terms fulfil time reversal symmetry, $j_s(\delta) = -j_s(-\delta)$, and thus the supercurrent density can be written as

$$j_s = \sum_{k=1}^{\infty} j_{ck} \sin(k\delta). \tag{A.1.5}$$

Equation (A.1.5) is the most general form of the supercurrent across the barrier fulfilling the fundamental symmetry principles, the gauge invariance and time reversal symmetry. For almost all junction types used in practice the Fourier series (A.1.5) converges rapidly and only the first term needs to be considered. We then have

$$j_s = j_0 \sin\delta \tag{A.1.6}$$

which is the first Josephson relation. The time evolution of δ is described by the second Josephson relation,

$$\hbar \frac{d\delta}{dt} = 2eU, \tag{A.1.7}$$

where U is the time dependent voltage drop across the Josephson junction. The equation can easily be obtained by taking the time derivative of δ, $\dot{\delta} = \dot{\varphi}_2 - \dot{\varphi}_1 - \frac{2\pi}{\Phi_0}\int_1^2 \dot{A}_z dz$. With $\psi \propto \exp(iEt/\hbar)$ the difference $\dot{\varphi}_2 - \dot{\varphi}_1$ is given by the differences in energy of the two superconductors, $\dot{\varphi}_2 - \dot{\varphi}_1 = (E_2 - E_1)/\hbar$, while the time derivative of the vector potential yields induced voltages, $-\frac{2\pi}{\Phi_0}\int_1^2 \dot{A}_z dz = 2eU_{ind}/\hbar$. The right-hand side of (A.1.7) is thus given by the total potential difference $2eU$ across the barrier. Note that if U is constant, equations (A.1.6) and (A.1.7) describe oscillations of the Josephson current with frequency $f = 2eU/\hbar$ (483.6 MHz/μV).

For $U \neq 0$, currents across the barrier do not only flow as supercurrents. Also quasiparticle currents j_q as well as displacement currents have to be taken into account. In general, j_q depends on voltage and frequency and needs to be determined microscopically. For example, for a Josephson tunnel junction with an insulating barrier between *s* wave superconductors, at zero temperature the quasiparticle current is zero for voltages below $2\Delta/e$ and increases linearly above $2\Delta/e$. The slope of the linear current–voltage characteristic corresponds to the normal resistance R_n. For this type of junction the supercurrent amplitude j_0 develops a singularity at voltages $2\Delta/e$ and there is also an interference term between the quasiparticle current and the supercurrent. It thus seems that many Josephson junctions require a complex description of their dynamics. However, in almost all cases being relevant for SQUIDs, it is sufficient to approximate the quasiparticle current by a linear relation, as discussed in Section 2.1. In the case of, for example, Nb SQUIDs, the Josephson tunnel junctions used are shunted by a normal resistor leading to a linear quasiparticle current with resistance R. Also in the case of YBCO grain boundary junctions, experiments show that the quasiparticle current indeed behaves in a linear way. The

current through the junction is thus simply given as the sum of supercurrent, quasiparticle current and displacement current,

$$I = I_0 \sin\delta + \frac{U}{R} + C\dot{U}. \tag{A.1.8}$$

This equation forms the basis of the Resistively Shunted Junction Model (see Section 2.1).

We next address the effect of the finite size of a Josephson junction. The basic effect is that, in the presence of magnetic fields, the phase difference δ will vary along the barrier layer. We consider the geometry shown in Figure A.1.3 where an external field is applied along y and a transport current is injected into the junction along z. The junction length along x is b. We consider the width of the junction along y to be small, such that δ is constant along y. We integrate the gradient of the phase φ inside the superconducting electrodes (Equation (A.1.1)) along the dashed path in Figure A.1.3. Integration from 2 to 1 gives

$$\varphi(1) - \varphi(2) = \frac{2\pi}{\Phi_0}\mu_0\lambda_L^2 \int_2^1 \vec{j}_s d\vec{l} + \frac{2\pi}{\Phi_0}\int_2^1 \vec{A} d\vec{l}. \tag{A.1.9a}$$

Integration from 1′ to 2′ yields

$$\varphi(2') - \varphi(1') = \frac{2\pi}{\Phi_0}\mu_0\lambda_L^2 \int_{1'}^{2'} \vec{j}_s d\vec{l} + \frac{2\pi}{\Phi_0}\int_{1'}^{2'} \vec{A} d\vec{l} \tag{A.1.9b}$$

Adding (A.1.9a) and (A.1.9b) and further adding the term $\frac{2\pi}{\Phi_0}\left[\int_{2'}^{2} \vec{A} d\vec{l} + \int_{1}^{1'} \vec{A} d\vec{l}\right]$ to both sides of the equation, yields

$$\varphi(2') - \varphi(2) - \frac{2\pi}{\Phi_0}\int_2^{2'} \vec{A} d\vec{l} - \left(\varphi(1') - \varphi(1) - \frac{2\pi}{\Phi_0}\int_1^{1'} \vec{A} d\vec{l}\right) = \frac{2\pi}{\Phi_0}\oint \vec{A} d\vec{l}$$
$$+ \frac{2\pi}{\Phi_0}\mu_0\lambda^2\left(\int_2^1 \vec{j} d\vec{l} + \int_{1'}^{2'} \vec{j} d\vec{l}\right). \tag{A.1.10}$$

The left-hand side of the equation can be written as $\delta(x+dx)-\delta(x)$. The integral over the vector potential is equal to the flux through the integration path yielding $Bt_{eff}dx$, with $t_{eff} \approx 2\lambda_L$, if the thickness of the superconducting electrodes is much larger than λ_L and the electrodes are in the Meissner state. In that limit the integrals over the current densities are also exponentially small and can be neglected. Equation (A.1.10) then reduces to

$$\frac{d\delta}{dx} = \frac{2\pi}{\Phi_0} B t_{eff}. \tag{A.1.11}$$

Combining (A.1.11) with Maxwell's relation $curl\vec{B} = \mu_0 \vec{j}$ yields

$$\frac{d^2\delta}{dx^2} = \frac{1}{\lambda_J^2} \cdot \frac{j_z}{j_0}, \tag{A.1.12}$$

with the Josephson length $\lambda_J = \sqrt{\Phi_0/2\pi\mu_0\lambda_L j_0}$ and the current j_z across the Josephson junction, for example, described by (A.1.8). The Josephson length λ_J plays a similar role as the London penetration depth for massive superconductors, however, it is typically of the order of microns. In particular, the size of Josephson vortices is about λ_J. If the Josephson junction is smaller than λ_J contributions of circulating currents to B can be neglected and (A.1.11) can be integrated, yielding a supercurrent density varying sinusoidally along x. If the critical current density j_0 is homogeneous, integration of the Josephson current over the junction area results in the maximum supercurrent across the junction, given by the Fraunhofer pattern

$$I_0(B) = I_0(0) \cdot \left|\sin(\pi B/B_0)/(\pi B/B_0)\right|, \text{ with } B_0 = \Phi_0/(t_{eff}\, b). \tag{A.1.13}$$

We finally consider the dc SQUID configuration of Fig. A.1.4 in order to introduce the kinetic inductance which is important for both dc and rf SQUIDs. Assuming that the size of the Josephson junction is much smaller than the size of the SQUID loop, an integration of the gradient of the phase φ along the dashed contour in Figure A.1.4 gives

$$\delta_2 - \delta_1 = \frac{2\pi}{\Phi_0}\left(\Phi + \mu_0\lambda_L^2\left(\int_2^1 \vec{j}_s d\vec{l} + \int_{1'}^{2'} \vec{j}_s d\vec{l}\right)\right) = \frac{2\pi}{\Phi_0}\Phi_T \tag{A.1.14}$$

in complete analogy to the derivation of (A.1.10). Φ_T is the total flux in the SQUID. The corresponding equation for an rf SQUID configuration can be obtained from (A.1.14) by setting $\delta_2 = \delta$ and $\delta_1 = 0$. The flux Φ through the SQUID loop is given by the sum of the applied flux $\Phi_a = BA_{eff}$ and the induced flux $L_g J$, with the geometric inductance L_g and the circulating current J. A_{eff} denotes the effective area of the SQUID. The integrals over current densities are usually small, however, they may contribute if the film thickness is comparable to λ_L and the width of the patterned structures is small. Since the sum of the two integrals provide a full integration of

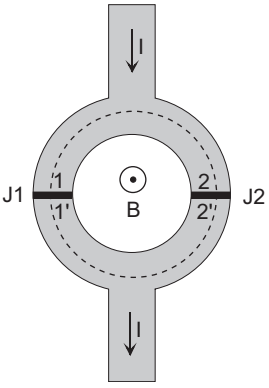

Fig. A.1.4 Configuration of a dc SQUID biased with a current I. The Josephson junctions are denoted J1 and J2. The dashed contour is an integration path used to obtain (A.1.14).

the supercurrent density around the SQUID loop they can be written as L_kJ, with the kinetic inductance L_k. Thus, the total flux can be written as

$$\Phi_T = BA_{eff} + LJ = \Phi_a + LJ, \tag{A.1.15}$$

with the total inductance $L = L_g + L_{kin}$.

References

1 Parks, R. D. (1989) *Superconductivity*. New York: Dekker.
2 de Gennes, P.G. (1989) *Superconductivity of Metals and Alloys*. Redwood City: Addison-Wesley.
3 Tinkham, M. (1996) *Introduction to superconductivity*. New York: McGraw-Hill.
4 Waldram, J. R. (1996) *Superconductivity of Metals and Cuprates*. London: IOP Publishing Ltd.
5 Ketterson, J. B., Song, S. N. (1999) *Superconductivity*. Cambridge: Cambridge University Press.
6 Orlando, T. P., Delin, K. A. (1991) *Foundations of Applied Superconductivity*. Reading (MA): Addison-Wesley Publishing Company, Inc.
7 Barone, A., Paterno, G. (1982) *Physics and Applications of the Josephson Effect*. New York: John Wiley & Sons.
8 Likharev, K. K. (1986) *Dynamics of Josephson Junctions and Circuits*. Philadelphia: Gordon and Breach Science Publishers.
9 Bardeen, J., Cooper, L. N., Shrieffer, J. R. (1957) Theory of superconductivity, *Phys. Rev.* **108**, 1175–1204.
10 Blatter, G., Feigel'man, M. V., Geshkenbein, V. B., Larkin, A. I., Vinokur, V. M. (1994) Vortices in high temperature superconductors, *Rev. Mod. Phys.* **66**, 1125–1388.
11 Pannetier, B., Courtois, H. (2000) Andreev reflection and proximity effect, *J. Low Temp. Phys.* **118**, 599–615.

Appendix 2

ac	alternating current
ADC	analog-to-digital converter
APF	additional positive feedback
BCF	bias current feedback
CFHX	counter-flow heat exchanger
CPR	current phase relation
DAC	digital-to-analog converter
dc	direct current
DLC	diamond-like carbon (thin-film etching mask of)
DROS	double relaxation oscillation SQUID
DSP	digital signal processor
EMI	electromagnetic interference
FA	field-applied
FEA	finite element analysis
FET	field-effect transistor
FLL	flux-locked loop
FR	field-removed
GBJ	grain boundary junction
GM	Gifford–McMahon
HTS	high-temperature superconductor (ing)
HX	heat exchangers
I	insulator
ISJ	intrinsically shunted junction
JT	Joule–Thomson
LAO	$LaAlO_3$
LSB	least-significant bit
LTS	low-temperature superconductor (ing)
MCG	magnetocardiography
MEG	magnetoencephalography
MLI	superinsulation, or multilayer insulation
MRI	magnetic resonance imaging
MTTF	mean-time-to-failure
MUSIC	multiple signal classification

N	normal conductor
NDE	nondestructive evaluation (of materials and structures)
NDT	non destructive testing
PBCO	$PrBa_2Cu_3O_7$
PECVD	plasma-enhanced chemical vapor deposition
$PI^{3/2}$ integrator	integrator with a gain slope of –30 dB/decade
PLD	pulsed laser deposition
PMMA	polymethylmethacrylate
RCSJ	resistively and capacitively shunted junction
rf	radio frequency
RIE	reactive ion etching
rms	root-mean-square
ROS	relaxation oscillation SQUID
RRR	residual resistivity ratio
RSFQ	rapid single flux quantum
RSJ	resistively shunted junction
RSJN	nonlinear resistive junction
RTS	random telegraph signal
S	superconductor
SAC	self-aligned contact
SHAD	second harmonic detection
SNAP	selective niobium anodization process
SNEP	selective niobium etch process
SNEAP	selective niobium etch and anodization process
SNIP	selective niobium insulation process
SNR	signal-to-noise ratio
SQUID	superconducting quantum interference device
SSP	signal space projection
STO	$SrTiO_3$
TEM	transient electromagnetic (geomagnetic exploration method)
TJM	tunnel junction microscopic
UHF	ultra-high frequency
W	working point
YBCO	$YBa_2Cu_3O_7$
YSZ	Yttria-stabilized zirconia
ZBCP	zero-bias conductance peak
ZES	zero energy state
ZFC	zero-field cooled

Constants

$e = 1.6022 \times 10^{-19}$ C	electron charge
$h = 6.6261 \times 10^{-34}$ Js	Planck constant
$\hbar = h/2\pi = 1.0546 \times 10^{-34}$ Js	Planck constant
$k_B = 1.3807 \times 10^{-23}$ J/K	Boltzmann constant
$\varepsilon_0 = 8.8542 \times 10^{-12}$ As/Vm	permittivity of vacuum
ε_r	relative permittivity
$\Phi_0 \equiv h/2e = 2.0678 \times 10^{-15}$ Vs	flux quantum
$\mu_0 = 4\pi \times 10^{-7}$ Vs/Am	permeability of vacuum

General

$\vec{A}$	vector potential
$\vec{B}$	magnetic flux density
B_0	cooling field
f	frequency
F_d	external driving force
$\vec{H}$	magnetic field
i	imaginary unit
m	mass
$\vec{r}$	spatial coordinate
t	time
T	temperature
Φ	magnetic flux
ω	angular frequency
ξ	friction coefficient

Superconductors General

B_T	threshold field for vortex entry
$D(U)$	distribution of activation energies for vortex motion
$H_c = B_c/\mu_0$	thermodynamic critical field of superconductor
$H_{c1} = B_{c1}/\mu_0$	lower critical field of type II superconductor
$H_{c2} = B_{c2}/\mu_0$	upper critical field of type II superconductor
I_s	supercurrent
j_c	maximum supercurrent density
$j_{c,p}$	depairing critical current density
j_s	supercurrent density
m_p	mass of Cooper pairs
n_p	density of Cooper pairs
n_{p0}	density of Cooper pairs in the absence of a supercurrent
q_p	charge of Cooper pairs
T_c	critical temperature of superconductor
v_p	velocity of Cooper pairs

α_{cp}	condensation energy per Cooper pair
Δ	energy gap for quasiparticle excitation
Δ_0	maximum value of energy gap
φ	phase of superconducting wave function
κ	Ginzburg–Landau parameter
λ_L	London penetration depth
ξ	Ginzburg–Landau coherence length
$\Psi(\vec{r}, t)$	superconducting wave function
Ψ_0	real amplitude of superconducting wave function

Josephson Junction

A_J	cross-section of Josephson junction
A_{Jp}	parasitic area of Josephson junction
C	total capacitance of Josephson junction
$c_J \equiv C/A_J$	capacitance per junction cross-section
C_{Jp}	parasitic capacitance of Josephson junction
$D(E)$	distribution of activation energies
$E_J \equiv I_0\Phi_0/2\pi$	Josephson coupling energy
$f_J \equiv \omega_J/2\pi = V/\Phi_0$	Josephson frequency
$f_\delta \equiv -\partial u_J/\partial\delta$	effective "force" (negative gradient) of tilted washboard potential
I	current through Josephson junction
$i \equiv I/I_0$	normalized current through Josephson junction
I_0	maximum supercurrent through Josephson junction
I_{ac}	amplitude of ac bias current
$i_{ac} \equiv I/I_{ac}$	normalized amplitude of ac bias current
I_d	displacement current
I_N	noise current
$i_N \equiv I_N/I_0$	normalized noise current
I_{qp}	quasiparticle tunneling current
I_r	return critical current of hysteretic Josephson junction
$i_r \equiv I/I_r$	normalized return critical current
$I_{th} \equiv \Gamma I_0 = 2\pi k_B T/\Phi_0$	thermal noise current
i_σ	probability flow
$j_0 \equiv I_0/A_J$	maximum supercurrent density across Josephson junction
L_{jp}	parasitic inductance of Josephson junction
R	shunt resistance of Josephson junction
R_n	normal resistance of Josephson tunnel junction
$S_I(f)$, $S_I(\omega)$	power spectral density of current noise
$S_i(f)$, $S_i(\omega)$	power spectral density of normalized current noise
t_{eff}	magnetic thickness of Josephson junction
U	time-dependent voltage across Josephson junction
$u \equiv U/I_0R$	normalized time-dependent voltage across Josephson junction
U_J	tilted washboard potential of Josephson junction

$u_J \equiv U_J/E_J$	normalized tilted washboard potential of Josephson junction
V	time-averaged voltage across Josephson junction
$v \equiv V/I_0R$	normalized time-averaged voltage across Josephson junction
$V_c \equiv I_0R$	characteristic voltage of Josephson junction
V_{gap}	gap voltage
V_n	voltage of n^{th} Shapiro step
V_r	return critical voltage of hysteretic Josephson junction
$\beta_c = \frac{2\pi}{\Phi_0} I_0 R^2 C$	Stewart–McCumber parameter
δ	gauge invariant phase difference across Josephson junction
ΔI_n	height of n^{th} Shapiro step
Δi_n	normalized height of n^{th} Shapiro step
$\Gamma \equiv k_B T/E_J = 2\pi k_B T/I_0\Phi_0$	noise parameter
$\lambda_J = \sqrt{\Phi_0/2\pi\mu_0 j_0}$	Josephson penetration depth
$\rho_J \equiv R \cdot A_J$	resistance times junction cross-section
ρ_n	normal resistivity of Josephson junction
$\sigma(t, \delta, u)$	probability density of finding system at point $[\delta,u]$ in phase space at the moment t.
$\tau \equiv t \cdot \omega_c$	normalized time
$\Omega_{ac} \equiv \omega_{ac}/\omega_c$	normalized frequency of ac bias current
ω_{ac}	frequency of ac bias current
$\omega_c \equiv 2\pi V_c/\Phi_0$	characteristic frequency of Josephson junction
$\omega_J \equiv 2\pi V/\Phi_0$	Josephson frequency
$\omega_p \equiv 2\pi I_0/C\Phi_0$	plasma frequency at zero bias current
$\omega_{p,i}$	plasma frequency of Josephson junction
$\omega_{RC} \equiv 1/RC$	frequency of RC circuit

SQUIDs General

a	outer dimension of pickup coil
$A_{eff} = \Phi_s/B_a$	effective area of SQUID
A_p	geometric area of the pickup coil
$A_{p,eff}$	effective area of the pickup coil
A_R	parasitic area of junction shunt resistor
A_{spoke}	parasitic area of coplanar microstripline "spokes" in "wagon-wheel" magnetometer
b	gradiometer baseline
b_{sl}	length of slit in SQUID ring
B_a	external field applied to the pickup coil
$B_N = \sqrt{S_\Phi}/A_{eff} = \sqrt{S_\Phi^{(p)}}/A_p$	magnetic field spectral resolution (field noise)

$B_\Phi = \partial B/\partial \Phi = 1/A_{\text{eff}}$	field sensitivity or field-flux conversion coefficient
C_{gp}	parasitic capacitance of groundplane over SQUID slit
C_{p}	parasitic capacitance across the SQUID inductance
C_{R}	parasitic capacitance of junction shunt resistor
C_{x}	capacitor of series $R_{\text{x}}C_{\text{x}}$ shunt across the input coil
C'_{strip}	input coil microstripline capacitance per unit length
d	inner side length or diameter of SQUID hole or pickup coil, wire diameter of wire-wound pickup coil
D	mean diameter of wire-wound pickup coil
F	coil factor for wire-wound pickup coils
f_{c}	$1/f$ noise corner frequency
f_{s}	microstripline resonant frequency of SQUID input coil
$f_{\text{op}} = 0.3 I_0 R/\Phi_0$	frequency corresponding to optimal SQUID operating point
f_{r}	SQUID *LC* resonant frequency
f_{w}	SQUID washer resonant frequency
$G_{1,\Phi}$	field gradient sensitivity, first-order gradiometer
$G_{2,\Phi}$	field gradient sensitivity, second-order gradiometer
h	dielectric insulator thickness
J	circulating current
$j = J/I_0$	normalized circulating current
J_s	current circulating in flux transformer
k_{i}	input coil coupling constant
ℓ	length of input coil microstripline, length of wire-wound pickup coil
ℓ_{eff}	effective length of input coil
L	inductance of the SQUID ring
$L_F = 2\pi k_{\text{B}} T/\Phi_0 I_0$	fluctuation threshold inductance
L_{g}	geometric inductance
L_{h}	inductance of SQUID ring hole
L_{i}	input coil inductance
L_{leads}	inductance of twisted pair leads
L_{loop}	inductance of a wire loop
L_{sl}	inductance of slit in SQUID ring
L_{tot}	total inductance of SQUID ring
L'_{strip}	input coil microstripline inductance per unit length
M_{i}	mutual inductance between SQUID loop and input coil
N	number of turns in wire-wound pickup coil
N_{i}	number of turns in input coil
L_{cop}	inductance of coplanar microstripline
L_{dc}	effective SQUID inductance including screening effect of the input coil
$L_{\text{i,eff}}$	effective input coil inductance including screening effect of the SQUID loop
L_{p}	inductance of pickup coil

L_{spoke}	parasitic inductance of coplanar microstripline "spokes" in "wagon-wheel" magnetometer
L_{kin}	kinetic inductance
p	pitch of wire-wound pickup coil
R_{x}	damping resistor of series $R_{\mathrm{x}}C_{\mathrm{x}}$ shunt across the input coil
s	input circuit screening factor
s_{c}	spacing between a pair of coplanar microstriplines
s_{i}	spacing between turns of input coil
$s_{\mathrm{in}} = L_{\mathrm{i}} / (L_{\mathrm{i}} + L_{\mathrm{p}})$	input coil screening factor
$S_B = S_\Phi / A_{\mathrm{eff}}^2$	power spectral density of magnetic field noise
$S_B = B_{\mathrm{N}}^2$	power spectral density of field noise
$S_{\mathrm{G},1}$	power spectral density of first-order gradiometer flux noise
$S_{\mathrm{G},2}$	power spectral density of second-order gradiometer flux noise
S_I	power spectral density of current noise referred to SQUID input
S_Φ	power spectral density of flux noise
$S_\Phi^{(p)}$	power spectral density of flux noise referred to the pickup coil
S_r	power spectral density of radial vortex motion
S_T	power spectral density of temperature fluctuations
t	superconducting film thickness
t_{i}	film thickness of SQUID input coil
U_{SQUID}	SQUID potential
$u_{\mathrm{SQUID}} = U_{\mathrm{SQUID}}/E_{\mathrm{J}}$	normalized SQUID potential
w	superconducting film width
w_{c}	linewidth of coplanar microstripline
w_{i}	linewidth of input coil
w_{p}	linewidth of pickup coil
Z	microstripline impedance
Z_{L}	impedance of a microstripline termination
$\varepsilon = S_\Phi / 2L$	energy resolution
$\varepsilon_{\mathrm{c}} = S_\Phi / 2k_{\mathrm{i}}^2 L = S_I L_{\mathrm{i}} / 2$	coupled energy resolution (spectral noise energy in input coil)
$\varepsilon^{(\mathrm{p})}$	energy resolution referred to the pickup coil
Γ_{r}	reflection coefficient at the termination of a microstripline
Φ_{a}	applied flux
$\phi_{\mathrm{a}} = \Phi_{\mathrm{a}}/\Phi_0$	normalized applied flux
$\Phi_{\mathrm{N}} = \sqrt{S_\Phi}$	magnetic flux resolution (flux noise)
Φ_{s}	flux coupled into the SQUID by a pickup coil structure
Φ_{T}	total flux
$\lambda_{L,w}$	London penetration depth of SQUID washer
$\lambda_{L,i}$	London penetration depth of SQUID input coil
σ	probability density distribution

dc SQUID

C	average junction capacitance
$e = s_\phi / 2\Gamma\beta_L = \varepsilon \cdot I_0 R / 2\Phi_0 k_B T$	normalized energy resolution
I	current through SQUID
$i \equiv I/I_0$	normalized current through SQUID
I_0	average junction critical current
I_b	SQUID bias current
I_c	critical current of SQUID
$M_{dyn} = R_{dyn}/V_\Phi$	current sensitivity of SQUID at working point
R	average junction resistance
R_d	damping resistor (shunting the SQUID inductance)
R_{dyn}	dynamic resistance of SQUID at working point
S_V	power spectral density of voltage noise
$s_v = S_V \dfrac{2\pi}{I_0 R \Phi_0}$	normalized power spectral density of voltage noise
$s_\phi = s_v / v_\phi^2 = S_\Phi \cdot 2\pi I_0 R / \Phi_0^3$	normalized power spectral density of flux noise
U	time-dependent voltage across SQUID
$u \equiv U/I_0 R$	normalized time-dependent voltage across SQUID
V_{pp}	peak-to-peak modulation of V–Φ_a characteristic
V	time-averaged voltage across SQUID
$v \equiv V/I_0 R$	normalized time-averaged voltage across SQUID
V_b	SQUID bias voltage
$\partial V/\Phi_a$	SQUID transfer coefficient
V_Φ	SQUID transfer coefficient optimized with respect to bias current and flux
$v_\phi = V_\Phi \Phi_0 / I_0 R$	normalized transfer function
$\bar{X}$	temporal average of quantity X
$\alpha = L/4L_F$	normalized SQUID inductance
α_C, α_I, α_R	asymmetry in junction capacitance, critical current, or resistance
α_L	asymmetry in SQUID loop inductance
$\beta_L \equiv \dfrac{2LI_0}{\Phi_0}$	screening parameter of dc SQUID
$\delta_+ \equiv (\delta_1+\delta_2)/2$; $\delta_- \equiv (\delta_2-\delta_1)/2$	rotated coordinates for dc SQUID potential
δI, δV, $\delta\Phi_a$	small change in current, voltage, or applied flux
δV^*	in-phase critical current or resistance fluctuation
$\delta\Phi^*$	out-of-phase critical current or resistance fluctuation
Φ_b	SQUID bias flux
$\Phi_{lin} = V_{pp}/V_\Phi$	linear flux range
$\gamma = R/R_d$	damping parameter for shunted SQUID inductance

rf SQUID

C_M	matching capacitance
C_T	capacitance of tank circuit
I_{rf}	peak rf current in tank circuit
$i_{rf} = I_{rf} M 2\pi/\Phi_0$	normalized rf current in tank circuit
$J_m(x)$	Bessel functions of first kind of order m and variable x
$k = M/\sqrt{LL_T}$	coupling coefficient between SQUID loop and tank circuit
L_T	inductance of tank circuit
M	mutual inductance between SQUID loop and tank circuit
$Q = R_T/\omega_0 L_T$	quality factor of tank circuit (loaded)
Q_0	unloaded quality factor of tank circuit
R_T	tank circuit impedance at resonance frequency (parallel resistance)
T_{eff}	effective noise temperature of the tank circuit, transmission line and preamplifier lumped together
V_T	SQUID output voltage (peak rf voltage across tank circuit)
$v_T = V_T(k/\omega_{rf})\sqrt{L/L_T}2\pi/\Phi_0$	normalized SQUID output voltage
$\partial V_T/\partial \Phi_a$	transfer function of rf SQUID
$<X>$	statistical average of quantity X
Z	output impedance of rf SQUID
α	step tilting parameter
$\beta_{rf} \equiv \frac{2\pi L I_0}{\Phi_0} = \pi\beta_L$	screening parameter of rf SQUID
$\Phi_{a,rf}$	external applied rf flux
$\phi_{a,rf} = \Phi_{a,rf}/\Phi_0$	normalized applied rf flux
Φ_c	critical magnetic flux (for which a quantum transition takes place)
Φ_{EMI}	magnetic flux of electromagnetic interference
λ	wavelength
ρ	phase difference between rf bias current I_{rf} and SQUID output rf voltage V_T.
$\omega_0 = 1/\sqrt{L_T C_T}$	tank circuit resonant frequency
$\omega_{cut} = R/L$	SQUID cutoff frequency
$\omega_R = \omega_{rf}/\omega_{cut}$	reduced operating frequency
$\omega_{rf} = 2\pi f_{rf}$	frequency of rf bias current
$\xi = (\omega_{rf} - \omega_0)/\omega_0$	detuning of drive frequency from tank circuit resonant frequency

SQUID Electronics

f_1	unity-gain frequency of open feedback loop
$f_{1,\max} = 1/4\pi t_d$	maximum unity-gain frequency
f_2, f_2'	corner frequencies of two-pole integrator
f_{3dB}	FLL bandwidth
$f_{3dB,\max} = 0.18/t_d$	maximum FLL bandwidth
f_{APF}	cutoff frequency of APF circuit
f_b	bias reversal frequency
f_{clk}	clock frequency
f_{GBW}	gain-bandwidth product of feedback electronics
f_{mod}	modulation frequency
f_{peak}	frequency of peak in closed-loop frequency response
f_{RO}	relaxation oscillation frequency
G_{APF}	low-frequency small-signal voltage gain obtained with APF
$G_{electronics}$	feedback electronics gain
G_{FLL}	closed-loop gain of FLL
G_{OL}	total gain of open feedback loop
$G_{SQUID} = V_\Phi M_f/R_f$	SQUID gain
G_Φ	low-frequency small-signal flux gain in two-stage configuration
L_{amp}	input coil inductance of amplifier SQUID
L_{APF}	inductance of APF coil
L_{sh}	shunt inductance of ROS or DROS
I_{clk}	comparator clock current
I_f	feedback current
I_{in}	current in SQUID input coil
I_{out}	output current of voltage-biased SQUID
M_{amp}	mutual inductance between amplifier input coil and amplifier SQUID
M_{APF}	mutual inductance between APF coil and SQUID
M_f	mutual inductance between feedback coil and SQUID
R_{APF}	APF resistance
R_b	bias resistance
R_f	feedback resistance
R_{in}	real part of preamplifier input impedance
R_{sh}	shunt resistance of ROS or DROS
$S_{I,amp}$	preamplifier current noise density
$S_{V,amp}$	preamplifier voltage noise density
$S_{V,APF}$	power spectral density of equivalent APF noise source
$S_{\Phi,amp}$	preamplifier flux noise contribution
$S_{\Phi,FLL}$	flux noise density in FLL mode
t_d	equivalent loop delay
V_0^*, V_Φ^*	offset voltage and slope of straight-line fit to V–Φ_a characteristic
V_f	voltage across feedback resistor
V_{in}	preamplifier input voltage

V_{out}	output voltage
β_{APF}	APF feedback parameter
δI_{out}	small change in output current
δV_{out}	small change in output voltage
$\delta\Phi$	deviation of flux in SQUID from value at working point (flux error)
$\delta\Phi_{n,pp}$	peak-to-peak noise flux fed back into SQUID operated in FLL mode
$\delta\Phi_{pp}$	peak-to-peak value of $\delta\Phi$
Φ_{amp}	flux applied to amplifier SQUID
Φ_f	feedback flux
$\dot{\Phi}_f \equiv \left\lvert \partial\Phi_f/\partial t \right\rvert_{max}$	system slew rate
$\dot{\Phi}_{f,max}$	maximum system slew rate
Φ_{LSB}	LSB of digital SQUID referred to flux input
Φ_{nl}	nonlinear error flux
φ_{OL}	total phase of open feedback loop

SQUID Systems

A	low-frequency noise constant of proportionality corresponding to the noise measured with gradiometer with baseline b
$\boldsymbol{A}$	matrix constructed from matrix of rotation elements and sensor gains
a	sensor gain equal to the inverse of the field-to-flux conversion coefficient
$\boldsymbol{a}$	matrix of rotation
$\boldsymbol{a}(t_n)$	vector of noise space waveforms at time t_n
a_B	minimum allowed reference magnetometer gain devised not to increase balanced gradiometer white noise (equal to the inverse of the field-to-flux conversion coefficient)
A_E	area of an eddy-current source
a_k	sensor gain for component k, $k = 11, 12, 13, 22, 23$ (equal to the inverse of the field-to-flux conversion coefficient)
$\boldsymbol{a}_k(t_n)$	component k of the vector of noise space waveforms at time t_n
A_o	low-frequency noise constant of proportionality corresponding to the noise measured with gradiometer with baseline b_o
A_p	magnetometer coil area
a_r	sensor gain for reference magnetometers (equal to the inverse of the field-to-flux conversion coefficient)
$\boldsymbol{B}$, B	field at a general position
$\dot{B}$	magnetic field slew rate in T/s
$\boldsymbol{b}(t_n)$	vector of signal waveforms at time t_n
$\boldsymbol{b}$, b, $\boldsymbol{b}_1$, b_1, $\boldsymbol{b}_o$, b_o	first-order gradiometer baseline
$\boldsymbol{b}_2$, b_2, $\boldsymbol{b}_2'$, b_2'	second-order gradiometer baseline
$\boldsymbol{b}_3$, b_3, $\boldsymbol{b}_3'$, b_3'	third-order gradiometer baseline

$\boldsymbol{B}_i^t$	vector of magnetic field time samples for a component B_i
B_{low}	square-root of low-frequency noise density
B_{N}	square-root of total noise density
$\boldsymbol{B}_o$, B_o	field at the coordinate origin
B_{rms}	rms noise
$\boldsymbol{B}_T$, $\boldsymbol{B}_{T1}$, $\boldsymbol{B}_{T2}$	total field acting on a magnetometer coil
B_w	square-root of white noise density
$b\delta G$	gradiometer system white noise in 1 Hz bandwidth multiplied by the gradiometer baseline (includes SQUID and electronics noise, dewar noise, etc.)
$\boldsymbol{C}_B$, $C_B = \|\mathbf{C}_B\|$	field common-mode vector and its magnitude
$\boldsymbol{C}_{G1}$	first gradient common-mode vector
$\boldsymbol{C}_{G2}$	second gradient common-mode vector
$\boldsymbol{C}_o$, C_o	"as made" field common-mode vector and its magnitude
C_{p}	specific heat
C_R	required level of the field common-mode vector balance
C_S	field common-mode vector magnitude which would be induced by the eddy current object if it were superconducting
D_{mag}, D_{grd}	dynamic range of magnetometer or gradiometer
D_{grd}^C, D_{grd}^G	gradiometer dynamic range imposed by field common-mode vector or by the environmental gradients
E	electric field intensity inside the shield
E_0	intensity of the electric field
$\boldsymbol{E}_B$, $E_B = \|\boldsymbol{E}_B\|$	field eddy-current vector and its magnitude
$\boldsymbol{E}_{Gi}$	i^{th} gradient eddy-current vector
E_R	required level of the field eddy-current vector balance
f_E	characteristic frequency of an eddy-current source
f_{min}	minimum frequency of interest
f_o	onset of low-frequency noise measured with gradiometer with baseline b_o
f_{ob}	onset of low-frequency noise measured with gradiometer with baseline b
$g^{(0)}$	magnetometer (0^{th}-order gradiometer) output
$g^{(1)}$	first-order gradiometer output
$g^{(2)}$	second-order gradiometer output
$g^{(3)}$	third-order gradiometer output
$\boldsymbol{G}$, $\boldsymbol{G}^{(1)}$, G, $G^{(1)}$	first gradient tensor
$\boldsymbol{G}^{(2)}$, $G^{(2)}$	second gradient tensor
$\boldsymbol{G}^{(3)}$, $G^{(3)}$	third gradient tensor
G_{11}, G_{12}, G_{13}, G_{22}, G_{23}	first gradient tensor components
G_{111}, G_{112}, G_{113}, G_{122}, G_{123}, G_{222}, G_{223}	second gradient tensor components
$\boldsymbol{G}_E$	first gradient tensor corresponding to the environmental gradients

$\boldsymbol{G}_i^t$	vector of time samples of a component i of the first gradient tensor projection into the gradiometer baseline
$G(k)$	gradiometer spatial transfer function
$g_k^{(1)}$	output of a first-order gradiometer component k, k = 11, 12, 13, 22, 23
g_k^R	component k (k = 11, 12, 13, 22, 23) of the rotated first gradient tensor
$\boldsymbol{g}^m$	measured output of first gradient tensor
$\boldsymbol{g}^R$	output of all components of the rotated first gradient tensor
$\boldsymbol{G}_R$	rotated first gradient tensors of the environmental gradient
$\boldsymbol{I}$	identity matrix
I_{cm}	common-mode current
I_{dm}	differential-mode current
K	number of channels
k	slope of low-frequency noise amplitude vs frequency on log–log scale
k_s	spatial frequency
K_N	number of noise components
K_S	number of signal components
L_E	inductance of an eddy-current source
L_{mag}, L_{grd}	permitted magnetometer or gradiometer nonlinearity
$\boldsymbol{m}$	$K \times N$ matrix of measurements
M_E	mutual inductance between an eddy-current source and a magnetometer coil
$\boldsymbol{m}_{noise}(t_n)$	K-component vector of noise measurement at time t_n
M_{source}, M_{dip}, M_1, M_2, M_3	magnetic dipole moments
N	number of time samples
N_{ave}	number of averages
n_{loc}	exponent in the field decay law with distance for a local anomaly
n_{reg}	exponent in the field decay law with distance for a regional anomaly
P	pressure
$\boldsymbol{P}_\perp$	orthogonal projection operator
$\boldsymbol{P}_\parallel$	parallel projection operator
$\boldsymbol{p}$, $\boldsymbol{p}'$	coil orientation vector
q	exponent which determines relationship between the system white noise in 1 Hz bandwidth and electronics bit resolution: $\delta B = 2^q \partial B$, $\delta G = 2^q \partial G$
Q_{H1}	rejection of heat
Q_{H2}	associated heat
Q_L	heat of expansion
$\boldsymbol{r}$, r	distance from magnetometer or gradiometer to a source

r_b	distance normalized by three times the gradiometer baseline
R_{g}	effective volume (responsivity)
r_i	reference outputs, $i = 1, 2, \ldots$
$\boldsymbol{r}_{ref}$	vector of reference outputs
S	synthetic system output
$\boldsymbol{S}$	vector of time samples of the synthetic system outputs
S_{cube}	shielding factor for a cube
S_{cylinder}	shielding factor for a cylinder
S_{sphere}	shielding factor for a sphere
$\|S\|_{\min}^{adapt}$	signal vector norm determined by minimizing the system noise
$\|S\|_{\min}^{grad}$	signal vector norm determined by requiring that the system be a gradiometer
t_1, t_2, t_i, t_k, t_n	time instances (time samples)
T_{H}	environmental high temperature
T_{L}	environmental low temperature
$\boldsymbol{U}$	$K \times K_S$ matrix composed of signal column vectors
$\boldsymbol{u}_k(t_n)$	component k of the signal space waveforms at time t_n
$\boldsymbol{U}_k$	signal column vector, $k = 1, 2, \ldots K_S$
$\boldsymbol{V}$	matrix composed of noise column vectors
$\boldsymbol{V}_k$	K-component noise column vectors, $k = 1, 2, \ldots K_N$
$\boldsymbol{X}$	crosstalk matrix for first gradient tensor components
$\boldsymbol{\gamma}_1$	vector of five independent components of a first gradient tensor
$\boldsymbol{\gamma}_2$	vector of seven independent components of second gradient tensor
$\boldsymbol{\gamma}_E$	vector of independent components of the tensor G_E
Z_{S}	intrinsic impedance of a shield
Z_{W}	wave impedance of the incident energy
Z_{WB}	B-field component of the wave impedance
Z_{WE}	E-field component of the wave impedance
∂B, $b\partial G$	electronic bit resolution of magnetometer or gradiometer multiplied by baseline (in T)
ΔB	field change applied to either a magnetometer coil, or a field difference between two first-order gradiometer coils
δB	magnetometer system white noise in 1 Hz bandwidth (includes SQUID and electronics noise, dewar noise, etc.)
Δd	amplitude of translational vibrations
Δf	bandwidth of measurement
δ	penetration depth or skin effect
$\delta t^{(1)}$	maximum allowed time delay between channels determined by the requirement of negligible eddy-current term
$\delta t^{(2)}$	maximum allowed time delay between channels when the eddy-current term is balanced out using constant coefficients

$\delta\Phi_B$	flux resolution of magnetometer systems (contains SQUID system and electronics noise, dewar noise, or any other system noise)
$\delta\Phi_G$	flux resolution of gradiometer systems (contains SQUID system and electronics noise, dewar noise, or any other system noise)
$\delta\Phi_r$	flux resolution of reference magnetometers (contains SQUID system and electronics noise, dewar noise, or any other system noise)
$\Delta\kappa$	difference of the eddy-current coupling constants between two gradiometer coils
$\mu = (\partial T/\partial P)_H$	Joule–Thomson coefficient
$\dot{\Phi}^C_{grd}$, $\dot{\Phi}^G_{grd}$	gradiometer slew rates imposed by field common-mode vector or by environmental gradients, in Φ_o/s
$\dot{\Phi}_{mag}$, $\dot{\Phi}_{grd}$	magnetometer or gradiometer slew rates in Φ_o/s
φ_n	coefficient for a power-law nonlinearity of n^{th} order
η	hysteresis parameter
κ, κ_1, κ_2	eddy-current coupling constants
$\boldsymbol{\nu}(t_n)$	K-component vector of sensor noise at time t_n
θ	amplitude of rotational vibrations
$\omega_E = 2\pi f_E$	characteristic frequency of an eddy-current source
ξ	vector of subtraction coefficients
ξ_i	component i of the subtraction coefficient
Ψ	constant containing all orientation dependent parts of the dipole equation
ψ	environmental noise attenuation
ψ_{grd}	environmental noise attenuation required for gradiometer operation
ψ_{mag}	environmental noise attenuation required for magnetometer operation
ζ	strength of inequality for the reference magnetometer gain design

Index

g